AD NUMBER

AD827594

LIMITATION CHANGES

TO:

Approved for public release; distribution is unlimited.

FROM:

Distribution authorized to U.S. Gov't. agencies and their contractors; Critical Technology; DEC 1967. Other requests shall be referred to Air Force Materials Laboratory, NonMetallic Materials Division, Wright-Patterson AFB, OH 45433. This document contains export-controlled technical data.

AUTHORITY

afml ltr, 7 dec 1972

AFML-TR-66-310
PART II

INTEGRATED RESEARCH ON CARBON COMPOSITE MATERIALS

UNION CARBIDE CORPORATION
CARBON PRODUCTS DIVISION
-IN ASSOCIATION WITH-
CASE WESTERN RESERVE UNIVERSITY
BELL AEROSYSTEMS COMPANY, A TEXTRON COMPANY

TECHNICAL REPORT AFML-TR-66-310, PART II
DECEMBER 1967

AIR FORCE MATERIALS LABORATORY
AIR FORCE SYSTEMS COMMAND
WRIGHT-PATTERSON AIR FORCE BASE, OHIO

DISCLAIMER NOTICE

THIS DOCUMENT IS THE BEST QUALITY AVAILABLE.

COPY FURNISHED CONTAINED A SIGNIFICANT NUMBER OF PAGES WHICH DO NOT REPRODUCE LEGIBLY.

INTEGRATED RESEARCH ON CARBON COMPOSITE MATERIALS

Summary Technical Report
AFML-TR-66-310, Part II
Covering Period
June 1966 to June 1967

Union Carbide Corporation
Carbon Products Division
in Association with
Case Western Reserve University
Bell Aerosystems Company, a Textron Company

Union Carbide Corporation
Carbon Products Division
Parma Technical Center
Parma, Ohio 44130

December 1967

NOTICES

When Government drawings, specifications, or other data are used for any purpose other than in connection with a definitely related Government procurement operation, the United States Government thereby incurs no responsibility nor any obligation whatsoever; and the fact that the Government may have formulated, furnished, or in any way supplied the said drawings, specifications or other data, is not to be regarded by implication or otherwise as in any manner licensing the holder or any other person or corporation, or conveying any rights or permission to manufacture, use, or sell any patented invention that may in any way be related thereto.

This document is subject to special export controls and each transmittal to foreign Governments or foreign Nationals may be made only with prior approval of the Nonmetallic Metals Division, MAN, Air Force Materials Laboratory, Wright-Patterson Air Force Base, Ohio 45433.

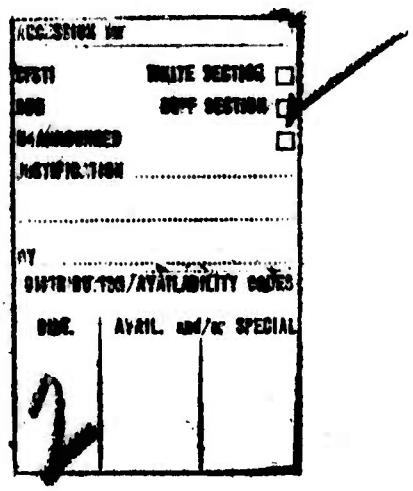

Copies of this report should not be returned unless return is required by security considerations, contractual obligations or notice on a specific document.

FOREWORD

The work reported herein was performed under the sponsorship of the Advanced Research Project Agency, Department of Defense, through a contract with the Air Force Materials Laboratory, MAN, Research and Technology Division, Wright-Patterson Air Force Base, Ohio, Contract No. AF 33(615)-3110, ARPA Order No. 719, Program Code No. 5950. Mr. H. S Schwartz, MAN, is the Air Force Program Manager.

The prime contractor is Union Carbide Corporation, Carbon Products Division; the subcontractors are Case Western Reserve University and Bell Aerosystems Company, a Textron Company. The program is administered by a committee composed of: J. C. Bowman (Chairman) and G. B. Spence (Program Supervisor) from Union Carbide; R. H. Thomas and L. A. Schmit (Program Supervisor) from Case Western Reserve University; and W. H. Dukes and F. M. Anthony (Program Supervisor) from Bell Aerosystems Company. Technical personnel participating in the program are indicated as authors of their portions of the report. The manuscript was released by the authors October 1967 for publication.

This report covers work performed from June 1966 to June 1967.

This technical report has been reviewed and is approved.

A. M. Lovelace
Director
Air Force Materials Laboratory

ABSTRACT

Results are reported on a continuing program directed toward developing a fabrication and structural design capability for graphite-fiber composites and toward extending the methods of structural synthesis to include material variables. Part of the current work is centered on the first phase of the design and fabrication of a ring- and stringer-stiffened tapered shell, representative of a subscale fuselage section. Other longer-range projects include work on analytical and experimental methods for obtaining reliable design data, on nonlinear analysis, and on synthesis studies. Studies on graphite-base refractory composites, begun before fiber composites were available, have been concluded; these include work on multiaxial stress failure criteria, statistical strength distributions for anisotropic materials, structural synthesis problems involving the selection of the best material, and nonlinear analysis of a rocket throat insert. Work on graphite-fiber, metal-matrix composites has been on processing studies and high temperature strength measurements of nickel-matrix composites. Graphite-fiber, resin-matrix composites have been fabricated with an epoxy (ERL 2256) matrix. The physical properties of the constituents have been determined; plates fabricated; and measurements made for membrane and bending stiffnesses, strengths, stress-strain behaviors, and thermal properties. Theoretical predictions of membrane and bending stiffnesses and tensile strengths correlated sufficiently well with experimental results for preliminary design purposes. Several common mechanical testing procedures for composite materials have been assessed; and a nondestructive plate buckling test apparatus and a new NOL ring test device have been built and applied. Structural element tests include angle bend and crippling tests on composite stringers as well as crippling and acoustic fatigue tests on composite panels. Several micromechanics and design data prediction investigations are reported. An elasto-plastic analysis of a cylindrical inclusion and a study of bonding stresses in laminated cylindrical shells have been completed. Projects in progress include microstress analysis and studies of photoelasticity and failure mechanisms. Several structural analysis and syntheses investigations aimed at developing the tools necessary to achieve superior structural designs with composite materials are reported. Several anisotropic discrete element formulations have been generated and numerically verified. New procedures are being developed for multiaxial stress analysis involving nonlinear and nonisotropic materials. Computer program packages have been created for unconstrained and inequality-constrained minimization techniques. The extension of structural synthesis to fiber composites is illustrated with a plate problem which treats material variables within the optimization process. Design activities associated with the tapered, stiffened cylinder began with weight efficiency comparisons of many candidate constructions and composite lay-up patterns. Parametric studies of the influence of fiber content and ply thickness on plate and column behavior are reported. Discrete element analyses are being made of stiffened panel element test configurations and of the behavior of the stiffened shell and end attachment.

BLANK PAGE

TABLE OF CONTENTS

TABLE OF CONTENTS (Cont'd)

TABLE OF CONTENTS (Cont'd)

TABLE OF CONTENTS (Cont'd)

ILLUSTRATIONS

ILLUSTRATIONS (Cont'd)

ILLUSTRATIONS (Cont'd)

ILLUSTRATIONS (Cont'd)

ILLUSTRATIONS (Cont'd)

ILLUSTRATIONS (Cont'd)

ILLUSTRATIONS

ILLUSTRATIONS (Cont'd)

ILLUSTRATIONS (Cont'd)

ILLUSTRATIONS (Cont'd)

ILLUSTRATIONS (Cont'd)

ILLUSTRATIONS (Cont'd)

ILLUSTRATIONS (Cont'd)

ILLUSTRATIONS (Cont'd)

TABLES

TABLES (Cont'd)

TABLE (Cont'd)

TABLES

SECTION I
INTRODUCTION

This report covers the second year's work of a program which represents a novel approach designed to fulfill three different but clearly interdependent needs of the Department of Defense: a materials need, a structural design capability need, and a need for more scientists and engineers trained in applied materials problems and advanced design methods. The Carbon Products Division of Union Carbide Corporation, Case Western Reserve University, and Bell Aerosystems Company have formed an Association to meet these needs.

The Association has formulated a broad program which includes the development of new materials, generation of advanced analyses and design methods, and education of graduate students. In brief, the major objectives are (1) to develop high modulus graphite fiber composites, (2) to extend the methods of structural mechanics, (3) to identify DOD applications toward which the program efforts should be directed, (4) to educate engineers capable of developing and using modern materials, and (5) to integrate materials research with the needs of the designer by extending the technique of structural synthesis to include material variables.

The general areas of responsibility of each member of the Association are defined in the following paragraphs. The technical program has been divided into eight parts and a survey of it is given in the latter parts of this section. Section II presents a summary of the results obtained during the second year's work. In the next eight sections, a more extensive discussion is given of the work that has been carried out on each part of the technical program.

The primary areas of responsibility of Union Carbide Corporation, Carbon Products Division, are to develop and produce composite materials and to measure those mechanical and thermal properties needed for the structural design work within the Association. The technical program at Union Carbide consists of: (1) materials research, a basic research program to develop new, improved composites of high modulus graphite fibers in both resin and metal matrices; (2) materials fabrication, an applied research program to produce materials for the joint research programs of the Association and to seek new ways of fabricating components which better utilize the superior properties of composite materials; (3) properties evaluation, the measurement of the mechanical and thermal properties of certain composites to provide data for the joint research programs of the Association; and (4) failure criteria, a basic research program to determine experimentally adequate failure criteria for anisotropic materials under multiaxial stress states and to find ways of representing the failure surface which can be used by the designer in practical calculations.

The primary objective of the work at Case Western Reserve University is to advance the basic structural mechanics technology required for rational design with composite materials. Composite materials offer the

structural design engineer the prospect of being able ultimately to carry on simultaneously the design of the structural configuration and material. Achieving this capability will require fundamental advances in structural synthesis as well as a substantially improved understanding of the behavior of composite materials. The objectives of the research program at Case are: (1) the quantitative formulation and efficient solution of the structural synthesis problem, including material variables, for elementary, but representative, components fabricated from composite materials; (2) experimental stress analysis studies and theoretical investigations in micromechanics with the objective of improving the measurement and calculation of stiffness properties and failure mode criteria for composite materials; and (3) the development of improved analysis methods for anisotropic, nonlinear, and nonconservative materials.

The primary pruposes of Bell Aerosystems Company's participation in this program are to interject user requirements into the appliedmaterial research efforts; to apply, at the prototype design level, the advanced analytical procedures and improved understanding of material behavior which will result from the research; and to establish application-related property specifications for materials research activities. To attain these objectives, a six-part technical program is being performed by Bell: (1) application selection, where the objective is to define representative configurations and environmental conditions that reflect DOD requirements; (2) recognition of failure modes, a task that involves the overall structural behavior such as elastic instability, deformation limits, and fracture and the material failure modes; (3) determination of the nature of and methods for the application of analytical tools needed to cope with the anisotropic, anelastic, and nonconservative material property behavior and the multiaxial stress distributions anticipated in structural configurations associated with the use of the subject materials; (4) structural synthesis, which involves the application of structural synthesis techniques at the practical level to define the most desirable material compositions within a particular class of composites; (5) study of creative design concepts which will be required because of the complex material behavior of composites; (6) testing, which is necessary to verify the value of analysis procedures used to design composite materials and the components made from composite materials.

In a project involving separate organizations, an attempt is usually made to divide the work so that each organization has separate and well-defined tasks. In the present case, a deliberate attempt has been made to do the opposite, that is, to achieve close coupling (1) between the Materials Laboratory and the Structural Design groups and (2) between the applied work in industry and the basic work at the university. A rather detailed program plan has been formulated to ensure this close coupling and to achieve the technical objectives set forth in this Introduction. A general review of this program, with emphasis on how the work of one member of the Association is coupled with that of the other two members, is given in Section II A of the First Annual Report.[1] In brief, many of the activities at the three organizations are centered around the design, fabrication, and testing of a ring- and stringer-stiffened tapered cylinder representative of a subscale fuselage section, as indicated in the more detailed discussion of the program objectives that follows. The program

also includes numerous relevant but fundamental studies that seek an improved understanding of the structural behavior of composite materials and a better analytic foundation for the design of advanced composite components. In the following paragraphs, the objectives for the second year of the eight parts of the technical program are discussed briefly.

1. Particulate Composite Studies

High modulus graphite fibers were not available at the start of the program; therefore, another class of materials, a series of particulate composites, was selected in order to carry through all aspects of an integrated approach to applied materials research. Except for documentation, the particulate composite studies have been completed. Descriptions and preliminary results for all the major projects were presented in Section V of the First Annual Report.[1] Concluding activities on these projects are given in this report.

2. Materials Research on Graphite-Fiber, Metal-Matrix Composites

Unlike the situation for resin matrix composites, fabrication processes for metal matrix composites, applicable to graphite fibers, did not exist at the beginning of the program. Therefore, the initial objective of the metal matrix research was to develop fabrication processes for composites which would be either light in weight or good in high temperature properties. Present work is on fabrication and high temperature testing of nickel matrix and aluminum matrix composites.

3. Materials Research on and Fabrication of Graphite-Fiber, Resin-Matrix Composites

A major part of the graphite-fiber, resin-matrix composite work is the preparation of materials for the physical properties and simple element testing programs and the fabrication of a stiffened tapered cylinder representative of a subscale fuselage section. This work must necessarily be done with present state-of-the-art technology. Concurrently, basic studies are being conducted to improve the composite material.

4. Physical Properties of Graphite-Fiber, Resin-Matrix Composites

Extensive physical property measurements are being made to support other programs of the Association. Property data for many lay-up patterns are needed for the design and analysis of the fuselage component, for analysis and synthesis studies, and for the evaluation of various analytical procedures used to predict composite properties from constituent properties.

5. Design Data Studies and Simple Element Testing on Fiber Composites

Investigations of various test methods are being conducted to find improved methods of obtaining design data of advanced composite materials. Conventional physical property data on plate and cylinder specimens are

being assembled, and structural elements are being tested for buckling and strength allowables. Studies have been made of the acoustic fatigue resistance of graphite fiber composites.

6. Micromechanics and Predicted Design Data for Fiber Composites

Design with fiber composite materials requires the ability to reliably predict composite properties from constituent properties. Such predictions, particularly those of strength, must be based on a detailed knowledge of the stresses both in the fiber and in the matrix. Several analytical and experimental projects have been initiated to predict elastic, thermal, and strength properties and to investigate internal stress distributions within laminated composites.

7. Structural Analysis and Synthesis Studies

Most composite lay-up patterns are anisotropic and exhibit nonlinear stress-strain behavior. Reliable design with such materials requires improvements in existing analysis and synthesis capabilities. Initial work has been concerned with improved computer programs and procedures for analysis and synthesis computations, with analysis procedures for nonlinear materials, and with methods for treating material variables in the automated design process. Applications are being made to the analysis of unstiffened and stiffened plates and shell and to the synthesis of a fiber composite plate.

8. Fuselage Component Design and Analysis

A stiffened cylinder 48 inches long and tapered from 20 to 24 inches in diameter is being designed and fabricated and will be tested as a performance demonstration of advanced graphite fiber composites in an aerospace application. In addition, this prototype activity will reveal technical areas where further studies are needed. Orthotropic shell buckling procedures and discrete element analyses are being employed in design studies which cover a range of representative fuselage loadings. The design activities include comparative weight efficiency studies, details of stiffening rings and end attachments, and evaluation of structural elements.

SECTION II
SUMMARY

A. Synopsis of Association Program

The activities of the Association formed by Union Carbide, Case Institute, and Bell Aerosystems are directed toward designing, fabricating, and evaluating a representative component; longer range investigations of selected, critical problem areas in advanced composite technology; and involvement of students in an important new technology. The component activity serves as a hardware performance demonstration and also serves to reveal new, or emphasize suspected, technological shortcomings. Investigations of these shortcomings and of other problems that clearly must be solved for the next generation of advanced composite applications form the basic, long range studies. Observations by the graduate students of the total program and their participation in specific projects contribute uniquely to the education of engineers skilled in advanced composite technology and the awareness of the nature of industrial research and development.

Two basic construction forms were considered during preliminary design of the fuselage component: stringer-stiffened skin and honeycomb stabilized sandwich. Structural weight efficiency studies indicated that, at low to moderate loadings, greater performance potential and design versatility with graphite fiber composites would be expected in stringer-stiffened constructions. This study provided guidance for many fabrication, design data, and advanced design activities.

Fabrication processes utilizing "Thornel" graphite yarn have been developed for thin gauge composites and realistic structural element geometries. Various types of design data, including finite layer effects and bending behavior, have been measured on "Thornel" 25 and 40 composites. Conventional buckling tests of "Thornel" 40 composite plates have yielded buckling allowables superior to those of 7075-T6 aluminum. The testing of high performance composites presents special difficulties; projects that have been initiated to obtain better data include a new plate buckling test for the nondestructive measurement of flexural rigidities and prediction of buckling allowables and a simple NOL ring test that avoids the bending moments and frictional effects of the split-D test.

Elastic properties under membrane and bending loadings have been calculated with existing methods, comparison with measured data has shown fair to good agreement. As with all types of fiber composites, the methods for predicting composite strengths are less satisfactory than those for predicting moduli. Several projects have been initiated to obtain improved predictions of design data and better knowledge of the internal stress distributions within the composite; two projects have been completed: an elastoplastic analysis of a cylindrical inclusion and a study of bonding stresses in laminated cylindrical shells.

Advanced design activities have included an orthotropic shell buckling analysis, based on a cylindrical shell idealization, that has established better candidate skin, stiffener, and stabilizing ring laminate constructions. The powerful methods of discrete element structural analysis have been generalized to account for material anisotropy. Several formulations for shell-type elements, verified on known solutions to plate and shell problems, have been applied to analyze stiffened-panel element test configurations. Other discrete element analyses are being made of the stiffened-shell behavior and of the component end attachment.

Extensive results have been obtained on several additional long range projects. Fabrication studies of high modulus graphite-fiber, nickel-matrix composites have resulted in improved processing conditions. High temperature tensile tests, to 1050°C, have yielded specific strengths at least twice those of TD nickel. An experimental acoustic fatigue test program has demonstrated good acoustic fatigue resistance for "Thornel"-fiber, epoxy-resin composites. New and improved procedures have been developed for multiaxial stress analysis of structures incorporating nonlinear and nonisotropic materials. One procedure employs a numerical minimization of the energy. A collection of operational computer program packages has been created for selected unconstrained and inequality constrained minimization techniques from the recent literature. These program packages have been used extensively in the nonlinear analysis work and in the automated optimum design studies. Work to include fiber composite material and processing variables within the structural synthesis (automated design) cycle has been initiated. The synthesis of a simple plate problem for which the number of lamina, the fiber angle, and the fiber modulus were variables, has been completed; this problem has demonstrated the feasibility of including material variables within the optimization process.

B. Particulate Composite Studies

Studies related to the particulate composites have been completed. These nonlinear, transversely isotropic materials, referred to as the JT-series, possess higher strengths and greatly improved oxidation resistance compared with conventional graphites, due to the addition of from 30 to 70 percent metallic elements to the graphitic base material. Many of the results and experiences obtained from these studies have been or will be applied in the studies of graphite fiber composites, thereby accelerating the fiber composite work. Other results are of intrinsic importance in applications involving materials which behave similarly to those in the JT-series.

So that a body of property data for the analysis and design work might be available, elastic properties, stress-strain curves, strengths, and thermal properties have been measured on nine materials having nominal compositions of 30, 50, and 70 percent additive and porosities of 5, 10, and 15 percent. As part of a study of failure criteria in anisotropic materials, average fracture strengths for composites of nominal 50 percent metallic additive and various porosities (including the commercially available grade JTA composite) have been determined for all

combinations of biaxial tensile and compressive stresses. A theoretical study has been made of the formulation of statistical strength distributions for anisotropic materials. Flexural strength distributions collected on bend bars cut at 30° and 60° with respect to the material symmetry could not be satisfactorily predicted from distributions for 0° and 90° bars. The shape of the failure surface under biaxial stresses was found to be a function of the probability of failure, indicating that very extensive multiaxial stress testing would be necessary for prediction of strength at the low probabilities of failure required in reliable structural design for aerospace applications.

The structural synthesis study of an axially symmetric, three-layer, thick-walled cylinder subject to high thermal and internal pressure loading, has been completed. The results of this study support the contention that the materials evaluation function is a useful concept. Further work on this problem should consider oxidation resistance as a function of porosity and percent additive and should be based upon a nonlinear multiaxial stress analysis that takes into account behavior differences in tension and compression. The structural synthesis study of a flat simply supported orthotropic rectangular panel has also been completed. This problem considers structural behavior characteristics such as bending, buckling, multiaxial stress states, and thermal stress response. Structural synthesis concepts can be applied to particulate composite structural systems subject to complex thermal and mechanical loads. The construction of a materials evaluation function based on synthesis results and the use of the materials evaluation function in guiding the selection of an optimum material composition for a particular application are illustrated by example.

The importance of considering material nonlinearity was demonstrated by analysis of a typical rocket engine throat insert and comparison of the results with those presented in Section V H of the First Annual Report.[1] Compared with the stress levels obtained with the linear analyses, the stress levels predicted on the basis of material nonlinearity were as much as an order of magnitude lower; and the maximum strains were only approximately one-half as large.

C. Materials Research on Graphite-Fiber, Metal-Matrix Composites

The need for greater productivity of nickel-plated graphite fibers required abandoning the batch yarn plating technique in favor of continuous electrocladding of the fibers. Three plating baths have been evaluated for this purpose: Watt's, nickel sulfate-boric acid, and nickel sulfamate. The Watt's bath yielded the best results. Since fiber misalignment is one of the factors considered to be deleterious to the physical properties, fabrication techniques were developed which result in more uniform fiber orientation. The effects of the fabrication variables (temperature, time, and pressure) on the physical properties of graphite-fiber, nickel-matrix composites have been investigated in detail. This work showed that the maximum forming pressure for optimum densification and minimum fiber damage is approximately 2500 lb/in.^{2} at both 900°C and 1050°C. Maximum composite strength was attained with 55 volume percent

fibers, but this strength level is still only 60 percent of the theoretical value based on the rule of mixtures. Forming pressures in excess of 2500 lb/in.^{2} cause increased fiber damage that results in lower composite strength. Three fiber damage mechanisms have been experimentally verified: longitudinal cleavage along the fiber axis, bridging between the fibers, and breakage of fibers into shorter length. In addition, surface damage to fibers is suspected. Thermal degradation of the fibers also contributes to the significant difference between the experimentally achieved and theoretically possible properties. This degradation was verified by annealing nickel clad fibers to temperatures between 500° and 1050°C for one hour. Physical testing of the fibers after removal of the Ni showed the fibers to be weaker by a factor of approximately 2/3. Since the elastic modulus remained unaffected, a surface rather than bulk effect is evidently present. Annealing of composites for 300 hours at temperatures of 500°, 700°, and 800°C caused a minor (approximately 10 percent at 800°C) decrease in room temperature composite tensile strength. High temperature tensile strength measurements showed that the specific strength of graphite-fiber, nickel-matrix composites exceeds that of TD nickel by at least a factor of two at all temperatures to 1050°C. Above 800°C, the composites also exceeded the specific strength of "Hastelloy" alloy X. The trend of composite tensile strength with test temperature appears to have a minimum at approximately 800°C. The reasons for this effect are under investigation. The preparation of graphite-fiber, aluminum-matrix composites, involving the concept of liquid phase sintering, is also described.

D. Materials Research and Fabrication of Graphite-Fiber, Resin-Matrix Composites

Four epoxy resin systems have been evaluated as matrix materials for graphite fiber composites. Low modulus graphite yarn and "Thornel" 25 graphite yarn were used in fabricating NOL rings with these resin systems. The system ERL 2256/MPDA was selected for the composite fabrication work because this system has good handling properties, has a relatively long pot life, and gives slightly higher strengths for "Thornel" composites than do the other three resin systems.

Some additional results have been obtained from the oxidation studies of low modulus graphite yarn that were started during the first contract year. Oxidation of the fiber surface by a solution of sodium dichromate in sulfuric acid significantly improved the wicking rates of all four epoxy resins used in the resin systems evaluation studies. A good correlation was observed between the increase in notched beam shear strength and the increase in wicking rate as the yarn immersion time was increased, a result that indicates wetting is a good measure of adhesion.

Approximately forty plates, each 1 ft by 1 ft, and several small cylinders have been fabricated from "Thornel" 25 and 40/ERL 2256 composites. In preparation for fabricating the ring- and stringer-stiffened subscale fuselage component, several types of stringers and rings and a single large unstiffened cylindrical shell (20 inches in diameter) have been made.

Properties of "Thornel" graphite fibers and of the ERL 2256/MPDA resin system are given for use in analytical studies. Lay-up patterns and fiber volume contents of the plates are included. Representative optical micrographs of the cross sections of the plates are also included.

E. Physical Properties of Graphite-Fiber, Resin-Matrix Composites

Data were obtained from measurements made on resin-matrix composites reinforced with "Thornel" 25 and 40 graphite fibers. These tests were carried out on specimens cut from unidirectional and multi-directional plates of from 2 to 9 plies in thickness and on hoop-wound cylinders. Test methods were developed for the measurement of tensile, compressive, bend, short beam shear, sonic resonant bar, hoop tensile, and cylinder torsion properties and for the measurement of thermal expansion and conductivity. The variations of ultimate tensile strength, Young's modulus, and Poisson's ratio were measured as functions of the angle of the test specimen. Complete tensile stress versus longitudinal and transverse strain curves were also measured as a function of test specimen angle.

Complete sets of Young's moduli, Poisson's ratios, and the in-plane shear modulus have been obtained for membrane loading of composites with various lay-up patterns and ply thicknesses; and Young's moduli and Poisson's ratios have been obtained for bend loading of most of these composites. For unidirectional "Thornel" 25 and 40 composite plates, the Young's moduli in the fiber direction were 11.1 and 24.6 x 10^6 lb/in.^{2}, respectively. For both unidirectional and cross-plied plates, the principal Young's moduli were approximately 85 to 90 percent of values given by the rule of mixtures.

Uniaxial tensile tests on coupon-type specimens of unidirectional "Thornel" 25 and 40 composite plates gave strengths as high as 92 and 140 x 10^3 lb/in.^{2}, respectively; and hoop tensile tests on cylinders gave 92 and 130 lb/in.^{2}, respectively. For the unidirectional and cross-plied plates, the tensile strengths in the principal directions were approximately 75 to 90 percent of values given by the rule of mixtures. Tests on several cross-plied "Thornel" 25 plates of different thicknesses showed no degradation in strength as the number of plies decreased from 9 to 2. In principal directions, compressive strengths were 70 to 85 percent of tensile strengths, due, in part, to poorer test techniques. Interlaminar shear strengths from short-beam flexure tests on "Thornel" 25 and 40 plates were 5000 and 4000 lb/in.^{2}, respectively; torsion tests on hoop wound cylinders gave interlaminar shear strengths of 4000 and 3300 lb/in.^{2}. Specimens cut from plates were boiled in water for 72 hours prior to testing; this treatment reduced the shortbeam shear strength 15 to 25 percentbut reduced the tensile and compressive strengths only 5 and 7 percent, respectively.

Preliminary measurements of thermal conductivity and thermal expansion are reported for "Thornel" 25 and 40 composite plates with unidirectional and cross-plied lay-up patterns.

F. Design Data Studies and Simple Element Testing of Fiber Composites

The split-D tensile test fixture for unidirectional NOL rings has been examined photoelastically and was found to be unsatisfactory for the establishment of reliable design data. Stress concentration in the region of the split due to bending of the ring element produces a stress state from which simple tensile data cannot be extracted. A new test device has been developed which induces a uniform tensile stress state and, thus, gives more reliable design data. Several configurations and sizes of flat tensile specimens have been investigated; a dog-bone tensile specimen with a hyperbolic fillet was found to give the most consistent results. The effects of gauge section widths on tensile strength of angle-ply specimens were found to be significant. A plot of tensile strength versus gauge width has a nonlinear character that can be interpreted as a dependency of the tensile strength on shear failure within and between the plies.

A buckling fixture for the determination of flexural rigidities and the buckling allowables of fiber composite plates has been developed. The fixture and a nondestructive test procedure have been verified by using metallic and glass fiber composite specimens. Several graphite fiber composite specimens have been investigated, and the correlation of buckling loads with those obtained analytically establishes this test procedure. The four point twist test for the determination of the twisting rigidity of fiber plates has been examined experimentally. The effects of specimen size, overhang, initial imperfection, and plate deflection were investigated, and limitations on these parameters were established. It has been experimentally verified that certain imperfect plates will yield spurious data. A test program based on the steady-state vibrational response of fiber plates has been initiated; the results of the vibration test can be correlated with analytical predictions and the results of the plate buckling tests. Test fixture design details of the support conditions required careful investigation. The fixture and test procedure will be evaluated by using the metallic and glass fiber composite specimens examined with the nondestructive buckling tests.

Various structural characteristics of fiber composite stringers have been investigated experimentally. Box, Zee, angle, and channel section stringers were examined for applicability to the representative fuselage component. Crippling tests on fiber composite panel elements have been conducted to obtain elastic instability and ultimate design data for "Thornel" 40 composites. Although the stress levels corresponding with elastic instability and ultimate strength were somewhat lower than expected, possibly due to testing difficulties, a structural efficiency advantage of approximately 30 percent was indicated for the "Thornel" 40 material as compared with aluminum alloy.

Results of a program funded by Bell Aerosystems on the acoustic fatigue resistance of advanced composites are reported. The "Thornel" graphite fiber was supplied to the program under the ARPA contract. This program, concerned with the acoustically excited panel which finds application in V/STOL aircraft and air cushion vehicles, included preliminary design, material evaluation, fabrication, and component testing.

Testing of rings provided quantitative data relative to damping, natural frequencies, and strengths. Results obtained from testing of panels under acoustic fatigue environments, although qualitative to a large degree, demonstrated that graphite and boron fiber composites possess potential for applications wherein resistance to fatigue is a significant factor.

G. Micromechanics and Predicted Design Data for Fiber Composites

A survey of the available micromechanic theories for the prediction of two-dimensional elastic properties of composite materials was conducted. It was established that further analytical and experimental work is needed on composites reinforced with orthotropic fibers. However, verification of predicted composite elastic properties which are sufficiently accurate for preliminary design purposes has been obtained through comparison with experimental data for graphite fiber composites. As a step toward the prediction of design strength allowables for graphite fiber composites, calculations of principal strength of properties of unidirectional and orthogonal composites have been satisfactorily compared with measured data on "Thornel" fiber laminates; strength predictions for angle ply laminates have not been as satisfactory. Thermal conductivities of graphite-fiber, epoxy-resin composites in pseudoisotropic lay-ups have been investigated by utilizing established methods. Calculations were made to determine the influence of fiber and matrix continuity on composite thermal properties.

Analytical procedures for the determination of internal elastic stress, strain, and displacement distributions of fiber composites have been investigated. The elastoplastic analysis of a cylindrical elastic inclusion in a uniformly stressed homogeneous matrix has been used to establish stress and strain distributions around the inclusion. The material properties of the inclusion and the matrix, including their stress-strain curves, are assumed to be arbitrary and independent of each other. Several examples, including the limiting cases of a hole and a rigid inclusion, are presented. Two- and three-dimensional models of fiber composites have been examined photoelastically. Shear-stress concentration factors in excess of 5 have been observed at fiber ends. Three-dimensional models are being examined to experimentally obtain complete stress states. Procedures to observe directly the failure of fiber reinforced composites are being developed. Glass and graphite fibers (actual size) have been observed during loading transverse to the reinforcement, and the regions of failure have been recorded photographically to guide the generation of failure mechanism hypotheses. Analytical studies to determine the bonding stress in laminated cylindrical shells have been completed. Stress concentration in and near the bond layer indicates a possible source of premature failure.

H. Structural Analysis and Synthesis Studies

Extension of discrete element methods of structural analysis to composite material structural systems requires that anisotropic behavior be considered. Several anisotropic discrete elements for analysis of stiffened thin shell structures have been developed. These include

triangular membrane and plate elements, quadrilateral membrane and plate elements, and a doubly curved axisymmetric ring element. These elements have been verified with example problems for which alternate solutions are available for comparison. This numerical verification task has been completed satisfactorily, and these discrete elements are being used in the analysis of a representative fuselage component. The use of incremental complementary energy methods to predict multiaxial stress distributions that take nonlinear material behavior into account has been introduced. Numerical results have been obtained for an isotropic plane stress problem with linear strain hardening. Correlation of these results with a previously published solution is satisfactory. Extension of the incremental complementary energy method to the case of nonlinear, transversely isotropic materials which behave differently in tension and compression has been undertaken. The formulation of a thick-walled infinite cylinder problem, including transverse isotropy and different behavior in tension and compression, has been completed. A reliable and efficient operational version of the method of feasible directions has been generated as an algorithmic tool for obtaining solutions to various structural synthesis problems. The potential role of the structural synthesis concept in design with fiber composites has been illustrated by carrying out the formulation and solution of a fiber composite panel design problem. Although this example is rather idealized, it exhibits many features characteristic of more realistic design problems for composite material structural systems.

I. Fuselage Component Design and Analysis

Preliminary design studies of the fuselage component have been completed. Structural efficiencies of various fuselage construction concepts were compared by using conventional procedures and assuming isotropic material behavior. For the range of loading indices of interest, the stringer- and ring-stiffened skin approach resulted in the lowest structural weights. Structural weights were estimated to be only 50 percent of the weights associated with aluminum alloy construction. The influence of laminate construction was exmained for plates, columns, wide columns, and unstiffened shells to serve as a guide for more refined shell analyses. In addition, finite layer effects and stringer configurations were investigated.

After design criteria and loading conditions for the fuselage component were established, orthotropic shell buckling analyses were conducted to investigate various laminate configurations and thicknesses. Unidirectional, bidirectional, and orthogonal skins, rings, and stringers were analyzed in various combinations. Elastic properties of the laminates were calculated on the basis of "Thornel" 25 fiber properties and a fiber volume content of 65 percent; the fiber was treated as anisotropic. With this level of refinement, the orthogonal skin and unidirectional stringer configuration, which was superior to others investigated, still indicated a 50 percent advantage over aluminum alloy construction. At this point in the design activities, a decision was made to employ "Thornel" 40 rather than "Thornel" 25 and to employ fiber contents currently available rather than those expected to result from fabrication procedure improvements.

Orthotropic buckling studies of "Thornel" 40 laminates with 50 percent fiber content indicated an approximate 30 percent weight advantage over aluminum.

Because of the inverse relationship between fiber content and ply thickness and the influence of these variables on buckling behavior, parametric studies of plates and columns were conducted. The results quantitatively define the influence of these variables for a constant number of plies. High fiber content appears desirable for unidirectional columns, but low fiber content appears desirable for orthogonal plates. Strength cut-off data are required before minimum fiber content can be defined.

Preliminary studies of the fuselage rings identified and qualitatively compared various concepts in addition to parametrically relating ring, torsional, and bending stiffnesses to fuselage buckling strength. Attachment design is now sufficiently advanced that detailed analyses can be initiated. The anisotropic discrete elements developed during the program were employed to determine the stresses and deflections in the fuselage shell.

SECTION III

PARTICULATE COMPOSITE STUDIES

The material selected at the beginning of the program for the first studies was a class of particulate composites designated as JT-series materials. These composites combine the good thermal shock resistance of graphite with oxidation resistance provided by incorporating ZrB_2 and Si into the graphite matrix. When this material is exposed to oxygen at elevated temperatures, a protective oxide coating is formed on the exposed surface by oxidation of the bulk material, thereby providing oxidation protection in depth. One member of this series, the commercial product JTA, is currently being used for rocket nozzle inserts and is being evaluated by the Air Force for additional applications. The physical properties of the JT-series materials can be varied by changing the composition (i. e., percent metallic additives) and the porosity of the particulate composite material. The thermal and mechanical properties of materials in this JT series can be thought of as functions of the material variables composition and porosity and of the operating temperature.

A logical extension of existing structural synthesis (automated design) methods is to add material variables to the design variables treated in the optimization process. The output of the structural synthesis process would be the specification not only of the best geometrical shape of the component to carry a certain load but also of the best material within a given class of materials from which to make the component. In this way, the material needs of the designer and the development of new materials by the materials supplier would be integrated into one process.

A primary goal of the particulate composite studies is to demonstrate this integrated approach to the simultaneous design of structural geometry and material. Consider the design of a simple component to perform a specified set of functional purposes. The design task is to determine the geometric proportions, material composition, and porosity in such a manner that the component will perform the functional purposes adequately and satisfy some desirable objective that, for this work, will be minimum weight. This task may be attacked by considering several discrete materials, each one within the JT series, and then obtaining an optimum design of the geometric proportions for each discrete material. These optimum design weights versus composition and porosity can be used to construct a function that estimates the optimum design weight as a function of composition and porosity. Functions of this kind will be referred to as materials evaluation functions. Seeking the minimum of the materials evaluation function, subject to constraints that limit the range of values of the arguments, leads to a quantitatively based recommendation for an improved material.

The JT materials which have been fabricated for this study are listed in Section IIIA, and the physical properties for these materials are summarized in Section IIIB. Failure criteria for nominal 50 percent additive material, obtained by multiaxial stress testing, are reported in Section IIIC. A theoretical investigation of statistical distributions of

strength in anisotropic materials has been completed and applied to data obtained from off-axis bend tests on JTA material. This work is given in Section IIID. Two analysis and synthesis studies have been made for the JT-series materials: a three-layer cylinder problem (see Section IIIE) and a flat-plate problem (see Section IIIF). In Section IIIG, the design of a more complicated component, a rocket nozzle throat insert of JTA material, is reported; analysis with a nonlinear, anisotropic material was investigated as the final part of this project.

A. Fabrication of JT-Series Materials
(R.G. Fenish, Union Carbide)

1. Description of JT-Series Materials

The JT-series materials are graphite-base refractory composites similar to the commercial material with the grade designation JTA produced by the Carbon Products Division (JTA is one member of the series). On a weight basis, grade JTA is composed of 48.1 percent C, 42.4 percent ZrB_2, and 9.5 percent Si. The minimum density limit for grade JTA is 3.0 g/cm^3. During manufacture, the silicon combines with part of the carbon to form silicon carbide.

In this work, the elements Zr, B, and Si are called the metallic additives; these elements will always be present in the same proportions as in JTA: 42.4 parts of ZrB_2 to 9.5 parts of Si. Let

c = mass fraction of metallic additive in the fabricated product and

ρ = density;

grade JTA may, then, be specified by composition $c = 51.9$ percent and density $\rho > 3.0$ g/cm^3.

The JT-series materials are a class of materials produced by varying the amount of metallic additives and the density. In order to vary the density at a fixed composition, variations must be made in processing temperatures or pressures; otherwise, the manufacturing conditions are kept as close as possible to those for grade JTA. To a good approximation, each member of the JT series can be identified by values of the compositional variable, c, and processing variable, the density, ρ. To the same approximation, the physical properties of the JT-series materials may be considered to be functions of only two material variables, c and ρ.

2. Material Symmetry, Coordinate Orientation, and Billet Notation

All of the JT-series materials are molded in cylindrical billets. This process yields material with the symmetry characteristic of transverse isotropy, i.e., all physical properties are invariant with respect to arbitrary rotations about the symmetry axis, which is parallel to the direction of molding and perpendicular to the molding ram face.

Throughout this study, physical properties of the JT-series materials will be specified with respect to a Cartesian coordinate system oriented with the x_1 and x_2 axes in the plane of transverse isotropy and the x_3 axis parallel to the axis of rotational symmetry. These symmetry-oriented coordinates should not be confused with other types and orientations of coordinate systems used in the stress analysis problems. In JT material, as in other molded material, the elongated graphite particles or grains tend to be aligned with their two larger dimensions parallel to the plane of transverse isotropy, a condition which has led to properties (Young's modulus, coefficient of thermal expansion, etc.) in directions parallel to the plane of isotropy being called "with-grain" properties and properties in the direction parallel to the symmetry axis being called "against-grain" or "across-grain" properties.

The billets of JT material fabricated especially for this program will be identified by the letters JT, followed by the designation for the nominal composition, and, finally, the sequential fabrication number. Thus, JT-30-4 designates that the billet is the fourth to be fabricated and that the composition is approximately 30 percent metallic additive.

Commercial JTA billets from the standard production material which are used for this program will be identified by the letters JTA followed by the sequential order number. Thus, JTA-9 designates the ninth piece of commercial JTA used for this program.

3. Calculation of Porosity

Because the density varies with the composition as well as with porosity in the material, it is better for some purposes to choose composition c and porosity p as the material variables, rather than composition and density. Part of the porosity is in closed pores, and the volume of these pores is not easily measured. Therefore, the porosity must be calculated from the measured bulk density ρ and the calculated theoretical maximum density ρ_m:

$$p = 1 - \rho/\rho_m \qquad \text{(IIIA-1)}$$

The procedure for calculating the theoretical maximum density is described in Section VA of the first Annual Report.[1]

4. Fabrication of JT-Series Billets

A series of JT materials has been fabricated for mechanical and thermal properties evaluation. Carefully controlled processing conditions were employed to hot press billets 3 inches in diameter and approximately 3.5 inches in length. Nominal compositions of 30, 50, and 70 percent metallic additive were used; at each composition the porosity was varied from a low of 2 to 6 percent to a high of 17 percent. Table I lists the composition, density, and porosity of the 27 billets fabricated. A more complete description of the fabrication process is given in Section VA of the First Annual Report.[1]

TABLE I

COMPOSITION, DENSITY, AND POROSITY OF JT-BILLETS USED FOR PROPERTY EVALUATION

Billet Number	Composition percent additive	Density g/cm^3	Porosity percent
JT30-16	31.5	2.61	6.2
JT30-48	31.5	2.57	7.9
JT30-40	31.5	2.54	8.8
JT30-38	31.5	2.48	11.1
JT30-32	31.5	2.45	11.9
JT30-35	31.5	2.32	16.8
JT30-31	31.5	2.30	17.6
JT50-46	51.9	3.14	4.0
JT50-22	51.9	3.11	4.9
JT50-23	51.9	3.08	5.7
JT50-43	51.9	3.08	5.7
JT50-21	51.9	3.07	6.1
JT50-44	51.9	3.05	6.7
JT50-45	51.9	3.04	7.0
JT50-28	51.9	3.02	7.7
JT50-42	51.9	2.95	9.8
JT50-27	51.9	2.94	10.1
JT50-29	51.9	2.82	13.9
JT50-26	51.9	2.71	17.3
JT70-19	71.4	3.86	1.6
JT70-47	71.4	3.84	2.0
JT70-20	71.4	3.83	2.2
JT70-18	71.4	3.82	2.6
JT70-33	71.4	3.57	8.9
JT70-34	71.4	3.45	11.9
JT70-37	71.4	3.42	12.9
JT70-17	71.4	3.26	16.9

B. Physical Properties of JT-Series Materials

(O. L. Blakslee, C. W. Nezbeda, and T. Weng, Union Carbide)

The objective of this work is to obtain physical property data to be used as input information to the stress analysis and structural synthesis calculations performed at Case Institute and Bell Aerosystems. The physical properties of interest are the elastic moduli, Poisson's ratios, stress-strain relations, fracture strengths, thermal conductivities, specific heats, and coefficients of thermal expansion. The results of multiaxial stress tests and torsion tests are given in Section IIIC.

1. Methods of Measurement

a. Ultrasonic. Elastic constants have been determined from the velocities of propagation of longitudinal and transverse ultrasonic pulses at one megacycle per second frequency. Due to the high attenuation of the JT-series material, a through-transmission method has been used with a path length of approximately 1.25 inches and with directions of propagation parallel, perpendicular, and at 45 degrees to the symmetry axis of the material.

b. Resonant Bar. Elastic constants have been determined from the frequencies of longitudinal, flexural, and torsional vibrations of bars of dimensions 1/4 x 1/4 x 3 inches. In addition, measurements have been made on the static tension and flexural specimens to detect defects and unusual characteristics of the specimens prior to static testing and to provide a check of the moduli determined from the initial slope of the stress-strain curves.

c. Tension and Compression Tests. Both longitudinal and transverse strains have been measured with pairs of strain gages mounted on dog bones in tension and on rectangular prisms in compression. The dog-bone blank dimensions were 1/4 x 5/8 x 2-3/4 inches, and the gauge-section dimensions were 1/4 x 1.4 x 1-1/2 inches. The size of the compression sample was 1/4 x 1/4 x 1 inch.

d. Flexural Test. Four-point loading on bars 1/4 x 1/4 x 3 inches was used for flexural testing. Transverse and longitudinal tensile and compressive strains were measured at the top and bottom surfaces with strain gages. Because the load versus strain relations are nonlinear and slightly different in tension and compression, the data obtained from flexural tests were converted to uniaxial stress-strain relations by means of Naidai's graphical method.[2] The effect of frictional forces at the loading and supporting edges was taken into account in the calculation of the true stresses.

e. Thermal Diffusivity. Thermal diffusivities have been measured from ambient to approximately 600° C by a flash method.[3] The sample size was 5/8 x 5/8 x 0.04 inch.

f. Specific Heat. Specific heats have been calculated by multiplying the weight percent of each constituent phase by the specific heat per unit mass of that phase (carbon,[4] zirconium diboride,[5] and silicon carbide,[6] assuming complete conversion of Si into SiC). The calculations were made at 100-degree intervals from room temperature to 700° C. These calculations have been checked from room temperature to 400° C by measurements made with a Perkin-Elmer Differential Scanning Calorimeter.

g. Coefficients of Thermal Expansion. The coefficients of thermal expansion from room temperature to 700° C have been measured by the Newton's rings method on 1/2-inch cubes. Measurements in the temperature range from room to 2000° C have been made on bars 2-1/2 inches in length heated in a tube furnace. Telescopes equipped with micrometer eyepieces were used to measure the elongation.

TABLE II

SUMMARY OF MECHANICAL PROPERTY DATA FOR JT MATERIALS

Metallic Additive (percent)	31.5			51.9			71.4		
Porosities (percent)	5	10	15	5	10	15	5	10	15
Densities (g/cm^3)	2.645	2.505	2.369	3.106	2.943	2.779	3.725	3.529	3.333
Young's Mod. ($1/s_{11}$) Sonic	5.67	4.46	3.34	10.41	7.87	6.10	22.00	16.80	14.00
Young's Mod. ($1/s_{11}$) Static	5.28	4.38	3.55	9.50	7.21	5.93	21.90	16.60	13.75
Young's Mod. ($1/s_{33}$) Sonic	2.26	1.86	1.51	4.42	3.50	2.77	11.90	9.04	7.33
Young's Mod. ($1/s_{33}$) Static	2.04	1.70	1.40	3.81	3.17	2.53	11.70	8.93	7.11
Shear Mod. ($1/s_{44}$) Sonic	1.42	1.15	0.91	2.84	2.13	1.69	6.86	5.28	4.32
Poisson's Ratio ($-s_{12}/s_{11}$)	.095	.089	.085	.110	.104	.099	.136	136	.136
Poisson's Ratio ($-s_{13}/s_{33}$)	.145	.133	.123	.143	.133	.122	.136	.129	.122
Flexural Strength (σ_{f_1})	8.22	6.46	4.85	11.40	8.20	6.51	16.17	10.70	5.47
Flexural Strength (σ_{f_3})	4.01	3.37	2.80	6.29	4.79	4.07	9.01	6.08	3.57
Tensile Strength (σ_{t_1})	6.31	5.33	4.51	11.13	7.58	5.67	13.50	9.15	7.00
Tensile Strength (σ_{t_1})	3.53	2.96	2.46	5.32	4.01	3.28	8.05	5.60	3.93
Compressive Strength (σ_{c_1})	17.6	15.0	12.5	31.5	25.1	19.7	70.0	56.0	41.6
Compressive Strength (σ_{c_3})	23.0	19.2	15.5	32.5	26.1	19.6	56.5	45.5	34.2

Units: Moduli - 10^6 lb/in.^{2}; Strengths - 10^3 lb/in.^{2}

2. Mechanical Properties

Room temperature mechanical property measurements on the billets listed in Table I have been made by ultrasonic and sonic resonant bar tests and by static tensile, flexural, and compressive tests. For each material composition and for each property, a graph of the property versus porosity was prepared on which the data points from the various test methods were plotted. A best-by-eye curve was drawn through the points and property values obtained from the curve at porosities of 5, 10, and 15 percent. These average values are listed in Table II. (The nominal composition used for identification differs slightly from the exact final billet composition.)

a. Moduli. In most cases, static values of the Young's moduli are approximately 10 percent less than the sonic values. This discrepancy is due to the uncertainty in determining the initial slopes of the static stress-strain curves and, possibly, to other systematic errors. The sonic modulus results are considered to be more accurate and should be used at near-zero stress levels; the static stress-strain curves must, of course, be used at higher stress levels. Typical stress-strain curves were given in Section VB-4 of the First Annual Report.[1] The variation of the with-grain and across-grain Young's moduli, with composition and porosity, determined by the sonic resonant bar test, is shown in Figure 1. The moduli increase with increasing metallic additive composition and decreasing porosity. The variation of Poisson's ratios with composition is negligible, and the Poisson's ratios decrease slightly with increasing porosity. The range of Poisson's ratios are: $-s_{12}/s_{11} = 0.08$ to 0.11, and $-s_{13}/s_{33} = 0.12$ to 0.15, and $-s_{13}/s_{11} = 0.28$ to 0.37.

The shear moduli follow the same general variation with composition and porosity as do the Young's moduli; i.e., the shear moduli increase with increasing composition and decreasing porosity. This variation of the shear moduli, determined by the sonic resonant bar test, is illustrated in Figure 2.

b. Strengths. The flexural test data have been corrected for nonlinearity in the shear-strain curves and for friction between the specimens and the fixture. The values given in Table II are less than values computed on the basis of linear elasticity and on friction by 23 percent. The tensile strengths, computed from load divided by cross-sectional area, have been increased by a factor of 1.06 to allow for stray bending moments in the gauge section. Even after these corrections are made, the tensile strength is consistently less than the flexural strength by approximately 10 to 20 percent. Two possible causes of this difference are a statistical dependence of strength on test volume and stress concentrations at the fillet of the dog-bone shaped tensile specimen. The variations of flexural, tensile, and compressive strengths with composition and porosity are shown in Figures 3, 4, and 5 for both the with-grain and across-grain properties. The strengths increase with increasing composition and decreasing porosity; the variation in the compressive strength is particularly large.

Figure 1. Variation of of Young's Moduli Versus Composition and Porosity.

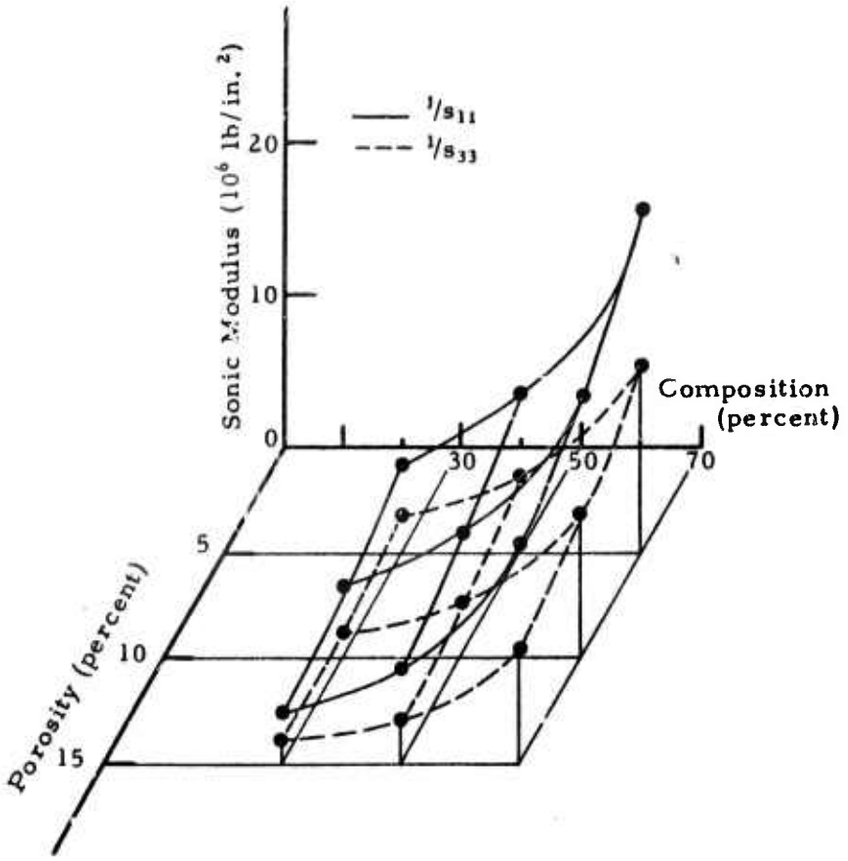

N-10155

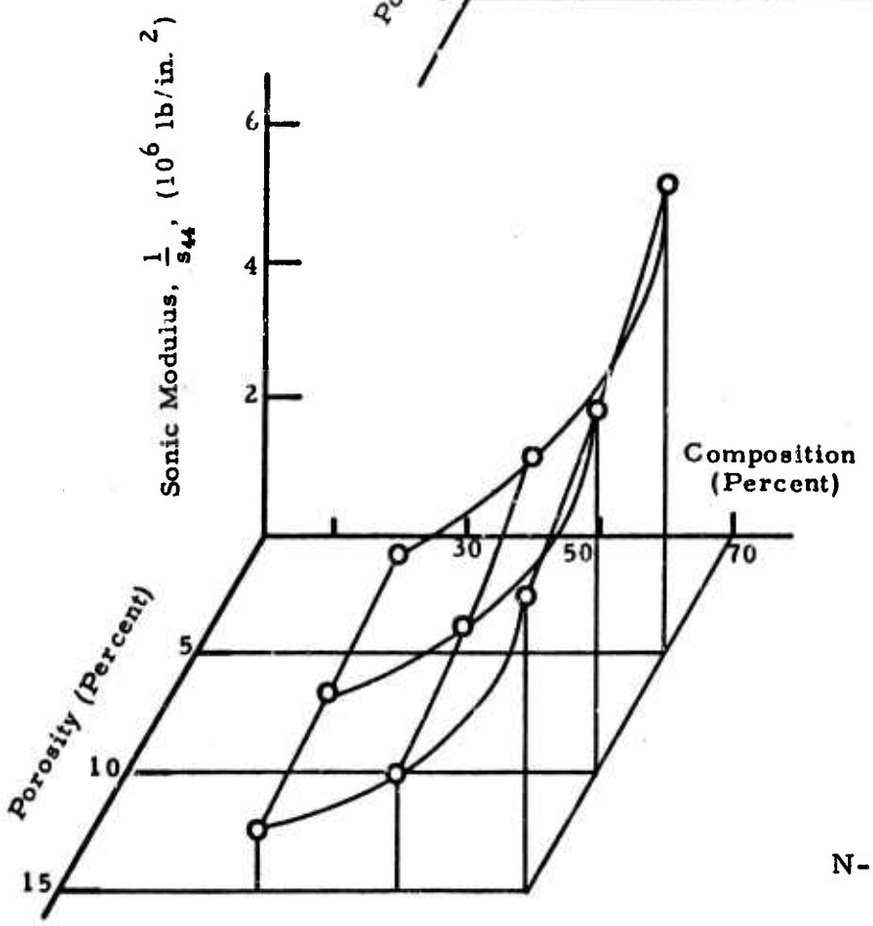

Figure 2. Variation of Young's Moduli Versus Composition and Porosity.

N-17224

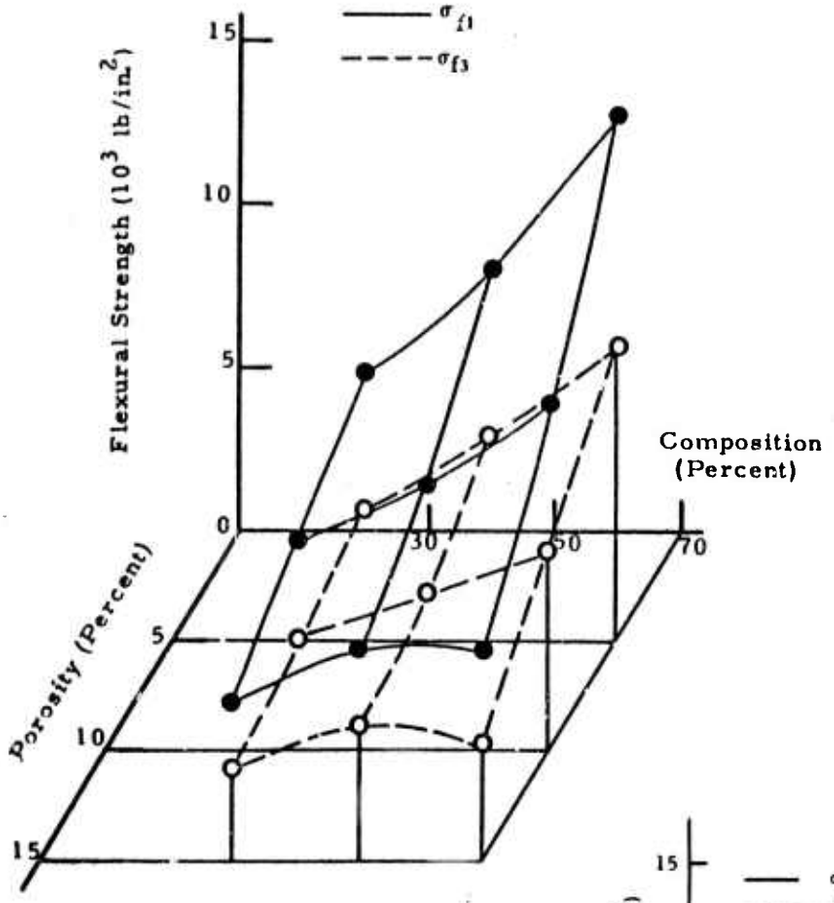

Figure 3. Variation of Flexural With-Grain and Across-Grain Strengths Versus Composition and Porosity.

N-17225

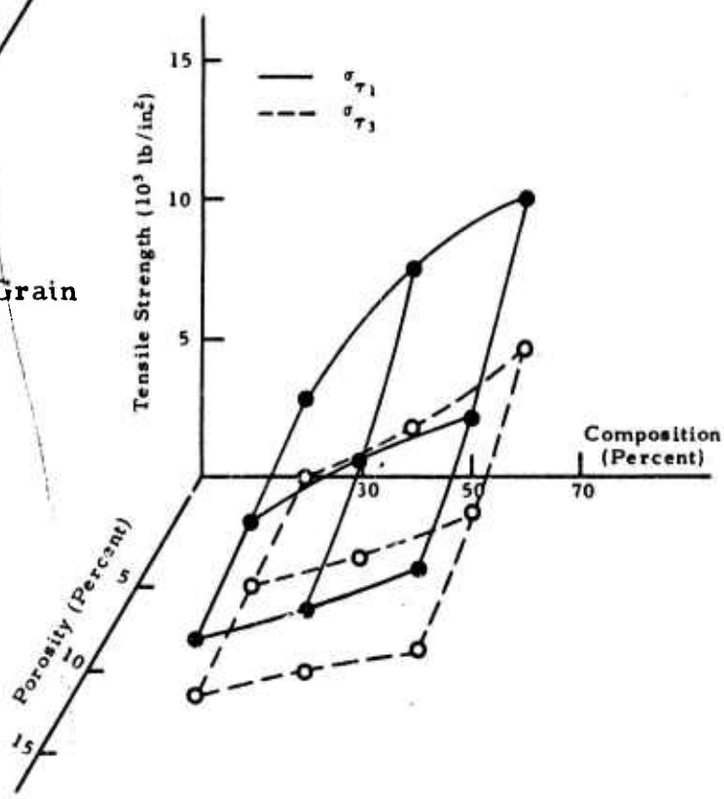

Figure 4. Variation of With-Grain and Across-Grain Tensile Strengths Versus Composition and Porosity.

N-17331

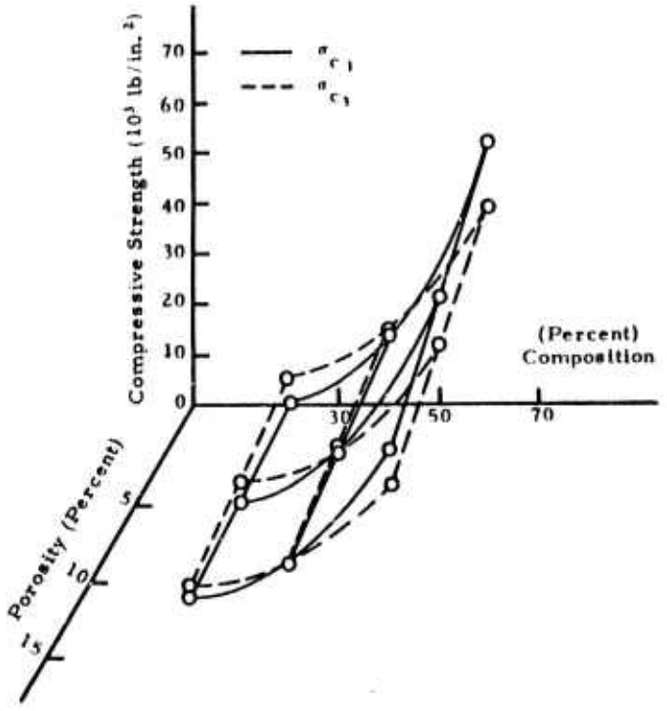

Figure 5. Variation of With-Grain and Across-Grain Compressive Strengths Versus Composition and Porosity.

N-17327

3. Thermal Properties

a. Specific Heat. The dependence of specific heat, c_p, on temperature is given in Figure 6 for the nominal compositions at 30, 50, and 70 percent. The curves were calculated from the specific heats of the constituent phases. The measured points are in very good agreement with the calculated values.

b. Thermal Diffusivity and Conductivity. The thermal diffusivity, κ_i, has been measured from room temperature to 600°C. The thermal conductivity k_i, has been calculated from the thermal diffusivity by means of the relation

$$k_i = \rho c_p \kappa_i, \qquad \text{(IIIB-1)}$$

where ρ is the density. The thermal diffusivity and thermal conductivity results for the nominal 30, 50, and 70 percent composition and 5, 10, and 15 percent porosities are reported in Tables III, IV, and V.

c. Thermal Expansion. The coefficient of thermal expansion data showed somewhat greater scatter than did the other property data. This scatter masked any dependence of the thermal expansion on porosity that might exist. The thermal expansion does depend slightly on composition, but the dependence is opposite for the with-grain and across-grain directions. The coefficients of thermal expansion α_1 and α_3 are almost equal for the 70 percent composition. The trends of α_1 and α_3 with temperature up to 1500°C are shown in Figure 7 for the nominal compositions of 30, 50, and 70 percent.

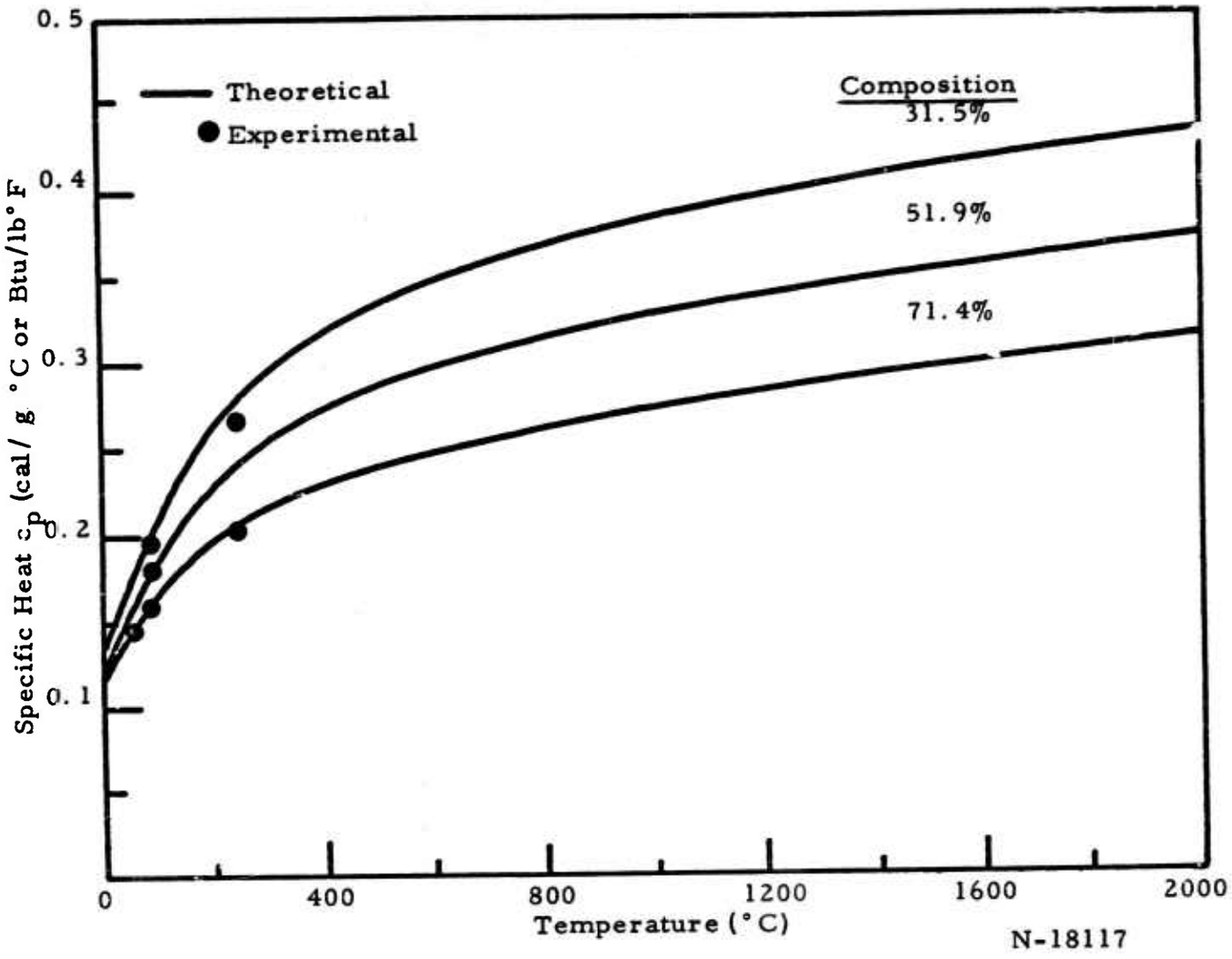

Figure 6. Specific Heat Versus Temperature for JT-Material

TABLE III

THERMAL DIFFUSIVITY AND THERMAL CONDUCTIVITY OF JT-30 MATERIAL

Temperature (°C)	THERMAL DIFFUSIVITY (cm²/sec)						THERMAL CONDUCTIVITY (cal/sec cm-deg)					
	5% porosity		10% porosity		15% porosity		5% porosity		10% porosity		15% porosity	
	K_1	K_3	K_1	K_3	K_1	K_3	k_1	k_3	k_1	k_3	k_1	k_3
100	.371	.186	.362	.183	.352	.179	.194	.097	.179	.091	.165	.089
200	.301	.151	.292	.148	.282	.144	.195	.098	.180	.091	.164	.084
300	.254	.127	.245	.123	.236	.119	.187	.093	.171	.086	.155	.078
400	.224	.108	.215	.104	.205	.100	.178	.086	.161	.078	.146	.071
500	.200	.094	.191	.090	.181	.087	.168	.079	.152	.072	.136	.065
600	.183	.083	.174	.079	.164	.075	.160	.073	.144	.066	.129	.059

TABLE IV

THERMAL DIFFUSIVITY AND THERMAL CONDUCTIVITY OF JT-50 MATERIAL

Temperature (°C)	THERMAL DIFFUSIVITY (cm²/sec)						THERMAL CONDUCTIVITY (cal/sec cm-deg)					
	5% porosity		10% porosity		15% porosity		5% porosity		10% porosity		15% porosity	
	K_1	K_3	K_1	K_3	K_1	K_3	k_1	k_3	k_1	k_3	k_1	k_3
100	0.361	0.212	0.346	0.202	0.331	0.191	0.200	0.117	0.172	0.100	0.164	0.094
200	0.304	0.175	0.289	0.164	0.274	0.153	0.204	0.117	0.174	0.099	0.164	0.092
300	0.264	0.143	0.250	0.135	0.235	0.128	0.198	0.107	0.175	0.094	0.157	0.086
400	0.237	0.125	0.222	0.118	0.207	0.111	0.190	0.100	0.160	0.085	0.148	0.080
500	0.215	0.108	0.200	0.103	0.186	0.097	0.182	0.091	0.152	0.078	0.140	0.073
600	0.201	0.095	0.186	0.091	0.172	0.087	0.177	0.084	0.147	0.072	0.135	0.068

There is a large uncertainty in the last significant figure.

TABLE V

THERMAL DIFFUSIVITY AND THERMAL CONDUCTIVITY
OF JT-70 MATERIAL

Temperature (°C)	THERMAL DIFFUSIVITY (cm^2/sec)						THERMAL CONDUCTIVITY (cal/sec-cm-deg)					
	5% porosity		10% porosity		15% porosity		5% porosity		10% porosity		15% porosity	
	K_1	K_3	K_1	K_3	K_1	K_3	k_1	k_3	k_1	k_3	k_1	k_3
100	.324	.215	.307	.204	.292	.192	193	.128	.174	.115	.109	.072
200	.274	.178	.257	.169	.241	.160	.192	.125	.171	.112	.106	.070
300	.238	.154	.224	.146	.211	.139	.183	.118	.163	.106	.101	.067
400	.214	.140	.200	.133	.186	.125	.175	.114	.155	.103	.095	.064
500	.196	.131	.183	.124	.170	.115	.167	.111	.147	.100	.090	.061
600	.176	.111	.166	.108	.156	.105	.155	.098	.139	.090	.086	.058

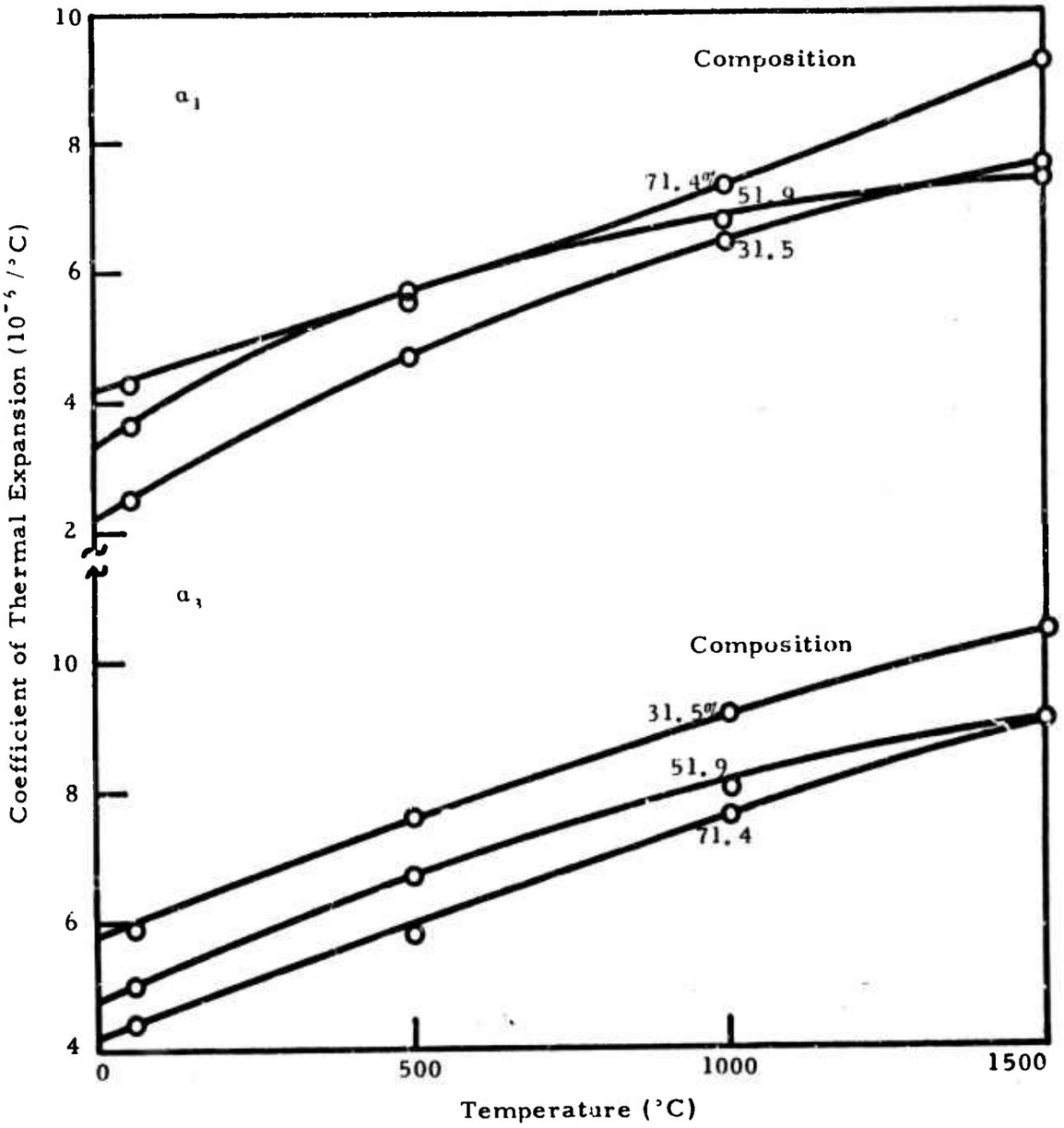

N-17328

Figure 7. Coefficient of Thermal Expansion Versus Temperature for JT-Material.

d. Effects of Annealing on Thermal Expansion and Mechanical Properties. Irreversible dimensional changes occur during the initial heating of the JT-material above approximately 1600°C. In the across-grain direction, the material expands between 1600° and 2000°C by

amounts of the same order as the intrinsic thermal expansion up to 1600° C. In the with-grain direction, the irreversible dimensional changes are much smaller and are sometimes positive and sometimes negative. During the fabrication process, the JT-billets are heated to temperatures greater than 2000° C and cooled under pressure; stress relief apparently occurs when the billets are reheated. When the same specimens are cycled a second time, irreversible changes still occur on a reduced scale.

Two simple experiments have been performed to study the dimensional changes that occur during reheating. Specimens of JT-30, 50, and 70 material were machined to precise dimensions for the first experiment. These specimens were repeatedly cycled in an induction furnace (argon atmosphere) from room temperature to various higher temperatures. After each temperature cycle, the specimen dimensions were checked with a micrometer. Table VI summarizes the results of this experiment, and Figure 8 shows a representative plot of the data for one of the specimens (JT-50-26). In Table VI and Figure 8, L_3 is in the across-grain direction and L_1 and L_2 are in the with-grain directions. In this experiment, several minutes were required before temperature equilibrium was achieved (the hold time was approximately 30 seconds), whereas several hours at high temperatures were required for the coefficient of thermal expansion tests.

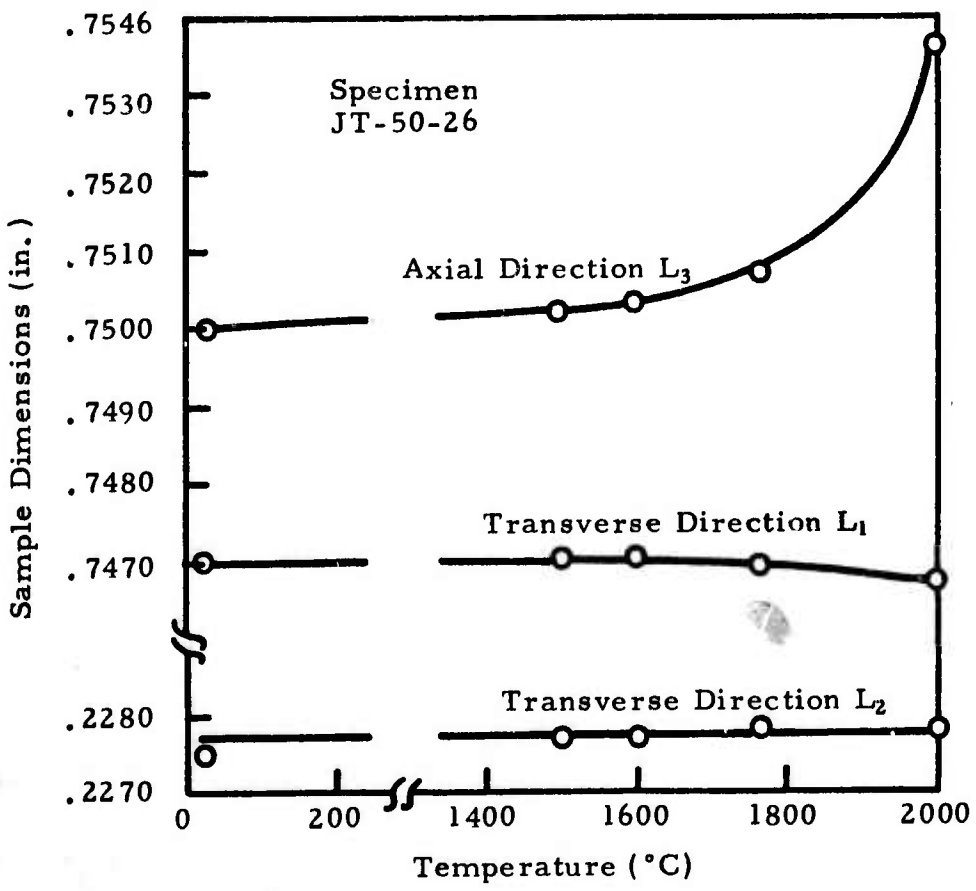

N-11413

Figure 8. Room Temperature Dimensions of JT-50 Material after Repeated Anneals to Each Higher Temperature.

TABLE VI

DIMENSIONS OF JT-MATERIAL AFTER CYCLING TO VARIOUS TEMPERATURES*

	As Received			1st Cycle to 1500°C			2nd Cycle to 1600°C			3rd Cycle to 1765°C			4th Cycle to 2000°C		
	L_1	L_2	L_3	L_1	L_2	L_3	L_1	L_2	L_3	L_1	L_2	L_3	L_1	L_2	L_3
JT 30-16	.7500	.2275	.7535	.7505	.2278	.7535	.7505	.2277	.7534	.7504	.2277	.7538	.7502	.2277	.7581
JT 30-35	.7535	.2275	.7505	.7536	.2276	.7504	.7538	.2275	.7502	.7539	.2276	.7506	.7538	.2275	.7559
JT 50-21	.753+	.2275	.7505	.7536	.2274	.7504	.7536	.2273	.7504	.7536	.2274	.7507	.7532	.2273	.7582
JT 50-26	.7470	.2275	.750+	.7470	.2277	.7502	.7470	.2277	.7503	.7469	.2278	.7507	.7467	.2278	.7536
JT 70-18	.7480	.227+	.7505	.7477	.2274	.7503	.7478	.2273	.7502	.7478	.2273	.7503	.7476	.2272	.7516
JT 70-34	.7470	.2265	.7505	.7469	.2267	.7505	.7468	.2267	.7505	.7468	.2267	.7508	.7467	.2266	.7531

*All dimensions measured in inches at room temperature.

TABLE VII

DIMENSIONS OF JT-MATERIAL AFTER CYCLING TO 2000°C*

	As Received			1st Cycle to 2000°C			2nd Cycle to 2000°C			3rd Cycle to 2000°C		
	L_1	L_2	L_3	L_1	L_2	L_3	L_1	L_2	L_3	L_1	L_2	L_3
JT 30-16	.7500	.0418	.7501	.7501	.0418	.7527	.7501	.0417	.7530	.7500	.0417	.7530
JT 50-21	.7501	.0414	.7504	.7499	.0415	.7541	.7499	.0414	.7546	.7498	.0414	.7546
JT 70-18	.7502	.0419	.7500	.7499	.0419	.7507	.7498	.0420	.7507	.7498	.0420	.7507

*All dimensions measured in inches at room temperature.

Since approximately the same amount of growth occurs in both instances, the growth is apparently independent of these heating rates.

Several additional specimens were machined for the second experiment. These specimens were repeatedly cycled between room temperature and 2000°C, and specimen dimensions were measured after each cycle. Table VII summarizes the results: after two temperature cycles, no further growth occurs in either the across-grain or with-grain directions.

The specimens should be pre-annealed or cycled several times to 2000°C before measuring the coefficient of thermal expansion at temperatures greater than 1600°C to insure that no growth will occur during measurement. This procedure should insure that only the intrinsic coefficient of thermal expansion of the material is measured above 1600°C.

A third experiment was run to determine the effect that annealing may have on mechanical properties. Two-thirds of a JT-billet was annealed at 2100°C for several hours. The remainder of this billet was left in the as-received state. Specimens were cut from both portions of the billet for mechanical property measurements. Preliminary results indicate that the Young's modulus and flexural strength in both the with-grain and across grain directions do not change significantly upon annealing.

C. Failure Criteria and Multiaxial Test Apparatus
(T. Weng, Union Carbide)

1. Multiaxial Stress Test Apparatus

A high pressure intensifier capable of generating a pressure as high as 50,000 lb/in.^{2} has been installed in the hydraulic system of the multiaxial stress test apparatus. The schematic diagram of the hydraulic system is shown in Figure 9. A torsion test machine has been constructed and is shown in Figure 10. A Baldwin Universal Test Machine is used to provide the torque by pulling a steel cable wound on one of the torque arms. The torque can be calculated from the tensile load in the cable, the load being measured by a strain-gage type load cell. The apparatus is designed so that the shaft to which the torque arms are welded can freely slide axially while rotating. This arrangement is necessary to reduce the combined coupling effects between axial load, torque, and internal pressure. The final version of the multiaxial stress test apparatus has been designed and is currently under construction.

2. Torsion Tests of JT-50 Composite Material

Four solid torsion specimens of JT-50 material have been tested. The overall length of the specimens was approximately 3.5 inches; the gauge section was 0.75 inch in diameter and 2.0 inches in length. The cylinder axis was oriented parallel to the symmetry axis of the material. Shear strain and longitudinal strain were measured with pairs of strain gages. The shear stress as a function of the shear-strain curve and the

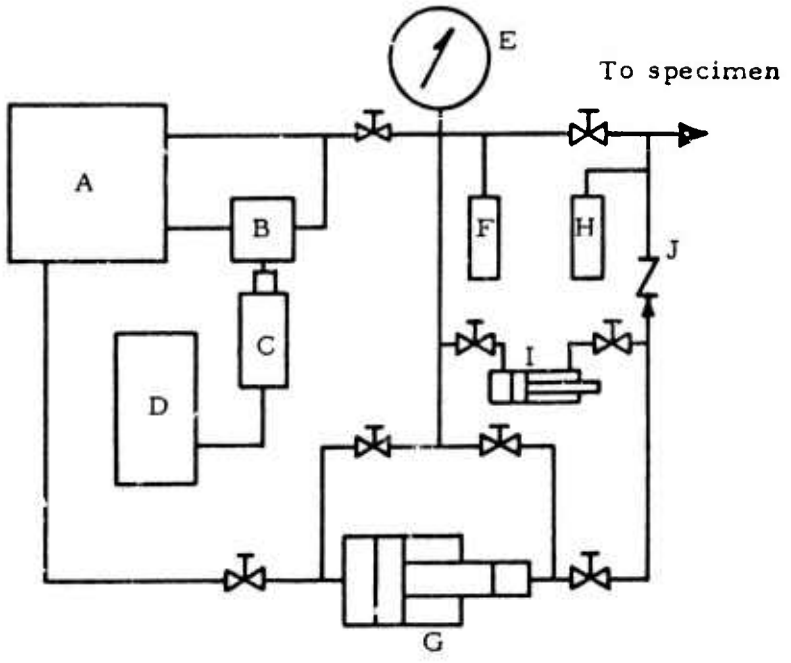

A. Hydraulic Pump (0-5, 000 psi)
B. Pressure Relief Valve
C. Linear Actuator
D. Control Box for Linear Actuator
E. Pressure Gage (0-5, 000 psi)
F. Pressure Transducer (0-5, 000 psi)
G. Pressure Intensifier (0-50, 000 psi)
H. Pressure Transducer (0-20, 000 psi)
I. Hydraulic Cylinder (0-10, 000 psi)
J. Pressure Check Valve

N-16890

Figure 9. Schematic Diagram of Hydraulic System for Multiaxial Stress Test Apparatus.

shear stress as a function of the longitudinal strain curve are shown in Figures 11 and 12 for one of the specimens. The stress-strain behavior for these specimens is similar to their uniaxial stress-strain behavior: nonlinear and nonconservative.

Since the torque, shear-strain curve for JT-series composites is nonlinear and nonconservative, Nadai's graphical method[7] was employed to obtain the shear-stress, shear-strain relationship from the torque, shear-strain curve. The shear properties for these specimens are also given in Table VIII. The shear-strain for specimen 1 was not properly recorded and, therefore, cannot be us ed for construction of the shear stress as a function of shear-strain curve. The nonlinearity correction on shear strength is approximately 9 percent.

The shear modulus and shear strength tend to increase and the shear strain to decrease with increasing density. The value of the shear strength is approximately 10 to 20 percent greater than the tensile strength in the across-grain direction. The specimens exhibited a small longitudinal elongation. Length changes in plastically twisted circular metal specimens have been observed by Swift.[8] The inherent characteristics of the torsion test and the anisotropy of the materials are believed to be

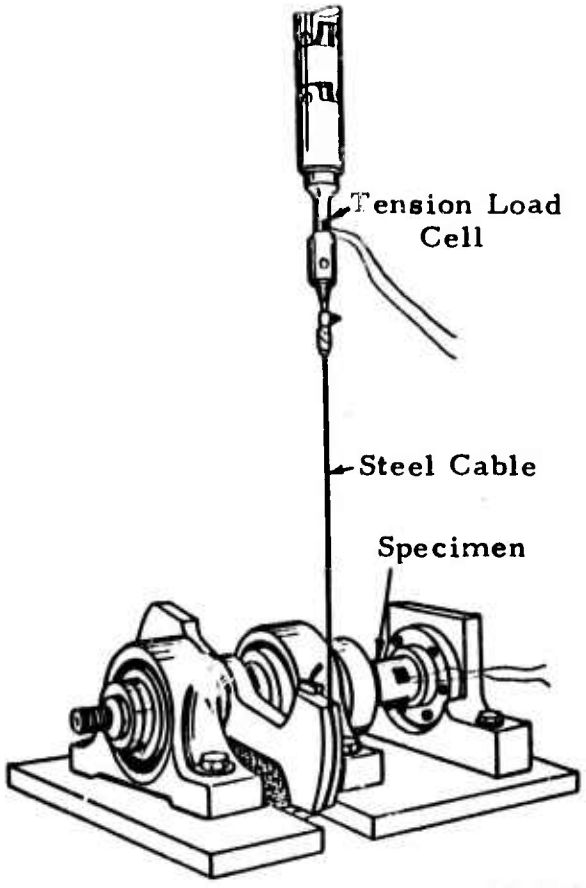

N-10143

Figure 10. Torsion Testing Machine.

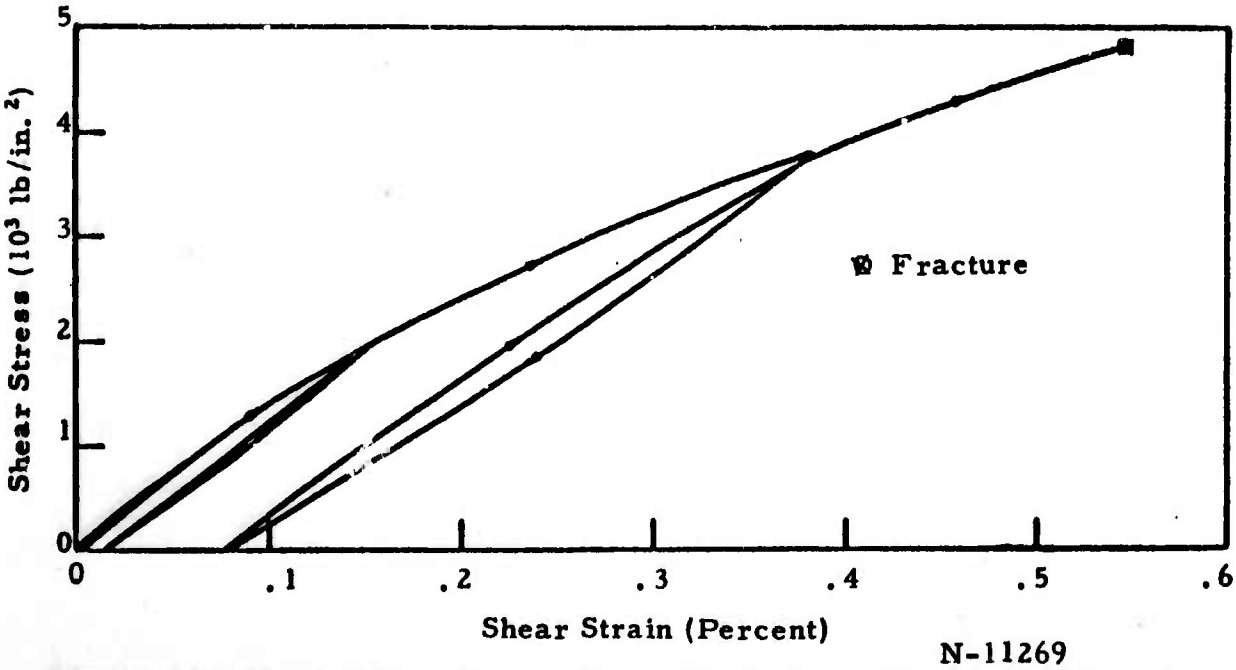

N-11269

Figure 11. Shear-Stress Versus Shear-Strain Curve for JT-50 Material.

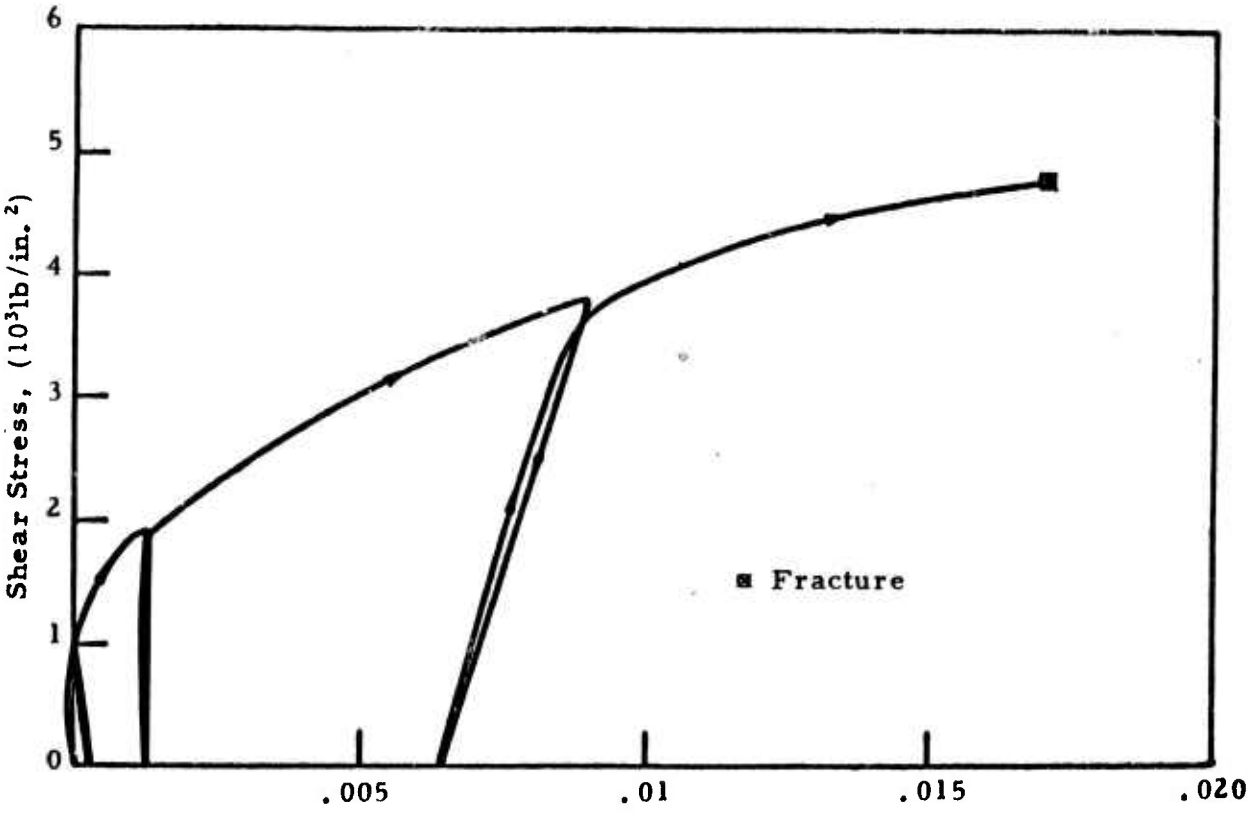

N-11270

Figure 12. Shear-Stress Versus Longitudinal-Strain Curve for JT-50 Composite Material.

TABLE VIII

SHEAR PROPERTIES FOR JT-50 COMPOSITE MATERIAL

Specimen	Density (g/cm^3)	Shear Modulus $1/s_{44}$ (10^6 lb/in.^{2}) sonic	static	Shear Strength (lb/in.^{2}) uncorrected	corrected	Shear Strain (percent)	Long. Strain (percent)
1	2.934	2.11	-	5750	-	-	0.01
2	2.931	2.11	1.98	5160	4740	0.55	0.03
3	3.014	2.27	2.43	6160	5630	0.44	0.03
4	3.012	2.28	2.43	6690	6080	0.48	0.04

the source of this phenomenon.([7,8,9]) The theory of anisotropic plastic flow developed by Hill([9]) also supports the explanation of the length change due to the anisotropy of the materials.

3. Failure Criteria for Nominal 50 Percent Additive JT-Composite Material

The fracture strength surface for JT-50 composite material has been determined. The fracture strength in the compression-tension quadrant ($-\sigma_{u3}$ and σ_{u1}) reported in Section V E of the First Annual Report[1] was obtained by the combination of internal pressure and axial compressive load. The fracture strengths in the other 3 stress-state quadrants were obtained by testing the specimens under combinations of external, internal, and axial end pressures in the pressure chamber shown in Figure 13. Strain gages were mounted on the outside surface of the test specimens to measure the hoop and longitudinal strains as well as to detect bending in the test specimens.

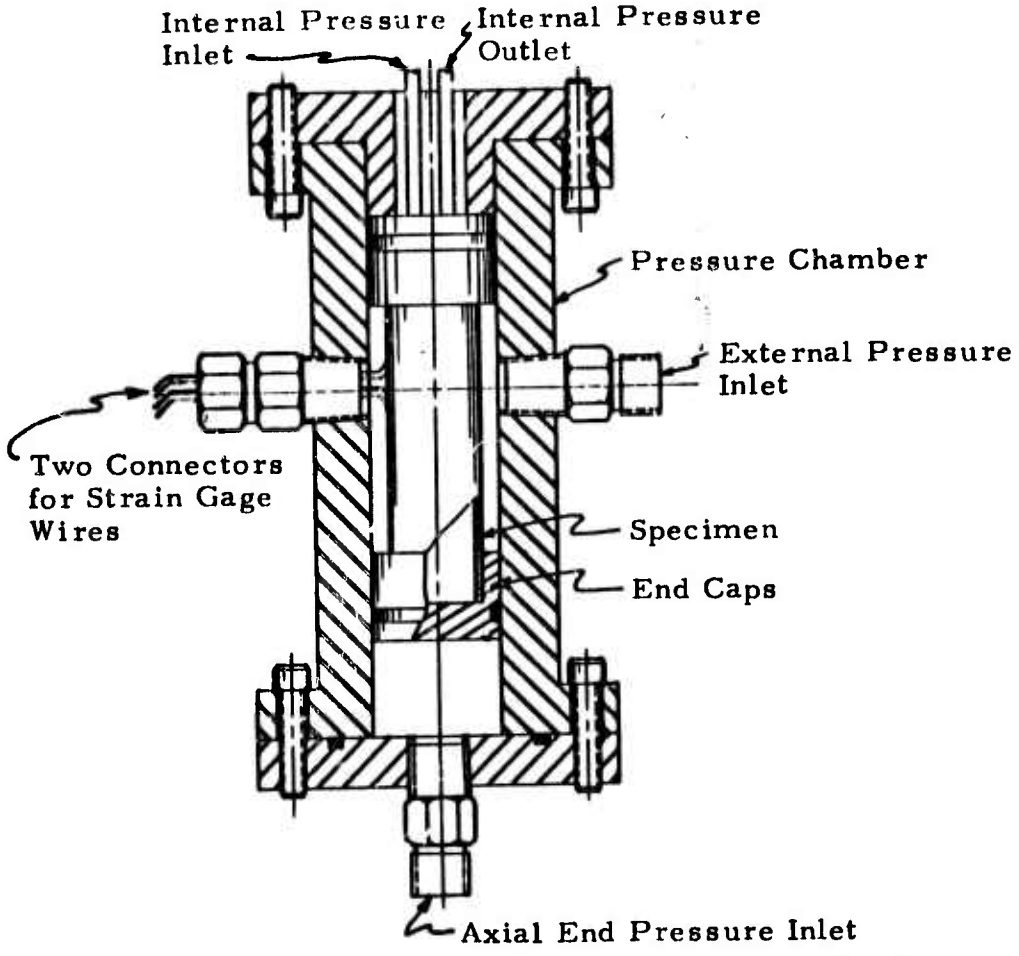

Figure 13. Pressure Chamber Assembly for Biaxial Stress Test.

Effects of the loading path on the nonlinear and nonconservative stress-strain behavior under combined stress states have been investigated with grade ATJ graphite. Since the strains were found to be dependent on the loading path, the stress-strain relation is also dependent on

the loading path. The effect of the loading path on the fracture strength was negligible. Because of the similarity between the stress-strain behavior of grade ATJ graphite and that of the JT-50 composite, the fracture stress surface of the JT-50 composite should also be independent of the loading paths under which the specimens were tested.

The fracture strength surface of JT-50 composite material is shown in Figure 14. Most of the scatter in the fracture strengths is probably due to the variation of porosity of the specimens. The estimated fracture strength surfaces for the isoporosities of 5, 10, and 15 percent are also shown in Figure 14. Since a maximum porosity limit for grade JTA is 8 percent, the fracture strength surface of grade JTA can be estimated from Figure 14. The shape of the fracture strength surface in the first and fourth stress-state quadrants is similar to the fracture strength surface for brittle materials, such as cast and inoculated irons.[10,11,12] An attempt will be made to determine how well the existing theories of fracture fit the experimental data on the JT-50 composite material.

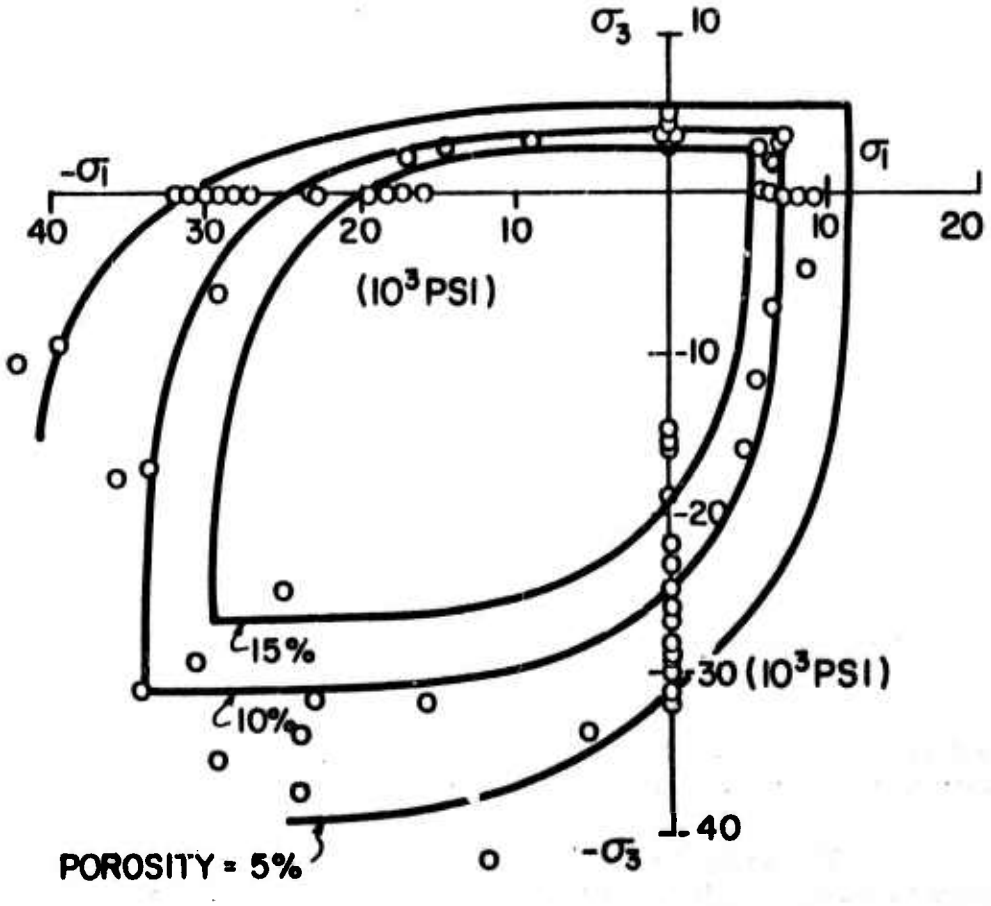

N-16943

Figure 14. Fracture Strength Surface of Nominal JT-50 Percent Additive Composite Material.

D. Statistical Aspects of Failure - Application to Grade JTA Graphite Composite Material

(J. Y. L. Ho and F. M. Anthony, Bell Aerosystems)

The basic purposes of this study were to investigate the importance of statistical considerations on material failure criteria with specific application to anisotropic particulate grade JTA graphite composite, and to investigate the practicality of predicting off-axis statistical strength behavior from measurements made in each of the major material axes. If the statistical nature of uniaxial strength under off-axis loadings can not be predicted from strength measurements in the major material directions, it is unlikely that multiaxial statistical strength behavior can be predicted from uniaxial measurements in the major material directions.

The interaction of probability of failure and multiaxial stress states was discussed in Section V D of the First Annual Report, (Reference 1). The failure surface of brittle materials was assumed to have an "ashtray" shape. Such a surface can be developed experimentally, but only at great expense. It was considered appropriate, therefore, to investigate a portion of the surface - the first quadrant - to see if a combination of analysis and select experiments could reduce the effort required by experiments alone.

1. Test Conducted and Analysis of Results

A JTA billet, 7-1/2 inches in diameter x 6 inches high, was cut into 1/2-inch thick slabs. Each slab was cut and machined to standard size bend bars (3.5 x 0.2 x 0.2 - inches) at the following angles with respect to the grain direction:

(a)	0° (with grain)	- 50 bars
(b)	30°	- 49 bars
(c)	60°	- 43 bars
(d)	90° (across grain)	- 42 bars

An attempt was made to cut the billet so as to obtain samples of different orientations from various locations in the billet.

Four-point bending tests were conducted with each sample supported on 3-inch centers and loaded on 1-inch centers. Failure loads were measured and maximum bending stresses were calculated.

The maximum bending stresses σ at the surfaces of the bars were calculated from $\sigma = Mc/I$ (where M is the applied moment, c is half the bar height and I is the moment of inertia of the bar cross-section) with no corrections made for material nonlinearity or for differences between tensile and compressive elastic moduli.

Since the flaws existing in the material are random in size and orientation, the rupture stresses of the test bars will be of statistical nature. The Weibull distribution function is assumed to apply, thus the probability of failure distribution function in terms of the maximum bending stress, σ^*, is

$$F(\sigma^*) = 1 - \exp\left[- \frac{V_b}{2(m+1)} \frac{(\sigma^* - \sigma_u)^{m+1}}{\sigma_0^m \sigma^*} \right] \qquad \text{(IIID-1)}$$

In equation IIID-1, $F_r = \frac{r}{N+1}$ ($r = 1, 2, 3 \ldots N$), r is the order of stress as listed in increasing order, and N is the total number of specimens in the population. The experimental data points (F_r, σ_r^*) are usually scattered near the distribution curve. To determine the constants σ_u, σ_0 and m so that the estimated distribution curve will best fit to the data points, a minimizing process is used which is similar to that described in Reference 13 for tensile loading.

Equation IIID-1 can be transformed into a linear function

$$y = (m+1)\,x - m \ln \sigma_0 + \ln \frac{V_b}{2} - \ln (m+1) \qquad \text{(IIID-2)}$$

where

$$y = \ln \ln \frac{1}{1-F} + \ln \sigma^* \qquad \text{(IIID-3)}$$

$$x = \ln (\sigma^* - \sigma_u) \qquad \text{(IIID-4)}$$

Equation IIID-2 represents a straight line relation between the two variables y and x. The experimental data points (F_r, σ_r^*) are also transformed into the y-x plane by the following transformation.

$$y_r = \ln \ln \frac{1}{1-F_r} + \ln \sigma_r^* \qquad \text{(IIID-5)}$$

$$x_r = \ln (\sigma_r^* - \sigma_u) \qquad \text{(IIID-6)}$$

By the method of least squares, the sum of squares of deviations from the data points to the estimated straight line is

$$S = \sum_{r=1}^{N} \left[\Delta y_r \right]^2 = \sum_{r=1}^{N} \left[y_r - y(\sigma_r^*) \right]^2 \qquad \text{(IIID-7)}$$

$$S = \sum_{r=1}^{N} \left[y_r - (m+1) \ln (\sigma_r^* - \sigma_u) + m \ln \sigma_0 - \ln\left(\frac{V_b}{2}\right) + \ln (m+1) \right]^2 \qquad \text{(IIID-8)}$$

For any given set of experimental data, the value of S is a function of the three variables σ_u, σ_0 and m. In order to minimize the value of S, the partial derivatives of S with respect to the three variables σ_u, σ_0 and m must vanish simultaneously. After the partials are removed, the Weibull constants can be found by solving three simultaneous equations. From $\frac{\partial S}{\partial \sigma_0} = 0$ and $\frac{\partial S}{\partial m} = 0$, the following relations are obtained.

$$m = m' = \frac{A_1 A_3 - N A_2}{A_3^2 - N A_4} - 1 \qquad \text{(IIID-9)}$$

$$\ln \sigma_0 = \ln \sigma_0' = \frac{1}{N m'} \left[-A_1 + (m'+1) A_3 + N \ln \frac{V_b}{2} - N \ln (m'+1) \right] \qquad \text{(IIID-10)}$$

If one substitutes Equation IIID-9 and IIID-10 into the expression for $\frac{\partial S}{\partial \sigma_u} = 0$, the residual function can be defined as

$$R(\sigma_u) = 2 (m'+1) \left\{ A_5 - (m'+1) A_6 + \left[m' \ln \sigma'_0 - \ln \frac{V_b}{2} + \ln (m'+1) \right] A_7 \right\} \qquad \text{(IIID-11)}$$

where

$$A_1 = \sum_{r=1}^{N} y_r \qquad \text{(IIID-12)}$$

$$A_2 = \sum_{r=1}^{N} y_r \ln (\sigma_r^* - \sigma_u) \qquad \text{(IIID-13)}$$

$$A_3 = \sum_{r=1}^{N} \ln (\sigma_r^* - \sigma_u) \qquad \text{(IIID-14)}$$

$$A_4 = \sum_{r=1}^{N} \left[\ln (\sigma_r^* - \sigma_u) \right]^2 \qquad \text{(IIID-15)}$$

$$A_5 = \sum_{r=1}^{N} \frac{y_r}{(\sigma_r^* - \sigma_u)} \qquad \text{(IIID-16)}$$

$$A_6 = \sum_{r=1}^{N} \frac{\ln(\sigma_r^* - \sigma_u)}{(\sigma_r^* - \sigma_u)} \qquad \text{(IIID-17)}$$

$$A_7 = \sum_{r=1}^{N} \frac{1}{(\sigma_r^* - \sigma_u)} \qquad \text{(IIID-18)}$$

Since A_i ($i = 1, 2, 3 \ldots 7$) are functions of σ_u, m' and $\ln \sigma_0'$ are also functions of σ_u. Hence, the residual function $R(\sigma_u)$ is a function of only one variable, σ_u. A computer program was set up to estimate successively the value of σ_u until

$$R(\sigma_u') = 0 \qquad \text{for} \qquad \sigma_u = \sigma_u' \qquad \text{(IIID-19)}$$

The partial derivatives of S with respect to σ_0, m and σ_u will vanish simultaneously when $\sigma_0 = \sigma_0'$, $m = m'$ and $\sigma_u = \sigma_u'$. The values of m' and σ_0' can be calculated from Equations IIID-9 and IIID-10 respectively with the values of A_i ($i = 1, 2, \ldots 7$) evaluated at $\sigma_u = \sigma_u'$.

Table IX shows the Weibull constants σ_u, σ_0 and m from the experimental data of four populations by the computer program.

TABLE IX

DETERMINATION OF WEIBULL CONSTANTS ($\sigma_u > 0$)

Grain Direction	N	σ_u (psi)	σ_0 (psi)	m
0°	50	6285	1762.8	3.231
30°	49	6533	1427.7	3.2584
60°	43	8323	383.5	3.1942
90°	42	5875	66.7	1.5327

Weibull constants were also computed with the assumption that the threshold stress of the material in all directions was zero, i.e., $\sigma_u = 0$, as shown in Table X.

TABLE X

DETERMINATION OF WEIBULL CONSTANTS ($\sigma_u = 0$)

Grain Direction	N	σ_u (psi)	σ_0 (psi)	m
0°	50	0	6788	6.424
30°	49	0	6759	7.3268
60°	43	0	7307	14.6711
90°	42	0	4300	8.1174

The Weibull distribution curves based on the estimated Weibull constants in the above tables are plotted in Figure 15 ($\sigma_u > 0$) and Figure 16 ($\sigma_u = 0$). In both cases, the curves fit the data points quite well.

The maximum bending rupture stresses at various probability of failure levels are calculated and plotted in Figure 17 ($\sigma_u > 0$) and Figure 18 ($\sigma_u = 0$). At high probability of failure levels, these bending rupture stresses show a "modified cosine" type of decrease as the angle of grain direction increases from zero to 90°, a performance which represents the strength characteristics of the anisotropic material. At very low probability of failure levels, this type of decrease in rupture strength does not hold. The rupture strengths of 60° bars fall into a very narrow range, indicating higher rupture strength at very low probability of failure levels compared with those at other angles of grain direction.

These predictions are solely dependent upon the available experimental results. Although the data points of each angle of grain direction can provide a statistical distribution curve, the rupture stress of each individual bar is dominated by the flaws existing in the particular portion of the material. The 60° bars may not vary as much as bars from other orientations. But this condition is not too likely, since an attempt was made to obtain samples of a particular orientation from various locations in the billet. Experimental shortcomings are also unlikely to have influenced only the 60° bars since the same personnel conducted all tests using the same equipment. A more likely possibility is that the mechanism of micro-fracture of JTA may have some type of transition as the angle between the grain direction of the material and the principal stress direction changes from 0° to 90°. The source of this apparent anomaly can be resolved only by more extensive investigations. Possible approaches include detailed examination of the fracture surface or additional tests using other billets. Without such studies, which are beyond the scope of the present effort, no firm conclusions can be made.

Angle	N	σ_u	σ_0	m
0°	50	6288	1762.8	3.231
30°	49	6533	1427.7	3.2589
60°	43	8325	383.5	3.1942
90°	42	5875	66.7	1.5327

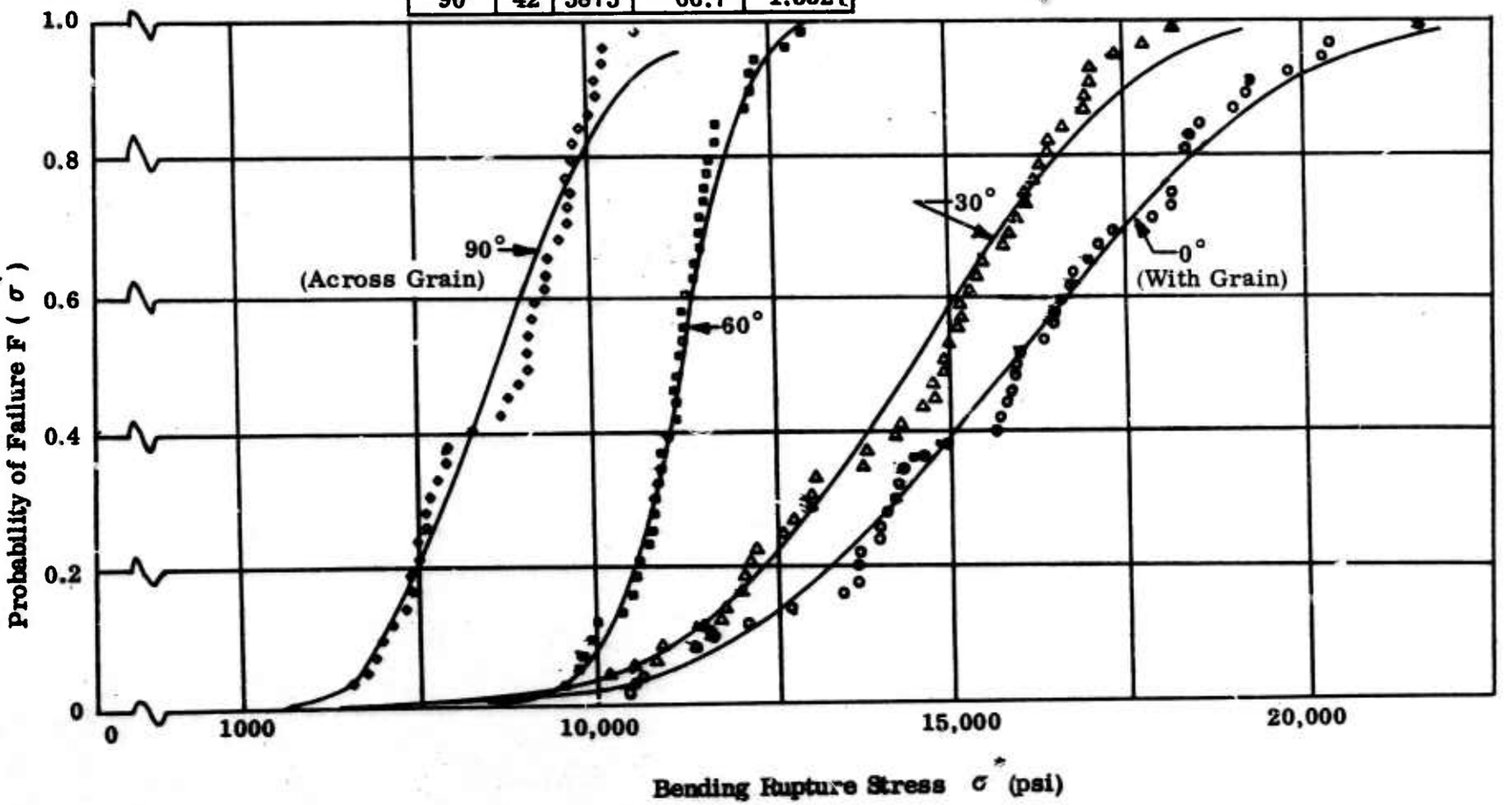

Figure 15. Cumulative Distributions Functions, $\sigma_u > 0$.

Angle	N	σ_u	σ_o	m
0°	50	0	6788	6.424
30°	49	0	6759	7.3268
60°	43	0	7307	14.6711
90°	42	0	4300	8.1174

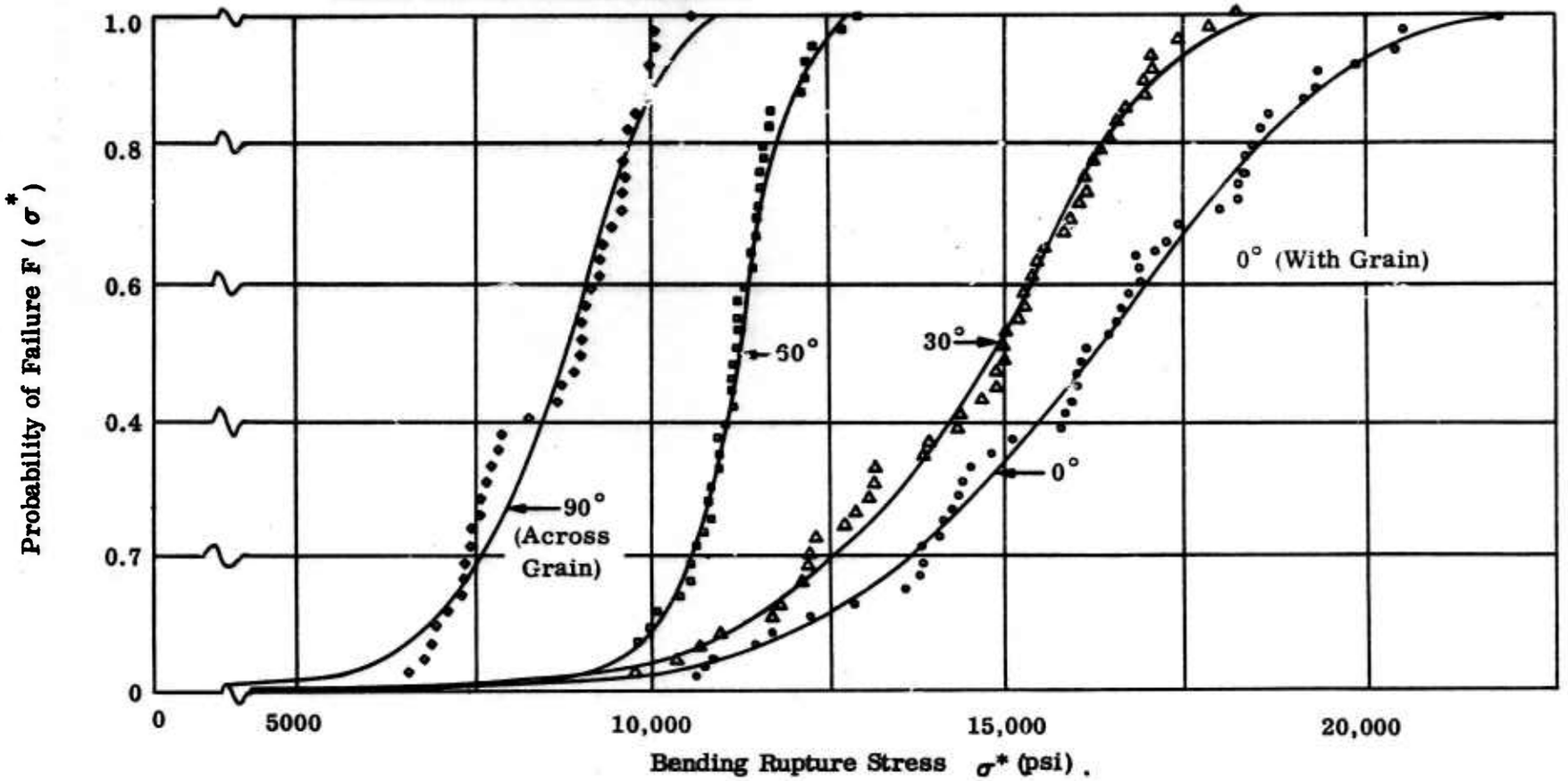

Figure 16. Cumulative distribution Functions, $\sigma_u = 0$.

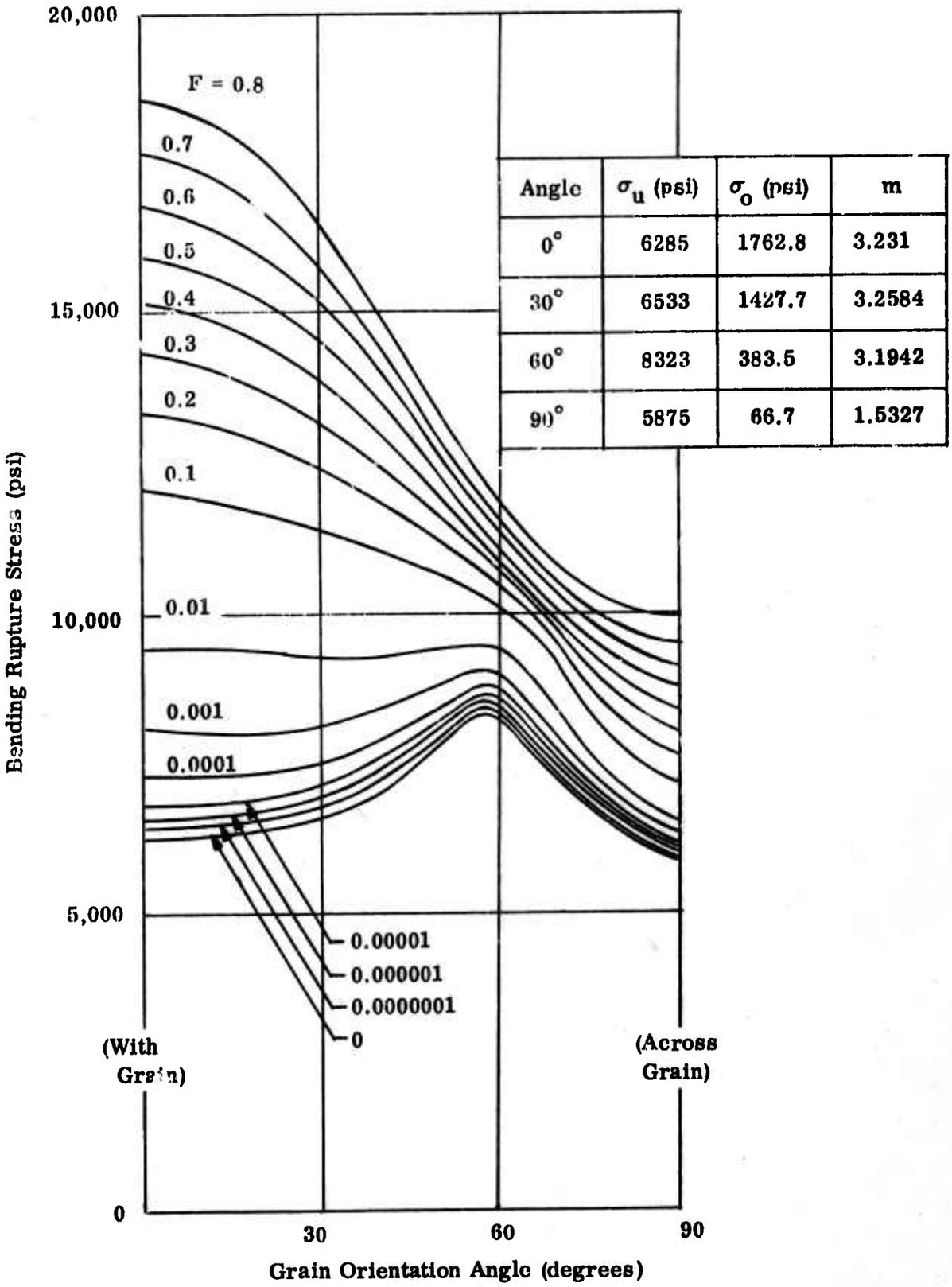

Angle	σ_u (psi)	σ_o (psi)	m
0°	6285	1762.8	3.231
30°	6533	1427.7	3.2584
60°	8323	383.5	3.1942
90°	5875	66.7	1.5327

Figure 17. Strength versus Grain Orientation at Various Probabilities of Failure, $\sigma_u > 0$.

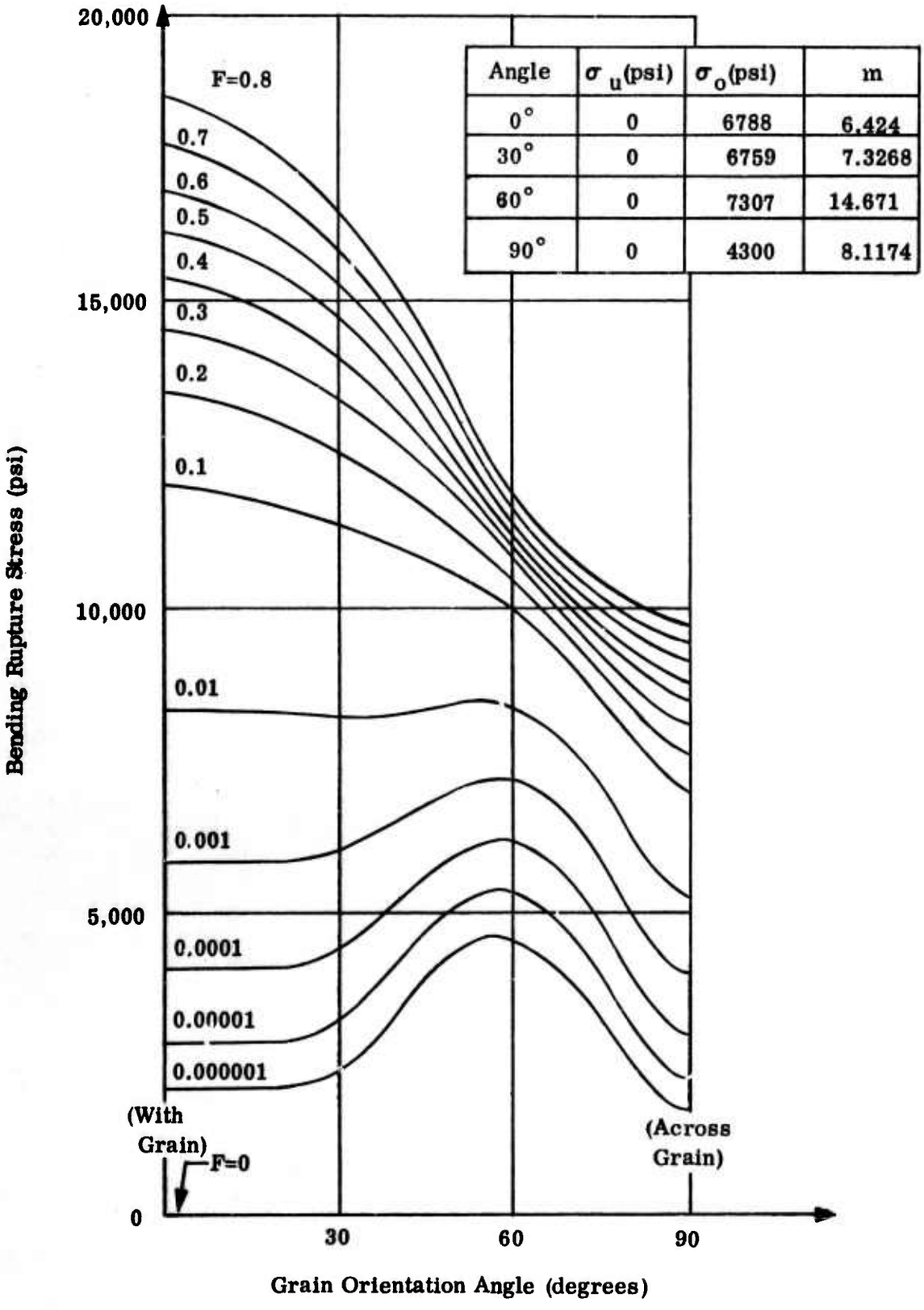

Angle	σ_u (psi)	σ_o (psi)	m
0°	0	6788	6.424
30°	0	6759	7.3268
60°	0	7307	14.671
90°	0	4300	8.1174

Figure 18. Strength versus Grain Orientation at Various Probabilities of Failure, $\sigma_u = 0$.

2. Failure Predictions

A major goal of this investigation was to examine the practicality of predicting the statistical strength distributions of the JTA particulate composites at any direction with respect to the principal material orientation axes from statistical data obtained in the two principal directions. The experimental data at 30° and 60° orientations could then be used to assess the suitability of the hypotheses employed. Three approaches were examined. First, the Weibull constants were assumed to vary linearly with angle of orientation. Second, the Weibull constants were assumed to vary as a trigonometric function which passed through the values at 0° and 90° in such a manner that the slope of the function was zero at these two orientations. This assumption preserves continuity of the function for both positive and negative values of orientation angles. Third, the assumption was made that failure at an off-angle could be predicted directly from the statistical data obtained at 0° and 90° by resolving the applied stress into the two principal material directions and treating the probability of survival of the sample as the product of the probabilities of survival in each direction.

The estimated Weibull constants of the distribution curves at various angles of grain directions are plotted in Figure 19. Obviously straight line or trigonometric functions based on 0° and 90° data alone would not provide good predictions of this unusual behavior. The degree of error due to such functional variations of Weibull parameters with angle was then determined.

The linear approximation had the form

$$(C)\ \phi = \frac{\phi}{90^\circ}\,(C)_{90^\circ} + \left[\,1 - \frac{\phi}{90^\circ}\,\right]\,(C)_{0^\circ} \qquad \text{(III D-20)}$$

The trigonometric function had the form

$$(C)\ \phi = (C)_{90^\circ} \sin^2 \phi + (C)_{0^\circ} \cos^2 \phi \qquad \text{(III D-21)}$$

The C's represent the Weibull constants σ_u , σ_0 and m.

The distribution curves based on the constants predicted with the linear function are plotted in Figure 20, do not coincide with 60° and 30° data. The fit with the trigonometric function was no better. The third approach gave the poorest correlation. The probability of failure is related to the probability of survival by F = 1 - S. If events are unrelated, the probability of survival of a component is the product of the probability of its surviving each event, i.e., $S = S_1 \times S_2 \ldots$, However, when the applied stress is resolved into components in the principal directions and the probability of survival under these normal stresses are computed, the resultant probability of component (test bar) failure is much less than the probability obtained experimentally. As applied, this approach neglects the influence of the shear stresses resulting from the rotation of stresses to the principal material directions. Inclusion of shear effects

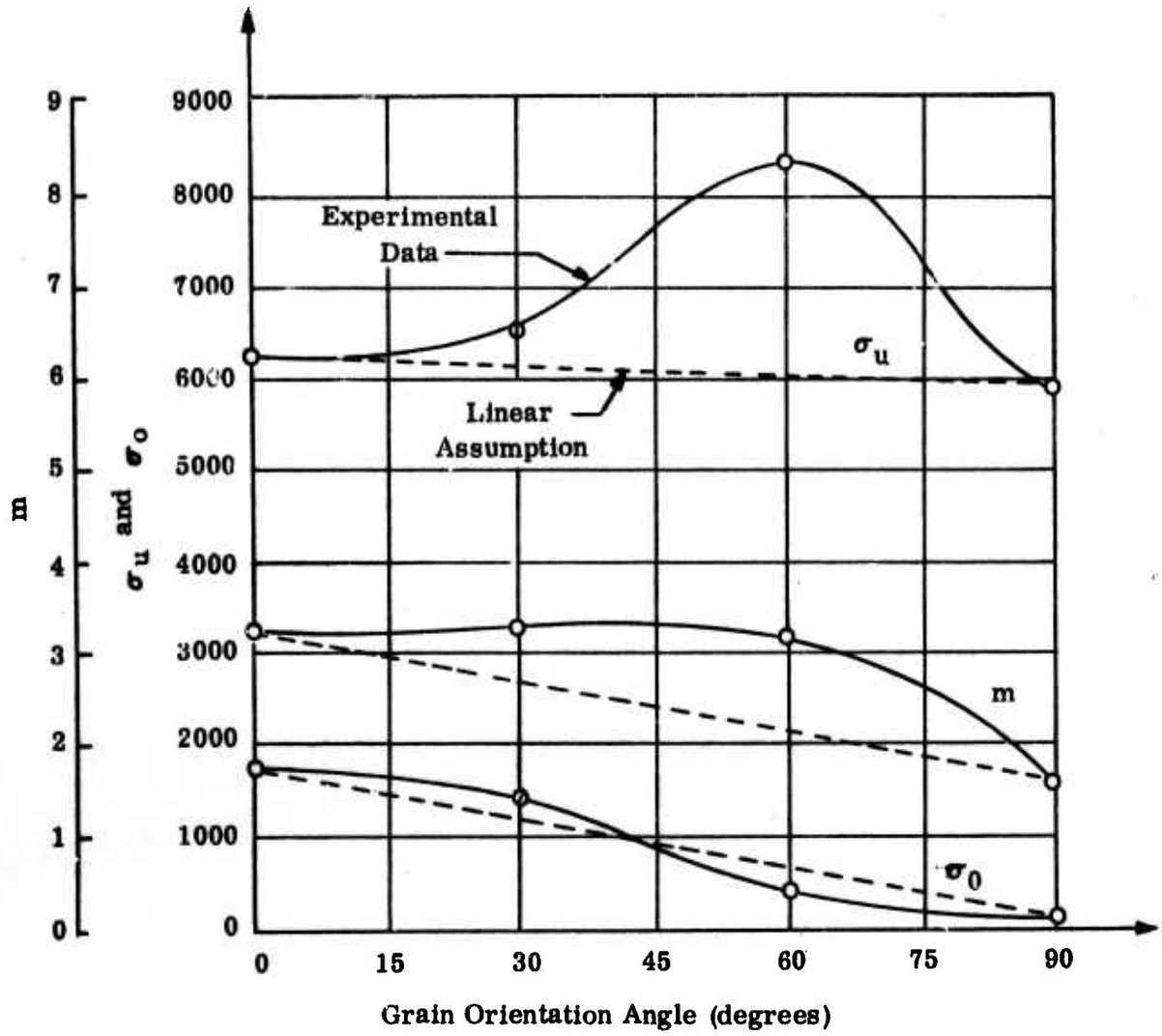

Figure 19. Weibull Constants as Functions of Grain Orientation.

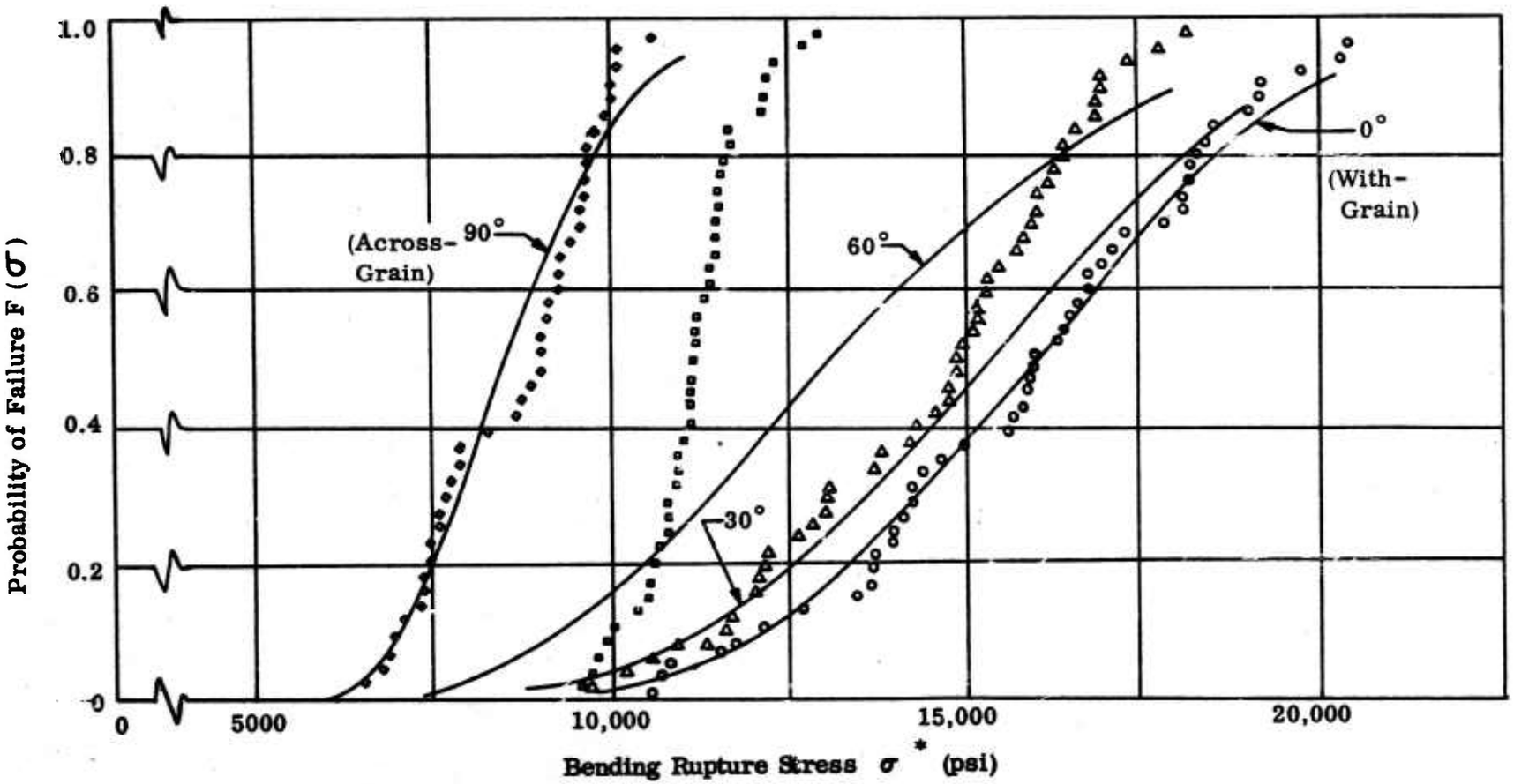

Figure 20. Predicted Distribution Curves at 60° and 30° Orientation, Linear Variation of Weibull Constants .

might improve the correlation, but, unfortunately, shear strength data are lacking. At this time, the statistical behavior of the JTA material, and perhaps other particulate anisotropic composites, can be determined only experimentally by evaluating samples cut at various angles to the principal material directions.

The data generated during this study, however, provide some verification of the "Ashtray" failure concept presented in First Annual Report, Section V D, (Reference 1).

Bending rupture stresses for JTA bend bars with various grain directions at different probability of failure levels F = 0.8, 0.2, 0.01 and 0 are plotted in polar coordinates as shown in Figure 21. For different assumptions ($\sigma_u > 0$ and $\sigma_u = 0$), the deviations from the elliptical shape that may have been expected are small at high F values and become larger as the F values decrease. These failure criteria are not the same as the conventional failure criteria because the maximum bending rupture stress (which is also the principal stress) is not in the same direction as the principal material direction for 30° and 60° bars.

A similar situation is apparent if the stress applied to a bar of arbitrary material orientation is resolved into normal components in the principal material directions. Figure 22 shows the normal stresses in the with-grain and across-grain directions due to the bending stress in a bar cut at an angle ϕ from the with-grain direction. The pictorial insert illustrates the resolution of the applied stress, σ_ϕ *, into two normal stresses and the shear stress (σ_ϕ *)$_{0°}$, (σ_ϕ *)$_{90°}$ and τ_ϕ respectively. In an approximate way, Figure 22 resembles the first quadrant of a biaxial failure criteria diagram. Of importance is the fact that the constant probability of failure contours change quite radically in shape at low probability of failure levels. The fact that shear stresses have been neglected will not alter this trend. If the shear effect is independent of the probability of failure, the relative shapes of the probability of failure contours would not change. If the shear effect is a function of probability of failure it is very unlikely that the functional relationship would cancel the observed trends for the normal stresses. These conclusions can have a significant influence on structural design efforts with particulate materials. There is an implication that the current procedure of verifying a multiaxial failure criterion, through the use of relatively few data points at various stress ratios, may lead to serious errors when brittle components of high reliability are to be designed.

As a result of this investigation, the following conclusions were reached.

(1) A statistical approach is required to achieve high reliability in predictions of failure.

(2) The shape of the failure criteria is a function of probability of failure.

(3) Interpolation of rupture strength statistical distributions at off-axis angles between major directions can lead to serious errors.

(4) Presently available data are insufficient to permit statistically significant predictions of failure contours.

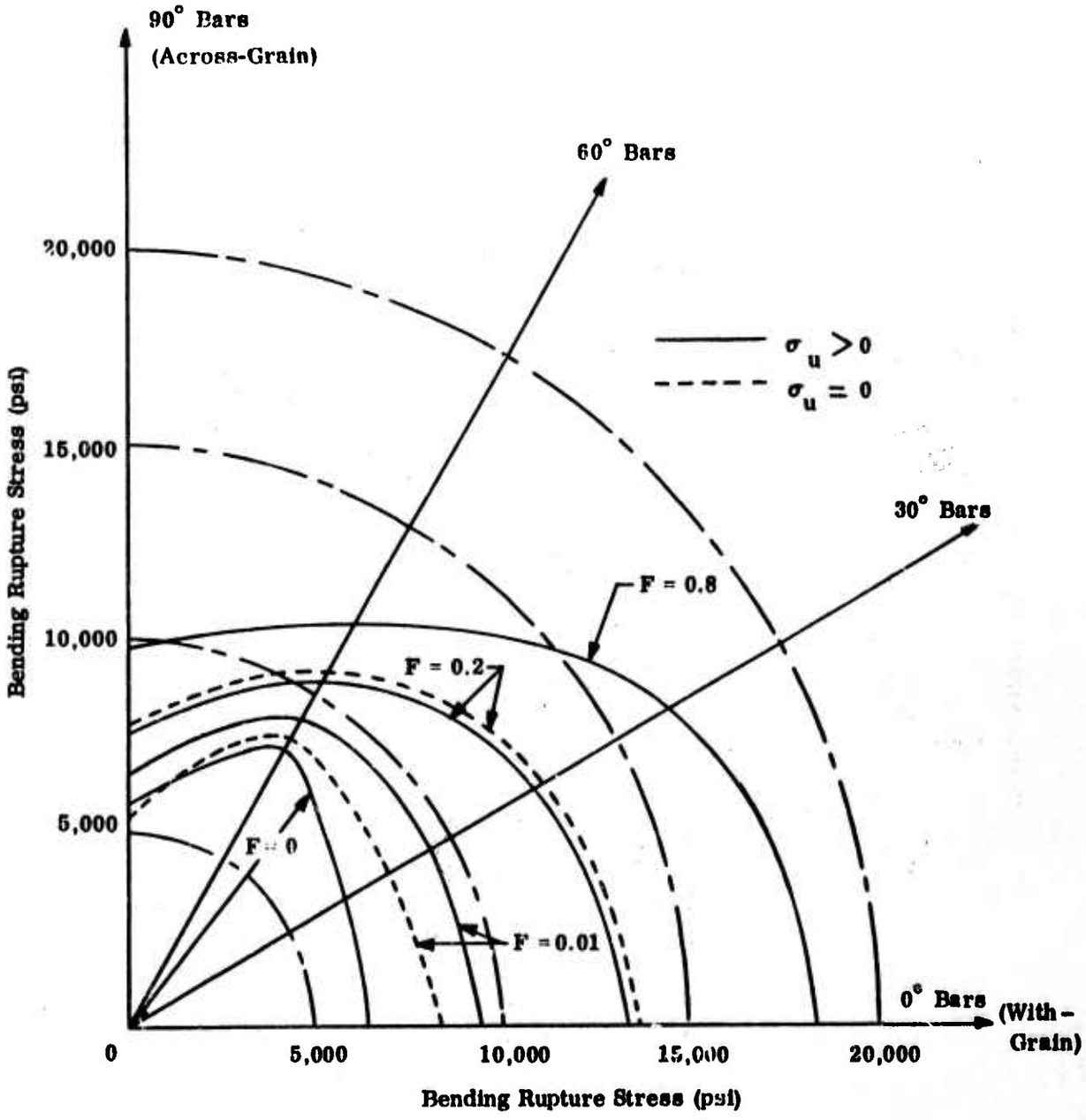

Figure 21. Bending Rupture Stresses of JTA Bend Bars with Various Grain Directions.

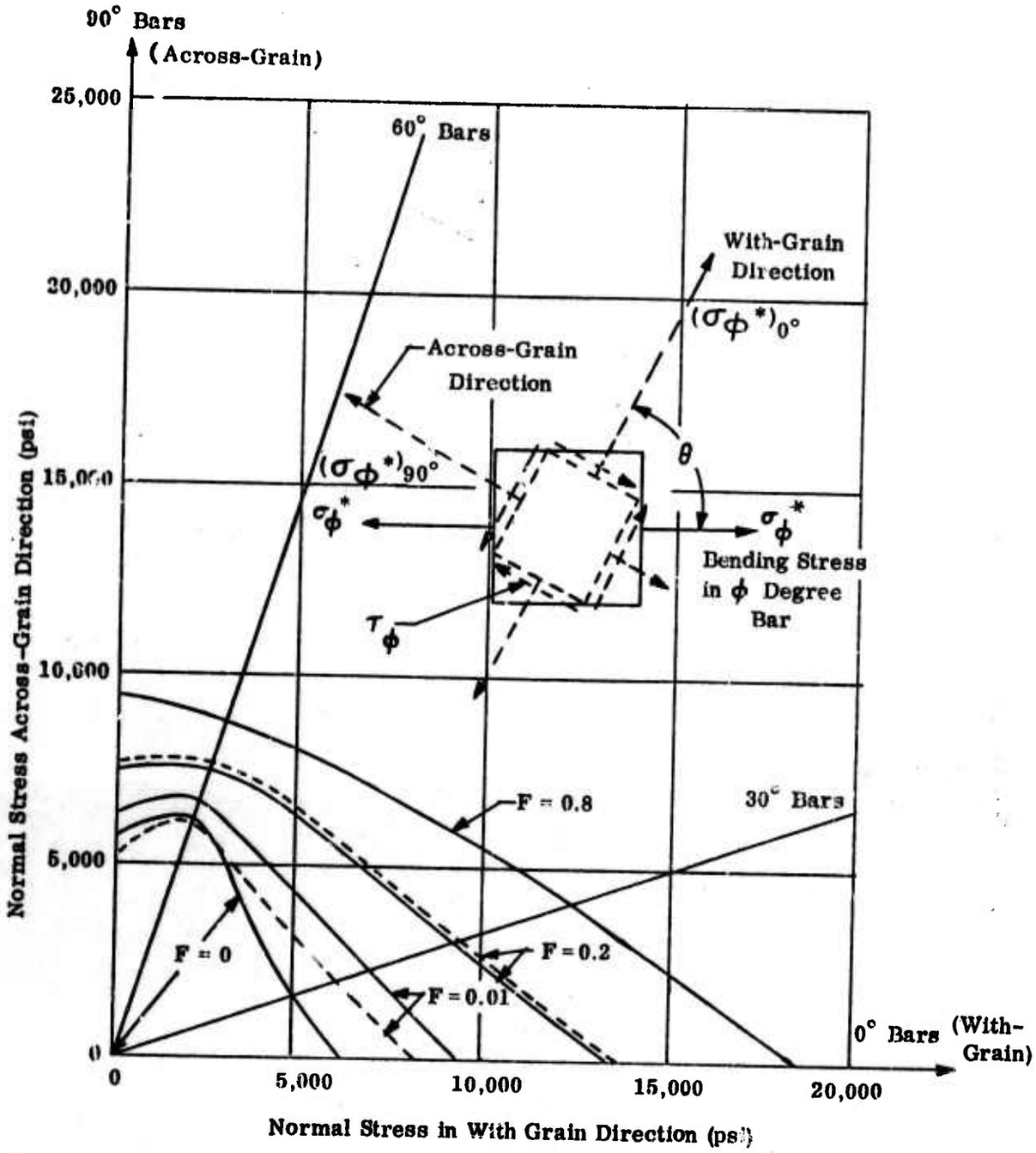

Figure 22. Normal Stresses in With-Grain and Across-Grain Directions Due the Bending Stress in ϕ-Degree Bars .

E. Analysis and Synthesis of Three Layer Cylinder - Application to JT Series Materials

(Professor Schmit and Mr. V. Genberg)

The structural synthesis study of an axially symmetric three layered thick-walled circular cylinder subject to high thermal and pressure loading on the inner surface has been completed. This idealized representative component was selected because it exhibits many of the characteristics found in certain high temperature nozzle inserts and thrust chambers.

Each of the three layers can be a cylindrically orthotropic material with temperature-dependent thermal and mechanical material properties. The internal radius (r_a) (see Figure 23) and the material properties are preassigned parameters. The individual layer thicknesses (D_1, D_2, and D_3) are the design variables. Each of several distinct load conditions is specified by giving the internal and external pressure and temperature as functions of time (the option to specify the heating rate as a function of time on the inner surface is included). The failure modes guarded against in each load condition include temperature and radial displacement limits as well as failure under combined stress. The objective function is assumed to be minimization of the weight per unit length of the cylinder. The thermal and stress analyses employed in this study will be found in Section V-F of the First Annual Report[1] and the synthesis algorithm used is a feasible directions method described in Section IX B5 of the same report. The further development of a preprogrammed feasible directions procedure is described in Section IX D of this report. The results and conclusions of this completed project are given in Reference 14.

Minimum weight optimum designs have been obtained for several example cases. In each case the outer layer is 6061 aluminum alloy, the middle layer is V204 asbestos felt, and the inner layer is a member of the JT particulate composite family. The internal radius and the load condition information summarized in Table XI were provided by Bell Aerosystems and are intended to be representative thrust chamber temperature and pressure conditions. Material property information for the two outer layers was obtained from Bell Aerosystems and the material property information on each of nine JT candidate materials for the inner layer was obtained from Union Carbide. Minimum weight designs have been obtained using each of eight JT candidate materials for the inner layer. The optimum designs found using the structural synthesis program are summarized in Table XII. Comparing the eight discrete optimum designs in Table XII, it is seen that the lightest weight is achieved with the JT 30-15%* porosity material (Figure 24).

The weight of each optimum design listed in Table XII is plotted versus the porosity and the percent additive in Figure 25. A materials evaluation function (MEF) expresses the merit of a material in a particular application as a function of variables which characterize the material within its class.

*The designation JT 30-15% refers to a JT series graphite composite containing 30% metallic additive and having 15% porosity.

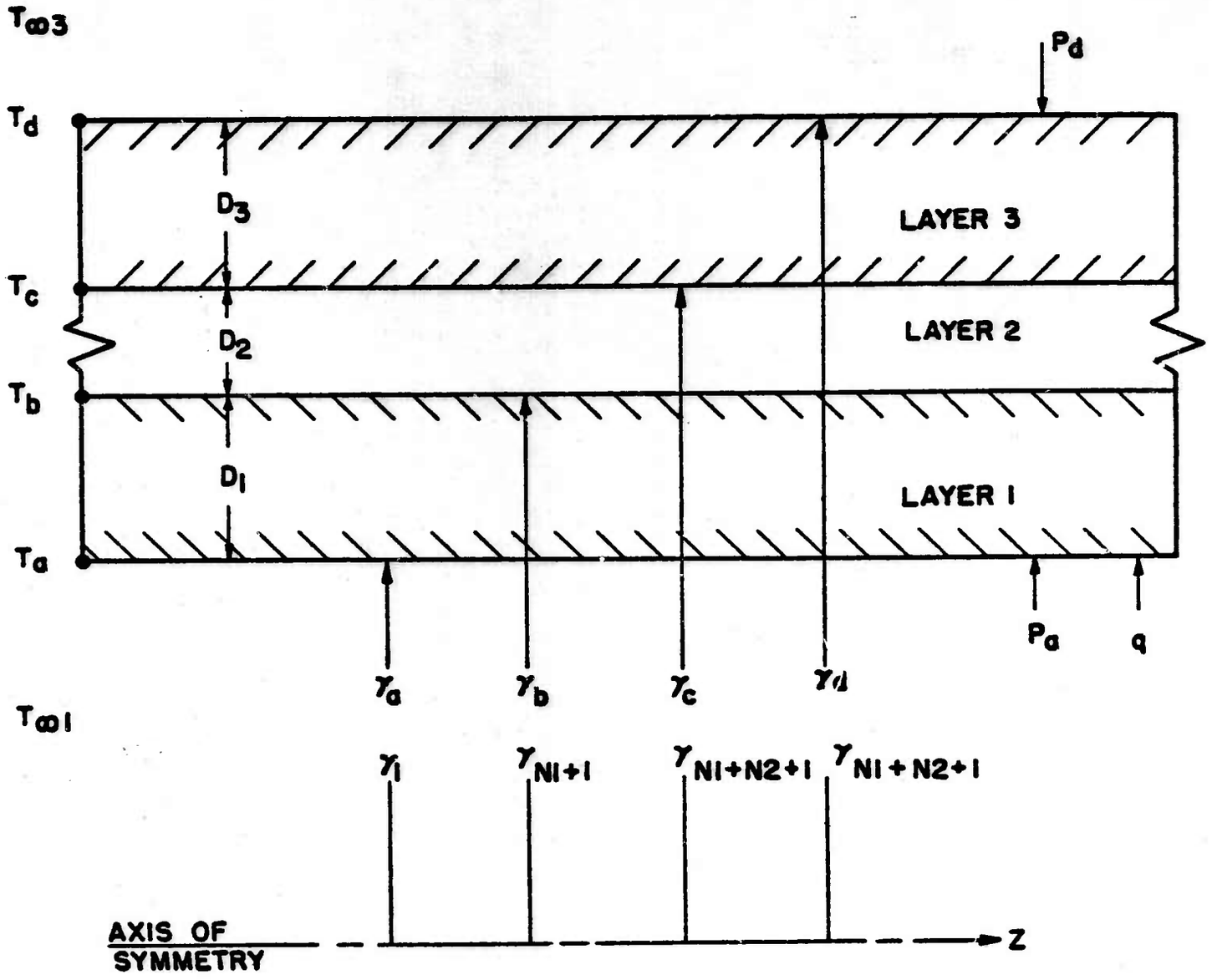

Figure 23. Three Layer Thick-Walled Cylinder

TABLE XI

INPUT DATA FOR CYLINDER SYNTHESIS PROBLEM

Internal Radius r_o	4.0"
Internal Pressure	120 psia
External Pressure	0 psia
Internal Gas Temperature	4200°F
External Gas Temperature	0°F
Heat Transfer Coefficient	160 $\frac{BTU}{FT^2 - HR - °F}$
Temperature Limit - Layer 1	4200°F
Temperature Limit - Layer 2	1500°F
Temperature Limit - Layer 3	500°F
During of Firing	100 sec.

TABLE XII

OPTIMUM DESIGNS FOR JT COMPOSITE CYLINDERS

	Layer Thicknesses (inches)			Weight (lb/in)
Material	D1	D2	D3	W
JT 30-5%	2.814	0.235	0.231	10.595
JT 30-10%	2.920	0.150	0.222	10.332
JT 30-15%	2.990	0.127	0.202	9.967
JT 50-5%	2.932	0.199	0.185	12.498
JT 50-10%	2.932	0.265	0.211	12.131
JT 50-15%	2.987	0.264	0.224	11.840
JT 70-5%	3.050	0.138	0.030	14.641
JT 70-10%	3.104	0.184	0.071	14.468
JT 70-15%	No Acceptable Design Found			

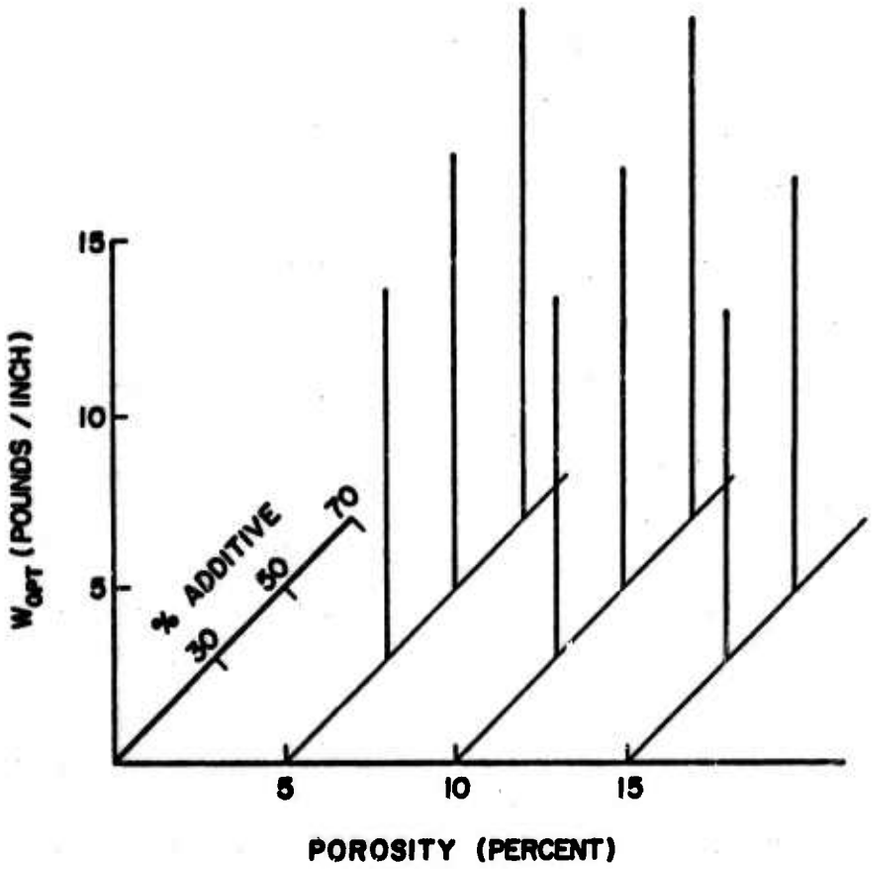

Figure 24. Materials Evaluation Function.

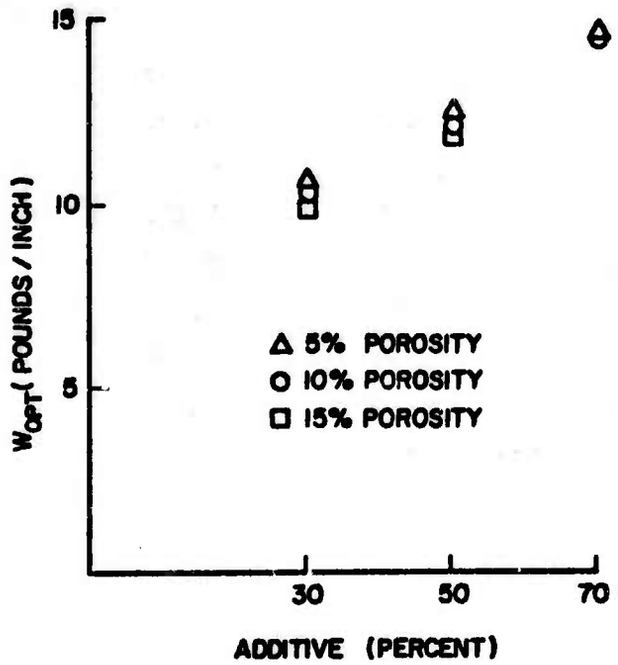

Figure 25. Optimum Weights Versus Amount of Additive for Fixed Porosities.

The essential conflict can be described qualitatively as follows. Increasing the percent additive increases the oxidation resistance, but also increases the final weight of the optimum design. Decreasing the porosity increases both the oxidation resistance and the final weight. Thus, a compromise dependent upon the desired performance is necessary. If oxidation resistance as a function of porosity and percent additive were known, the information could be used as a constraint while the minimum of the MEF was being determined. Currently, this constraint is represented by planes at 30% additive and 15% porosity.

This study indicates that future investigators should include material nonlinearity in addition to the cylindrical orthotropy and the temperature dependent mechanical properties accounted for by the stress analysis employed herein. Nonlinear stress analysis studies aimed in this direction are currently underway. A logical extension of this project would be to incorporate porosity, and composition as design variables within the structural synthesis program. Basically, this extension requires that the objective function and the failure modes be expressed as functions of the two additional design variables (porosity and percent additive of the JT layer). Expressing the objective function and its analytical gradient as a function of the three layer thicknesses as well as the porosity and composition of the JT layer is straight forward. The failure mode functions, however, depend upon those material variables through the mechanical and thermal properties of the JT layer. Therefore, since interpolation between available material data points would be used to represent the dependence of the material properties of the JT layer on the porosity and the percent additive, experimental data for several additional JT materials would be required to obtain reasonable accuracy. Extension of the current structural synthesis program to include porosity and composition of the JT layer as design variables is described further in Appendix E of Reference 14. It would not be profitable to program this extension for the present case until a relation for oxidation resistance as a function of porosity and percent additive is established.

F. Analysis and Synthesis of Flat Plate
(Professor Schmit and Mr. C. Chamis)

1. Introduction

A flat, simply supported orthotropic rectangular panel (see Figure 26) was chosen as a second idealized representative component. This system exhibits several important structural behavior characteristics such as bending, buckling, multiaxial stress states, and thermal stress response. The loadings on this panel include thermal inputs on the exposed surface [for example, q(t)], transverse pressure loading (p), and in-plane membrane forces (N_x, N_y, and N_{xy}). The planform dimensions of the plate (a,b) are preassigned parameters, and, initially, the material of the plate will also be preassigned. When the material is preassigned, the temperature dependent thermal and mechanical properties of the plate are assumed to be known. Initially, then, the design variables are the plate thickness and the angel θ orienting the material axes (1, 2) with respect to the planform axes of the plate (x,y). Failure modes to be guarded against in each load condition include temperature and transverse displacement limits as well as failure under combined stress. The objective of the structural synthesis is assumed to be minimization of the total weight of the plate.

The underlying analysis for this synthesis study, which will be found in Section V G of the First Annual Report[1], consists of three parts: the transient temperature distribution solution, the displacement response, and the stress analysis. The thermal analysis is carried out through the use of the one-dimensional heat conduction equation including temperature-dependent thermal properties. The transient temperature response through the thickness of the plate is obtained using an implicit finite difference solution technique. The displacement analysis is based on small deflection elastic thin plate theory. The basic field equation is a vertical equilibrium equation in terms of the unknown transverse displacement w(x,y). The series expansion selected to represent approximately the transverse displacement w(x,y) satisfies the imposed boundary conditions (namely, the w(x,y) = 0 on all four simply supported edges). The field equation subject to the natural boundary conditions (namely, M = 0 on all four simply supported edges) is solved approximately by applying the generalized Galerkin method which yields a system of linear simultaneous equations. Solution of this system of simultaneous equations gives the values of the coefficients in the series expansion for w(x,y) and, hence, an approximate functional expression for the transverse displacement pattern of the plate. The stress analysis is based on the stress displacement relations, and the end result essentially expresses the stresses in terms of the applied temperature distribution, the applied in-plane forces, and the applied transverse load distribution.

In this report, a combined stress failure criterion in the form of an interaction equation, which is used in the synthesis, is discussed; the synthesis problem of the particulate composite is defined; and synthesis results for the nine candidate materials from which the materials evaluation function is to be constructed are presented. Lastly, the materials evaluation function is formed.

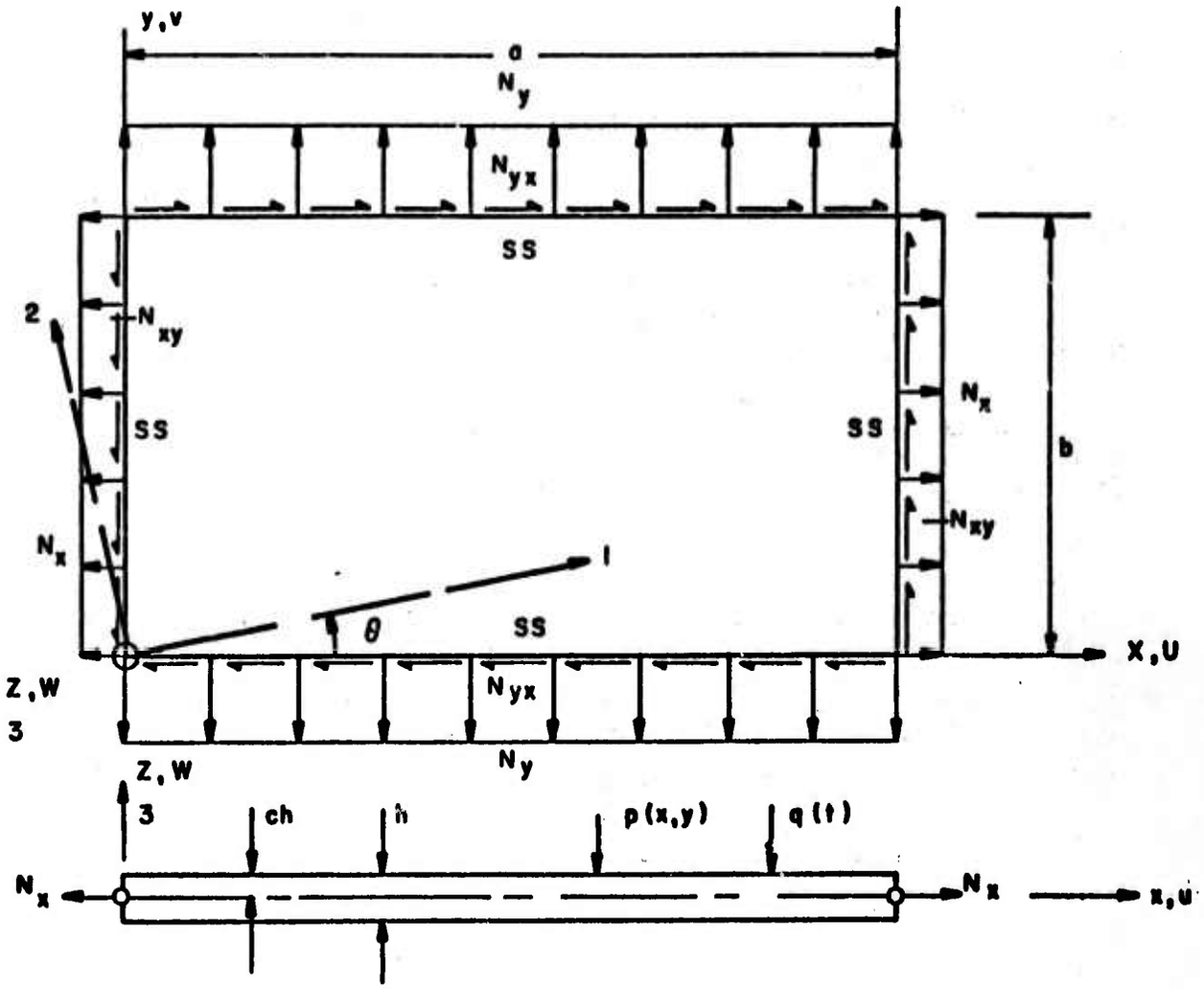

Figure 26. Schematic of Flat Plate.

2. Combined-Stress Strength-Criterion

The combined-stress strength-criterion used as a behavior constraint in the synthesis has the following form:

$$\left(\frac{\sigma_{11\alpha}}{S_{11\alpha}}\right)^2 + \left(\frac{\sigma_{22\beta}}{S_{22\beta}}\right)^2 + \left(\frac{\sigma_{12}}{S_{12}}\right)^2 - K_{12\alpha\beta}\,\frac{\sigma_{11\alpha}}{|S_{11\alpha}|}\,\frac{\sigma_{22\beta}}{|S_{22\beta}|} \leq 1 \qquad \text{(III F-1)}$$

where σ and S are the applied stress and uniaxial strength, respectively. The subscripts α and β become T(tension) or C(compression) depending upon the type of applied stress. The constant $K_{12\alpha\beta}$ is an empirical factor which is to be evaluated from tests on specimens loaded in the appropriate quadrant, i.e., TT, TC, CT and CC for the cases of tension-tension, tension-compression, compression-tension, and compression-compression, respectively.

Equation III F-1 is derived by postulating that the distortion energy of a generally orthotropic body remains invarient under simple and combined loading. In this derivation, the constant $K_{12\alpha\beta}$ is a function of the elastic constants of the material. However, the assumptions on which the distortion energy formulation is based do not strictly hold for the particulate composites under consideration. Therefore, it is more realistic to choose $K_{12\alpha\beta}$ so that experimental results and predicted values from Equation III F-1 agree reasonably well. Figure 27 illustrates this concept.

This approach is illustrated in Figure 27, where the experimental results reported in Section III C are superimposed on a curve based upon Equation III F-1. The values of $K_{12\alpha\beta}$ chosen for the theoretical curves are indicated in their respective quadrants in Figure 27. The point to be noted here is that values of $K_{12\alpha\beta}$ can be chosen so that Equation III F-1 gives results that fit the experimental data reasonably well.

3. Synthesis Formulation and Results

The synthesis formulation of the particulate composite plate is given by

$$W = \rho h \rightarrow \min \qquad \text{(III F-2)}$$

subject to

$$h - h_\ell \geq 0 \qquad \text{(III F-3)}$$

$$\left(\frac{1}{10}\right) \min (a,b) - h \geq 0$$

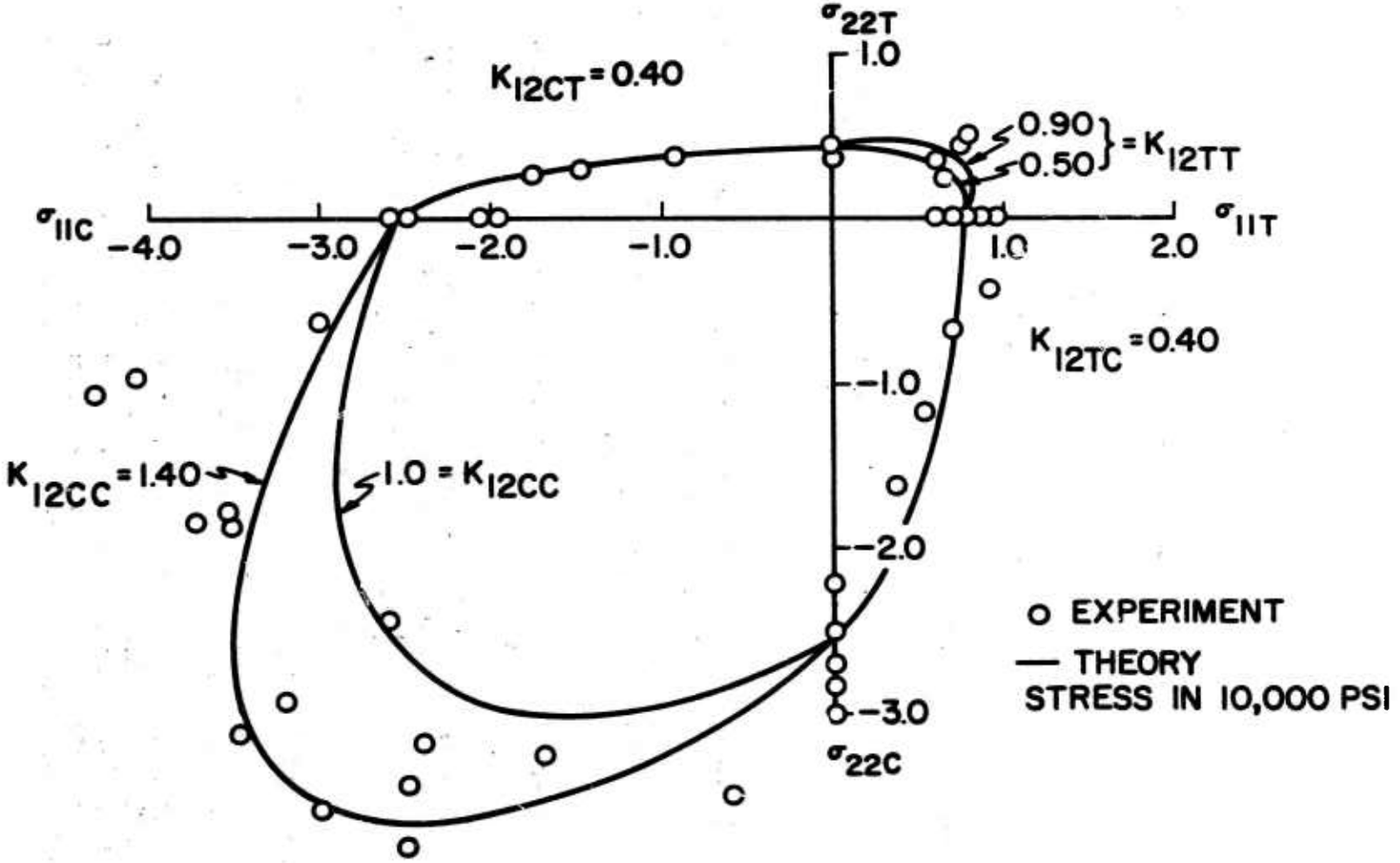

Figure 27. Modified Distortion Energy Failure Criterion For Particulate Composite of JT 50-10% Graphite

$$\theta \geq 0$$

$$\pi/2 - \theta \geq 0 \qquad \text{(III F-4)}$$

$$T_{max} - T(z,t) \geq 0 \qquad \text{(III F-5)}$$

$$h - |w(x,y,T,\theta)| \geq 0 \qquad \text{(III F-6)}$$

$$1.0 - IEC(x,y,z,T,\theta) \geq 0 \qquad \text{(III F-7)}$$

where, in synthesis terminology,

- W is the objective function (weight of the panel in pounds per square inch of panel surface)
- ρ is the material density
- h and θ (panel thickness and orientation angle) are the design variables
- h_ℓ and $\frac{1}{10}$ min (a,b) are the side constraints (lower and upper bound) on h
- 0 and $\pi/2$ are the side constraints (lower and upper bounds) on θ.
- $T(z,t)$, $w(z,y,T,\theta)$ and $IEC(x,y,z,T,\theta)$ (interaction equation constraint, i.e., combined stress failure criterion) are the significant behavior variables that depend on the design variables through the displacement and stress analyses.

Equations III F-5, 6, and 7 are the behavior constraints and T_{max}, h and 1.0 are the upper bounds on the temperature, lateral displacement, and the combined stress-state interaction expression, respectively.

It is interesting to note that temperature (T) plays the role of a load condition in addition to that of a behavior variable: it is a load condition, since both the lateral displacement and the combined stress state, through the interaction equation, are functions of its gradient; and it is a behavior variable, since it is dependent on the design variable h.

It is further noted from Equation III F-5 that T is a function of z and t only. It is independent of θ and, therefore, a simplification can be obtained by including the temperature limitation through the lower bound on the plate thickness h_ℓ. This condition is particularly helpful when one is to optimize various panel aspect ratios using the same material. The temperature limitation can be treated indirectly by selecting h_ℓ the lower bound on the design variable h, such that

$$T_{max}(z,t) = T_{max,allowable} \qquad \text{(III F-8)}$$

where

$$0 \leq t \leq t_f$$

and t_f is the real time period of interest. This alternate means of handling the temperature limitation was incorporated into the computer program as an option.

The minimization of W is accomplished by a sequential procedure which is a combination of steepest descent for a free point and optimum feasible directions for a constrained point. The feasible directions algorithm employed in this synthesis study was essentially available as a preprogrammed procedure as a result of an effort first reported in Section IX B5 of the First Annual Report[1] and described further in Section IX D of this report.

The operational structural synthesis program has been used to obtain minimum weight optimum designs for a variety of example cases. In particular, the capability has been used to seek minimum weight optimum designs for a 36" x 24" panel employing each of nine candidate materials in the JT particulate composite family. The thermal and mechanical load conditions are summarized in Table XIII. The results for each of eight distinct structural synthesis runs are given in Table XIV. The best optimum design was obtained using the JT 50-5% material. Table XIV shows that the optimum design for the JT 50-5% material is such that two constraints are active, namely, the temperature limit and the combined stress limit. It has not been possible to find an acceptable design using the JT 70-15% material. The design space for the optimum 36" x 24" panel using JT 50-5% material is shown in Figure 28. The acceptable region in this design space is disjoint and contains relative minima at $\theta = 90°$ and $0°$.

4. Materials Evaluation Function

The materials evaluation function concept applied to the results of the (36" x 24") panel turned out to be simple curve fitting. This curve fitting is shown in Figure 29 and provides all the information that could have been obtained from a more sophisticated choice of optimum-designs-surface function.

TABLE XIII

MECHANICAL AND THERMAL LOAD CONDITIONS

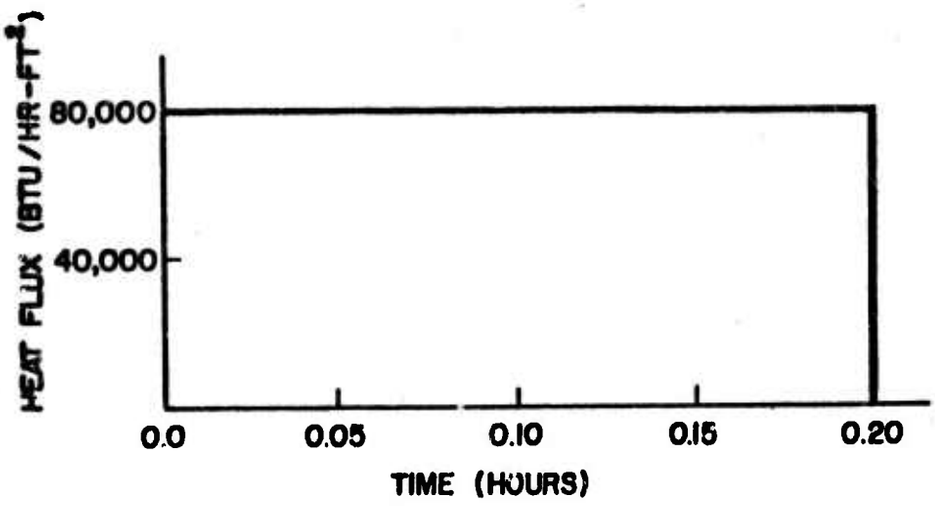

THERMAL LOAD CONDITION

LOAD CONDITION	TRANSVERSE PRESSURE $\bar{P}$ PSI	MEMBRANE LOADS			
		$\bar{N}$ LB/IN.	$\bar{N}_y/\bar{N}$	$\bar{N}_y/\bar{N}$	$\bar{N}_{xy}/\bar{N}$
1	40.0	12,000	1.0	0.0	0.0
2	30.0	"	0.375	-0.20	0.25
3	0.0	"	0.0	0.0	0.0
4	10.0	"	0.0	0.5	0.0
5	10.0	"	0.0	0.0	0.0
6	5.0	"	0.5	0.25	0.40

MECHANICAL LOAD CONDITIONS

TABLE XIV OPTIMIZED JT-MATERIAL PARTICULATE COMPOSITES

Material	Density lb/cu.in.		Planform Dimensions Inches		Optimum Design Point Variables		Design Weight	Behavior Variables at Optimum Normalized		
	Theor.	Actual	a	b	h inches	θ degrees	W lb/sq.in.	T/T*	|w|/w*	IEC/IEC*
30,.05	0.1005	0.0956	36.0	24.0	2.041	90.0	0.196	0.836	0.066	1.015
30,.10	0.1005	0.0905	36.0	24.0	2.192	90.0	0.198	0.843	0.063	0.998
30,.15	0.1005	0.0855	36.0	24.0	2.400	90.0	0.205	0.818	0.055	1.045
50,.05	0.1180	0.1122	36.0	24.0	1.566	90.0	0.175	0.977	0.078	0.994
50,.10	0.1180	0.1062	36.0	24.0	1.834	90.0	0.194	0.917	0.057	0.976
50,.15	0.1180	0.1004	36.0	24.0	2.102	90.0	0.211	0.877	0.044	0.989
70,.05	0.1415	0.1345	36.0	24.0	1.515	90.0	0.203	1.002	0.073	0.383
70,.10	0.1415	0.1274	36.0	24.0	1.648	90.0	0.210	0.984	0.075	0.851
70,.15	0.1415	0.1203	36.0	24.0	**	**	**	**	**	**

** Incompatible Material with Planform Dimensions of Panel

T* = Temperature Behavior Constraint = 3000°F

w* = Displacement Behavior Constraint = h

IEC* = Combined Stress Behavior Constraint = 1.0

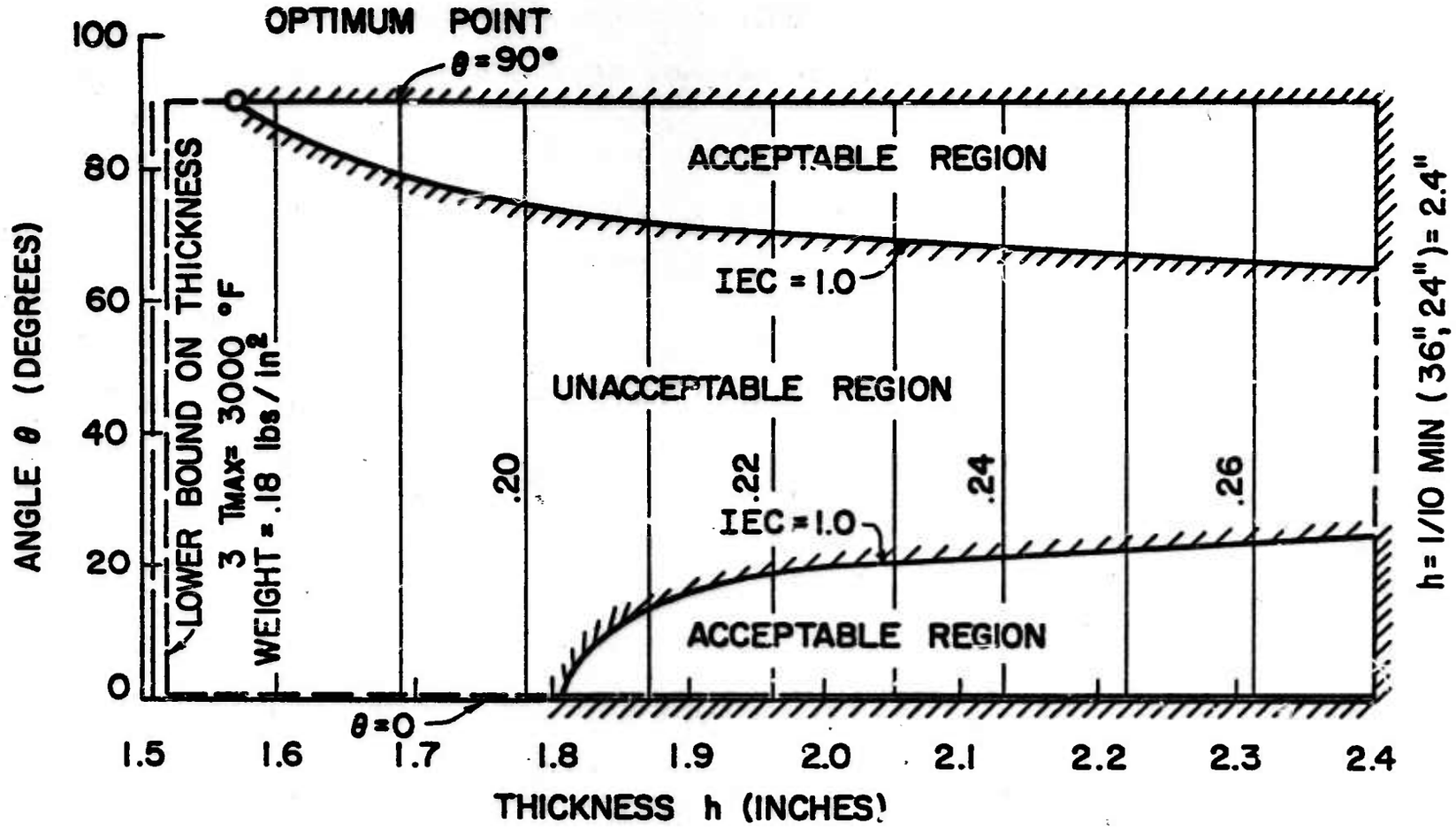

Figure 28. Design Space for Jt - 50, .05 - 36 in. x 24 in.

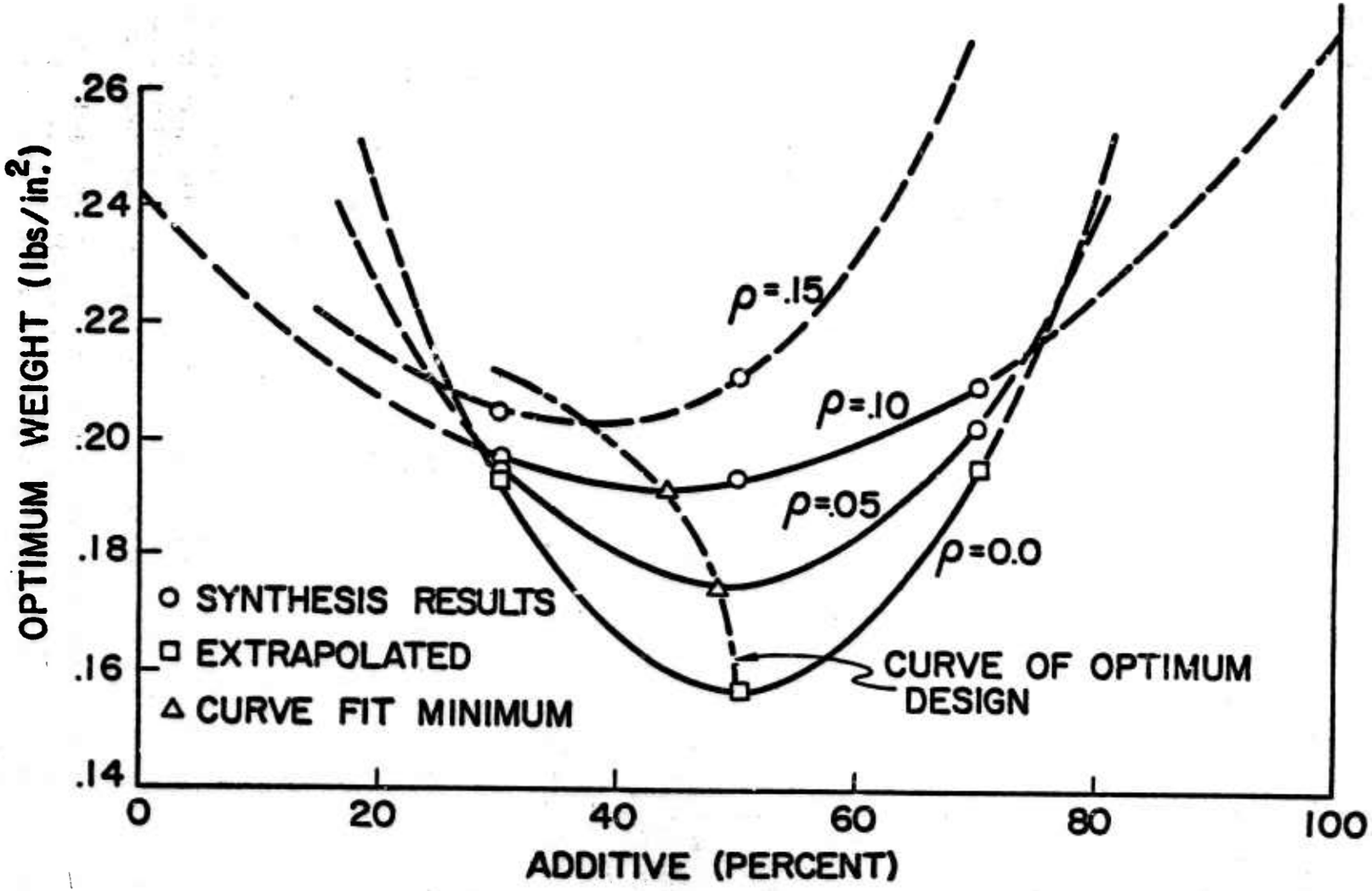

Figure 29. Optimum Weight Versus Percent Additive for Various Porosity Ratios, 36 x 24 Panel.

In Figure 29 four curves are shown as labeled. The zero-porosity curve was obtained by linear extrapolation of optimum weight versus percent porosity at 30%, 50%, and 70% additive. Parabolas were fitted through the points representing optimum designs for 10%, 5%, and zero porosity and the minimum points of these parabolas were connected with a curve labeled "Curve of Optimum Designs" in Figure 29.

From Figure 29 the following best optimum designs corresponding to fixed porosities can be estimated:

Porosity	Metallic Additive	Optimum Weight
0%	50%	0.157 lb/in.^{2}
5%	48%	0.175 lb/in.^{2}
10%	44%	0.192 lb/in.^{2}
15%	38%	0.203 lb/in.^{2}

An equation of the optimum designs path shown in Figure 29 was derived by fitting a parabola through the best optimum design points at porosities of 10%, 5%, and zero. The location of the curve is not known accurately below 40% metallic additive because of the limited data available (i.e., optimum designs for only eight candidate materials).

On the basis of the materials evaluation function results, a material with 50% metallic additive at 0% porosity should yield the optimum design for the (36" x 24") panel for the load conditions in Table XIII.

5. Conclusions

From the results of the flat panel studies, the following conclusions can be drawn:

(1) Structural synthesis concepts can be applied successfully to particulate composites which are subjected to complex thermal and mechanical loads and which have temperature dependent properties.

(2) Materials evaluation functions can be constructed from synthesis results.

(3) Recommendations on material composition which will result in improved designs can be made from the information provided by the materials evaluation function. This fact, in a way, closes the loop between structural design and materials development.

(4) A combined-stress strength-criterion can be constructed utilizing the distortion energy hypothesis by allowing the coefficients, which arise naturally in the formulation to be determined experimentally.

G. Stress Analysis of a Rocket Nozzle Throat Insert of Grade JTA Graphite Composite Material

1. Linear Analysis

(F.M. Anthony and A.L. Mistretta, Bell Aerosystems)

Analyses were presented in Section V H of the first Annual Report (Reference 1) for the representative JTA rocket nozzle throat insert in order to define the relationships among operational conditions, geometric variables, external restraint, and thermal stresses and assumed linear stress-strain relationships. More recent data obtained from Union Carbide indicated significant differences in mechanical properties as compared to the previous data. Selected analyses described in this section were re-run to ascertain the influence of the more accurate material properties.

Before comparing the analytical results, one should first examine the differences in mechanical properties. Table XV summarizes the original and revised property data at several specific temperatures. The newer elastic moduli values are only approximately two-thirds of the original values, whereas the expansion coefficients are from 0 to 25% higher, depending upon direction and temperature level. The new αE products in the with-grain and across-grain directions are 60 to 70% and 70 to 90% of the original values, respectively. Poisson's ratio data are significantly different, partly due to mis-interpretation of the original literature data.

The resulting stresses at the throat obtained from each set of property data are presented in Table XVI for two chamber pressures and two nozzle sizes. Despite the lower αE product in the across-grain direction, little difference is present in the maximum axial compressive stress. The circumferential stresses are reduced; but, for the maximum compressive stresses, the reductions are less than would be expected from the change in the $\alpha E/(1-\nu)$ term. This difference is due to the more complex interaction of the elastic constants for anisotropic materials.

2. Non-linear Analysis

(Dr. P.V. Marcal, Bell Aerosystems)

The high temperatures associated with the rocket nozzle throat insert application, coupled with the non-linear stress-strain behavior of the JTA material, could result in significant plastic yielding. Non-linear stress analyses were conducted, therefore, to determine the effect upon induced thermal stresses and strains. An available tangent-modulus method of elastic-plastic analysis based on finite element techniques was employed (Reference 15). The method provided linearized the material stress-strain behavior for each load increment by treating the problem in a piece-by-piece linear manner. Modifications in the analysis account for the anisotropic elastic and plastic behavior of the JTA material. The analyses were carried out utilizing the von Mises yield criterion and two possible generalizations thereof in order to obtain comparative results.

TABLE XV

COMPARISON OF MECHANICAL PROPERTIES OF JTA COMPOSITE

PROPERTY	ORIGINAL	REVISED
E_w, 10^6 psi: 80°F	17.0	11.5
3000°	21.5	12.2
E_A, 10^6 psi: 80°	6.0	4.5
3000°	7.4	5.5
α_w, 10^{-6} IN./IN. °F: 80°	2.9	2.7
2600°	—	3.9
3000°	3.1	3.9
α_A, 10^{-6} IN./IN. °F: 80°	3.2	3.0
3000°	3.7	4.3
ν (80°F TO 3000°F)	0.22 TO 0.27	0.38 TO 0.47
ν_{aw} (80°F TO 3000°F)	0.08 TO 0.10	0.15 TO 0.21
ν_{ww}^{wa} (80°F TO 3000°F)	0.22 TO 0.27	0.06 TO 0.10

TABLE XVI

EFFECT OF MATERIAL PROPERTIES ON THERMAL STRESS

CONDITIONS	MAXIMUM AXIAL STRESS, psi		MAXIMUM CIRCUMFERENTIAL STRESS, psi	
	TENSION	COMPRESSION	TENSION	COMPRESSION
2.0" I. D., 100 psi	(-9000) -8000	(37, 000) 38, 000	(-22, 000) -16, 000	(130, 000) 101, 000
2.0" I. D., 500 psi	(-5000) 1000	(120, 000) 112, 000	(-10, 000) -5000	(325, 000) 275, 000
24" I. D., 500 psi	(-3000) 0	(120, 000) 120, 000	(-5000) -5000	(315, 000) 228, 000

NOTES:

1. COMPLETE RESTRAINT
2. (XXX) ORIGINAL PROPERTIES
   XXX REVISED PROPERTIES

a. Theoretical Considerations

Anisotropy is usually introduced in the theory of plasticity by generalizing the von Mises yield criterion. In cylindrical coordinates, specialized to the present problem of rotational symmetry, the von Mises yield criterion is

$$(\sigma_r - \sigma_\theta)^2 + (\sigma_\theta - \sigma_z)^2 + (\sigma_z - \sigma_r)^2 + 6 \sigma_{rz}^2 = 2 \bar{\sigma}^2 \qquad \text{(IIIG-1)}$$

where $\bar{\sigma}$ is the equivalent yield stress and the yield surface is defined in stress space with σ_r, σ_θ, σ_z and σ_{rz} as coordinates. Despite the fact that anisotropic elastic constants are used to determine stress distributions, this criterion assumes that the yield stress is equal in all directions.

A generalization of this equation accounting for anisotropy has been suggested in Reference 16. This criterion is given by

$$F (\sigma_r - \sigma_\theta)^2 + G (\sigma_\theta - \sigma_z)^2 + H (\sigma_z - \sigma_r)^2 + 2L \sigma_{rz}^2 = 2 \bar{\sigma}^2 \qquad \text{(IIIG-2)}$$

where the constants F, G. H, and L may be determined from simple uniaxial and torsion tests. This second criterion was originally suggested for work-hardened metals (Reference 16) and has subsequently also been applied (Reference 17) for fibrous composites.

Another generalization is obtained by weighting the effect of the stress according to

$$(\sigma_{r/R} - \sigma_\theta / \theta)^2 + (\sigma_\theta / \theta - \sigma_{z/Z})^2 + (\sigma_{z/Z} - \sigma_{r/R})^2 + 6 (\sigma_{rz/RZ})^2 = 2 \bar{\sigma}^2 \qquad \text{(IIIG-3)}$$

where R, θ , Z, and RZ are the yield stresses in the appropriate directions. This equation has been used as an interaction curve for fiberglass composites (Reference 18).

b. Stress-Strain Relations

Once the yield criterion is defined, the normal flow rule of plasticity defines the plastic components of strain:

$$\left\{ de_p \right\} = de_p \left\{ \frac{\partial \bar{\sigma}}{\partial \sigma} \right\} \qquad \text{(IIIG-4)}$$

where $\left\{ de_p \right\}$ = vector of plastic strain increments

$\left\{ \frac{\partial \bar{\sigma}}{\partial \sigma} \right\}$ = gradient of the yield surface

$d\bar{e}_p$ = equivalent plastic strain increment.

The Prandtl-Reuss equations then give

$$\begin{aligned} \left\{ de \right\} &= \left\{ de_e \right\} + \left\{ de_p \right\} \\ &= \left[S \right]^{-1} \left\{ d\sigma \right\} + \left\{ \frac{\partial \bar{\sigma}}{\partial \sigma} \right\} d\bar{e}_p \end{aligned} \qquad \text{(IIIG-5)}$$

where

$\left[S \right]^{-1}$ = inverse of the elastic stiffness matrix

$\left\{ d\sigma \right\}$ = vector of stress increments

$\left\{ de \right\}$ = vector of total strain increments

$\left\{ de_e \right\}$ = vector of elastic component of the strain increment.

The formulation of the linear stress-strain laws in the increment may be completed if the yield criterion is written in the form of an implicit differential

$$\left[\frac{\partial \bar{\sigma}}{\partial \sigma} \right] \left\{ d\sigma \right\} = d\bar{\sigma} = H' \, d\bar{e}_p \qquad \text{(IIIG-6)}$$

where H' is the local tangent modulus of the equivalent stress/equivalent strain curve.

Equations IIIG-5 and -6 are then assembled into a matrix equation.

$$\left[\begin{array}{c|c} S^{-1} & \dfrac{\partial \bar{\sigma}}{\partial \sigma} \\ \hline \dfrac{\partial \bar{\sigma}}{\partial \sigma} & -H' \end{array}\right] \left\{\begin{array}{c} d\sigma \\ \hline d\bar{\varepsilon}_p \end{array}\right\} = \left\{\begin{array}{c} de \\ \hline 0 \end{array}\right\} \qquad \text{(IIIG-7)}$$

Equation IIIG-7 can be rewritten

$$\left\{\begin{array}{c} d\sigma \\ \hline d\bar{\varepsilon}_p \end{array}\right\} = \left[p\right] \left\{\begin{array}{c} de \\ \hline 0 \end{array}\right\} \qquad \text{(IIIG-8)}$$

where $[p]$ is the inverse of the matrix on the left of equation IIIG-7. Equation IIIG-8 transforms the total strain increment into a stress increment in a linear fashion.

Equation IIIG-8 is used to form the stiffness matrix in the finite element analysis; thus the elastic-plastic problem is approximated by a series of piece-by-piece linear problems.

c. Analysis of the Nozzle Insert

A nozzle insert with an external diameter of two inches and a maximum wall thickness of one inch was analyzed to determine the maximum thermal gradients for a chamber pressure of 100 psi. The most severe thermal conditions were found to occur two seconds after ignition. The analysis was conducted with the assumption that a linear increase of temperature with time occurred until the most severe thermal gradient was reached. The insert was represented by 126 toroidal rings of triangular cross-section, resulting in 93 nodal points. The mesh idealization is shown in Figure 30. The insert was assumed to be fully restrained along the exterior and side surfaces. The computer program as developed does not allow for variation of yield stress with temperature. A stress-strain curve was assumed which was based on room temperature data, but flattened at the higher stresses. This lower tangent modulus was introduced to account for the expected increase in ductility of JTA at elevated temperature. The non-linear stress-strain curve approximations used for the with-grain and across-grain directions are shown in Figure 31.

Fine Grid 126 Elements

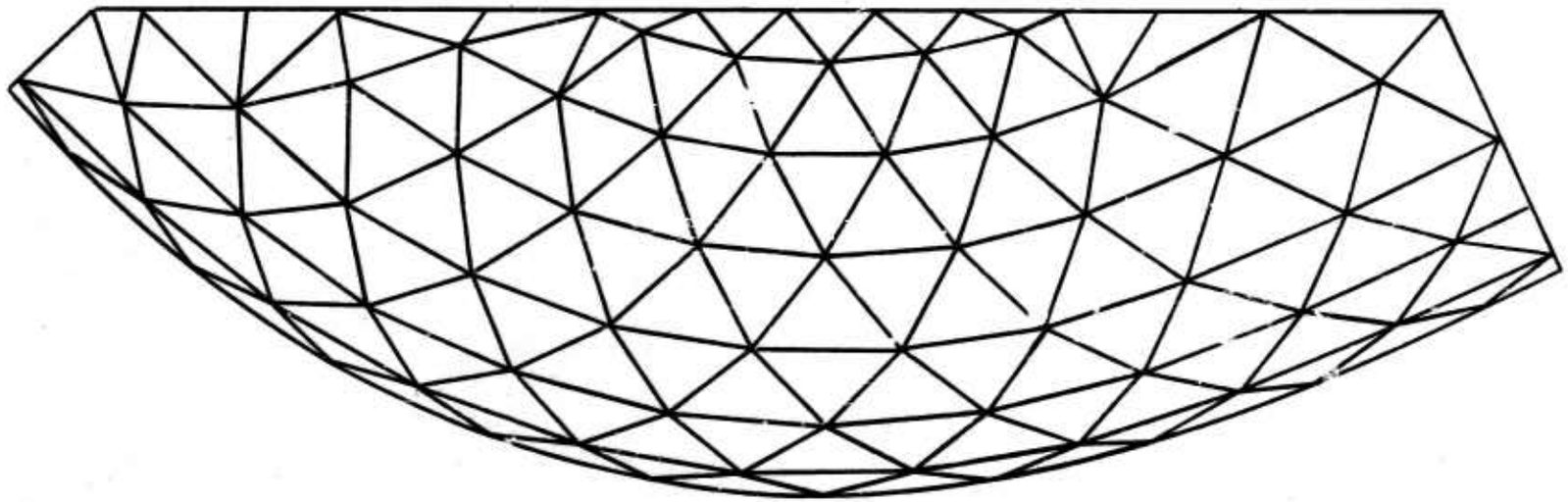

Figure 30. Structural Idealization of Throat Insert

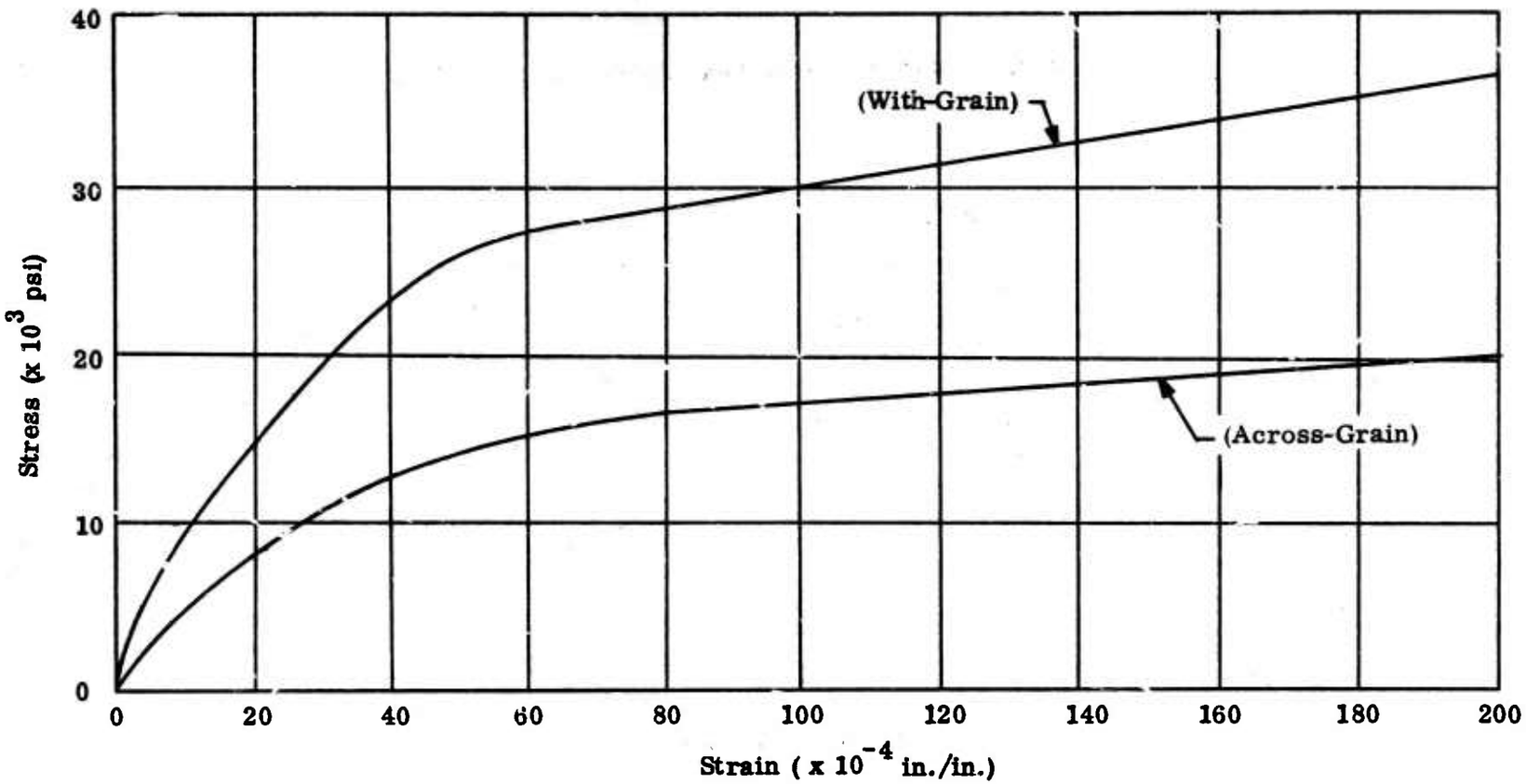

Figure 31. Stress-Strain Curves Used in Nonlinear Analysis

d. Results

Figure 32 shows the temperature distribution and equivalent plastic strain distribution on the inside surface two seconds after ignition. The values are plotted against distance in the axial direction. The stresses induced at the minimum throat section are shown in Table XVII. An examination of the results shows that the yield criterion of equation IIIG-2 effectively suppresses the plastic strains. Because the thermal strains are more or less fixed, a high elastic component of stress is induced.

It is of interest to examine the shape of the three yield criteria applied to conditions at the inside insert surface. Here the shear and radial stresses disappear so that the circumferential and axial stresses can be plotted against each other to obtain the loci of yield shown in Figure 33. The ellipse for equation IIIG-2 is for a ratio of yield in the two directions of 1 to 0.51. A ratio of 1 to 0.5 results in an infinitely elongated elipse. For a given overall strain through use of the data in Figure 33, it can be seen that the yield criterion of equation IIIG-2 tends to suppress plastic yielding, and the yield criterion of equation IIIG-3 leads to larger plastic strains as compared with the isotropic yield criterion. The validity of the various yield criteria for anisotropic non-linear materials must ultimately be established by experiment.

The non-linear analysis together with reasonable assumptions results in lower thermal stresses than those predicted by linear material response assumptions. The large differences in thermal stresses between the linear and non-linear analysis results illustrate clearly the importance of accounting for non-linear stress-strain behavior.

TABLE XVII

RESULTS OF NONLINEAR STRESS ANALYSIS OF THROAT INSERT
(CHAMBER PRESSURE 100 psi)

Stress or Strain Parameter	Yield Criterion			Elastic Analysis
	(Isotropic)	Equation IIIG-2	Equation IIIG-3	
Circumferential stress (psi)	-35,000	-100,000	-25,000	-130,000
Axial stress (psi)	-25,000	-45,000	-7,000	-52,000
Equivalent stress (psi)	-36,000	-15,000	-32,000	-133,000
Equivalent plastic strain (percent)	0.30	0.02	1.15	-

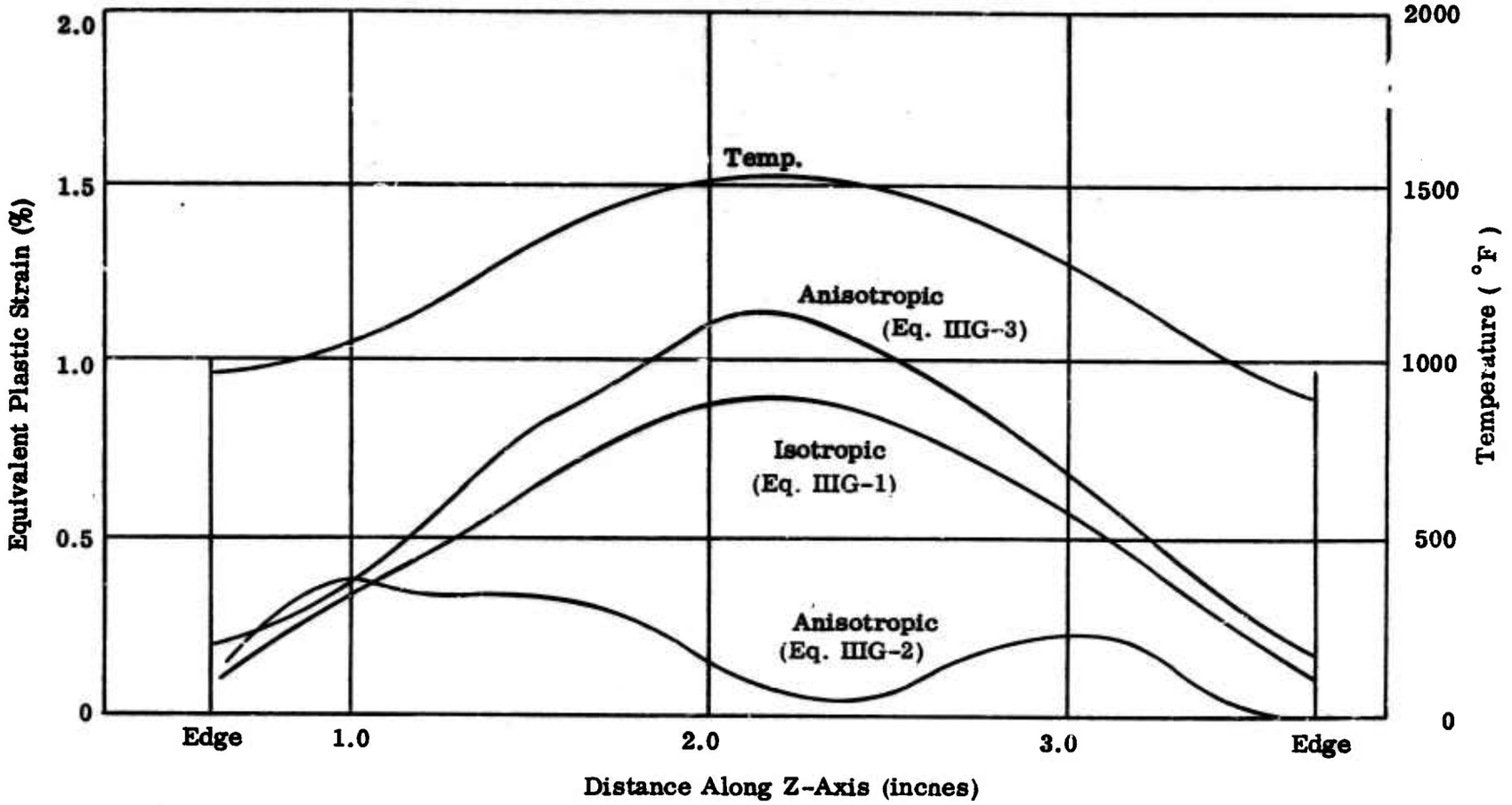

Figure 32. Equivalent Strain and Temperature Distribution on Inside Surface of Insert

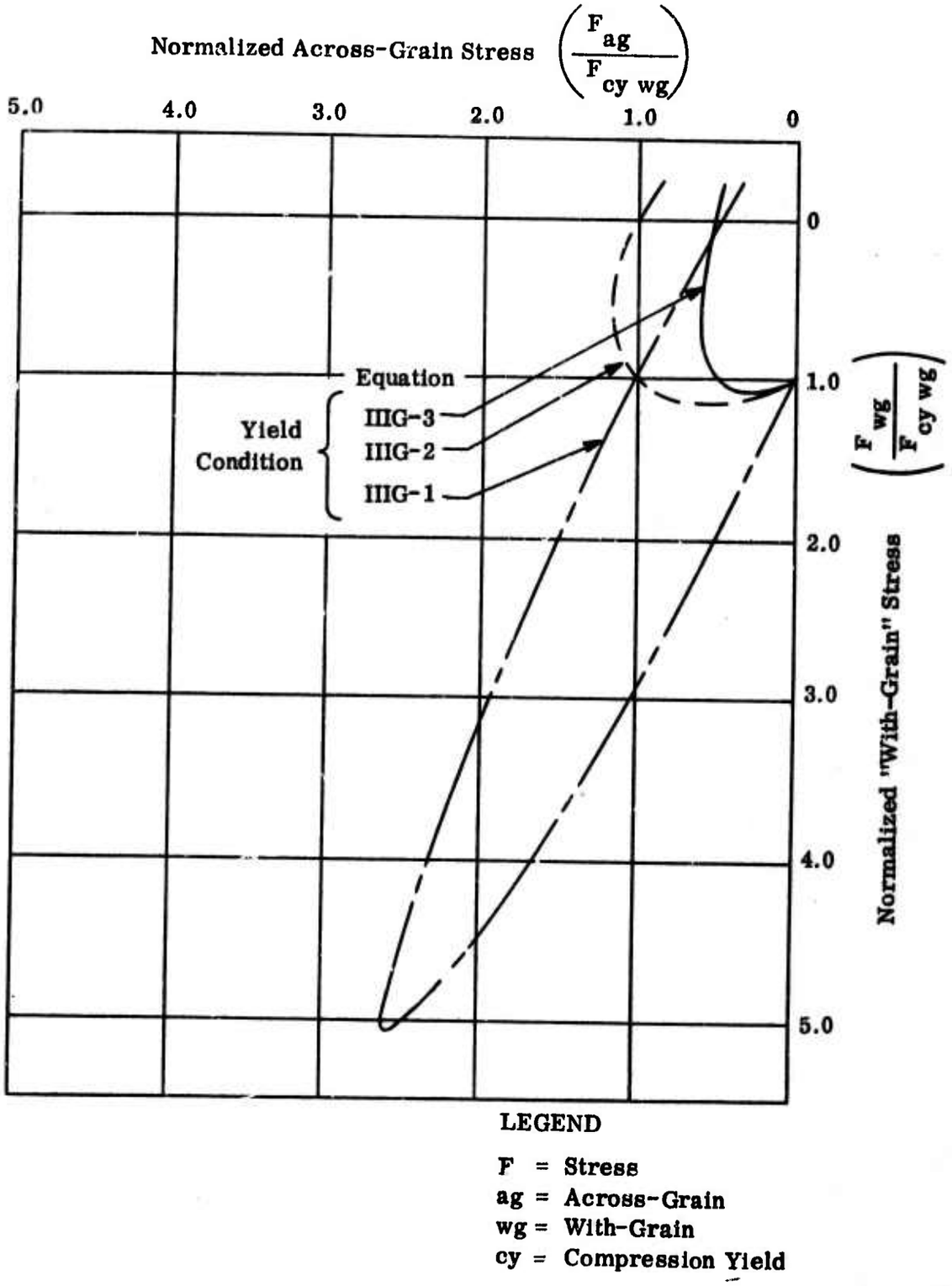

Figure 33. Biaxial Compressive Yield Criteria Used For Nonlinear Analyses of Throat Insert

3. Thermal Properties

(M.S. Janis and J. Palumbo, Bell Aerosystems)

Design studies of the nozzle throat insert described in Section IX D of the first Annual Report (Reference 1) concluded with predictions of transient temperatures in JTA assumed isotropic with across-grain properties. These temperatures at various depths from the heated surface of the isotropic insert are compared in Figure 34 with comparative results for the transversely isotropic insert. It is evident that the inner surface temperatures are appreciably reduced as a result of material thermal anisotropy. Figure 34 supplements data shown in Figure 141 of the first Annual Report which treated JTA as isotropic with with-grain properties.

Of more significance than temperatures is the anisotropy influence on the thermal gradient, shown in Figure 35, since this determines the local stress. It is seen that the maximum local gradient (occurring 2 seconds after ignition at the hot gas surface) would be even more pronounced for a material having a lesser degree of anisotropy, thus suggesting a means of specifying materials properties based on functional design requirements. Previous thermal stress studies, Section V H of the first Annual Report (Reference 1), also indicated that material anisotropy could be used to advantage in rocket throat insert applications.

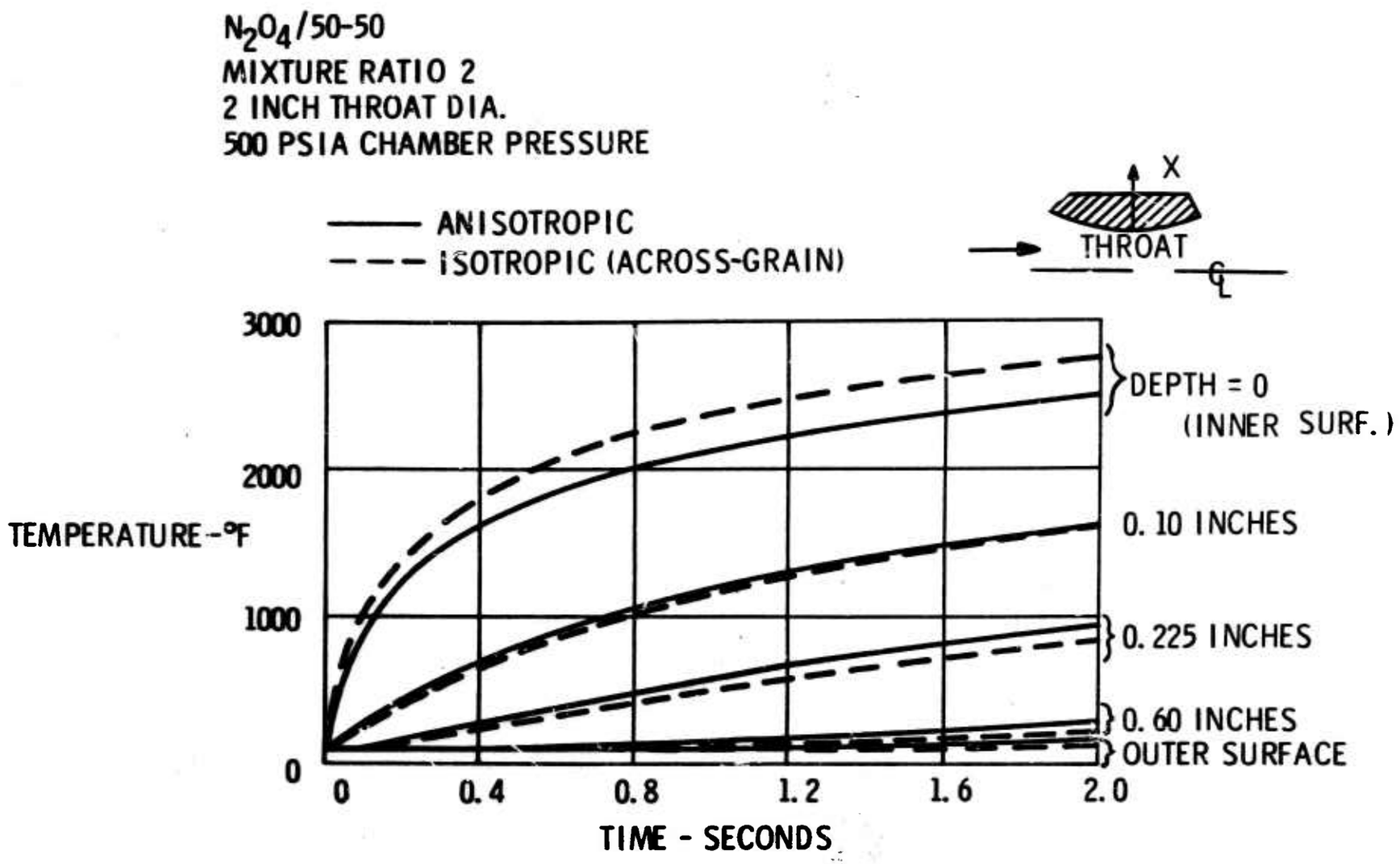

Figure 34. Transient Temperatures At Throat

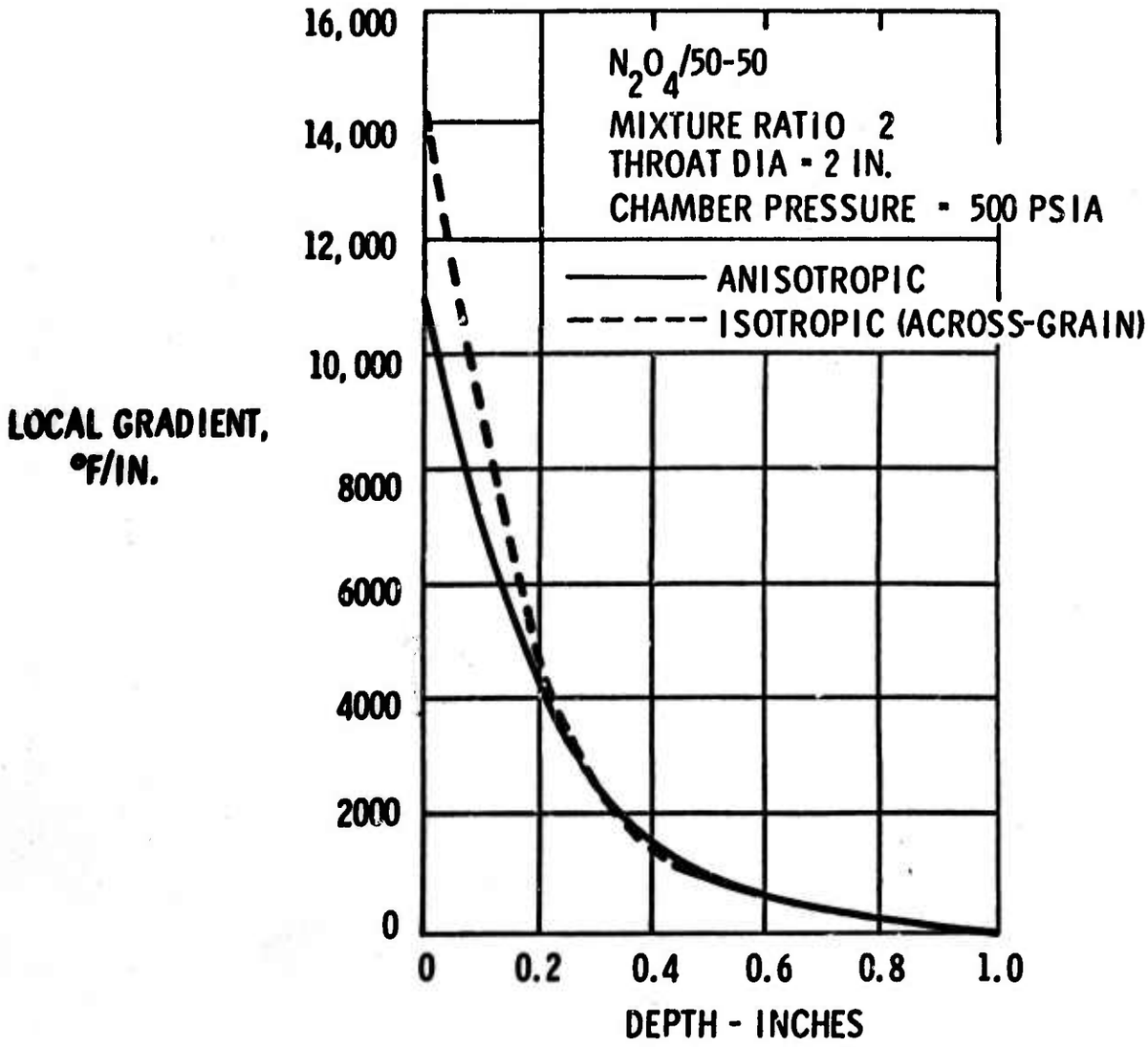

Figure 35. Thermal Gradient at Throat Station 2 Seconds after Ignition

SECTION IV

MATERIALS RESEARCH ON GRAPHITE-FIBER, METAL-MATRIX COMPOSITES

High modulus graphite fibers are an ideal reinforcing agent for metals both because the graphite fiber modulus and strength are essentially independent of temperature up to, at least, 2000°C and because the fibers have a much lower density than metals. Goals of the metal-matrix work are to develop composites with high modulus-to-density ratios, strength-to-density ratios, and superior high temperature properties.

The major effort of the research on graphite-fiber, metal-matrix composites has been with nickel and aluminum matrices. The nickel-matrix studies are reported in Section IV A. High modulus graphite fibers are electroclad with nickel, and the coated fibers are hot pressed to form the composite. The original batch plating process has been replaced by a continuous plating operation. Fabrication studies investigated the effects on composite properties of three coating baths and various forming pressures and temperatures. Tensile properties of unidirectional composites have been measured from room temperature to 1050°C. The aluminum matrix work, reported in Section IV B, has attempted to reduce fiber damage during aluminum infiltration by utilizing precoated fibers.

A. Nickel Matrix Studies

(R. V. Sara, Union Carbide)

1. Fiber Properties

Three types of graphite fibers have been used for the preparation of composites containing nickel. As shown in Table XVIII, the fiber lots differed significantly in their properties at each stage of exploration; the most advanced fiber material available in sufficient quantities was used.

TABLE XVIII

PROPERTIES OF GRAPHITE FIBERS USED IN NICKEL-MATRIX COMPOSITES

Modulus E ($lb/in.^2$)	Strength ult σ ($lb/in.^2$)	Density ρ (g/cm^3)	Cross-Sectional Area-A (μ^2)
34.5×10^6	200,000	1.60	38.2
49.2×10^6	260,000	1.63	33.8
60.8×10^6	270,000	1.70	30.8
62.1×10^6	345,000	1.71	30.1

The first generation of composites discussed below included fibers having a lower modulus of elasticity and tensile strength. For the fabrication studies (effect of forming pressure on properties) and thermal degradation analysis the 50 and 60 million modulus fibers were available. The yarn with 50 million modulus was used for tensile and 300 hour stability tests at elevated temperatures, and the 60 million modulus fibers were used in the fiber loading evaluation.

Graphite yarn has a two-ply construction with 720 filaments per ply. The two plies were separated before electroplating; but as shown in Figure 36, the filaments within a given ply had a twist that could not be removed without completely destroying the integrity of the yarn. This feature complicated attempts to achieve perfect fiber alignment within the composite.

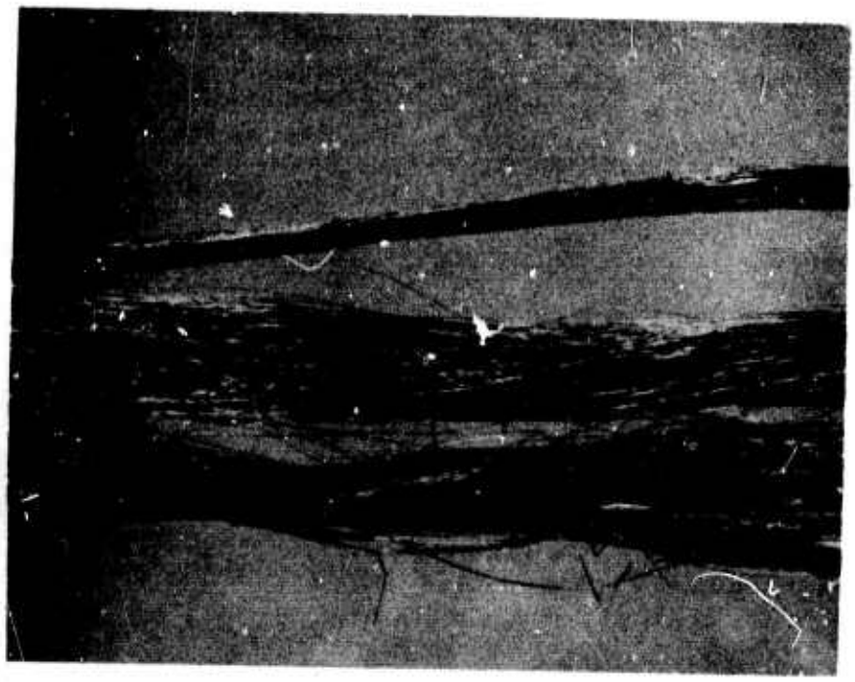

N-17489

Figure 36. Residual Twist in Graphite Yarn. 5X Magnification

2. Nickel Electrocladding Procedures

The procedure for preparing composites containing aligned graphite fibers in a nickel matrix consists of electrocladding nickel around each of the 720 filaments comprising a single ply of yarn and then consolidating multisegments of the metal-coated yarn into a solid shape by hot forming. The coating thickness on the filaments governs the volume content of matrix in the final composite.

Nickel was deposited around all the filaments comprising a ply of yarn by electrolytic deposition from an aqueous solution. The first electroplating of nickel was conducted on a batch basis with nickel sulfate-boric acid and nickel sulfate-boric acid and nickel sulfamate plating baths. By the batch method, three inches of coated single ply yarn could be prepared in 2 to 5 minutes. A continuous plating operation was designed to overcome the limitations of the batch method and to provide uniform nickel coatings on all the filaments of the yarn. The schematic diagram in Figure 37 briefly outlines features of the continuous plating operation. The spool (A) rotates in two directions to remove twist in the yarn and to permit free feeding through the plating bath. The furnace (B) heats the yarn to 550°C under normal atmospheric environment in order to oxidize slightly the filaments, thereby promoting better wetting in the plating bath. Metallographic evidence indicates that this procedure results in a more uniform metal deposition on the multifilaments. Two wire loops at (C) separate the two plies of yarn. Electrical contact is made at (D); the lower set of rollers is made of copper, and the upper set is made of soft sponge rubber. Satisfactory results have been obtained with an anode/cathode ratio of approximately 9:1 and a current density of 30 amps/ft^2. With this plating apparatus, two-ply yarn has been coated continuously with 50 volume percent nickel at a rate of approximately 1.25 inches per minute. A larger version of the continuous plating equipment described above is currently under construction and should be capable of plating at approximately ten times the present rate.

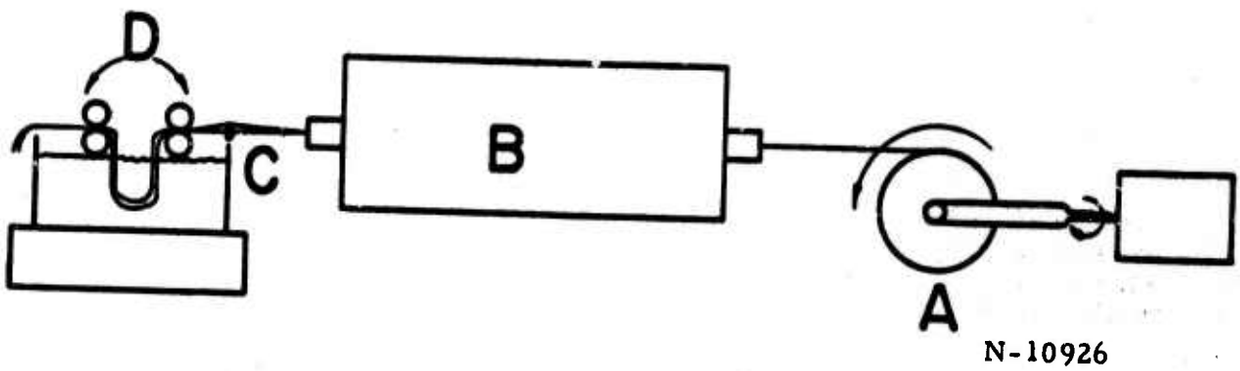

Figure 37. Schematic Diagram for Continuous Nickel Plating of Two-Ply Graphite Yarn.

Three plating baths (Watt's, nickel sulfate-boric acid, and sulfamate) were evaluated as part of this study on continuous plating of nickel on graphite yarn. The three plating baths provided comparable coating homogeneity around all the filaments, as shown by the photomicrograph in Figure 38. The physical appearance of the yarn from the three plating baths was remarkably different. Gas evolution (hydrogen) around the filaments in the sulfate bath resulted in a rather bulky yarn. The sulfamate solution provided yarn with very little filament separation. The Watt's bath provided a yarn which was somewhat intermediate between the two others in bulk density.

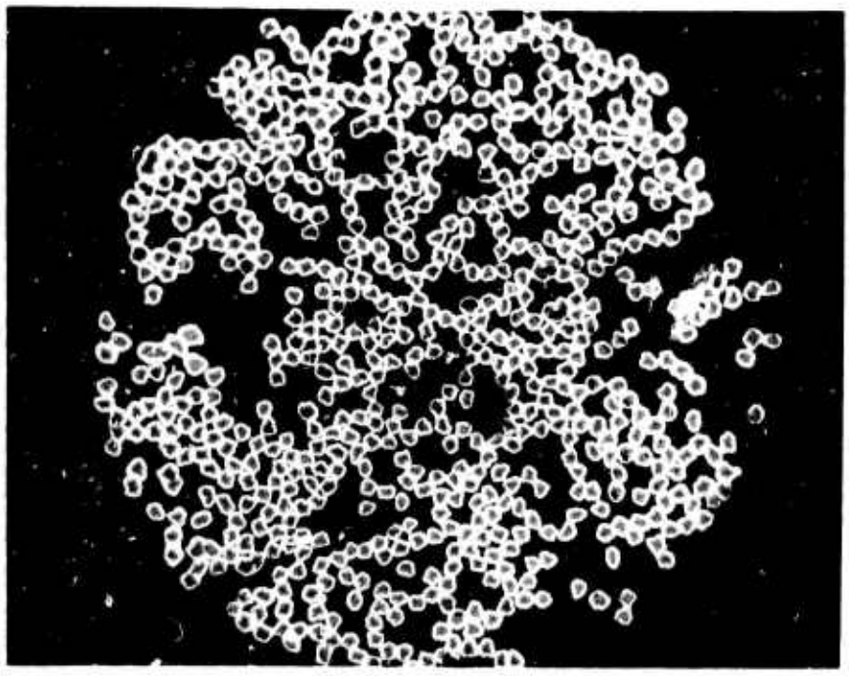

N-17490

Figure 38. A Single Ply of Nickel-Coated Graphite Filaments, Magnification 250X.

Fibers were coated with nickel to approximately 52 v/o from the three plating baths and formed into composites at 1050°C and 2500 lb/in.^{2} pressure. The as-received filaments had a Young's modulus of 34.5 x 10^6 lb/in.^{2} and a tensile strength of 200,000 lb/in.^{2}. Data for the three specimens are shown in Table XIX.

TABLE XIX

PROPERTIES OF COMPOSITES PREPARED FROM CONTINUOUSLY PLATED FIBERS

Plating Bath	Young's Modulus E (10^6 lb/in.^{2})	Shear Modulus G (10^6 lb/in.^{2})	Density ρ (g/cm^3)	Strength ultσ (lb/in.^{2})
Watts	28.7	4.5	5.147	65,900
Sulfamate	29.6	4.2	5.047	61,000
Sulfate	28.9	4.3	5.127	54,600

The filaments coated with nickel from the Watt's bath provided the highest composite strength, and according to stress-strain behavior, less yielding at high stress levels. Comparable amounts of uncoated fibers or structural irregularities were observed in the three microstructures. Some microporosity (approximately 1 to 2 percent) was found in composites fabricated both from batch plated and from continuously plated yarn.

The results shown in Table XIX indicate a slight superiority of the Watt's bath over other plating solutions. Further advantages of the Watt's bath include more uniform cation replenishment, which is highly desirable in order to obtain uniform coatings, and a more ductile nickel deposit.[19] Consequently, the more recent composite data cited in this report (the high temperature properties and a portion of the pressure forming studies) have been obtained on composites fabricated from continuously plated yarn using a Watt's bath; the photomicrograph in Figure 39 is representative of these specimens. The remaining specimens were prepared from batch plated yarn, plated from nickel sulfate-boric acid solutions, unless otherwise specified in the discussion.

N-17491

Figure 39. A Graphite-Fiber, Nickel-Matrix Composite Containing 46 Volume Percent Fibers, 100X Magnification.

3. Composite Fabrication Studies

Bar specimens (1/8 x 1/16 x 1 inch) for test purposes were prepared by hot pressing the nickel-coated fibers in vacuum at various forming pressures, temperatures, and fiber loadings. The hot pressing mold was shaped from graphite and employed a single wedge acting against the confined fibers. The pressing time in all cases was one hour at the peak temperature.

Metallographic studies of longitudinal composite sections showed some potentially serious fiber misalignment: the misalignment may reduce the axial strength and modulus properties. A typical example of this fiber irregularity is shown in the photomicrograph in Figure 40; this condition is representative of most composites prepared and evaluated to date. The microstructure shows that certain areas of the composite contain a number of fibers with their axes at approximately 30 degrees to that of the specimen axis. The difficulty in achieving highly aligned fibers in the nickel matrix is basically due to curvature in the plated yarn and a tendency for the yarn segments to shift as they are being positioned in the mold cavity. No practical method has yet been developed for anchoring the yarn segments in position as they are charged in the mold. Two methods have been attempted for achieving better alignment, but both approaches required an initial heat treatment before final compaction.

N-17492
Figure 40. Longitudinal Section of Graphite-Fiber, Nickel-Matrix Composite Showing Fiber Misorientation, 20X Magnification

The first approach was an attempt to correct the curvature and bulkiness by drawing the yarn at 1000°C through a graphite orifice with a diameter of 0.014 inch. (An orifice diameter of 0.011 would have consolidated the yarn to near theoretical density.) The graphite die used is shown in Figure 41. The extent of consolidation is evident from the yarn appearance on either side of the orifice. The appearance and quantity of yarn required for the preparation of one test specimen is shown in Figure 42. As evidenced by this photograph, perfectly straight yarn was not obtained, but there is a considerable improvement over the as-plated yarn.

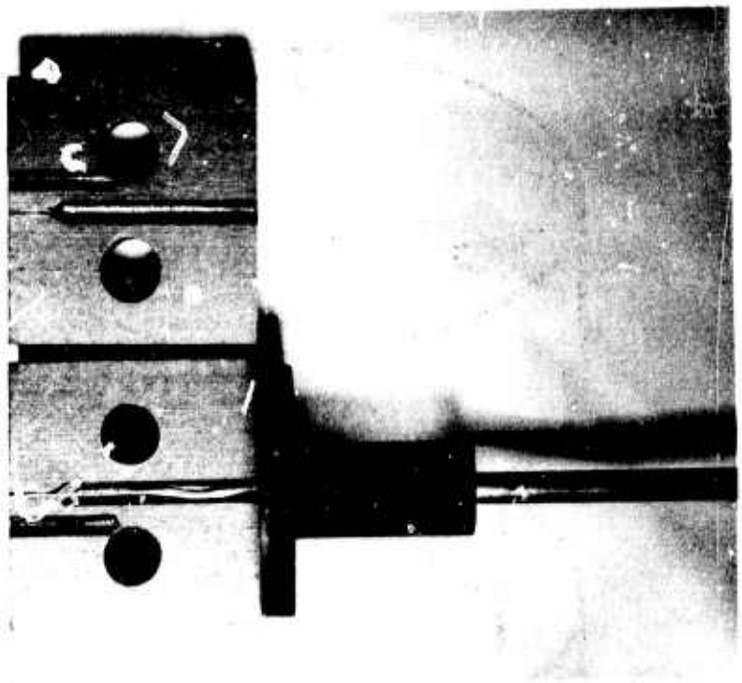

N-11579

Figure 41. Graphite Die for Consolidating Nickel-Coated Yarn, 1.4X Magnification.

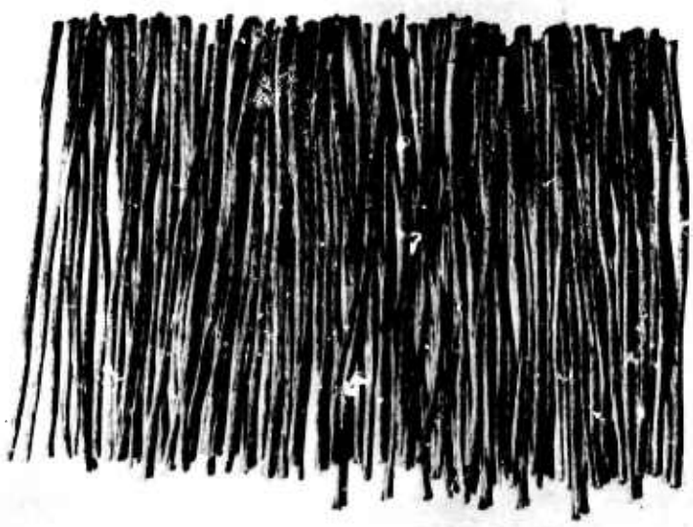

N-11580

Figure 42. Nickel-Coated Yarn after Drawing Through Die, 2.5X Magnification.

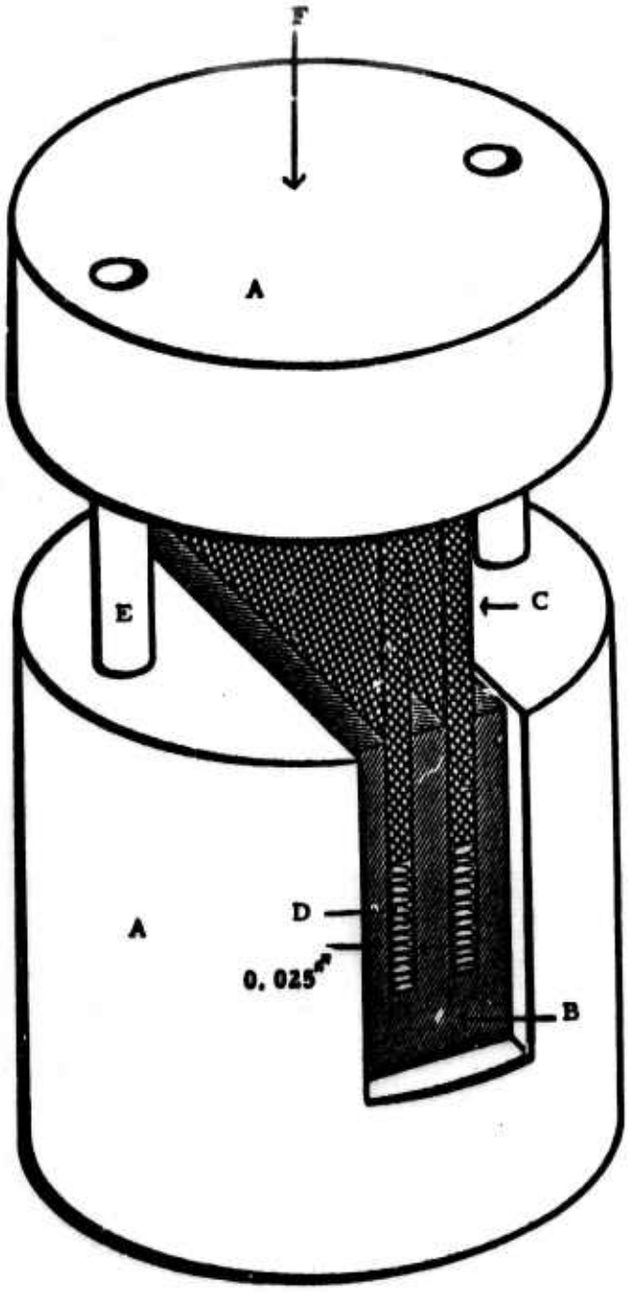

N-17090

A. Graphite Mold Components
B. Ceramic Insert
C. Ceramic Plungers
D. Nickel-coated Yarn
E. Stainless Steel Guide Pins
F. Applied Pressure

Figure 43. Mold Configuration for Preforming Wafers.

The second method for attaining better fiber collimation consisted of forming a number of thin wafers with a mold, as shown in Figure 43. The objective of this mold configuration was to confine the yarn in a cavity having a width (0.025") only slightly greater than the diameter of a single ply, thereby imposing a high probability of alignment. Two wafers were formed simultaneously at 1000°C under an applied pressure of 300 lb/in.^{2}. Approximately 70 percent of theoretical density was achieved. The final composite was prepared by stacking four such wafers in a larger mold and hot pressing normal to the smallest wafer dimensions. The microstructure for a composite prepared in this manner (Figure 44) showed very good axial alignment of the fibers. The tensile fracture in Figure 44 shows little, if any, fiber pull-out and is more regular than normally encountered with misaligned fibers.

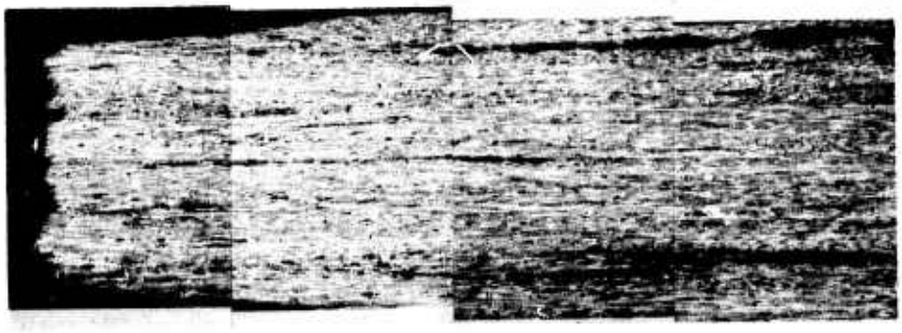

N-17493

Figure 44. Longitudinal Section of Graphite-Fiber, Nickel-Matrix Composite Showing Fracture Edge and Fiber Orientation 20X Magnification.

Properties representative of a conventionally fabricated composite (with fiber misalignment), a composite prepared from higher bulk density yarn (previously drawn through a graphite orifice at an elevated temperature), and a composite made from preformed wafers are shown in Table XX. The theoretical modulus and strength (based on the rule of mixtures) are 40 x 10^6 lb/in.^{2} and 130,000 lb/in.^{2}, respectively. The composite prepared from preformed wafers has a tensile strength virtually equivalent to that of conventionally prepared specimens containing a relatively high degree of fiber misalignment. These results suggest that additional weakening mechanisms prevail in the system. A number of these detrimental factors have been identified and are discussed in Section IV A 4 in conjunction with additional fabricational studies. The composite prepared from wafers has a higher modulus of elasticity than that of either of the other specimens represented in Table XX. The modulus for the conventionally prepared specimen is typical of values derived for approximately thirty other specimens fabricated in the same manner. The specimen prepared from high bulk

density fibers failed to densify; ply-overlapping with this type yarn evidently requires greater forming pressures.

TABLE XX

PROPERTIES OF CONVENTIONAL COMPOSITES AND OF COMPOSITES WITH IMPROVED FIBER ALIGNMENT

Specimen	Young's Modulus E (10^6 lb/in.^{2})	Shear Modulus G (10^6 lb/in.^{2})	Strength ult σ (lb/in.^{2})	Density ρ (g/cm^3)
Conventional	31.2	4.49	79,500	5.027
High Bulk Density Yarn	29.9	3.99	73,700	4.802
Preformed Wafers	34.5	4.39	81,150	5.118

All data presented in subsequent sections pertain to composites fabricated by conventional hot pressing, i.e., without using the listed precautions to achieve the highest degree of fiber alignment. The efforts discussed in the following sections were attempts to define problem areas other than fiber collimation that are detracting from the anticipated strength values. The process of hot pressing rather delicate metal-coated filaments is relatively involved, and each of the conventional variables of pressure, temperature, time, and environment, individually and collectively, have some effect on the properties of this system. It became obvious after initial probing studies that all of these parameters had to be considered in detail if their effects are to be understood.

4. Influence of Fabrication Parameters on Room-Temperature Composite Properties

a. Preliminary Studies

A series of specimens was prepared with an intended fiber loading of approximately 56 v/o for the purpose of determining the effect of forming pressure and temperature on composite properties. Yarn with a 34.5 million lb/in.^{2} modulus was used for these studies (for fiber properties see Table XVIII). The properties of these specimens are shown in Tables XXI and XXII. Metallographic examination showed that essentially theoretical density was achieved at pressures equal to or greater than 4500 lb/in.^{2} and temperatures of 900°C or higher. The conditions of 900°C and 4500 lb/in.^{2} for achieving maximum density, therefore, were used in forming the composites shown in Table XXIII. Microstructural studies on all the specimens gave no evidence of fiber degradation due to dissolution of carbon in nickel or of graphite precipitation in the matrix.

TABLE XXI

GRAPHITE-FIBER, NICKEL-MATRIX
COMPOSITES FORMED AT 900°C

Forming Pressure ($lb/in.^2$)	Young's Modulus E ($10^6 lb/in.^2$)	Shear Modulus G ($10^6 lb/in.^2$)	Strength ult σ ($lb/in.^2$)	Density ρ (g/cm^3)	Fiber Volume Percent
2250	26.3	3.20	49,700	4.15	48.0
4500	28.6	4.01	48,800	4.84	55.5
6750	28.8	4.07	47,300	4.81	55.5

TABLE XXII

GRAPHITE-FIBER, NICKEL-MATRIX COMPOSITES
FORMED AT 4500 $lb/in.^2$

Form. Temp. (°C)	Young's Modulus E (10^6 $lb/in.^2$)	Shear Modulus G (10^6 $lb/in.^2$)	Strength ult σ ($lb/in.^2$)	Density ρ (g/cm^3)	Fiber Volume Percent
800	27.9	3.75	58,000	4.54	52.7
900	28.6	4.01	48,800	4.84	55.5
1000	29.6	3.95	57,200	4.75	56.8
1100	29.2	3.80	46,600	4.78	56.4

TABLE XXIII

GRAPHITE-FIBER, NICKEL-MATRIX COMPOSITES
FORMED AT 4500 $lb/in.^2$ AND 900°C

Young's Modulus E ($10^6 lb/in.^2$)	Shear Modulus G ($10^6 lb/in.^2$)	Strength ult σ ($lb/in.^2$)	Density ρ (g/cm^3)	Fiber Volume Percent
25.7	1.62	18,600	3.31	76.6
28.6	4.01	48,800	4.84	55.5
28.2	4.86	45,400	5.33	49.1
29.1	7.71	50,000	6.84	28.3

The values of the tensile strength for these composites failed to show any significant response to the various parameters considered in this investigation, and the values achieved represent a negligible improvement over the matrix metal. The poor strength for the 76.6 v/o fiber composite (Table XXIII) is due largely to the excessive porosity and laminations prevalent in the structure. The absence of any appreciable reinforcement in these composites is due, in part, to similarity of the fiber modulus (34.5×10^6 lb/in.^{2}) to that of the matrix (31×10^6 lb/in.^{2}) and, in part, to the high forming pressure of 4500 lb/in.^{2}. Subsequent work has shown that fiber damage is excessive at pressures of 4500 lb/in.^{2} and contributes to weakening the structure. The modulus of elasticity also does not under go significant change with processing variations. The maximum value of 29.6×10^6 lb/in.^{2} is approximately ten percent lower than the modulus obtained by the rule of mixtures. Part of this discrepancy may be due to fiber misalignment.

b. Forming Pressure Studies

The effect of forming pressure on composite properties has been studied in greater detail by employing smaller pressure increments than those shown in Table XXI. The principal objective of this work was to determine the densification behavior and the minimum pressure required for maximum densification of the composites.

Composites containing 49, 57, and 62 v/o fibers were fabricated by hot pressing the nickel-coated fibers at 1050°C for one hour; 49 v/o fiber composites were also formed at 900°C for one hour. The quoted fiber contents are average values with a deviation of approximately ± 2 percent. Pressing for one hour at 1050°C gave maximum densification (theoretical density) at approximately 2500 lb/in.^{2} for the 57 v/o fiber composite (see Figure 45). At fiber loadings of 62 v/o, however, only 96.5 percent of the theoretical density could be obtained, although a forming pressure as high as 4500 lb/in.^{2} was employed. Metallographic studies revealed that porosity in the 62 v/o composites was caused by laminations resulting from metal deficiency around many of the fibers (see Figure 46). Pressing at 900°C required higher pressures in order to achieve fully densified composites. The curve for the 49 v/o fiber composite in Figure 45 suggests that the minimum pressure necessary to achieve maximum density at 900°C is 3300 lb/in.^{2}.

c. Tensile Strength Results

The tensile strength of the composite specimens is a function of forming pressure, forming temperature, and fiber loading (see Figure 47). For example, the tensile strength of a 57 v/o composite formed at 1050°C shows a maximum of 78,000 lb/in.^{2} at a forming pressure of 2,500 lb/in.^{2}, whereas pressing at 4500 lb/in.^{2} results in a strength of only 50,000 lb/in.^{2}. For this particular composite, a pressure of 2500 lb/in.^{2} is also the minimum pressure required to achieve full densification. This relationship may, however, be only coincidental, because the strength of the 49 v/o composite pressed at 900°C is likewise highest at a forming pressure of 2500 lb/in.^{2}, whereas full densification requires a pressure of 3300 lb/in.^{2}.

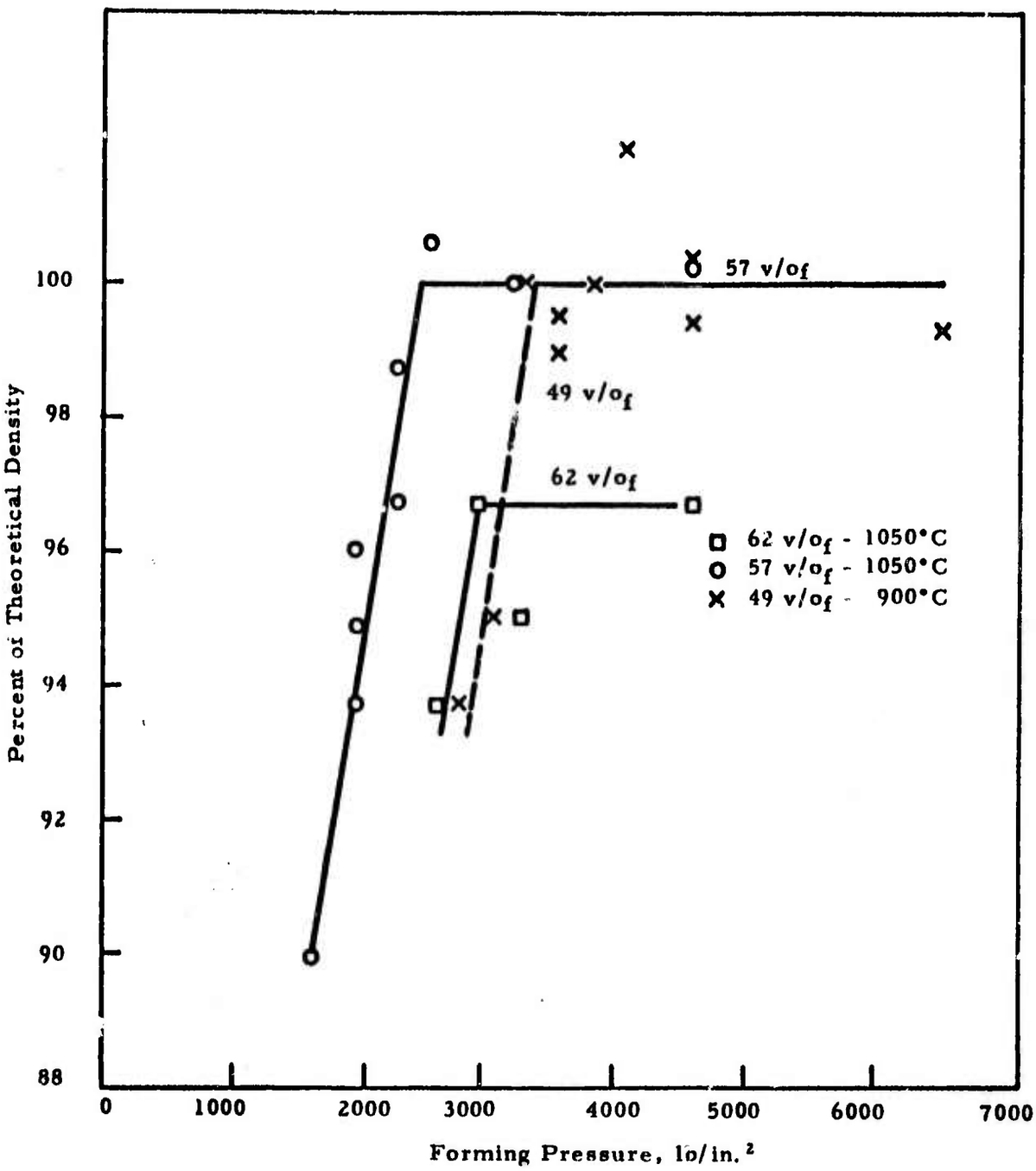

N-17087

Figure 45. Densification of Graphite-Fiber, Nickel-Matrix Composites at 900° and 1050°C.

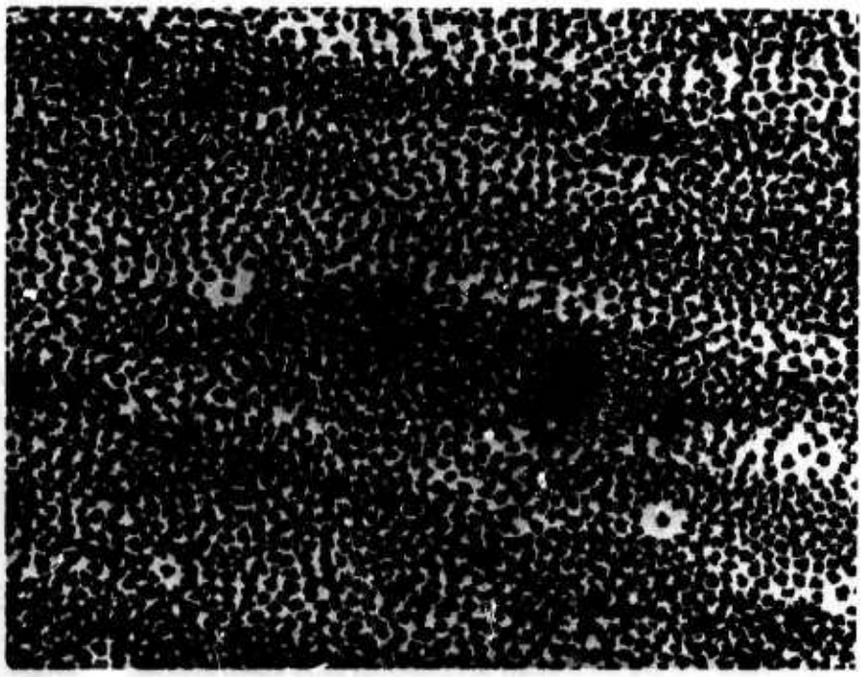

N-10582

Figure 46. Laminations in Graphite-Fiber, Nickel-Matrix Composite Containing 62 Volume Percent Fibers. 250X Magnification.

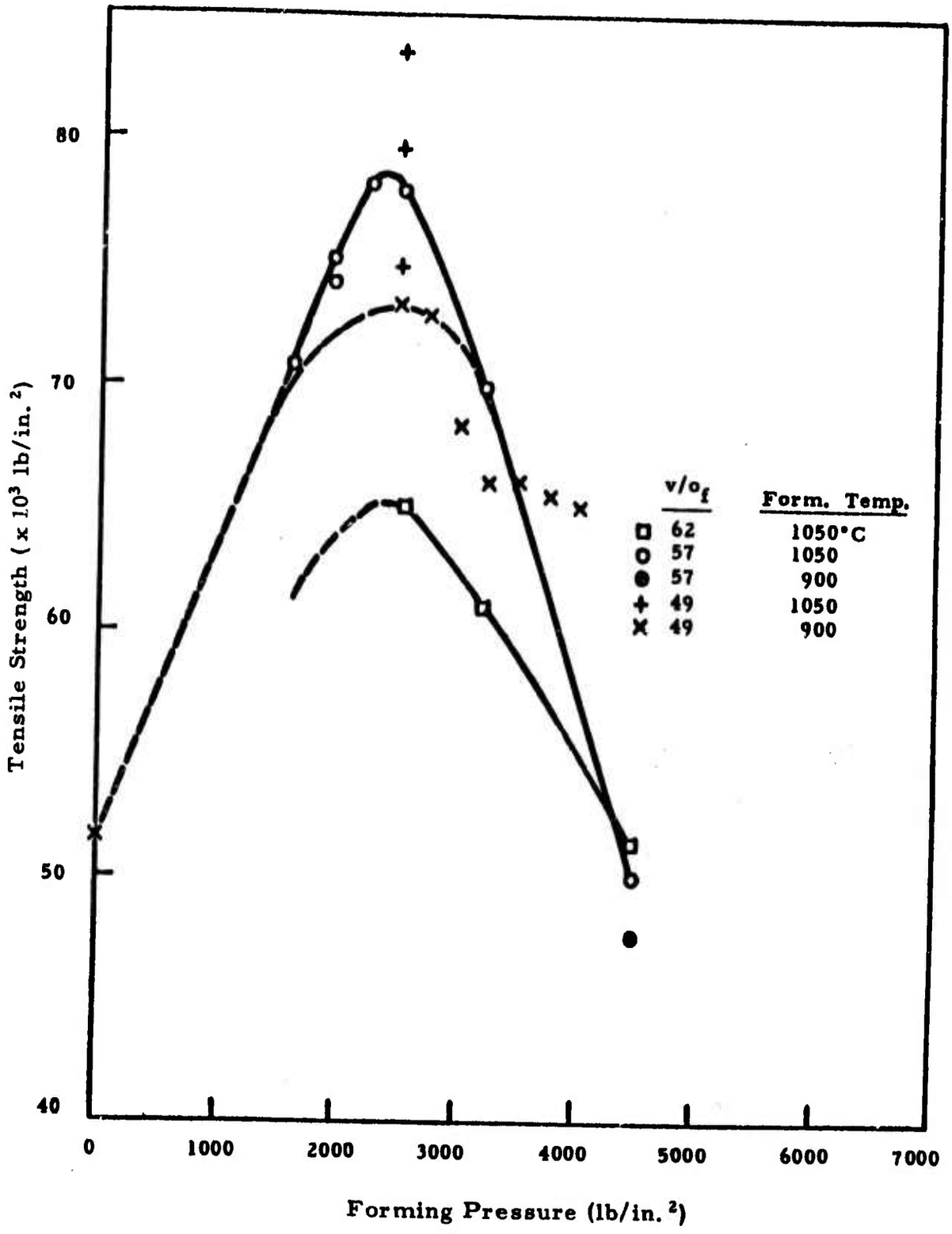

N-17757

Figure 47. Effect of Forming Pressure on Graphite-Fiber, Nickel-Matrix Composite Strength.

The porosity of the 49 v/o composites can be eliminated by raising the forming temperature to 1050°C; this temperature also improves the strength, as shown for three specimens in Figure 47. The data in Figure 47 also indicate that, for fiber contents above 49 v/o, the maximum obtainable strength decreases with increased fiber loadings. Limited experimental evidence shows that the curves in Figure 47 should not be extrapolated toward higher forming pressures; rather, a strength plateau appears to prevail at pressures of 4500 lb/in.^{2} and higher. This strength plateau may be strongly dependent on fiber content. Composites containing 57-62 v/o fibers formed at 4500 lb/in.^{2} had a strength of 50,000 lb/in.^{2}, whereas a single composite containing 46 v/o fibers formed at the same pressure had a strength of approximately 75,000 lb/in.^{2}.

The data in Figure 47 show that a strength maximum occurs at a forming pressure of 2500 lb/in.^{2} at pressing temperatures of either 900 or 1050°C. Cratchley and Baker[20] observed a similar strength maximum at a certain forming pressure in their studies of glass fiber-aluminum composites. They attributed this behavior to the opposing effects of increased bonding between adjacent metal-coated fibers (densification) versus increased fiber damage (decreased fiber strength) as the pressing pressure increased. Their model is shown in Figure 48. This same reasoning seems applicable to the carbon fiber, nickel-matrix composites, since the data show that, as porosity diminishes with increasing forming pressures up to 2500 lb/in.^{2}, the strength also increases. However, forming pressures higher than 2500 lb/in.^{2} evidently damage the fibers more extensively, thereby weakening the structure.

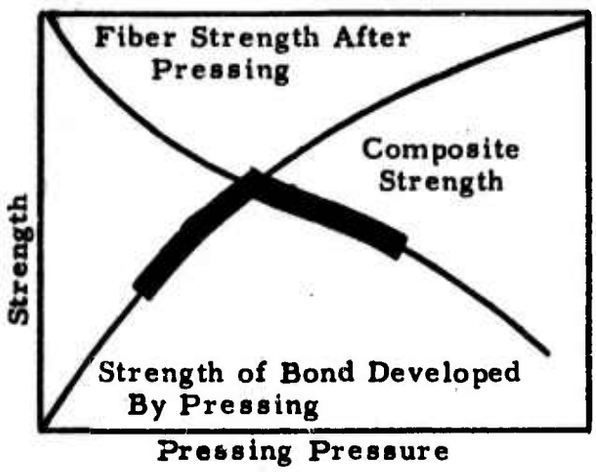

N-10053

Figure 48. Model Proposed for the Effect of Pressure on Strength by Cratchley and Baker.

d. Physical Damage of Fibers

Four modes of fiber damage or fiber irregularities in the graphite fiber, nickel-matrix composites have been proposed that can be attributed to forming pressure. Three of these damage mechanisms have been confirmed by microscopic studies; the fourth, which concerns surface damage, has not been verified experimentally. The following evidence, although qualitative, is of fundamental importance in guiding subsequent endeavors to achieve better composite properties.

Fiber Cleavage. Fibers which fragmented longitudinally as a result of high pressure have been observed in microstructures, as evidenced by the circled regions in the photomicrograph of Figure 49. The cleaved fibers were found most frequently in composites with high volume fractions of fiber. The fragmentation may be a consequence of fiber-fiber attrition or may result from applying pressure to the notched regions which characterize the fiber cross-section.

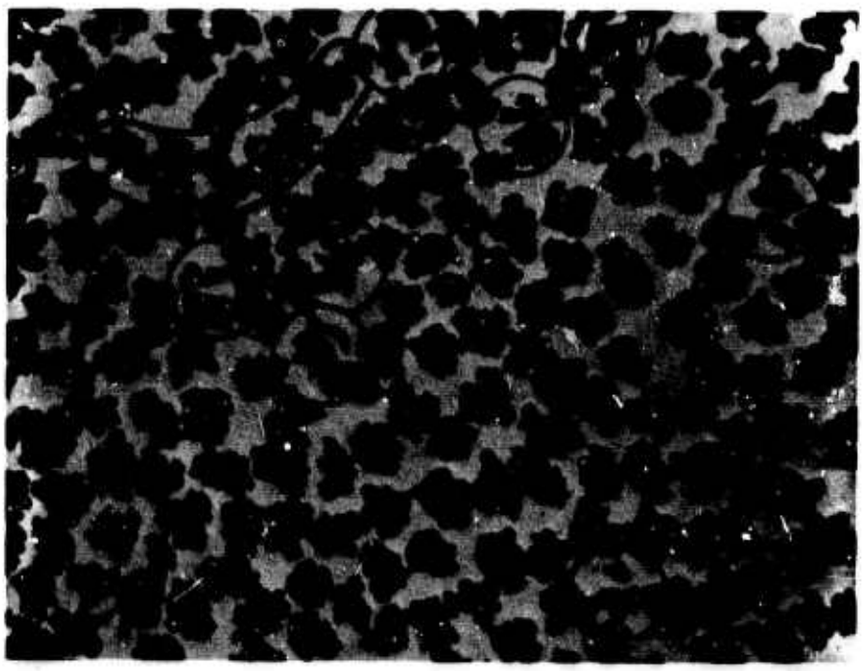

N-17494

Figure 49. Fiber Damage and Fiber-Fiber Contact in Graphite-Fiber, Nickel-Matrix Composite, 1000X Magnification.

Fiber Chain-Like Networks. The second anomaly observed in high fiber volume microstructures consists of the bridged fiber configurations outlined in Figure 49. The fibers appear to be interconnected

by carbon which has diffused into regions between the fibers. At high temperatures, the system will tend to minimize the free surface energy by reducing the high fiber surface area and forming larger and energetically more favorable cross sections. The fiber bridging seen in Figure 49 may be the first stage of this process.

Shortened Fibers. The third effect concerns fiber breakage into short lengths due to high forming pressures. As a result, the aspect ratios decrease from essentially infinity to a distribution of smaller values. Although this matter has not been pursued in detail, an investigation of fibers extracted from a composite which had been pressed at 2500 lb/in.^{2} shows that the upper limit in the aspect ratio distribution is 1000. Due to a tendency for the longer fibers to interlock, sampling and portraying a representative fiber length distribution is difficult. Underneath a mat of longer fibers shown in Figure 50, for example, is a large concentration of shorter fibers (see Figure 51). Furthermore, as a result of the extraction operation, the filter paper trapped a large quantity of fibers with smaller lengths than are shown in Figure 51.

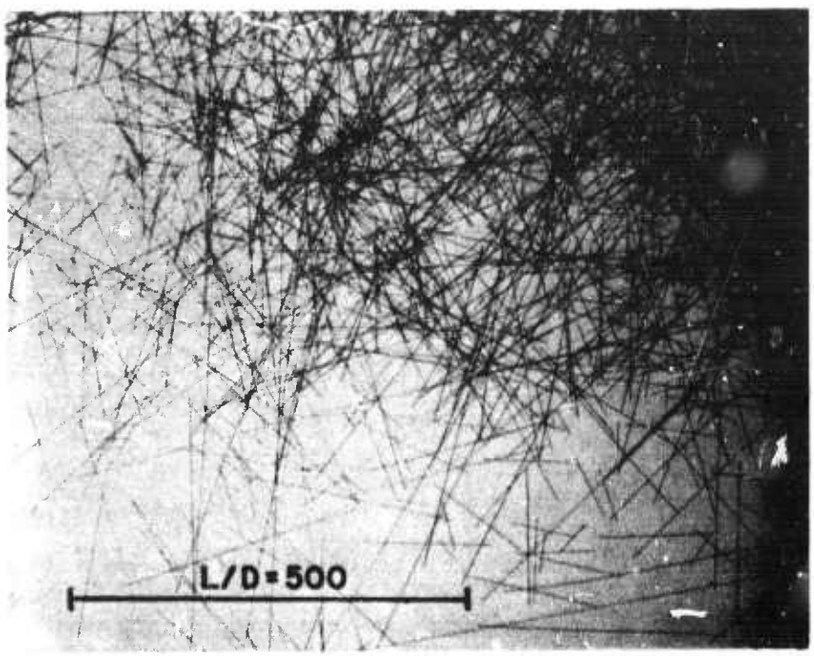

N-17495

Figure 50. Longest Fibers Extracted from Graphite-Fiber, Nickel-Matrix Composite after Pressing at 2500 lb/in.^{2}.

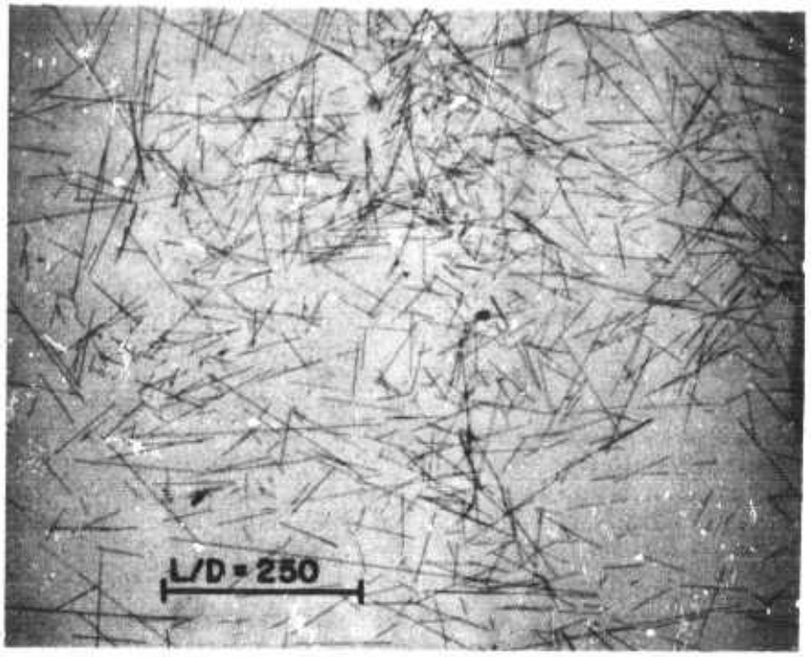

N-17496

Figure 51. Intermediate Length Fibers Extracted from Graphite-Fiber, Nickel-Matrix Composite after Pressing at 2500 lb/in.^{2}.

There is reason to believe that, in this case, the majority of fibers exceeded the critical aspect ratio, but this condition may not prevail in composites formed a pressures greater than 2500 lb/in.^{2}. Similar studies, contemplated for composites formed at pressures greater than 2500 lb/in.^{2}, should reveal whetner the decrease in strength at the high-forming pressures is a consequence of abnormally short fiber lengths.

Surface Damage. The damage to fiber surfaces as a result of compaction pressure has not been ascertained. If the pressures employed are capable of cleaving the fibers, they may also be great enough to introduce surface imperfections. Efforts are now being made to extract fibers from fabricated composites for physical testing. Mounting and testing the shortened fibers, however, is extremely difficult.

e. Young's and Shear Modulus Results

The variation in modulus of elasticity with forming pressure for the composites containing 49, 57, and 62 percent fibers is shown in Figure 52. The curves show the expected improvement in modulus as the porosity decreases with forming pressure. The 57 and 62 v/o fiber composites contained 61 x 10^6 lb/in.^{2} modulus fibers, whereas 49 x 10^6 lb/in.^{2} modulus fibers were used in the 49 v/o fiber composites. The

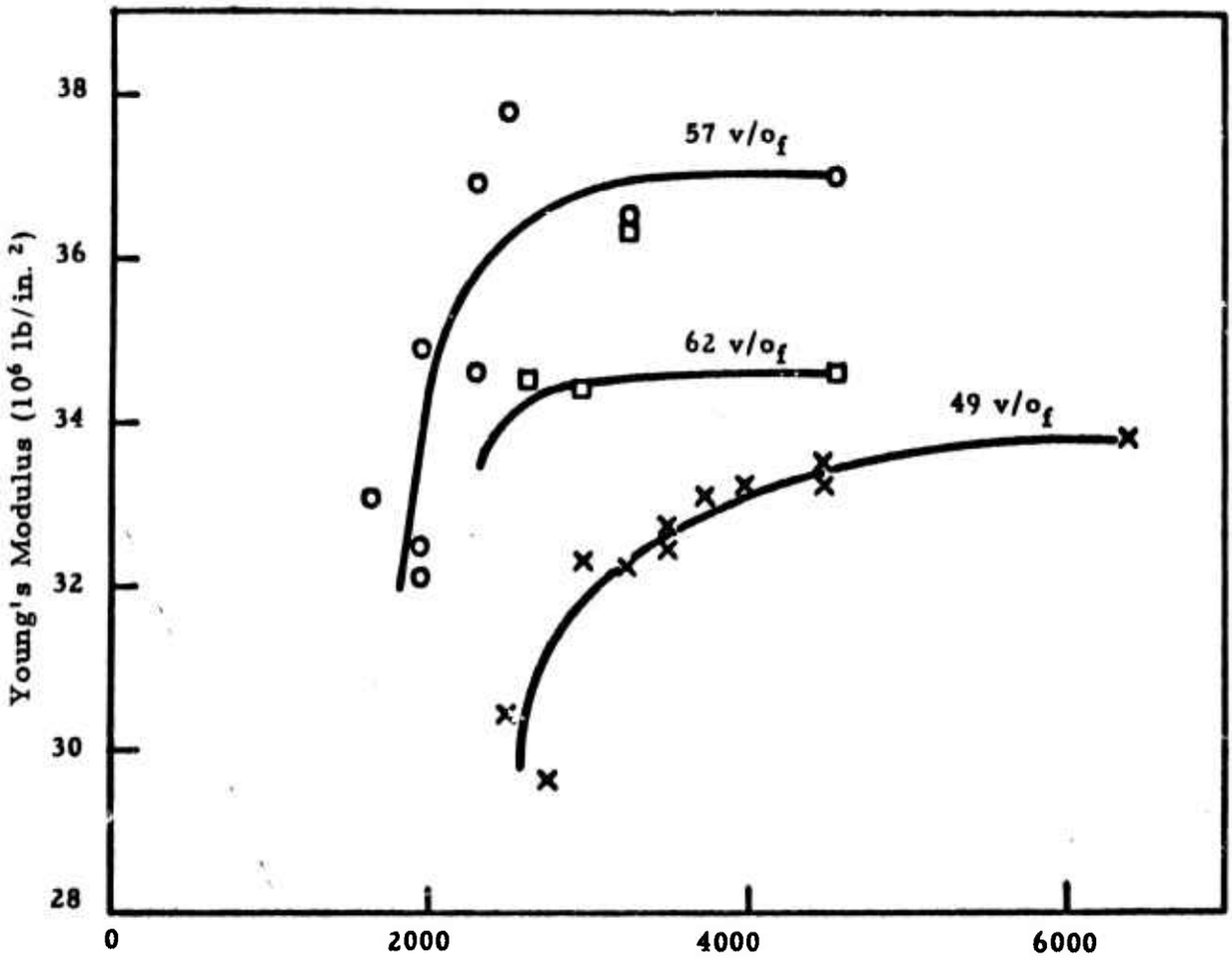

N-17085

Figure 52. Young's Modulus for Graphite-Fiber, Nickel-Matrix Composites.

composite modulus values are in accord with the fiber properties, but only 85 and 77 percent of rule of mixtures modulus was achieved for the 49 and 57 percent fiber specimens, respectively. Abnormally low modulus values for the 62 v/o composites are due to excessive porosity. Failure to achieve rule-of-mixtures values is due, in part, to fiber misalignment and, in part, to unknown factors.

The effect of forming pressure or densification on shear modulus (measured by torsional resonant vibrations) for composites containing 49, 57, and 62 v/o fibers is shown in Figure 53. A reduction in porosity and higher metal contents increase the shear modulus.

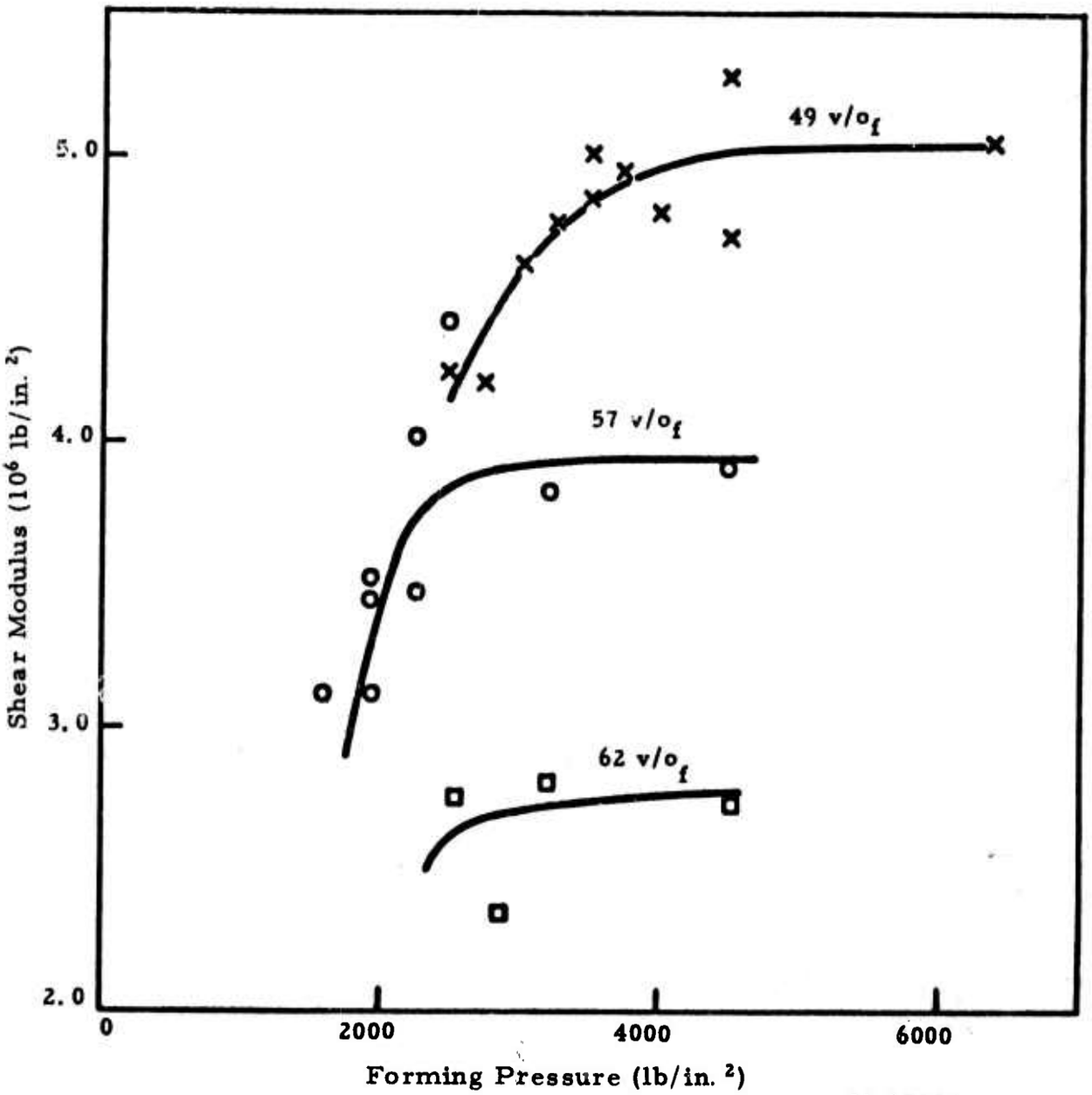

N-17084

Figure 53. Shear Modulus for Graphite-Fiber, Nickel-Matrix Composites.

f. Fiber Loading Studies

Composites containing different volume fractions of fibers were prepared by first electroplating nickel on the filaments to the appropriate thickness and then hot pressing the aligned metal-coated fibers in vacuum at 1050°C for one hour under the optimized pressure of 2500 lb/in.^{2}. The plating was done on a batch basis with a nickel sulfamate or nickel sulfate-boric acid plating solution. Microstructural studies and bulk density calculations indicated that porosity was less than 5 percent.

The variation in tensile strength for composites with fiber volume fractions between 29 and 62 percent is show in Figure 54. A curve showing the theoretical composite strength as a function of fiber

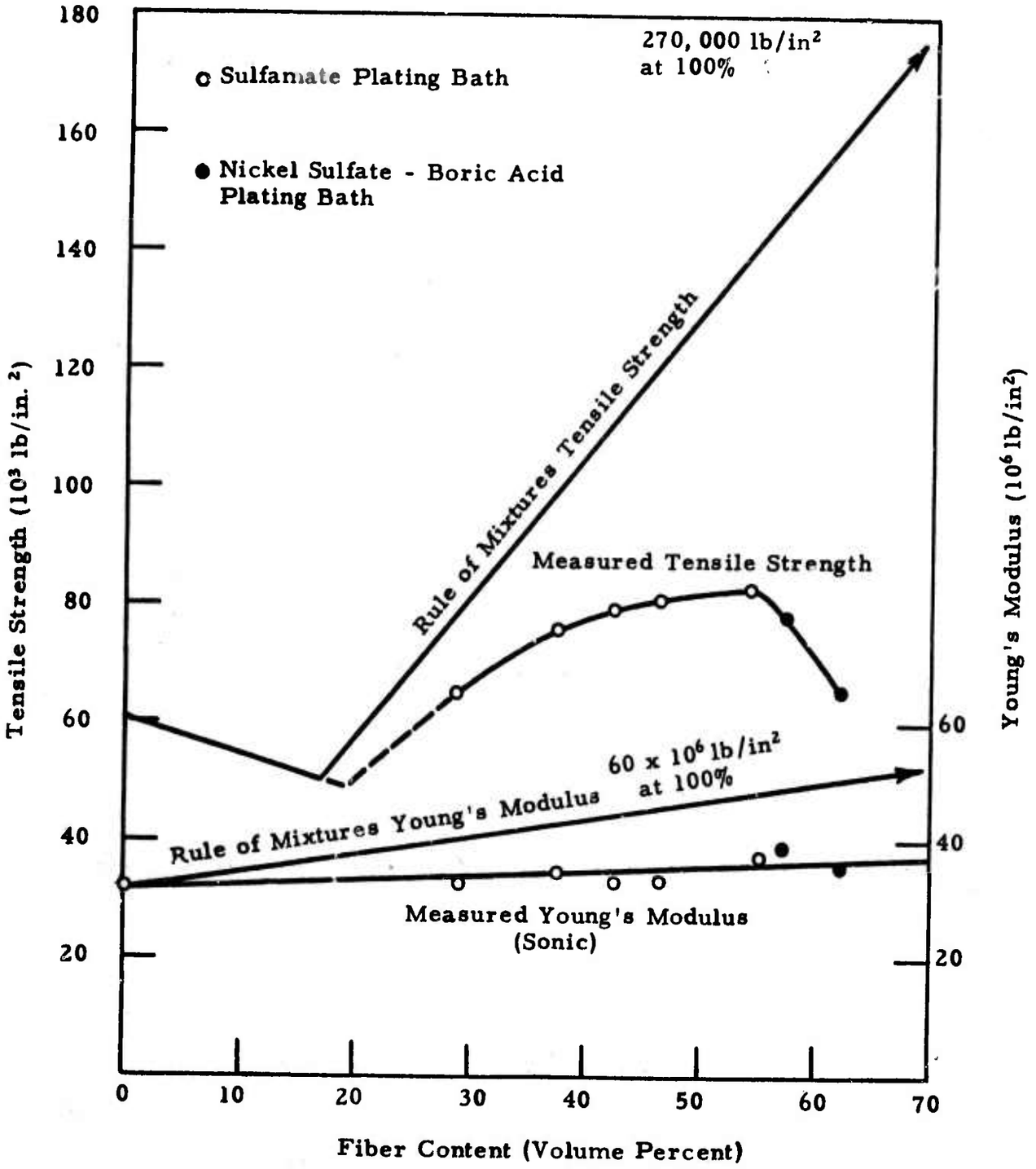

N-10882

Figure 54. Tensile Strength and Young's Modulus for Graphite-Fiber, Nickel-Matrix Composites Versus Fiber Content.

loading was constructed by using properties for Nickel "A" which had previously been annealed at the 1050°C hot pressing temperature and a fiber tensile strength of 270,000 lb/in.^{2}. According to Figure 54, the maximum composite strength of 82,000 lb/in.^{2} occurs at 55 v/o fibers and represents approximately 60 percent of the rule-of-mixtures value. The strength drop-off depicted at the highest fiber loadings can be attributed to inferior microstructures (see Figures 46 and 49).

The shear modulus (Figure 55) for the composites varies non-linearly with fiber content and decreases from 12 x 10^6 lb/in.^{2} for pure Nickle to an extrapolated value of 1 to 2 x 10^6 lb/in.^{2} for the fiber.

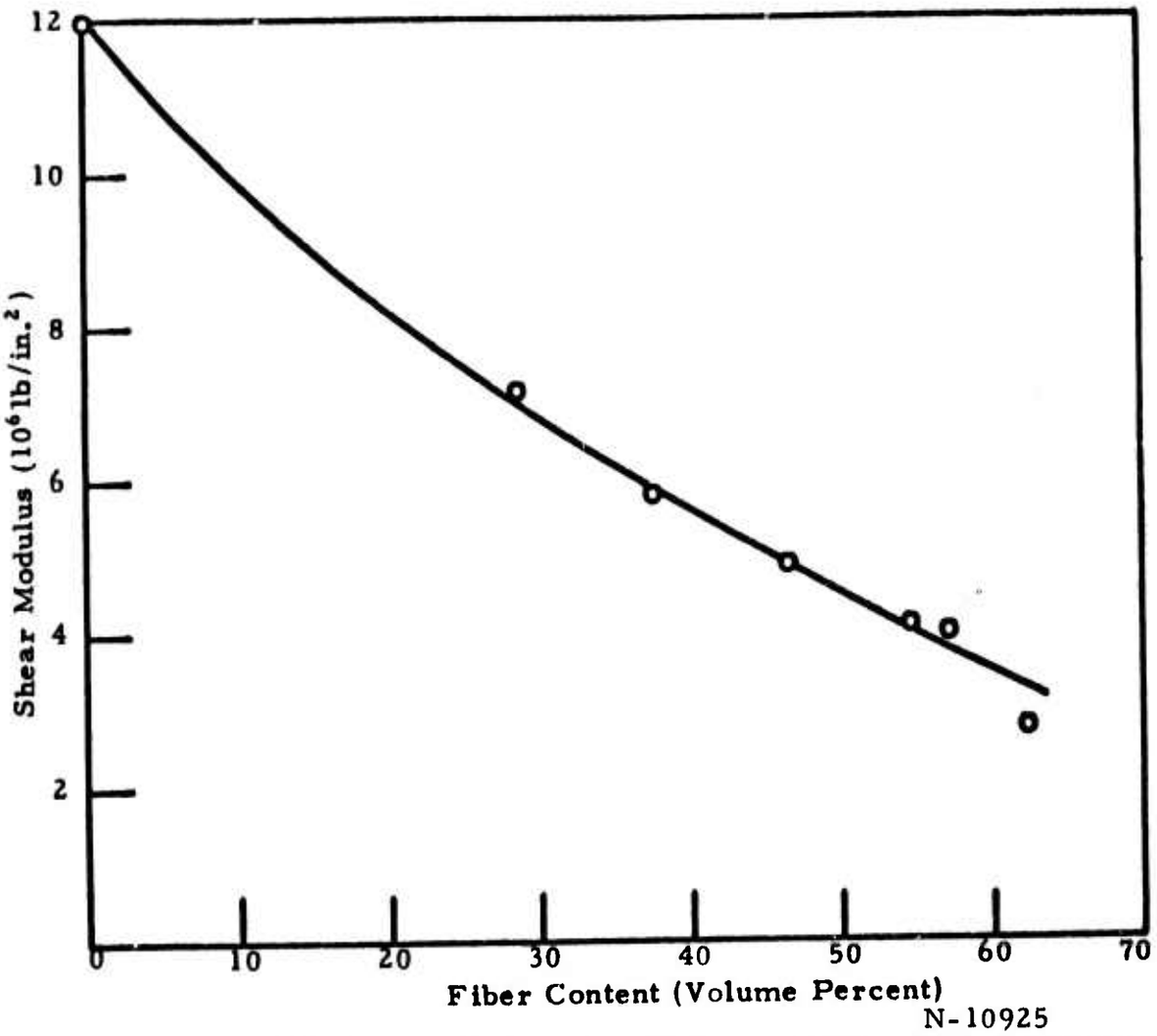

Figure 55. Shear Modulus for Graphite-Fiber, Nickel-Matrix Composites Versus Fiber Content.

The stress-strain relationships of annealed nickel and of a graphite fiber, nickel-matrix composite containing 55 v/o fibers are shown in Figure 56. The stress-strain behavior for the composite in Figure 56 is typical of other fiber loadings for this system. A proportional limit of approximately 20,000 lb/in.^{2} was observed in all cases, and strain at fracture increased slightly as the fiber content decreased. The stress-strain curve provided moduli which either matched or exceeded the dynamic values shown in Figure 54.

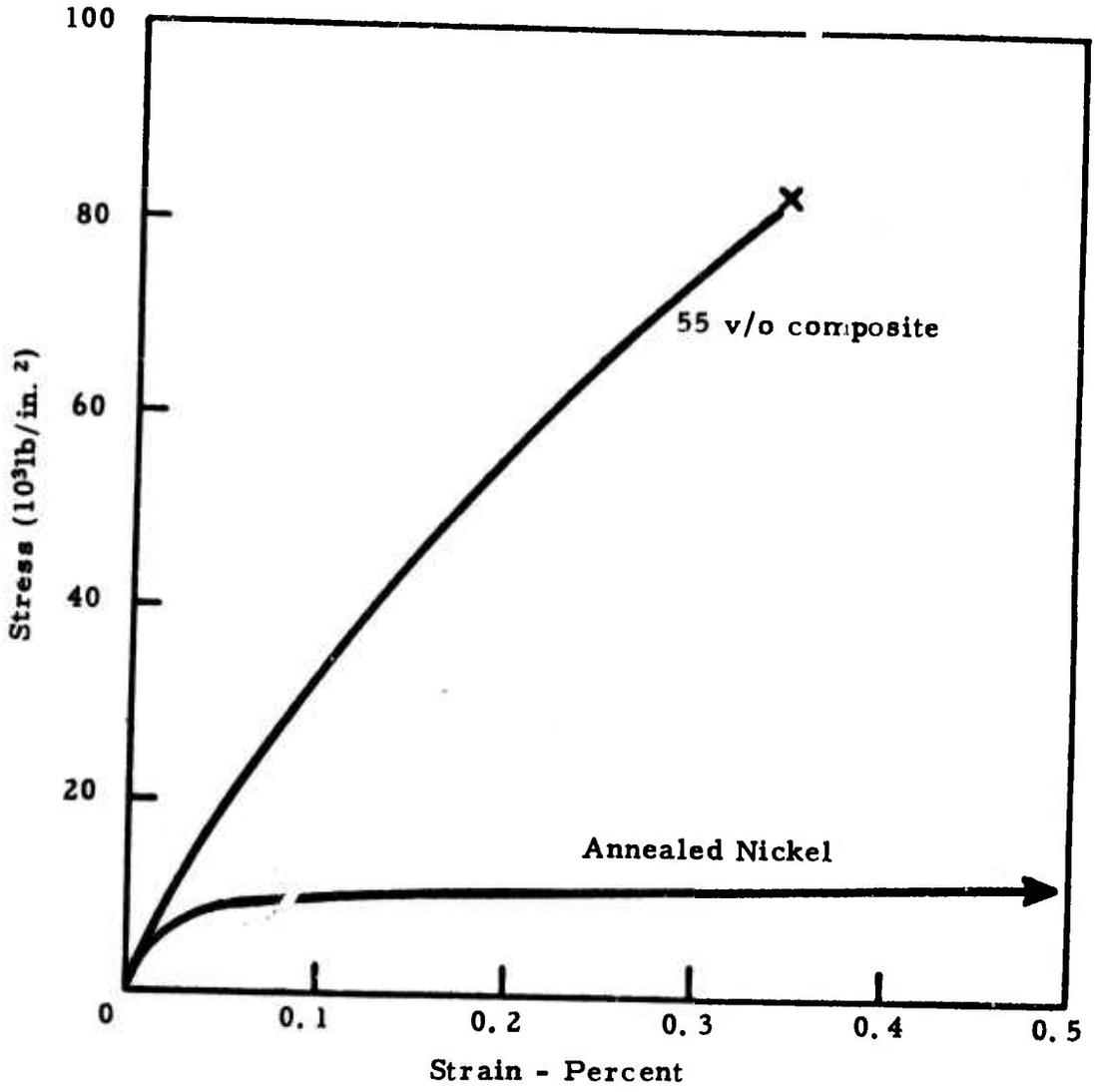

N-17082

Figure 56. Stress-Strain Relationships for Graphite-Fiber, Nickel-Matrix Composite and Annealed Nickel.

g. Thermal Degradation of Fibers

The rather significant difference between experimental and theoretical strength values for these composites indicates that the semi-optimized fabrication pressure used in consolidating the yarn segments is not the complete solution for obtaining high strength composites. It was noted previously that fiber damage is an important consideration, and pertinent irregularities were identified in composites fabricated at pressure higher than 2500 lb/in.^{2}. The threshold pressure for physical fiber damage has not yet been conclusively established. However, a pressure of 2500 lb/in.^{2} is suspected since the composite strengths in Figure 47 peak at this forming pressure quite independent of densification. To supplement investigations of physical degradation, the strength of the fibers was measured after they had been heated in a nickel environment. The slight solid solubility of carbon in nickel[21] (of the order of 1.5 atomic percent at 1050°C) could damage and weaken the fibers.

Segments of nickel-coated yarn (50 and 60 x 10^6 lb/in.^{2} modulus) were heated to various temperatures between 500 and 1050°C for one hour and the nickel removed by solution in 50 percent HCl before the yarn was physically tested. The tensile strength results for the two fiber lots after these heat treatments are shown in Figure 57. The data show that the fibers are, in fact, weakened appreciably. The phase diagram data in Figure 57 show that the solid solubility of carbon in nickel starts at approximately 700°C, the temperature at which fiber fiber weakening becomes noticeable. Control specimens revealed that acid does not affect the fibers, and uncoated fibers do not suffer strength loss after being heated to 1050°C. On the basis of a reduced fiber strength of 200,000 lb/in.^{2}, the experimental composite strength agrees with the theoretical strength for the 30 v/o composite in Figure 54, but is only 75 percent of the theoretical strength for the 55 v/o composite.

According to the data given in Figure 58, the fiber modulus of elasticity is not degraded as a result of heat treatment in a nickel environment, a fact which suggests that the strength degradation is due to surface or localized conditions rather than to bulk changes in the fiber. The experimental modulus of elasticity for the composites reported in Figure 54 reflects a marked deviation from the anticipated values. The effective modulus of the fibers in the composite is approximately 40 x 10^6 lb/in.^{2} as opposed to a measured value of 60 x 10^6 lb/in.^{2} for the as-received yarn. As mentioned previously, part of this difference is due to misalignment and slight porosity; but the major factors are not well understood at this time.

h. Elevated Temperature Composite Properties

A vacuum capsule, specimen grips, and extension rods assembly, obtained from the Instron Company, were used for tensile testing of pure nickel and of graphite fiber, nickel-matrix composites at elevated temperatures. The equipment was modified slightly and special devices were designed to facilitate better specimen alignment and loading without dang

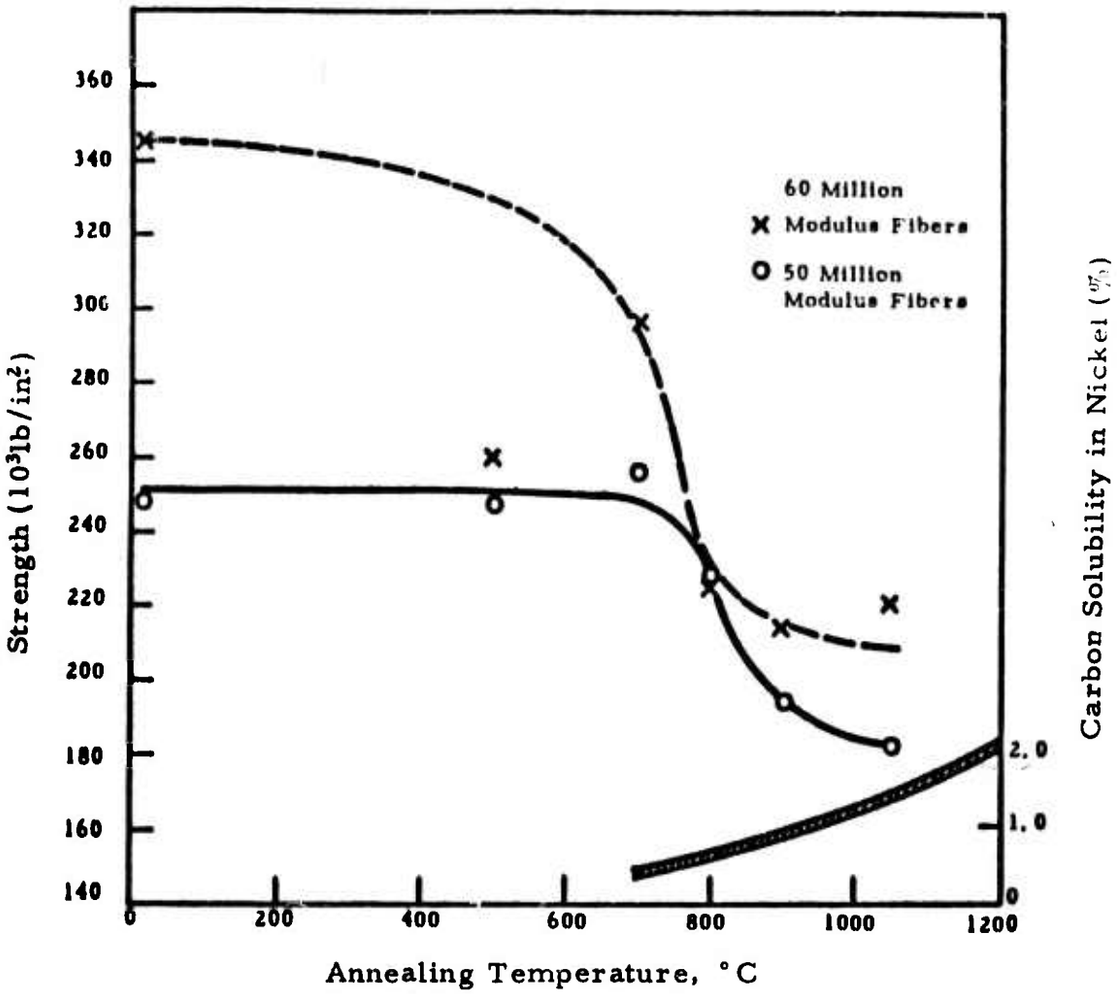

N-17089

Figure 57. Graphite Fiber Tensile Strength after Interaction with Nickel at Various Temperatures.

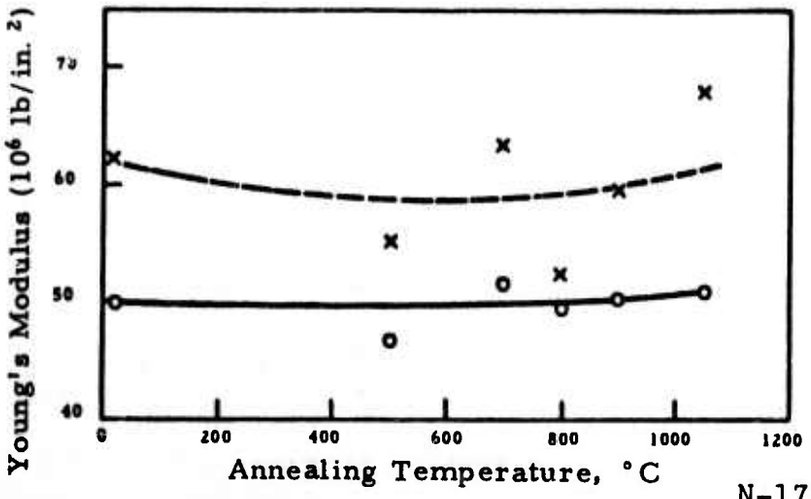

N-17086

Figure 58. Graphite Fiber Modulus after Interaction with Nickel at Various Temperatures.

of prematurely breaking the samples. A series of eight annealed Nickel "A" specimens was tested in tension at elevated temperatures to establish confidence in the test equipment before composites were tested. The results of these measurements generally confirm published values[21], as evidenced by the information presented in Figure 59.

The fibers used in the preparation of graphite fiber, nickel-matrix composites for study of elevated temperature tensile properties were characterized by a modulus of elasticity and tensile strength of 49.2×10^6 lb/in.^{2} and 261,000 lb/in.^{2}, respectively. The continuous plating operation was used to electroclad the yarn with nickel. The specimens were formed from the coated yarn segments by pressing at 1050°C and 2500 lb/in.^{2} for one hour. The composites contained approximately 50 v/o fibers; the average properties for 25 specimens prepared for these tests were: density, 5.217 g/cm^3; Young's modulus, 32.3×10^6 lb/in.^{2}; and shear modulus, 4.62×10^6 lb/in.^{2}.

The composites were studied in tension at selected temperatures between 25 and 1050°C. The specimens were held at temperature in vacuum for approximately five minutes before they were loaded with a cross-head movement of 0.02 in./min. Initially, frequent breakage in the grips or slippage out of the grips was encountered. This problem was eliminated by close wrapping of the specimen ends with 0.005-inch diameter tantalum wire. All reported results were obtained on specimens which broke in the gauge area with the exception of the tests at 1050°C. At this temperature, all three specimens could not be tested to fracture due to slippage from the gripping plates at 35,000 lb/in.^{2}.

The results of elevated temperature tensile strength measurements on the composites are shown in Figure 60. Three tests each were made at room temperature, 700°, 900°, and 1050°C, whereas two and a single measurement were made at 500 and 300°C, respectively. The composite strength decreased from 79,200 lb/in.^{2} at room temperature to 29,000 lb/in.^{2} at 900°C, essentially following the trend for annealed Nickel "A" but displayed toward higher strength values by 15,000 to 25,000 lb/in.^{2}. At 1050°C, the tensile strength exceeded 35,000 lb/in.^{2} this result indicates that the composite strength is somewhat greater at this higher temperature than at 700°C. The strength curve appears to have a minimum at approximately 800°C. A mismatch of fiber and matrix thermal expansion coefficients could induce stresses on cooling from the fabrication temperature which are subsequently relieved at the higher test temperatures. Other causes might be re-solution of precipitated graphite in the nickel at temperatures above 850°C and/or improved bondings between fiber and matrix metal; evidently, bondings in the 700° to 900°C temperature range is quite poor, as suggested by fiber pull-out in the fracture areas. Experiments are now being conducted to confirm the validity of this reasoning and to determine the causes of the apparent strength minimum at 800°C.

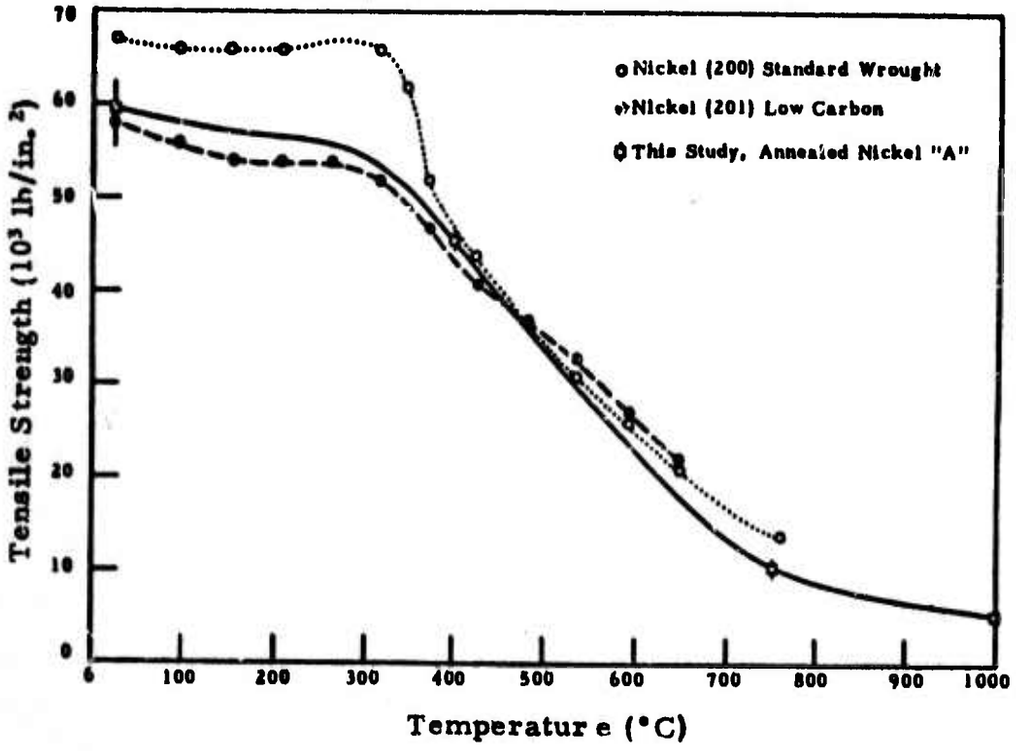

N-17220

Figure 59. Tensile Strength of Nickel Versus Temperature.

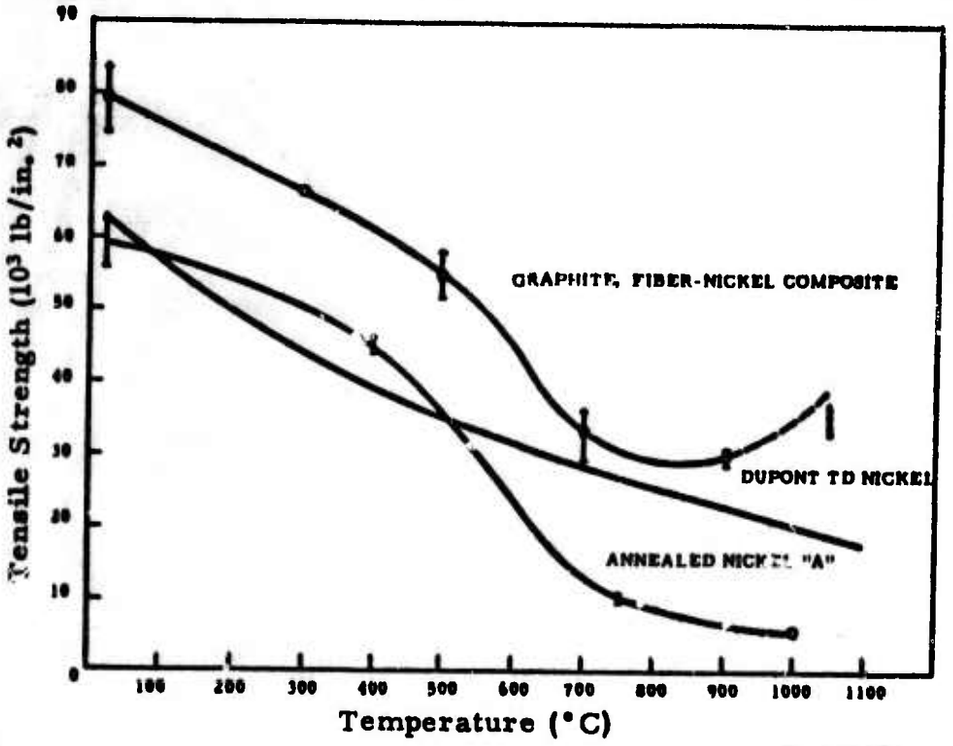

N-17083

Figure 60. Tensile Strength of Various Temperatures for Graphite-Fiber, Nickel-Matrix Composite, TD Nickel at Annealed Nickel "A".

Specific strengths as a function of temperature for the nickel composite, TD Nickel, pure nickel, and "Hastelloy" X are shown in Figure 61. Due to the lower density, the composite specific strength is at least twice that of nickel or TD Nickel at all temperatures considered; the composite also shows superiority over "Hastelloy" X at temperatures above 800°C.

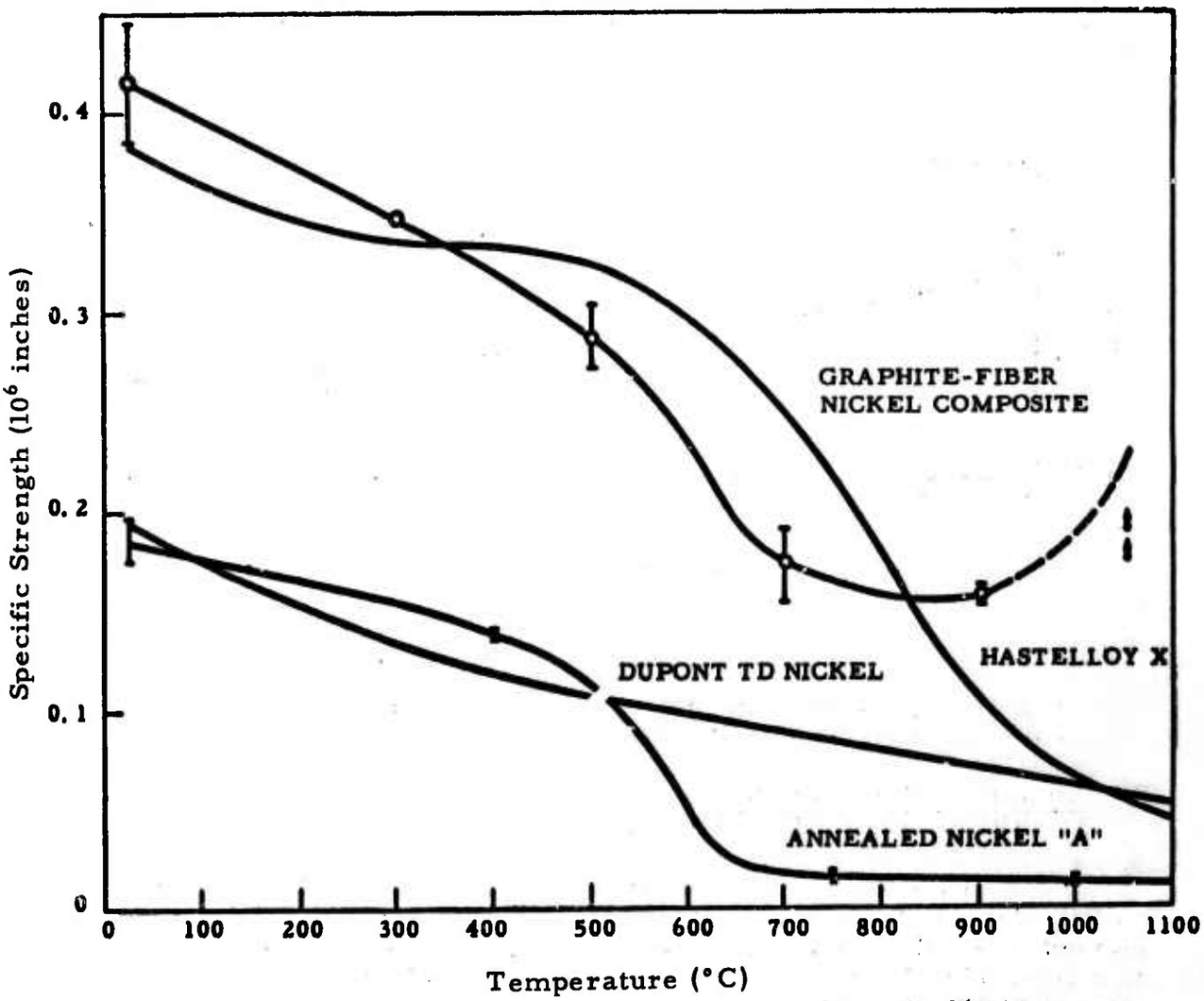

N-16850

Figure 61 Specific Strength Versus Temperature for Graphite-Fiber, Nickel-Matrix Composite and Several Refractory Metal Systems.

Specimens similar to those used for high temperature tensile testing were annealed at 500, 700, and 900°C for 300 hours in vacuum and then evaluated at room temperature. Microstructures of the composite showed a slight increase in fiber bridging but no pronounced deterioration in the fiber morphology. A slight expansion was detected in the specimen dimension that was parallel to the applied fabrication pressure. Young's and shear moduli were slightly lower by constant amounts after the fibers

were annealed at the three temperatures. The average Young's modulus of six specimens decreased from 32.7 to 31.9 x 10^6 lb/in.^{2}, and the shear modulus decreased from 4.76 to 4.40 x 10^6 lb/in.^{2}. The tensile strength decreased as an almost linear function of the annealing temperature from a room temperature value of 79,200 lb/in.^{2} to 68,800 lb/in.^{2} after 300 hours at 900°C (see Figure 62). These high temperature stability tests revealed only slight degradation in composite properties, and the deterioration might be rectified by choosing composites having greater fiber-fiber separation and, hence, less opportunity for fiber bridging.

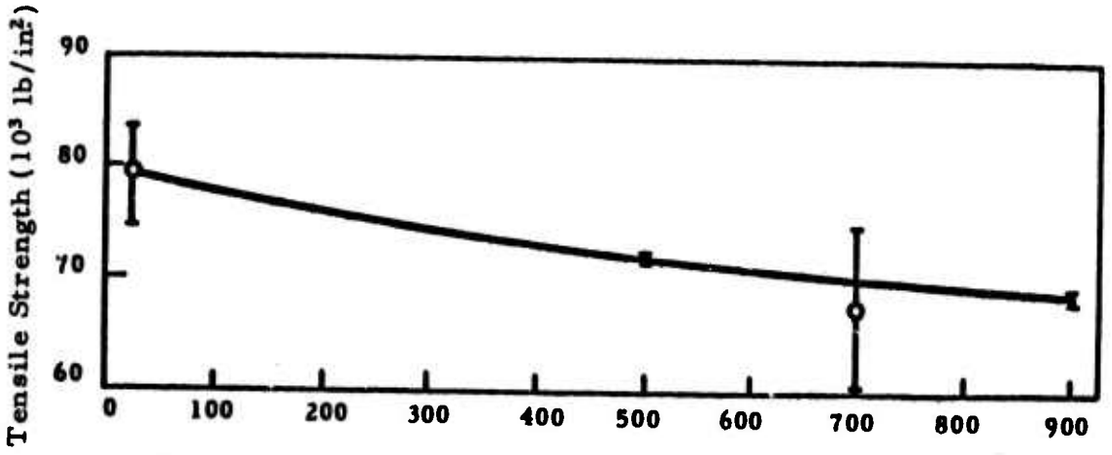

N-17081

Figure 62. Room-Temperature Tensile Strength of Graphite-Fiber, Nickel-Matrix Composite After 300 Hours at Annealing Temperature.

B. Aluminum Matrix Studies
(R. V. Sara, Union Carbide)

Prior attempts at incorporating graphite fibers in an aluminum matrix involved the concepts of pressure infiltrating molten aluminum into networks of uncoated metal fibers. For uncoated fibers, a pressure as high as 1080 lb/in.^{2} was still inadequate for infiltrating the fiber networks. Metal-coated fibers, on the other hand, were readily infiltrated with aluminum. However, tantalum was the only suitable coupling agent found which would not react with or dissolve in the molten aluminum. Because of the problem in obtaining uniform tantalum coatings, this approach was abandoned for the present time.

The approach considered in the present study for preparing a graphite-fiber, aluminum-matrix composite entailed the concept of liquid phase sintering. This technique has been used successfully by other investigators in the field.[22, 23] Alternate layers of alloy foil and fibers are arranged in an array, and the array hot pressed at a temperature just above that of the solidus. Pure aluminum cannot be used because it

has a distinct melting temperature. If one uses 2024 alloy foils, molten metal can be forced around most of the fibers under an applied pressure of 4500 lb/in.^{2} (Figure 63A). At one-half this pressure, however, very little metal migrated into the yarn (Figure 63B). The necessity of using high pressures is unfortunate; photomicrographs reveal that the fibers undergo considerable damage at the higher pressure, a result similar to that found in the nickel studies. An attempt was made to reduce this damage by using fibers that were plated with silver. Silver was used since it is one of the few metals which alloys extensively with aluminum. By using silver-coated fibers laminated between foils of 2024 alloy, consolidation was possible at 2250 lb/in.^{2} (see Figure 64). The composite strength and modulus of elasticity values shown in Table XXIV are improvements over the annealed matrix metal and are consistent with the rule-of-mixtures values. Various modifications on this general theme were tried. For example, pure aluminum and 2024 alloy foils were silver plated and used individually in conjunction with uncoated and silver-coated fibers. The best results, however, were achieved with the initial procedure described above. The fabrication temperature proved to be critical, since optimum structures were achieved only when incipient melting occurred at the silver-aluminum interface. Excessive liquid formation results in microstructures similar to that shown in Figure 63B. This method of liquid phase sintering was found to be more reproducible if slow heating rates were used prior to the final consolidating temperature.

TABLE XXIV

GRAPHITE-FIBER, ALUMINUM-MATRIX COMPOSITES SINTERED WITH UNCOATED AND SILVER-COATED FIBERS

Form. Press. (lb/in.^{2})	Young's Modulus E (10^6 lb/in.^{2})	Strength ult σ (lb/in.^{2})	Density ρ (g/cm^3)	Fiber Volume Percent
		2024 Matrix Metal		
-	10.4	36,100	2.76	-
		2024+Uncoated Fibers		
4500	12.2	27,100	2.46	18
		2024+Ag-Coated Fibers		
2250	11.0	36,700	2.76	11
2250	13.0	44,100	3.16	16
2250	14.3	54,700	3.34	28

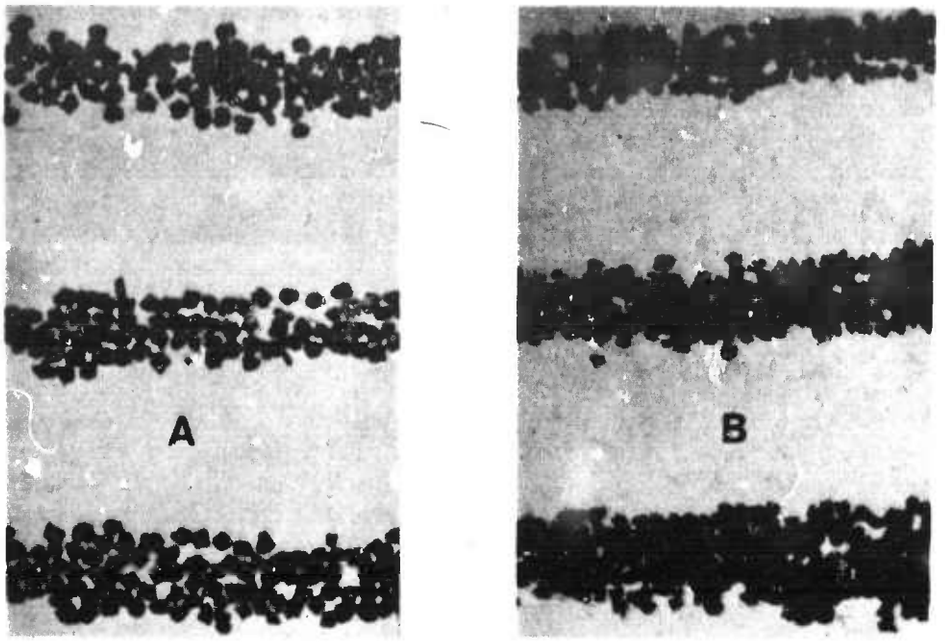

N-10584

Figure 63. Infiltration of Aluminum into Graphite Fibers at (A) 4500 lb/in.^{2} and (B) 2250 lb/in.^{2} 300X Magnification.

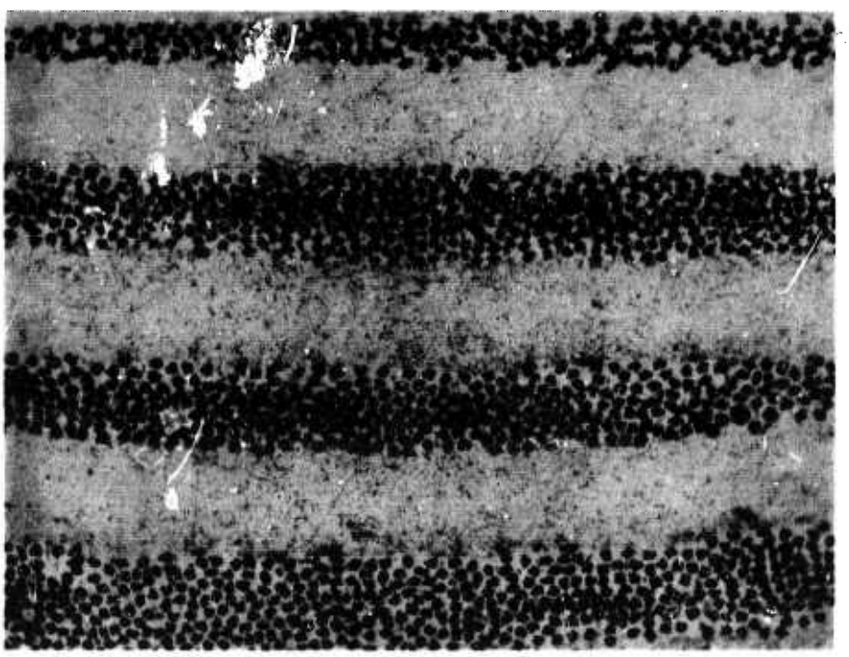

N-10585

Figure 64. Silver-Coated Graphite Fibers between Foils of Aluminum. 200X Magnification.

SECTION V

MATERIALS RESEARCH ON AND FABRICATION OF GRAPHITE-FIBER, RESIN-MATRIX COMPOSITES

Composites of "Thornel" graphite yarn and a resin matrix can be fabricated by essentially the same technology that is used for glass fiber reinforced plastics. Conventional procedures for filament winding, preparing prepreg tape, and molding laminated composites are readily adapted to "Thornel" yarn composites. Through the use of existing technology, the fabrication of plates and cylinders was started as soon as the "Thornel" yarn became available. Because the "Thornel" yarn can be formed around curves of small radius, structural elements such as rings, stringers, and stiffened panels are also easily fabricated.

Before the extensive plate fabrication program was undertaken, four epoxy resin systems were evaluated as matrix materials for fiber composites (see Section V A); the ERL 2256/MPDA system gave slightly better properties and was selected for future work. A study of the effects of oxidizing graphite yarn on resin wicking rates and composite shear strengths is reported in Section V B. Physical properties of "Thornel" fibers and of the ERL 2256/MPDA resin system are given in Section V E. The fabrication procedures for the "Thornel"-fiber, epoxy-resin composites are described in Section V D; and the lay-up pattern, average fiber properties and content, and optical micrographs of the plates are presented in Section V E.

A. Evaluation of Four Epoxy Resin Systems for Graphite Fiber Composites

(A. A. Pallozzi, Union Carbide)

An evaluation of the mechanical performance of "Thornel" graphite yarn and low modulus graphite yarn in various resin matrices was performed prior to the selection of a resin system for the fabrication of flat plates and stringers.

Four epoxy resins were selected for evaluation on the basis of chemical structure and type of hardener employed in polymerization:

ERLA 4305/MPDA	MPDA = Metaphenylenediamine
ERL 4221/MNA	MNA = Methyl"Nadic"Anhydride
ERL 2256/MPDA	
ERL 2272/MNA.	

The ERLA 4305 and ERL 4221 are both cyclic aliphatic-based epoxy resins reacted with different type hardeners. The ERL 2772 is an aromatic-based resin consisting of diglycidyl ether of bisphenol-A that is reacted with an anhydride hardener. The ERL 2256 is a hybrid mixture of a cyclic aliphatic-based resin and diglycidyl ether of bisphenol-A polymerized with an amine hardener.

Low modulus graphite yarn was used in the preliminary experimental work because of the limited availability of "Thornel" graphite yarn at that time. "Thornel" 25 graphite yarn was incorporated into the

program when it became available. Table XXV presents filament properties measured on the fibers used in this study. Filament-wound ring specimens

TABLE XXV

FILAMENT PROPERTIES FOR RING SPECIMENS

	Low Modulus Graphite Yarn	"Thornel" 25
Elastic Modulus (10^6 lb/in.^{2})	6.2	25.2
Tensile Strength (10^3 lb/in.^{2})	89.3	194

were prepared in accordance with ASTM Designation D 2291-64T, "Tentative Recommendation for Fabrication of Ring Test Specimens." The mechanical properties measured on the rings were elastic modulus and tensile, flexural, short beam shear, and notched beam shear strengths.

The values for the elastic modulus of the rings made with "Thornel" 25 and low modulus graphite yarns and with the four resin systems are compared in Figure 65. None of the resin systems yielded a composite elastic modulus significantly superior to those of the other resin systems. The fourfold higher elastic modulus of the "Thornel" 25 yarn is effectively translated into an approximately similar increase in the modulus of the composite rings. The modulus values measured on the rings are in agreement with values calculated by using the rule of mixtures for a fiber content of approximately 65 percent.

The values for the tensile, flexural, short beam shear, and notched beam shear strengths of the rings are compared in Figures 66, 67, 68, and 69, respectively. The strength values measured on rings made with resin system ERL 2256/MPDA and "Thornel" 25 yarn are slightly, but consistently, higher than the values for rings made with the other resin systems. In addition, the system ERL 2256/MPDA has good handling properties and a relatively long pot life. Consequently, this system was selected for use in the other segments of the resin matrix composite program.

The "Thornel" 25 yarn reinforced rings show higher tensile strength and, to a lesser extent, higher flexural strength than the rings made with low modulus graphite yarn. The values of tensile and flexural strength for the "Thornel" rings are approximately one-half the tensile strength of the filament and, thus, somewhat below the 65 percent value for composite strength based on the rule of mixtures. This low translation of fiber strength into composite strength may be due, in part, to shortcomings of the split D ring tests that are magnified with the high modulus "Thornel" yarn.

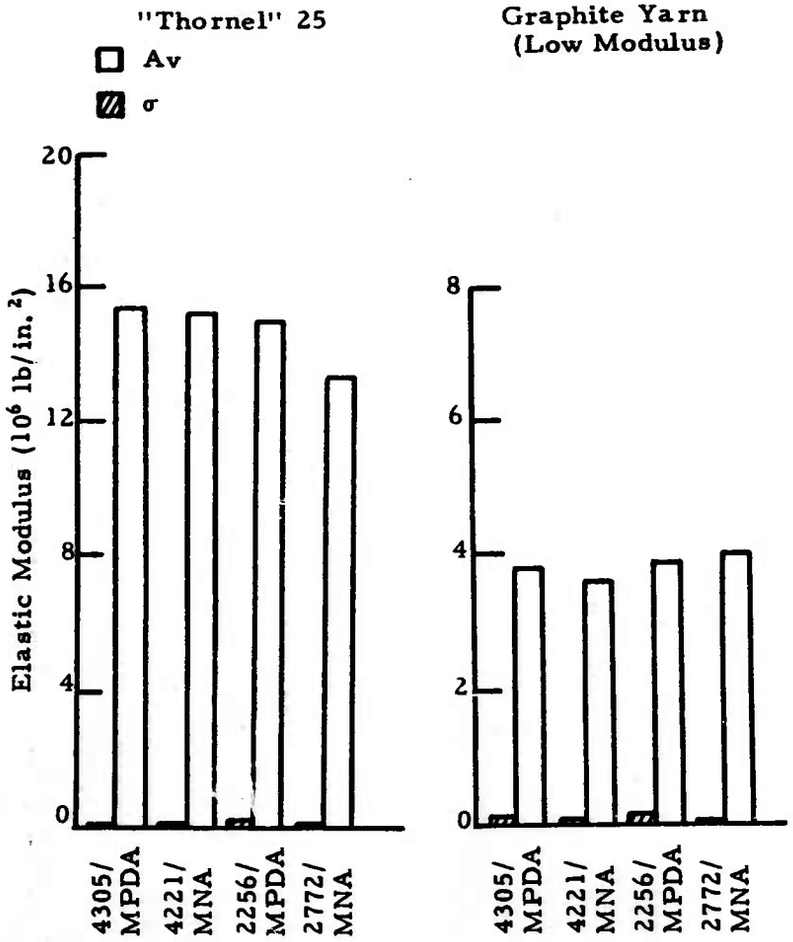

Figure 65. Elastic Modulus of Rings with Different Resin Systems.

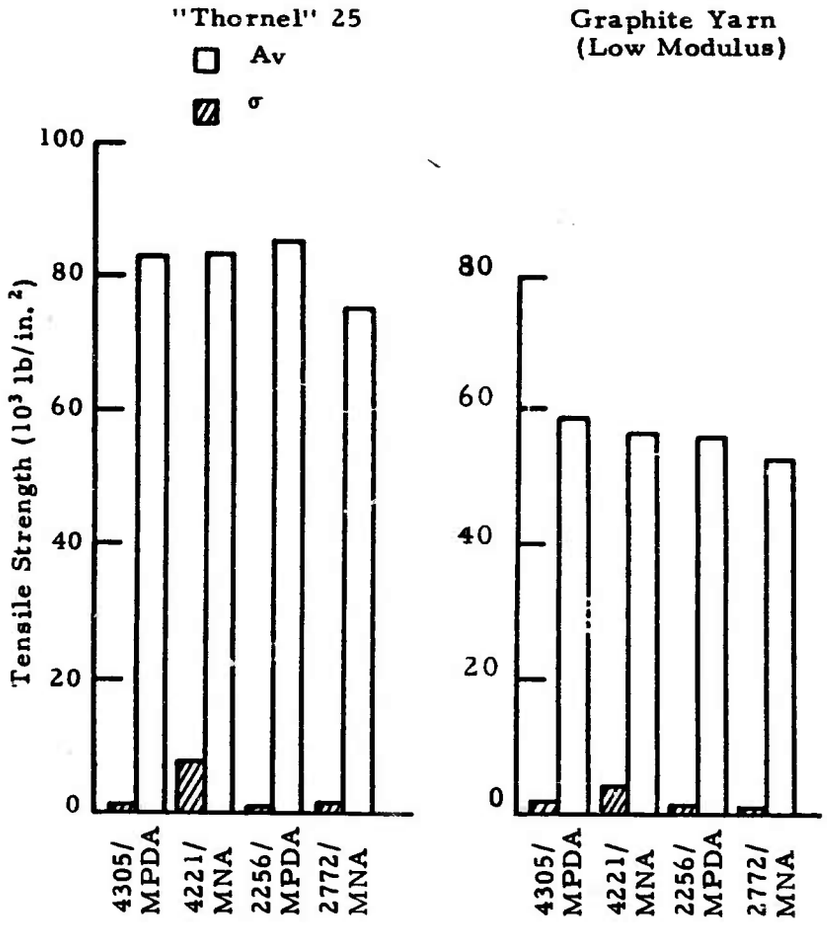

Figure 66. Tensile Strength of Rings with Different Resin Systems.

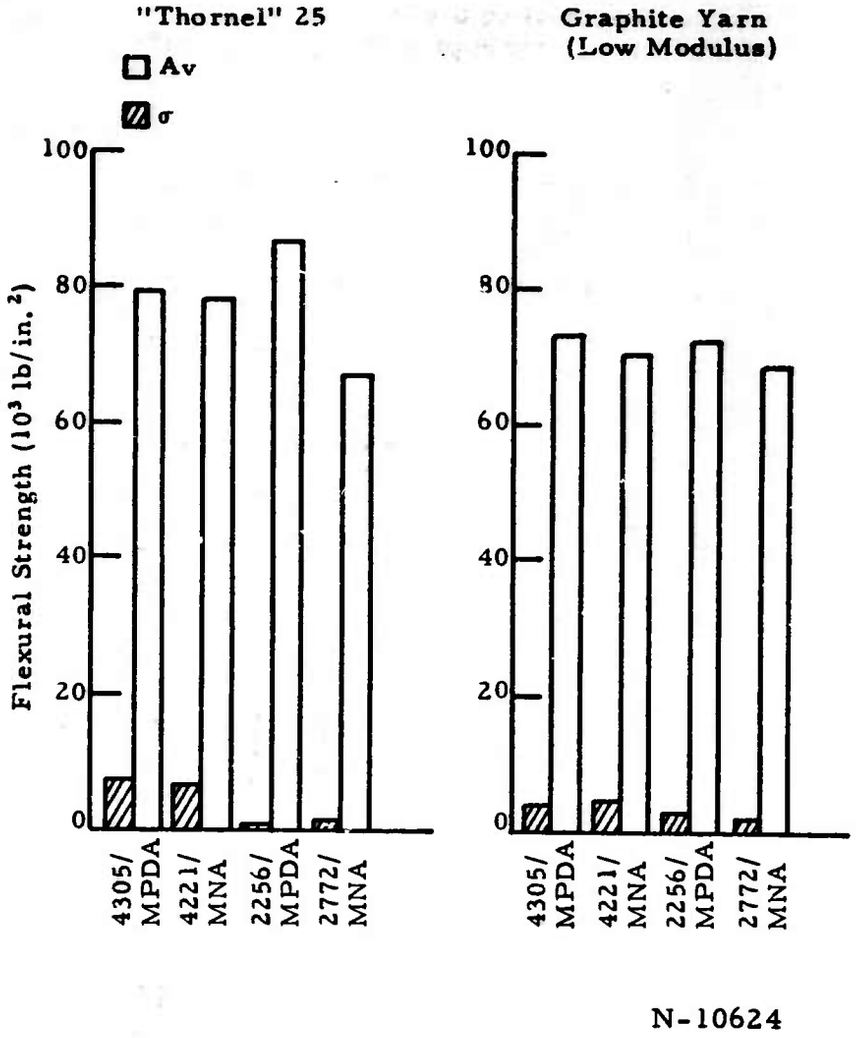

Figure 67. Flexural Strength of Rings with Different Resin Systems.

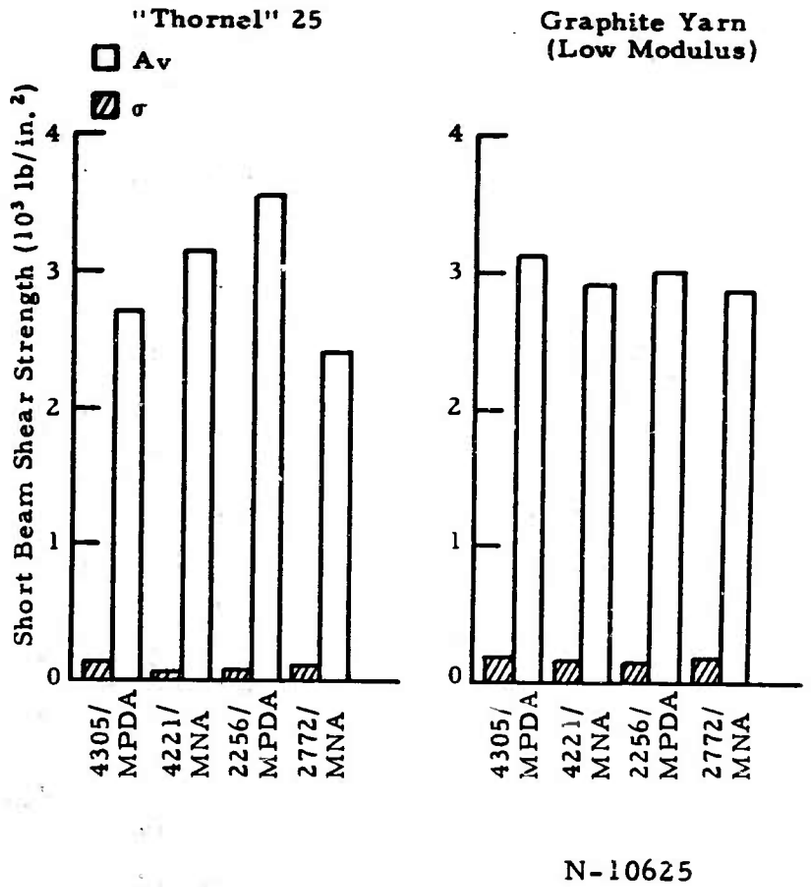

Figure 68. Short Beam Shear Strength of Rings with Different Resin Systems.

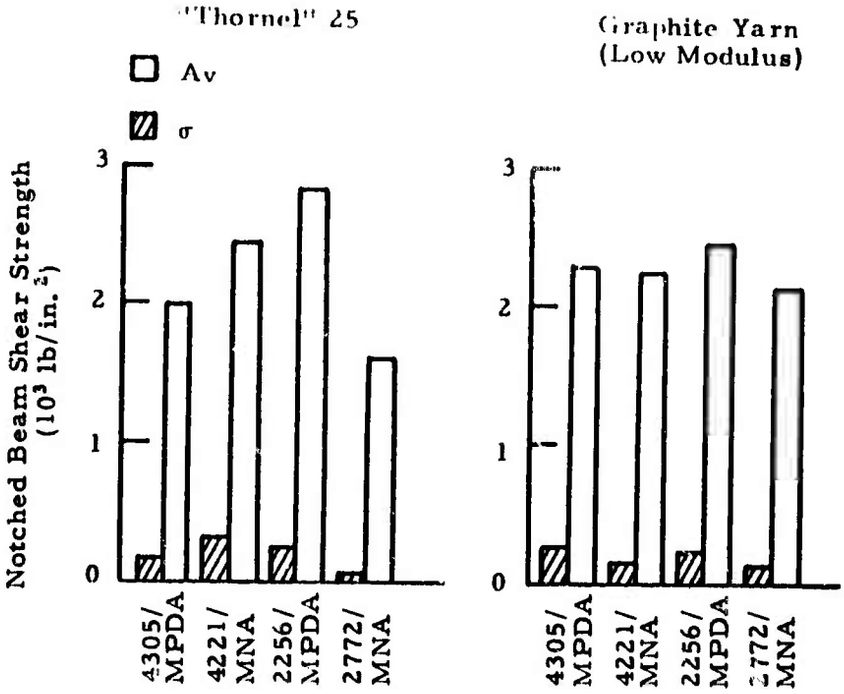

N-10626

Figure 69. Notched Beam Shear Strength of Rings with Different Resin Systems.

An improved ring test, not available at the time of this work, is described in Section VII A.

The shear strengths shown in Figures 68 and 69 are low; significant differences in shear strengths have not been observed between the two types of yarn reinforcement.

B. Surface Treatments and Wicking Rate Studies on Graphite Yarn

1. Effect of Yarn Surface Treatment Upon Composite Properties (A. A. Pallozzi, Union Carbide)

The low shear strengths obtained from ring specimens made with either "Thornel" or low-modulus graphite yarn are indicative of poor bonding at the fiber-resin interface. Results discussed previously (page 133 of the First Annual Report[1]) have indicated bonding to be more of a problem with graphite yarn than with carbon yarn. A hypothesis has been offered that the poorer bonding is associated with the lower surface area of graphite yarn. The previous work showed that etching low-modulus graphite yarn with a solution of sodium dichromate in sulfuric acid increases the surface area of the fiber, increases the composite compressive strength by a factor of approximately two, and decreases the composite tensile and flexural strengths.

Additional results for low modulus fibers have been obtained in this study and are shown in Table XXVI. The oxygen content of the fibers is

TABLE XXVI

PROPERTIES OF ETCHED LOW MODULUS GRAPHITE YARN
(FILAMENT MODULUS APPROXIMATELY 6 x 10^6 lb/in.^{2})

Solution Temp. °C	Immersion Time for Yarn, min	Surface Area of Yarn m^2/g	Oxygen Content %
Control	---	1-2	0.18
55	5	4	0.19
55	10	4	0.23
95-100	5	8	0.43
95-100	10	17	0.49
95-100	24	23	1.66

Oxidizing Solution $H_2SO_4 \cdot Na_2Cr_2O_7$

increased as the severity of the etch is increased. The magnitude of the increase in oxygen content does not correlate well with the change in composite physical properties. Additional tensile, flexural, and compressive strength tests have confirmed the trends reported previously. New measurements of the notched beam shear strength and wicking rates of rings made with low modulus graphite yarn are shown in Figure 70 (a discussion of wicking rates is given in Section V B-2). The oxidation treatment increases the composite shear strength by a factor of approximately two, similar to the increase in the compressive strength. Since there is no reason to believe that these preliminary treatments were optimum, even greater improvements in composite compressive and shear strengths are expected to result from more extensive surface treatment and/or coupling agent studies.

2. Correlation of Resin Wicking Rates with Shear Properties of Composites

(R. Didchenko, Union Carbide)

Measurements of wicking rates of epoxy resins on unsized graphite yarn provide a rapid method for evaluating the wetting characteristics of these materials. The experimental techniques and some preliminary results were reported in Section VI E of the First Annual Report.[1] The method has been used to study the effect of the fiber oxidation treatment on the wetting behavior of the four resin systems discussed in Section V A of this report.

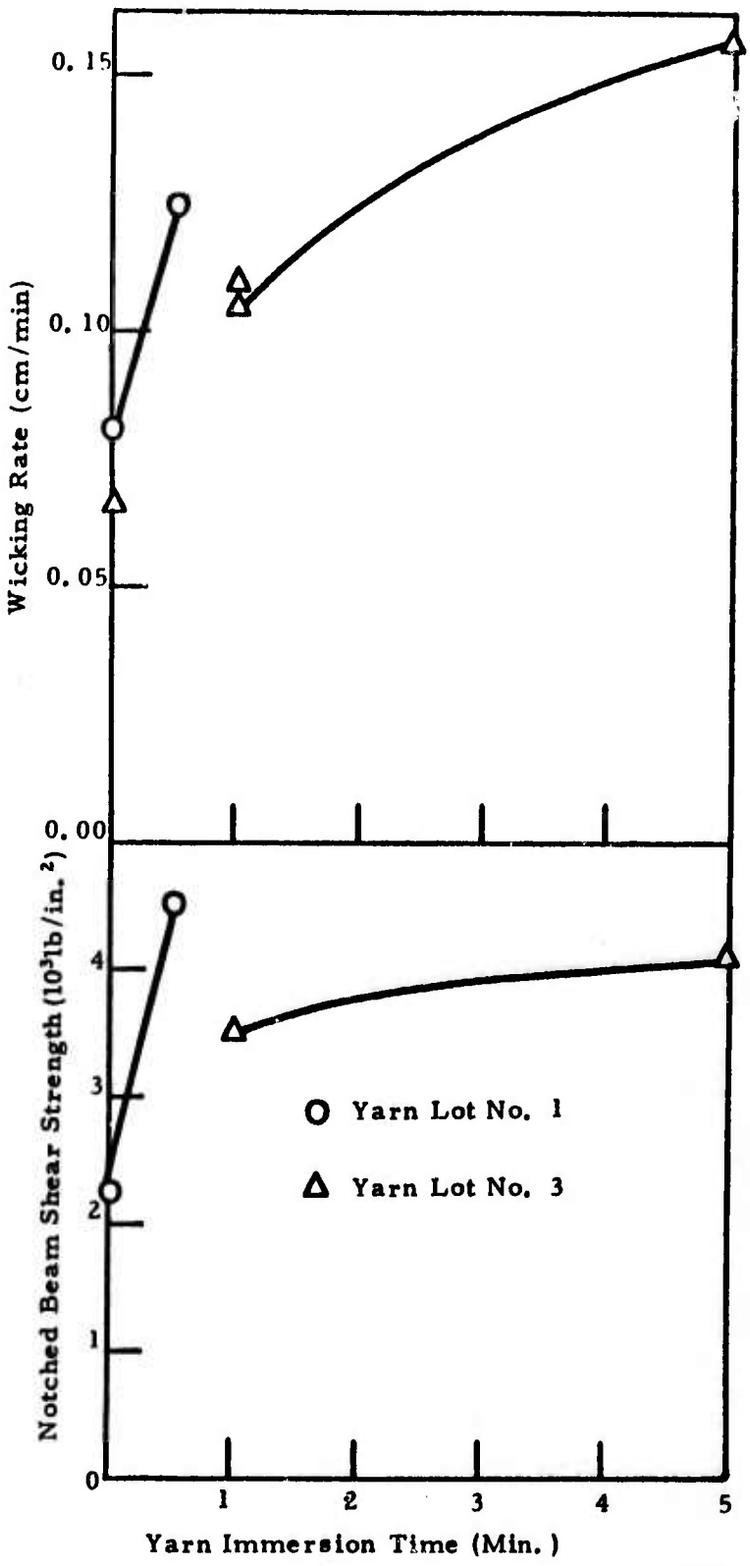

N-10998

Figure 70. Comparison of Wicking Rates of ERL 2256/MPDA Epoxy Resin on Oxidized Low Modulus Graphite Yarn with Notched Beam Shear Strength of Fiber-Resin Rings.

Materials prepared for, but not used during the studies of yarn oxidation with chromic acid, were used for this exploratory study. The yarn had been stored in tightly closed containers flushed with nitrogen, a condition that assured no changes in the surface during the time period between preparation of the yarn and the present experiments. Although the available samples were insufficient for a complete and systematic study, they were considered adequate to establish existing trends and to lay a foundation for a future, more satisfactory experimental design.

The wicking rates for the four epoxy resins are shown in Table XXVII for two lots of low modulus graphite yarn that had been oxidized in sodium

TABLE XXVII

WICKING RATES OF FOUR EPOXY RESINS ON GRAPHITE YARN TREATED WITH CHROMIC ACID SOLUTION*

	Yarn Lot No. 1				Yarn Lot No. 3	
	Yarn Immersion Time in Chromic Acid Solution (Minutes)					
Resin	0.0	1.0	1.0	5.0	0.0	0.5
ERL 4221/MNA	---	0.204	0.221	0.191	0.153	0.330
ERL 2772/MNA	---	0.106	0.132	0.167	0.079	0.150
ERL 2256/MPDA	0.0666	0.112	0.104	0.160	0.081	0.125
ERLA 4305/MPDA	---	0.078	0.096	0.083	0.042	0.059

*Average wicking rate in cm/min over 2 cm length of yarn.

dichromate "cleaning solution" (approximately 4.5 percent $NaCr_2O_7$ in concentrated sulphuric acid) at 56°C and 52°C, respectively, for time periods between 0.5 and 5 minutes. Untreated yarn from yarn Lot 1 was available in an amount sufficient only to measure the wicking rates with one resin, ERL 2256/MPDA. The wicking rates shown in Table XXVII are averages of three to seven individual determinations on different samples from each lot of oxidized yarn. The differences between the second and third columns (measured on two different pieces of the same yarn given duplicate chemical treatment) show that the reproducibility of this evaluation is rather poor but appears to be adequate to establish major trends.

There is a significant difference in the wetting characteristics of different resins towards the oxidized graphite yarn. The ERL 4221/MNA resin wicks significantly better than the others. This effect cannot be

accounted for by differences in viscosity, since the viscosity of ERL/4221 MNA system over aging periods corresponding to the duration of these experiments is actually higher than that of ERL 2256/MPDA or of 2272/MNA. Oxidation of the fiber surface with chromic acid significantly improves the wicking rates of epoxy resin. Prolonged fiber surface oxidation does not show any advantage over treatments of 0.5 to 1 minute duration. These short duration treatments are sufficient to approximately double the wicking rate. Comparison of plots of the notched beam shear strength of the composites and of the corresponding wicking rates versus the surface oxidation time shown in Figure 70 reveals a parallel behavior strongly indicating that wetting is a measure of adhesion and that the notched beam shear strength is limited by the adhesive failure at the fiber-resin interface.

C. Properties of "Thornel" Graphite Fibers and of the ERL 2256/MPDA Resin System

1. Properties of "Thornel" Graphite Fibers and Yarns (G. B. Spence, Union Carbide)

Average properties of "Thornel" 25 and 40 graphite fibers and yarns have been supplied by Union Carbide Corporation based on tests on the first several months of production material. Measured properties on production grade material are given in Table XXVIII. Properties obtained from limited quantities of experimental material are given for 50 and 60 x 10^6 lb/in.^{2} graphite fibers. The modulus-to-density ratio for "Thornel" 40 is higher than that of the boron fiber on a tungsten core, and the strength-to-density ratio for experimental graphite fibers with a modulus of 50 x 10^6 lb/in.^{2} is higher than that of boron.

TABLE XXVIII

AVERAGE PROPERTIES OF "THORNEL" GRAPHITE FIBERS, BORON, AND GLASS

Properties		"Thornel" Present 25	"Thornel" Present 40	"Thornel" Future 50	"Thornel" Future 60	Boron on W*	"S" Glass**
Modulus	(10^6 psi)	25	40	50	60	60	12.4
Sp. Mod.	(10^6 in.)	480	710	850	980	630	138
Strength	(10^3 psi)	180	250	285	315	450	700
Sp. Str.	(10^6 in.)	3.5	4.4	4.8	5.1	4.7	7.8
Density	(g/cm^3)	1.43	1.56	1.63	1.7	2.63	2.49
	(lb/in.^{3})	.052	.056	.059	.061	.095	.090
Equiv.	(μ)	7.5	6.9	6.6	6.2	102	10.2
Diam.	(mil)	.30	.27	.26	.24	4	.40

* Data from Reference 27
**Data from Reference 28

The "Thornel" fibers are strongly anisotropic. The transverse properties have not been measured, but Young's modulus transverse to the fiber may be as low as 1 to 3 x 10^6 lb/in.^{2}. The shear modulus for rotation about the fiber axis is probably in the range 2 to 4 x 10^6 lb/in.^{2}. Poisson's ratios are expected to be in the range of 0.1 to 0.3. In accordance with the behavior of all other forms of graphite, the strength and moduli are expected to be independent of temperature to approximately 1000°C and then to increase slightly to 2000°C.

Estimated thermal and electrical properties are given in Table XXIX. The specific heat of the graphite fiber is assumed to be the

TABLE XXIX

ESTIMATED "THORNEL" 25 AND 40 GRAPHITE FIBER PROPERTIES

Surface Area		1-4	m^2/g
Specific Heat	25°C = 77°F	0.17	cal/g°C
	150°C = 302°F	.26	or
	500°C = 932°F	.39	Btu/lb°F
	1000°C = 1832°F	.45	
Axial Coefficient of Thermal Expansion			
	-273°C	0.0	$°C^{-1}$
	25°C	~ -1.0 x 10^{-6}	
	400°C	0.0	
	>1500°C	~+1.5 x 10^{-6}	
Axial Thermal Conductivity			
	25°C	~ 0.2	cal/sec cm°C
	>1500°C	~ .08	
	72°F	~ 60	Btu/hr ft°F
	>2700°F	~ 20	
Axial Electrical Resistivity at 25°C			
	"Thornel" 25	15 x 10^{-4}	ohm cm
	" 40	12	

same as that for all other forms of graphite. Preliminary measurements of the fiber coefficient of thermal expansion in the axial direction indicate that the axial expansion is approximately the same as that for a basal plane direction in the graphite single crystal; single crystal values[24] are given in the table. The fiber coefficient of thermal expansion in the radial direction is expected to be positive and of the order of magnitude of .0 x 10^{-6} / C. Table XXIX lists measured values of fiber electrical resistivity in the axial direction. From these values, an estimate has been made of the fiber thermal conductivity in the axial direction by

using a typical ratio of thermal-to-electrical conductivity for other types of graphite. The axial thermal conductivity is expected to increase with increasing fiber modulus.

The "Thornel" fibers are supplied as essentially continuous fibers in a multi-fiber; average yarn properties are given in Table XXX. Although

TABLE XXX

AVERAGE "THORNEL" GRAPHITE YARN PROPERTIES

	"Thornel" 25	"Thornel" 40
Plies/Yarn	2	2
Filaments/Ply	720	720
Twist-Ply/Ply	1.6	1.5 turns/in.
Yarn Diameter	~.02	~.02 in.
Yield	5600	6300 yd/lb.
Breaking Strength	~8	~7 lb.

the nominal number of fibers is 1440 fibers per 2-ply yarn, the actual number tends to be slightly less. Fiber counts from a few samples were approximately 1470 for "Thornel" 25 and approximately 1360 for "Thornel" 40. These numbers are not well-established averages and may increase in the future. To facilitate handling, "Thornel" 25 and 40 yarn is supplied with a polyvinyl alcohol (PVA) finish of approximately one percent by weight.

2. Properties of ERL 2256/MPDA Epoxy Resin System (O. L. Blakslee, Union Carbide)

The resin system used for most of the composites program has been Union Carbide epoxy resin ERL 2256 with metaphenylenediamine hardener, mixed in the weight ratio of 19.2 parts hardener to 100 parts resin. This system was chosen for the reasons discussed in Section V A. In order to obtain the properties of the bulk resin, plates approximately 0.75 x 8 x 8 inches were cast from which test specimens were cut. The cure cycle used for these plates was 35 minutes at 85°C and 5 hours at 160°C.

Compressive stress-strain curves were run on 0.5 inch diameter cylinders 1.0 inch long. Stress was calculated by dividing the force by the original area. Figure 71 shows a typical compressive stress versus longitudinal strain curve to fracture. Cyclic loading at stress levels

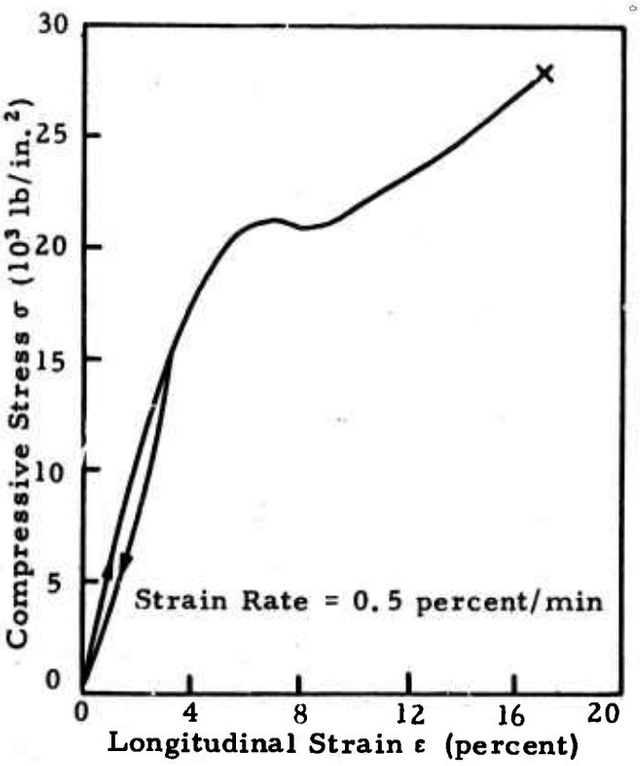

N-10621

Figure 71. Compressive Stress Versus Longitudinal Strain for Epoxy Resin System ERL 2256/MPDA.

below 20,000 lb/in.^{2} showed hysteresis effects but very little residual longitudinal strain when the stress was removed. Figure 72 shows the first part of the compressive stress versus transverse strain curve. Cyclic loading at all stress levels revealed both hysteresis and residual transverse strain effects.

The compressive yield strength (stress at top of knee) and the ultimate strength in compression increase slightly as the strain-rate increases by several decades, as shown by the data given in Table XXXI. The initial Young's modulus also increases slightly with large increases in strain rate, as shown in Figure 73. At a given strain rate, the initial modulus in compression is approximately 5 percent larger than that in tension. The gauge section of the tensile dog-bone specimen was 0.5 x 0.5 x 1.5 inches. Values of Young's modulus E, the shear modulus G, and Poisson's ratio ν, determined from static, sonic resonant bar, and ultrasonic tests, are given in Table XXXII. At present, insufficient data are available to determine whether the significant increases in E and G from static to sonic to ultrasonic values are to be attributed to strain rate or frequency effects.

The density, coefficient of thermal expansion, and thermal diffusivity have been measured on this resin system at room temperature.

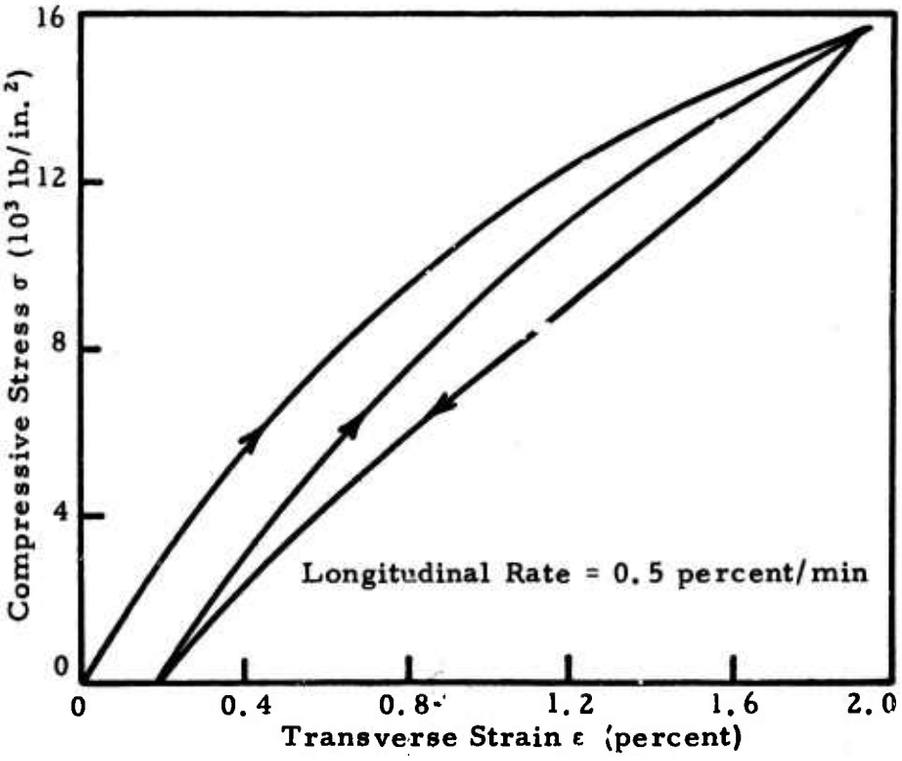

N-10620

Figure 72. Compressive Stress Versus Transverse Strain for Epoxy Resin System ERL 2256/MPDA.

These results and nominal values for other physical properties are given in Table XXXIII.

TABLE XXXI

COMPRESSIVE YIELD AND ULTIMATE STRENGTH AT VARIOUS STRAIN RATES OF RESIN SYSTEM ERL 2256/MPDA

Strain Rate percent/min	Yield Strength 10^3 lb/in.^{2}	Ultimate Strength 10^3 lb/in.^{2}
0.5	21.1	---
1.0	21.2	---
10.0	22.3	29.0
20.0	23.6*	49.8*
200.0	24.5	34.6

*Specimen only 0.5 in. long; all others 1.0 in. long; all 0.5 in. diam.

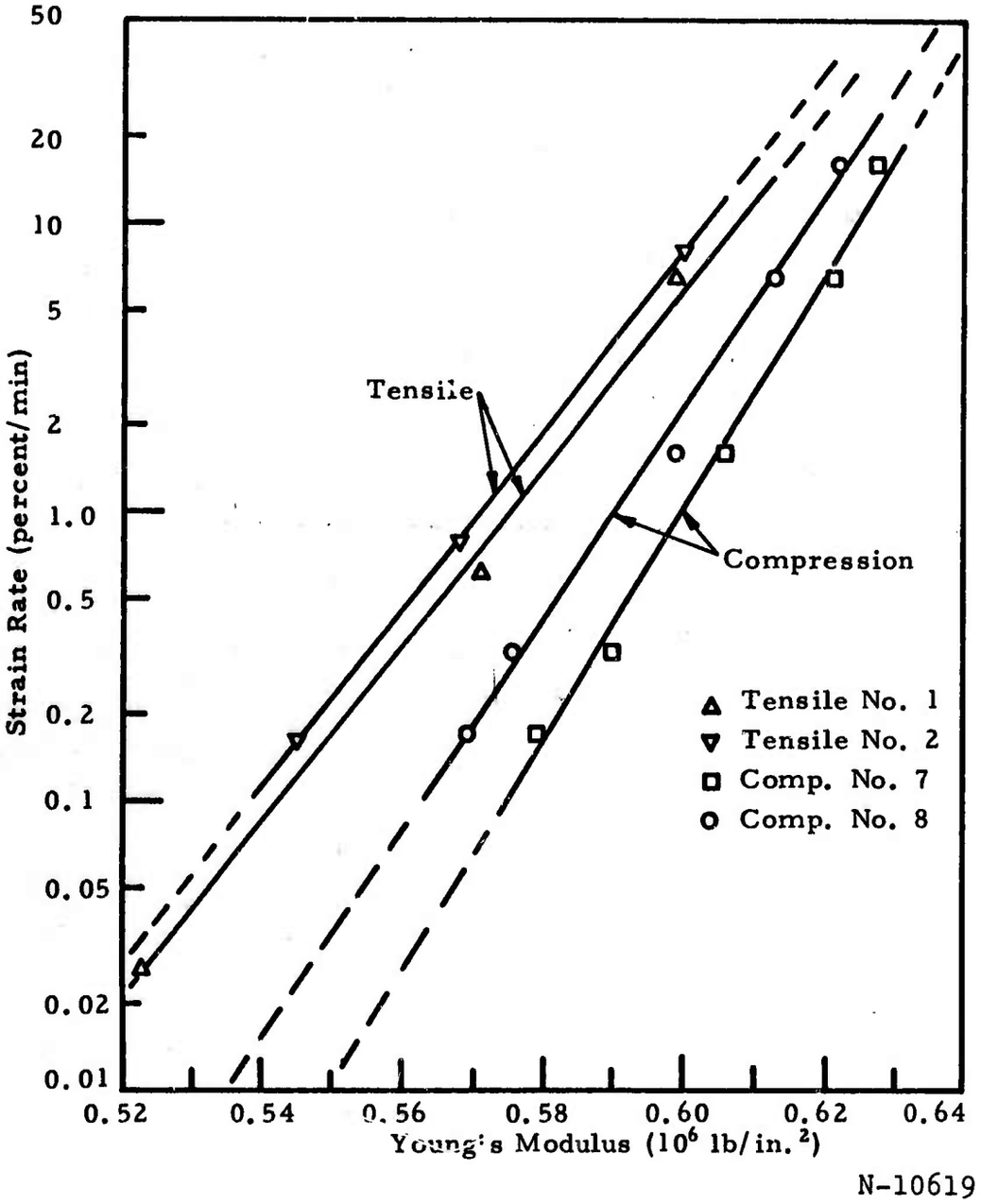

Figure 73. Initial Young's Modulus Versus Strain Rate of Resin System ERL 2256/MPDA.

TABLE XXXII

STATIC, SONIC, AND ULTRASONIC VALUES OF THE ELASTIC CONSTANTS OF RESIN SYSTEM ERL 2256/MPDA

Constant	Static*	Sonic**	Ultrasonic***
E (10^6 lb/in.^{2})	0.545	0.649	0.736
G (10^6 lb/in.^{2})	.200	.239	.271
Poisson's Ratio ν Experimental	.36	---	---
Calc. ν = E/2G-1	.36	.36	.36

* E by tensile test at 0.16 percent/min. strain rate; G by static torsion test.

**Resonant bar test at about 5 kHz.

*** Pulse velocity test at 1 mHz.

There is a large uncertainty in the third significant figure.

TABLE XXXIII

OTHER PHYSICAL PROPERTIES OF RESIN SYSTEM ERL 2256/MPDA

Property			
Density ρ	1.226 ± 0.005 0.0443 ± 0.0002	g/cm^3 lb/in.^{3}	Exp.
Coeff. Thermal Exp. α(25°C)	79 x 10^{-6}	°C^{-1}	Exp.
Specific Heat c_p (25°C)	0.25	cal/g°C	Ref. 25
Thermal Diffusivity κ(25°C)	1.4 x 10^{-3}	cm^2/sec	Exp.
Thermal Conductivity k(25°C)	4.3 x 10^{-4}	cal/cm sec°C	$k = \rho\kappa c_p$
Heat Distortion Temperature	160	°C	Ref. 26
Flexural Strength, Ultimate	22 x 10^3	lb/in.^{2}	Ref. 26
Tensile Strength, Ultimate	14 x 10^3	lb/in.^{2}	Ref. 26
Tensile Elongation, Fracture	~4	percent	Ref. 26

D. Fabrication of "Thornel"-Fiber, Epoxy-Resin Composites
(W. A. Doig and A. A. Pallozzi, Union Carbide)

1. Fabrication of Flat Plates

Flat plates have been fabricated by laminating unidirectional layers of prepreg "Thornel" graphite yarn. The prepreg was prepared by simultaneously passing six strands of "Thornel" Yarn through a resin bath and winding a single ply on a Mylar-covered cylindrical mandrel, as shown in Figure 74. Teflon pulleys were used as guides in order to minimize yarn damage. To prevent fiber catenary during winding, a tension of 1/4 to 1/2 pound was applied to each yarn by means of a friction brake.

The resin system ERL 2256/MPDA was maintained at room temperature. The resin bath contained 65 weight percent resin solids in acetone which gave a fiber content of approximately 55 weight percent in the prepreg material. This concentration of resin solids was the minimum amount that permitted sufficient resin pickup to hold adjacent yarns together after the material had been B-staged. The volatilization of the acetone solvent and resin advancement were accomplished in a forced air convection oven. Uniform resin distribution in the prepreg material was assured by slowly rotating the mandrel during the heating schedule. In more recent work, a sheet of Mylar has been used to cover the wet layup prior to heating as a precautionary measure to maintain

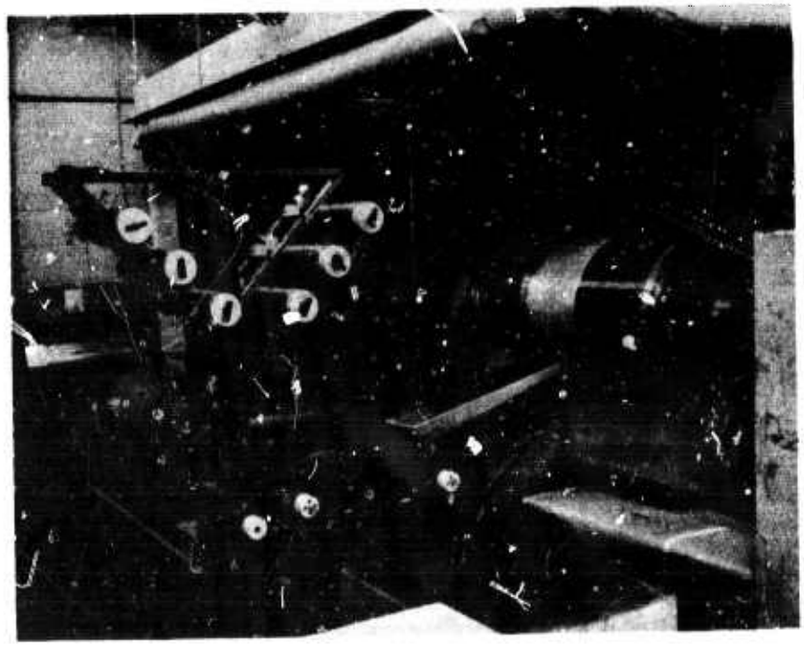

N-17502

Figure 74. Wet Winding of "Thornel" Graphite Yarn and Epoxy-Resin System ERL 2256/MPDA on a Mylar-Covered Mandrel.

the resin-hardener stoichiometry during B-staging. This procedure does not appear to hinder the complete volatilization of the solvent, since acetone odors have not been detected from the prepreg yarn. The PVA coating was not removed from the "Thornel" prior to resin impregnation. Typical B-staging schedules are given in Table XXXIV.

The initial fabrication work utilized "Thornel" 25 yarn but, in the spring of 1967, when "Thornel" 40 yarn became available, "Thornel" 25 was replaced by the higher modulus yarn for most of the work. The flat plates made with "Thornel" 25 were laminated between two caul plates of 1/8-inch thick stainless steel sheet. A low degree of resin advancement during B-staging resulted in good resin flow during pressing. However, the sides of the layup had no restraints, and fiber wash caused fiber misalignment. In order to minimize fiber wash, additional resin advancement was obtained by heating the "Thornel" 25 plies during lay-up.

Cavity molds had been fabricated by the time the "Thornel" 40 yarn became available. Close dimensional tolerances were held during the machining of the cavity molds so that during molding, a gradual seepage of excess resin from the prepreg may occur without fiber wash. This procedure essentially eliminates the difficulties experienced in fabricating the "Thornel" 25 composite plates. Fiber content has been increased and the thickness per ply decreased in "Thornel" 40 composite plates. Typical molding schedules are given in Table XXXIV.

TABLE XXXIV

TYPICAL B-STAGING AND MOLDING SCHEDULES FOR COMPOSITE PLATES

"Thornel" 25 ERL 2256/MPDA Composites	"Thornel" 40 ERL 2256/MPDA Composites
B-Staging Schedule	
15 min at 90°C 15 min at 100°C 5 min at 105°C	15 min at 95°C 15 min at 105°C
Molding Schedule	
60 min at 75°C & 90 psi 60 min at 90°C & 90 psi 60 min at 110°C & 180 psi 120 min at 160°C & 180 psi 120 min at 160°C post cure	30 min at 70°C & 90 psi 30 min at 100°C & 180 psi 60 min at 160°C & 180 psi

2. Fabrication of Cylinders

Cylinders with diameters of 1, 2, and 4-inches have been hoop wound for hoop tensile stress tests. For torsion tests, 2-inch diameter by 6.5-inches long cylinders were hoop wound and the ends overwrapped with glass fibers. The 1-inch cylinder was wound on the NOL ring winder. The 2 and 4-inch cylinders were wet wound on the large winder on graphite mandrels which were removed by machining after the composite was cured. A problem of circumferential cracking at the gauge-section end of the glass fiber overwrap was corrected by covering the mandrel with a sheet of Mylar and by overwrapping the entire cylinder with glass fibers applied at an angle. Resin shrinkage during curing then resulted in overall shortening of the cylinder rather than in opening up circumferential cracks. After the cylinder was cured, the glass fibers were machined from the gauge section.

A thin-walled cylinder 20 inches in diameter by 30 inches long was filament wound as a forerunner of the fuselage component. Two layers (i.e., four plies) were formed at ±45° C; the length of the mandrel used for this cylinder was chosen to produce a simple winding pattern. The plaster mandrel was coated first with carnauba wax and then with polyvinyl alcohol solution before winding. The composite was partially cured with quartz tube infrared heaters while rotating on the filament winding machine. The composite was then placed in an oven and fully cured. The cured composite was cut to length and the plaster mandrel was broken out of the cylinder. Figure 75 shows the cylinder with light aluminum bands attached to protect the ends.

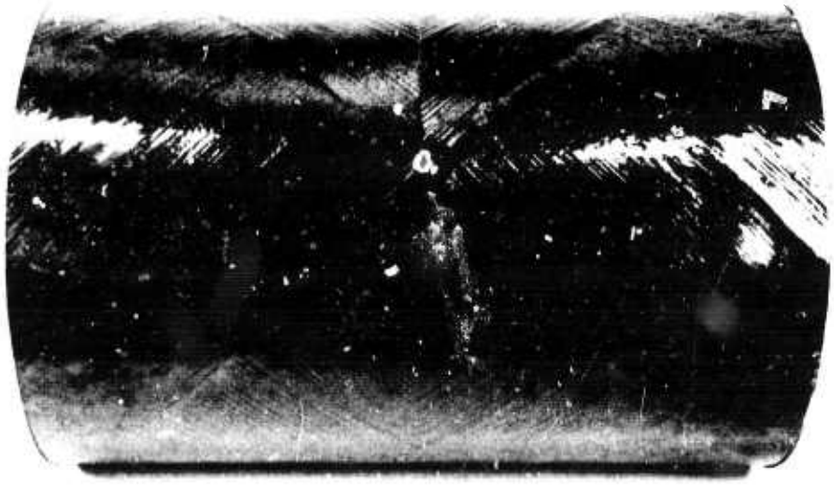

N-10732

Figure 75. Two-Layer Cylinder 20 Inches in Diameter x 30 Inches Long Wound with "Thornel" 25/ERL 2256.

3. Fabrication of Ring Stiffeners

Four hollow stabilizing rings are required in the design of the Representative Fuselage Component No. 1 to give the component circumferential stability. Several subscale (1/4 size) hollow rings have been fabricated with "Thornel" 25 graphite yarn and resin system ERL 2256/MPDA to obtain experience in ring fabrication.

A cutaway sectional view of a partially cured ring containing a low melting alloy insert (Cerrotru) is shown in Figure 76. The molten alloy was allowed to drain during the complete cure schedule, resulting in the structure shown in Figure 77. Two small holes, 1/8 inch in diameter, were drilled diametrically opposite in the ring's outer perimeter to allow the molten metal insert to drain during the cure cycle.

Several difficulties in fabricating hollow rings become evident during the preliminary studies. Slag adhered to the inner wall of the ring, as shown in Figure 77, resulting in a significant weight penalty for the structure. The slag formation is due to the molten metal combining with the release agent used to coat the metal insert. In addition, transverse cracks were formed due to the restraint of the metal insert on resin shrinkage upon the shrinkage of the resin matrix during the curing cycle.

An alternate type of ring stiffener is presently under evaluation consisting of segments of balsa wood as a core material sandwiched between flat composite panels made from "Thornel" 40 yarn and ERL 2256/MPDA. Figure 78 shows the parts of an unassembled straight beam; each side panel has 3 plies oriented at (0°, +45°, -45°). Two of the completed beams are shown in Figure 79; these beams will be destructively tested to evaluate their potential as stiffening elements. In the fuselage component, hat-shaped stringers will pass through the holes in the beams. The side panels of one beam are twice as long as those of the other and the end joints are staggered on opposite sides of the beam. Additional designs (for example, with different lay-up patterns and/or core weights) will be evaluated as straight beam elements; if a design appears to be satisfactory, a circular ring element will be fabricated and tested.

4. Fabrication of Stringers and Stiffened Panels

Several L-shaped stringers were fabricated with different radii of curvature to determine the influence of fiber strain introduced when "Thornel" is formed over curves of small radii. The testing and evaluation of these stringers are reported in Section VII F. All stringers were of 3-ply construction with plies oriented at (90°, 0°, 90°) with respect to the stringer axis. Three types of stringers were made with inner radii of curvature of 0.050, 0.100, and 0.200 inch, as shown in Figure 80.

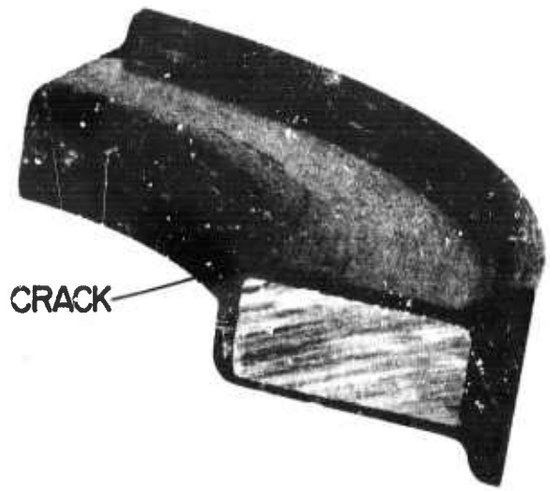

N-17503

Figure 76. Selection of "Thornel" 25/ERL 2256 Ring before Low-Melting Alloy Insert was Removed.

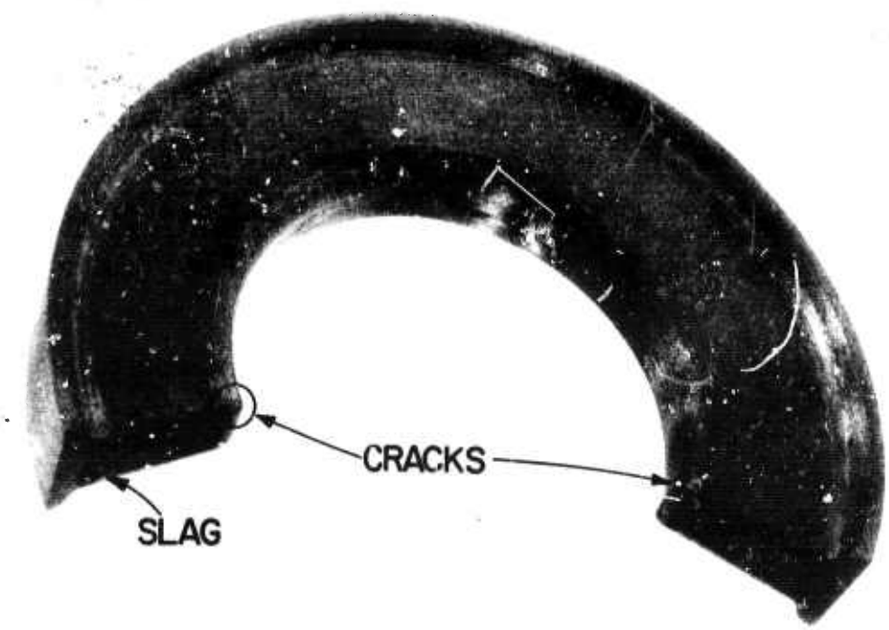

N-17504

Figure 77. Section of Hollow "Thornel" 25/ERL 2256 Ring.

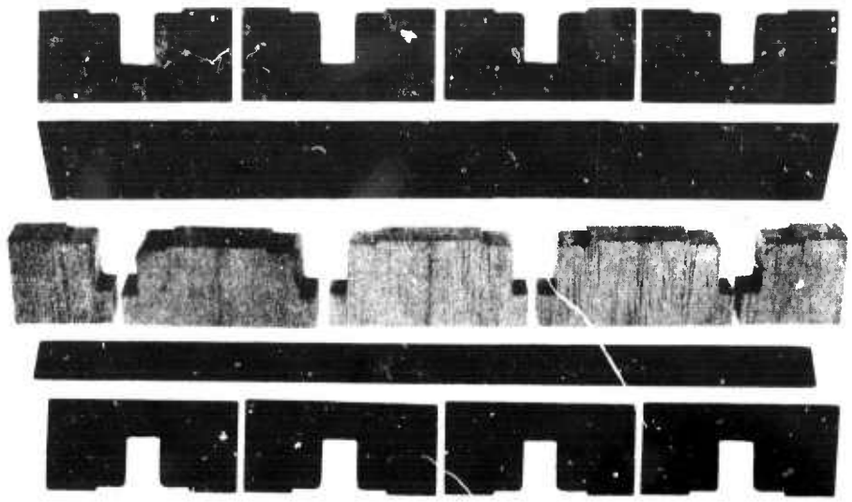

N-17505

Figure 78. Components of Balsa-Core Beam Ready for Assemble.

N-17506

Figure 79. "Thornel" 40/ERL 2256 Beams with Balsa Wood Cored.

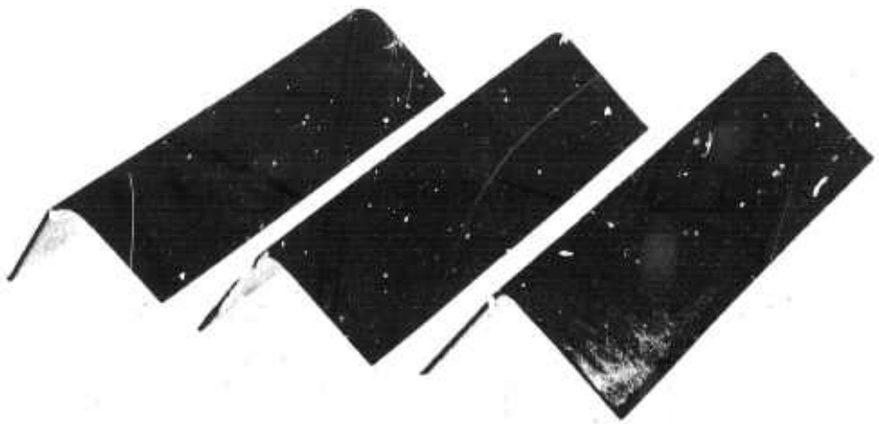

N-17507
Figure 80. Three L-Shaped Stringers with Radii of Curvature of 0.100, 0.200, and 0.050 Inch.

Stiffeners for thin panels are an important configuration in the program. As an exploratory effort, four different types of stringers were fabricated: Z-shaped, box-beam, U-shaped (cut from box beams), and hat-shaped. The Z- and hat-shaped stringers were molded in a matched-die mold from three-ply and four-ply lay-ups in a manner similar to that used for molding plates. Box beam stringers were filament wound on salt mandrels 0.6 by 0.6 inch by 15 inches long. These mandrels were wound at ±60° and ±45° angles in two layer (four-ply) thickness. The wet-wound composite was cured and the salt dissolved to leave a hollow, box-beam stringer. In one case, the wound mandrel was placed in a press and cured to produce a beam with two flat surfaces ready for bonding to a plate. Some of the box-beam stringers were cut to make U-shaped stringers measuring 0.4 x 0.6 x 0.4 inch.

A three-ply "Thornel" 25 composite plate stiffened with Z-shaped stringers is shown in Figure 81. The stringers and plate were fabricated separately and bonded with epoxy adhesive ERL 2772/ZZL0325. The inner radius of curvature of the stringer is 0.050 inch. Figure 82 shows two hat-shaped stringers. Difficulty with fiber wash has been experienced in fabricating long hat-shaped stringers, and further studies of alternate fabrication methods are in progress.

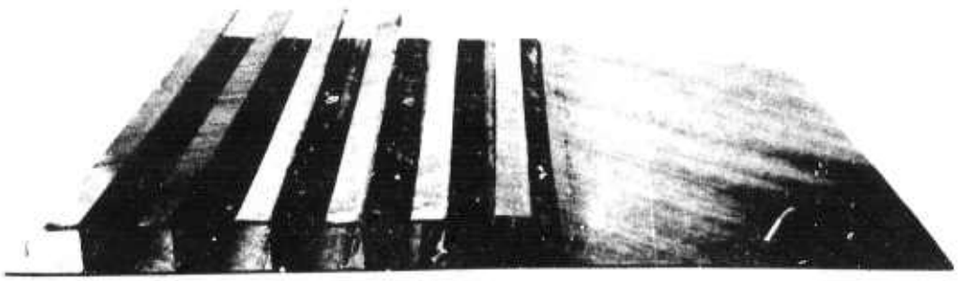

N-10731
Figure 81. "Thornel" 25/ERL 2256 Z Stiffeners Bonded to 12 x 12 Inch Plate.

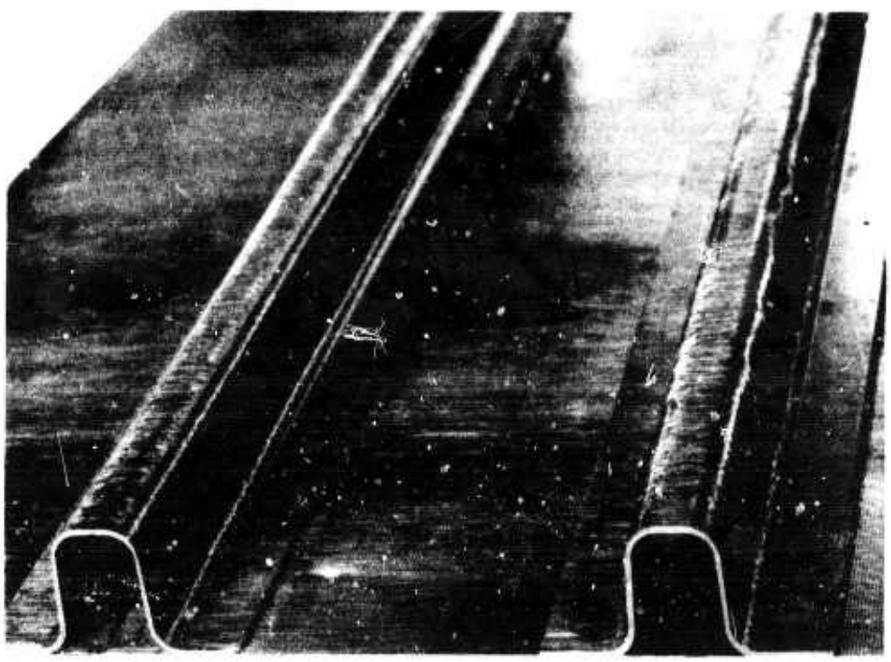

N-17508
Figure 82. "Thornel" 40/ERL 2256 Hat-Shaped Stringers.

E. Lay-Up Pattern, Average Fiber Properties and Content, and Optical Micrographs of Plates

1. Lay-Up Pattern of Plates

Over twenty-five composite plates made from "Thornel" 25 and 40 have been partially or fully cut into test specimens. The number and orientation of the monolayer sheets or plies average plate thickness, and average thickness per ply are given in Table XXXV for the "Thornel" 25 composites and in Table XXXVI for the "Thornel" 40 composites. A standard method is used throughout this report for describing the fiber orientations in the lay-up patterns. Angles are counted positive in a counterclockwise sense when looking down on the plate. The first angle given is the orientation of the bottom ply and the last angle is the orientation of the top ply. For example, for the (0, -45, 90, 45) plate, if the bottom ply is in the east-west direction, the top ply is in the northeast-southwest direction.

Most of the plates were 12 x 12 inches; a few (denoted by asterisks in Table XXXVI) were 7-3/4 x 20 inches. Because of resin shrinkage, the thin plates with an unbalanced lay-up were strongly curved, even after the plates were cured and post-cured between flat platens. The description "strongly curved" indicates that the plate, when placed on a flat surface, would deviate from that surface by one to several inches. A few plates were slightly curved i.e., the plates deviated from the flat support by one-quarter to one inch.

2. Average Fiber Properties
(G. B. Spence)

Individual filament properties of "Thornel" graphite yarn vary both along the yarn length and across the yarn cross section. Test data have shown that the variations of filament properties within a one-pound ball of yarn are approximately the same as variations from pound to pound of the material. The standard testing procedure for each one-pound ball of "Thornel" is to test five filaments selected at random from a cross section.

Table XXXVII shows the average filament properties for each one-pound ball and the average of the six balls of "Thornel" used in fabricating each plate (plate number P25-11 was fabricated from a single strand line on the filament winder before the six strand line was introduced). The plus-minus limits assigned each property give the boundaries of fairly well-defined scatter bands within which most of the measured values occurred.

TABLE XXXV

LAY-UP PATTERN OF "THORNEL" 25 PLATES USED FOR PHYSICAL TESTING

Plate Number (Size, in. 12x12)	Number of Plies	Orientation of Plies (deg.)	Ply Thickness (in.)	Ply Thickness (10^{-3} in.)	Remarks
P25-4	9	(0. . .0)	0.120	13.4	---
P25-14	9	(0. . .0)	.137	15.2	---
P25-5	2	(0,0)	.028	14.1	Slightly curved, very fragile
P25-1	9	(0,90,0. . .0)	.121	13.4	Partially delaminated
P25-11	9	(0,90,0. . .0)	.141	15.7	Bad fiber wash
P25-12	9	(0,90,0. . .0)	121	13.4	---
P25-9	6	(0,90,0,90,0,90)	.077	12.8	Slightly curved, insuf. res. flow
P25-2	5	(0,90,0,90,0)	.063	12.6	Insufficient resin flow
P25-3	4	(0,90,90,0)	.046	11.5	---
P25-10	3	(0,90, 0)	.040	13.5	Slightly curved
P25-7	2	(0,90)	.027	13.6	Strongly curved, insuf. res. flow
P25-8	4	(0,-45,90,45)	.052	13.0	Strongly curved, slight fiber wash
P25-6	3	(0,-60,60)	.043	14.2	Strongly curved, insuf. res. flow
P25-13	3	(90,60,-60)	.037	12.2	Strongly curved

TABLE XXXVI

LAY-UP PATTERN OF "THORNEL" 40 PLATES USED FOR PHYSICAL TESTING

Plate Number	Number of Plies	Orientation of Plies deg	Plate Thickness in.	Plate Thickness 10^{-3} in.	Remarks
P40-1	9	(0. . .0)	0.077	8.6	---
P40-9	7	(0. . .0)	.062	8.9	---
P40-14	6	(10,-10,45,-45,10,-10)	.056	9.3	slightly curved
P40-15*	6	(10,-10,45,-45,10,-10)	.057	9.5	slightly curved
P40-2	4	(90,0,0,90)	.029	7.3	---
P40-11	4	(90,0,0,90)	.032	8.0	Fiber wash and surface wrinkled
P40-12	4	(90,0,0,90)	.034	8.5	Fiber separation in some sections
P40-3	4	(45,-45,-45,45)	.029	7.3	delamination due to insuf. res.
P40-4*	4	(45,-45,-45,45)	.032	8.0	slightly curved
P40-10	4	(45,-45,-45,45)	.032	8.0	---
P40-5	4	(10,-10,-10,10)	.034	8.5	---
P40-6*	4	(10,-10,-10,10)	.036	9.0	---
P40-13*	4	(10,-10,-10,10)	.036	9.0	---
P40-16	4	(90,10,-10,90)	.039	9.8	---

*Size 7.75 x 20 in.; all others 12 x 12 in.

TABLE XXXVII

AVERAGE PROPERTIES OF "THORNEL" GRAPHITE FIBERS USED IN PLATES

Plate Number	Modulus (10^6 lb/in.^{2})	Strength (10^3 lb/in.^{2})	Density (g/cm^3)
P25-11	29.4 ± 4	197 ± 30	1.48 ± .08
P25-1, 2, 3	29.4 ± 4	197 ± 30	1.48 ± .08
	25.0 ± 4	197 ± 30	1.48 ± .08
	25.0 ± 4	197 ± 30	1.48 ± .08
	27.5 ± 3	190 ± 30	1.45 ± .07
	23.5 ± 3	170 ± 30	1.42 ± .07
	23.2 ± 3	166 ± 30	1.42 ± .07
ave.	25.6	186	1.46
P25-5, 7	29.4 ± 4	197 ± 30	1.48 ± .08
	25.0 ± 4	197 ± 30	1.48 ± .08
	27.5 ± 3	190 ± 30	1.45 ± .07
	25.5 ± 3	180 ± 30	1.43 ± .07
	23.5 ± 3	170 ± 30	1.42 ± .07
	23.2 ± 3	166 ± 30	1.42 ± .07
ave.	25.7	183	1.45
P25-8, 12	22.9 ± 4	171 ± 35	1.48 ± .10
	22.9 ± 4	165 ± 35	1.45 ± .10
	22.2 ± 4	165 ± 35	1.45 ± .10
	28.5 ± 3	194 ± 30	1.45 ± .07
	24.5 ± 3	175 ± 30	1.43 ± .07
	27.5 ± 3	179 ± 30	1.47 ± .07
ave.	24.6	175	1.46
P25-4, 9, 13	22.9 ± 4	171 ± 35	1.48 ± .10
	22.2 ± 4	165 ± 35	1.45 ± .10
	22.2 ± 4	165 ± 35	1.45 ± .10
	28.5 ± 3	194 ± 30	1.46 ± .07
	27.5 ± 3	179 ± 30	1.47 ± .07
	27.5 ± 3	179 ± 30	1.47 ± .07
ave.	25.1	175	1.46
P25-6, 10	27.5 ± 3	179 ± 30	1.47 ± .07
	27.5 ± 3	179 ± 30	1.47 ± .07
	26.0 ± 3	181 ± 30	1.44 ± .07
	26.0 ± 3	181 ± 30	1.44 ± .07
	24.3 ± 3	181 ± 30	1.42 ± .07
	24.3 ± 3	181 ± 30	1.42 ± .07
ave.	25.9	180	1.44
P25-14	27.5 ± 3	190 ± 30	1.45 ± .07
	25.5 ± 3	190 ± 30	1.45 ± .07
	24.5 ± 3	175 ± 30	1.43 ± .07
	28.5 ± 3	194 ± 30	1.46 ± .07
	23.2 ± 3	166 ± 30	1.42 ± .07
	23.2 ± 3	166 ± 30	1.42 ± .07
ave.	25.4	180	1.44
P40-1 through 12	39.8 ± 4	260 ± 40	1.56 ± .05
	39.8 ± 4	260 ± 40	1.56 ± .05
	39.8 ± 4	260 ± 40	1.56 ± .05
	39.8 ± 4	260 ± 40	1.56 ± .05
	39.8 ± 4	260 ± 40	1.56 ± .05
	39.8 ± 4	260 ± 40	1.56 ± .05
ave.	39.8	260	1.56
P40-13 through 16	39.8 ± 4	260 ± 40	1.56 ± .05
	39.8 ± 4	260 ± 40	1.56 ± .05
	39.8 ± 4	260 ± 40	1.56 ± .05
	39.8 ± 4	260 ± 40	1.56 ± .05
	41.6 ± 4	248 ± 40	1.56 ± .05
	41.6 ± 4	248 ± 40	1.56 ± .05
ave.	40.4	256	1.56

Most of the fiber densities on which the data of Table XXXVII are based were determined by dividing the mass per unit length of yarn by the total cross-sectional area. The total cross-sectional area was taken to be the average filament area based on the measured area of 20 filaments) multiplied by 1420 for "Thornel" 25 yarn and by 1365 for "Thornel" 40 yarn. A limited number of density measurements have been made by immersing the fibers in mercury in a porosimeter. The fiber densities determined in this way have been in good agreement with those obtained by the geometrical method.

The problem of determining the fiber density is being investigated further and more information will be given in a future report.

3. Fiber Volume Content
(G. B. Spence)

The volume fraction of fibers in composites has been determined by three methods. The Kjeldahl method determines the mass fraction of nitrogen in the composite. This number divided by the mass fraction of nitrogen in the pure resin system ERL 2256/MPDA (i.e., by 0.0374) gives the mass fraction of resin in the composite. A second method employs nitric acid to dissolve the resin.[29] The weight of fibers remaining then gives the mass fraction of fibers in the composite. The optical method is a point counting technique of modal analysis. A grid of several thousand points is established on an optically polished cross-sectional surface of the composite; then, at each point, the surface is identified as being fiber, resin, or void. The volume fractions of fiber, resin, and voids are assumed to be equal to the corresponding area fractions.

The mass fractions are converted to volume fractions by density ratios. The necessary formulas are as follows: let

m_f & v_f = mass & volume fraction of fiber in composite

m_m & v_m = mass & volume fraction of matrix in composite

v_v = volume fraction of void in composite

ρ_f, ρ_m, & ρ_c = density of fiber, matrix, & composite.

Then, $m_f = 1 - m_m$,

$$v_f = \rho_c m_f / \rho_f,\ v_m = \rho_c m_m / \rho_m, \text{ and } v_v = 1 - v_f - v_m. \qquad \text{(VE-1,2)}$$

The accuracy of the Kjeldahl method has been investigated by determining the resin content of glass-fiber, ERL 2256/MPDA composite rings by this method and by the reliable resin burn-off method. The mass fraction of resin was approximately 5 percent less by the Kjeldahl method. Whether or not the deviation will be the same for other batches of resin remains to be investigated.

Table XXXVIII gives the results of the measurements of volume fractions of fibers and voids in the plates. In many cases, the same method was used on several samples from the same plate. The measurement of the composite density was inadvertently omitted on some samples, in which case the composite density of neighboring material was used. The error from this source is probably less than 2 percent.

The optical method is the most accurate, the uncertainty in the fiber content being less than 2 percent. The analytical laboratory personnel are less familiar with the nitric acid method, a fact that may account for the greater variability in these results. This method seems capable of good reproducibility. The Kjeldahl method has always yielded good reproducibility; but for plates numbered P 25-1, 2, 3, 5, and, possibly, 8, the fiber content by the Kjeldahl method is lower than that obtained by the nitric acid method. Since the Kjeldahl determinations on the same plate were made at widely different times, there is no chance of systematic experimental error. For plates numbered P 25-1, 2, and 3, the good physical properties and the optical result (on plate number 3) indicate that the Kjeldahl results are in error. The discrepancy is thought to be caused by nonuniformity of nitrogen fraction in the resin; and, at present, we have less confidence in the Kjeldahl method than in the nitric acid method, provided that duplicate results by the nitric acid method agree. For this reason, the Kjeldahl measurement was not used on the "Thornel" 40 plates. For plate number P 25-5, fiber spacing in optical micrographs of the cross section and the low values of the modulus and strength indicate that the Kjeldahl result is more accurate (in this 2-ply unidirectional plate, the variability in fiber content across the plate may be greater than for any other plate). The column labelled "Average" is based on the measurements which are thought to be the most reliable.

The calculated void contents are not very accurate (note calculated negative void contents) because of the lack of an accurate fiber density. Evidently, when there was sufficient resin flow present to give a smooth surface, the void content was between 0.1 and 1.5 percent. When insufficient resin flow was present, the void content was between 1.5 and 5 percent.

4. Optical Micrographs of Plates

At fiber contents lower than approximately 50 volume percent, excess resin accumulates between the yarn strands, as shown in Figure 83 depicting a plate with approximately 42 v/o "Thornel" 25 fibers. Each of the two plies can be identified, but little resin accumulation is evident between plies. At approximately 46 v/o fibers, the strands are touching, but resin-rich areas are present as shown in Figure 84. There is good penetration of the resin into the yarn bundles; the porosity almost always occurs between plies or yard strands. The porosity has been observed to be extensive enough to cause poor bonding between plies. This condition results from insufficient resin flow during molding. In cross-plied laminates with high fiber content, cracks often developed within a ply, with the crack surface generally normal to the plane of the ply parallel to the fiber axis; a few such cracks are evident in Figure 84.

TABLE XXXVIII

FIBER AND VOID VOLUME CONTENT OF PLATES

Plate No.	No. of Plies & Orientation	Fiber Vol. Content (Void Vol. Content in Parentheses)				
		Average**	Kjeldahl Method	HNO_3 Method		Optical Method
P25-4	9(0)	50	49.2(1.4);49.9*(1.6)	52.6(1.9);43.1*(.3)		50.6(.1)
P25-14	9(0)	45	---	44.5(2.0)		---
P25-5	2(0)	34	33.7(-.3);38.5*(.1)	52.7(2.6)		---
P25-1	9(0,90)	43	34.5(.1);36.9*(2.2)	42.6(1.9);44.1*(3.8)		---
P25-11	9(0,90)	47	47.6(.2);45.7(.2);46.6(1.2)	47.8(1.4)		---
P25-12	9(0,90)	48	---	48.2(4.1)		---
P25-9	6(0,90)	50	49.7(2.3);50.1*(2.8)	50.9*(2.9)		---
P25-2	5(0,90)	42	24.1(-.1);26.8*(.6);28.2*(.9)	42.6(6.2);42.3*(3.5)		---
P25-3	4(0,90,90,0)	50	37.6(.1);36.0*(.2)	50.3(2.4);50.7*(3.0)		50.3(.4)
P25-10	3(0,90,0)	46	44.7(.4);47.0*(1.8)	47.1(1.5);66.1*(4.8)		---
P25-7	2(0,90)	41	41.2(2.9);37.3*(2.4)	41.5*(3.1)		---
P25-8	4(0,-45,90,45)	50	44.3(1.3);44.9*(2.4)	50.0(2.6);50.5*(3.5)		---
P25-6	3(0,-60,60)	46	44.7(1.7);46.8*(2.2)	45.8*(2.0)		---
P40-1	9(0)	67	---	71.1	66.6	66.7(.1)
P40-9	7(0)	65	---	65.6		
P40-14	6(+10,±45,±10)	56	---	56.5	56.8	
P40-5	4(10,-10,-10,10)	69	---	69.0	68.6	
P40-6	4(10,-10,-10,10)	64	---	63.6		
P40-12	4(90,0,0,90)	64	---	63.1	66.1	
P40-10	4(45,-45-45,45)	67	---	67.7	67.4	
P40-16	4(90,±10,90)	57	---	57.7	57.5	

*Based on estimate of composite density.
** Average of reliable values, see text on next page.

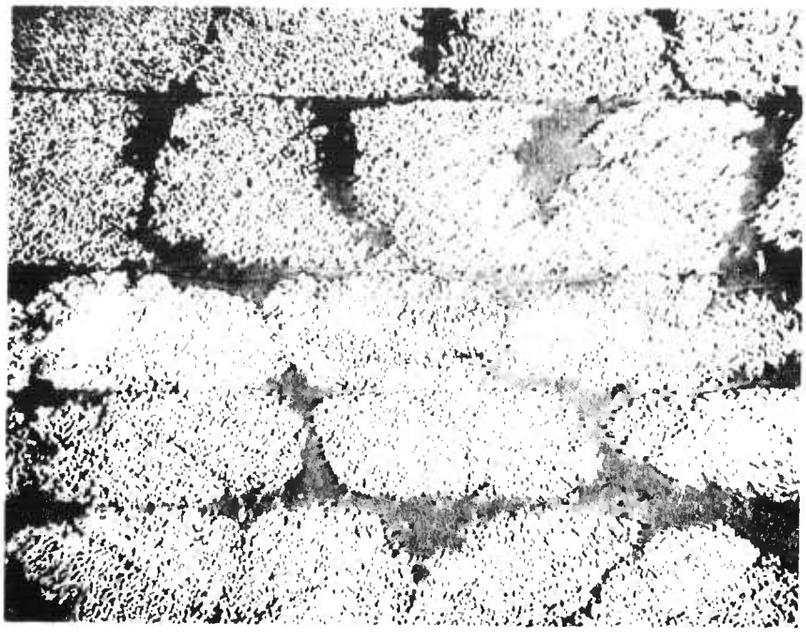

N-10733

Figure 83. Plate P25-2, 5 Plies (0°, 90°) Lay-Up, Fiber Volume Content 42 Percent. Surface at 45° to Fiber Axes. 50X Magnification.

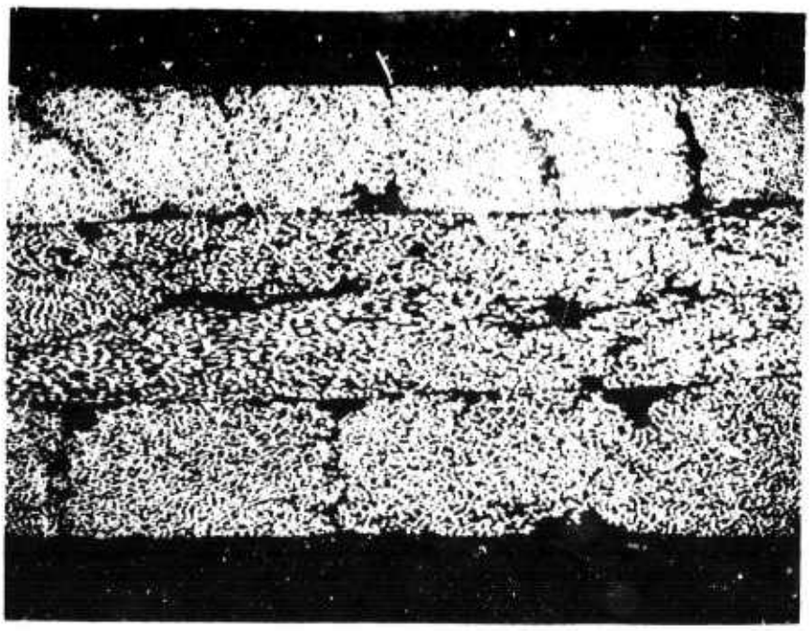

N-10734

Figure 84. Plate P25-6, 3 Plies (0°, ±60°) Lay-Up, Fiber Volume Content 46 Percent. Surface Normal to Fibers in Top Ply. 50X Magnification.

Figure 85 shows a surface at 45 degrees to the fiber axes of plate number P25-3. Since the lay-up pattern was (0°, 90°, 90°, 0°) the fibers in the two center plies are parallel, resulting in a nestling together of the strands. At 50 v/o fibers, very few resin-rich areas are present, and individual yarn strands are difficult to distinguish (see Figure 86). This figure also illustrates an appreciable variation in ply thickness, a variation that may be caused, in part, by nonuniform resin pickup in different plies. Another cause may be related to the fact that the surface between plies (observed at delaminations) is almost always wavy, with a wave length of approximately 0.2 inch. Since the outside surfaces are flat, these waves can occur only if there is a variation in ply thickness. It is not known whether the waves are due to some systematic nonuniformity in the plies or to a more fundamental mechanism, such as a buckling of one ply due to the resin shrinkage of the neighboring cross plies.

Figure 87 shows the cross section of a unidirectional lay-up with 50 v/o fibers. The strands nestle so completely that it is difficult to detect the original plies. Since internal cracking has never been observed in unidirectional lay-ups, the cracks are possibly due to the resin shrinkage within one layer being restricted by the very stiff cross plies on either side.

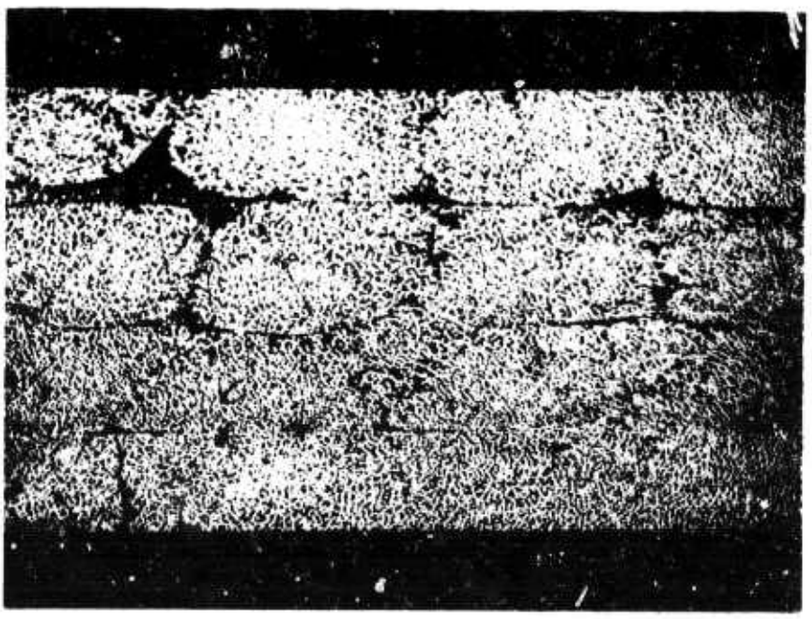

N-10735

Figure 85. Plate P25-3, 4 Plies (0°, 90°, 90°, 0°) Lay-Up, Fiber Volume Content 50 Percent. Surface at 45° to Fiber Axes. 50X Magnification.

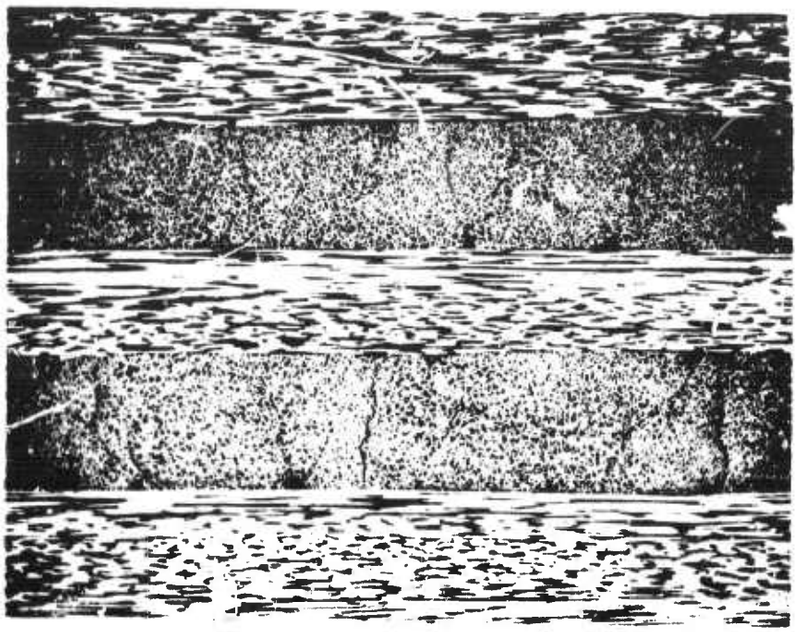

N-10736

Figure 86. Plate P25-9, 6 Plies (0°, 90°) Lay-Up, Fiber Volume Content 50 Percent. Surface Normal to Fibers in Top Ply. 50X Magnification.

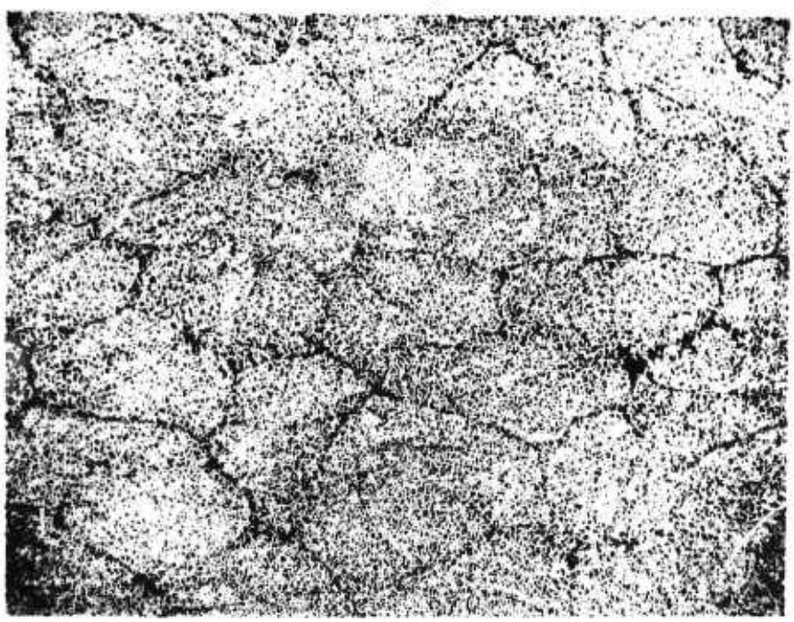

N-10737

Figure 87. Plate P25-4, 9 Plies (0°) Lay-Up, Fiber Volume Content 50 Percent. Surface Normal to Fiber Axis. 50X Magnification.

Optical micrographs of composites containing "Thornel" 40 fibers are similar to those for "Thornel"25. In Figure 88 of a unidirectional composite with 68 v/o "Thornel" 40 fibers, the boundaries between yarns have almost disappeared. Figure 89 shows the same surface at higher magnification; fiber-fiber contacts are common at high fiber loadings.

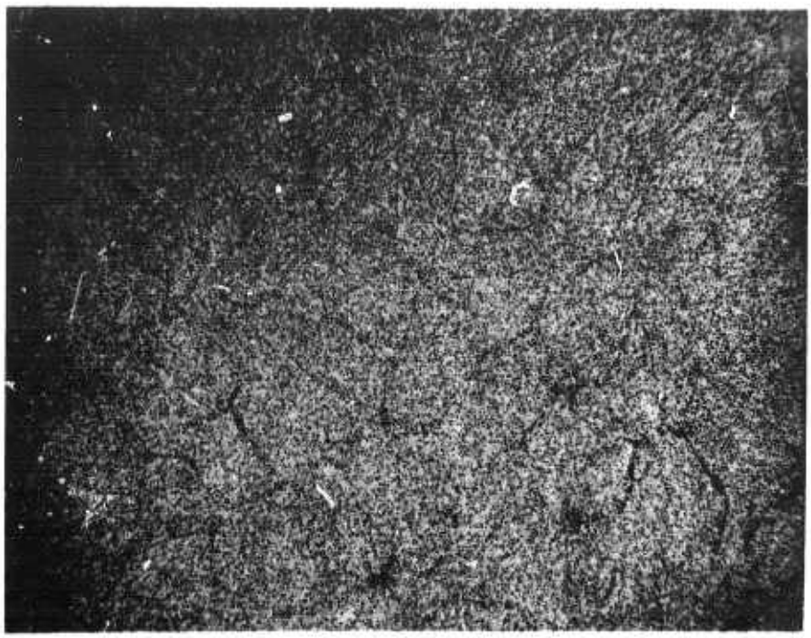

N-17508

Figure 88. Plate P40-1, 9 Plies (0°) Lay-Up, Fiber Volume Content 68 Percent. Surface Normal to Fiber Axis. 50X Magnification.

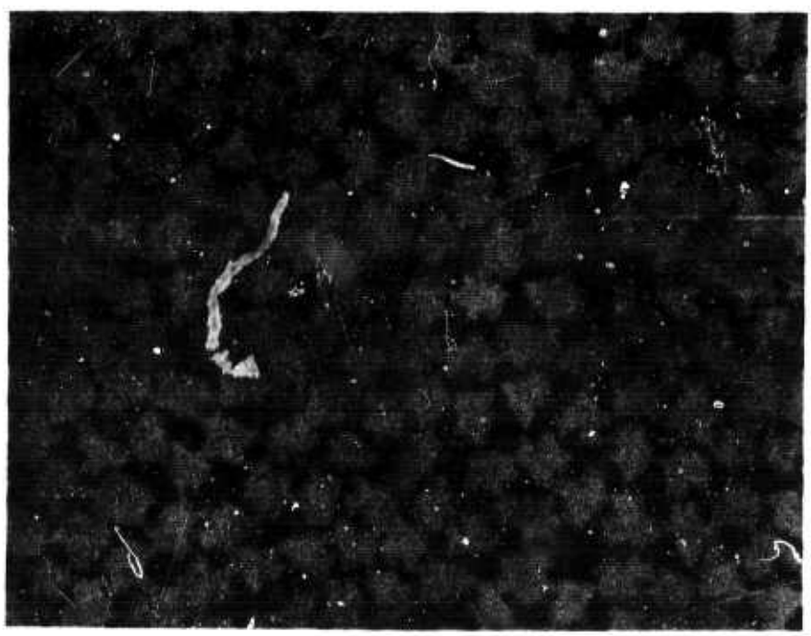

N-17509

Figure 89. Plate P40-1, 9 Plies (0°) Lay-Up, Fiber Volume Content 68 Percent. Surface Normal to Fiber Axis. 1000X Magnification.

SECTION VI

PHYSICAL PROPERTIES OF GRAPHITE-FIBER, RESIN-MATRIX COMPOSITES

The initial physical properties measurement program on the "Thornel" 25 series of resin matrix composites had the objectives of determining the extent to which the fiber properties could be realized in a composite and of determining the principal elastic properties and strength allowables needed for the design activities. Additional data were obtained on off-axis elastic and strength properties and on the effects, particularly on the strength and flexural rigidities, of decreasing the number of plies in the laminate. Subsequent work on the "Thornel" 40 composites has been devoted mainly to determining the strength allowables for nonorthogonal lay-up patterns and to determining complete sets of membrane and bending elastic properties.

The physical properties test procedures are described in Section VI A. Membrane and bending elastic properties are reported in Section VI B, and membrane stress-strain curves are shown in Section VI C. Tensile, compressive, and short-beam shear strengths of plate specimens and hoop-tensile and torsional strengths of cylinders are given in Section VI D. The results of a limited study of the effects produced by submersion in boiling water are reported in Section VI E. Section VI F presents preliminary measurements of thermal expansion and conductivity.

A. Test Procedures for Fiber Composites

(O. L. Blakslee, Union Carbide Corporation)

Tensile Tests. Tensile tests have been made on "dog-bone" shaped composite specimens; except for three specimens, the gauge section was 0.25-inch wide and 1- or 2-inches long. Figure 90 shows typical specimen shapes. The wide-shank specimen (Type A) was used for multidirectional composite specimens and for unidirectional composite specimens tested off-axis; the long, narrow-shank specimen (Type B) was used for unidirectional composite specimens tested in the fiber direction. The specimen ends were reinforced with reusable steel doubler plates bonded to the specimens with ERL 2795/ERL 2793 epoxy resin as shown in Figure 91. The shape of the Type B doubler plate was chosen to obtain a more uniform distribution of shear stress in the specimen than that which occurs with the simpler Type A plate. Satisfactory tensile breaks could not be obtained on unidirectional "Thornel" 40 composites with either a Type A plate or an elongated rectangular but nontapered plate. A pin was placed in the small hole in the Type B specimen to insure alignment during bonding of the doubler plates. For both the Type A and B specimens, a pin-clevis loading fixture was chosen instead of the clamp-grip loading fixture because of the superior aligning characteristics of the former under load. Longitudinal and transverse strains were measured by pairs of high elongation strain gages mounted on both sides of the specimen and wired so as to cancel bending effects. The cross-head rate was either 0.01 or 0.02 inch/min.

Compression Tests. Edgewise compression tests were made on 3.5 x 0.5-inch "dog-bone" shaped specimens with a 2.75 x 0.375-inch

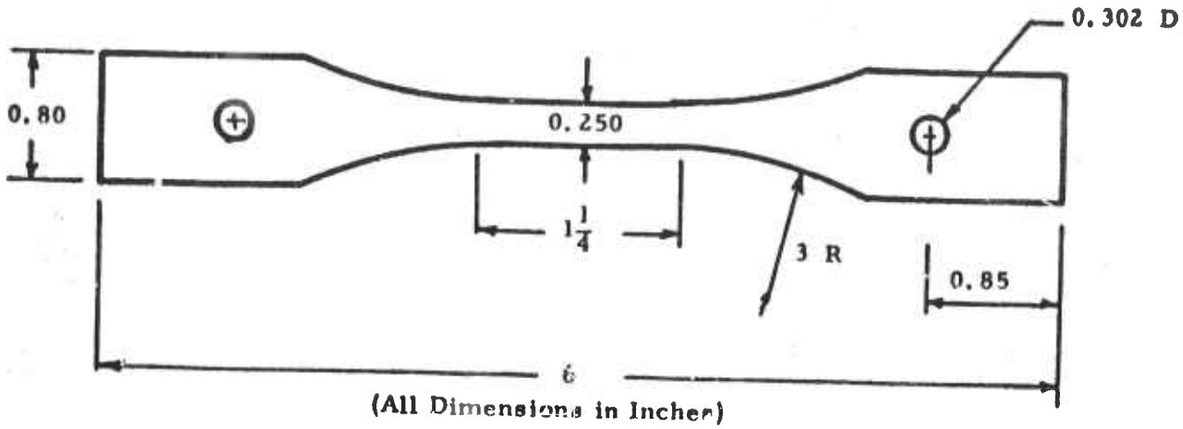

Type A

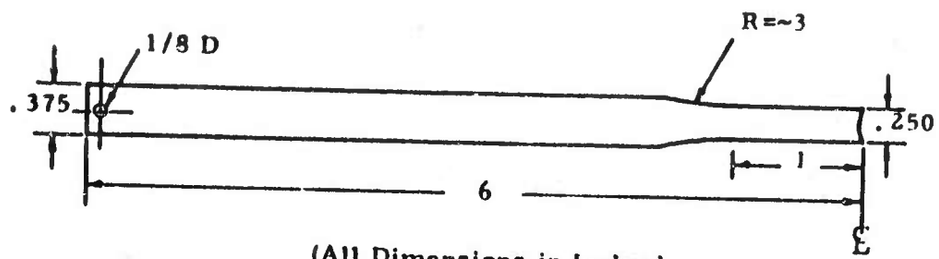

(All Dimensions in Inches)

Type B

N-10617

Figure 90. Geometry of Typical Tensile Test Specimens.

gauge section. The specimens were clamped on the ends to prevent "brooming" and supported by the fixture described in Federal Test Method Std. No. 406, Method 1021 (shown in Figure 92). Strain was measured on several of the "Thornel" 25 composite specimens. On thick specimens, both strain gages mounted on the edges and a strain-gage compressometer were used; on thin specimens, only the compressometer was used. The cross-head rate was either 0.01 or 0.02 inch/min.

Bend Tests. Bend (flexural) tests were made with the fixture shown in Figure 93. The distance between the middle load points is 1.33 inches and between the outer support points is 4.0 inches. The effect of friction between the specimen and the fixture is minimized by supporting the load and support rods in ball bearings. The support carriage is balanced in ball bearings so that the fixture will automatically adjust for specimens with an initial curvature along the specimen axis.

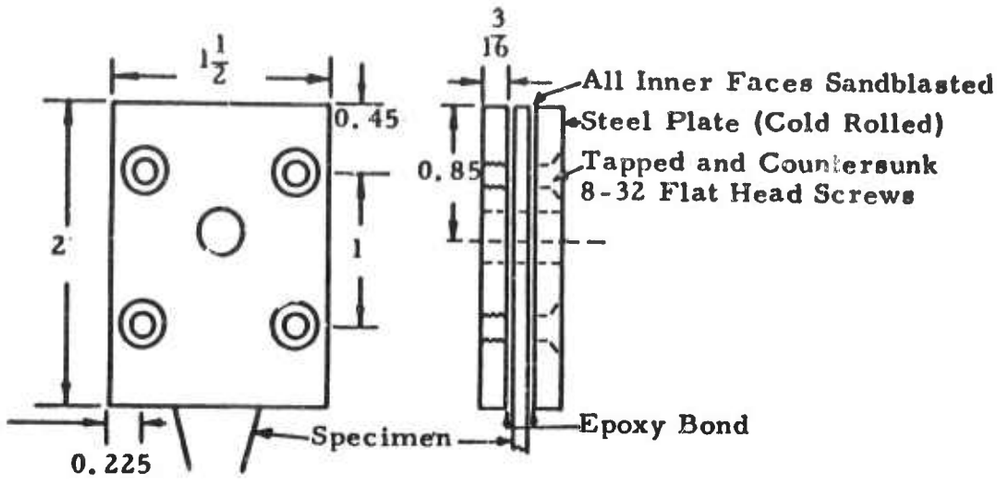

(All Dimensions in Inches)

Type A

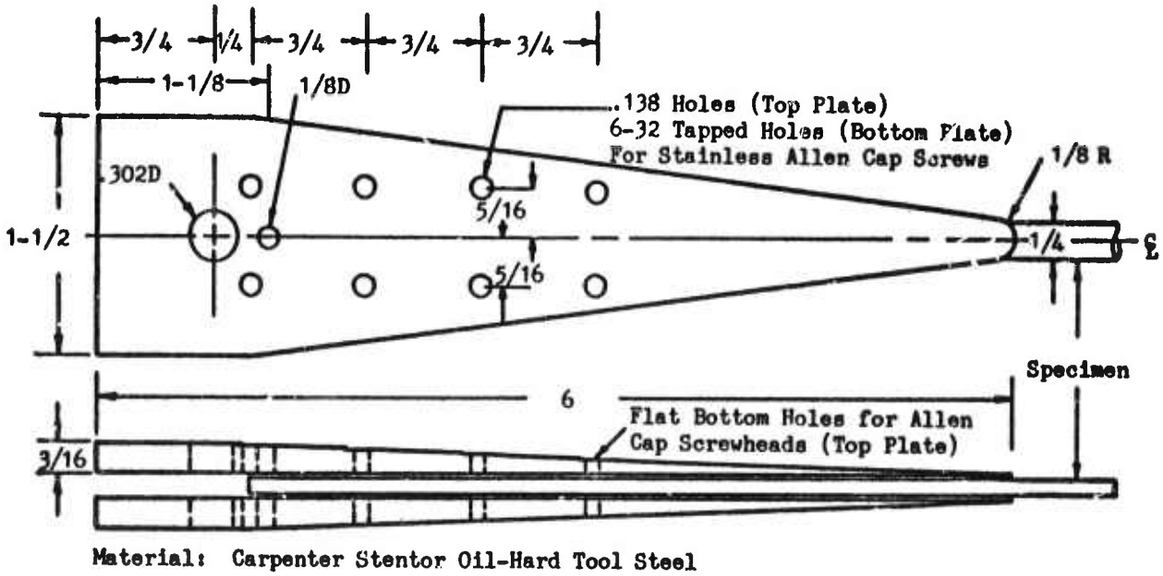

Material: Carpenter Stentor Oil-Hard Tool Steel

(All Dimensions in Inches)
Type B

N-10616

Figure 91. Reinforcing Doubler Plates for Tensile Specimens.

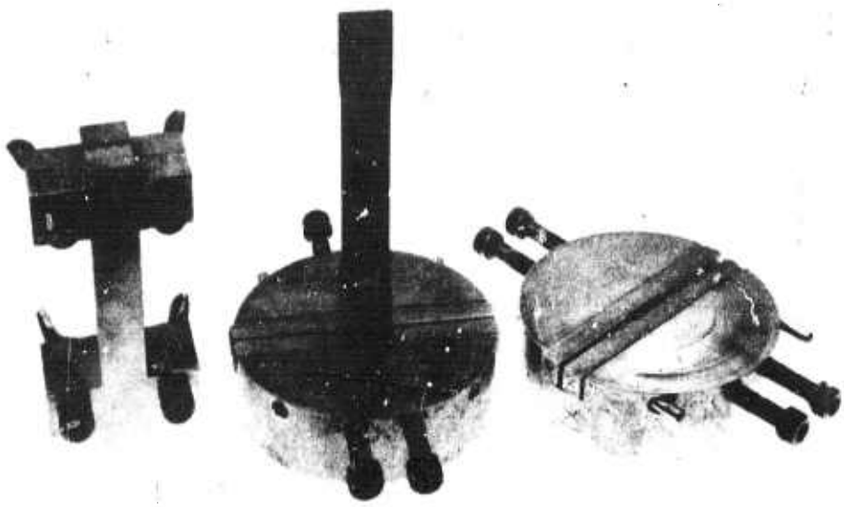

N-17510

Figure 92. Edgewise Compression Fixtures.

Friction between the two parts of the fixture had to be limited to less than 0.03 pound because the loads applied to thin composite specimens to measure elastic properties were, in some instances, only 0.2 pound. On most tests, the curvatures both along and transverse to the specimen axis were measured with pairs of strain gages mounted on both sides of the specimen, usually, all four strains were monitored separately. Occasional large deviations between the magnitudes of the transverse strains on the top and bottom surfaces indicate that, in some specimens, the loading was not a pure bending moment, probably because of material nonhomogeneities and geometrical irregularities in the specimens. The cross-head rate was either 0.05 or 0.1 inch/min.

Shear Tests. Shear strengths were obtained by the flexure of a short beam loaded at three points. (Specimen dimensions are discussed later in connection with the results.) A few shear strengths were measured by the torsion of thin-walled hollow cylinders which were hoop wound. The torsion tests were made on the torsion apparatus described in Section III C 1 (see Figure 10).

Sonic and Ultrasonic Tests. Nondestructive sonic resonant bar tests were made on all tensile, compression, and bend specimens before the specimens were machined to "dog-bone" shape and/or statically

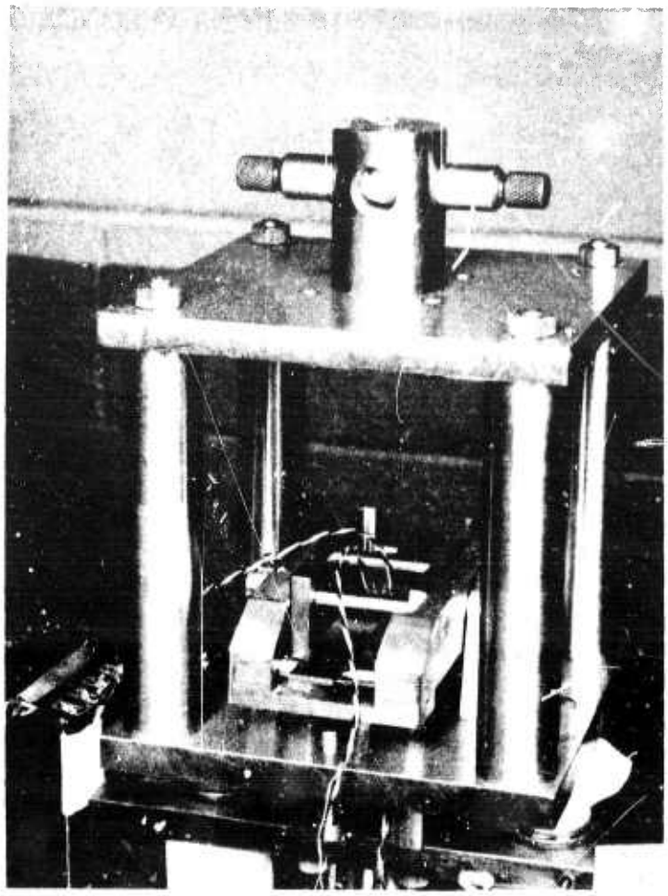

N-17511

Figure 93. Bend Fixture.

tested. The sonic resonant bar test used longitudinal and flexural resonances parallel to the laminate to measure membrane (extension) moduli and used flexural resonances perpendicular to the laminate to measure bend moduli.

A limited number of direct shear moduli measurements were made by the ultrasonic pulse velocity method. The shear constants c_{44}, c_{55}, and c_{66} were measured by a 1 mHz shear wave using a transmit-receive technique.

Thermal Expansion and Conductivity Tests. The coefficient of thermal expansion was determined from the change in length between room and steam temperatures compared with that of an Invar standard. The thermal conductivity was calculated from the room-temperature thermal diffusivity measured by the flash method and from the specific heat calculated from the specific heats of the fiber and the resin.

B. Composite Elastic Properties
(O. L. Blakslee and G. B. Spence, Union Carbide)

Tensile specimens and a limited number of resonant bar, compression and bend specimens were cut at various angles from the "Thornel" 25 and 40 composite plates. Typical cutting patterns are shown in Figure 94.

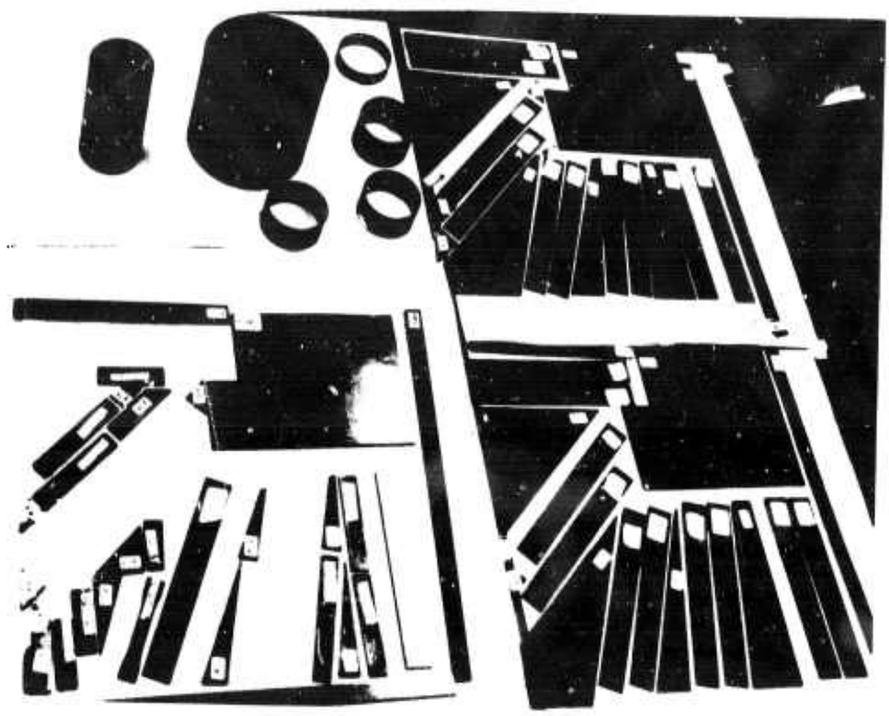

N-10730
Figure 94. Plates and Cylinders of "Thornel" 25/ERL 2256 Partially Cut into Specimens for Testing.

The tensile specimen orientations were as follows:

Plates	Specimen Orientation
P25-1, 2, 3, 4, 10	0°, 10°, 20°, 45°, 90°
P25-6	0°, 10°, 20°, 30°, 90°
P25-8	0°, 10°, 22.5°, 45°, 90°
P25-5	0°
P25-7, 9	0°, 90°
P40-1, 6, 9, 14, 16	0°, 45°, 90°
P40-5, 12	0°, 90°
P40-10	0°

All of the data in this section were measured on bars with a gauge section width of 0.25 inch; the gauge section length-to-width ratio was 4 or greater.

Section VI B 1 contains a discussion of the Young's moduli values at low stress levels, obtained from sonic tests on the rectangular tensile bars from which the tensile "dog-bone" specimens were cut and from the initial slopes of static tensile stress-strain curves. So that data from different plates might be compared, the data must be reduced to a common fiber modulus and fiber volume content. In Section VI B 2, these normalized data are compared and evaluated with respect to moduli predicted from constituent properties by the rule-of-mixtures. The Poisson's ratios and shear moduli are given in Tables XXXIX and XL of Section VI B 1 and are discussed in Section VI B 3. The complete tensile stress-strain curves are reported in Section VI C.

Definition of Standard Coordinate System and Notation for Elastic Properties. A standard coordinate system is chosen such that the x_1 axis is in the plane of the plate and in the zero degree direction. Angles are positive on rotating counterclockwise as one views the plate from above. The x_2 axis is in the plane of the plate and points in the positive 90 degree direction; the x_3 axis is perpendicular to the plate and points up. The elastic compliance constants s_{ij} (defined by $\varepsilon_i = s_{ij}\sigma_j$) and the elastic stiffness constants c_{ij} (defined by $\sigma_i = c_{ij}\varepsilon_j$) are determined with reference to the standard coordinate system. The Young's moduli in the 0 and 90 degree directions are:

$$E_1 = 1/s_{11} \text{ and } E_2 = 1/s_{22} \qquad \text{(VIB-1)}$$

The Poisson's ratios for stresses in the 0 and 90 degree directions are:

$$\nu_{12} = -s_{12}/s_{11} \text{ and } \nu_{21} = -s_{12}/s_{22} \qquad \text{(VIB-2)}$$

and the in-plane shear modulus is:

$$G = c_{66} = 1/s_{66} \qquad \text{(VIB-3)}$$

Procedure for Analyzing the Data. Elastic moduli were measured on tensile bars cut at various angles from the "Thornel" 25 composite plates. In the zero stress limit, the Young's modulus and Poisson's ratio for a bar at an angle θ with respect to the x_1 axis can be calculated from the elastic constants relative to the standard coordinate axes. This fact has been utilized in analyzing the present moduli data.

The Young's modulus $E'(\theta)$, Poisson's ratio $\nu'(\theta)$, and the in-plane shear modulus $G'(\theta)$ of a bar in the $x_1 x_2$ plane at an angle θ with x_1 axis can be expressed in terms of the standard compliance constants by the following formulas (orthorhombic symmetry is assumed):

$$E'(\theta) = 1/s_{11}'(\theta) \qquad \text{(VIB-4)}$$

$$\nu'(\theta) = -s_{12}'(\theta)/s_{11}'(\theta) \qquad \text{(VIB-5)}$$

$$G'(\theta) = 1/s_{66}'(\theta) \qquad \text{(VIB-6)}$$

in which

$$s_{11}'(\theta) = s_{11} + S_1 \sin^2\theta + S_2 \sin^4\theta \qquad \text{(VIB-7)}$$

$$s_{12}'(\theta) = s_{12} + S_2(\sin^2\theta - \sin^4\theta) \qquad \text{(VIB-8)}$$

$$s_{66}'(\theta) = s_{66} + 4S_2(\sin^2\theta - \sin^4\theta) \qquad \text{(VIB-9)}$$

and

$$S_1 = -2s_{11} + 2s_{12} + s_{66} \qquad \text{(VIB-10)}$$

$$S_2 = s_{11} + s_{22} - 2s_{12} - s_{66} \qquad \text{(VIB-11)}$$

If one sets $y(\theta) = \sin^2\theta$ and $S_0 = s_{11}$, equation VIB-7 may be written as a second degree polynominal in y:

$$s_{11}'(\theta) = S_0 + S_1 y(\theta) + S_2 y^2(\theta) \qquad \text{(VIB-12)}$$

A standard computer program was used to make a least squares fit of the data to equation VIB-12. The computer input consisted of the experimental values of $s_{11}'(\theta)$ from the static, sonic longitudinal, and sonic in-plane flexural tests and the corresponding values of $y(\theta)$ for all bars of a given plate. The computer output was a set of best values for S_0, S_1, and S_2 for the plate. In this way, all of the data were treated equally.

Since S_2 is a large negative number and s_{12} is a small negative number, experimental errors in S_2 preclude the use of equation VIB-8 and experimental values of $s_{12}'(\theta)$ at $0°<\theta<90°$ to compute a best value of s_{12}. However, since $s_{12}'(\theta) = s_{12}$ at $\theta = 0°$ and 90°, the best value of s_{12} was taken to be the average of the values for the 0° and 90° bars:

$$s_{12} = [s_{12}'(0°) + s_{12}'(90°)]/2 \qquad \text{(VIB-13)}$$

The best values for the remaining standard compliance constants for the plate were computed from:

$$s_{11} = S_0 \qquad \text{(VIB-14)}$$

$$s_{22} = S_0 + S_1 + S_2 \qquad \text{(VIB-15)}$$

and

$$s_{66} = 2S_0 + S_1 - 2s_{12} \qquad \text{(VIB-16)}$$

The best engineering moduli for the plate were computed from these values with equations VIB-1, 2, 3.

Plates numbered P25-6 and P25-8 have approximately transversely isotropic symmetry instead of orthorhombic symmetry. Consider a plate made up of a large number of thin packets, each packet consisting of n plies oriented uniformly at an angle of 180/n degrees apart. By invoking the consequences of symmetry on the transformation formulas for the

extensional elastic constants, one can show that if n is equal to or greater than 3, the extensional elastic properties of the plate will have transversely isotropic symmetry.* Even though plates P25-6 and P25-8 have unbalanced lay-ups of only one packet, it will be assumed that their symmetry is strictly transverse isotropy. In practice, any deviation of the extensional moduli from transverse isotropy is within the scatter of the data. The average of the values of $1/s_{11}$ for each bar from plates P25-6 or P25-8 is always greater than the reciprocal of the average of the values of s_{11} for each bar, but the difference is only approximately 1 or 2 percent. So that the transversely isotropic and orthorhombic plates might be treated similarly, the procedure used for plates P25-6 and P25-8 was to average all the values of s_{11} and the values of s_{12} to obtain the best compliance constants for the plates. The Young's modulus and Poisson's ratio for the plate were computed from these values with equations VIB-1 and 2. For transverse isotropy, the in-plane shear modulus is given by

$$G = (c_{11} - c_{12})/2 = 1/2(s_{11} - s_{12}) \qquad \text{(VIB-17)}$$

For plate number P25-5, the only tensile specimen tested was in the 0° direction. For plates P25-7 and P25-9, a tensile bar was tested in the 0° and 90° directions only; sonic and static values of the compliance constants were averaged.

At present, only measurements at 0°, 45°, and 90° have been made on the series of plates made of "Thornel" 40 yarn. Values of E_1, E_2, ν_{12} and ν_{21} were obtained from the 0° and 90° specimens. The in-plane shear modulus was calculated from data for the 45° specimens by using the relation

$$G = E'(45°)/2[1 + \nu'(45°)], \qquad \text{(VIB-18)}$$

which follows from equations VIB-3 through 11.

1. Young's Moduli Membrane and Bending

Young's modulus in the limit of zero stress has been measured under membrane loading by static tensile and sonic resonant bar tests and, in a few cases, by compression tests. Since the values obtained in compression agreed well with sonic measurements on the same specimen and with static tensile measurements on similar samples, the moduli measurements in compression were discontinued due to the difficulty of obtaining the compression strain. A small amount of compression modulus data is given at the end of this (VIB-1) section.

The so-called equivalent Young's modulus in bending has been determined from static bend tests. In addition, an exploratory study was initiated to see if Young's modulus in bending could be determined from the sonic resonant vibrations of a freely-supported bar. A discussion of the sonic work is given in the next subsection; this review is followed by a presentation of the experimental result.

Sonic Resonant Bar Test Method. An effort has been made to evaluate the sonic resonant bar method for determining the zero stress

*The authors are indebted to Mr. L. B. Greszczuk for bringing this property to their attention.

level elastic constants of strongly anisotropic fiber-reinforced, epoxy composites. Since the study has not been completed, and only a status report can be given at this time, the bars were supported at their nodal points; both ends were free. Resonant frequencies were measured for several harmonics (first harmonic = fundamental) of four types of vibrations. Longitudinal vibrations parallel to the axis of the bar and flexural vibrations with the plane of vibrations parallel to the plies both yield the membrane Young's modulus. Flexural vibrations with the plane of vibration perpendicular to the plies presumably yield the flexural rigidity relating bending moment to curvature. However, the data from the out-of-plane vibrations are reported here as equivalent Young's moduli in bending since, by comparing moduli in membrane and in bending, we wish to emphasize the large difference between these numbers when the plates have only a few plies. The data from the torsional vibrations have not yet been analysed. The failure of the torsional frequencies to follow an integer harmonic series indicates that the bars were not vibrating in a purely torsional mode. It remains to be seen whether a reliable value of a shear modulus or a torsional rigidity can be obtained from the torsional resonant frequencies.

A modulus was calculated for each resonant frequency of each type of vibration. For the longitudinal vibrations and for the in-plane flexural vibrations, the modulus values for all the harmonics were averaged to obtain the data reported here. The spread in the values indicates an uncertainty in the average of approximately 2 to 4 percent. For the out-of-plane flexural vibrations, the equivalent modulus in bending invariably decreased as the harmonic number increased from 1 to 3 or 4 As an example, the following results were obtained on bars from plate number P25-3:

	Equivalent Modulus in Bending (10^6 lb/in.^{2})	
Harmonic	Tensile Bar No. 1 at 0°	Flexure Bar No. 1 at 0°
1	80.1	---
2	14.2	---
3	10.9	12.2
4	9.80	10.1
5	9.61	9.35
6	---	9.42
7	---	9.62
8	---	9.58
9	---	9.67
10	---	9.68
11	---	9.46

The membrane Young's modulus is only 5.6×10^6 lb/in.^{2}. There is an additional uncertainty in this procedure in that the values of Young's modulus calculated from the higher harmonics depend strongly on the value of the shear constant which is used as a correction factor in Timoshenko's equation([30]) for the flexural vibrations of a resonant bar.

Only 5 or 6 harmonics were measured on the tensile specimen blanks; the sonic value of the equivalent modulus in bending reported in the following subsection is the mean of the values calculated from the highest 2 or 3 harmonic frequencies.

Results from Static Tensile Static Bend, and Sonic Resonant Bar Tests. The results reported here for the "Thornel" 25 composites are based, at each angle, on sonic and static tests of only one tensile specimen and on bend tests of one bend specimen. Additional testing is underway to determine the degree of reproducibility of the data.

The sets of best values of the membrane moduli, obtained by the procedures discussed above, are given in Table XXXIX for the "Thornel" 25 composite plates (the values of the Young's modulus in bending, obtained from static bend tests, are given later in Table XLI.) The values of Young's modulus from individual static tensile, static bend, sonic longitudinal, and sonic in-plane and out-of-plane flexural tests are shown in Figures 96 through 102 for plates numbered P25-4, 1, 2, 3, 10, 8, and 6; the symbols used in these figures are explained in Figure 95. The solid curve is the membrane Young's modulus values calculated from equations VIB-4, 7, 10, and 11 and the average plate moduli given in Table XXXIX. The dashed curve in Figures 96 through 102 is an attempt to represent the bending modulus data by equations VIB-4 and 12, in which the three constants S_0, S_1, and S_2 are determined by requiring the curve to pass through the experimental sonic bending modulus values at θ equal to 0, 45, and 90 degrees.

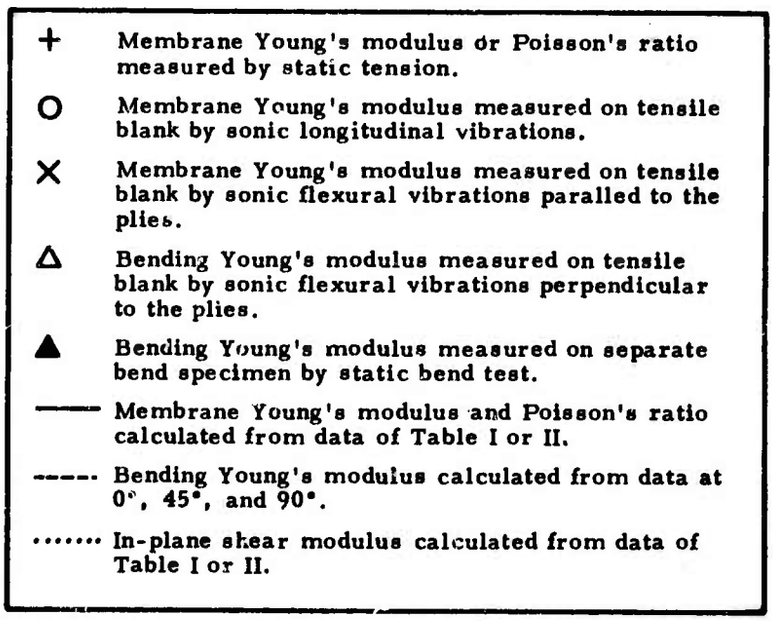

N-17244

Figure 95. Symbols Used for Elasticity Data.

TABLE XXXIX

AVERAGE VALUES OF MEMBRANE ELASTIC MODULI AND COMPLIANCE CONSTANTS FOR "THORNEL" 25/ERL 2256 PLATES

Plate Number	Plies & Lay-Up	E_1 (10^6 lb/in.^{2})	E_2 (10^6 lb/in.^{2})	G (10^6 lb/in.^{2})	$\nu_{12} = -s_{12}/s_{11}$	$\nu_{21} = -s_{12}/s_{22}$
P25-4	9(0)	11.07	1.05	0.604	0.29	0.027
P25-5	2(0)	8.70	----	-----	.32	-----
P25-1	9(0,90)	5.53	4.41	.433	.052	.041
P25-9	6(0,90)	5.78	5.91	-----	.052	.053
P25-2	5(0,90)	6.02	3.56	.475	.063	.038
P25-3	4(0,90,90,0)	5.70	5.65	.520	.049	.049
P25-10	3(0,90)	7.25	4.45	.502	.088	.054
P25-7	2(0,90)	4.8	4.8	-----	-----	-----
P25-8	4(0,-45,90,45)	4.10	----	1.57	.30	-----
P25-6	3(0,-60,60)	3.28	----	1.28	.28	-----

Plate Number	s_{11} (10^{-6} in.^{2}/lb)	s_{22} (10^{-6} in.^{2}/lb)	s_{66} (10^{-6} in.^{2}/lb)	s_{12} (10^{-6} in.^{2}/lb)
P25-4	0.0903	0.949	1.66	-0.026
P25-5	.115	-----	----	-.037
P25-1	.181	.227	2.31	-.0094
P25-9	.173	.169	----	-.0090
P25-2	.166	.281	2.10	-.011
P25-3	.175	.177	1.92	-.0086
P25-10	.138	.225	1.99	-.012
P25-7	.21	.21	----	-.04 (?)
P25-8	.244	-----	.636	-.074
P25-6	.305	-----	.779	-.085

There is a large uncertainty in the last significant figure.

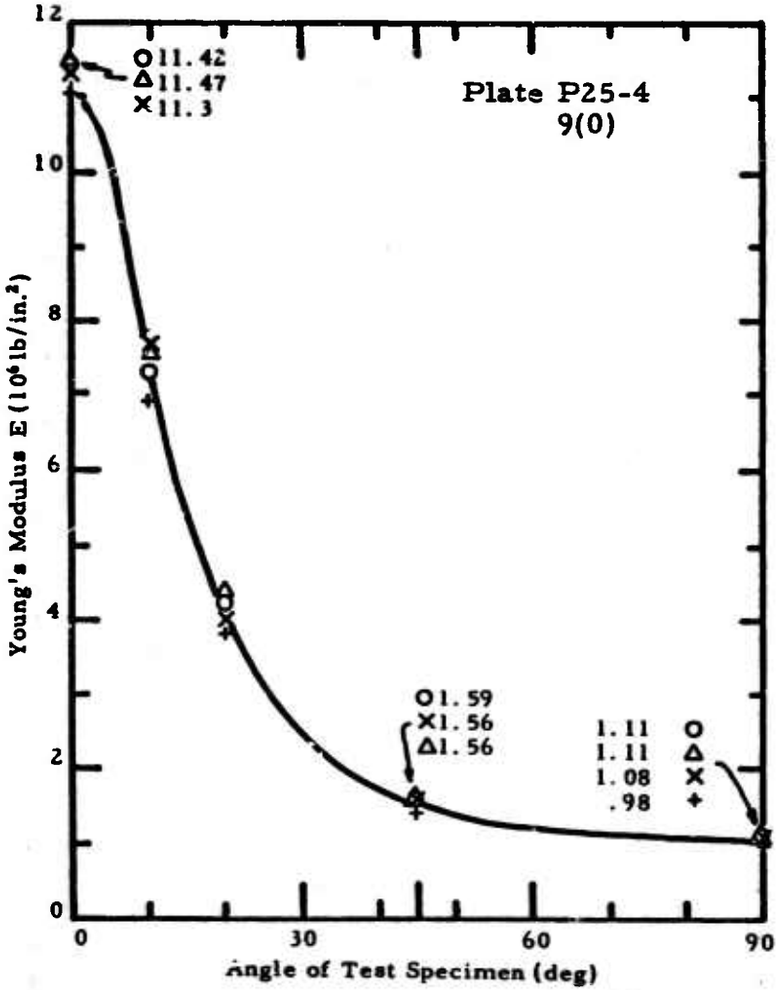

N-10649

Figure 96. Young's Modulus Versus Angle of Test Specimen for "Thornel" 25/ERL 2256 Plate P25-4. See Figure 95 for Explanation of Symbols.

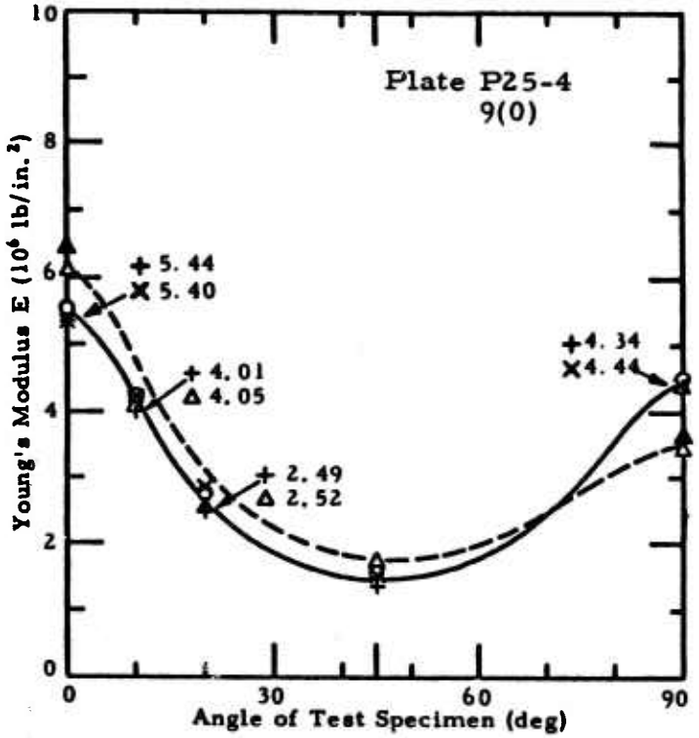

N-17138

Figure 97. Young's Modulus Versus Angle of Test Specimen for "Thornel" 25/ERL 2256 Plate P25-1. See Figure 95 for Explanation of Symbols.

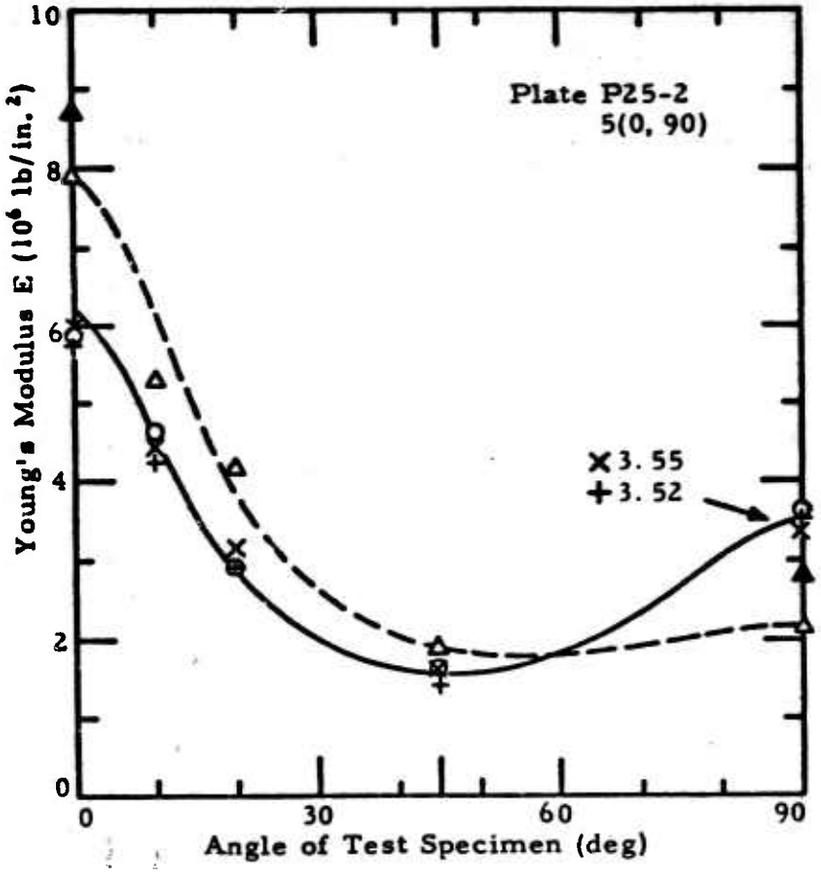

N-17136

Figure 98. Young's Modulus Versus Angle of Test Specimen for "Thornel" 25/ERL 2256 Plate P25-2. See Figure 95 for Explanation of Symbols.

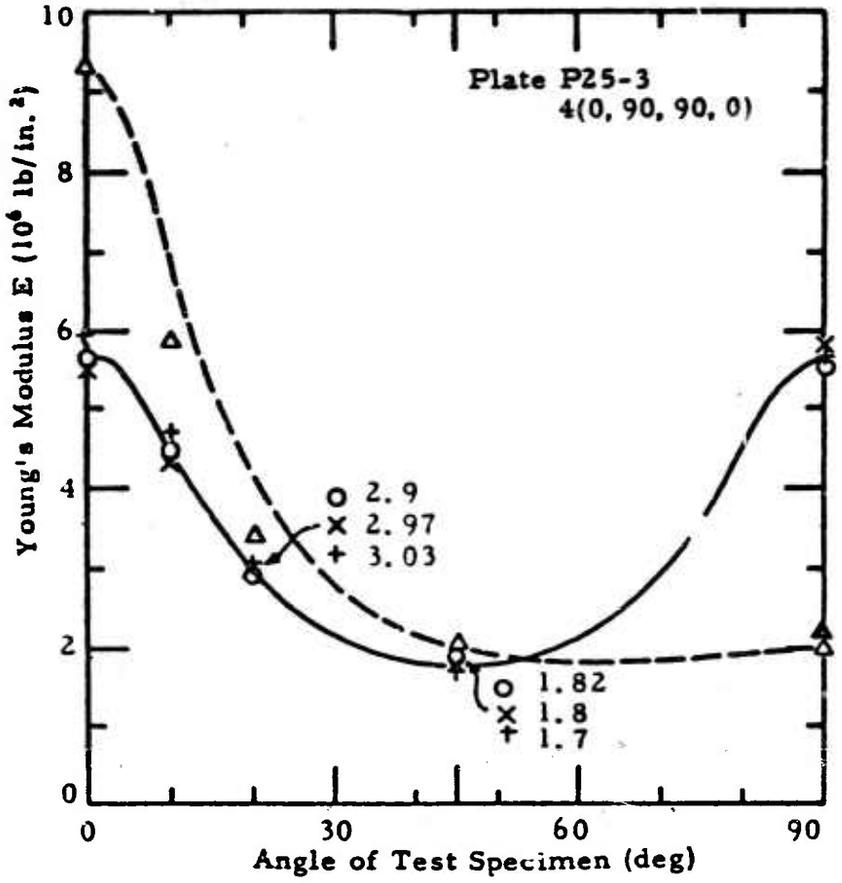

N-17137

Figure 99. Young's Modulus Versus Angle of Test Specimen for "Thornel" 25/ERL 2256 Plate P25-3. See Figure 95 for Explanation of Symbols.

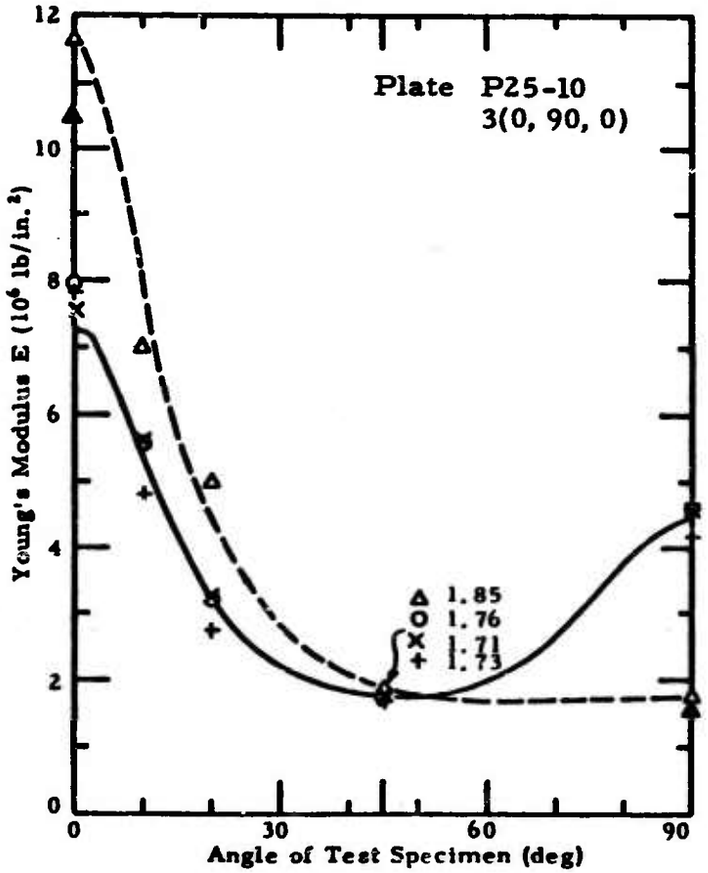

N-17139

Figure 100. Young's Modulus Versus Angle of Test Specimen for "Thornel" 25/ERL 2256 Plate P25-10. See Figure 95 for Explanation of Symbols.

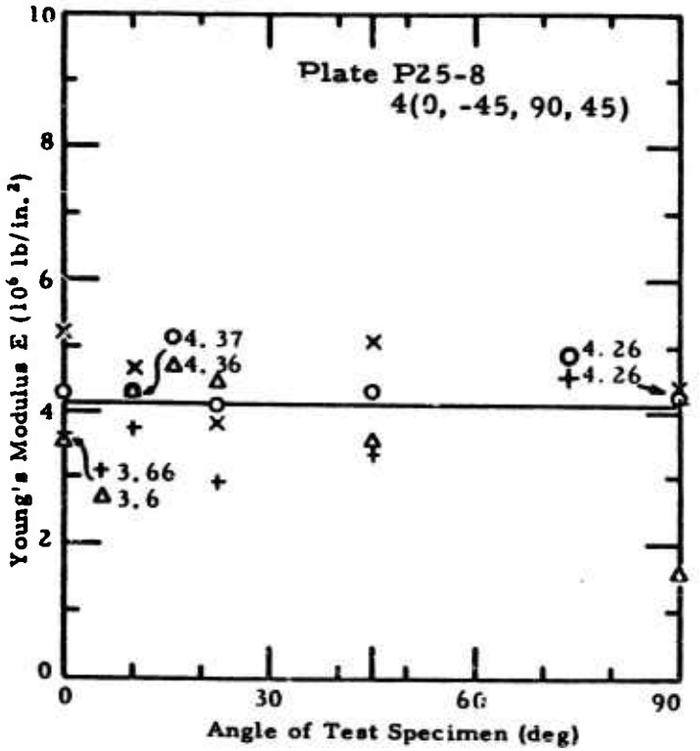

N-10688

Figure 101. Young's Modulus Versus Angle of Test Specimen for "Thornel" 25/ERL 2256 Plate P25-8. See Figure 95 for Explanation of Symbols.

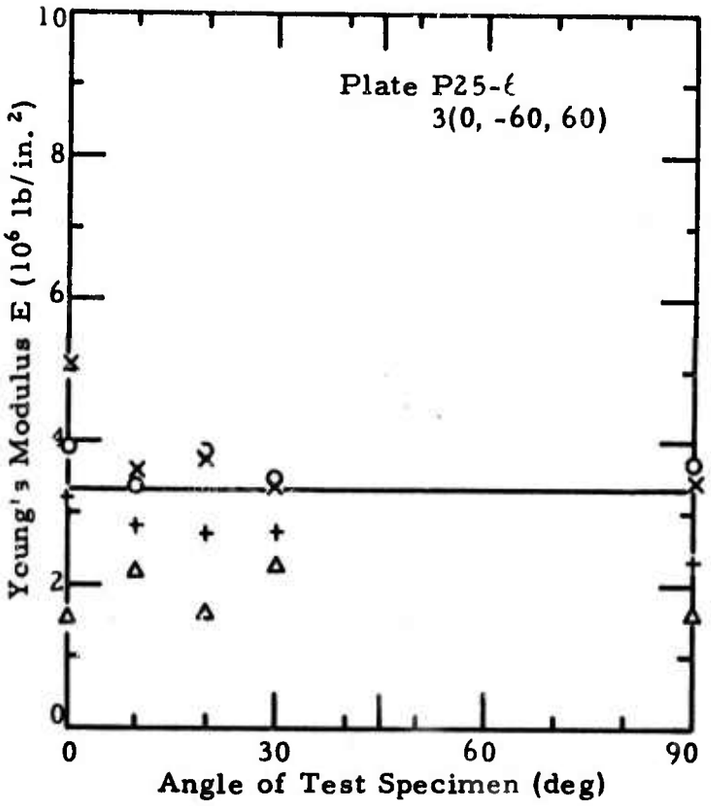

N-10707

Figure 102. Young's Modulus Versus Angle of Test Specimen for "Thornel" 25/ERL 2256 Plate P25-6. See Figure 95 for Explanation of Symbols.

The sonic longitudinal value of the membrane Young's modulus agreed closely with the sonic in-plane flexural value on all plates except P25-6 and 8. The tensile blanks from these plates were both curved along and twisted about the bar axis (the warping was due to the unbalanced lay-up pattern). With very few exceptions, the static tensile values either agreed with the sonic values or varied from them by less than 10 percent. Since the number of measurements is larger than the number of elastic constants determined from the measurements, the good agreement of the calculated curve of $E'(\theta)$ with the experimental results at all angles indicates that the test methods for the membrane modulus are satisfactory. The agreement also indicates that off-axis elastic properties of graphite-fiber composites can be accurately computed when the principal elastic constants are reliably known.

The sonic and static values of the bending modulus are in good agreement in view of the variation in the harmonic series of the flexural vibrations discussed previously. The modulus deduced from higher harmonics such as the fifth harmonic, appears to be accurate to within approximately 10 percent; by changing the sample dimensions, it may be

possible to use a lower harmonic number and still deduce a reliable bending modulus. As the number of plies decreases, a difference between the membrane and bending moduli increases, a trend clearly illustrated by the data of Figures 97, 98, and 100. (An analytical investigation of this point is discussed in Section VIIIB.) Consequently, in laminates with a small number of plies, it is important to measure the bending modulus as well as the membrane modulus. The sonic test has the potential of being a quick and inexpensive way of obtaining both types of moduli.

The correct dependence of modulus on test specimen orientation was confirmed on the "Thornel" 25 composites; therefore, "Thornel" 40 composites were tested only at 0° and 90°, to provide the principal Young's moduli and Poisson's ratios, and at 45°, to provide the in-plane shear modulus. The results reported here for the "Thornel" 40 composites are based, at each angle, on sonic and static tests of two or more tensile bars from each plate and, in some cases, on tests of bars from different plates with the same lay-up pattern. The greater scatter in the data compared with that for the single specimen "Thornel" 25 data gives some indication of the variability among specimens from the same plate and among specimens from different plates. The sets of best values of the membrane moduli are given in Table XL for the "Thornel" 40 composite plates. The values of Young's modulus from static tensile, sonic longitudinal, and sonic in-plane flexural tests are shown in Figures 103 through 107 for plates numbered P40-1, 9, 14, 5, 6, 10, 12, and 16. As with the "Thornel" 25 composite data, the static and sonic values are in good agreement.

TABLE XL

AVERAGE VALUES OF MEMBRANE ELASTIC MODULI AND COMPLIANCE CONSTANTS FOR "THORNEL" 40/ERL 2256 PLATES

Plate Number	Plies & Lay-Up	E_1 (10^6 lb/in.^{2})	E_2 (10^6 lb/in.^{2})	G (10^6 lb/in.^{2})	$\nu_{12} = -s_{12}/s_{11}$	$\nu_{21} = -s_{12}/s_{22}$
P40-1,9	9(0), 7(0)	24.6	0.95	0.74	0.29	0.011
P40-14	6(±10, ±45, ±10)	14.2	2.0	2.7	0.82	0.12
P40-12*	4(90, 0, 0, 90)	11.8	12.0	0.62	0.024	0.024
P40-16	4(90, ±10, 90)	9.4	11.0	0.84	0.042	0.050
P40-5, 6	4(10, -10, -10, 10)	21.6	1.05	1.5	0.97	0.047

Plate Number	s_{11}	s_{22}	s_{66}	s_{12}
	(10^{-6} lb/in.^{2})			
P40-1, 9	0.0406	1.05	1.35	-0.0118
P40-14	0.0704	0.50	0.370	-0.0577
P40-12*	0.0847	0.0833	1.61	-0.00203
P40-16	0.106	0.0909	1.19	-0.00447
P40-5, 6	0.0463	0.952	0.667	-0.0449

There is a large uncertainty in the last significant figure.

*Plate P40-10 was tested at 0° in lieu of testing P40-12 at 45°.

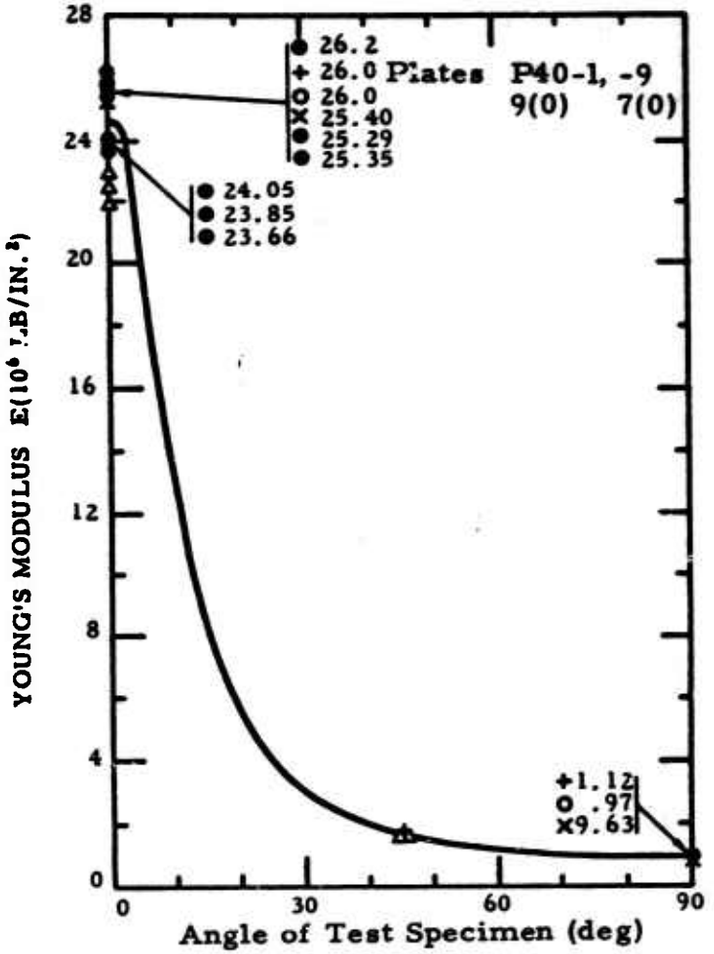

Figure 103. Young's Modulus Versus Angle of Test Specimen for "Thornel" 40/ERL 2256 Plates P40-1 and 9. See Figure 95 for Explanation of Symbols.

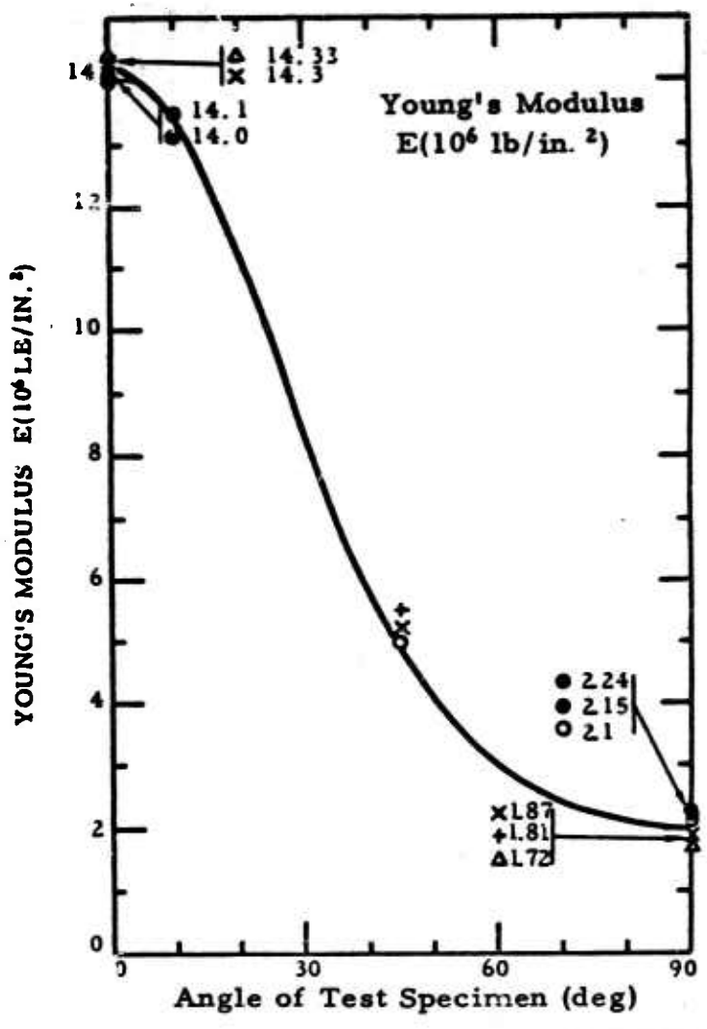

Figure 104. Young's Modulus Versus Angle of Test Specimen for "Thornel" 40/ERL 2256 Plate P40-14. See Figure 95 for Explanation of Symbols.

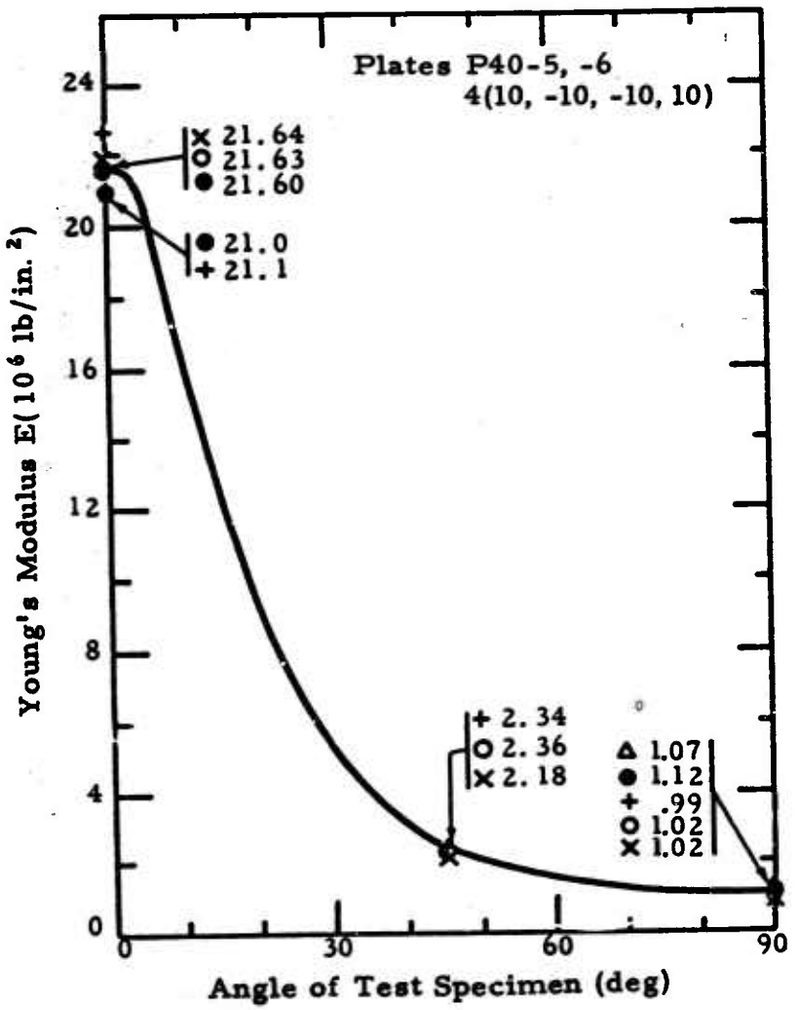

N-17240

Figure 105. Young's Modulus Versus Angle of Test Specimen for "Thornel" 40/ERL 2256 Plates P40-5 and 6. See Figure 95 for Explanation of Symbols.

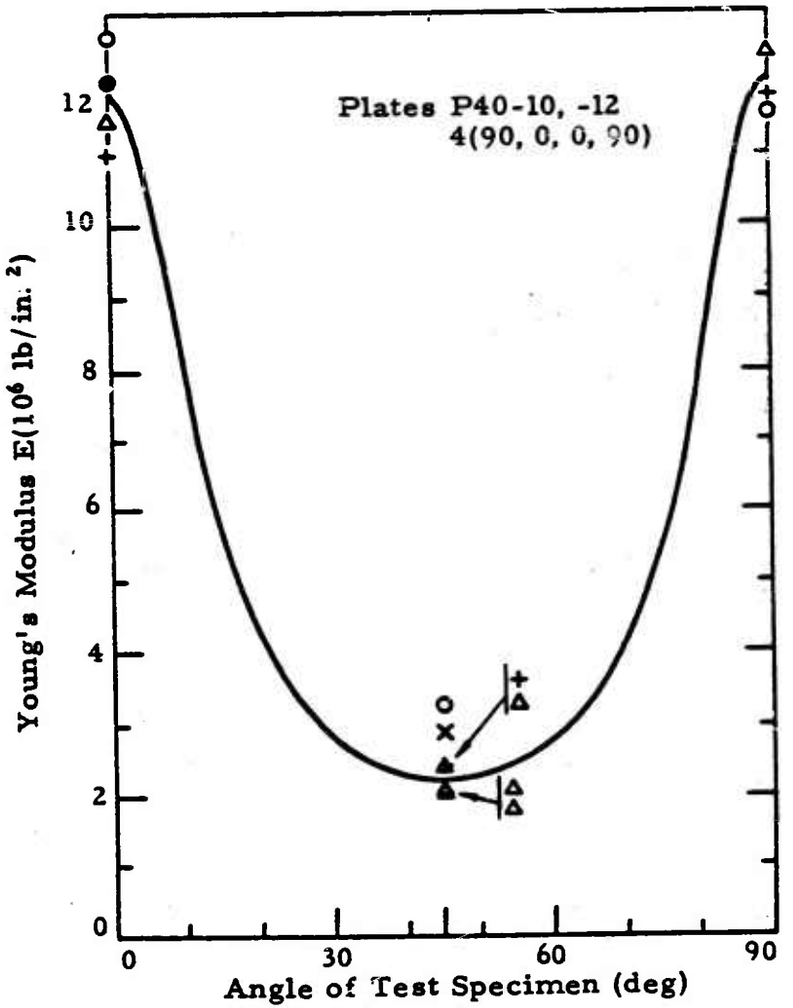

N-17228

Figure 106. Young's Modulus Versus Angle of Test Specimen for "Thornel" 40/ERL 2256 Plates P40-10 and 12. See Figure 95 for Explanation of Symbols.

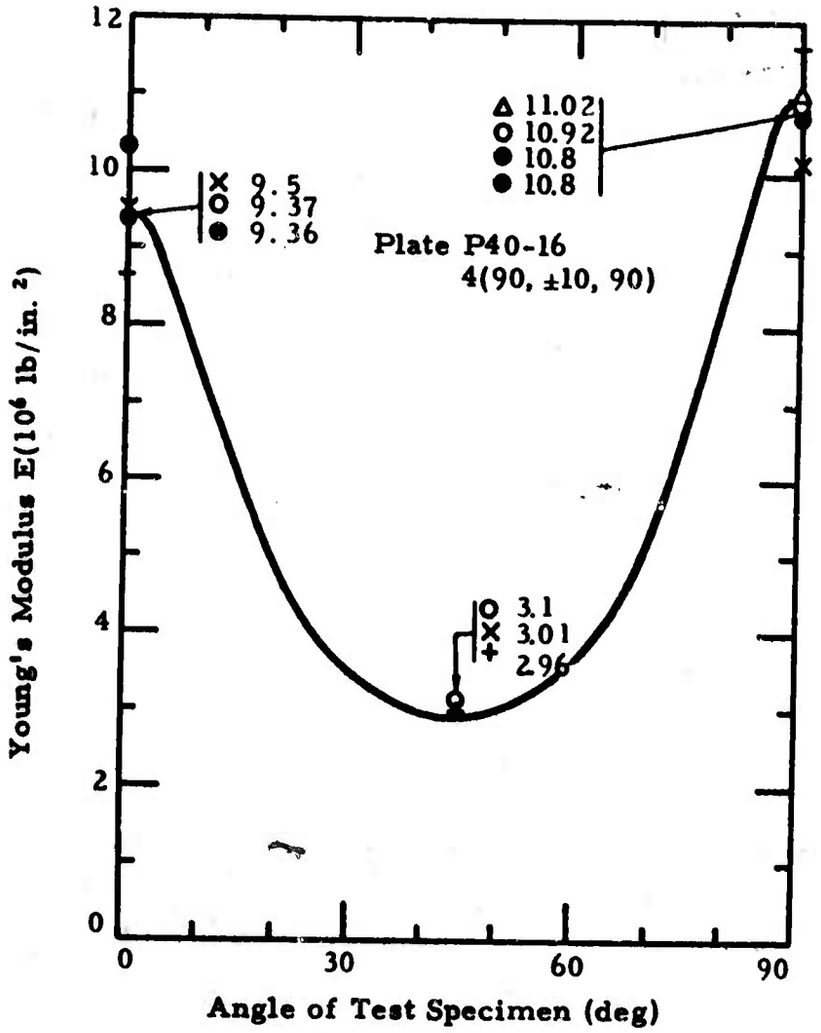

N-17238

Figure 107. Young's Modulus Versus Angle of Test Specimen for "Thornel" 40/ERL 2256 Plate P40-16. See Figure 95 for Explanation of Symbols.

Values of Young's moduli and Poisson's ratios in bending, obtained from static bend tests, are given in Table XLI. The unidirectional plates (P25-4 and P40-1) are homogeneous. As expected, the values of the membrane and bending Young's moduli are in agreement; in most other cases, the membrane and bending moduli are very different. The Poisson's ratios in bending are discussed in Section VI B 3.

For many of the lay-up patterns considered here, the complete membrane and bending elastic properties have been calculated, based on fiber and matrix constituent properties and various micromechanics models. Summaries of these calculations and comparisons with the present measured data are given in Sections VIII A and B.

TABLE XLI

BENDING MODULUS FOR "THORNEL" 25
AND 40/ERL 2256 PLATES

Plate No.	Plies & Lay-Up	$E_1(B)$	$E_2(B)$	$\nu_{12}(B)$	$\nu_{21}(B)$
		10^6 lb/in.^{2}			
P25-4	9(0)	11.1	1.00	0.30	0.021
P25-1	9(0, 90)	6.45	3.65		
P25-9	6(0, 90	5.01*	6.29*	0.06*	0.05*
P25-2	5(0, 90)	8.76	2.89	0.11	0.04
P25-3	4(0, 90, 90, 0)	---	2.20		
P25-10	3(0, 90, 0)	10.41	1.64		
P25-7	2(0, 90)	3.02 *	---*		
P40-1	9(0)	24.8	1.03	0.29	
P40-14	6($\pm$10, $\pm$45, $\pm$10)	17.3	1.20	0.8	0.07
P40-6	4(10, -10, -10, 10)	19.0	1.25	0.76	0.019
P40-12	4(90, 0, 0, 90)	4.17	17.3	0.01	0.062
P40-16	4(90, $\pm$10, 90)	3.12	16.7	0.03	0.098
P40-10	4(45, -45, -45, 45)	2.06*	---*		

* Values at 0° and 90° should be equal by symmetry.

Results from Compression Tests. Values of the zero-stress-level Young's modulus, obtained from static compression tests, are given in Table XLII. These data are based on strains measured with a compressometer. Comparison of the values in Table XLII with those in Figures 96, 97, and 99 shows approximately 15 percent deviation between the compression values and the average tensile and sonic values. However, there is no indication that the initial modulus values in tension and compression are different.

2. Normalized Membrane Young's Moduli

In this section, the measured Young's modulus values are normalized to a standard fiber volume fraction and fiber modulus, and these normalized values for the various cross-plied plates are compared. An elementary discussion, based on the rule of mixtures, described the extent to which the theoretical composite properties have been attained.

TABLE XLII

MEMBRANE YOUNG'S MODULUS FROM COMPRESSION TESTS FOR "THORNEL" 25/ERL 2256 PLATES

Plate Number	Plies & Lay-Up	Specimen Orientation Degrees	Young's Modulus 10^6 lb/in.^{2}
P25-4	9(0)	0	10.4
		45	1.31
		90	1.03
P25-1	9(0, 90)	0	5.84
		10	4.38
		20	2.35
		45	1.26
		90	4.04
P25-3	4(0, 90, 90, 0)	0	5.29

A dimensionless modulus normalization factor N_E is defined for each plate by:

$$N_E = v_{fs} E_{fs} / v_f E_f \qquad \text{(VIB-19)}$$

in which v_f and E_f are the actual fiber volume fraction and fiber modulus for each plate and v_{fs} and E_{fs} specify corresponding quantities for a standard plate. We have chosen:

$$v_{fs} = 0.50 \text{ and } E_{fs} = 25 \times 10^6 \text{ lb/in.}^2 \qquad \text{(VIB-20)}$$

for the "Thornel" 25 series plates and:

$$v_{fs} = 0.65 \text{ and } E_{fs} = 40 \times 10^6 \text{ lb/in.}^2 \qquad \text{(VIB-21)}$$

for the "Thornel" 40 series plates.

The principal plate extensional moduli E_1 and E_2 have been averaged to eliminate the effects on the moduli due to the number of plies in each plate. Table XLIII gives the modulus normalization factor N_E, the average modulus $(E_1 + E_2)/2$, and the normalized average $N_E(E_1 + E_2)/2$.

TABLE XLIII

MODULUS NORMALIZATION FACTOR, AVERAGE EXTENSIONAL YOUNG'S MODULUS, AND NORMALIZED AVERAGE EXTENSIONAL YOUNG'S MODULUS FOR "THORNEL" FIBER/ERL 2256 PLATES

Plate Number	Plies & Lay-Up	Modulus Normalization Factor N_E	$(E_1 + E_2)/2$ 10^6lb/in.^{2}	$N_E(E_1 + E_2)/2$ 10^6lb/in.^{2}
P25-4	9(0)	1.00	6.06	6.06
P25-5	2(0)	1.43	---	---
P25-1	9(0, 90)	1.14	4.97	5.66
P25-14	9(0, 90)	1.06	5.79	6.13
P25-9	6(0, 90)	1.00	5.84	5.84
P25-2	5(0, 90)	1.16	4.79	5.56
P25-3	4(0, 90, 90, 0)	0.98	5.68	5.57
P25-10	3(0, 90)	1.05	5.85	6.14
P25-7	2(0, 90)	1.19	4.8	5.7
Average for plates P25-1, 14, 9, 2, 3, 10, 7			5.39	5.80
P25-8	4(0, -45, 90, 45)	1.02	---	---
P25-6	3(0, -60, 60)	1.05	---	---
P40-1	9(0)	.97	12.77	12.39
P40-14	6(±10, ±45, ±10)	1.15	8.14	9.36
P40-5	4(10, -10, -10, 10)	.95	11.32	10.75
P40-12	4(90, 0, 0, 90)	1.02	11.90	12.13
P40-16	4(90, ±10, 90)	1.13	10.22	11.54
Average for plates P40-14, 5, 12, 16			10.40	10.95

For the unidirectional plate with standard properties, the rule of mixture gives, for $E_m = 0.6 \times 10^6$ lb/in.^{2},

$$E_{1\,\text{unid.}} = v_{fs}E_{fs} + (1 - v_{fs})E_m \qquad \text{(VIB-22)}$$

$$= 12.8 \times 10^6 \text{lb/in.}^2 \qquad \text{(VIB-23)}$$

for the "Thornel" 25 series and

$$E_{1\,\text{unid.}} = 26.2 \times 10^6 \text{lb/in.}^2 \qquad \text{(VIB-24)}$$

for the "Thornel" 40 series. For plate P25-4, the measured value of $N_E E$ is 11.4×10^6 lb/in.^{2}; this value is 89 percent of the predicted rule-of-mixtures value. For plate P40-1, the measured value of $N_E E_1$ is 23.9×10^6 lb/in.^{2} or 91 percent of the theoretical modulus.

For the standard cross-plied (0°, 90°) plates, the rule-of-mixtures values for the average modulus are:

$$(E_1 + E_2)/2 = (E_{1\,\text{unid.}} + E_{2\text{unid.}})/2 \qquad \text{(VIB-25)}$$

$$= 6.9 \times 10^6 \text{ lb/in.}^2 \qquad \text{(VIB-26)}$$

for the "Thornel" 25 composites and

$$(E_1 + E_2)/2 = 13.6 \times 10^6 \text{ lb/in.}^2 \qquad \text{(VIB-27)}$$

for the "Thornel" 40 composites. These estimates are based on a value of $E_{2\text{unid.}}$ of 1.0×10^6 lb/in.^{2}. For the seven "Thornel" 25 cross-plied plates, the average of the measured values of $N_E(E_1 + E_2)/2$ is 5.80×10^6 lb/in.^{2}, a value which is 84 percent of the predicted 6.9×10^6 lb/in.^{2}. For the one "Thornel" 40 cross-plied plate, the measured value of $N_E(E_1 + E_2)/2$ is 12.13×10^6 lb/in.^{2} or 89 percent of the predicted value.

The reasons for the lower measured values can only be suggested. The twist of the fibers within a yarn strand and misalignment of yarn strands within a plate both contribute to fiber misalignment, a condition that reduces the modulus. Imperfect fiber-matrix adhesion would lower the modulus as well as the strength. For the cross-plied plates, the waviness in the plies discussed in Section V E 4, causes fiber misalignment; in addition, vertical cracks in the transverse layers may reduce the effective value of $E_{2\text{unid.}}$ in these plies. These two factors could account for the slightly greater loss in fiber efficiency for the cross-plied plates than that for the unidirectional plates.

3. Poisson's Ratios and Shear Modulus-Membrane and Bending

The procedures used to analyze the tensile bar data to obtain the principal membrane Poisson's ratio and in-plane shear modulus are discussed in the introduction to this section, and the average experimental values of ν_{12} and G are given in Tables XXXIX and XL for the various "Thornel" 25 and 40 composite plates. Equations VIB 5 through 11 give the variation of Poisson's ratio and the shear modulus versus the angle θ of the test specimen or, equivalently, the variation in $\nu_{12}'(\theta)$ and $G'(\theta)$ as the coordinate system is rotated through an angle θ in the plane of the plate.

Figures 108 through 119 show the experimental values of Poisson's ratio for plates numbered P25-4, 1, 2, 3, 10, 8, and 6 and P40-1, 9, 14, 5, 6, 10, 12, and 16; the solid curves give the calculated values of Poisson's ratio $\nu_{12}'(\theta)$ based on the data of Tables XXXIX and XL.

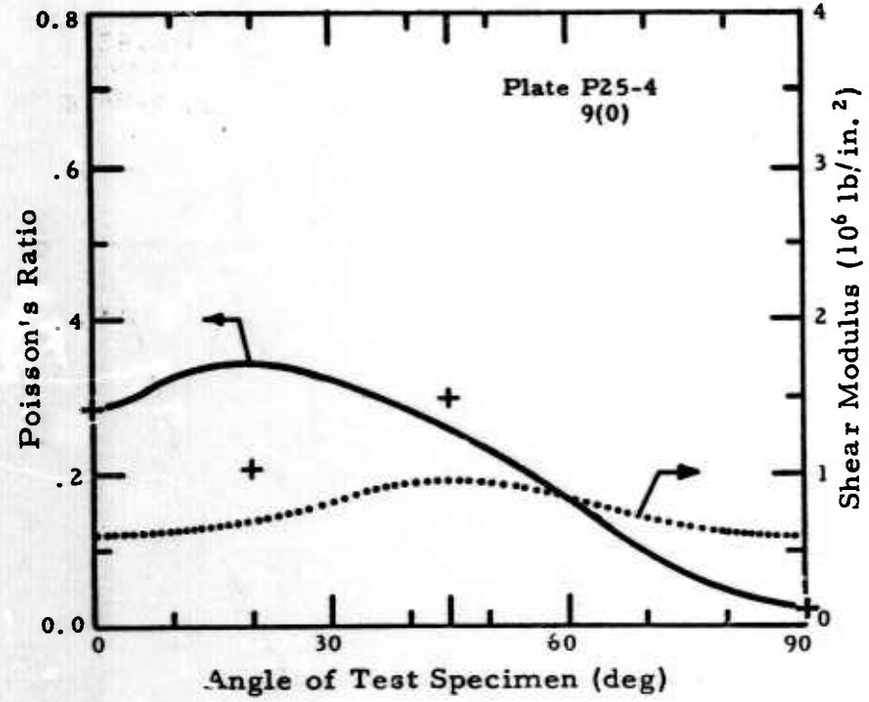

N-10708

Figure 108. Poisson's Ratio and Shear Modulus Versus Angle of Test Specimen for "Thornel" 25/ERL 2256 Plate P25-4. See Figure 95 for Explanation of Symbols.

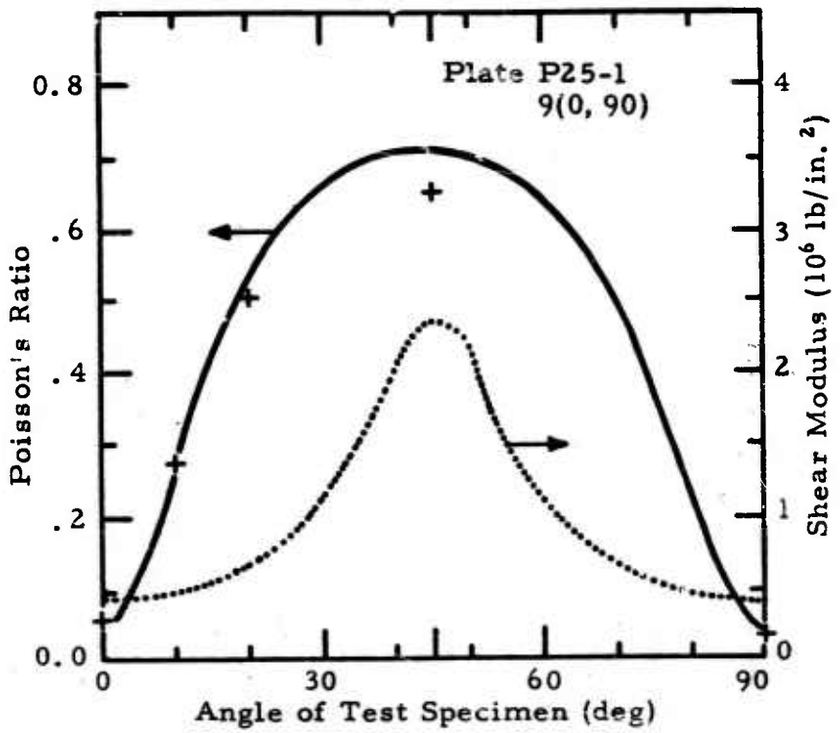

N-10706

Figure 109. Poisson's Ratio and Shear Modulus Versus Angle of Test Specimen for "Thornel" 25/ERL 2256 Plate P25-1. See Figure 95 for Explanation of Symbols.

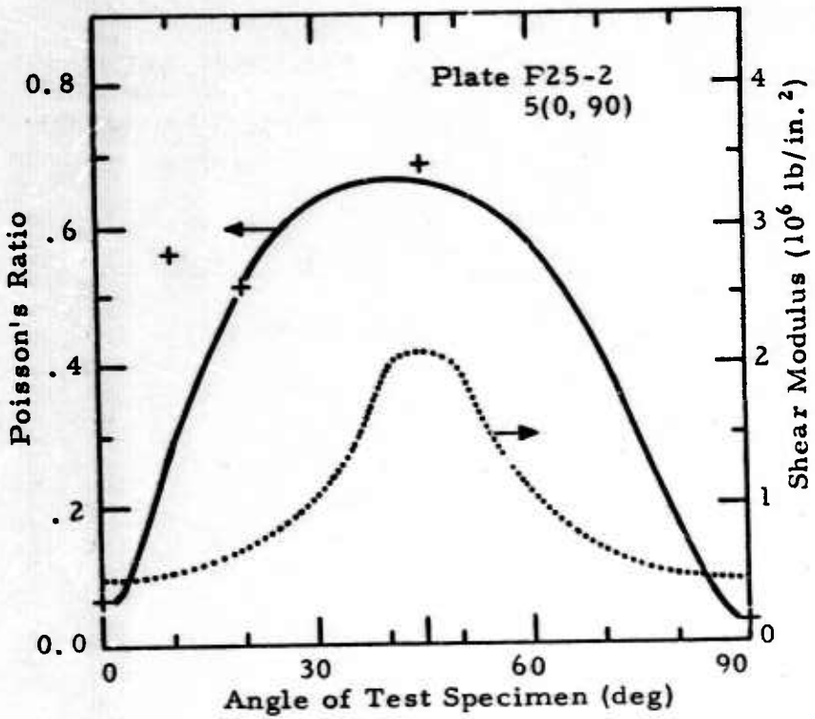

N-10705

Figure 110. Poisson's Ratio and Shear Modulus Versus Angle of Test Specimen for "Thornel" 25/ERL 2256 Plate P25-2. See Figure 95 for Explanation of Symbols.

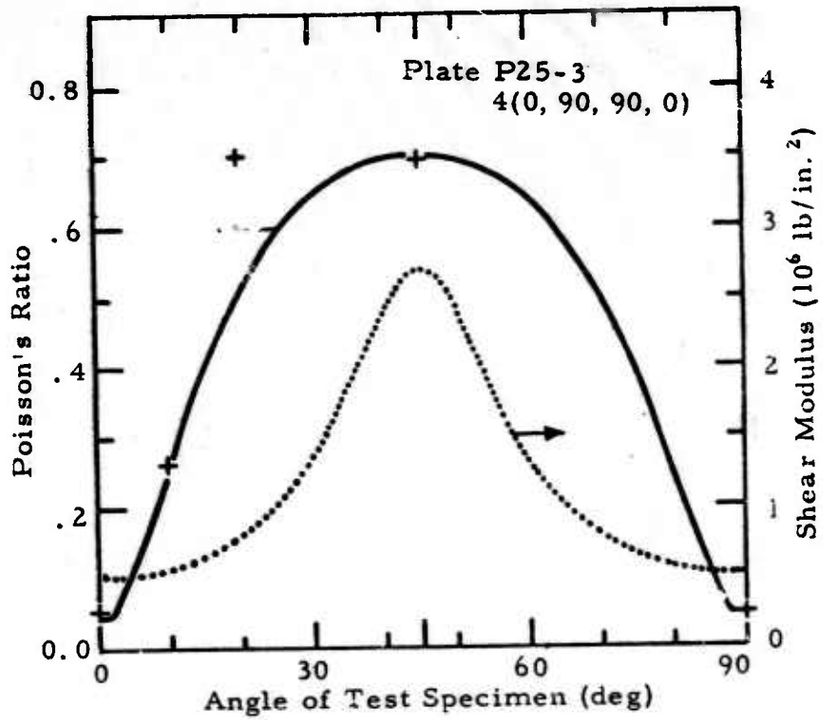

N-10709

Figure 111. Poisson's Ratio and Shear Modulus Versus Angle of Test Specimen for "Thornel" 25/ERL 2256 Plate P25-3. See Figure 95 for Explanation of Symbols.

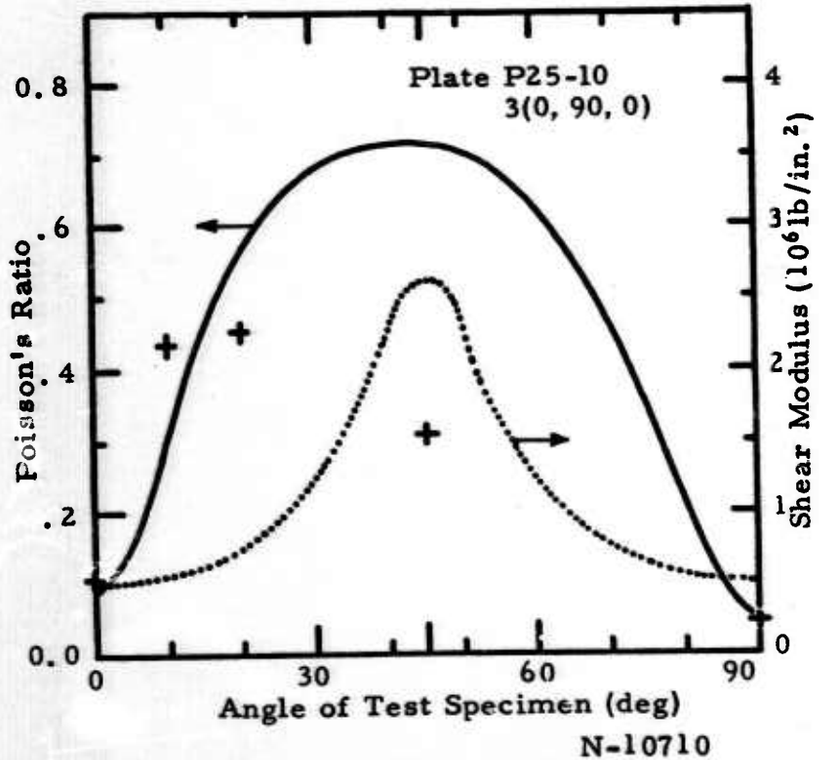

Figure 112. Poisson's Ratio and Shear Modulus Versus Angle of Test Specimen for "Thornel" 25/ERL 2256 Plate P25-10. See Figure 95 for Explanation of Symbols.

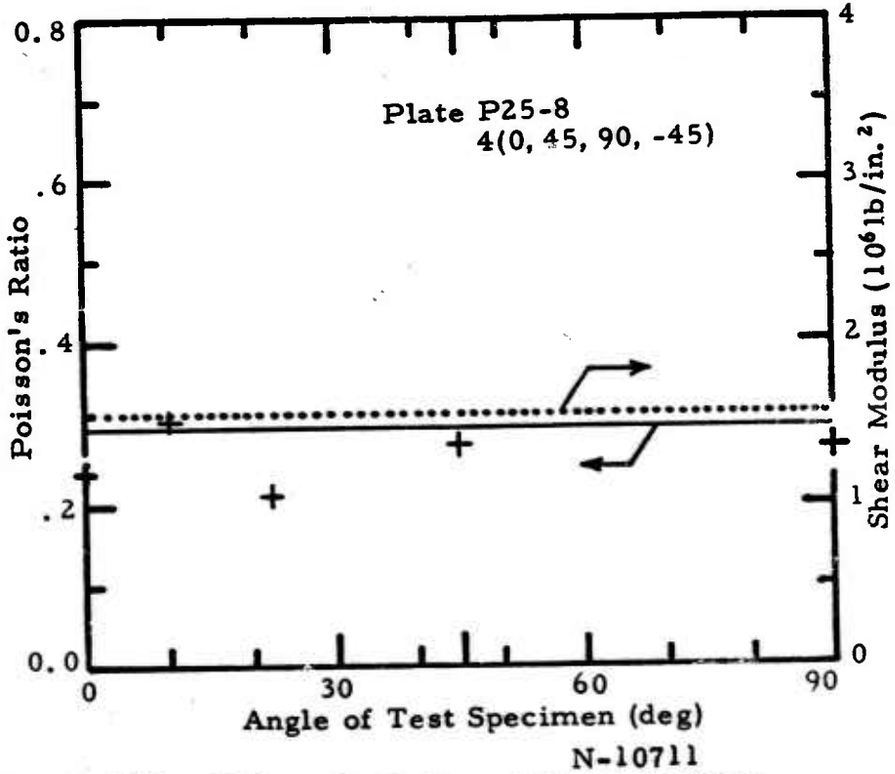

Figure 113. Poisson's Ratio and Shear Modulus Versus Angle of Test Specimen for "Thornel" 25/ERL 2256 Plate P25-8. See Figure 95 for Explanation of Symbols.

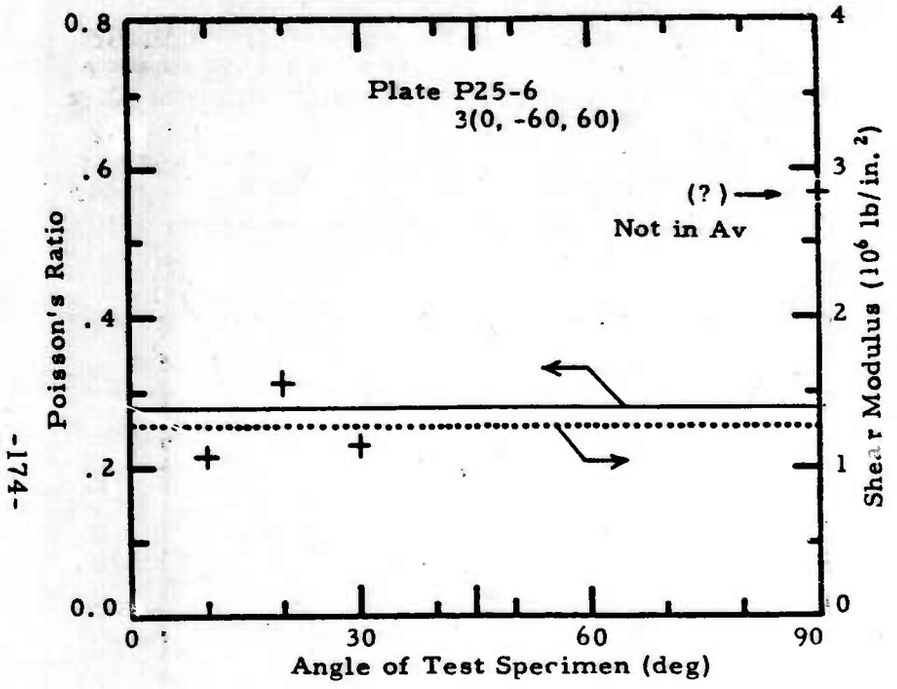

N-10648

Figure 114. Poisson's Ratio and Shear Modulus Versus Angle of Test Specimen for "Thornel" 25/ERL 2256 Plate P25-6. See Figure 95 for Explanation of Symbols.

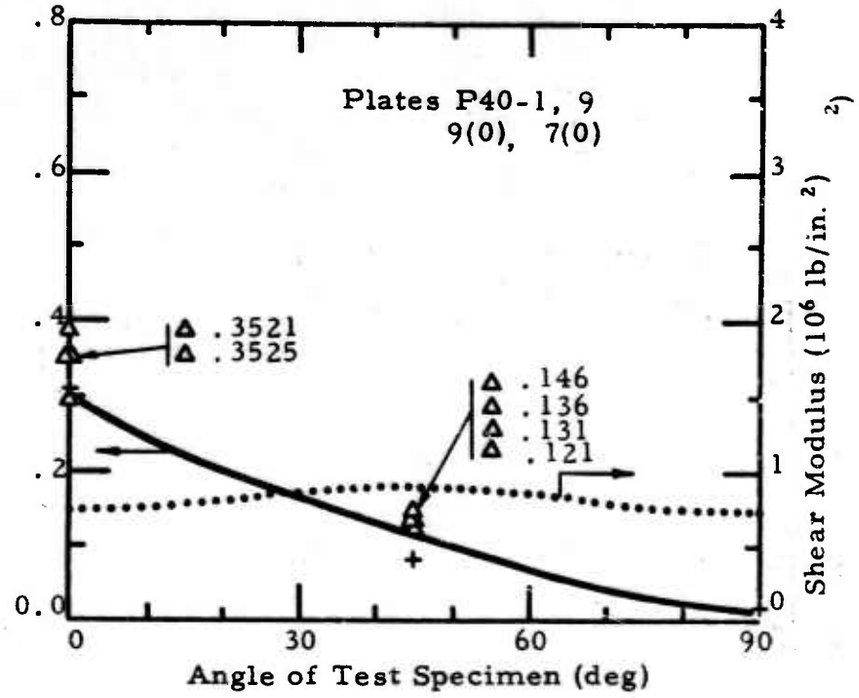

N-17235

Figure 115. Poisson's Ratio and Shear Modulus Versus Angle of Test Specimen for "Thornel" 40/ERL 2256 Plates P40-1, 9. See Figure 95 for Explanation of Symbols.

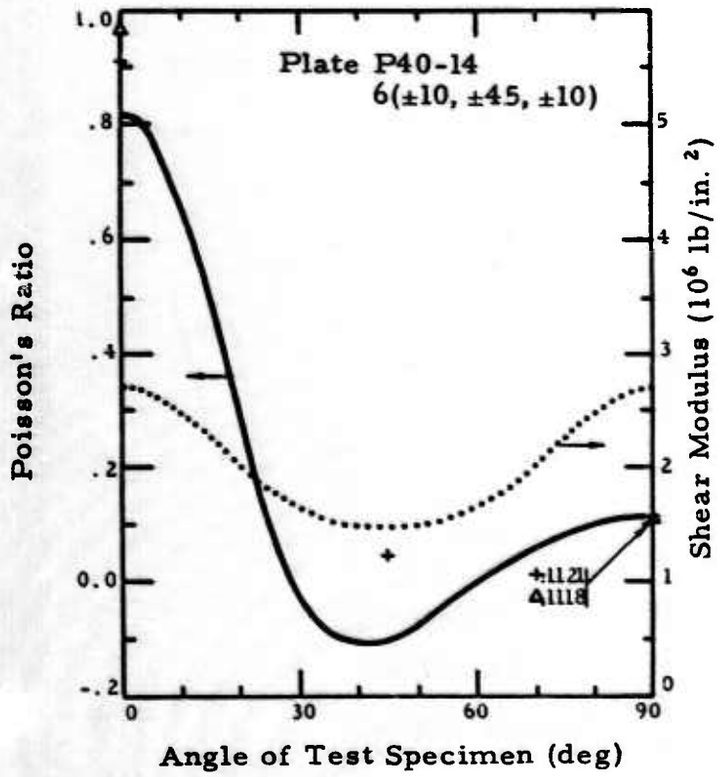

N-17234

Figure 116. Poisson's Ratio and Shear Modulus Versus Angle of Test Specimen for "Thornel" 40/ERL 2256 Plate P40-14. See Figure 95 for Explanation of Symbols.

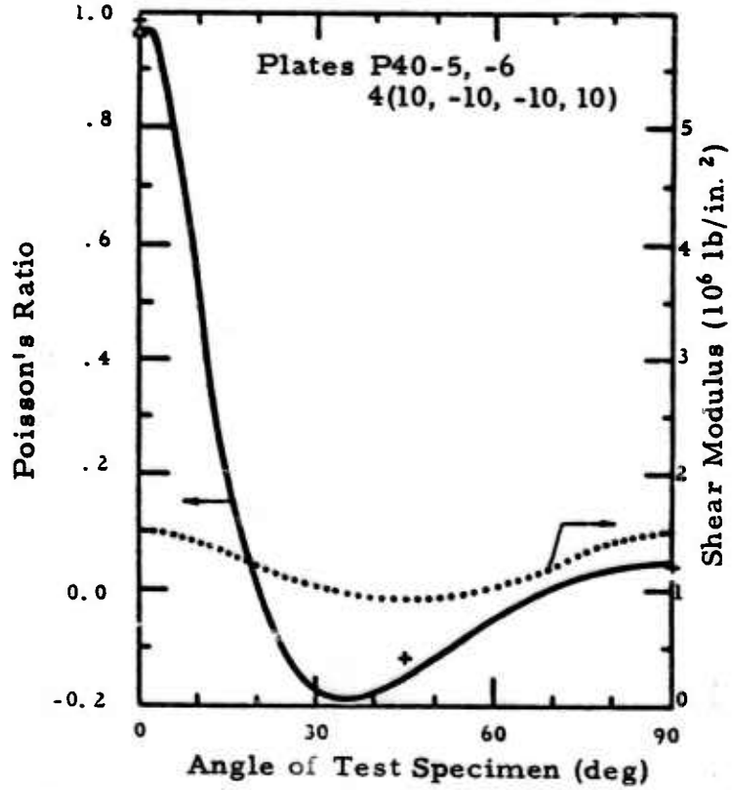

N-17236

Figure 117. Poisson's Ratio and Shear Modulus Versus Angle of Test Specimen for "Thornel" 40/ERL 2256 Plates P40-5,6. See Figure 95 for Explanation of Symbols.

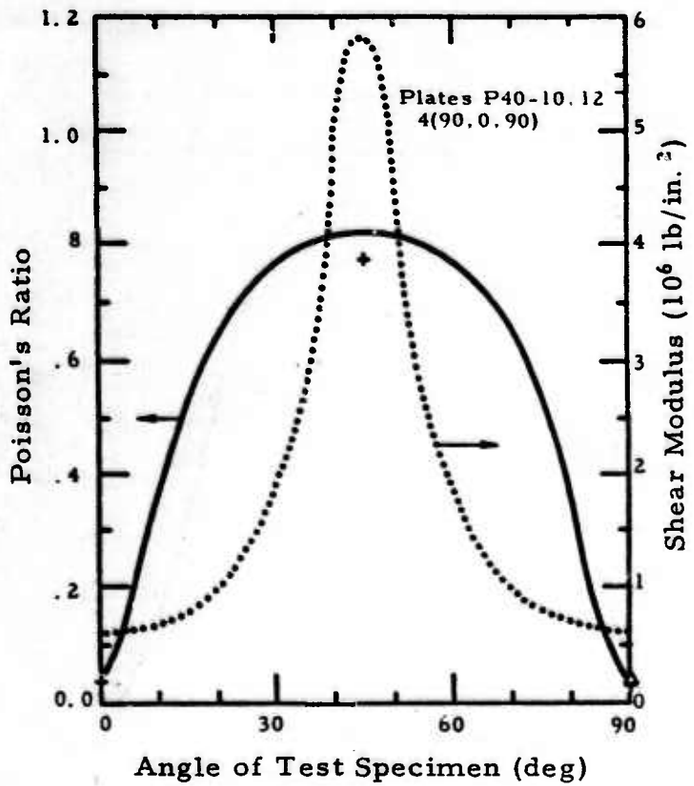

N-17237

Figure 118. Poisson's Ratio and Shear Modulus Versus Angle of Test Specimens for "Thornel" 40/ERL 2256 Plates P40-10, 12. See Figure 95 for Explanation of Symbols.

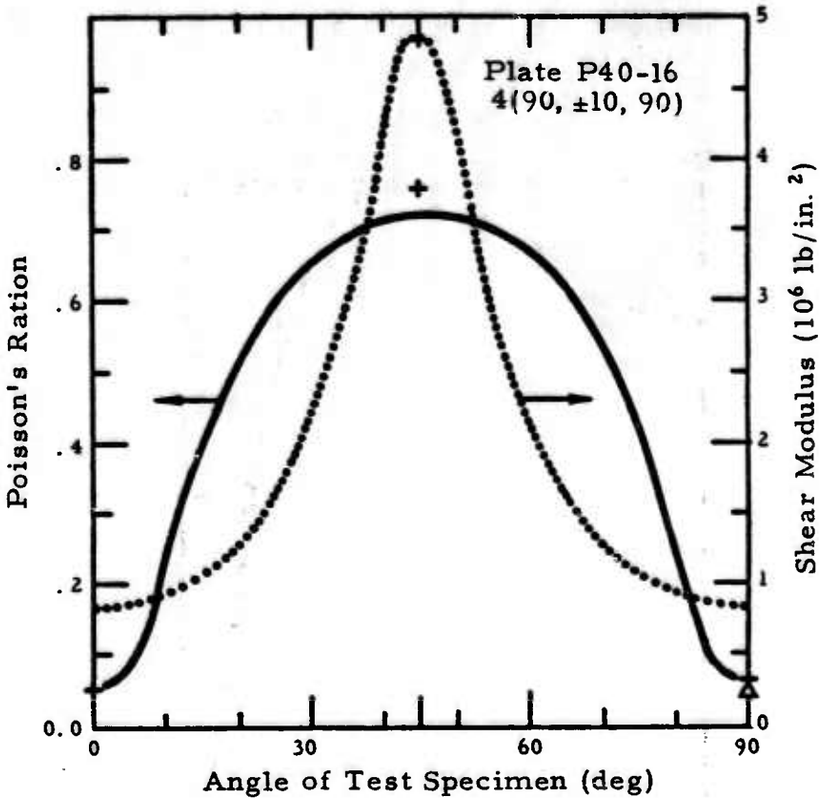

N-17229

Figure 119. Poisson's Ratio and Shear Modulus Versus Angle of Test Specimen for "Thornel" 40/ERL 2256 Plate P40-16. See Figure 95 for Explanation of Symbols.

Usually, the experimental and calculated values are in reasonable agreement, but occasionally an experimental point will deviate by a factor of 2. The value of $\theta = 45°$ for a (0°,90°) plate is of interest, since this value would also be obtained at $\theta = 0°$ for a (±45°) plate. The low Poisson's ratio at $\theta = 0°$ and the high value at $\theta = 45°$ suggest that difficulties in bonding metal attachments for these orientations may be present. The maximum at approximately 17° in the Poisson's ratio curve for the unidirectional "Thornel" 25 composite (Figure 108) does not occur in the curve for the more strongly anisotropic unidirectional "Thornel" 40 composite (Figure 115). For the 4(10°, -10°, -10°, 10°) and 6(±10°, ±45°, ±10°) lay-ups of the "Thornel"40 composites (Figures 116 and 117), the predicted Poisson's ratios are negative at test angles near 45°; the measured value at 45° was negative for the 4(10°, -10°, -10°, 10°) plate but was slightly positive for the 6(±10°, ±45°, ±10°) plate.

The values of Poisson's ratios measured in the bend test are given in Table XLI. By definition, the Poisson's ratio in bending is the negative of the ratio of the transverse curvature to the longitudinal curvature (the curvatures are normally of opposite sign). Under the condition that plane sections remain plane for a constant bending moment, the Poisson's ratio in bending is given by

$$\nu_{ij}(B) = \frac{-(\varepsilon_t - \varepsilon_c) \text{ in trans. dir. } j,}{(\varepsilon_t - \varepsilon_c) \text{ in long. dir. } i} \qquad \text{(VIB-28)}$$

where ε_t and ε_c are the strains on the tensile and compressive stress sides of the bar, respectively (contractive strains are negative numbers). Usually, the bar was turned over and remeasured in which case the Young's modulus values always agreed to within 10 percent. In some cases, the Poisson's ratio values deviated by more than 10 percent, indicative of nonhomogeneity in the specimen. The data in Table XLI are only representative values; more specimens would have to be tested to obtain reliable averages.

In some cases, the Poisson's ratios under membrane and bending loads are predicted to be different, and the experimental results confirm this difference. A more detailed comparison of the membrane and bending values is given in Section VIIIB.

The dotted curves in Figures 108 through 119 give the calculated values of the in-plane shear modulus $G'(\theta)$ based on the data of Tables XXXIX and XL. For the (0, 90) degree plates, the shear modulus at $\theta = 45°$ is approximately 5 times larger than the value at $\theta = 0°$ or 90°, but the 45° orientation has the lowest Young's modulus. For the "Thornel" 40 composites, the shear modulus curve at 45° test angle has a maximum for the unidirectional composite (Figure 115) and a minimum for the 4(10°, -10°, -10°, 10°) lay-up (Figure 117); therefore, there is a (±α) lay-up for $0° < \alpha < 10°$ for which the shear modulus is essentially constant for all test angles θ.

C. Composite Stress-Strain Curves
(O. L. Blakslee, Union Carbide Corporation)

The tensile stress-strain curves for both longitudinal and transverse strain are given in Figures 120 through 131 for plates numbered P25-4, 1, 2, 3, 10, 8, and 6 and P40-1, 9, 14, 5, 6, 10, 12, and 16. The tangent modulus for the longitudinal strain curve was either constant or increased slightly to a load of approximately 90 percent of ultimate for unidirectional and cross-plied composites tested in the direction of the fibers. Often in these and other cases, the curve "hooked-over" from 90 percent of ultimate to failure (see, for example, the 0° test angle curve in Figure 129). The tangent modulus usually decreased slightly for unidirectional composites tested off-axis; but no evidence of resin crazing or permanent damage was present if the "hook-over" did not occur. The stress-strain curves were significantly nonlinear for multidirectional composites with many or all of the fibers at a large angle to the test direction. If the tangent modulus became small, the fracture strain tended to vary widely from a few tenths to several percent. The transverse strain curves were complicated in shape, but the pattern was usually similar from plate to plate. One exception was the transverse strain measured at 45° for the "Thornel" 40-4(10°, -10°, -10°, 10°) plate (Figure 129); this curve is almost linear and has a positive slope, yielding the negative Poisson's ratio reported earlier. The ERL 2256/MPDA resin system has a relatively large fracture elongation; and, correspondingly, the composite tensile specimens showed little resin crazing.

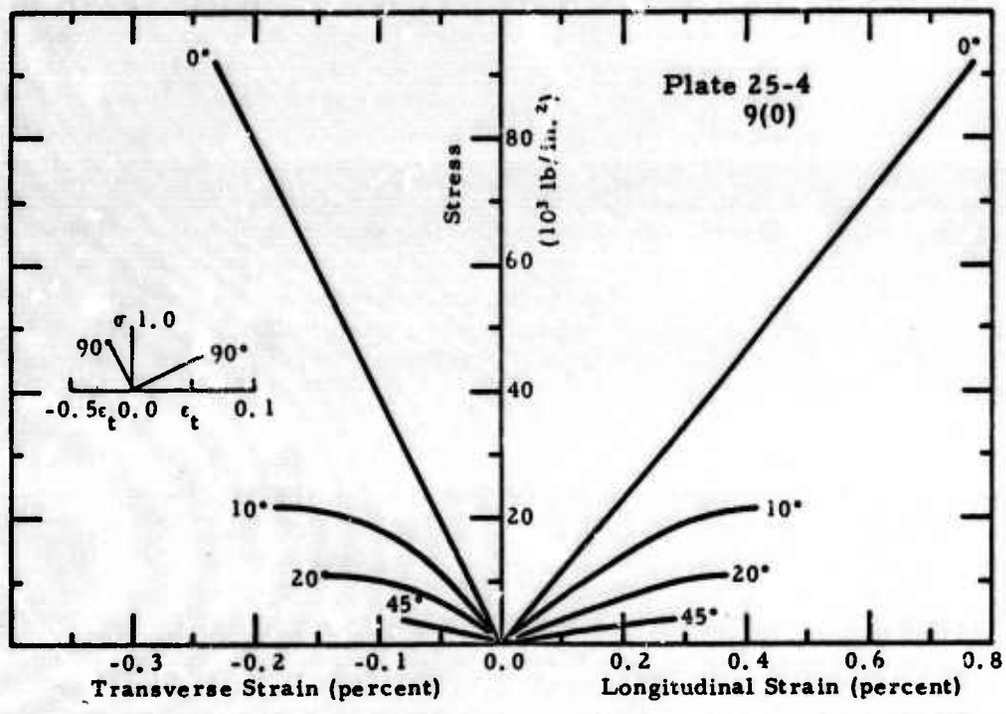

N-10703

Figure 120. Tensile Stress-Strain Curves for "Thornel" 25/ERL 2256 Plate P25-4. Angles Give Test Specimen Orientation.

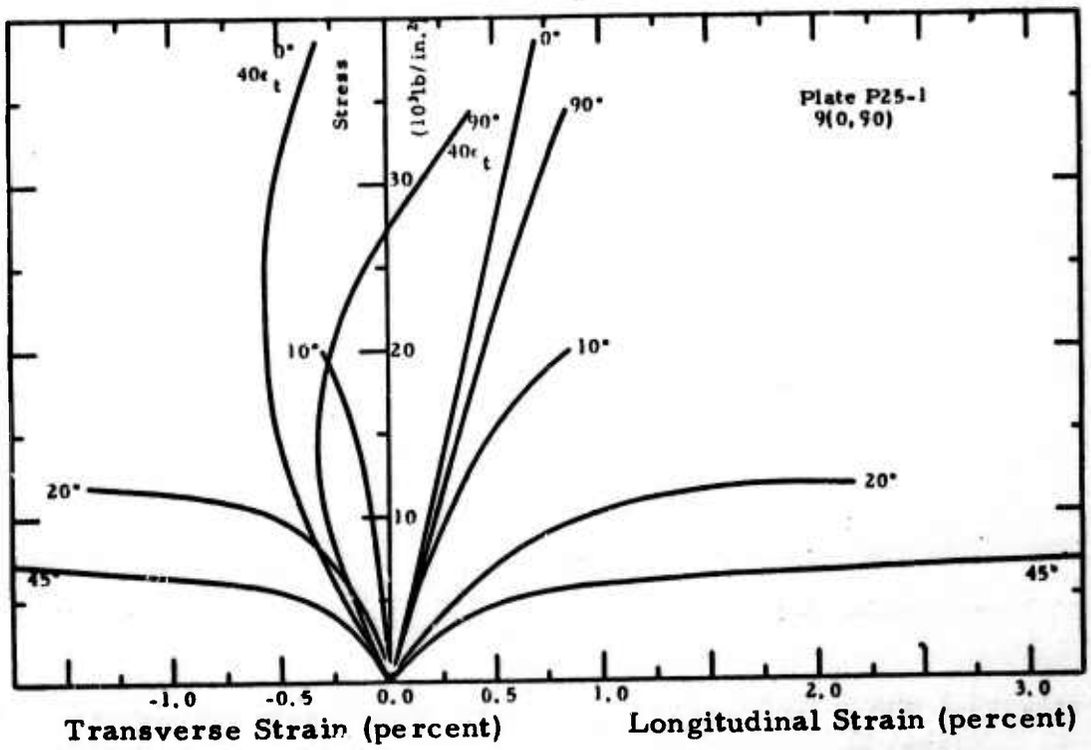

N-10703

Figure 121. Tensile Stress-Strain Curves for "Thornel" 25/ERL 2256 Plate P25-1. Angles Give Test Specimen Orientation.

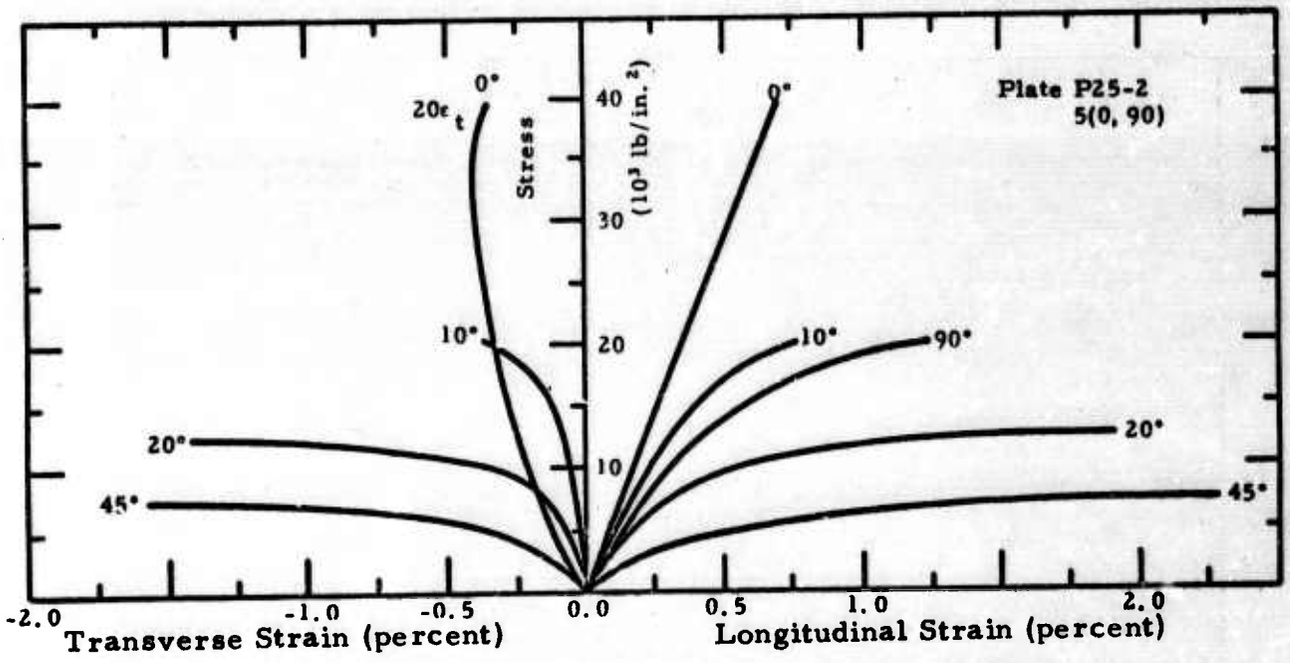

N-10699

Figure 122. Tensile Stress-Strain Curves for "Thornel" 25/ERL 2256 Plate P25-2. Angles Give Test Specimen Orientation.

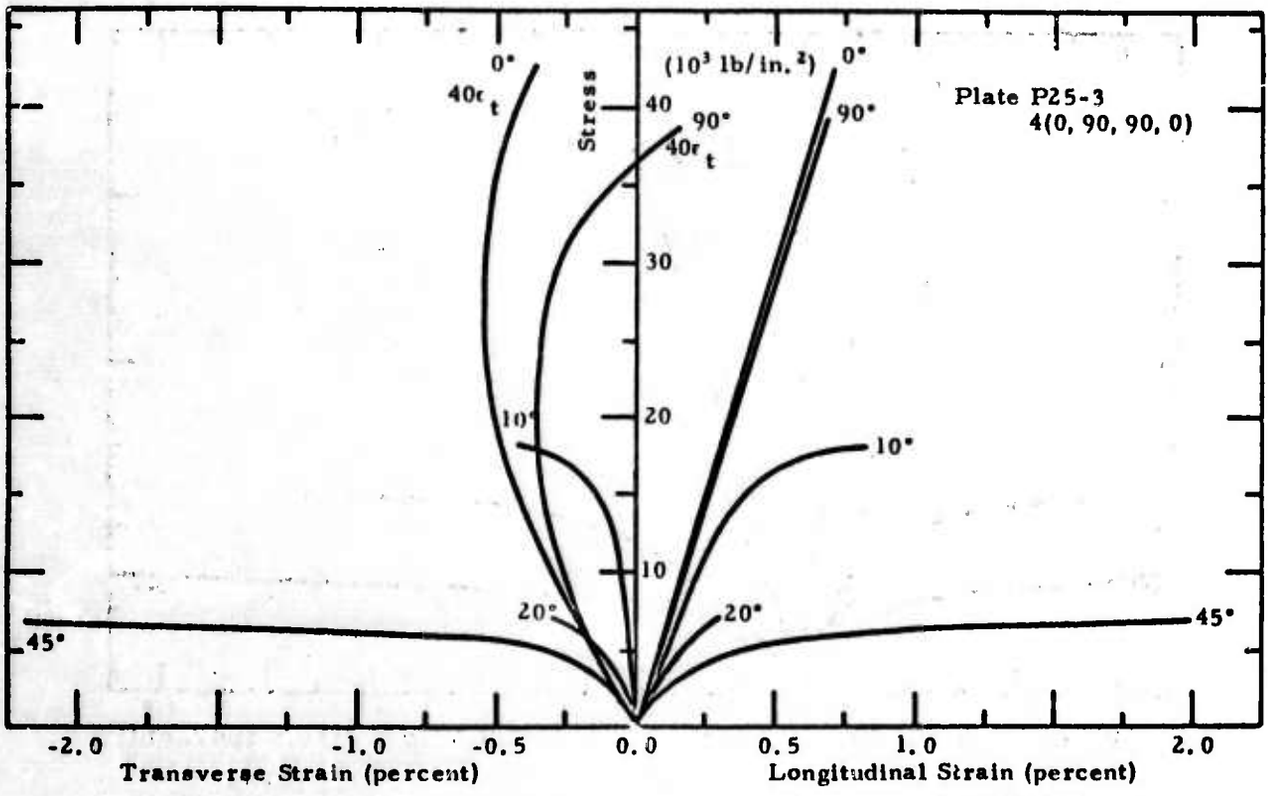

N-10697

Figure 123. Tensile Stress-Strain Curves for "Thornel" 25/ERL 2256 Plate P25-3. Angles Give Test Specimen Orientation.

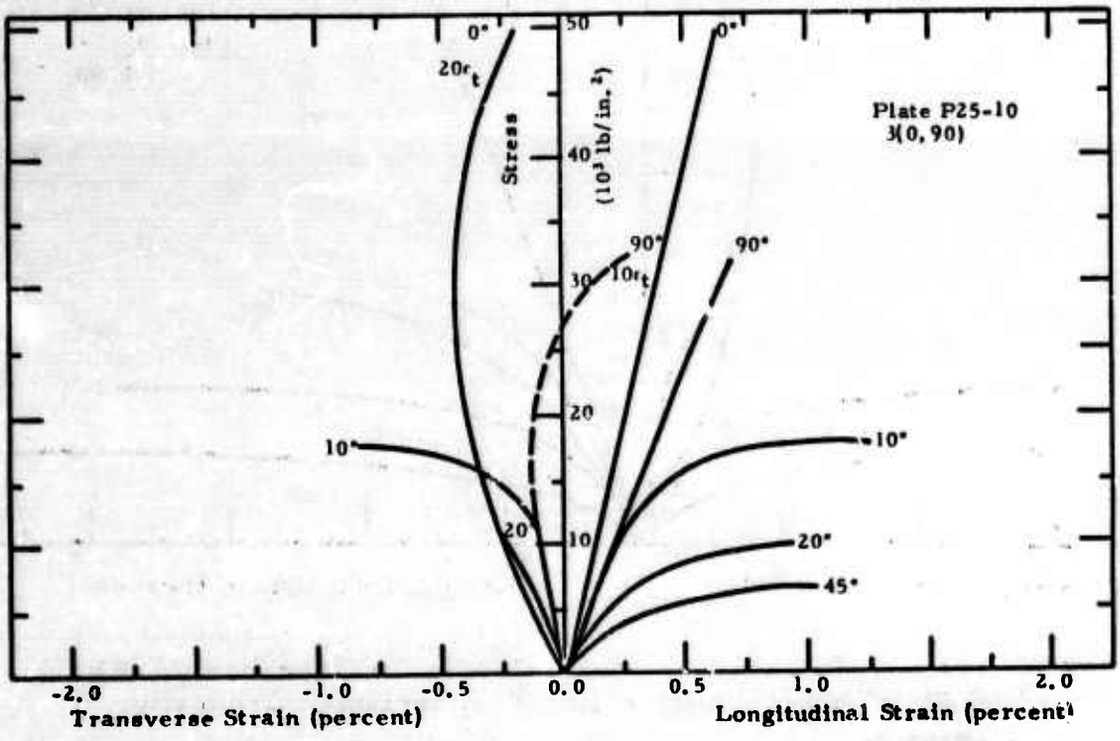

N-10696

Figure 124. Tensile Stress-Strain Curves for "Thornel" 25/ERL 2256 Plate P25-10. Angles Give Test Specimen Orientation.

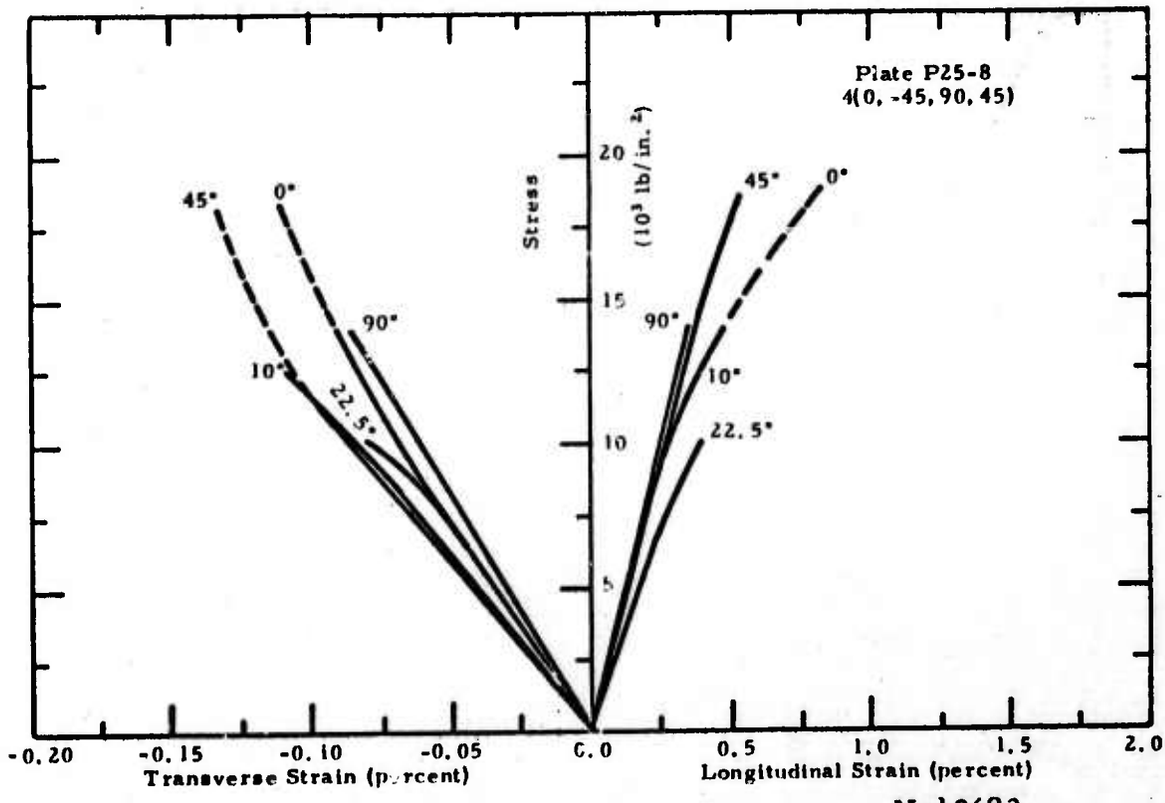

N-10693

Figure 125. Tensile Stress-Strain Curves for "Thornel" 25/ERL 2256 Plate P25-8. Angles Give Test Specimen Orientation.

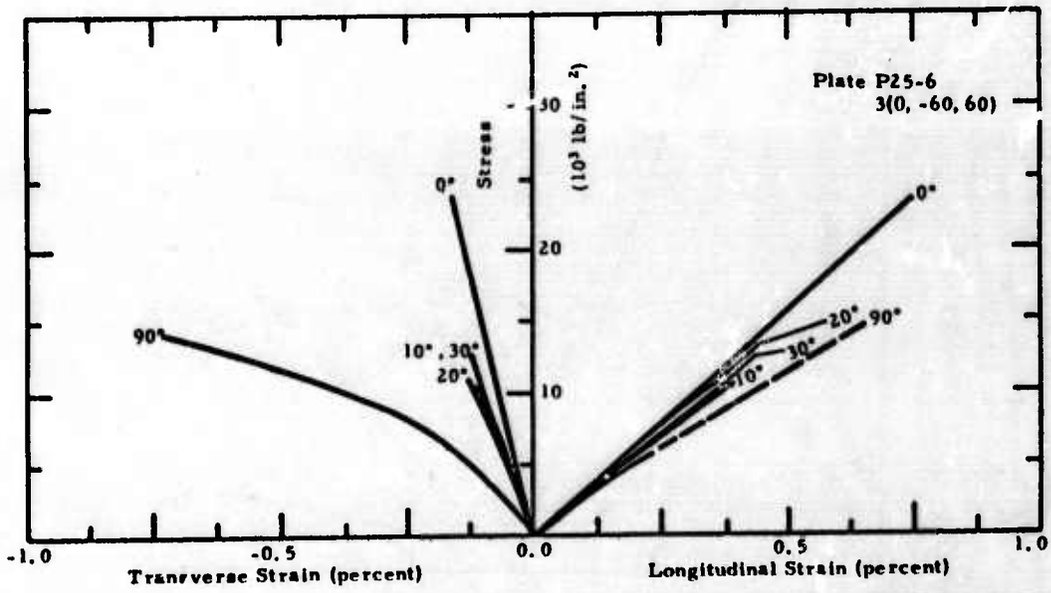

N-10694

Figure 126. Tensile Stress-Strain Curves for "Thornel" 25/ERL 2256 Plate P25-6. Angles Give Test Specimen Orientation.

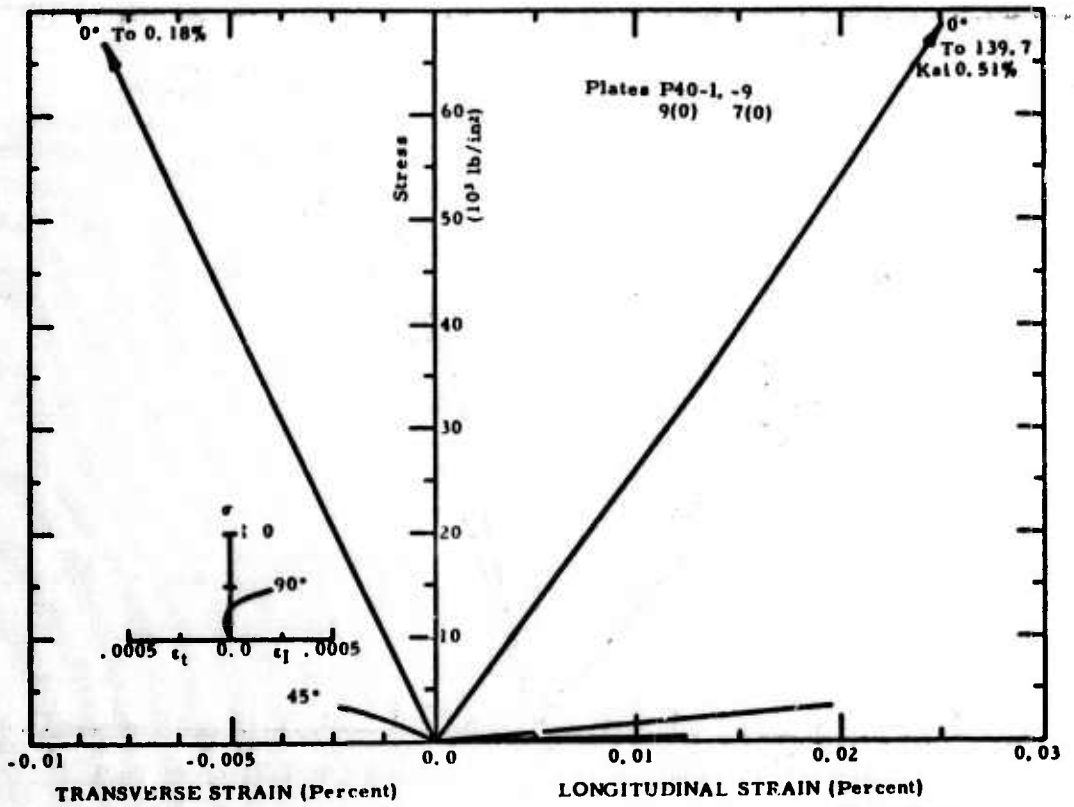

N-17247

Figure 127. Tensile Stress-Strain Curves for "Thornel" 40/ERL 2256 Plates P40-1, 9. Angles Give Test Specimen Orientation.

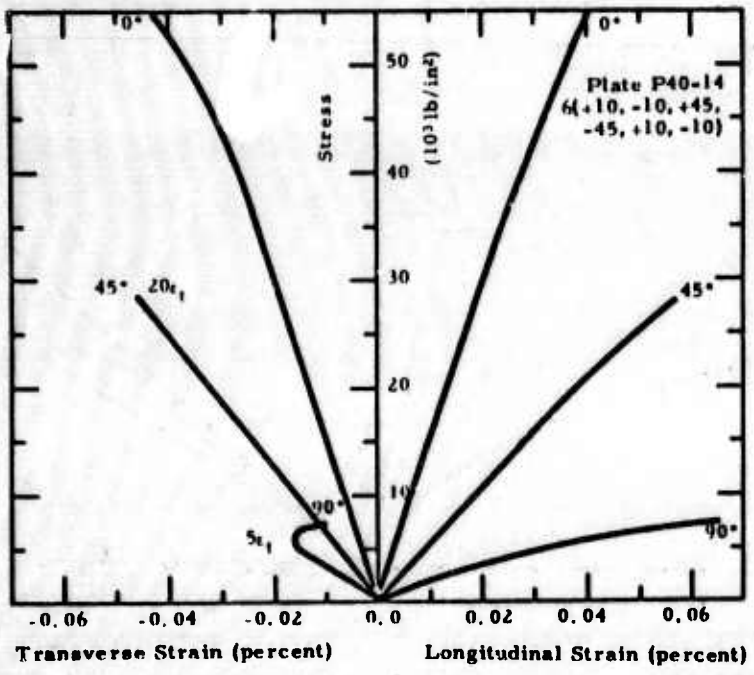

N-17246

Figure 128. Tensile Stress-Strain Curves for "Thornel" 40/ERL 2256 Plate P40-14. Angles Give Test Specimen Orientation.

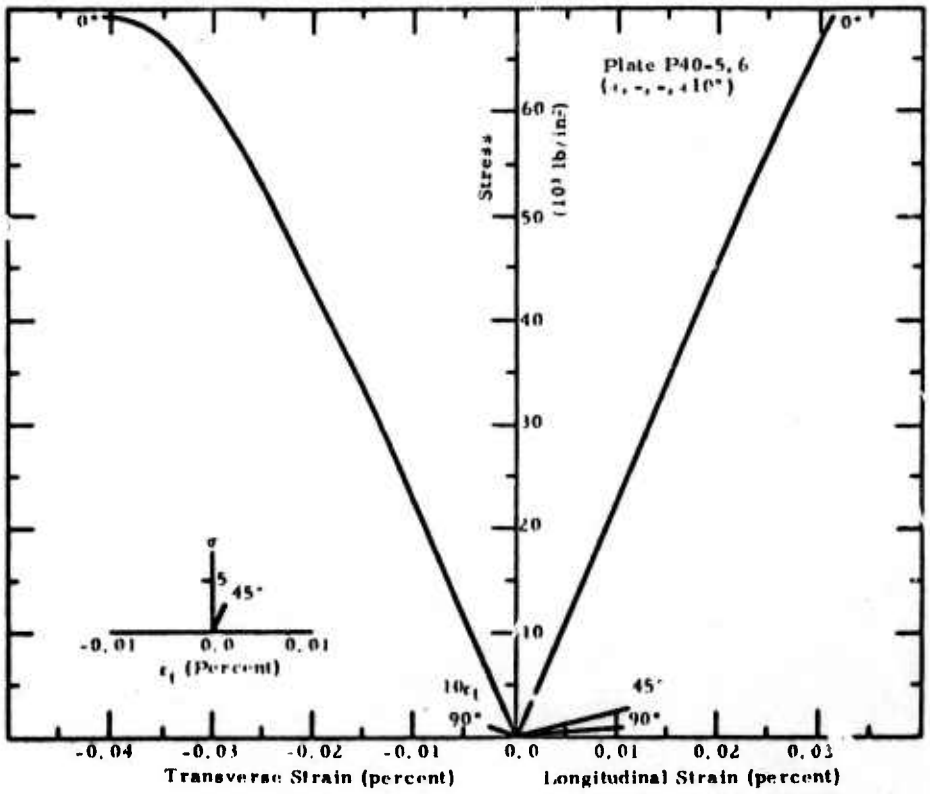

N-17248

Figure 129. Tensile Stress-Strain Curves for "Thornel" 40/ERL 2256 Plates P40-5, 6. Angles Give Test Specimen Orientation.

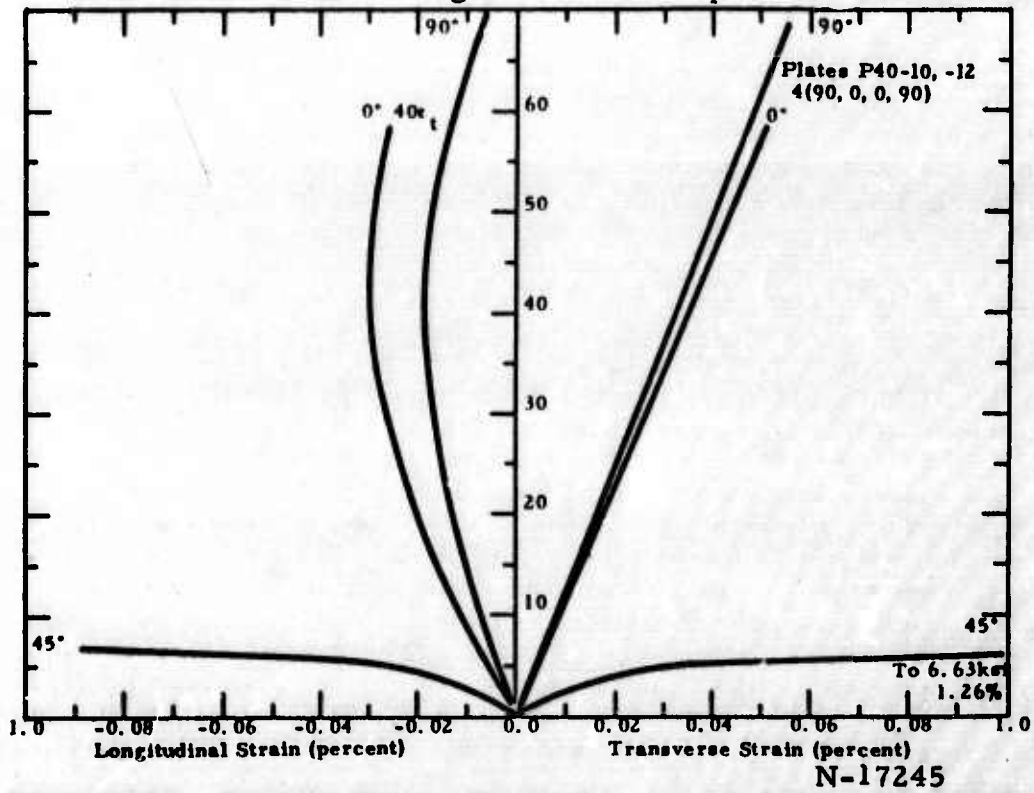

N-17245

Figure 130. Tensile Stress-Strain Curves for "Thornel" 40/ERL 2256 Plates P40-10, 12. Angles Give Test Specimen Orientation.

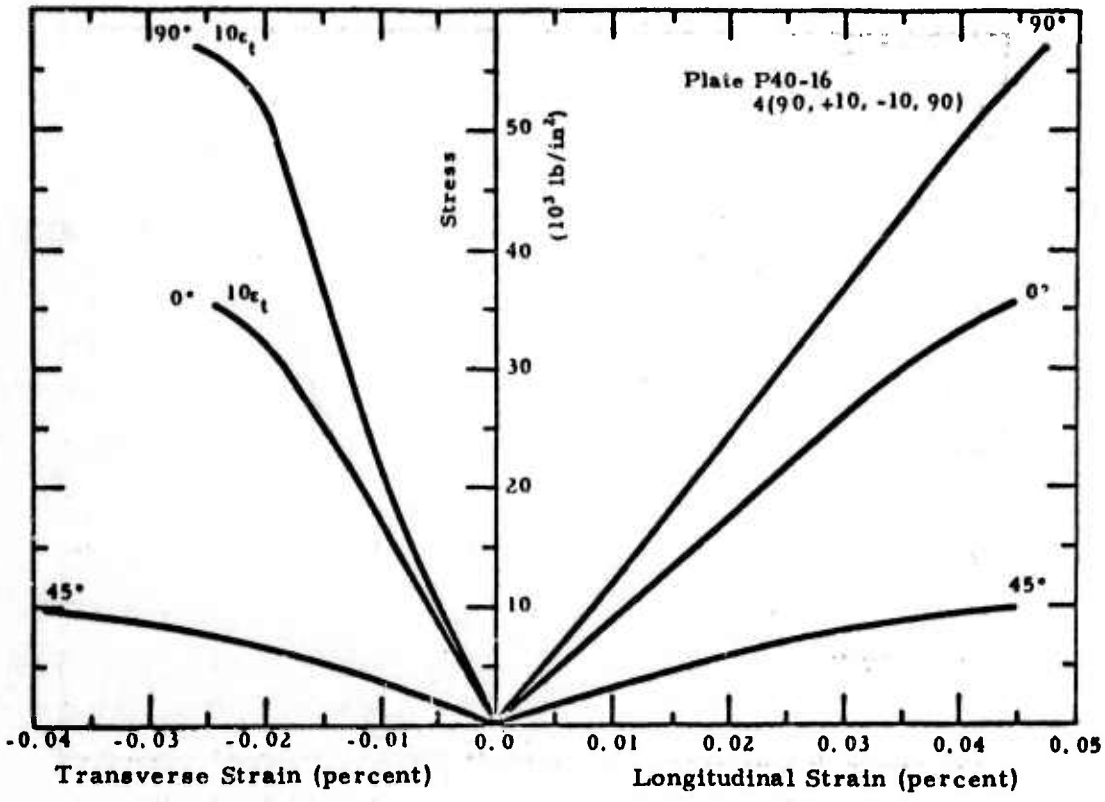

N-17230

Figure 131. Tensile Stress-Strain Curves for "Thornel" 40/ERL 2256 Plate P40-16. Angles Give Test Specimen Orientation.

The compressive stress-strain curves were qualitatively similar to the tensile stress-strain curves. The only significant difference is that the compressive stress-strain curves for the 45° and 90° specimens from the unidirectional plate number P25-4 went to much higher stress levels. The compressive stress-strain curves for plate P25-4 are shown in Figure 132.

D. Composite Strengths

(O. L. Blakslee and T. Weng, Union Carbide)

For both "Thornel" 25 and 40 composites, tensile, compressive, and short-beam shear strengths have been measured on flat specimens; hoop tensile and torsion strengths have been measured on hoop-wound cylinders. In Section VID-1, tensile strengths are given for the specimens for which moduli data were reported in Section VIB. Selected data were normalized to a common value of fiber modulus and fiber volume content so that results from different plates could be compared and evaluated with respect to strengths predicted from constituent properties by the rule-of-mixtures. These results are given in Section VID-2. The compressive strengths are discussed in Section VID-3 and shear strengths are reported in Section VID-4. Results from hoop tensile stress tests of thin-walled cylinders are given in Section VID-5; torsion tests on cylinders provide another measure of the shear strength (Section VID-6).

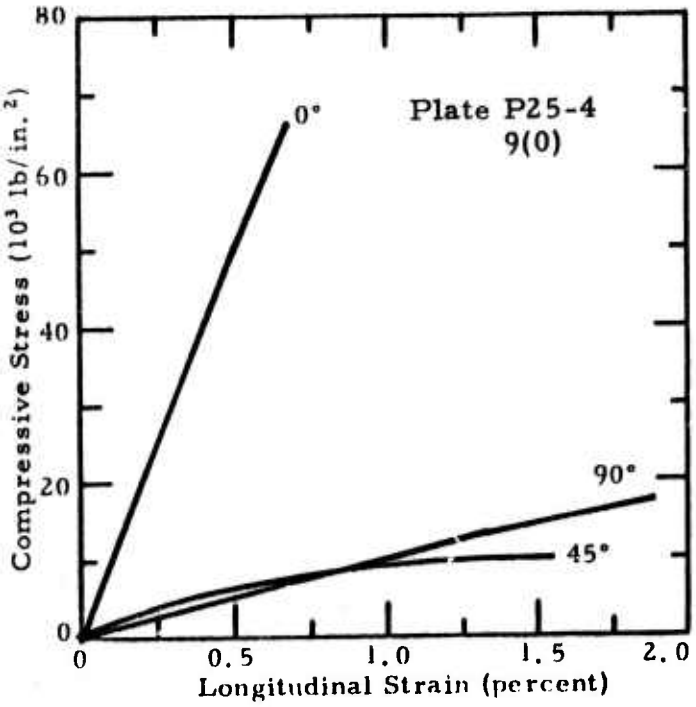

N-10700

Figure 132. Compressive Stress-Strain Curves for "Thornel" 25/ERL 2256 Plate P25-4 Angles Give Test Specimen Orientation.

Average strength data for all types of tests are given in Table XLIV for selected lay-up patterns of interest in the fuselage design studies. The methods used to predict multidirectional composite tensile strengths from unidirectional composite strengths are described in Section VIII C and D. A more detailed discussion is given in Section VIII D.

1. Measured Tensile Strengths

Since the width of the gauge section of the tensile dog-bone was only 0.25 inch, the tensile strengths reported here are often referred to as narrow-specimen tensile strengths. These results are considered to be applicable for the design of long, thin stringers and rings to be used as stiffeners for a thin skin. Wide-specimen tensile strengths are required to understand the behavior of the skin material. Preliminary work on wide-specimen testing is reported in Section VII B 2.

Tensile strengths are shown in Figures 133 through 139 of the specimens used to obtain the moduli data in Section VI B. The curves in the figures are intended to show general trends and are not predicted analytically. The tensile strength of the 90° specimens from the unidirectional plates was only 570 and 465 lb/in.^{2} for the plates P25-4 and P40-1, respectively. The specimens were either damaged in preparation or other difficulties were encountered in testing, because flexural tests on 90° specimens from plate P40-1 have given strengths of 2,900 lb/in.^{2}. The transverse tensile strength of the unidirectional composites is estimated to be at least 2,000 lb/in.^{2}.

TABLE XLIV
ULTIMATE STRENGTHS OF "THORNEL" 25 AND 40/ERL 2256 COMPOSITES

Property Unit - 10^3 psi	Plate Number, Number of Plies, and Lay-Up Pattern "Thornel" 25				"Thornel" 40			
	P25-4 9(0°)	P25-3 4(0, 90, 90, 0)	P25-1, 12 9(0°, 90°, ...)	P40-1, 9 9(0°), 7(0°)	P40-10, 12 4(90°, 0°, 0°, 90°)	P40-16 4(90°, 10°, -10°, 90°)	P40-5, 6 4(10°, -10°, -10°, 10°)	P40-14 6(±10°, ±45°, ±10°)
Tensile								
σ_{t1} - Meas.	92	43	42	140	57	36	67	54
Pred.	-	31.1	35.0	-	56.1	51.6	106.5	71.0
σ_{t2} Meas.	-	39	38	-	67	56	1	7
Pred.	-	31.1	27.4	-	56.1	56.1	2.1	6.1
Flexural								
σ_{f1}			64	114				
σ_{f2}				3				
Compressive								
σ_{c1}	67	38	37	91	44	38	54	48
σ_{c2}	21		30	19	51	49	12	16
Short-Beam Shear								
τ_{13}	5.0		3.7	3.7				3.8
τ_{23}			2.5					
Torsion								
τ_{12}	4.0			3.2 @ 57%				
Fiber Volume Content (percent)	50	50	~50	67	64	57	69	56

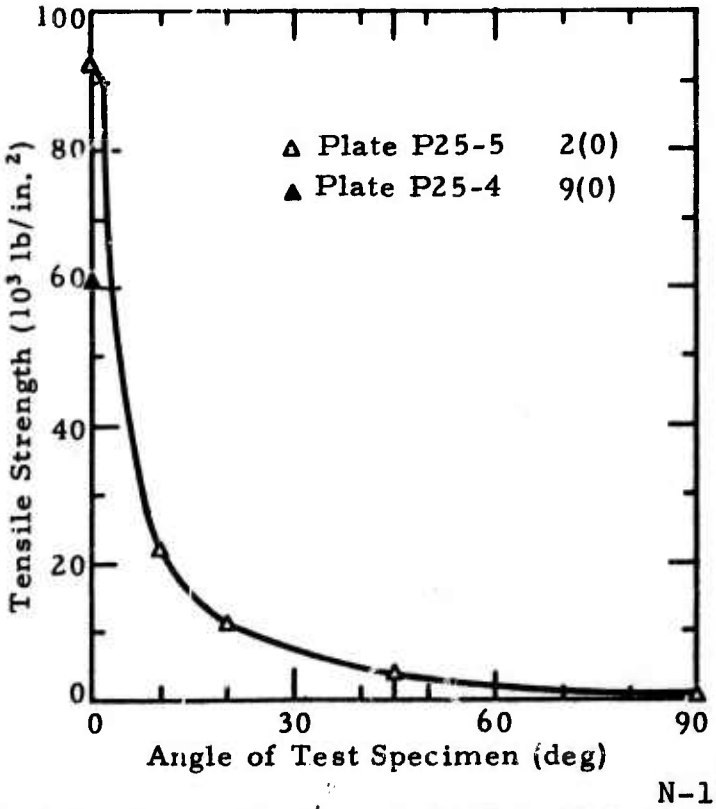

Figure 133. Tensile Strength Versus Angle of Test Specimen for "Thornel" 25/ERL 2256 Plates P25-4,-5.

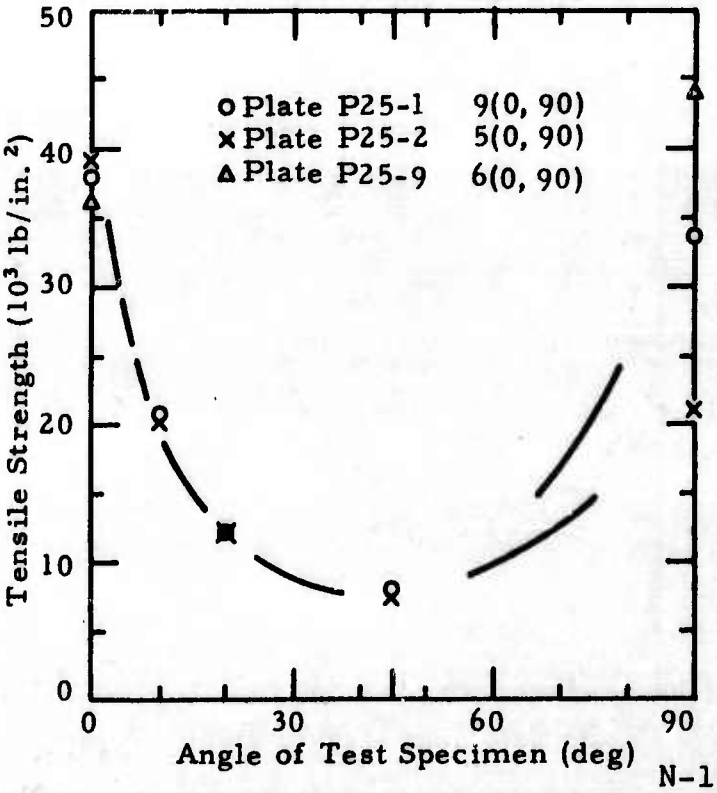

Figure 134. Tensile Strength Versus Angle of Test Specimen for "Thornel" 25/ERL 2256 Plates P25-1,-9,-2.

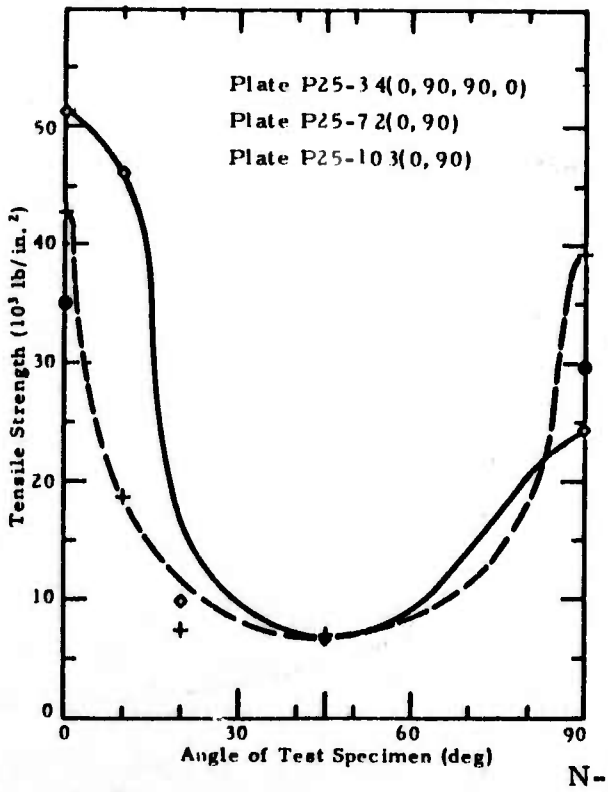

N-10701

Figure 135. Tensile Strength Versus Angle of Test Specimen for "Thornel" 25/ERL 2256 Plates 3, 10, and 7.

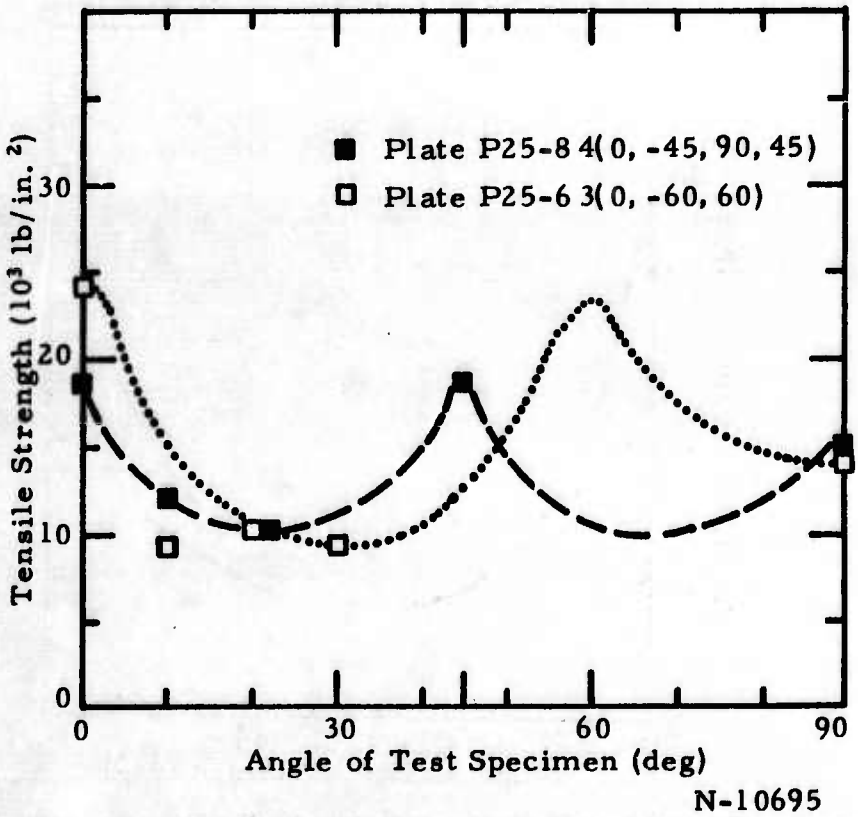

N-10695

Figure 136. Tensile Strength Versus Angle of Test Specimen for "Thornel" 25/ERL 2256 Plates P25-8 and 6

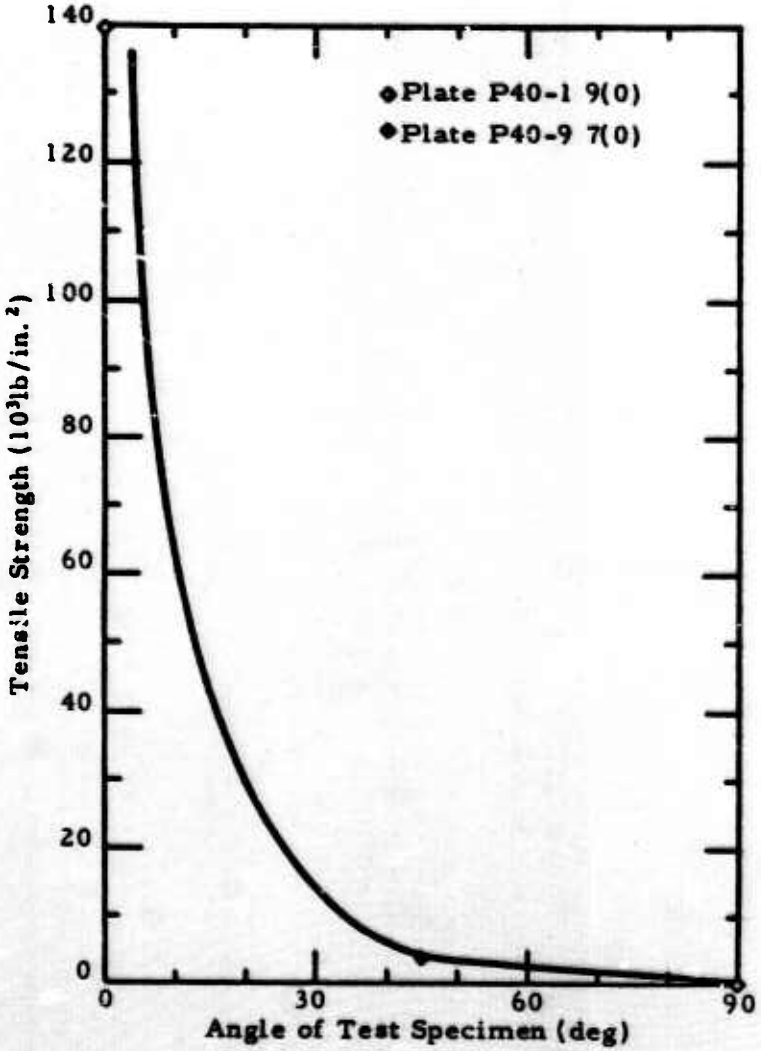

N-17233

Figure 137. Tensile Strength Versus Angle of Test Specimen for "Thornel" 40/ERL 2256 Plates P40-14, 5, and 6.

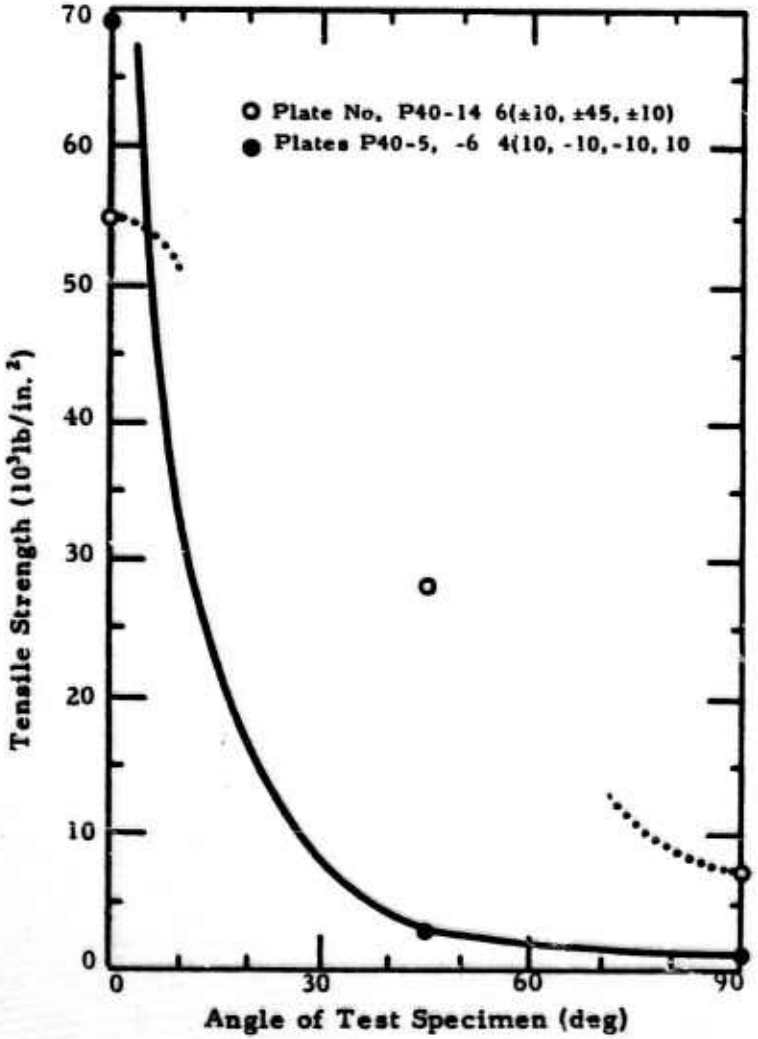

N-17227

Figure 138. Tensile Strength Versus Angle of Test Specimen for "Thornel" 40/ERL 2256 Plates P40-14, 5, and 6.

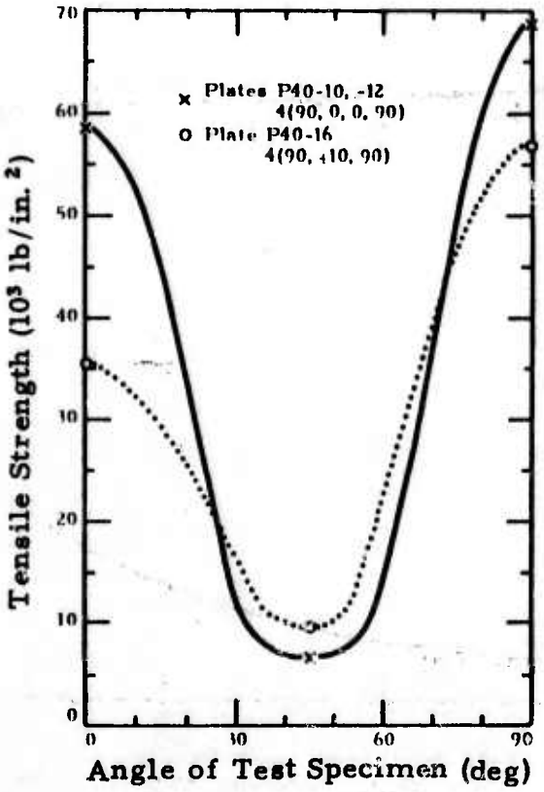

N-17232

Figure 139. Tensile Strength Versus Angle of Test Specimen for "Thornel" 40/ERL 2256 Plates P40-10, 12, and 16.

The failure surfaces of the 0° specimens of the unidirectional composites were ragged with massive longitudinal splintering. The 10°, 20°, and 45° specimens failed in the gauge section by shear parallel to the fibers. The 90° specimens failed in the transition region.

The failure surface was perpendicular to the specimen axis for the various (0°, 90°) lay-ups and the (90°, ±10°, 90°) lay-up. The 0° and 90° specimens broke at the beginning of the transition from the gauge section to the shank. The 10°, 20°, and 45° specimens failed in the gauge section; the tendency was for each individual ply to fail by shear parallel to the fibers in that ply and for neighboring plies to separate by interlaminar shear, resulting in a saw-toothed fracture surface that changed direction by 90° with each ply.

For the (0°-60°, 60°), (0°, -45°, 90°, 45°), and (20°, -10°, -10°, 10°) lay-ups, the fracture surfaces were like those for the (10°, 20°, and 45°) specimens from the (0°, 90°) degree lay-ups. When the specimen's axis was parallel to the fiber direction in one of the plies, approximately one-half of the breaks occurred at the beginning of the transition section.

2. Normalized Tensile Strengths

As in the treatment of the Young's moduli, a scaling factor is used to account for the major part of the differences between strengths of various plates due to variation in constituent properties and fiber loading. A dimensionless strength normalization factor N_σ is defined for each plate by

$$N_\sigma = v_{fs}\sigma_{fs}/v_f\sigma_f, \qquad \text{(VID-1)}$$

in which v_f and σ_f are the actual fiber volume fraction and fiber tensile strength for each plate and v_{fs} and σ_{fs} specify corresponding quantities for a standard plate. We have chosen

$$v_{fs} = 0.50 \text{ and } \sigma_{fs} = 180,000 \text{ lb/in.}^2 \qquad \text{(VID-2)}$$

for the "Thornel" 25 plates and

$$v_{fs} = 0.65 \text{ and } \sigma_{fs} = 250,000 \text{ lb/in.}^2 \qquad \text{(VID-3)}$$

for the "Thornel" 40 plates.

The principal ultimate tensile strengths σ_{ut1} and σ_{ut2} have been averaged to eliminate the major effects on the strengths due to the number of plies in each plate. The strength normalization factor N_σ, the average ultimate tensile strength $(\sigma_{ut1} + \sigma_{ut2})/2$, and the normalized strength $N_\sigma(\sigma_{ut1} + \sigma_{ut2})/2$ are given in Table XLV.

For the unidirectional plate with standard properties, the ultimate tensile strength in the fiber direction, as given by the rule-of-mixtures, is

$$\sigma_{ut1,\,unid.} = [v_{fs} + (1 - v_{fs})E_m/E_{fs}]\sigma_{fs} \qquad \text{(VID-4)}$$

$$= 92,200 \text{ lb/in.}^2 \qquad \text{(VID-5)}$$

for the "Thornel" 25 composites and

$$\sigma_{ut1,\,unid.} = 163,800 \text{ lb/in.}^2 \qquad \text{(VID-6)}$$

for the "Thornel" 40 composites; a value of 0.6×10^6 lb/in.^{2} was used for the matrix modulus E_m. For plate P25-4, the average measured value $N_\sigma \sigma_{ut1}$ for the two specimens tested is 95,100 lb/in.^{2}. In view of the modulus results and the known fiber misalignment in the plate, the measured strength was expected to be less than the theoretical value. The fact that it is not may be due to statistical fluctuation for that plate or may indicate that the effective strength of the fibers in the composite is greater than that measured on free fibers at a one-inch gauge length. The measured value of $N_\sigma \sigma_{ut1}$ for plate P40-1 is 130,000 lb/in.^{2}, which is only 80 percent of the predicted value.

For the (0°, 90°) plates, it is assumed that, at fracture, the plies transverse to the applied load are contributing essentially nothing to the

TABLE XLV

STRENGTH NORMALIZATION FACTOR, AVERAGE ULTIMATE TENSILE STRENGTH, AND NORMALIZED AVERAGE ULTIMATE TENSILE STRENGTH FOR "THORNEL" FIBER/ERL 2256 PLATES

Plate Number	Plies & Lay-up	Strength Normalization Factor N_σ	$(\sigma_{ut1} + \sigma_{ut2})/2$ 10^3 lb/in.^{2}	$N_\sigma(\sigma_{ut1} + \sigma_{ut2})/2$ 10^3 lb/in.^{2}
P25-4	9(0)	1.03	46.2	47.6
P25-5	2(0)	1.45	-	-
P25-1	9(0, 90)	1.13	35.8	40.5
P25-9	6(0, 90)	1.03	40.0	41.2
P25-2	5(0, 90)	1.15	30.2	34.7
P25-3	4(0, 90, 90, 0)	0.97	41.0	39.8
P25-10	3(0, 90)	1.09	40.2	43.8
P25-7	2(0, 90)	1.20	32.3	38.8
	Average for Plates P25-1, 9, 2, 3, 10, 7		38.0	40.9
P25-8	4(0, -45, 90, 45)	1.03	-	-
P25-6	3(0, -60, 60)	1.09	-	-
P40-1	9(0)	.93	70.5	65.6
P40-14	6(±10, ±45, ±10)	1.13	30.5	34.5
P40-5	4(10, -10, -10, 10)	.92	34.0	31.3
P40-12	4(90, 0, 0, 90)	.98	62.0	60.7
P40-16	4(90, ±10, 90)	1.11	46.0	51.1

strength of 0° and 90° tensile specimens. The theoretical average strength of the standard (0°, 90°) plate is then just one-half of the unidirectional strength, or 46,100 lb/in.^{2} for the "Thornel" 25 plates and 81,900 lb/in.^{2} for the "Thornel" 40 plates. For the six cross-plied "Thornel" 25 plates, the measured average value of $N_\sigma(\sigma_{ut1} + \sigma_{ut2})/2$ is 40,900 lb/in.^{2}, or 89 percent of 46,100 lb/in.^{2}. The only cross-plied "Thornel" 40 plate is P40-12 for which the measured value of $N_\sigma(\sigma_{ut1} + \sigma_{ut2})/2$ is 50.7, or 74 percent of 81,900 lb/in.^{2}. At first, it was thought that the greater difficulty experienced in testing the unidirectional "Thornel" 40 composite might account for its lower percent of theoretical strength compared with that for the "Thornel" 25 composite. However, the fact that the percent of theoretical strength is also lower for the cross-plied "Thornel" 40 composite (where no testing difficulty was noted) suggests that possibly the full potential of the higher modulus "Thornel" 40 fibers is not being utilized. The lower resin content of the "Thornel" 40 composites may also be a contributing factor. These questions are being investigated further.

The trend of the normalized ultimate tensile strengths in the 0° and 90° directions with number of plies is shown in Figure 140 for the

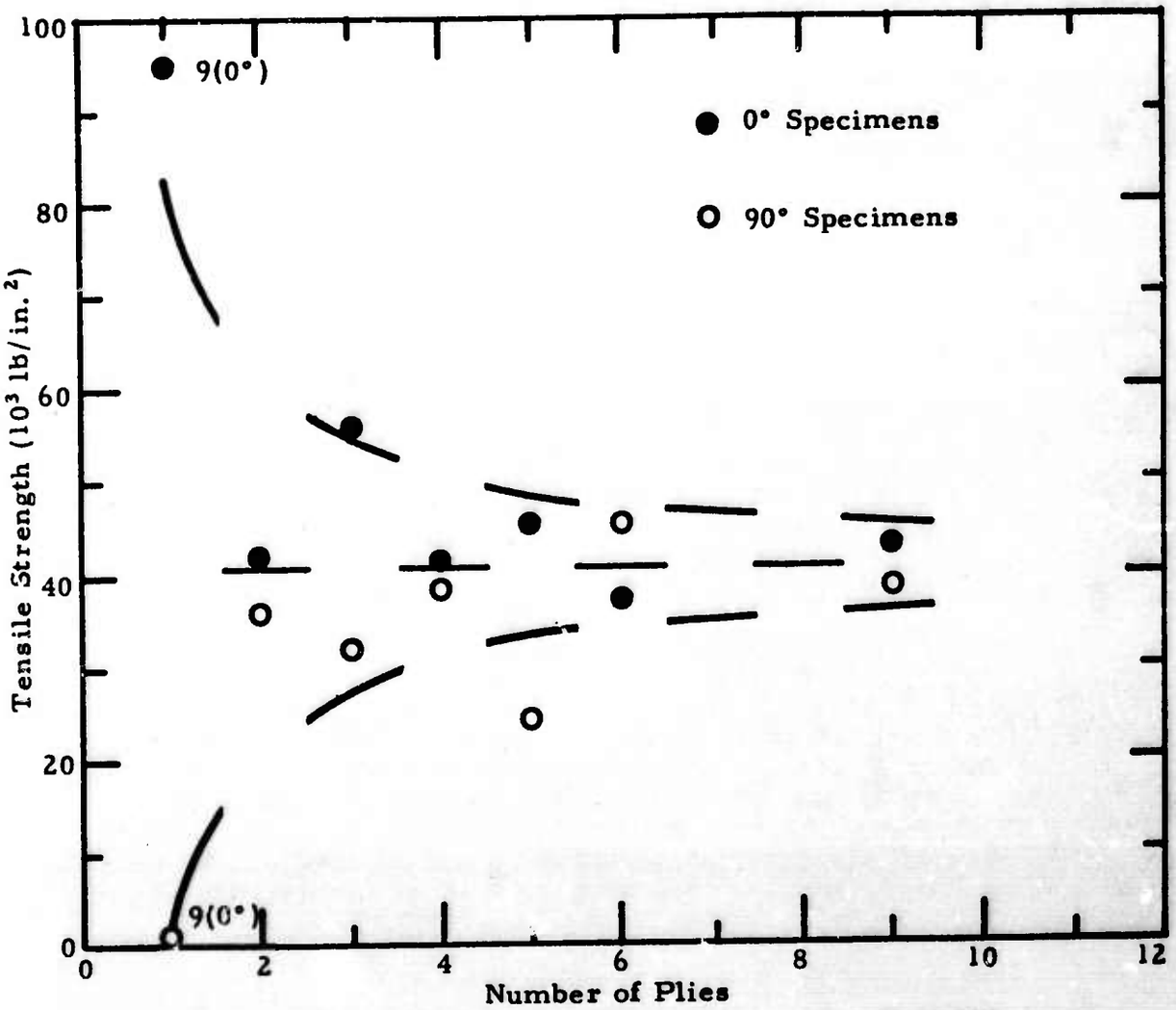

Figure 140. Normalized Ultimate Tensile Strengths Versus Number of Plies for Cross-Plied "Thornel" 25/ERL 2256 Plates.

cross-plied "Thornel" 25 plates. The curves for the strength of plates with an odd number of plies were computed from

$$\sigma_{ut1} = k \frac{n+1}{2n} \sigma_{ut1,\,unid.} \qquad \text{(VID-7)}$$

$$\sigma_{ut2} = k \frac{n-1}{2n} \sigma_{ut1,\,unid.} \qquad \text{(VID-8)}$$

in which the value of $\sigma_{ut1,\,unid.}$ is given by Equation VID-5 and the value of 0.89 for k was selected to convert from theoretical to average measured values. The deviation of the point from the average indicates the extent of the scatter in the data for the plates with 2, 4 and 6 plies. The experimental

points follow the trend of the theoretical curves for plates with 1, 3, 5, and 9 plies (the 9-ply 0° plate was used in lieu of a one-ply plate).

One of the important objectives of studying plates with various numbers of plies was to see if there was a degradation of properties as the number of plies decreased. No degradation in the strength is evident as the number of plies decreased from 9 to 2.

3. Compressive Strengths

The strengths reported here should be classified as narrow-specimen compressive strengths, since the gauge section was only 0.375 inch wide. Table XLVI summarizes the compression failure data. All the data are averages for 2 to 4 specimens except that only single measurements were made for the 10, 20, and 45 degree specimens from plate P25-1. The compressive strength is usually less than the tensile strength when a large number of the fibers lie in or near the test direction and is always greater than the tensile strength when most of the fibers lie at a large angle with respect to the test direction. That is, if the mode of failure of the tensile specimen is primarily shear between fibers, the compressive strength for a similar specimen will be greater than the tensile strength.

The 45° specimen from plate P25-1 did not break; at 6 percent deformation, the platens hit the fixture. The strength value is considered accurate because there was no significant increase in load after 2 percent strain. Two 0° specimens from plate P25-3 failed by brooming at the ends. All other specimens failed in the gauge section. The 0° specimen from the unidirectional plates failed by local crushing across a surface roughly perpendicular to the load axis. The remaining specimens failed by shear across a plane, intersecting the edge of the specimen at 45 degrees and intersecting each ply either parallel or perpendicular to the fibers.

4. Short-Beam Shear Strengths

Over 50 shear strength measurements were made by the flexure of a short beam in three point loading in order to see if there was any appreciable dependence of shear strength on span-to-depth or width-to-depth ratios. These measurements were made on the central region of plate P25-11, a 9-ply (0°, 90°) plate which had strong fiber wash around the edges during molding.

The depth (thickness) of plate P25-11 was 0.141 inch, and span-to-depth ratios of 4, 5, and 6 were chosen. Specimen widths of 0.3, 0.4, and 0.5 inch were used; two to four specimens of each type were cut at 0° and 90° orientations from the plate. The averages of the test results are given in Table XLVII. Significant trends are not evident, although there is a tendency for the shear strength to decrease with increasing span-to-depth ratio. This effect may be due to the decrease in compressive stress across the shear plane as the span-to-depth ratio is increased.

TABLE XLVI

FRACTURE STRAINS AND ULTIMATE STRENGTH FROM COMPRESSION TESTS FOR "THORNEL" FIBER/ERL 2256 PLATES

"THORNEL" 25					"THORNEL" 40			
Plate Number	Plies & Lay-Up	Specimen Orientation degrees	Fracture Strain percent	Ult. Comp. Strength 10^3 lb/in.^{2}	Plate Number	Plies & Lay-Up	Specimen Orientation degrees	Ult. Comp. Strength 10^3 lb/in.^{2}
P25-4	9(0)	0	0.68	67	P40-1	9(0)	0	92
		45	1.5	10			90	19
		90	1.9	21	P40-9	7(0)	0	91
P25-1	9(0, 90)	0	0.49	26	P40-14	6(±10, ±45, ±10)	0	48
		10	0.46	19			90	16
		20	2.5	15	P40-5	4(10, -10, -10, 10)	0	54
		45	>6.0	>13			90	12
		90	0.66	28	P40-12	4(90, 0, 0, 90)	0	44
P25-14	9(0, 90)	0	-	37			45	6
P25-3	4(0, 90, 90, 0)	0	> 0.75	>36			90	51
					P40-16	4(90, ±10, 90)	0	38
							90	49

TABLE XLVII

AVERAGE SHORT-BEAM SHEAR STRENGTH FOR "THORNEL" 25/ERL 2256 PLATE NUMBER P25-11

Width to Depth Ratio	Span/Depth 4.0	5.0	6.0
	0° Direction		
2.1	2.88	2.75	2.79
2.8	3.04	2.91	2.75
3.5	3.17	3.01	2.55
	90° Direction		
2.1	2.44	2.40	2.26
2.8	2.56	2.23	2.27
3.5	2.55	2.28	2.26

Unit: 10^3 lb/in.^{2}

No clear dependence on width-to-depth was evident. The common span-to-depth ratio of 5 appears to be satisfactory for "Thornel" fiber composites.

A similar experiment was performed with samples cut in the 0° direction from the unidirectional plate P25-4. A constant span-to-depth ratio of 5.3 was used, but the widths were 0.12, 0.3, and 0.4 inch for a depth of 0.12 inch. No significant variation of shear strength with width-to-depth ratio was found, and the average of all specimens is given in Table XLVIII. An additional eight samples with square cross section were

TABLE XLVIII

AVERAGE SHORT-BEAM SHEAR STRENGTH FOR "THORNEL" FIBER/ERL 2256 PLATES

Plate Number	Plies & Lay-Up	Span to Depth Ratio	Specimen Orientation 0°	Specimen Orientation 90°	Load Application
P25-4	9(0)	5.3	5.49	-	Edge of Plies
			4.89	-	Face of Plies
P25-14	9(0)	5.3	4.94	-	Face of Plies
P25-1	9(0,90)	5.3	3.68	2.52	Face of Plies
P25-11	9(0,90)	5.3	2.86	2.36	Face of Plies
P25-12	9(0,90)	5.3	3.55	-	Face of Plies
P40-1	9(0)	12	3.68	-	Face of Plies
P40-9	7(0)	5	4.32	-	Face of Plies
P40-14	6(±10, ±45, ±10)	5	3.7	-	Face of Plies

Unit: 10^3 lb/in.^{2}

tested on edge, i.e., the load was applied to the edges of the plies rather than to the plies which formed the outer surfaces of the plate; the shear strength with edge loading was approximately 10 percent higher than that measured with face loading.

Short-beam strengths for several other "Thornel" 25 and 40 plates are also given in Table XLVIII. An attempt to test the 4-ply "Thornel" 40 plates in short-beam shear was not successful. The span was 0.25 inch, which gave a span-to-depth ratio of 8. The measured strengths were erratic and are not reported. The higher shear strength of the unidirectional "Thornel" 25 plates compared to that of the cross-plied plates is probably due to the fact that the original flat ply surfaces have been largely broken up in the unidirectional plates as shown in the optical micrographs of Section VE-4. The shear strength of the

unidirectional "Thornel" 40 composites is less than that of the unidirectional "Thornel" 25 composites. This result is consistent with the work of Simon, Prosen, and Duffy[31] and is thought to be due to a change in fiber surface properties with increasing fiber modulus.

The tests were stopped when there was a marked break in the load-deflection curve. There was no catastrophic failure, and it was usually very difficult to see the place of fracture without magnification. Although examination of the specimens has not been completed, many of the cross-plied samples that have been analyzed fractured near the surface between two plies.

5. Hoop Tensile Stress Test of Cylinders

Hoop tensile stress test fixtures similar to one reported in Section VE of the First Annual Report[1] have been constructed for cylindrical specimens with diameters of 2 and 4 inches. The test fixtures can be used for specimens having lengths of 0.5, 1, 2, and 4 inches by interchanging the steel spacers. With these test fixtures, the preliminary work conducted on the JT-series composites can be extended to study the effects of diameter and length on the uniaxial tensile strength of graphite-fiber, resin-matrix composite cylinders.

During the initial stage of this experimental program, some of the specimens were not tested to failure because of premature rupture of the neoprene bags. This premature rupture is generally caused by the large space created between the end plates of the test fixture and the test specimen due to the axial contraction of the test specimen under hoop stress and the separation of the end plates from the specimen by hydraulic pressure in the neoprene bag. Attempts to maintain a close tolerance between the end plates and the specimen by the application of additional compressive load on the end plates during the test were found to be partially successful. The premature rupture of the neoprene bags was eliminated by making several modifications in the test fixtures and using neoprene bags having more uniform thickness and higher strength.

For the hoop-wound cylinders used in this study, the hoop stress-strain curve is linear up to fracture. The axial (transverse to the fiber direction) stress-strain behavior is initially linearly elastic; it becomes gradually nonlinear with increasing stress; and, finally, it shows considerable plasticity near fracture. The summary of the hoop tensile stress tests is given in Table XLIX. "Thornel" 25 specimens marked with (**) were not tested to fracture, due to premature rupture of the neoprene bags; and, therefore, the values of the hoop stress corresponding to the rupture of the neoprene bags are given. "Thornel" 25 specimens marked with (*) were cylinders with a uniform wall thickness. These specimens failed at hoop stresses lower than those predicted because the fracture of these specimens initiated from the edges of the specimens due to severe end effects. The configuration of the test specimen was modified to have the

TABLE XLIX

HOOP TENSILE STRESS TEST RESULTS ON HOOP-WOUND CYLINDERS OF "THORNEL" FIBER/ERL 2256 COMPOSITES

Specimen	Inside Diam. (in.)	Thickness (in.)	Length (in.)	Fiber Vol. Content (percent)	Max Hoop Stress lb/in.^{2}	Young's Modulus $10^6 1/s_{11}$ lb/in.^{2}	Poisson's Ratio (ν_{12})
"Thornel"25 /ERL 2256							
1*	.885	.05	1.0	-	62,100**	16.5	.24
2*	.885	.05	1.0	-	91,600**	17.5	.17
3*	2.000	.04	1.0	-	57,000**	13.2	.20
4*	2.000	.04	1.0	58.4	49,800	14.1	-
5*	2.000	.04	2.0	56.3	66,700	12.0	.24
6	2.000	.04	2.0	53.9	82,800	13.3	.40
7*	4.000	.04	2.0	-	42,600**	14.0	.27
"Thornel" 40/ERL 2256							
1	2.000	.03	2.0	55.5	128,600	23.3	.30
2	2.000	.03	2.0	56.5	93,600	19.2	.20

* Specimens had uniform wall thickness.
**Specimens were not tested to fracture.

curved exterior surface shown in Figure 141 in order to eliminate the failure of test specimens at the edges. The reduced section insures that the initiation of fracture occurs in the gauge section. The thickness at the reduced section for the 2-inch diameter "Thornel" 25 and 40 composite specimens are, respectively, 0.04 and 0.03 inch. The values of Young's modulus and Poisson's ratio were determined at the origin of the stress-strain curve, and the fiber volume content was measured by the nitric acid method.

"Thornel" 25 specimen 2 was tested to an internal pressure of 9,600 lb/in.^{2} without catastrophic failure. The hoop stress at the inside surface of the specimen under this pressure was 91,600 lb/in.^{2}, supporting the average tensile strength value of 92,300 lb/in.^{2} obtained for the unidirectional plate P25-4. The lower values of the fracture hoop stress for specimens 4 and 5 were due to edge failures caused by end effects. The fracture hoop stresses for the "Thornel" 25 specimen 6 and the "Thornel" 40 specimen 1 are 84 and 89 percent, respectively, of the values predicted by the rule-of-mixtures.

The fracture hoop stress for the "Thornel" 40 specimen 2 is considerably lower than the predicted value; but examination of the

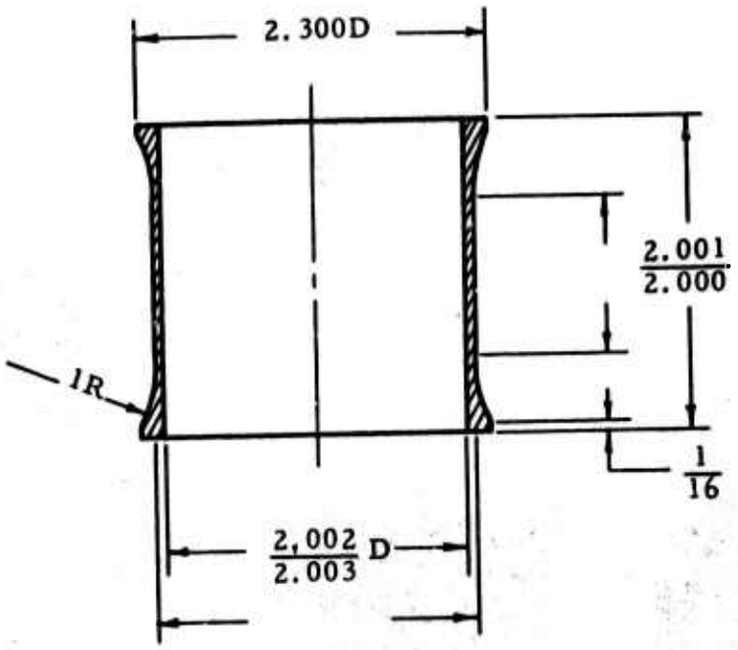

Hoop Tensile Test Specimen

N-17231

Figure 141. Hoop Tensile Test Specimen for Graphite-Fiber, Resin-Matrix Composites.

longitudinal stress-strain curves indicates that the specimen appears to be damaged prematurely. The values of Young's modulus agree within 15 percent with the predicted values. The scatter in the values of Poisson's ratio may be due to the variations in the longitudinal strain, which is influenced strongly by the friction between the neoprene bag and the test specimen and by end effects. A photograph of a fractured "Thornel" 40/ERL 2256 composite specimen in the test fixture is shown in Figure 142.

6. Torsion Tests of Cylinders

Five hoop-wound "Thornel" 25 and 40/ERL 2256 hollow cylinders were tested in torsion with the apparatus described in Section IIIC. The specimens had an outside diameter of 2.20 inches, a thickness of 0.1 inch, and a gauge length of approximately 3.0 inches. The shear strain and longitudinal strain at the outside surface were measured, respectively, with a pair of 45° oriented rosettes and a pair of foil gages.

Torque-shear strain curves and torque-axial (parallel to the cylinder axis) strain curves were nonlinear, with the exception of one of "Thornel" 25 specimen which appeared to fail prematurely. The specimens exhibited a small longitudinal extension, and the rate of the extension increased rapidly as the specimens approached fracture. Since the material exhibits nonlinear torque-shear strain behavior, nonlinearity must be taken into account in the calculation of the shear strength.

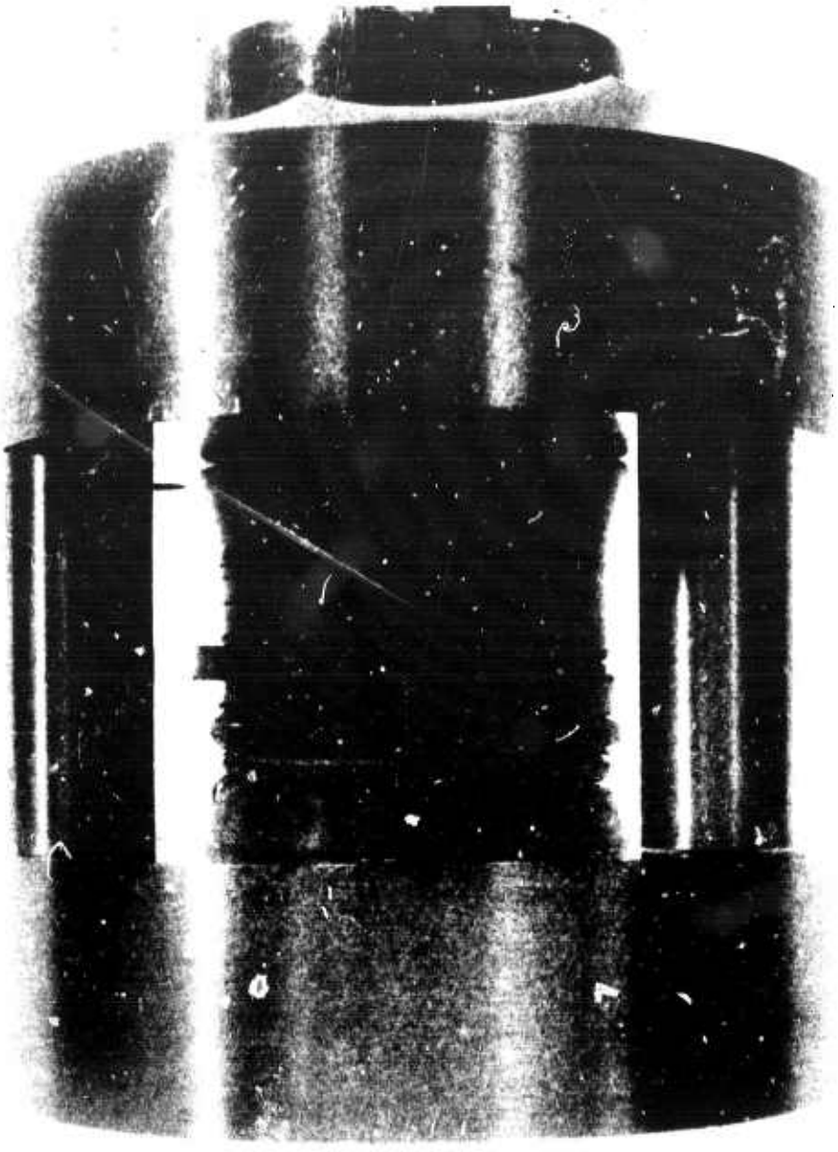

THORNEL 40
HOOP WOUND COMPOSITE

N-17512

Figure 142. Hoop-Wound "Thornel" 40/ERL 2256 Composite Cylinder Fractured in Hoop Tension.

Ellington[32] extended Nadai's graphical solution for plastic torsion of a circular solid bar to a thin hollow cylinder. The shear strengths were calculated with (1) Ellington's graphical method, (2) a formula for thin hollow cylinders in which shear stress is assumed to be distributed uniformly across the thickness, and (3) a formula derived from linear elasticity theory. Shear strengths determined by the first two methods are practically identical and slightly lower than that calculated with the linear elasticity formula.

The results of the torsion tests are given in Table L. The shear modulus is the slope at the origin of the shear stress-strain curve. The

TABLE L

TORSION TEST RESULTS ON HOOP-WOUND HOLLOW CYLINDER OF "THORNEL" FIBER/ERL 2256 COMPOSITES

Specimen	Fiber Vol. Content (Percent)	Shear Modulus ($1/s_{66}$, 10^6 lb/in.^{2})	Shear Strength (lb/in.^{2})	Shear Strain (Percent)	Axial Strain (Percent)
"Thornel" 25/ERL 2256					
1	56	0.55	1390	0.26	0.003
2	55	0.61	3280	0.74	0.01
3	48	0.56	4070	1.51	0.043
"Thornel" 40/ERL 2256					
1	57	0.62	3120	0.67	0.0
2	57	0.65	3310	0.69	0.014

shear strength given in the table was calculated with the thin hollow cylinder formula. The fiber volume content was determined by the nitric acid method. The increase in shear strength of the first three "Thornel" 25 cylinders is thought to be due to an increase in the quality of the material as fabrication experience was obtained. The 4,070 lb/in.^{2} shear strength is considered to be representative of "Thornel" 25 composites. If so, the torsion test results indicate the composite shear strength decreases as the fiber modulus increases, as noted in the discussion of the short-beam shear strengths. The short-beam shear strengths listed in Table XLVIII are approximately 800 lb/in.^{2}, higher than the torsion test shear strengths given in Table L. The approximate agreement between the torsion shear strengths and the short-beam shear strengths justify the use of the simple short-beam test, but further comparative work is required.

The value of $1/s_{66}$ for the hoop-wound "Thornel" 25 cylinder number 3 in torsion is in fair agreement with the value 0.604×10^6 lb/in.^{2} (see Table XXXIX of Section VIB) obtained from off-axis tensile

tests of the unidirectional plate number P25-4. The comparison of these results with ultrasonic measurements at 1 mHz is of interest. The ultrasonic values of the shear moduli of plate P25-4 are:

$$1/s_{44} = 0.39 \times 10^6 \text{ lb/in.}^2$$
$$1/s_{55} = 0.43$$
$$1/s_{66} = 0.69.$$

The fact that the ultrasonic value of $1/s_{66}$ is higher than the static values correlates with similar results for the pure resin. For the "Thornel" 40 composites, the torsion test results for the shear modulus cannot be directly compared with the values obtained by the off-axis tensile tests because the fiber volume contents of the cylinders and plates are different; the shear modulus is a strong function of fiber volume content.

E. Water Sensitivity of Composite Properties
(O. L. Blakslee, Union Carbide)

Tests to determine the sensitivity of the mechanical properties of "Thornel"-fiber, epoxy-resin composites to high humidity environments were made on two "Thornel" 25 and one "Thornel" 40 plates: P25-62, a 9-ply (0°, 90°) plate; P25-64, a 9-ply (0°) plate; and P40-1, a 9-ply (0°) plate. Half of the specimens were boiled in water for 72 hours prior to testing, and the other half were kept dry. The results of the strength measurements are summarized in Table LI. After the water boil treatment, the tensile, flexural, and compressive strengths decreased by

TABLE LI

EFFECT OF 72 HOUR WATER BOIL ON STRENGTH OF "THORNEL"-FIBER, ERL 2256/MPDA COMPOSITES

Strength Property	Initial (10^3lb/in.^{2})	Change After Boil (percent)	Initial (10^3lb/in.^{2})	Change After Boil (percent)	Initial (10^3lb/in.^{2})	Change After Boil (percent)
Tensile σ_1	42.3	-5	---	---	---	---
Flexural σ_1	63.8*	-11	---	---	---	---
Compressive σ_1	37.3	-7	---	---	---	---
Short-Beam Shear τ	3.55	-16	4.94	-17	3.68	-23

*Breaking occurred under load point.

11 percent or less. The short-beam shear strength decreased by 17 percent for the "Thornel" 25 composites and by 23 percent for the "Thornel" 40 composite.

These tests also showed that, after the specimens were subjected to the water boil, the thickness had increased 1 to 2 percent and the other

dimensions had decreased ~0.1 percent. Measured on a percentage basis, the decrease in Young's modulus was the same as the increase in thickness or cross-sectional area. No measurable change was found in Poisson's ratio.

F. Composite Thermal Properties
(O. L. Blakslee, Union Carbide)

Preliminary measurements have been made of the thermal expansion and conductivity of "Thornel" 25 and 40 composites at or near room temperature. Even though some of the results are accurate to only one significant figure, the results are included to illustrate the strong anisotropy in these properties. The specific heats of the composites have been calculated from the specific heats of the constituent fiber and matrix. The thermal data are given in Table LII.

TABLE LII

THERMAL EXPANSION AND CONDUCTIVITY OF "THORNEL" 25 AND 40/ERL 2256 COMPOSITES

Property	P25-4 9(0°)	P25-3 4(0°, 90°, 90°, 0°)	P40-1 9(0°)	P40-12 4(90°, 0°, 0°, 90°)
Thermal Conductivity (at 25°C) - cal/sec cm°C				
K_1 cal/sec cm°C	0.029	0.0039	0.13	0.0095
K_2 cal/sec cm°C	-	-	0.0025	-
K_3 cal/sec cm°C	0.0015	0.0015	0.0023	0.0026
K_1 Btu in/hr ft²°F	84.	11.	380.	28.
K_2 Btu in/hr ft²°F	-	-	7.3	-
K_3 Btu in/hr ft²°F	4.4	4.4	6.7	7.5
Coefficient of Linear Expansion (over 25 to 100°C) - 10^{-6}/°C				
α_1	0.4	2.6	-0.7	-0.02
α_2	41.	4.2	29.	-0.19
Specific Heat (Calculated at 25°C) - cal/g°C and Btu/lb°F				
c_p	0.21	0.21	0.19	0.20
Fiber Volume Content-percent				
V_f	50.	50.	67.	63.

Thermal Conductivity. The value of the thermal conductivity parallel to the fibers, k_1, measured on the unidirectional "Thornel" 40 composite agrees with the value calculated through the use of the parallel heat flow model[33] and a value of 0.2 cal/sec. cm°C for the axial thermal conductivity of the fiber. The value of k_1 measured on the unidirectional "Thornel" 25 composite is approximately 1/3 the predicted value based on 0.2 for the fiber conductivity. The axial thermal conductivity of the "Thornel" 25 fiber is not expected to be sufficiently less than that of the

"Thornel" 40 fiber to account for the discrepancy between the measured and predicted composite values. As expected, the measured thermal conductivity in the direction perpendicular to the laminate, k_3, is approximately the same for both unidirectional and cross-plied composites of equal fiber volume. For "Thornel" 40 composites, the value of 0.0018 was calculated for k_3 through the use of Springer and Tsai's equation(9) for their square filament model[34]; a value of 0.02 was assumed for the transverse thermal conductivity of the fiber. The measured values of k_1 for the cross-plied composites are much less than the values predicted by the rule-of-mixtures. The strong anisotropy in the thermal conductivities of the crossed plies may have caused an error in the measured values. Further studies on predicting the thermal conductivity are reported in Section VIIIE.

Thermal Expansion. The values of the coefficient of thermal expansion parallel to the fibers, α_1, measured on unidirectional "Thornel" 25 and 40 composites are +0.4 and $-0.7 \times 10^{-6}/°C$. The negative value is due to the negative coefficient of expansion of the fiber (approximately $-1 \times 10^{-6}/°C$) near room temperature and to the high fiber content and high fiber modulus of the "Thornel" 40 composites. The values of α_1 predicted through the use of the rule-of-mixtures and strain compatibility[35] are $+0.57$ and $-0.51 \times 10^{-6}/°C$ respectively. The differences between the measured values of α_1 and α_2 for the cross-plied composites (α_1 should equal α_2) are probably due to experimental difficulties associated with non-uniform strain within the composite. The predicted values are +3.8 and +0.44 for the "Thornel" 25 and 40 cross-plied composites, respectively; the agreement between measured and predicted values, on an absolute rather than a percentage basis, is relatively good.

SECTION VII

DESIGN DATA STUDIES AND SIMPLE ELEMENT TESTING ON FIBER COMPOSITES

The development of theoretical methods for reliably predicting design data of fiber composite materials is a difficult task, and the attainment of satisfactory methods for use in immediate applications is highly uncertain. In the interim, fundamental design data and the response of new composite systems to destabilizing and dynamic loading environments is being obtained from empirical formulations based on experimental investigations. These data will be used subsequently in correlative studies with analytical prediction. Efforts to establish tests for accomplishing this goal were expanded during this report period.

The evaluation of the split-D test for NOL rings and the subsequent development of an improved ring tensile test are reported in Section VII A. A study of flat tensile specimen sizes and shapes and the interpretation of data are presented in Section VII B. Buckling tests on fiber composite plates are described in Section VII C. An extensive experimental investigation on the four point twist test is discussed in Section VII D. A study of the steady state dynamic response of plates, which parallels the buckling studies reported in Section VII C, is described in Section VII E. A description of the composite stringer testing program and a summary of the resulting experimental data obtained are presented in Section VII F. Section VII G contains a description of the test program and a graphical presentation of the results for crippling tests on fiber composite panel elements. Section VII H describes an acoustic fatigue resistance test program conducted on advanced composites.

A. Tensile Test Studies on NOL Rings

(Professors Goble and Kicher and Mr. F. Campbell)

Unidirectionally reinforced fibrous composites are the fundamental building blocks for the design of simple components. Reliable strength and stiffness data on unidirectional composites are necessary for a rational design proceedure.

When a substantial percentage of the fibers in a reinforced composite are colinear with the load, the fiber fails in a brittle manner. In this instance, the initiation of failure is heavily dependent upon the peak stress caused by the applied load and the distribution of flaws. A tensile test of such a composite should induce a uniform tensile state over a substantial portion of the specimen. A photoelastic investigation of the split-D tensile test was conducted to determine the presence and amount of bending which can be viewed as a linearly varying tensile stress distribution. A light weight split-D fixture, for use in the polariscope, was constructed and is shown in Figure 143. Photoelastic specimens to simulate both the 1/16" and 1/8" thick NOL rings were fabricated, annealed and dried. Figure 144 shows the photoelastic stress distribution for the entire specimen at a strain simulating that of failure for a reinforced composite. The fringes between the split -D and a point over the load are caused by friction between the ring and the fixture. The fringes in the vicinity of the split indicate the presence and intensity

Figure 143. Polariscope Loading Fixture.

Figure 144. Photoelastic NOL Ring Specimen.

Figure 145. Photoelastic Stress Distribution in the Vicinity of the Splint.

of bending. Figure 145 is a closeup of the fringe pattern in the vicinity of the split at the same load intensity. The tensile stress varies by a factor of five from inside the ring to the outside. Since brittle failure is predominantly a point phenomenon, this test is unsatisfactory for testing fibrous composites. These observations become more pronounced as the modulus and strength of the reinforced composite increase. A tensile test which produces a more uniform state of stress is needed for high performance composites.

A hydraulically loaded NOL ring would produce a more uniform state of tensile stress. However, the problems associated with seals, strain measurements, and safety led to the development of a new test device.

The new test fixture induces a tensile load into an NOL ring through contact with a ring shaped rubber insert. The insert expands against the test ring when subjected to a longitudinally compressive load, due to the Poisson's expansion of the rubber. Figure 146 is a schematic of the test device showing the loading piston, the rubber insert, the test ring, and the restraining rings.

Several difficulties encountered in the development of this test are summarized below. The rubber inserts were first cast in a mold using a room temperature vulcanizing material. Although this material was adequate for testing 1/16 inch thick rings (see Figure 147), the rubber underwent excessive permanent deformation during the testing of a 1/8 inch thick ring. Bell Aerosystems then recommended a material (Neoprene Elastromer 17942, Goodyear Tire and Rubber Co.) which they use in a sheet forming process. This material proved to be superior. A 1/8-inch-thick ring tested to failure is shown in Figure 148.

During the test, the retainer rings must expand at approximately the same rate as the test ring; otherwise, a variation of the deformation and stress distribution will occur in the axial direction in the test specimen. If the stiffnesses of the retainer rings are approximately matched (something less than an order of magnitude), a uniform stress state will be established in the test specimen. Since tensile specimens of varying modulus and strength are to be tested, several sets of rings must be available and calibrated.

Finally, there was a tendency for the top retainer ring to shift vertically during the test, particularly at higher loads. By fastening the top ring to the base of the test fixture, this problem could be alleviated. The final assembled test fixture is shown in Figure 149 and the disassembled component parts are shown in Figure 150.

Several steel specimens have been instrumented and tested in order to determine experimentally the relationship between the axial load applied to the test device and the load in the ring specimen. The results obtained were in agreement with the analytical predictions for a thin ring under internal pressure once a small amount of load has been applied to the specimen. The irregularities in this initial loading region seemed to be caused

by the initial irregularity of both the test specimen and the rubber insert. Upon application of subsequent load, the load-strain curves were virtually linear and the stress-strain curves gave the known modulus of the steel calibration rings. Modulus data taken from this test must therefore be derived from data at loads above this initial loading region. No steel specimens were tested to failure but rather a limited number of carbon specimens were failed while the device was being developed. Photoelastic specimens will be examined in this test device using the frozen stress technique at strains simulating those of failure in graphite fiber composites. These photoelastic studies will disclose any irregularities in stress distribution causing deviations from a pure tensile test and will also serve to validate the calibration curves upto failure.

A carefully planned series of tests comparing the results of tensile tests using the split-D and the rubber insert device will be conducted. Union Caribde Corporation has fabricated pairs of near-identical NOL ring specimens to be used in this parallel study to substantiate the validity of this new test method for unidirectional composites.

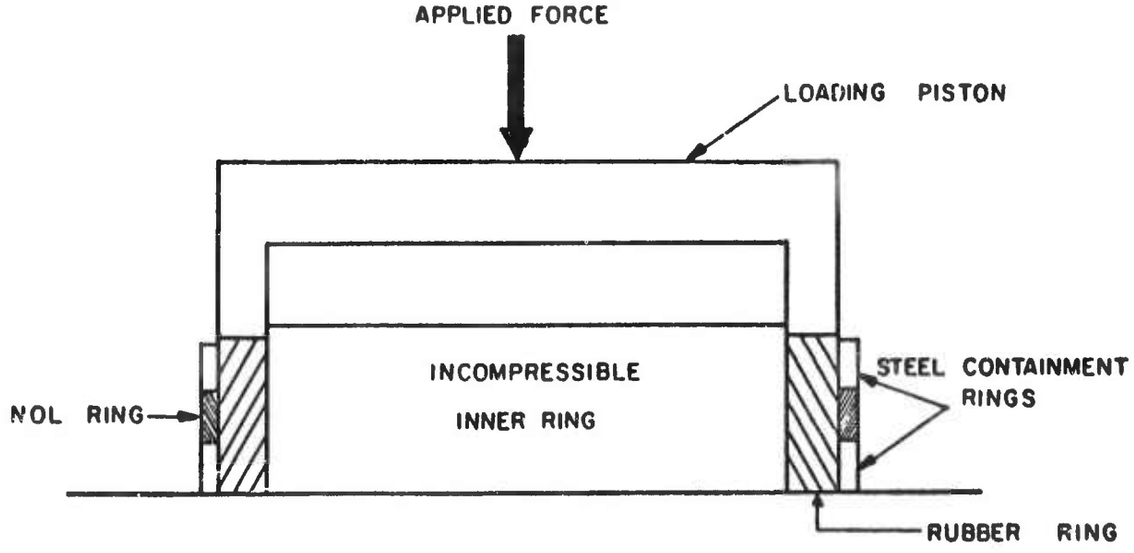

Figure 146. A Mechanical Fixture for a Uniform Tensile Loading of Standard NOL Rings.

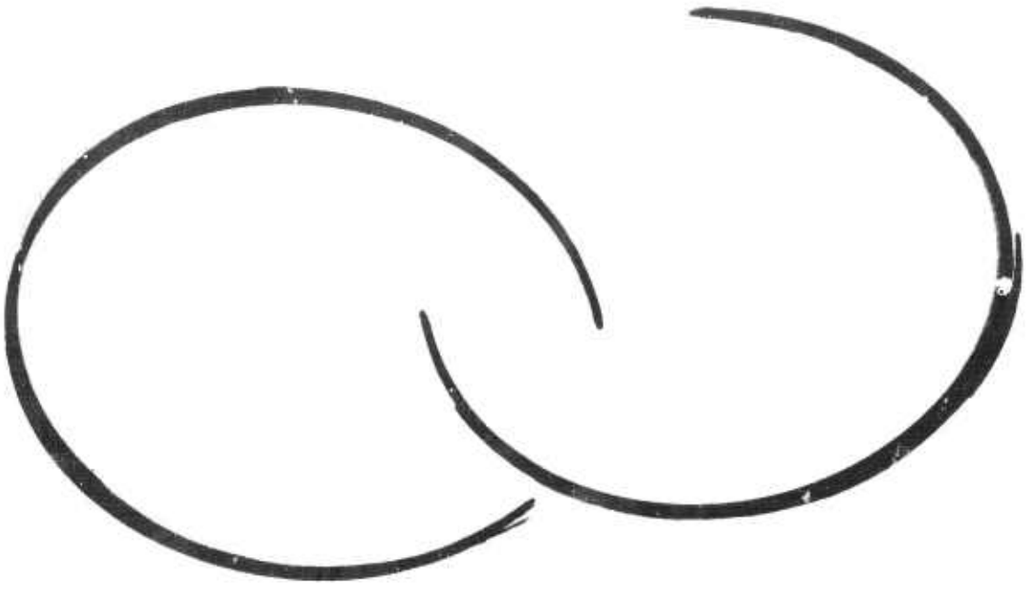

Figure 147. NOL Ring (1/16 Inch Thick) Specimen.

Figure 148. NOL Ring (1/8 Inch Thick) Specimen.

Figure 149. Assembled Rubber Insert Tensile Test Device.

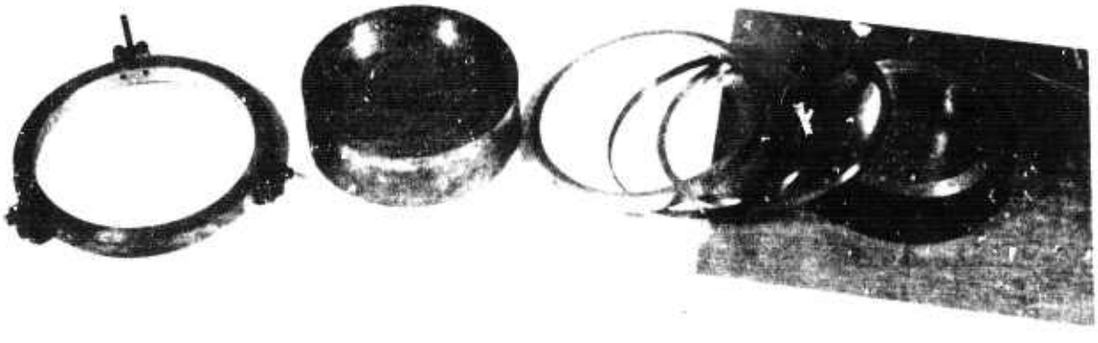

Figure 150. Component Parts of the Rubber Insert Tensile Test Device.

B. Coupon Tensile Tests on Fiber Composites
(Professor Kicher and Mr. C.-H. Wu)

1. Effect of Specimen Shape

The objective of this work is to obtain the modulus of elasticity, ultimate strength, and the Poisson's ratio by the uniaxial tensile test. Since the test specimens are made of composite materials, an optimum shape of the test specimen had to be selected for these particular materials. The experimental work conducted as part of this investigation was limited to tensile specimens of both the cross-ply and angle-ply configurations. The specimens shown in Figures 151 and 152 are all cross-ply specimens. Various shapes have been investigated for these constructions.

Type I of the ASTM Standards with radius of the fillets varying from 1 to 3 inches was tried. It is known that the stress concentration in a circular fillet is inevitable. This stress concentration caused premature failure in the fillet, as shown in Figure 151.

A shape analogous to the profile of a hydraulic flow through an orifice,[36] shown in Figure 152 was tried next. A photoelastic investigation with isotropic material was conducted using this shape of fillet. The results shown in Figure 153 indicate that there was no stress concentration in the fillet of the isotropic model. However, a series of tensile tests on composite specimens showed that the specimens failed outside the gage section.

A new shape of the tensile specimen was then developed. The hyperbolic curve

$$y = \left(\frac{B}{A}\right)\left[A^n - (A-x)^n\right]^{\frac{1}{n}} \qquad \text{(VII B-1)}$$

with various exponents n and coefficients A and B has been tried. The curve with A = 2.0, B = 0.5, and n = 0.75, gave a tensile specimen that did not consistently break in the fillet. The Federal Test Standards Method 1011, Type II has also been investigated. The results were in fair agreement with the results from the hyperbolic fillet test specimen.

The shape with hyperbolic fillet was chosen for the final test specimen. Type II of the Federal Test Method Standards will also be tested for the purpose of comparison A series of trial tests on the glass fiber specimens has been completed, and the testing on the carbon composite specimens has been started.

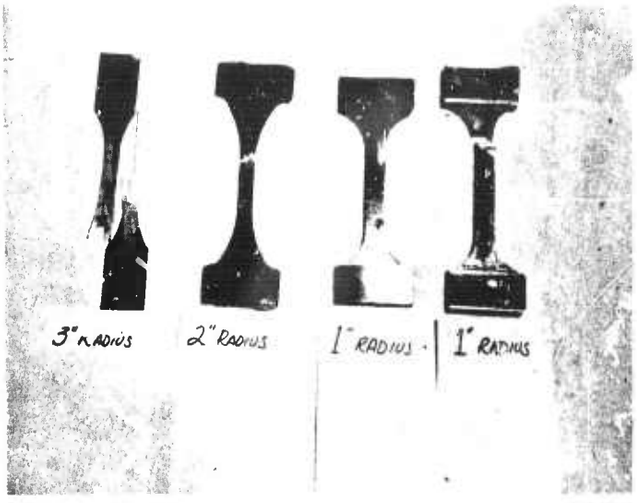

Figure 151. Tensile Specimens with Circular Fillets of Various Radii.

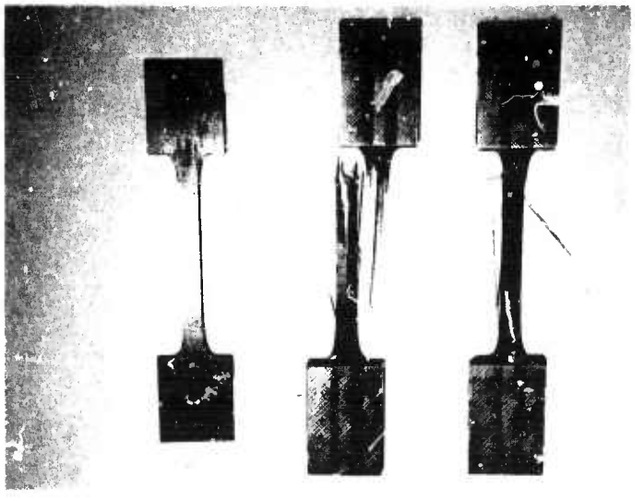

Figure 152. Tensile Specimens with Isotensoid Fillets.

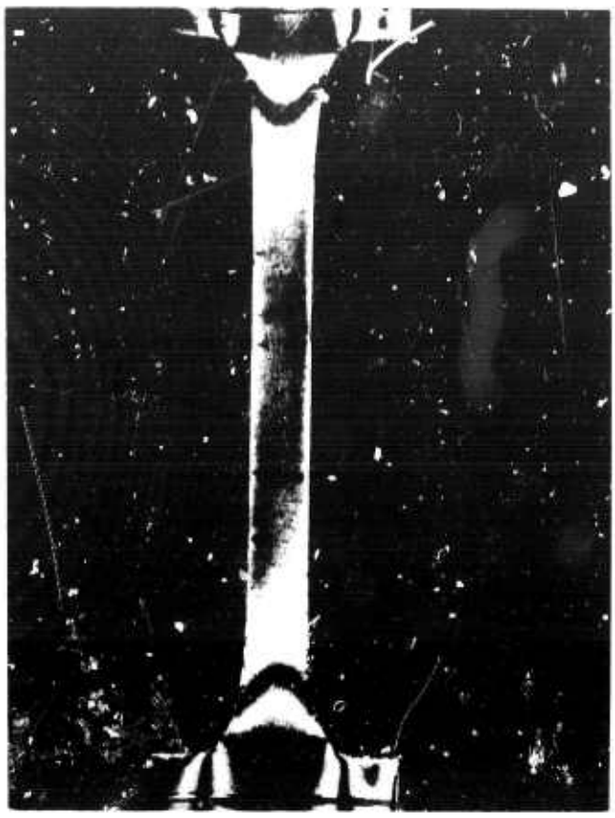

Figure 153. Photoelastic Stress Distribution of an Isotensoid Specimen.

2. Effect of Gauge Configuration on Properties Measured by Off-Axis Tensile Specimens.
(O. L. Blakslee, Union Carbide)

A series of measurements has been made to determine the variation of tensile stress at failure with gauge-section size and shape. The type A specimen shown in Figure 154 illustrates the configuration for the "narrow-gauge" specimens, i.e., specimens having no lateral restraint at the edges and having many fibers that run from one edge of the gauge section to the other. The Type B specimen shown in Figure 154 illustrates the shape of the "wide-gauge" specimens with few fibers ending in the gauge section (although the gauge length is not well defined, the length is small compared to the width).

Preliminary tests using the Type A specimen were made on a 3-ply (0°, 90°) plate fabricated from "S" glass and ERL 2256/MPDA resin; the specimens were cut at 45°. Figure 155 shows the tensile stress at failure as a function of the gauge width. Similar data are shown in Figures 156, 157, and 158 for "Thornel" fiber/ERL 2256 composites having lay-ups 3(90°, ±60°), 4(45°, -45°, -45°, 45°), and 4(10°, -10°, -10°, 10°), respectively; the Type A specimens were cut at 0°. In Figure 157, the low strength of the 2.5-inch wide specimen is thought to be due to either a faulty test or to a nonhomogeneity in the material. Stress-strain curves obtained for these three plates were not significantly different for specimens with different gauge widths.

It had originally been hoped that the curves of tensile strength versus gauge width would asymptotically approach a maximum strength which could be considered the intrinsic material strength. With the possible exception of the 4(10°, -10°, -10°, 10°) data, no such behavior was found; and it is concluded that at least for the specimens investigated, the uniaxial tensile strength must be treated as a function of the size of the region under stress.

A second attempt to measure the strength of angle-ply composites was made with the Type B specimen (i.e., with the wide-gauge specimen). Results for four "Thornel" composites are given in Table LIII. Strengths obtained with a 1/4-inch wide Type A(narrow-gauge) specimen are also included for comparison. The wide-gauge strengths are greater than the corresponding narrow-gauge strength in every case (in one case, by a factor of 8). Although it was known that the Type B specimen does not produce a homogeneous unidirectional tensile stress in the gauge section, it was hypothesized that this specimen might give a useful approximation to the intrinsic material strength. Comparison of the wide-gauge strengths of Table LIII with the curves in Figures 156, 157, and 158 casts doubt on the validity of this hypothesis. Some composite strengths predicted at Bell Aerosystems by the procedures discussed in Section VIII D are listed in Table LIII. On the whole, the predicted values are in better agreement with the narrow-gauge strengths than with the wide-gauge strengths; a result which casts further doubt on the hypothesis that the wide-gauge strengths are a useful measure of uniaxial tensile strengths.

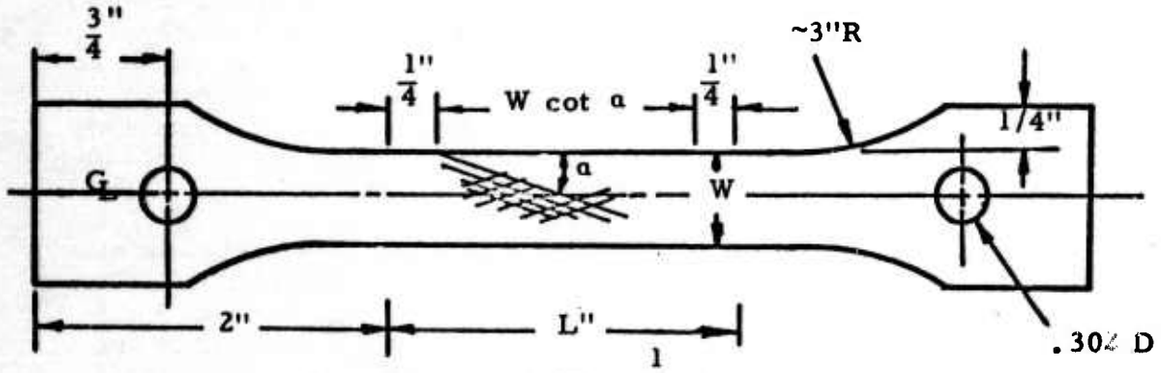

L = Greater of 4W or $\frac{1}{2}$ + W cot α

TYPE A

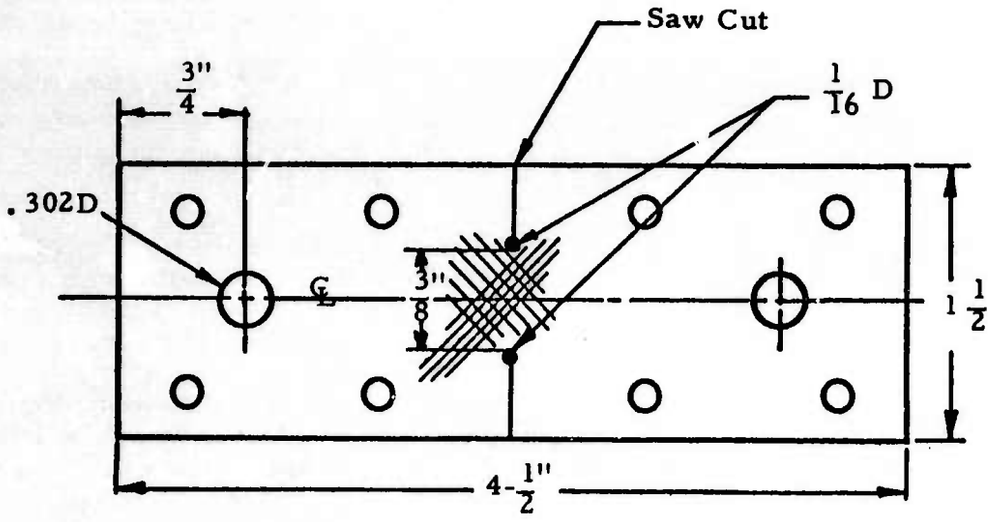

N-17397

Figure 154. Tensile Test Specimens Used to Investigate the Influence of Gauge Section Size and Shape on Tensile Strength and Moduli Measurements on Fiber Composite Plates.

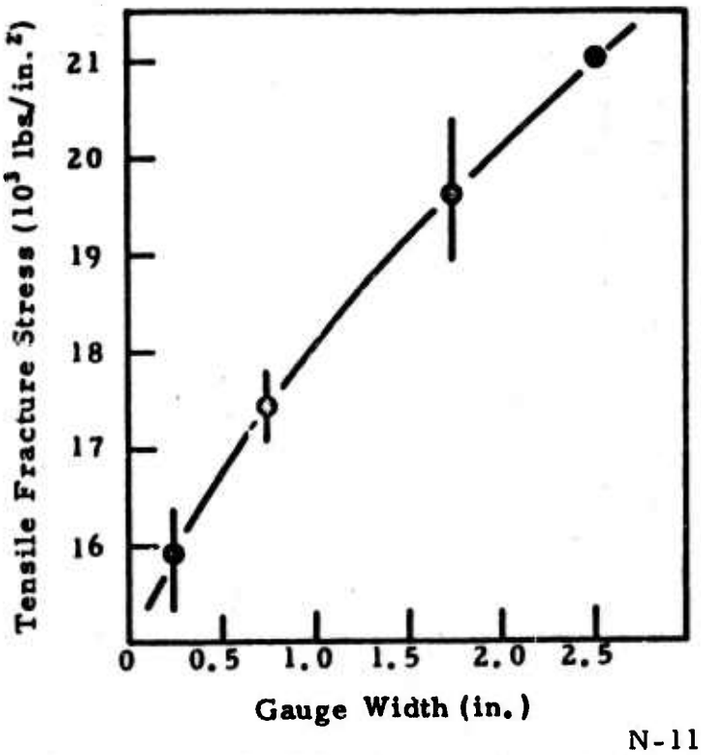

N-11412

Figure 155. Variation of Tensile Stress at Failure with Gauge Width of "S" glass, Epoxy-Resin Composite, 3-ply (0°, 90°) Lay-Up. Bidirectional Fibers Oriented at ±45° to Specimen Axis.

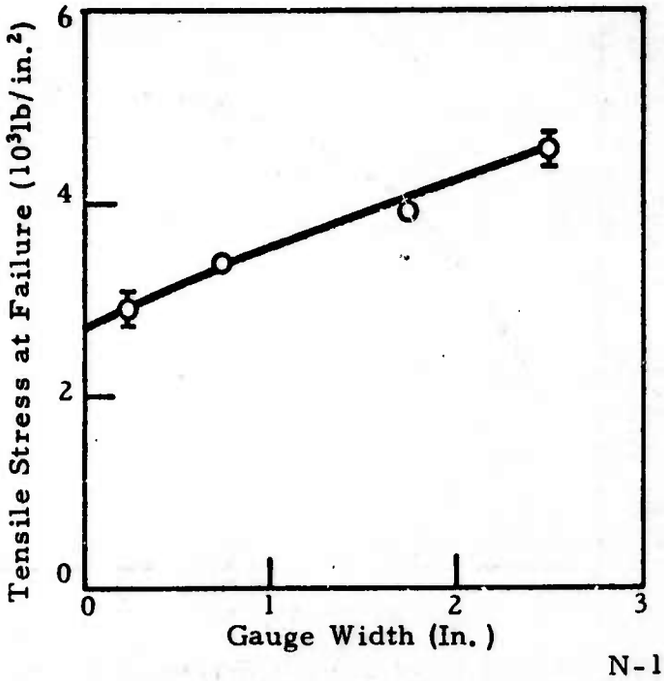

N-17263

Figure 156. Variation of Tensile Stress at Failure with Gauge Width of "Thornel" 25/ERL 2256 Plate P25-13, 3-ply (90°, +60, -60°) Lay-Up. Test Specimens Oriented at 0°.

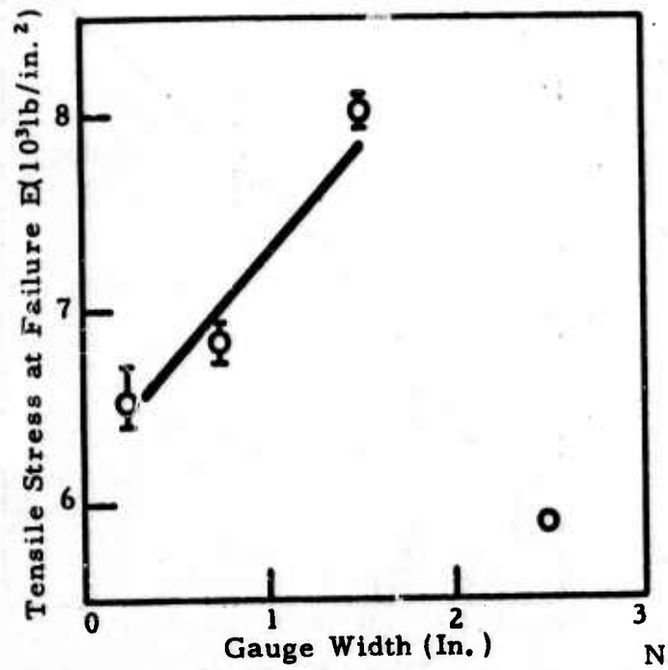

Figure 157. Variation of Tensile Stress at Failure with Gauge Width of "Thornel" 40/ERL 2256 Plate P40-10, 4-ply (45°, -45° -45°, 45°) Lay-Up. Bidirectional Fibers Oriented at ±45° to Specimen Axis.

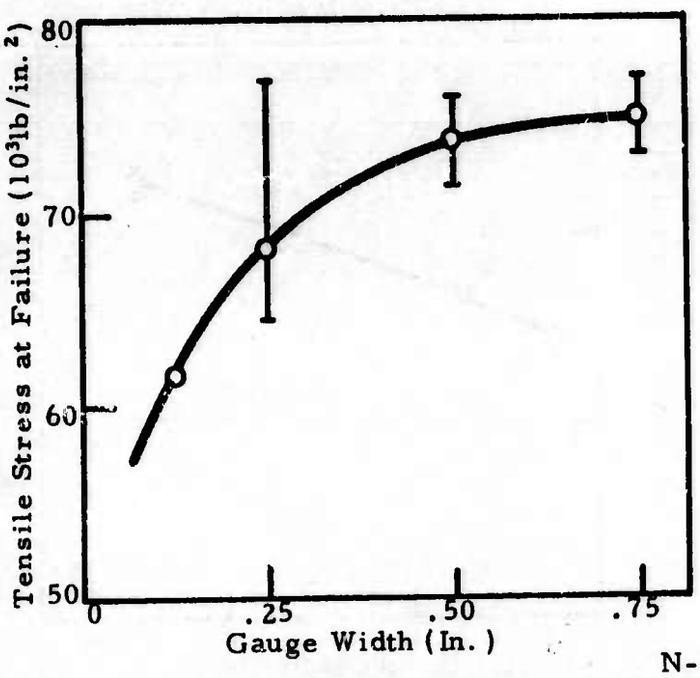

Figure 158. Variation of Tensile Stress at Failure with Gauge Width of "Thornel" 40/ERL 2256 Plate P40-5 and 6, 4-ply (±10°, -10°, -10°, +10°) Lay-Up. Test Specimen Oriented at 0°.

TABLE LIII

TENSILE STRENGTHS OF "THORNEL" FIBER/ERL 2256 PLATES MEASURED WITH NARROW- AND WIDE-GAUGE SPECIMENS

Plate Number	Lay Up Pattern	Test Specimen Orientation	Narrow-Gauge Strength (10^3 lb/in.^{2})	Wide-Gauge Strength (10^3 lb/in.^{2})
P25-2	5(0°,90°)	45°	7.3	20.8
P25-13	3(90°,±60°)	0°	2.9	10.8
P40-10	4(+45°,-45°,-45°,+45°)	0°	6.6	52.7
P40-5	4(+10°,-10°,-10°,+10°)	0°	69.3	99.3

The present results represent only a progress report of a continuing project on the strength of angle-ply composites. Fundamental advances are needed both in test procedures and in analytical concepts for characterizing the strength as a function of the size and shape of the stressed region.

C. Buckling Tests on Fiber Composite Plates
(Professor Kicher and Mr. J. Mandell)

Plate buckling tests are being used primarily as a means of determining the flexural and torsional rigidities of fiber reinforced composite plates. Thus far, the emphasis has been on unstiffened, ten-inch-square plates, though some stiffened plates will be tested in the future. The tests are nondestructive, and the test fixture can accommodate ten-inch-square plates of variable thicknesses with or without initial imperfections or stiffeners.

The plates are subjected to an evenly distributed compressive edge load in one direction. The plates are either simply supported on all four sides or simply supported on the two loaded sides only and free on the other two. As the plate is loaded, the center point deflection is measured with a movable linear variable differential transformer (L.V.D.T.). Any other deflections which might be necessary to determine the mode shape are measured with the same L.V.D.T. If the plate has an initial imperfection, it will deform into some mode shape, usually the first mode, as the load is applied. If the plate is flat, however, it must be perturbed into the correct mode shape as the load is applied. A small constant force acting at the center of the plate is used to achieve this perturbation.

The test fixture originally developed was found to yield results which were in good agreement with theory for the case of only two sides simply supported. For the case of all four sides simply supported, however, the results were found to be in poor agreement with theory, particularly for very thin plates. Two basic reasons were found for this inaccuracy. First, the load shifted toward the outside edges as the deflection increased until the load was no longer evenly distributed. Second, the supporting knife edges bonded to the edges of the plate tended to add stiffness to the plate, since they resisted any variation in the rotation along an edge.

Recently, a new test fixture (see Figures 159, 160, and 161) has been developed which corrects these problems and gives accurate results for the torsional as well as the flexural rigidities. The new test fixture applies the load through a number of independent, spring loaded pistons so that the load remains evenly distributed throughout the test. The supports have also been altered so as to minimize their stiffening effect.

Accurate theories are available to describe the buckling of orthotropic plates with the fibers running colinear with the edges. For the case of the loaded sides simply supported and the other two sides free, the governing differential equation is

$$D_{11} \frac{\partial^4 w}{\partial x^4} + N_x \frac{\partial^2 w}{\partial x^2} = 0 \qquad \text{(VII C-1)}$$

where the plate is loaded in the one direction. If the deflection pattern is assumed to be

$$w = A_n \sin \frac{n\pi x}{a} . \qquad \text{(VII C-2)}$$

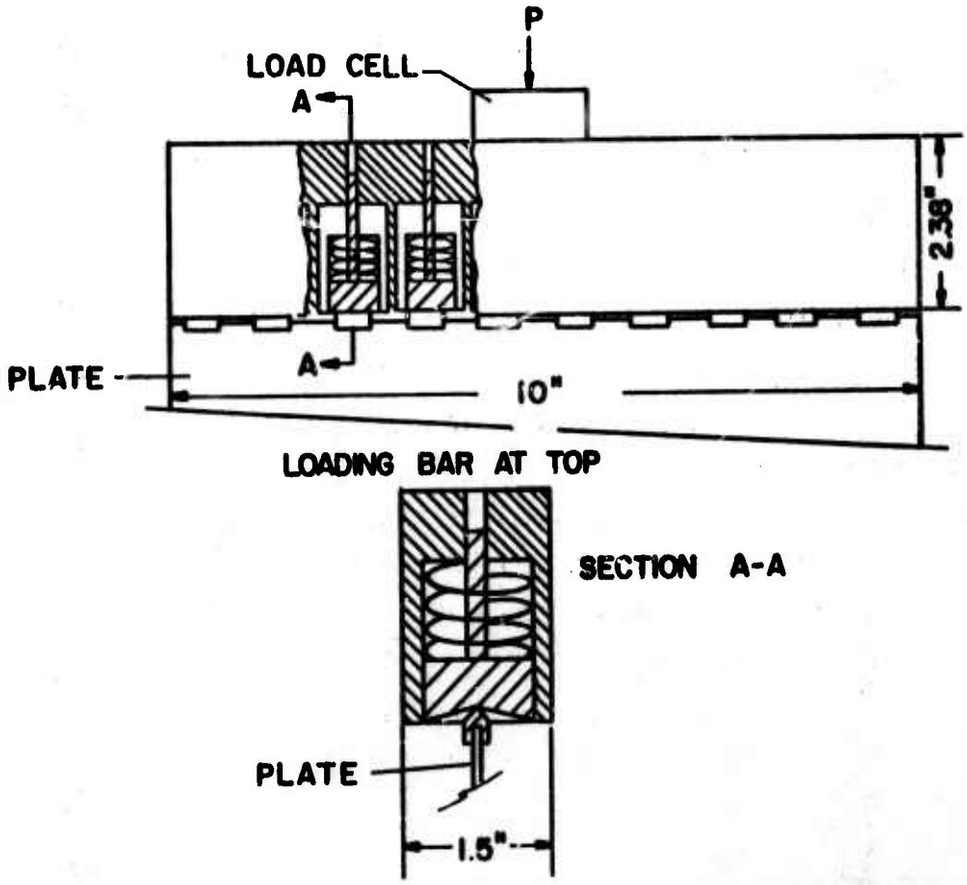

Figure 159. Loading Head for Plate Buckling Tests.

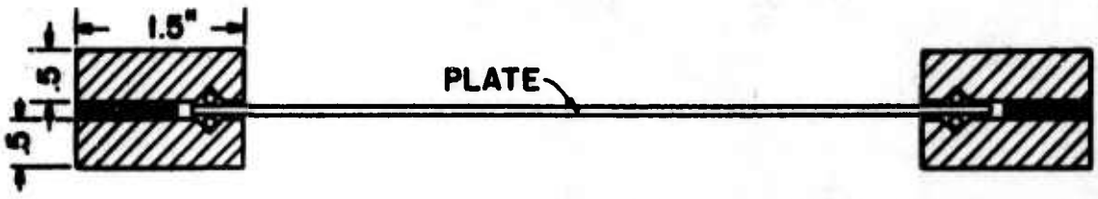

Figure 160. Side Supports for Plate Buckling Tests.

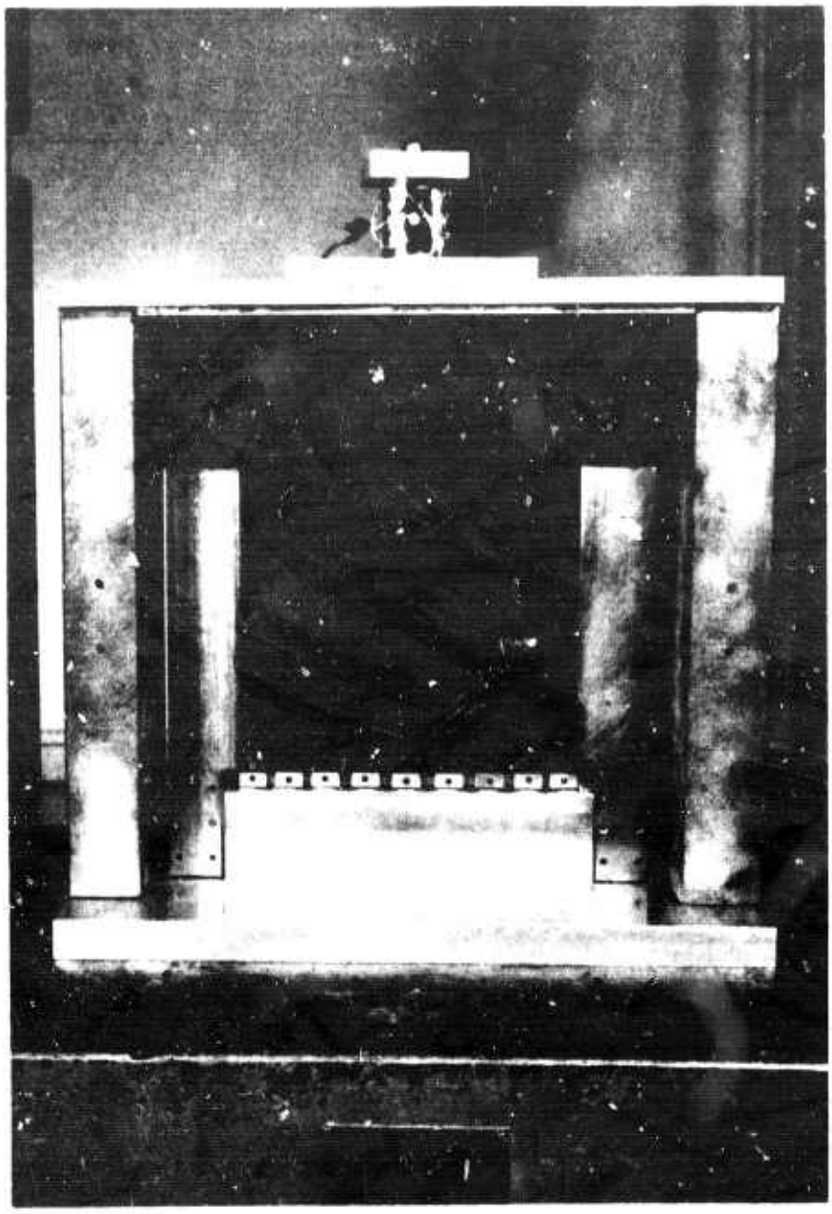

Figure 161. Assembled Buckling Test Fixture with a Carbon Plate in Place.

Then the critical load for the first mode is

$$(N_x^1)_{cr} = D_{11}\pi^2/a^2. \qquad \text{(VII C-3)}$$

Or, if the plate is turned 90° and loaded in the two direction, the critical load is

$$(N_x^2)_{cr} = D_{22}\pi^2/b^2 \qquad \text{(VII C-4)}$$

where a and b are the lengths of the sides of the plate. Thus, if the critical loads in the two directions can be determined experimentally, the bending stiffnesses can be determined as follows

$$D_{11} = \frac{a^2 (N_x^1)_{cr}}{\pi^2}$$

$$D_{22} = \frac{b^2 (N_x^2)_{cr}}{\pi^2} . \qquad \text{(VII C-5)}$$

If all four sides of the plate are simply supported, the differential equation becomes

$$D_{11}\frac{\partial^4 w}{\partial x^4} + 4 D_{16}\frac{\partial^4 w}{\partial x^3 \partial y} + 2(\nu_{21} D_{11} + 2 D_{66})\frac{\partial^4 w}{\partial x^2 \partial y^2} + 4 D_{26}\frac{\partial^4 w}{\partial x \partial y^3}$$

$$+ D_{22}\frac{\partial^4 w}{\partial y^4} + N_x\frac{\partial^2 w}{\partial x^2} = 0. \qquad \text{(VII C-6)}$$

For the special case where the fiber directions are colinear with the sides, the differential equation becomes

$$D_{11}\frac{\partial^4 w}{\partial x^4} + (\nu_{21} D_{11} + 2 D_{66})\frac{\partial^4 w}{\partial x^2 \partial y^2} + D_{22}\frac{\partial^4 w}{\partial y^4} + N_x\frac{\partial^2 w}{\partial x^2} = 0. \qquad \text{(VII C-7)}$$

If a deflection pattern of the form

$$w = A_{mn} \sin\frac{m\pi x}{a} \sin\frac{n\pi y}{b} \qquad \text{(VII C-8)}$$

is assumed, then for the first mode the critical load will be

$$(N_x)_{cr} = \frac{\pi^2\sqrt{D_{11}\,D_{22}}}{b^2}\left[\sqrt{\frac{D_{11}}{D_{22}}} + \frac{2(\nu_{21}\,D_{11} + 2D_{66})}{D_{11}\,D_{22}} + \frac{D_{22}}{D_{11}}\right] . \qquad \text{(VII C-9)}$$

Since D_{11} and D_{22} are known either from theory or from the test with only two sides supported, D_{66} can be determined if the critical load is known.

For the tests to be nondestructive, it is necessary to predict the buckling load without actually buckling the plate. Southwell developed a technique for predicting the buckling load of columns, and this technique can be applied to a plate with the loaded sides simply supported and the other two sides free by considering the plate to be a wide column. If the plate has a first mode imperfection, the deflection pattern can be assumed to be

$$w = w_0 + w_1 = \frac{a_1}{1-\alpha} \sin \frac{\pi x}{a} \qquad \text{(VII C-10)}$$

where $w_0 = a_1 \sin \pi x/a$

$$w_1 = a_1 \left[\frac{1}{1-\alpha} - 1\right] \sin \pi x/a. \qquad \text{(VII C-11)}$$

At $x = a/2$

$$w_1 = \frac{\alpha a_1}{1-\alpha} = \delta$$

$$\alpha = N_x/(N_x)_{cr}. \qquad \text{(VII C-12)}$$

Thus,

$$\frac{\delta}{N_x} = \frac{1}{(N_x)_{cr}} (\delta + a_1) \qquad \text{(VII C-13)}$$

and a plot of $\frac{\delta}{N_x}$ vs δ will yield a straight line with slope $\frac{1}{(N_x)_{cr}}$ and an intercept of a $a_1/(N_x)_{cr}$.

This technique can be further applied to an isotropic plate with all four sides simply supported and a first mode imperfection. Here, the deflection will be given by

$$w = w_0 + w_1 = \frac{a_{11}}{1-\alpha} \sin \frac{\pi x}{a} \sin \frac{\pi y}{b} \qquad \text{(VII C-14)}$$

where, at $x = a/2$, $y = b/2$,

$$\alpha = \frac{N_x}{\frac{\pi^2 D}{2}\left[1 + \frac{a^2}{b^2}\right]^2} = \frac{N_x}{(N_x)_{cr}}$$

$$\delta = a_{11}\left[\frac{1}{1-\alpha} - 1\right]. \qquad \text{(VII C-15)}$$

And, as before,

$$\frac{\delta}{N_x} = \frac{1}{(N_x)_{cr}}(\delta + a_{11}). \qquad \text{(VII C-16)}$$

As previously mentioned, tests with only two sides supported show very good correlation with theory for all cases. Tests using the new test fixture with all four sides simply supported display a characteristic and reproducible plot of δ/N_x vs δ. On many plates, the first few points are quite random and reflect the lack of a well-defined mode shape. The middle portion of the curve, however, is the well-defined straight line described in the previous paragraph. After the deflection reaches about one-third to one-half the thickness of the plate, bending becomes prominent and the curve tails off from the straight line. This behavior is reflected in the plot of N_x vs δ, which should be a rectangular hyperbola with asymtotes at zero deflection and at $(N_x)_{cr}$, but which is not well defined in the beginning and tends to become linear near the end.

Representative test curves are presented in Figures 162 through 167 for one aluminum and two Thornel 25 fiber reinforced composite plates. The fiber volumes for the composite plates were not known exactly, but it was believed that the 9(0,90) plate had a fiber volume of between 40 and 42 percent, whereas the (0,90,90,0) plate had a fiber volume of between 48 and 50 percent. All tests were run on the new test fixture with sides simply supported. At the time the tests were run, however, the linear variable differential transformer was not used to measure the deflections. Instead, a temporary dial indicator was used which may have introduced error. Also the (0,90,90,0) plate was not loaded in the usual manner, causing considerable friction as witnessed by the variation of the data from a smooth curve. Only enough data to define the curve are included for the (0,90,90,0) plate; all data are included for the other plates. Theoretical buckling loads found using the stiffnesses calculated by T.L. Chao and these are listed in Table LIV along with the experimental results.

Efforts to determine if this buckling test is truly nondestructive have been limited to low magnification observations during and after the tests. No strain gages were applied to the fibrous composite panels to determine if the stress-strain curve reached its knee. The strongest point in support of this test is that the experiments were repeated approximately ten to twelve times for each panel with no apparent delamination and no degradation of the buckling load.

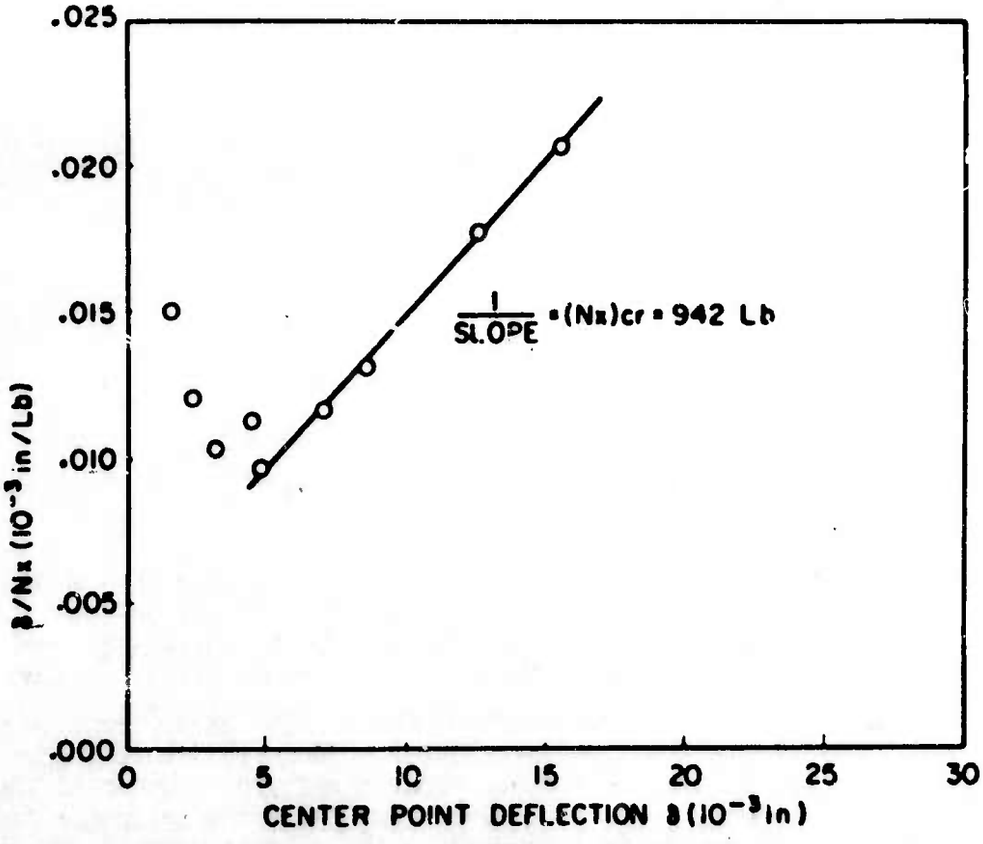

Figure 162. Center Point Deflection Divided by Load vs. Center Point Deflection for an Aluminum Plate (t=0.063) Under Edgewise Compression.

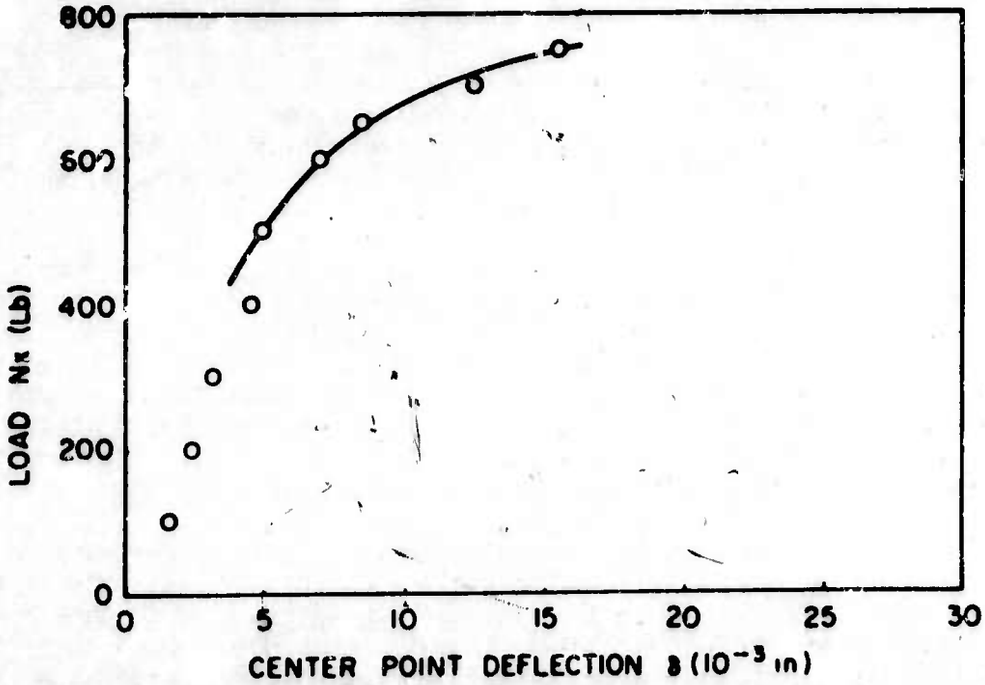

Figure 163. Load vs. Center Point Deflection for an Aluminum Plate (t=0.063) Under Edgewise Compression.

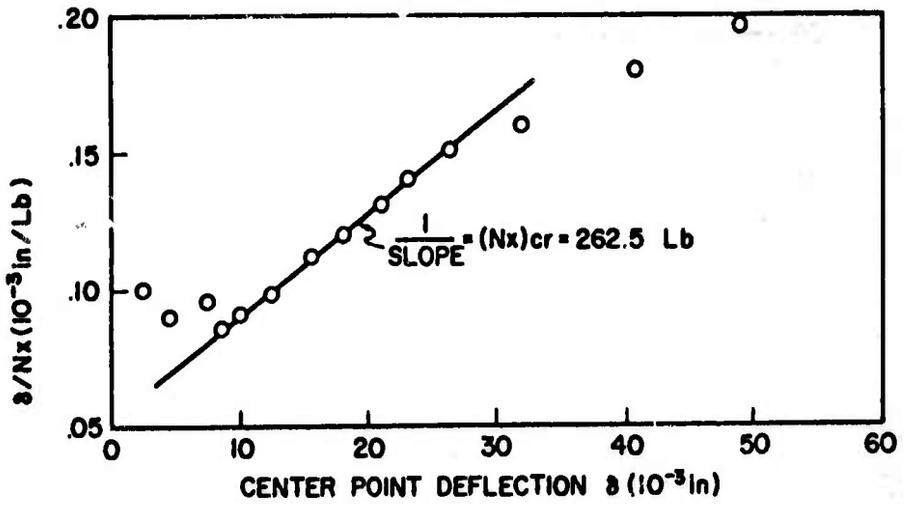

Figure 164. Center Point Deflection Divided by Load vs. Center Point Deflection for a (0,90,90,0) Graphite Fiber Composite Plate Under Edgewise Compression.

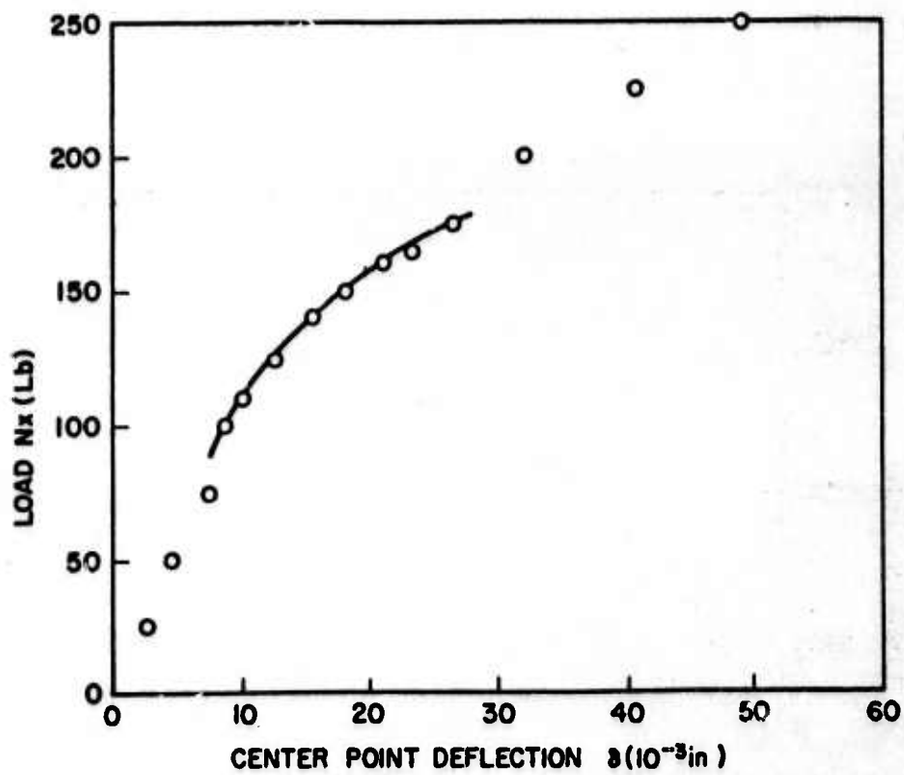

Figure 165. Load vs. Center Point Deflection for a (0,90,90,0) Graphite Fiber Composite Plate Under Edgewise Compression.

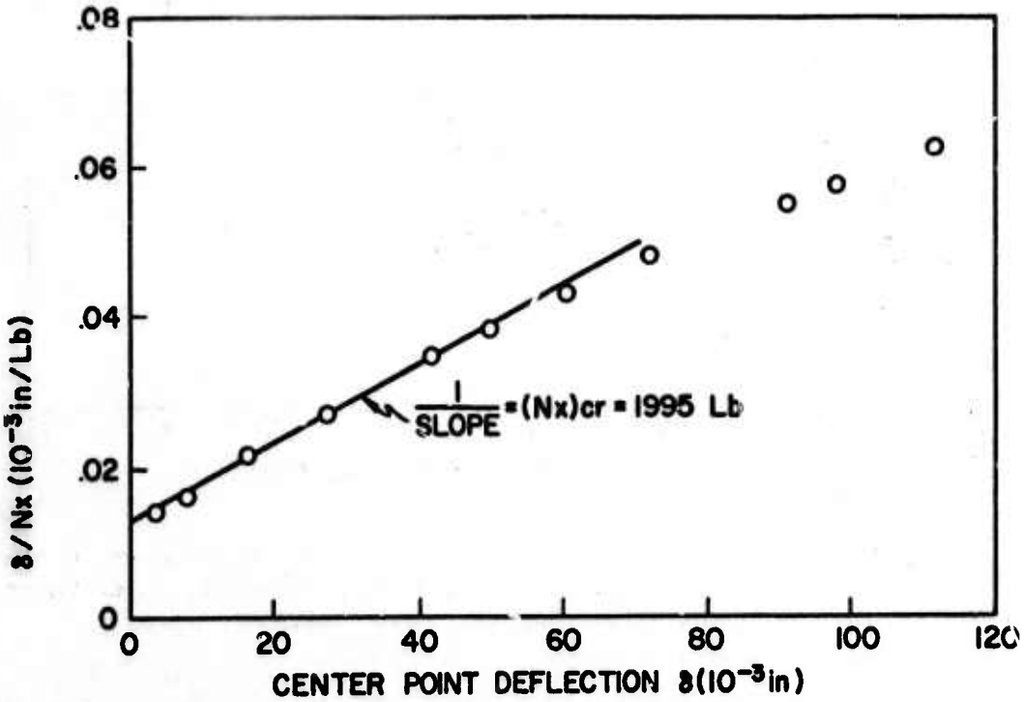

Figure 166. Center Point Deflection Divided by Load vs. Center Point Deflection for a 9(0,90) Graphite Fiber Composite Plate Under Edgewise Compression.

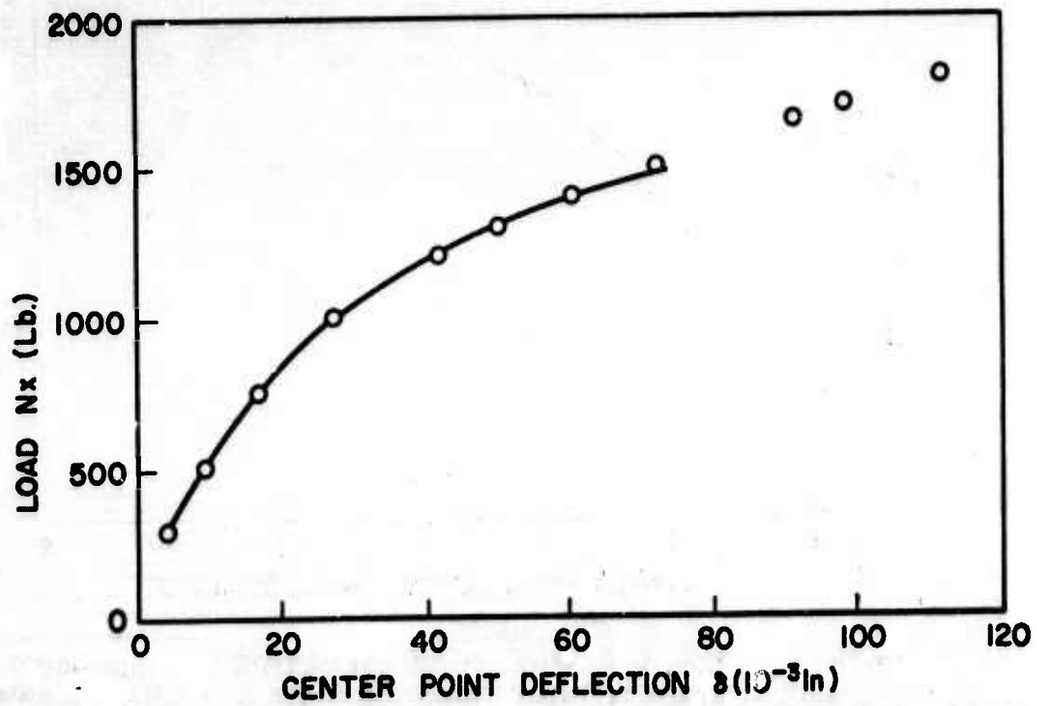

Figure 167. Load vs. Center Point Deflection for a 9(0,90) Graphite Fiber Composite Plate Under Edgewise Compression.

TABLE LIV

THEORETICAL AND EXPERIMENTAL BUCKLING LOADS

		$(N_x)_{cr}$ (lb)		
Material	Configuration	Theory	Experiment	Error %
6061-T6 Aluminum	t = .0630"	933	942	1.0
Graphite Fiber Composite	(0,90,90,0)	251(50% vol)	262.5	4.6
Graphite Fiber Composite	9(0,90)	2060(40% vol)	1995	3.1

D. Four Point Twist Test On Fiber Composite Plates
(Professor Goble and Mr. F. Campbell)

The four point twist test has been used extensively to determine the torsional flexural rigidity of orthotropic composite plates. However, several difficulties associated with initial imperfections, nonlinearities, and scatter of results have been reported. An extensive experimental program to study these difficulties and the effects of specimen overhang, length-to-thickness ratio, and methods of loading has been initiated.

A test device[37] which loads the specimens near the corners and measures the twist curvature near the center of the plate is not satisfactory for thin gage composite specimens. The dial indicators used to determine the twist curvature through a finite difference scheme introduce a load, causing a deviation from the desired hyperbolic paraboloidal shape. Although their effects could be included, the desire to retain simplicity in the data reduction led to an alternative loading scheme. A test device which holds two diagonally opposite corners fixed while inducing a known displacement and measures the load at the remaining diagonal corners gives satisfactory results. The desire to read extremely small loads (0.001 pounds) required a flexible load cell which needs only a minor correction in data reduction. Figure 168 is a photograph of this test device styled after the one described by Tsai[38].

So that the effects of specimen length-to-thickness ratio, might be determined, several aluminum and steel plates having a planform dimension of 11" by 11" were tested. The plates were then cut to reduce the planform dimension and the tests repeated. This procedure was repeated several times until the plates were 4" by 4". This method gave a consistant set of data from which the following preliminary conclusions were drawn:

1. Range of length-to-thickness ratio:
   ℓ/t should not be much less than 40 nor much greater than 200;

2. Deflection limitations for a linear load-deflection curve:
   thin plates ($\ell/t \simeq 200$) 1 to 2 plate thicknesses moderate thickness ($\ell/t \simeq 120$) one plate thickness thickplates ($\ell/t \simeq 40$) much less than one plate thickness;

3. Geometric imperfections:
   Thin plates ($\ell/t \simeq 200$) less than a plate thickness; for thin plates with an imperfection exceeding one plate thickness, errors on the order of 20% in the twist rigidity were observed. However, this relationship is not linear, since plates having an imperfection on the order of two plate thickness have been observed to be in error by 300%.

The effects of specimen overhang were also studied both experimentally and analytically. Assuming that the four point test fixture deform the plate into a hyperbolic paraboloid, a uniform state of twisting exists and the strain energy becomes

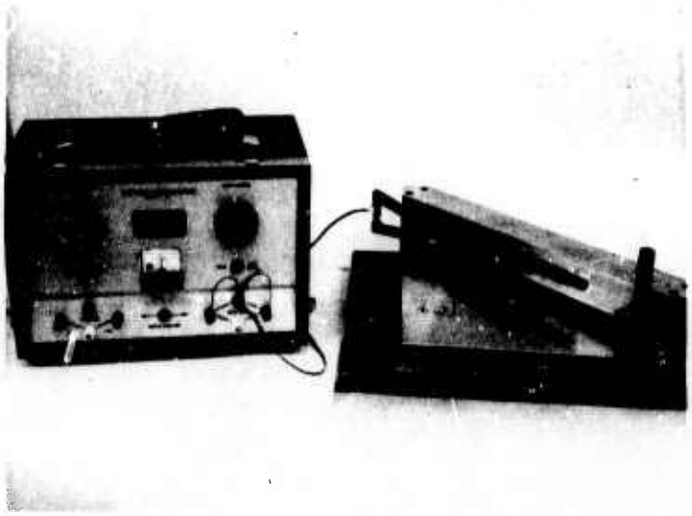

Figure 168. Four Point Twist Test Apparatus

$$U = \int_V 1/2\, G_{xy}\, \epsilon_{xy} dV = \int 1/2\, G_{xy} (\epsilon^{\circ}_{xy} - 2zK_{xy})^2 dxdydz. \quad \text{(VII D-1)}$$

Assuming the membrane shear strain vanishes

$$U = 2D_{xy}\, K_{xy}^2\, A_T \quad \text{(VII D-2)}$$

where

K_{xy} = Twist curvature, $\frac{\partial^2 w}{\partial x \partial y}$

A_T = Total area of the plate

$D_{xy} = \int G_{xy}\, z^2 dz$ = torsional flexural rigidity.

The work done by the external loads can be expressed in terms of the twist curvature as

$$W = K_{xy} \ell_x \ell_y F \quad \text{(VII D-3)}$$

where F is the load at a corner and ℓ_x and ℓ_y are the spans between load points as shown in Figure 169. From the stationary condition on the total energy, the following expression for the torsional flexural rigidity can be established

$$D_{xy} = \frac{A_L F}{4 A_T K_{xy}} . \quad \text{(VII D-4)}$$

Where A_L is ℓ_x times ℓ_y, the area bounded by the four load points. This expression for the flexural rigidity differs from that found in the published literature in that the calculations must be modified by the area ratio A_L/A_T. It arises because of the assumption that the loading induces a uniform state of constant twist curvature throughout the entire plate both within the loading points and within the overhang region. While it is an assumption that this curvature is the same within the loaded area and the overhang, it appears to be a better approximation than neglecting the strain energy of twisting in the overhang region. For example, the testing of a 10 inch square flat aluminum panel with a 1/2 inch overhang on all four sides gave a torsional flexural rigidity which was approximately 20 percent in error when the twisting of the overhang was assumed to be zero. However, the application of the Equation VII D-4 yielded a torsional flexural rigidity within 1 percent of the analytical results. Certainly this assumption of a uniform curvature is not valid for a substantial amount of overhang but it appears to be superior then neglecting the effects of the overhang for most practical experimental tests. This correction for specimen overhang has been verified experimentally for moderate area ratios, on the order of $A_L/A_T = 0.80$.

The more difficult problems of the effects of initial imperfections, causes of the nonlinearities, and the scatter of results have only been partially resolved. At this time, the study has not been completed; thus, only a limited number of results are available and the conclusion is only speculative. There is a strong correlation between an apparent nonlinearity and initial imperfections even for small deformations. Several metal plates of selected thicknesses and random imperfections were loaded in the four-point-twist test device in various configurations. For example, a complete load-deflection curve, for both the positive and negative loads, can be obtained by inverting the plate or rotating it by 90° in its own plane. For metallic test specimens with an initial imperfection greater than a plate thickness and a length-to-thickness ratio greater than 160, the initial slopes of the load-deflection curve have differed by a factor of three. These same plates display a pronounced nonlinearity, bordering on an unstable behavior when the imposed

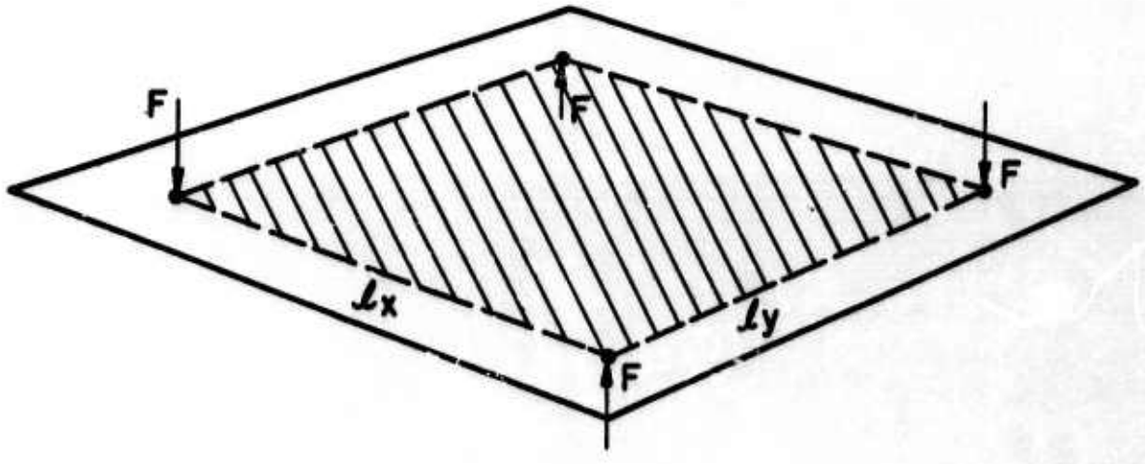

Figure 169. Four Point Load Test Showing the Specimen Overhang.

displacement exceeds two plate thicknesses. This larger displacement phenomenon has been observed analytically by Foye[39]. The discrepancies in slope in the vicinity of the origin of the load-deflection curve indicate that the deformed shape is not a hyperbolic paraboloid as assumed in the analytical development. The response could be some form of shell behavior involving the flexural rigidities. For example, consider a plate with a cylindrical initial imperfection skewed to the sides of the plate. The generatrix of the cylindrical imperfection will lie along the diagonal and be supported by two of the four loading points. The other diagonal will have a circular imperfection and lie at the remaining two loading points. When a load is applied, the straight diagonal will serve as an arch, causing all of the deformation to occur in bending perpendicular to the arch. The torsional mode of response will not be excited in this case and the slope of the load-displacement curve will be some function of the bending rigidity. The effects of other imperfections will be studied to determine the limitations of the four point tests.

E. Static and Dynamic Flexural Tests on Fiber Composites
(Professor Kicher and Mr. Y. Hikami)

Two experimental methods have been studied for determining the rigidities of composite material plates. First, pure static four point bending of long rectangular plates similar to the beam test was used to obtain the flexural rigidities. The results agreed with those obtained by the buckling test; however, this test generally cannot be applied to thin or imperfect plates. Second, a vibration test on square plates in which natural frequencies of plates are found and used to determine rigidities of plates was undertaken. The basic idea of this method is that when the plate is subjected to flexural vibrations with various boundary conditions, the frequencies of the plate maybe obtained. With these experimentally obtained frequencies and theoretically derived relations, the elastic constants of the plate are obtained. For the free vibration of a thin rectangular plate of elastic orthotropic material of constant thickness, the expression for the circular frequency P_{mn} is

$$P_{mn} = \frac{\pi^2}{b^2\sqrt{h\rho}} \left[D_x \left(\frac{mb}{a}\right)^4 + 2D_3 n^2 \left(\frac{mb}{a}\right)^2 + D_y n^4\right]^{1/2} \qquad \text{(VII E-1)}$$

for all four sides simply supported.

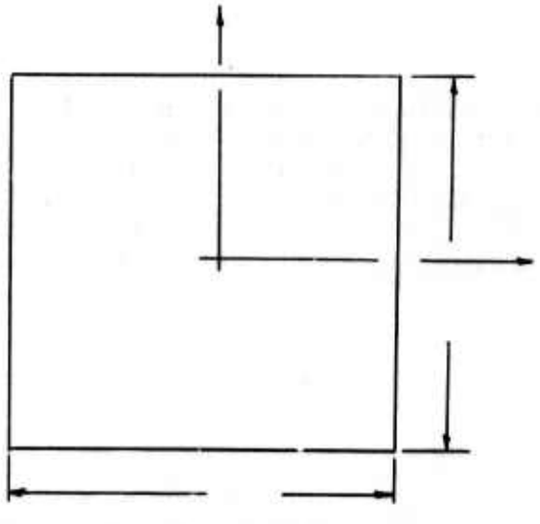

Figure 170. Rectangular Plate Dimensions

where P_{mn} = circular frequency of m-n mode of vibration of rectangular plate

m,n = mode number corresponding to x-direction and y-direction respectively.

D_x, D_y = flexural rigidity of plate in x-direction and y-direction, respectively.

$D_3 = \nu_{xy} D_x + 2D_{xy}$

ρ = mass density

h = thickness of plate

a,b = dimension of plate (see Figure 170).

In these tests, a 10 x 10 inch square plate is subjected to the flexural vibration of a known fundamental mode. The flexural rigidities of the plate are obtained with the boundary condition of two opposite edges being simply supported and other two edges being free. The torsional rigidity is obtained by simply supporting all four edges. In order to determine the fundamental frequency of flexural vibration of the plate, a strain gage will be attached at the center of the plate and the maximum amplitude will be recorded. A Strobe-

light will be used to check that the vibration is a fundamental mode.

One major difficulty encountered was the design of a test apparatus which gives an ideal simply supported boundary condition. The use of rubber as a device for simply supporting the plate edges (Figures 171a and 171b) was tried, and the apparatus was tested with an 8 x 2 x 0.125-inch aluminum plate. The results of the test indicated that the values of flexural rigidity were different (11% for the plate with knife edges (Figure 171a) and 22% for the plate with square corner edges (Figure 171b) as compared with the plate having knife edges which were supported by V-notch grooves (Figure 172). It was concluded that this type of support was not sufficiently accurate.

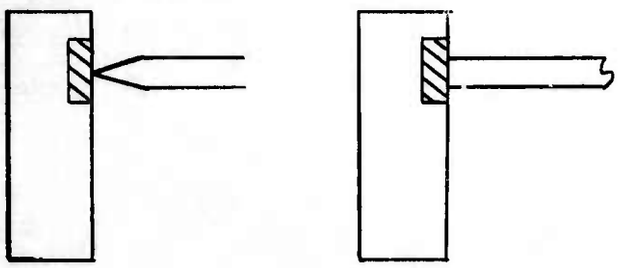

Figure 171. Approximate Simply Supported Edge

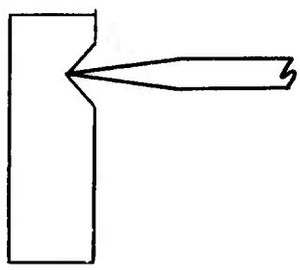

Figure 172. Simply Supported Edge

The test apparatus with roller bearings (Figure 173) was then constructed (see Figure 174). This device has an advantage over the one with the knife edge stiffeners (Figure 175) in that the axes of rotation coincide with the edges of the plate. The effect upon frequency of the moment produced due to the inertia of rods was investigated. The rods are attached to the edges of the plate so that the plate edge lines coincide with the axes of rotation of the rods.

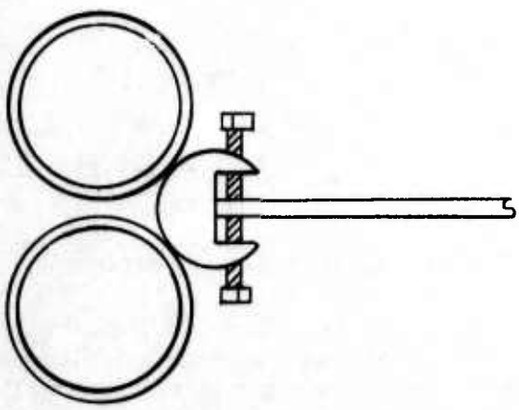

Figure 173. Roller Bearing Supported Edges

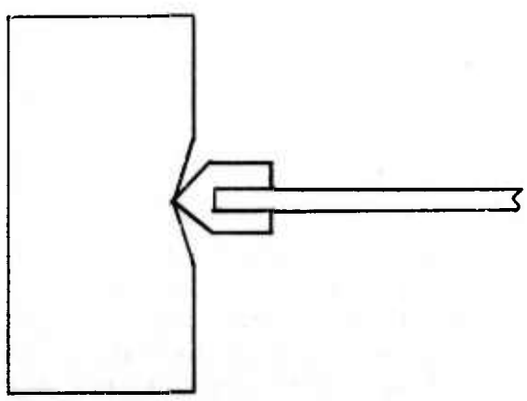

Figure 175. Knife Edge Stiffeners

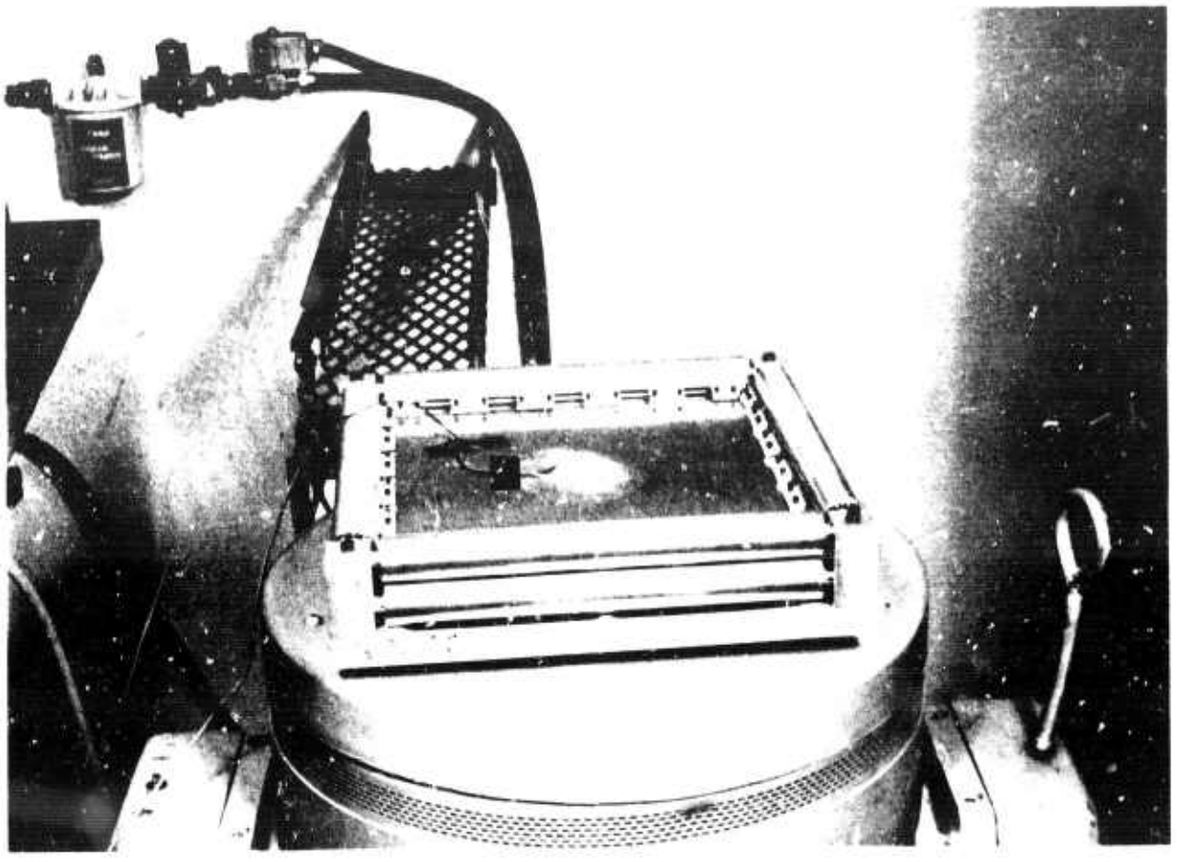

Figure 174. Roller Bearing Supported Plate for Vibration Tests.

The difficulties encountered with this experimental apparatus were:

1. When the plate is subjected to vibration with four sides supported, there is a component of bending moment at the boundary violating the simply supported boundary condition. The bending moment is due to the restraint of variable rotation of the plate edges within its sides with respect to the plate edge lines by both of the torsional rigidity of the rods and same angular displacement for whole length of the roller bearings. There is also a contribution to the bending moment due to the angular inertia of the rods and roller bearings.

2. The attachment of the rods to the plate must be extremely accurate so that when the plate is fitted to the apparatus the rods are in contact with the roller bearings along two lines.

These difficulties may be overcome if, the rods are cut into small pieces, eliminating the bending moment, and an allignment fixture for the attachment of the rods to the plate is constructed.

The test was, in spite of these problems, run on an aluminum plate, and a 3.3% error in the torsional rigidity and a 7.4% error in the flexural rigidity were obtained. The results of the test are not sufficiently reliable, but they do indicate the potentiality of this apparatus to give good results.

F. Tests on Fiber Composite Stringers

1. Angle Bend Tests of L-Shaped Stringers

(O. L. Blakslee, Union Carbide, and W. N. Meholick Bell Aerosystems)

The possible mechanical damage and/or residual stress resulting from bending graphite fibers around corners (such as occur in stringers) has been investigated. A series of L-shaped stringers has been tested to failure in the manner shown in Figure 176 to determine the effects of the sharp curvature at the corner. The fabrication of this series of stringers is described in Section V D4. Three different curvature radii were used: 0.050, 0.100, and 0.200 inch. The samples were approximately one inch in length, and the undeformed moment arms were 0.400 inch. The stringers were of 3-ply (90°,0°,90°) construction, as shown in the inset in Figure 176. The data recorded (see Table LV) were the fracture load per unit-length and the horizontal and vertical deformations at fracture. Since the vertical deflection does not enter the calculation, it was not measured during the tests on the "Thornel" 40 stringers.

The thicknesses and fiber contents of the L-shaped stringers with 0.050-inch and 0.200-inch radii are sufficiently similar that the failure loads per unit-length can be directly compared for both "Thornel" 25 and 40 composites; no significant weakening of the bend is evident for bend radii as small as 0.050-inch. Peak tensile and compressive stresses at the outside and inside surfaces, respectively, of the bend region have been computed by using classical curved-beam theory.[40] The computed stresses given in Table LV, cannot be directly compared with uniaxial composite strengths because the fibers are subjected to two additional stress systems; the flexural prestresses in each fiber due to its being bent and the reactive prestresses of the matrix on the fibers which keep the fibers bent even when the stringer is unloaded. These reactive stresses and their changes as the stringer is loaded are not known. Most of the computed tensile and compressive stresses given in Table LV seem reasonable if rough allowance is made for the prestresses in the fibers. The compressive stresses in the "Thornel" 40 stringers are about the same as the uniaxial compressive strength of a unidirectional composite, but the computed tensile stresses are much less than the unidirectional composite tensile strength; as expected, these stringers broke in compression. For the "Thornel" 25 stringers, the computed tensile stresses are much closer to the unidirectional tensile strength (about 75,000 $lb/in.^2$); and, in practice, many of these stringers broke in tension. An interesting feature of the "Thornel" 25 stringer tests is the indication that the maximum compressive stress in the curved composite increased as the bend radius decreased.

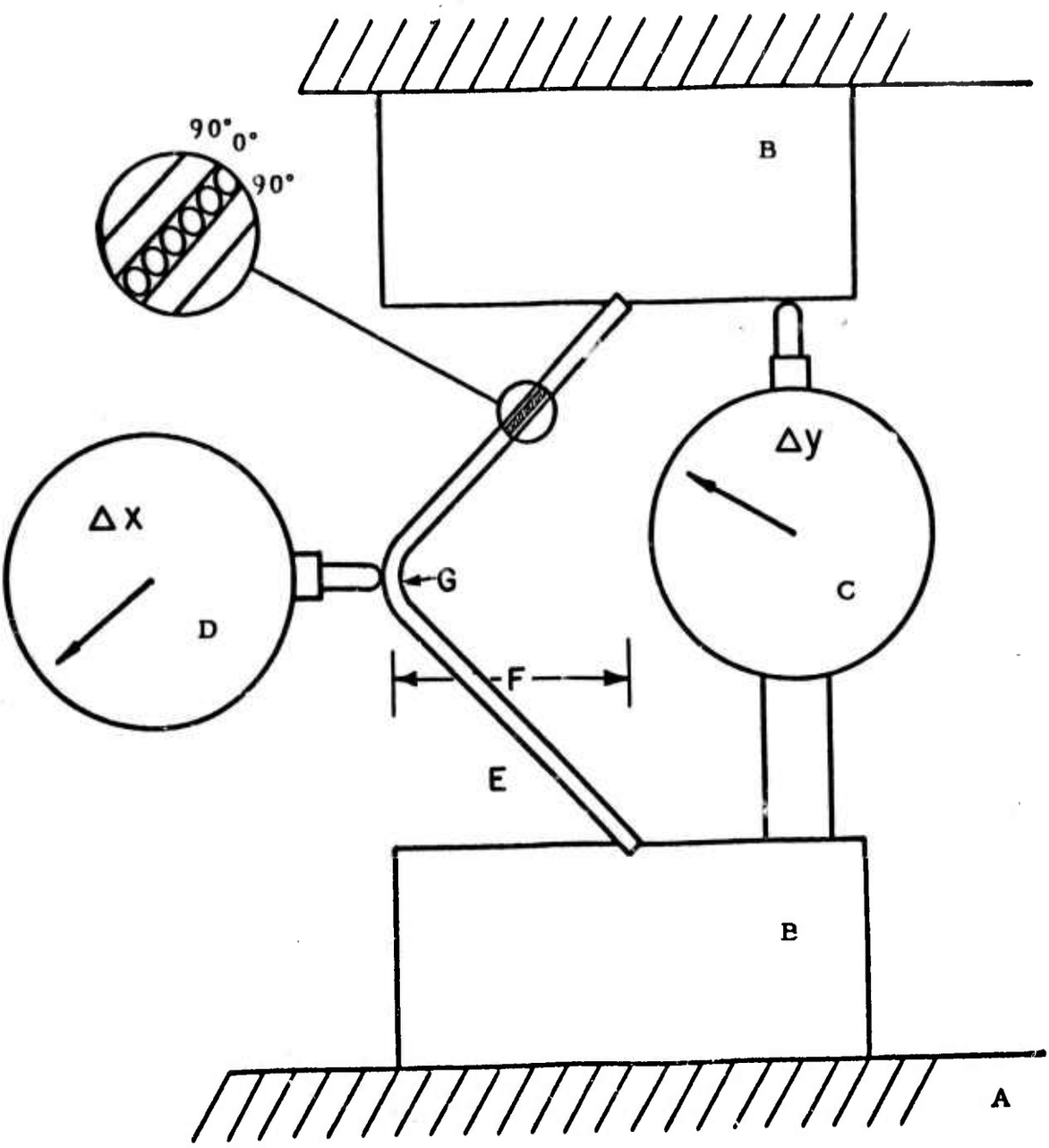

A-Instron Platens; B-Notched Aluminum Blocks;
C, D-Dial Indicators Measuring Vertical and Horizontal Deformation;
E-Sample

N-17135

Figure 176. Angle Bend Test Procedure for L-Shaped Stringer.

TABLE LV

ANGLE BEND FRACTURE LOADS OF L-SHAPED STRINGERS

Sample		Fiber Volume (percent)	Radius (in.)	Thickness (in.)	Failure Load/Length (lb/in.)	Failure ΔX (in.)	Failure ΔY (in.)	Stress Comp. (10^3lb/in.^{2})	Stress Tensile (10^3lb/in.^{2})	Failure Surface*
"Thornel" 25										
L25-1-	1		.050	.0494	58.9	.035	.090	96.5	45.0	AX
	2		"	.0494	64.4	.032	.083	104.8	48.8	BZ & AX
	3		"	.0485	71.9	.032	.074	120.1	56.9	BZ
	4	43.1	"	.0486	74.8	.037	.077	126.0	59.6	BZ
L25-2-	1		"	.0484	66.5	.031	.075	111.2	52.8	BZ
	2		"	.0482	67.4	.029	.075	112.9	53.8	BY
	3		"	.0481	72.0	.031	.079	121.5	58.0	BY
	4	41.1	"	.0481	70.7	.031	.079	119.3	56.9	BZ
L25-3-	1		.100	.0437	61.8	.040	.088	101.2	73.0	BY & CY
	2		"	.0429	61.6	.036	.091	104.1	75.2	BY & CY
	3		"	.0435	56.7	.036	.083	93.0	67.0	BZ & CZ
	4	41.9	"	.0423	54.5	.036	.079	94.6	68.7	CY
L25-4-	1		.200	.0480	69.1	.042	.094	89.6	73.5	CY
	2		"	.0478	66.4	.036	.074	86.1	70.7	CY
	3		"	.0480	69.5	.038	.077	89.2	73.2	CY
	4	39.9	"	.0476	70.6	.042	.087	94.4	77.5	CY
L25-5-	1	40.1	"	.0490	50.7	.049	.099	63.0	51.6	CY
	2	40.3	"	.0486	60.2	.038	.072	74.1	61.0	CY
	3		"	.0485	71.6	.041	.083	86.8	71.2	BY & CY
	4	41.1	"	.0490	76.1	.043	.088	93.4	76.4	CY
"Thornel" 40										
L40-5-1	1		.050	.0300	20.7	.042	--	77.1	49.8	CY & CZ
	2		"	.031	26.1	.027	--	88.5	56.3	CY & CZ
L40-6-	1		.100	.0395	45.8	.036	--	89.7	66.6	CY
	2		"	.0360	37.4	.034	--	86.8	66.2	CY
L40-4-	1		.200	.0273	22.9	.037	--	84.7	75.8	CY
	2		"	.0282	30.9	.039	--	106.3	94.7	CZ

*Type and Location of Failure Surface:

A - Interlaminar Failure
B - Tensile Failure
C - Compressive Failure

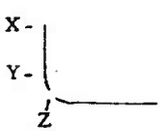

Although the test results cannot be analyzed in detail, the angle bend tests have demonstrated that "Thornel" 25 and 40 graphite fibers can be used safely to fabricate structural elements with small radii of curvature. The ability to be formed over curves of small radius is an important asset of these nigh modulus fibers.

2. Axial Crippling Tests of Stringers
(O. L. Blakslee, Union Carbide)

Candidate stringers for the reinforcing of plates and cylinders have been tested to determine suitability and optimum processing conditions. The selection criterion was the endwise compressive strength.

The samples were trimmed to shape with a thin cut-off wheel in a surface grinder. Particular care was taken to assure that the ends were plane parallel. The length was made short enough to insure that failure would not occur due to column buckling of the entire stringer. This length was approximately four inches for the box, the Z-, and the U-shaped sections but only approximately two inches for the L-shaped sections. High elongation epoxy-backed foil strain gages were attached to at least two flanges of each specimen. The samples were then placed between the platens of an Instron esting machine in such a manner that the load was uniformly distributed along the platen-stringer interface, and the specimens were loaded to failure. The strains measured by the strain gages were continuously and individually plotted versus the load on X-Y recorders.

The five different shapes and sizes tested are shown in Figure 177. The wound box beams were tested as box, U-, and L-shaped sections (Figure 177-A, -B, and -C, respectively). The shapes tested for the Z molded stringers were the L and Z sections (Figure 177-C and -D, respectively). The L-shaped stringers were tested in the L configuration (Figure 177-E). Table LVI lists the number of plies and describes the lay-up patterns for the stringers tested. The first number in parentheses is the angle (in degrees) that the fibers in the first (outside) ply make with the longitudinal axis of the stringer.

The results of these tests are summarized in Table LVI. The data are listed in approximate chronological order. Estimates of stringer properties are listed also; these estimates are based on the plate tensile and compression data given in Sections VI B and D. The filament wound stringers had severe variations in wall thickness (adjacent to the end of a cross-over, the thickness was occasionally only approximately one-half of the nominal value). All the stringers for this series failed by shear along the fibers, and this shear always originated at one of the thin regions. The molded specimens of $4(\pm 45°)$, $3(\pm 45°)$, and $3(\pm 10°)$ all failed due to shear along the fibers. The $\overline{4}(90°,0°,0°,\overline{90}°)$ samples failed at one flange by shear along a plane which lay at 45° to the plies. The unidirectional samples failed by local buckling of one flange. The $3(0°,90°,0°)$ specimens failed by "brooming" of the ends at the specimen-platen interface.

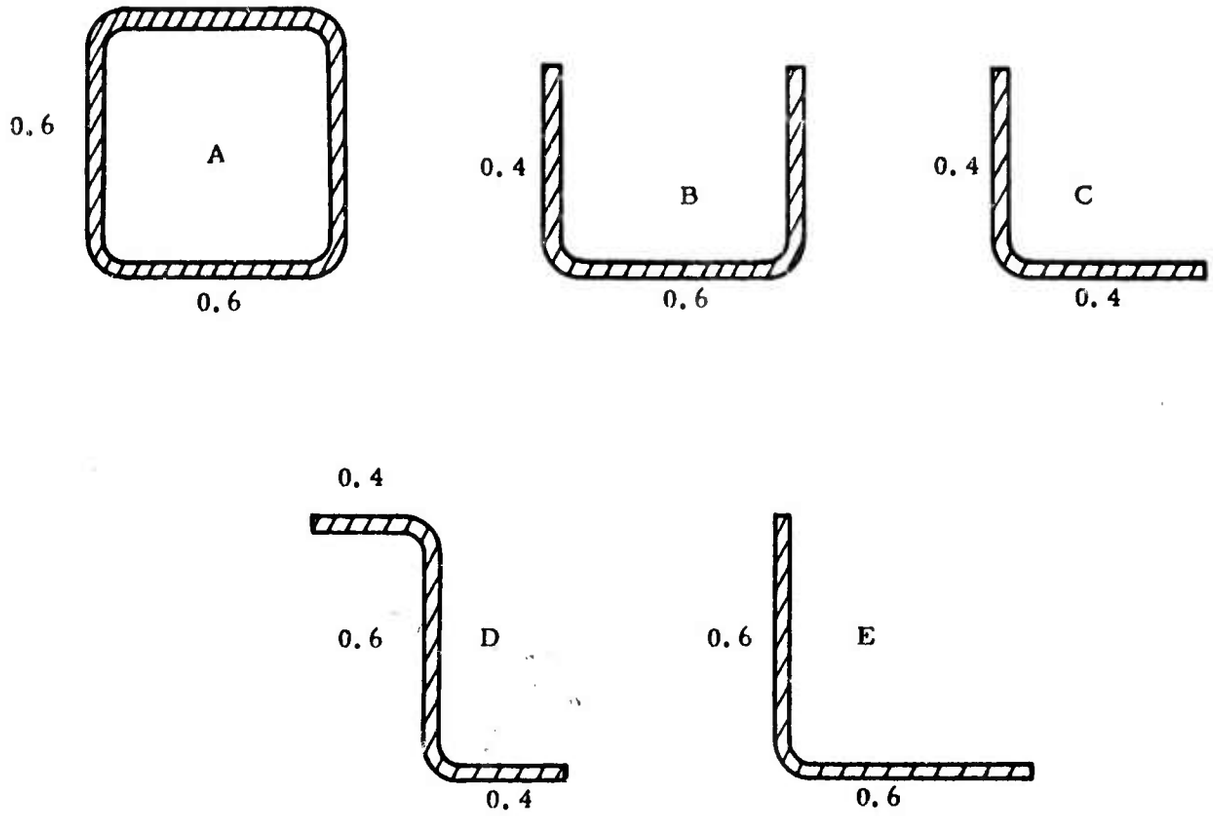

All Dimensions are in Inches;
Inside Radii at Corners are 0.050 Inch.

N-10997

Figure 177. Cross-Sectional Shapes and Sizes of Stringers Tested.

The differences between the measured and estimated values appear to be due to manufacturing and/or testing difficulties. Both processing and testing techniques were improved on the latter samples; good agreement between estimated and measured values was then obtained. The one large discrepancy occurred for the unidirectional 3(0°) stringer. A compressive strength 66 x 10^3 lb/in.^{2} and a Young's modulus of 11 x 10^6 lbs/in.^{2} have been measured previously on unidirectional plate samples, but only 25 x 10^3 lbs/in.^{2} strength and 7.2 x 10^6 lbs/in.^{2} modulus were measured on the stringer. Because of these results, compression testing was carried out on small plate specimens cut from the flanges of the untested 3(0°) stringer samples. These plates failed at only 30 x 10^3 lbs/in.^{2} This result suggests that the test procedure on the stringer was reasonably valid but that

TABLE LVI

MEASURED AND ESTIMATED COMPRESSIVE INITIAL MODULUS AND ULTIMATE STRENGTH OF STRINGER CANDIDATES OF "THORNEL" 25/ERL 2256 COMPOSITES

Shape	Number Tested	Plies & Lay-Up	Young's Mod. (10^6 lb/in.^{2}) Meas.	Young's Mod. (10^6 lb/in.^{2}) Est.	Strength (10^3 lb/in.^{2}) Meas.	Strength (10^3 lb/in.^{2}) Est.
Filament Wound						
Box	1	4(±45°)	1.4	1.3	7.2	15
L	4	"	1.4	1.3	7.6	15
U	3	"	1.4	1.3	7.5	15
Z Mold						
Z	2	"	1.2	1.3	9.0	15
L	1	"	1.3	1.3	10.5	15
Z	2	3(±45°)	1.1	1.3	4.7	15
L	1	"	1.1	1.3	7.1	15
Z	3	4(90°, 0°, 0°, 90°)	5.0	5.3	13.9	37
L	1	"	3.8	5.3	10.5	37
Z	1	3(0°)	7.2	11.0	17.5	66
L	2	"	-	11.0	25.3	66
*	2	"	-	11.0	30.4	66
L Mold						
L	1	3(±10°)	-	-	15.8	16
L	4	3(0°, 90°, 0°)	7.0	7.9	32.8	33

*Flat plate cut from preceding Z - 3(0°) shape.

the stringer material was different. The fiber volumes of the 3(0°), 3(±10°), and 3(0°,90°,0°) stringers were measured and found to be 38, 37, and 42 percent, respectively. These fiber volumes account for most of the difference between stringer and plate strengths. Further work on stringer fabrication is being carried out which should result in improved stringer properties.

G. Crippling Tests on Fiber Composite Panel Elements

(K. H. Sayers, W. N. Meholick, and D. P. Hanley, Bell Aerosystems)

A plate compression test program has been conducted to generate design data on initial buckling and crippling allowables for web-type elements. Such elements occur in the thin-gage, stiffened skin construction of the fuselage component (see Section X, Fuselage Component Design and Analysis). An aspect ratio of four was chosen for the plate elements with the approximate width-to-thickness ratio b/t ranging from 20 to 60. Plate elements of the skin and stringers for the fuselage component are considered to have infinite aspect ratios. Since buckling allowables from panels with aspect ratios equal to or greater than four may be treated as infinite, the proportions selected for the test specimens are considered to cover adequately the range of necessary design values.

A plate element and test assembly is shown in Figure 178. The test fixture for the large plate size is shown disassembled with glass fiber composite specimens in Figure 178a. The protruding drill rods are used to approximate simply supported boundary conditions. On the right-hand side of the figure is a fixture which is used to make parallel the "tear-drop" metal end caps. These caps ride in grooved metal parts shown above and below the large specimen. Figure 178b shows an assembled fixture with an instrumented "Thornel" 40 composite test panel of intermediate size. An adjustment feature to translate and rotate the plate element is provided in the test fixture at each loading end to assure load alignment. The alignment has been checked satisfactorily by the output of back-to-back strain gages at the ends of each specimen. Engineering drawings of the test fixtures and assemblies are given in Figure 179.

Panel compression tests were made on four "Thornel" 40 composites with overall specimen dimensions of 1.12 x 2.50, 1.75 x 5.00, and 3.00 x 10.00 in. A 0.25 in. overhang beyond the drill rod line of contact was allowed on each long edge, and the depth of insert into the loading caps of the short panel edges was 0.50 in. Thus, the simply supported plate dimensions were 0.62 x 1.50, 1.25 x 4.00, and 2.50 x 9.00 in. Usually, three specimens were tested of each size for each of the following four composites:

Plate No.	Lay-Up	Fiber Volume Content (percent)	Average Thickness (in.)
1	4(0°, 90°, 90°, 0°)	68	0.032
2	4(90°, 0°, 0°, 90°)	62	0.036
3	4(90°, ±10°, 90°)	55	0.042
4	6(±10°, ±45°, ±10°)	56	0.061

In each case, the direction of loading was at 0 degrees; e.g., plate number 2 was tested with the outer plies perpendicular to the load direction.

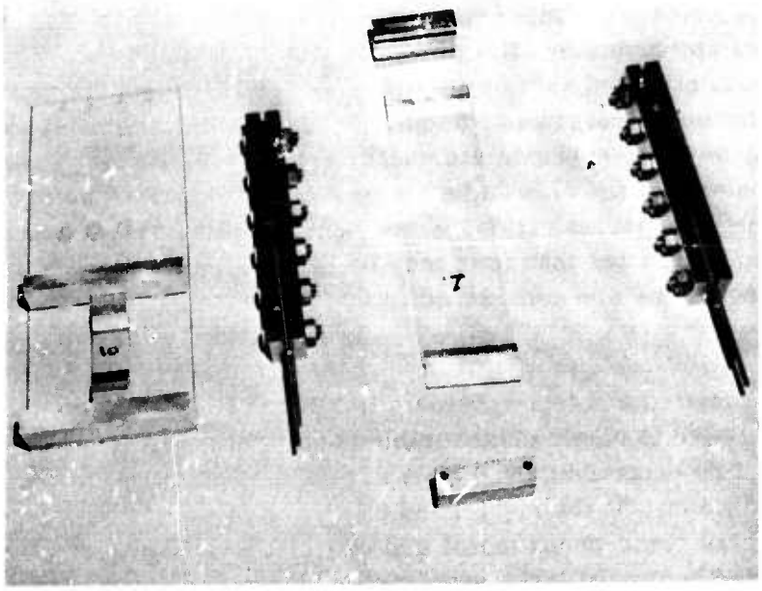

(a) Fixture Disassembled.

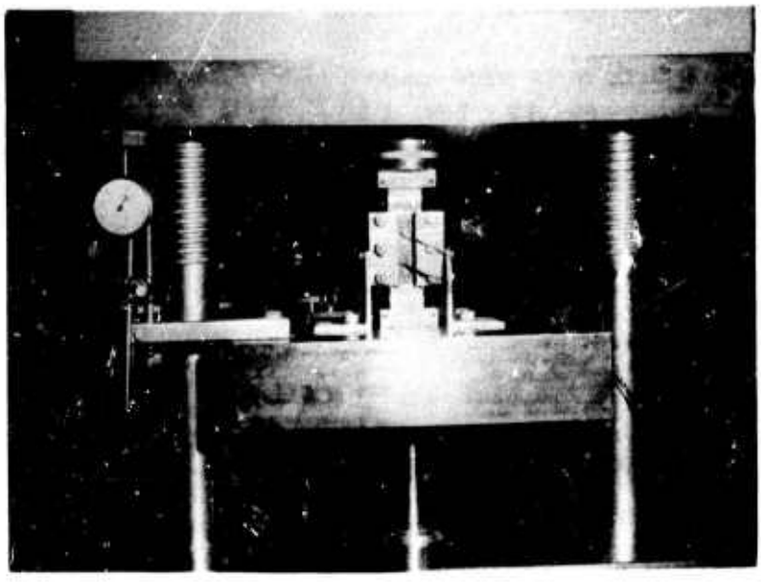

(b) Assembled Fixture and Instrumented Specimen.

Figure 178. Plate Element Crippling Test Apparatus.

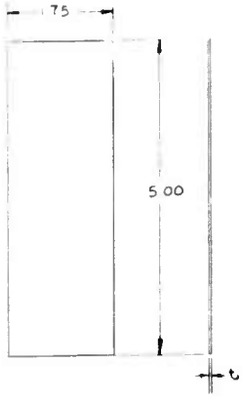

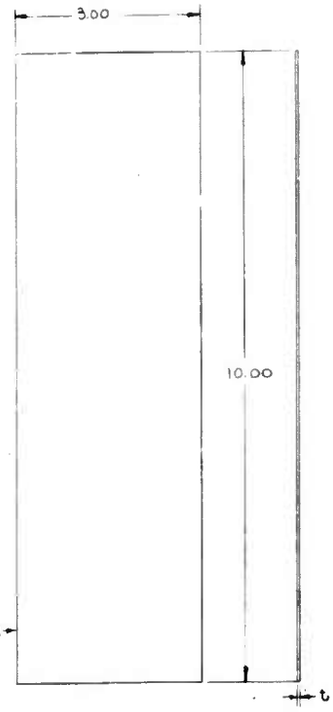

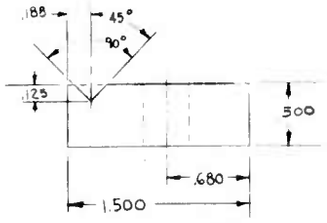

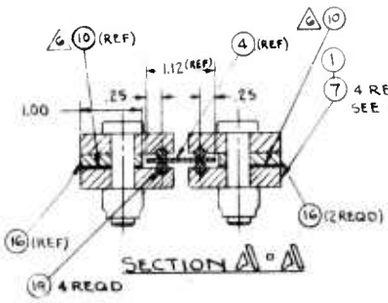

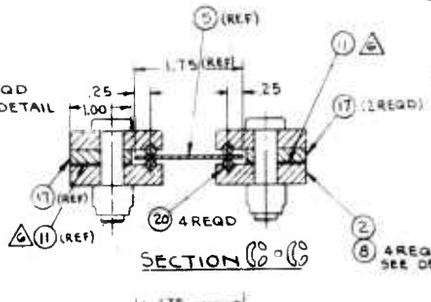

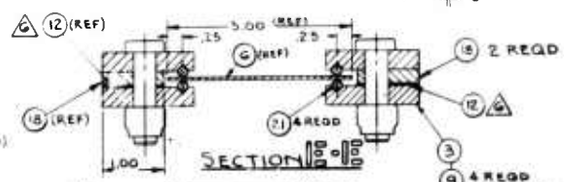

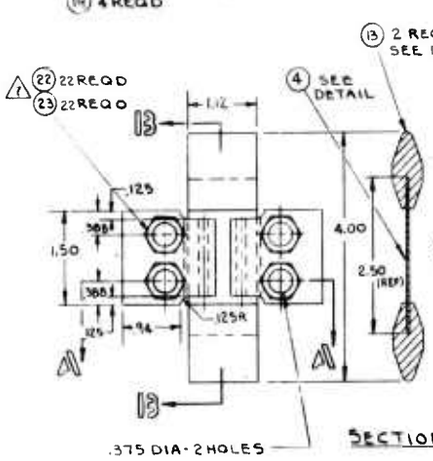

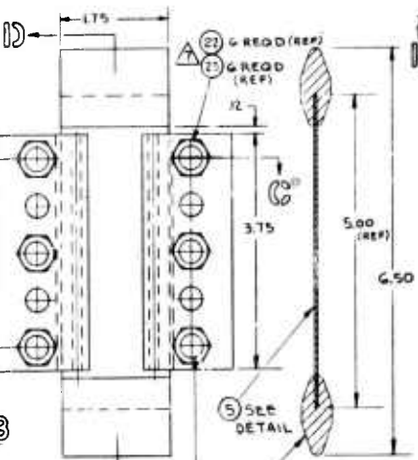

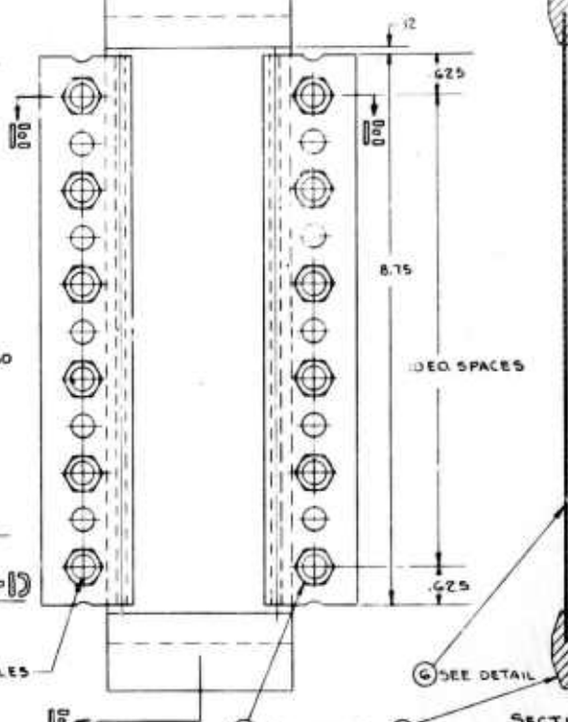

DASH NUMBER
8506-150008-4
8506-150008-4
8506-150008-4
8506-150008-4
8506-150008 5
8506-150008-5

△8 CENTER LINE OF .090R & CENTER LINE OF SLOT TO BE PARALLEL WITH SURFACE WITHIN .005 TIR

△7 TORQUE TO 00$^{\pm10}$ LBS PER BPS4018

△6 SHIM AS REQUIRED TO PROVIDE A SLIDING FIT OF TEST SPECIMEN ON RODS

△5 PURCHASE FROM LAMINATED SHIM CO INC. GLENBROOK, CONN OR U.S. GASKET & SHIM CO. CUYAHOGA FALLS, OHIO

△4 TOOL STEEL MAY BE USED AS ALTERNATE

△3 CFRP UCC PLATE NO.

△2 CFRP UCC PLATE NO.

△1 CFRP UCC PLATE NO.

NOTES.

A

MIL-S-7742
BPS 4018
EO NO.
NUMBER

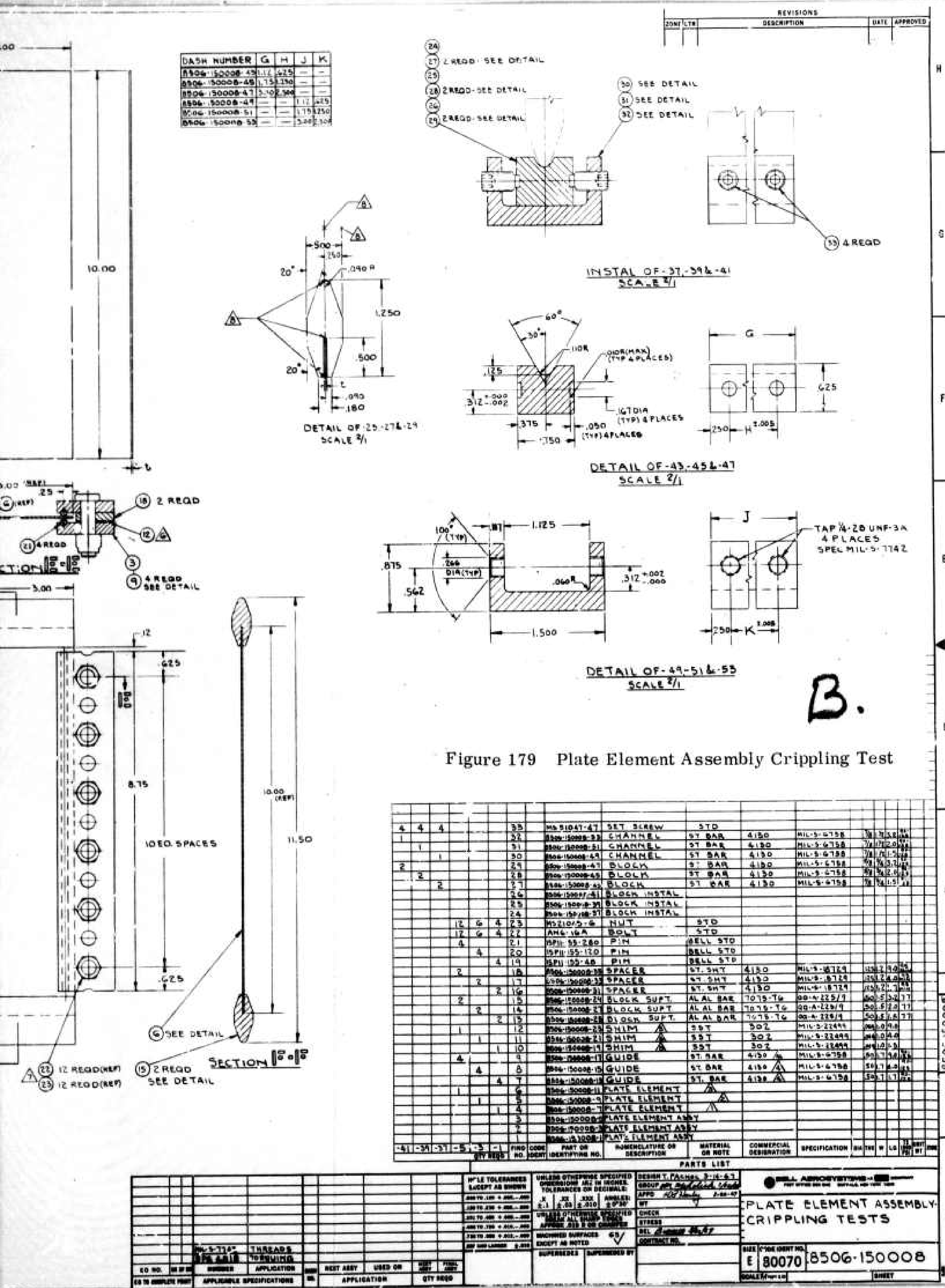

Figure 179 Plate Element Assembly Crippling Test

DASH NUMBER	G	H	J	K
8506-150008-43	1.12	.625	—	—
8506-150008-45	1.75	1.250	—	—
8506-150008-47	3.10	2.500	—	—
8506-150008-49	—	—	1.12	.625
8506-150008-51	—	—	1.75	1.250
8506-150008-53	—	—	3.10	2.500

-41	-39	-37	-5	-3	-1	FIND NO.	CODE IDENT	PART OR IDENTIFYING NO.	NOMENCLATURE OR DESCRIPTION	MATERIAL OR NOTE	COMMERCIAL DESIGNATION	SPECIFICATION	DIA	THK	W	LG
4	4	4				33		MS51047-47	SET SCREW	STD						
1						32		8506-150008-53	CHANNEL	ST BAR	4130	MIL-S-6758	[illegible]	[illegible]	[illegible]	[illegible]
	1					31		8506-150008-51	CHANNEL	ST BAR	4130	MIL-S-6758	[illegible]	[illegible]	2.0	[illegible]
		1				30		8506-150008-49	CHANNEL	ST BAR	4130	MIL-S-6758	[illegible]	[illegible]	1.5	[illegible]
2						29		8506-150008-47	BLOCK	ST BAR	4130	MIL-S-6758	[illegible]	[illegible]	3.2	[illegible]
	2					28		8506-150008-45	BLOCK	ST BAR	4130	MIL-S-6758	[illegible]	[illegible]	2.0	[illegible]
		2				27		8506-150008-43	BLOCK	ST BAR	4130	MIL-S-6758	[illegible]	[illegible]	1.5	[illegible]
						26		8506-150008-41	BLOCK INSTAL							
						25		8506-150008-39	BLOCK INSTAL							
						24		8506-150008-37	BLOCK INSTAL							
			12	6	4	23		MS21045-4	NUT	STD						
			12	6	4	22		AN6-16A	BOLT	STD						
			4			21		15P11-55-280	PIN	BELL STD						
				4		20		15P11-155-120	PIN	BELL STD						
					4	19		15P11-155-48	PIN	BELL STD						
			2			18		8506-150008-35	SPACER	ST. SHT	4130	MIL-S-18729	[illegible]	[illegible]	[illegible]	[illegible]
				2		17		8506-150008-33	SPACER	ST. SHT	4130	MIL-S-18729	[illegible]	[illegible]	[illegible]	[illegible]
					2	16		8506-150008-31	SPACER	ST. SHT	4130	MIL-S-18729	[illegible]	[illegible]	[illegible]	[illegible]
			2			15		8506-150008-29	BLOCK SUPT.	AL AL BAR	7075-T6	QQ-A-225/9	.50	.5	3.2	7.7
				2		14		8506-150008-27	BLOCK SUPT.	AL AL BAR	7075-T6	QQ-A-225/9	.50	.5	2.0	7.7
					2	13		8506-150008-25	BLOCK SUPT.	AL AL BAR	7075-T6	QQ-A-225/9	.50	.5	1.5	7.7
			1			12		8506-150008-23	SHIM △	SST	302	MIL-S-22499	[illegible]	1.0	9.0	
				1		11		8506-150008-21	SHIM △	SST	302	MIL-S-22499	[illegible]	1.0	4.0	
					1	10		8506-150008-19	SHIM △	SST	302	MIL-S-22499	[illegible]	1.0	[illegible]	
			4			9		8506-150008-17	GUIDE	ST. BAR	4130 △	MIL-S-6758	.50	.7	[illegible]	[illegible]
				4		8		8506-150008-15	GUIDE	ST. BAR	4130 △	MIL-S-6758	.50	.7	[illegible]	[illegible]
					4	7		8506-150008-13	GUIDE	ST. BAR	4130 △	MIL-S-6758	.50	.7	1.7	[illegible]
			1			6		8506-150008-11	PLATE ELEMENT	△						
				1		5		8506-150008-9	PLATE ELEMENT	△						
					1	4		8506-150008-7	PLATE ELEMENT	△						
						3		8506-150008-5	PLATE ELEMENT ASSY							
						2		8506-150008-3	PLATE ELEMENT ASSY							
						1		8506-150008-1	PLATE ELEMENT ASSY							
QTY REQD																

PARTS LIST

MIL-S-7742 THREADS
SPEC 6818 TUBING
APPLICABLE SPECIFICATIONS

UNLESS OTHERWISE SPECIFIED DIMENSIONS ARE IN INCHES TOLERANCES ON DECIMALS: .X ±.1 .XX ±.03 .XXX ±.010 ANGLES: ±0°30'

MACHINED SURFACES EXCEPT AS NOTED 63

DESIGN T. FACHER 3-16-67

BELL AEROSYSTEMS

PLATE ELEMENT ASSEMBLY-CRIPPLING TESTS

SIZE E CODE IDENT NO. 80070 8506-150008

Figures 180 and 181 give the results in the manner suggested by Dow (Reference 41) the structural weight parameter (plate weight per unit area W divided by plate width between supports b) is plotted against N_x/b, where N_x is the load per inch based on actual plate width. Both the initial buckling test data and the theoretical curves are given in Figure 180; ultimate failure test data are given in Figure 181. Reference curves for two widely used aircraft alloys, 7075-T6 clad aluminum and 6A1-4V titanium, are included for comparison. The operation of the test fixture was investigated by conducting tests on 7075-T6 aluminum panels of the same three sizes as those for the composite. The measured values for initial buckling, plotted in Figure 180, agree well with the reference curve. The ultimate compressive failure data shown in Figure 181 generally fall at slightly lower loads than those predicted by the reference curves, a condition which indicates the existence of minor edge restraint and end cap fitting problems with the test fixture. The theoretical initial buckling curves were predicted from the equations

$$W/b = \rho\, t/b = \rho\,/(b/t) \qquad \text{(VIIG-1)}$$

and

$$N_x/b = \sigma_{cr}\, t/b \qquad \text{(VIIG-2)}$$

where

$$\sigma_{cr} = (2\pi^2/t\, b^2)\,(D_3 + \sqrt{D_1\, D_2}). \qquad \text{(VIIG-3)}$$

The D_1, D_2, and D_3 are the flexural properties as defined by Hearmon (Reference 42), t is the plate thickness, and ρ is the density. Theory is not available for the prediction of post-yield composite buckling behavior.

The theoretical initial buckling curves for the graphite fiber composites represent approximately 40 and 50 percent lighter construction than that for aluminum and titanium, respectively. Most of the composite experimental data points lie somewhat to the left of their respective performance curves, resulting in a lower load capability than that expected. Nevertheless, the experimental initial buckling points for the composites lie below the aluminum curve, indicating that the composites will result in lighter structures. In addition, the measured buckling capability for the composites may be low due to difficulties in determining initial buckling.*

*During each test, the load-shortening curve was determined from the deflection between the loading platens; and the stress-strain curve was measured with strain gages. The initial buckling stress when bending first occurs is determined from the stress-strain curve, and the ultimate crippling stress is obtained from the maximum load carried. In all crippling tests, a constant crosshead rate of ~ 0.005 in./min. was used.

BLANK PAGE

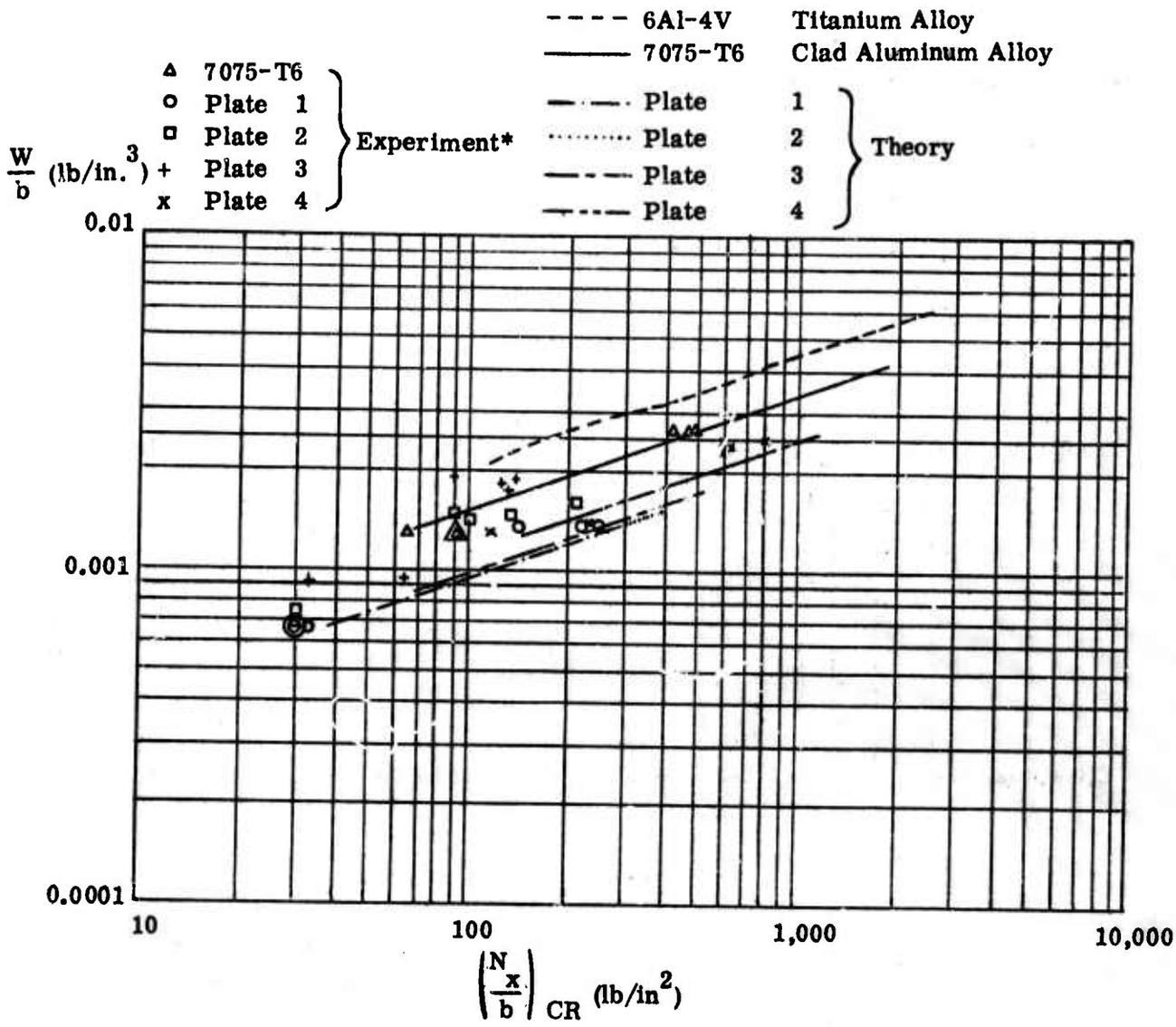

* Data to be Treated with Caution due to Difficulty Experienced in Detecting Initial Buckling, Especially Plate 3

Figure 180. Weight-Strength Comparison for Initial Buckling of Long, Flat, Simply-Supported Rectangular Panels of "Thornel" 40/ERL 2256 Composites

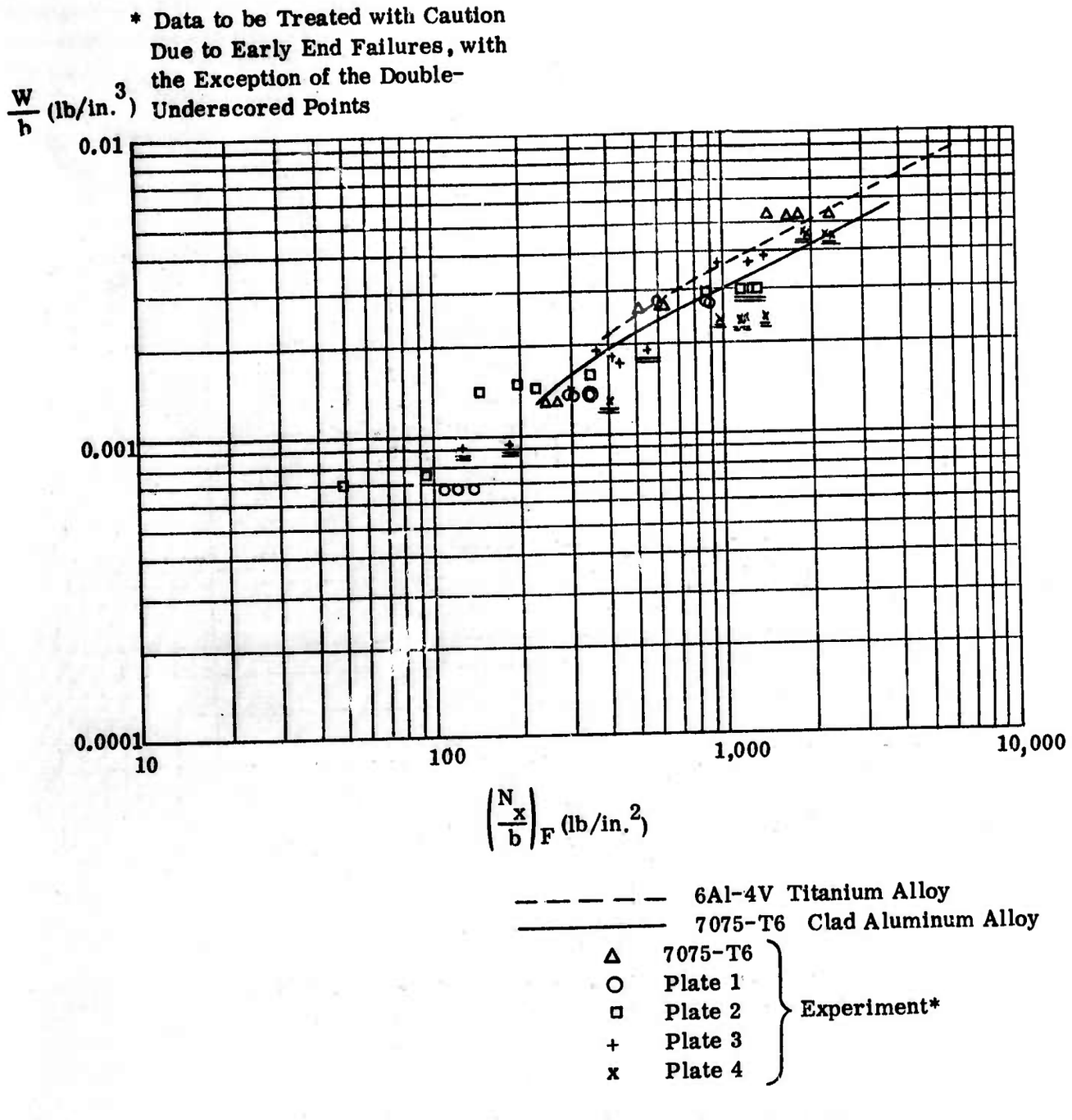

Figure 181. Weight-Strength Comparison for Compressive Failure of Long, Flat, Simply-Supported Rectangular Panels of "Thornel" 40/ERL 2256 Composites

With respect to ultimate compressive failure, the test points for the composites lie about the aluminum reference curve, indicating no performance advantage. However, for several of the composite specimens (denoted by double scoring in Figure 181) the failures occurred in areas away from the edges or were due to crushing. These points are below the aluminum curve, suggesting that the composite performance should be improved after improvements are made in the test fixture (shorter unsupported distances) and in specimen fabrication (less fiber wash and greater flatness).

The aluminum panels exhibited rather smooth load-deflection curves, and initial buckling was observed visually. The large and intermediate size aluminum specimens generally buckled into three axial half-waves, and ultimate failure was due to local plastic bending near the loaded ends. For the orthogonal composites, when the outer plies were perpendicular to the load direction (plate 2), five half-waves were observed; ultimate failure appeared to be transverse normal fracture of the outer ply or plies. When the outer plies were parallel to the load direction (plate 1), initial buckling was generally observed as two half-waves which snapped-through to three half-waves; this behavior resulted in a "stepped" load-deflection curve. The failure of specimens from plate 1 was generally more catastrophic (accompanied by audible noise and cracking). Fiber failures occurred in the outer layer(s), although the specimens did not necessarily come apart into two. Most of the specimens were weak in flexur- when they were removed from the test fixture and quite often broke when the end caps were removed. Most of the composite specimens tested appeared to have localized damage near the ends; the remaining surface area, apparently undamaged, recovered elastically.

H. Acoustic Fatigue Resistance of Advanced Composites

(S.L. Cross and D.P. Hanley, Bell Aerosystems)

In June 1966, Bell initiated a six-month Company-funded exploratory program to gain and broaden experience with composites in fatigue applications. A specific structural element was chosen for study - the acoustically excited panel - which finds application in ducted fan V/STOL aircraft and air cushion vehicles. The "Thornel" fiber was supplied under the ARPA contract. This report section highlights the results of the six-month study.

The scope of the study included preliminary design, material evaluation, fabrication, and component testing. Material selections were based on strength, fabrication, and damping characteristics of various composites. Analytical studies and correlation were conducted in parallel with the testing program. The acoustic environment for evaluation of materials was provided with existing Bell facilities. Panel attachment and hardware design were established to provide well defined boundary conditions and acoustic tests with glass, boron, and graphite composites were then conducted.

1. Material Selection

The criteria in selecting materials for acoustic panel testing were strength, fabrication, and damping characteristics. Filament and tape-wound rings (6-inch O.D. x 1/4-inch wide x 1/16-inch thick) were used initially to provide simple elements readily adaptable to relative strength and damping property measurements. In addition, material handling and fabrication techniques could be assessed for later application to flat panels.

Rings were fabricated of fiberglass, boron, and graphite ("Thornel" 25) fibers with resin systems ranging in modulus from (approximately) two-tenths of a million to one million psi. As a basis for comparison, rings were also made of machined 2024-T3 aluminum.

Ultimate strength properties were determined by the standard Split-D method. Relative damping factors were calculated from logarithmic decay and transmissibility data from free and forced vibration.

Typical frequency response curves are shown on Figure 182. The ratio of output/input acceleration is shown on the ordinate while the ratio of forced to natural frequency is plotted on the abscissa. The damping factor (b) is inversely proportional to the amplification at resonance. These tests were performed on a standard vibration tester. The rings were held vertically with respect to the table and vibrated in-plane by a sinusoidal input as shown in Figure 183.

Figure 184 shows the response of fiberglass, boron, and graphite rings undergoing free vibration. This mode was impulsively excited. In this case, the damping factor (b) is a function of the oscillation decay rate. Peak-to-peak amplitude,

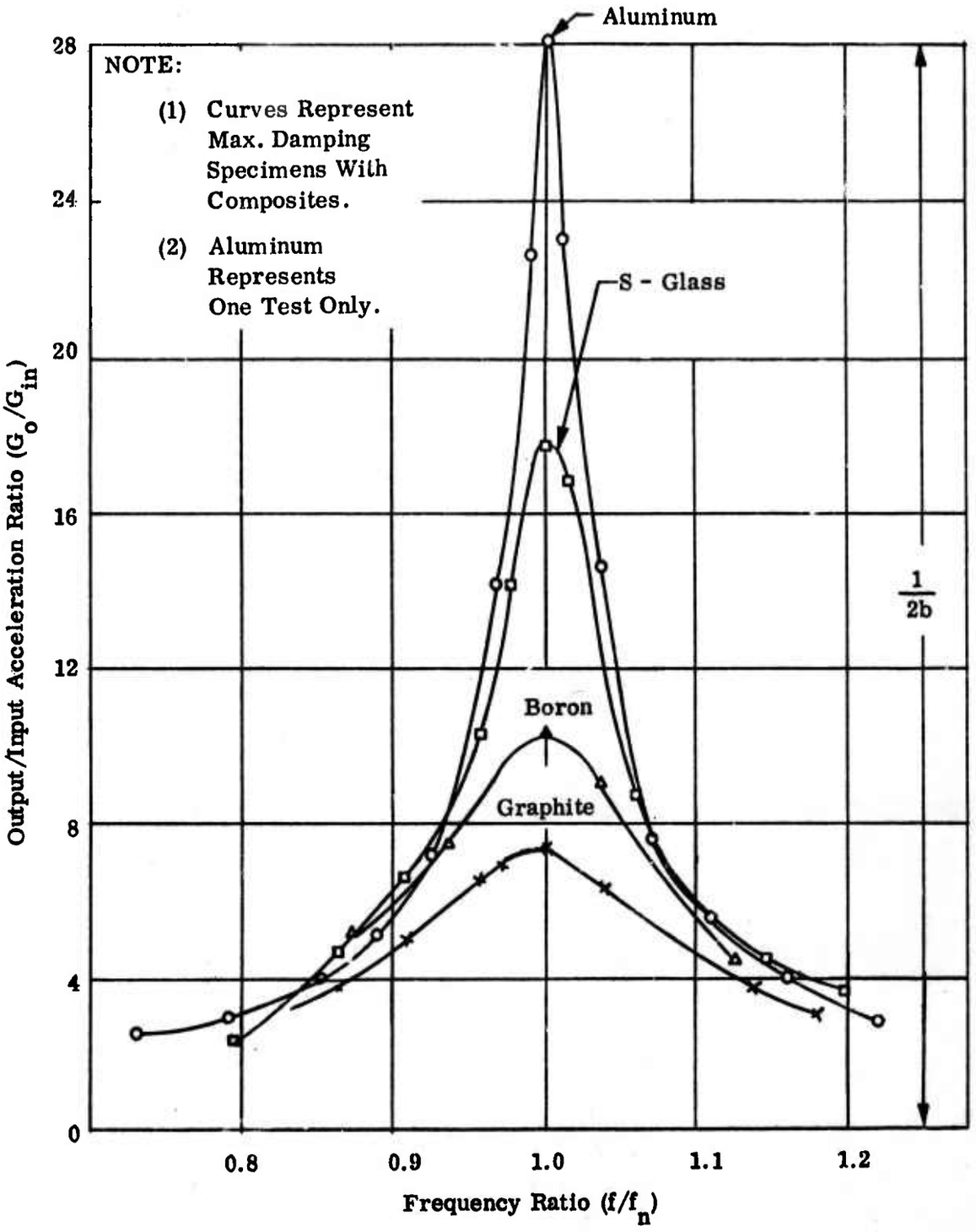

Figure 182. Forced Vibration Transmissibility (2 g Input)

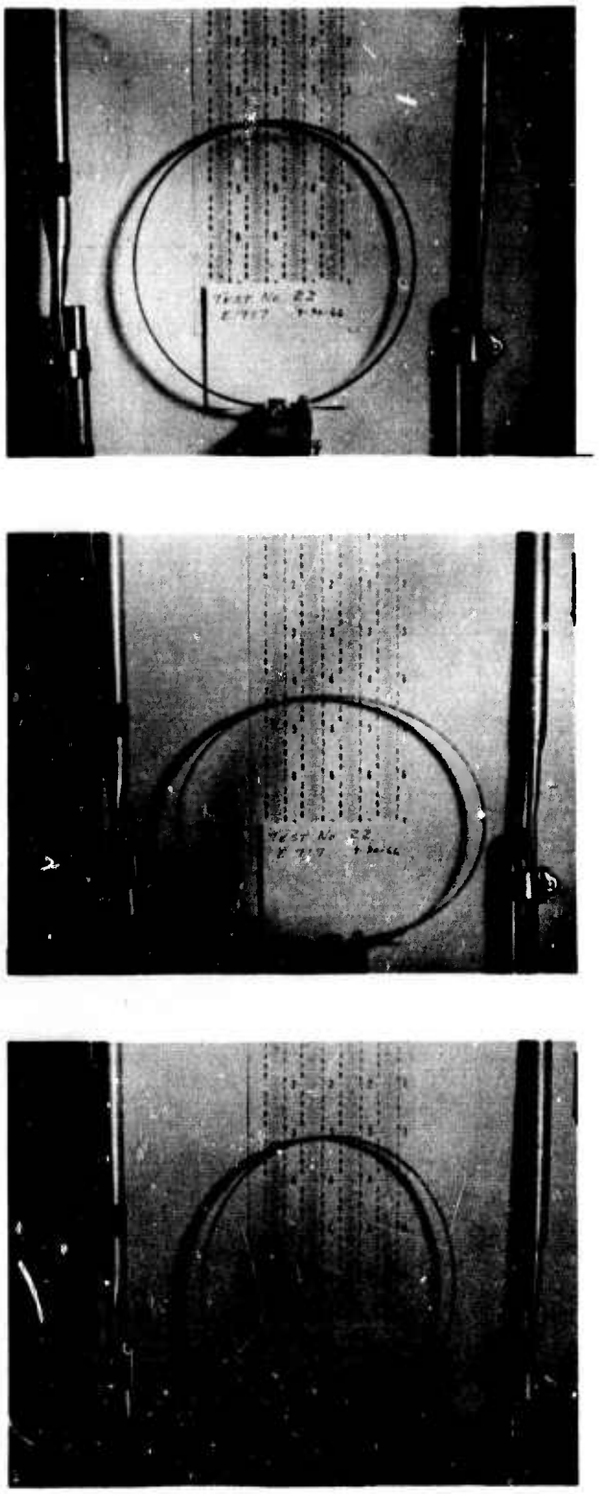

Figure 183. Fiberglass Ring Response Modes at 10g Excitation

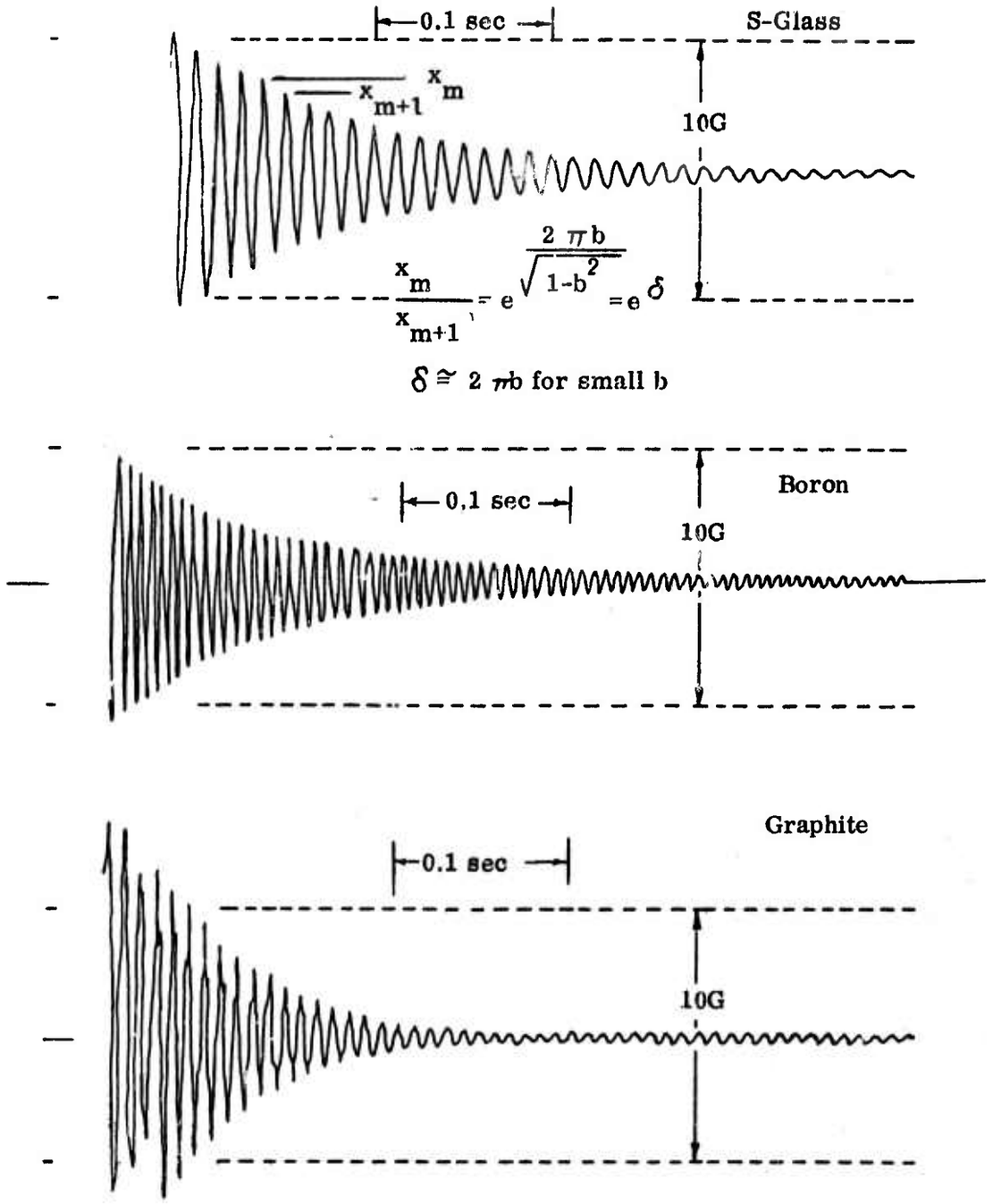

Figure 184. Free Vibration of Composite Rings

shown by the dotted lines, is equivalent to 10g's and the time scale is one-tenth of a second. Damping factors determined from forced vibrations agreed very well with those determined from free vibration.

A summary of the data determined from these ring tests is shown in Table LVII.

TABLE LVII

RING TEST RESULTS

Ring Material	Nat. Freq. fn (cps)	Damping Factor (b)	Ring Density ($lb/in.^3$)	Ult. Ten. Strength F_{tu} (psi)
S-Glass	109	0.0208	0.0695	206,000
	107	0.0237	0.0801	279,000
	116	0.0336	0.0702	258,000
Boron	207	0.0183	0.0741	120,000
	207	0.0297	0.0760	129,000
	199	0.0398	0.0801	131,000
Graphite	178	0.0273	0.0472	94,000
	173	0.0584	0.0492	90,300
	186	0.0260	0.0496	89,200
Aluminum	110	0.0179	0.100	68,300

Natural frequencies, average damping factors, density, and ultimate tensile strengths are given. The data are tabulated for each fibrous reinforcement with three matrix materials in the order of increasing resin modulus,~ 0.2, 0.5, and 1.0 x 10^6 psi. It had been anticipated that higher damping would be associated with the lower-modulus resin systems, since they were more elastomeric and dissipative; however, this trend was generally not observed. The relative stiffness-to-density ratios of the various materials are reflected in the natural frequency levels. As expected, higher stiffness-to-density ratios corresponded to higher natural frequencies. In general, the composite materials offered 1.5 to 3 times greater damping factors than aluminum. The potential of graphite, in particular, is noted with the highest measured structural damping capacity. With the exception of the boron data, the ultimate strength values

are generally in agreement with the literature. Photomicrographs of the boron rings indicated void and fiber wetting problems, which are believed associated with their somewhat lower strength levels.

Poor fiber wetting was also experienced with the high-modulus resin system (ERL 4305) and carbon fiber. An indication of this is reflected in the low damping factor for graphite with the high-modulus resin. The low-modulus system (ERL 4221) offered lower damping and low stiffness. In view of these factors and processing considerations, the medium-range modulus resin (Epon 828/1031) was selected for the fabrication of panels.

To supplement the experimental ring testing, studies were also made to define analytically the dynamic stress and deflection response of the rings at resonance. A discrete element computer program was utilized to verify the stress profiles under forced vibration. The theoretical and experimental results, the latter obtained from strain gage and displacement measurements, compared extremely well.

2. Acoustic Environment

Following the preliminary material evaluation, a study was completed to determine the desirable acoustic operating levels. The facilities at Bell have the capabilities of operating at discrete or random frequencies between 130 and 450 cps. Sound pressure level may be controlled within the range of 135 to 164 db.

Discrete frequencies at panel resonance were desired in view of the potential application to the X-22A V/STOL duct structure. A panel size of 8 x 8-inches was, therefore, chosen based upon: (1) resonance between 130 and 450 cps, (2) acoustic chamber size, and (3) sound pressure level. Analysis of the aluminum panels indicated that a sound pressure level of 157 db would be required for fatigue within the preselected time of two hours for a panel thickness of 0.025-inch.

The composite panels were initially designed to be of weight approximately equal to the aluminum panels. Thus, with an orthogonal 0-90° lay-up, 6-plies of fiberglass, 5-plies of boron, and 5-plies of graphite were required. Difficulties were encountered with the fabrication of the 6-ply fiberglass panels. Anticlastic curvature was observed upon removal of the panels from the molds. This problem was resolved by going to a 5-ply thickness to provide symmetry about the geometric center of the panel cross-section. Panel natural frequencies were predicted based on theory by Hearmon (Reference 42). Composite stiffnesses and elastic property data were obtained from Bell's computer program. Predicted natural frequencies were 165 cps, 145 cps, 199 cps, and 281 cps for the aluminum, fiberglass, boron, and graphite panels. Calculations were made to determine the desired sound pressure level. Based on stress predictions, it was determined that a sound pressure level of 160 db was required.

3. Hardware Design

Since the acoustic chamber has a rectangular (21 x 36-inch) test section, it was possible to design hardware for mounting three panels in-line. Bonded edge constraint was used so that inherent stress concentrations associated with mechanical fasteners might be eliminated. The design is shown in Figure 185. Epon 927 room curing adhesive was used for bonding the panels to the frames. As noted in the diagram, pins were provided to ensure alignment between the top and bottom frames.

Three of these bonded assemblies were clamped between two main support plates which were in turn mounted in the acoustic chamber. A complete assembly in the acoustic chamber is shown in Figure 186. Although somewhat difficult to see in this figure, the basic operation of the facility may be described as follows. The sound source progresses through from right to left in the enclosed portion below the panels. Sound is generated through air-driven modulators and passed through exponential horns into the test compartment.

4. Test Results

The acoustic test conditions and general results are shown in Table LVIII.

TABLE LVIII

PANEL TEST CONDITIONS

Material	Freq. (cps)	Sound Pressure Level (db)	Total No. Cycles	RMS Stress 2 - Ply Dir.
Aluminum	148	152	9×10^6	7,070
S-Glass	150	160	2.5×10^6	14,000
Boron	190	160	2.9×10^6	37,900
Graphite	230	160	4.6×10^6	14,100

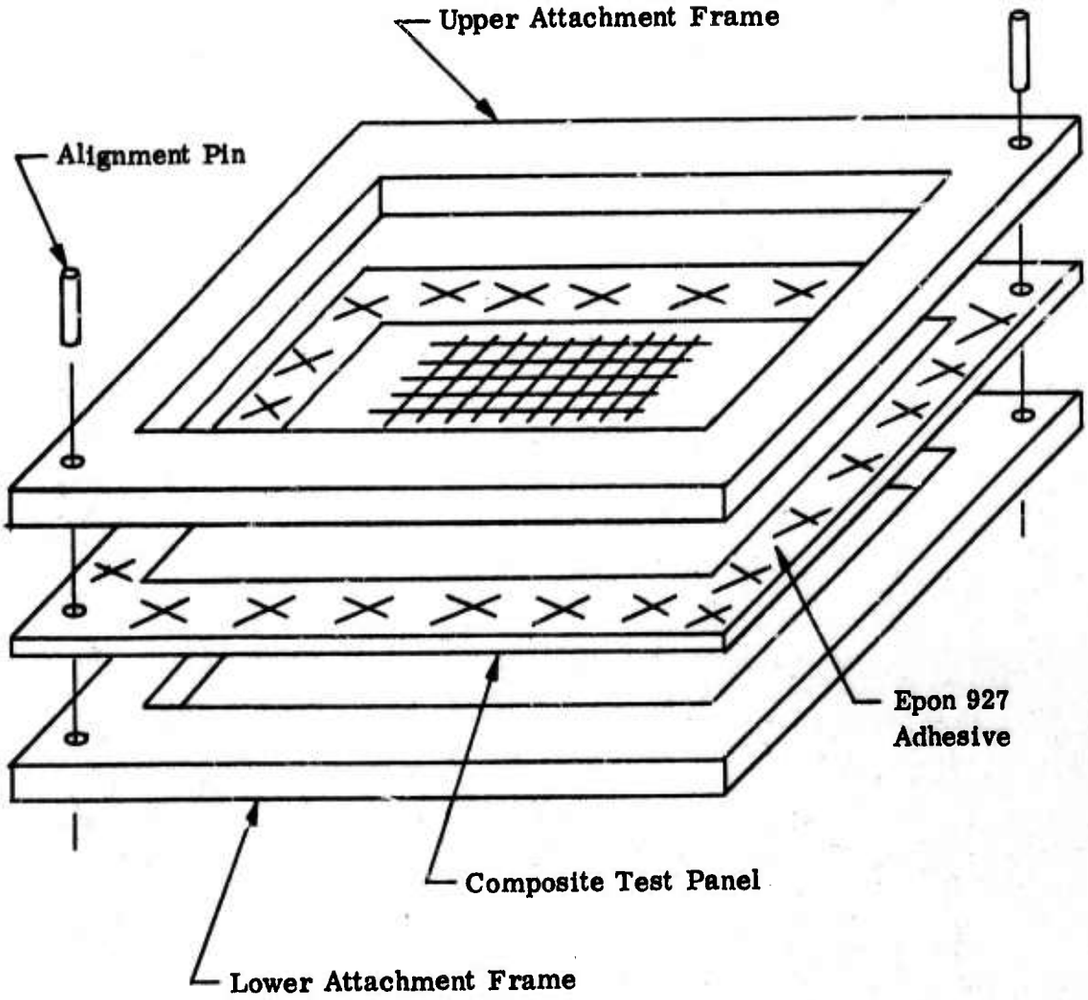

Figure 185. Panel Bonding Method

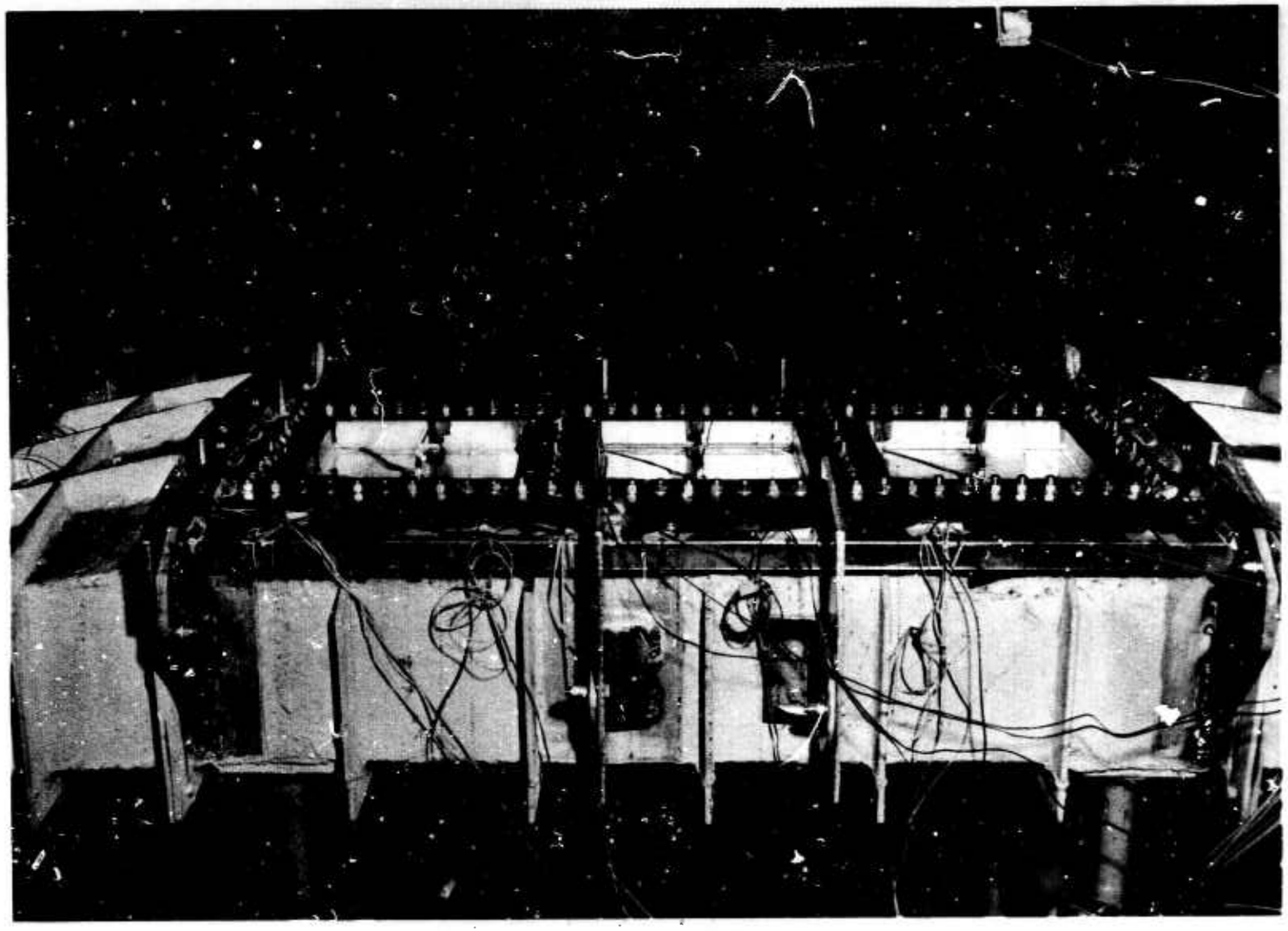

Figure 186. Panel Installation in Acoustic Chamber

Frequency, sound pressure level, total cycles of exposure, and RMS stress are tabulated. The total number of cycles do not represent fatigue failure. Time limitations of the program and earlier difficulties in materials procurement precluded longer duration tests.

Natural frequencies were determined while the frequency was scanned at low sound pressure level by monitoring strain gages and accelerometers. Aluminum and fiberglass resonance was verified as indicated. Boron panels resonated at 230 cps while resonant peaks at 180, 230, 350, and 380 cps were observed on the graphite panels. The three carbon panels did not show resonance at the same frequency. This same problem was encountered with the other panel materials but to a lesser degree. Slight differences, as experienced with aluminum, fiberglass, and boron were anticipated because of minor changes in the sound field through the acoustic chamber.

When the sound pressure was raised to the desired operating level, a major problem developed which had not been anticipated. At 142 db, two of the three aluminum panels experienced snap-through or "oil-canning". Fatigue failure resulting from this type of response would not be comparable to conventionally encountered fatigue environments. As a consequence, the two panels were damped and the sound pressure was raised to 152 db. The test was continued at this level for 9 million cycles at an indicated RMS stress of 7,070 psi. No failure was observed. Similar conditions resulted with fiberglass and boron but at much higher db levels. One fiberglass panel was damped and the other two exposed to 160 db for the period shown.

A history of progressive resin crazing was observed with the fiberglass. At 43 minutes, resin crazing was noted at the edges. This crazing became more severe after one hour, although still confined to the edges. After approximately three hours, the crazing was noted over the entire panel. The test was continued for another hour and terminated. No fiber breakage was observed.

Operating conditions were altered slightly with the boron in light of "oil-canning" at 155 db. Frequency was dropped off resonance to 190 cps and the sound pressure raised to 160 db with no "oil-canning". The test was terminated after 2.9 million cycles with no visible resin crazing or fiber breakage. Upon removal from the acoustic chamber, bond failure was noted between the panels and the aluminum frames. From the appearance of the bond surface, poor bonding was suspected.

No problems with "oil-canning" were experienced with the graphite panels. As noted, operation continued at 160 db for 4.6 million cycles. No resin crazing or fiber breakage was observed; however, a degree of panel unbonding was discovered following removal of the panels from the chamber.

5. Summary

A six-month exploratory program involving fabrication and testing of fiber-composite materials under dynamic loading conditions has been completed.

Ring testing provided quantitative data relative to material damping, frequency, and strength. Although results obtained on panel testing were qualitative to a large degree, definite potential has been demonstrated by certain composite materials. High damping and evidently equivalent accustic fatigue resistance was shown by graphite and boron, however, actual fatigue life was not determined. Specimens will be cut from these panels and tension tested. Results will be compared with specimens cut from control panels which were not subjected to the fatigue environment.

Manufacturing feasibility of representative skin elements was also demonstrated. Curved panels (~ 24 x 24-inches) of five ply, ±20° bidirectional, glass and graphite tape were fabricated . These duct-section elements, Figure 187 showing the configuration, are demonstration items for the potential X-22A application.

Work in the ARPA graphite fiber composite materials program has continued to show large potential weight advantages of graphite composite over aluminum construction for the representative fuselage application. The present X-22A aluminum duct structure weighs 295 lb/aircraft. Preliminary design calculations estimate that this weight might be reduced to 143 lb/aircraft with graphite composite redesign. This structural weight reduction would allow for a ~ 20% payload increase for the aircraft. Future efforts in Bell's internally supported research will be applied toward verification of this potential contributing simultaneously toward the goals of the present program.

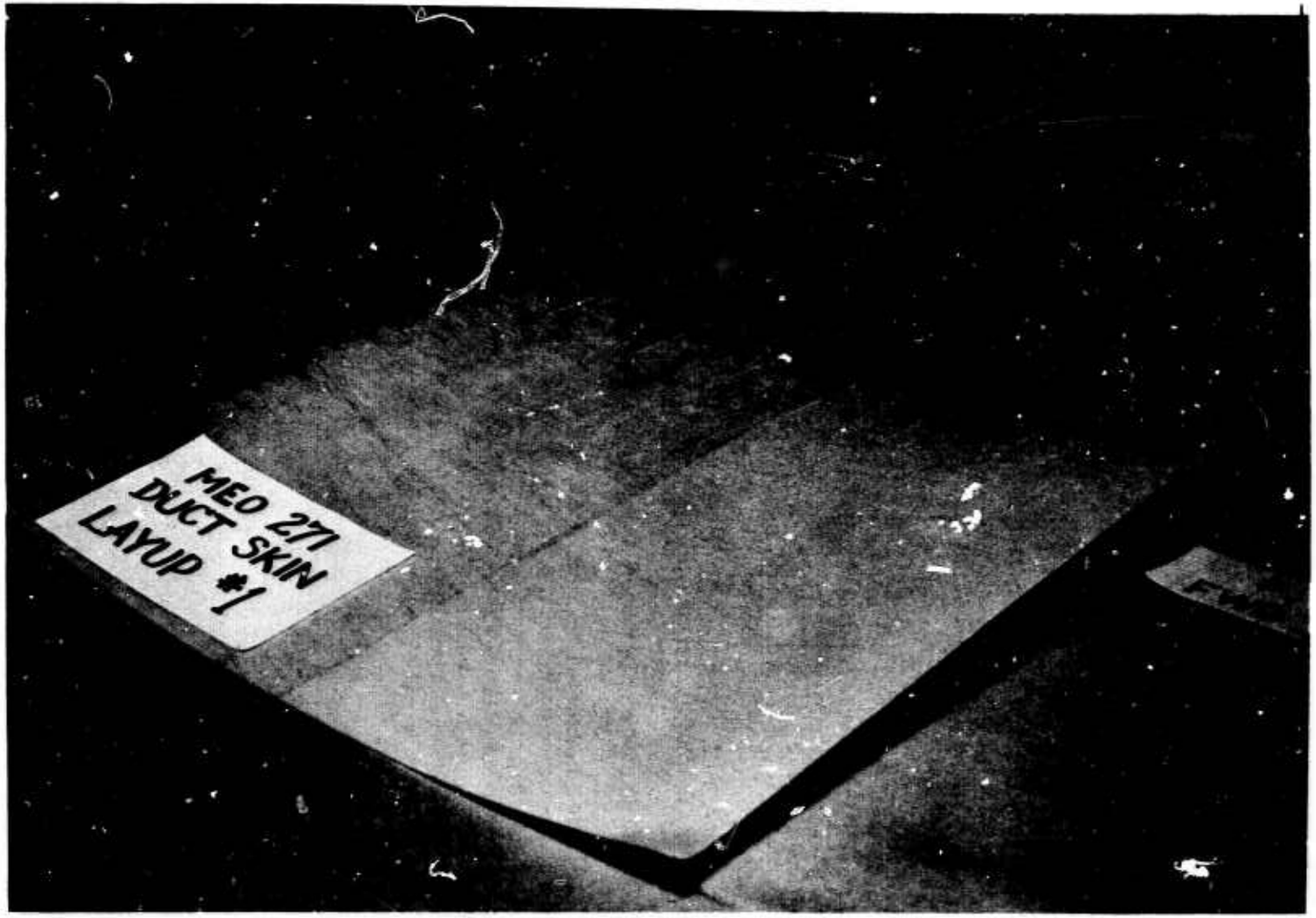

Figure 187. Composite Duct Panel

SECTION VIII

MICROMECHANICS AND PREDICTED DESIGN DATA FOR FIBER COMPOSITES

The initial adaptation of a new constituent material, design concept, or fabrication technique to a single composite application can be accomplished through an iterative, but often expensive, design test program. However, efficient and economical utilization of these advances in a variety of structural applications requires reliable micromechanic theories for the prediction of design data. Microstress analyses also provide a basis for seeking to improve the design of composites at the ply or laminate level. The full potential of composite materials in widespread structural applications can be realized only if reliable design data can be generated analytically from constituent material properties.

In order to establish validated design procedure and generate engineering property data for graphite fiber composites, the following projects were undertaken. Section VIII A reports on a survey and comparison of the present analytical methods available for the prediction and orthotropic elasticity properties and raises a question concerning the graphite fiber shear modulus. A comparison of predicted and experimental composite elastic properties is given in Section VIII B for "Thornel" 25 and 40 systems. Available failure criteria for glass and graphite fiber composites subjected to multiaxial stresses are compared with test results in Section VIII C. Section VIII D reports comparisons of predicted and measured multidirectional composite strengths. Section VIII E describes research in microstress analysis of fiber composite mathematical models. Section VIII F contains an analytical study of the stress and strain concentration due to a cylindrical inclusion in an elasto plastic matrix material. Photoelasticity work on two- and three-dimensional physical models is reported in Section VIII G. Preliminary experimental failure mechanics studies are described in Section VIII H. Finally, a bonding stress analysis of laminated cylindrical shells subjected to various loadings is reported in Section VIII I.

A. Elastic Properties for Fiber Composites
(Professor Kicher and Mr. D. Chao)

A survey on the elastic properties of fiber composites was made during the last year. The main purposes of this survey are to compile information from the existing analytical methods for predicting elastic constants of fiber composites and to study the possibilities of applying these methods to composites reinforced with anisotropic carbon fibers.

A detailed report[43] of this work has been released recently, titled "A Study of Elastic Properties of Filamentary Composites, Part I - Two Dimensional Mechanical Properties".

Analytical methods for various models were briefly described in this report. Numerical results of the principal elastic constants from different theories are compared with one another and with experimental data. Methods for determining the elastic properties of anisotropic laminates are also given

in the report. The subsequent results for anisotropic laminates are presented for comparisons. The most interesting observation is that the transverse modulus for an orthotropic fiber composite is virtually independent of fiber volume as shown in Figure 188.

Recently, more experimental data concerning the graphite fiber composites have been obtained. A comparison of predicted and measured composite properties was made at Bell (see Section VIII B). The shear moduli of the carbon fibers, 5 x 10^6 psi for "Thornel" 25 and 4 x 10^6 for "Thornel" 40, must be examined carefully. These values were obtained by selecting fiber shear moduli which yielded a "best fit" with the experimental data using Whitney's micromechanics model.[44] It can be established that Whitney's expression

$$G_{12} = \frac{[(G_f + G_m) + (G_f - G_m) V_f] G_m}{(G_f + G_m) - (G_f - G_m) V_f} \qquad \text{(VIII A-1)}$$

gives a modulus about 30% lower than the experimental data for glass fiber composites as shown in Figure 189. Since this expression is valid for both isotropic and orthotropic fibers, it is reasonable to assume that it will also give a value approximately 30% lower than test data for graphite fiber composites. If the shear modulus as calculated using Equation VIII A-1 is multiplied by a factor of 1.4, better correlation with experimental data is obtained. The shear modulus thus obtained using a "best fit" with experimental data is approximately 1.2 x 10^6 psi for both "Thornel" 25 and 40. The fiber data and elastic constants for both "Thornel" 25 and 40 using a fiber shear modulus of 1.2 x 10^6 psi are given in Tables LIX and LX respectively. Further studies to determine a more reliable value for the fiber shear modulus are therefore indicated.

TABLE LIX

FIBER AND MATRIX PROPERTIES
USED IN ANALYTICAL PREDICTIONS

Property	Resin ERL 2256 /MPDA	"Thornel" Fiber 25	40
E_L	0.57	25.	40.
E_T	----	1.2	1.1
G_{LT}	0.209	1.2	1.2
ν_{LT}	0.36	0.25	0.25
ν_{TT}	----	0.25	0.25

Unit: Modul: -10^6 psi

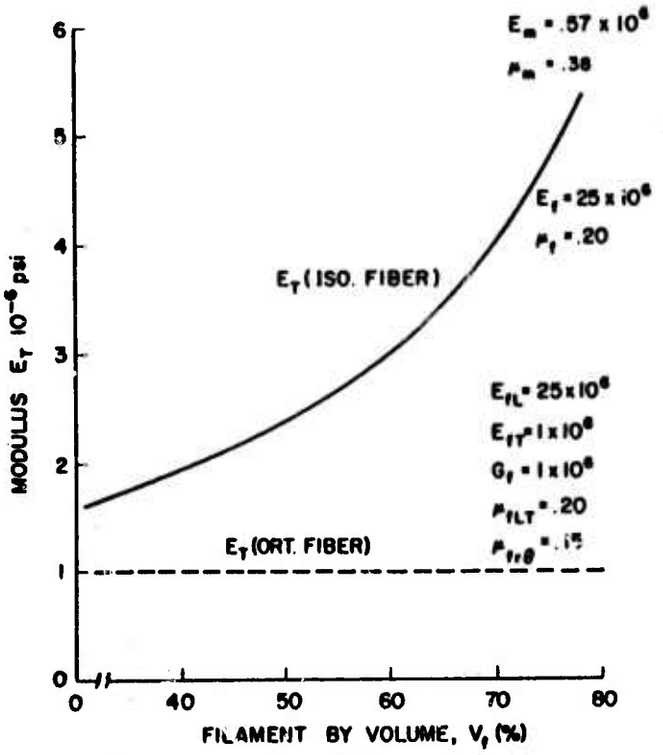

Figure 188. E_T Of Carbon-Epoxy Matrix Composites Vs. V_f.

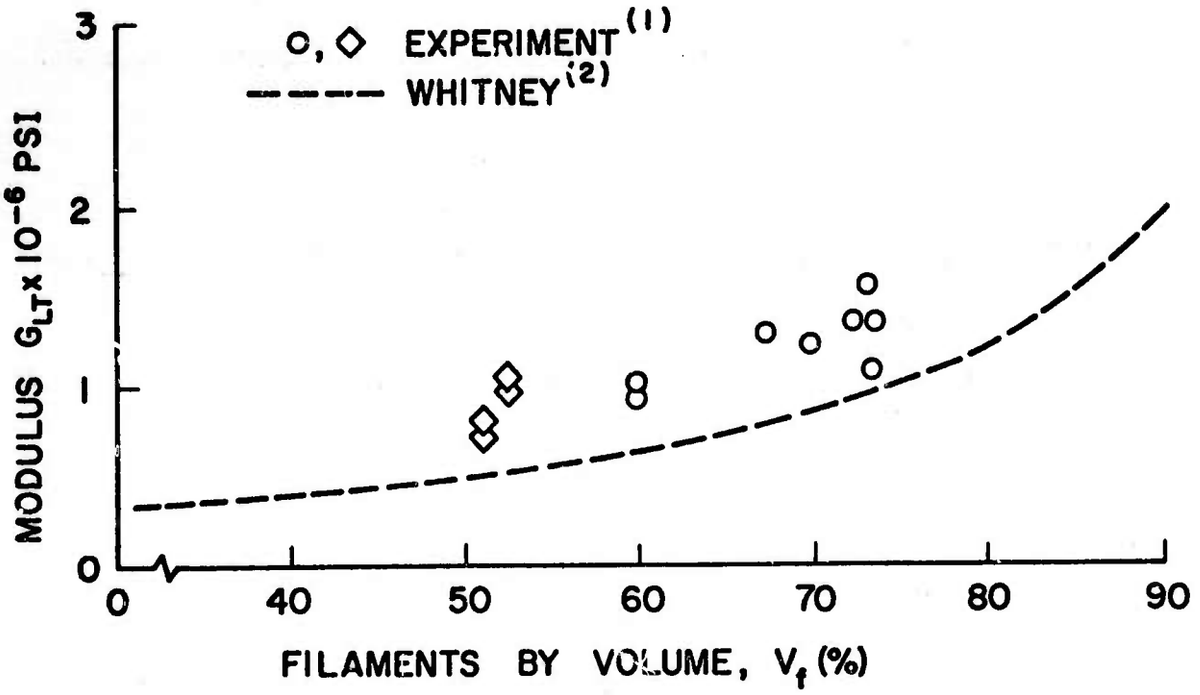

Figure 189. G_{LT} of E Glass-Epoxy Composites Versus V_f.

TABLE LX

PREDICTED AND MEASURED ELASTIC PROPERTIES
FOR UNIDIRECTIONAL "THORNEL" 25 AND 40 /ERL 2256 COMPOSITES

	"Thornel" 25(V_f = 50%)		"Thornel" 40(V_f = 65%)	
Property	Measured	Predicted	Measured	Predicted
E_1	11.07	12.78	24.6	26.2
E_2	1.05	1.06	0.95	1.05
G_{12}	0.60	0.610	0.74	0.785
ν_{12}	0.29	0.31	0.29	0.295
ν_{21}	0.027	0.026	0.011	0.012

Unit: Moduli - 10^6 psi

B. Comparison of Predicted and Measured Composite Elastic Properties
(D.P. Hanley, Bell Aerosystems, and G.B. Spence, Union Carbide)

Since measuring the elastic properties of all composite lay-up patterns of interest to the designer is prohibitively expensive, methods of proven reliability must be employed for predicting these properties. For the properties of unidirectional composites, Whitney's micromechanics model (Reference 44) which takes into consideration the anisotropy in the fiber properties, has been used. So that the effects of fiber anisotropy might be investigated, calculations have also been made with isotropic fiber properties. The fiber and matrix properties used as input data for these calculations are given in Table LXI.

TABLE LXI

FIBER AND MATRIX PROPERTIES
USED IN ANALYTICAL PREDICTIONS

Property	Resin ERL 2256 /MPDA	"Thornel" 25 Isotropic	"Thornel" 25 Anisotropic	"Thornel" 40 Isotropic	"Thornel" 40 Anisotropic
$E_L = 1/s_{11}$	0.57	25	25	40	40
$E_T = 1/s_{22}$		25	1.2	40	1.1
$G_{LT} = 1/s_{66}$	0.209	10	5	16	4
$\nu_{LT} = -s_{12}/s_{11}$	0.36	0.25	0.25	0.25	0.25
$\nu_{LT} = -s_{12}/s_{22}$		0.25	0.012	0.25	0.0069
$\nu_{TT} = -s_{23}/s_{22}$		0.25	0.25	0.25	0.25

Unit: Moduli - 10^6 psi

Transformations and laminate stacking procedures used in predicting the elastic properties of multidirectional composites have been based on Greszczuk s equations (Reference 45). Unidirectional composite properties based on both values have been used as the input data for the prediction of multidirectional composite properties.

In Section VIII A, evidence was cited that, if true values of the fiber and matrix shear moduli are used, the composite modulus, given by Equation VIIIA-1, should be multiplied by a factor of approximately 1.4. Alternatively, another analytical procedure for computing the unidirectional composite shear modulus might be more accurate. In order to be able to procede with the present studies before these questions are resolved and because the true shear modulus of the graphite fiber is not known, a

somewhat empirical procedure was adopted. Values of the shear modulus of the fiber were chosen so that the unidirectional shear modulus given by Equation VIIIA-1 without a correction factor agrees with the measured value. This procedure led to the use of 5 and 4 x 10^6 psi for the shear modulus of "Thornel" 25 and 40, respectively, in contrast to the use of 1.2 x 10^6 psi when a correction of 1.4 is applied to Equation VIIIA-1.

The elastic properties of unidirectional "Thornel" 25 and 40 composites have been predicted with both the isotropic and anisotropic fiber models. The results, given in Table LXII, may be compared with values measured on a single plate of each composite.

TABLE LXII

PREDICTED AND MEASURED ELASTIC PROPERTIES FOR UNIDIRECTIONAL "THORNEL" 25 AND 40/ERL 2256 COMPOSITES

Fiber and Property	Predicted for Isotropic Fiber	Predicted for Anisotropic Fiber	Measured
"Thornel" 25 Composites: Fiber Volume = 50 percent			
$E_1 = 1/s_{11}$	12.78	12.78	11.07
$E_2 = 1/s_{22}$	2.12	1.05	1.05
$G_{12} = 1/s_{66}$	0.518	0.565	0.60
$\nu_{12} = -s_{12}/s_{11}$	0.309	0.310	0.29
$\nu_{21} = -s_{12}/s_{22}$	0.051	0.025	0.027
"Thornel" 40 Composites: Fiber Volume = 65 percent			
$E_1 = 1/s_{11}$	26.20	26.19	24.60
$E_2 = 1/s_{22}$	3.29	1.04	0.95
$G_{12} = 1/s_{66}$	0.931	0.799	0.74
$\nu_{12} = -s_{12}/s_{11}$	0.292	0.293	0.29
$\nu_{21} = -s_{12}/s_{22}$	0.037	0.012	0.011

Unit: Moduli - 10^6 psi

Estimated experimental errors are 5 percent in E_1 and E_2, 10 percent in G, ν_{21}

and ν_{12}, 5 percent in the modulus of the fibers used in these plates, and 2 percent in the fiber volume content of the plates; fiber misalignment caused an additional but unknown error. Several iterations with different input anisotropic fiber properties indicate that the values given in Table LXI are physically reasonable and give, with the anisotropic fiber micromechanics model, satisfactory predictions of unidirectional composite elastic properties. On the other hand, the isotropic fiber model gives unsatisfactory predictions of the transverse modulus and, therefore, of ν_{21}. The present work suggests that, for the graphite fiber, E_T and G_{LT} (and probably ν_{LT} and ν_{TT}) depend upon the longitudinal fiber modulus E_L; but further work over wider ranges of fiber modulus and fiber volume content must be made before these dependences can be determined.

The variation of Young's modulus E, Poisson's ratio ν, and shear modulus G with polar angle θ has been calculated through the use of standard transformation formulas and the principal elastic properties E_1, E_2, ν_{12}, and G_{12}. Curves based on the three sets of properties given in Table LXII for a 9-ply unidirectional "Thornel" 25 composite are shown in Figure 190; experimental data obtained from tensile specimens oriented at 0, 10, 20, 45, and 90 degrees are also shown. The dotted curve for the anisotropic fiber model is in good agreement with the solid curve, which represents a best-fit of the experimental data; but the large error in the value of E_2 predicted by the isotropic fiber model causes correspondingly large errors in the ν-versus-θ and G-versus θ dashed curves for this model. Similar curves and measured data are given in Figure 191 for a 4-ply "Thornel" 25 composite with a (0°, 30°, 90°, 0°) lay-up. Bidirectional composite properties (dotted curve) predicted from properties measured on a unidirectional composite of the same fiber volume content are in good agreement with measured bidirectional data (solid curve). For most preliminary design studies, bidirectional composite properties predicted from constituent properties with the anisotropic fiber model (dashed curve) would also be satisfactory; however, the greater accuracy of properties based on measured unidirectional values is evident.

Only a small number of plies are needed in many applications of advanced composite materials. In such cases, the response of the material in bending is very different from the response to an in-plane membrane load. This difference is illustrated in Figure 192, which gives the so-called principal equivalent moduli in bending, E_1B and E_2B, and the ordinary principal membrane moduli, E_1M and E_2M, versus number of plies for "Thornel" 25 composites with alternating 0° and 90° lay-ups. The curves were calculated from the measured unidirectional composite properties given in Table LXII. Each point represents one static tensile or bend test measurement, but the data for each plate have been normalized to a standard fiber volume of 50 percent and fiber modulus of 25 million psi. For composites with an odd number of plies, the difference between membrane and bending moduli is very pronounced if the number of plies is less than approximately fifteen. For an even number of plies, the difference is much less but is still significant for 2 and 4 plies.

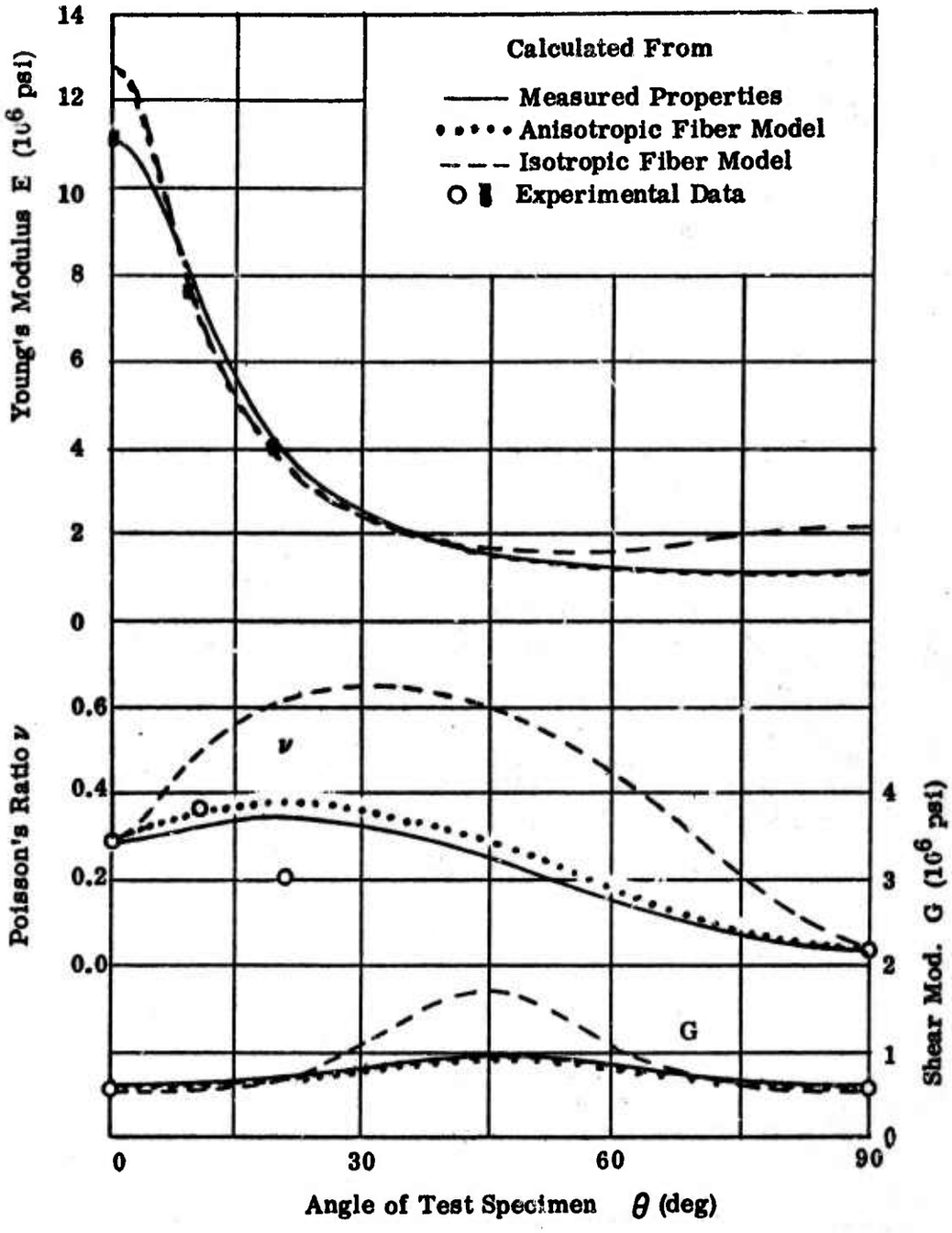

Figure 190. Elastic Properties Versus Angle of Test Specimen for Unidirectional "Thornel" 25/ERL 2256 Composites

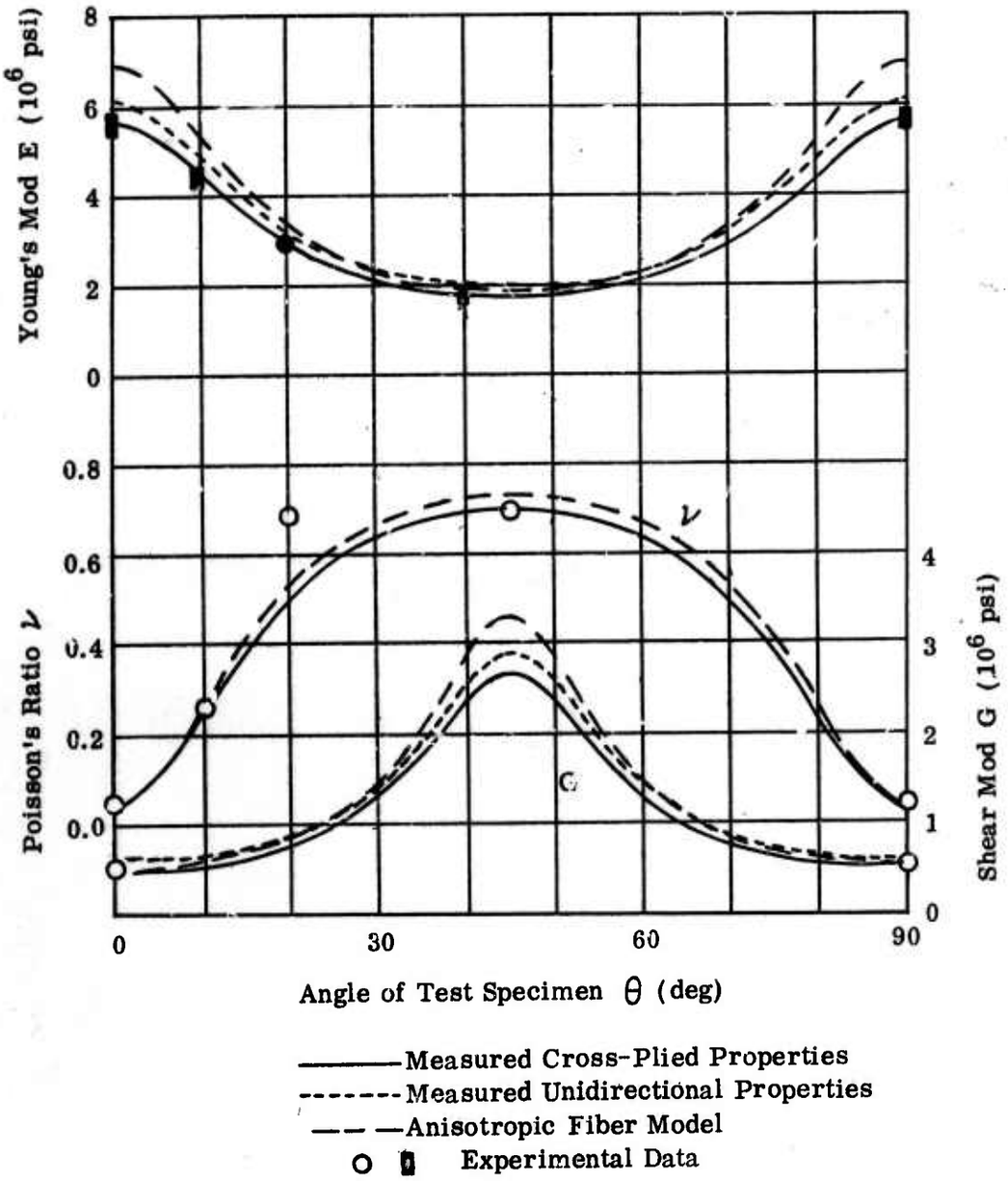

Figure 191. Elastic Properties versus Angle of Test Specimen for Four-Ply $(0^\circ, 90^\circ, 90^\circ, 0^\circ)$ "Thornel" 25/ERL 2256 Composite

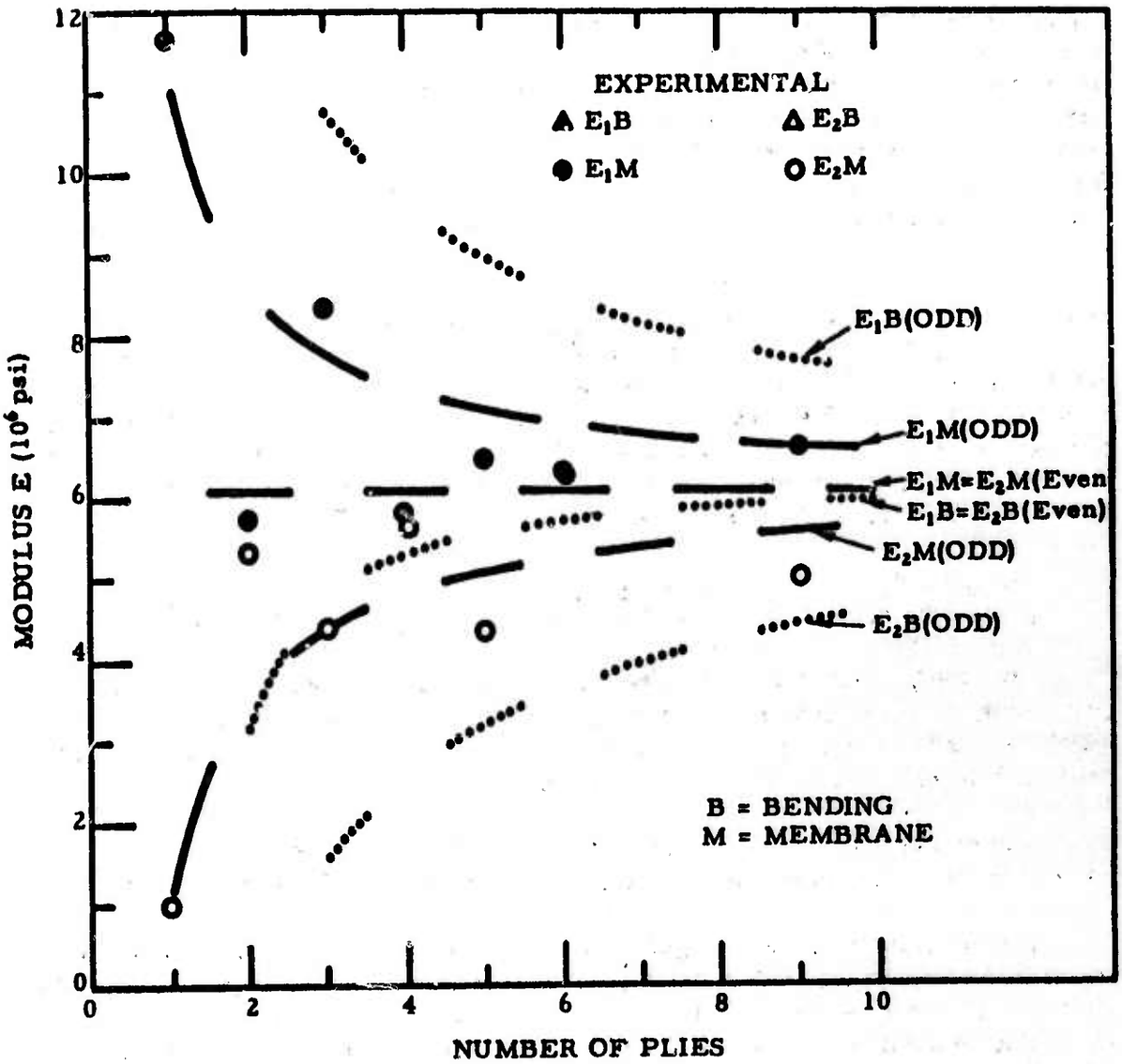

Figure 192. Membrane and Bending Moduli Versus Number of Plies for Cross-Plied "Thornel" 25/ERL 2256 Composites

Only a limited amount of experimental data is available for "Thornel" 40 composites. Initial measurements of elastic properties are given in Table LXIII for four candidate skin and stringer lay-up patterns. The predicted values are based on the measured unidirectional properties given in Table LXII and on an assumed thickness per ply of 0.010 inch. When allowance is made for the difference between the true fiber volume content of the plates and the value of 65 percent used in the calculations, the measured and predicted membrane properties usually differ by less than 10 percent. For all of the lay-up patterns listed in Table LXIII except the 4 ($10^\circ, -10^\circ, -10^\circ, 10^\circ$) pattern, the predicted values of Poisson's ratios are different for bending loads than for membrane loads. Although the experimental values are not very accurate, particularly for bending loads, the trend of the data confirms the theoretical predictions.

The present work indicates that the elastic properties of multidirectional high-modulus graphite fiber composites with resin matrices can be predicted to within approximately 10 percent, based on measured unidirectional composite properties, and to within approximately 20 percent, based on constituent properties and the anisotropic fiber model. This capability is satisfactory for preliminary design with graphite fiber composites. As additional fabrication experience is obtained and as the fiber properties become more uniform and better known, the agreement between measured and predicted values will certainly improve.

C. Failure Criteria for Fiber Composites

(K.H. Sayers, D.P. Hanley, Bell Aerosystems, and G.B. Spence, Union Carbide)

This report section considers the prediction of the strength of a single layer (lamina) of composite material. This layer may be one of many within a laminate, in which case the stresses acting on each lamina are first calculated from the applied loads and the characteristics of the laminate.

The problem then is to predict those combinations of stresses (σ_1, σ_2, and τ_{12}) applied to the lamina shown in Figure 193 which cause the lamina to fail.

It is assumed that the strengths in the 1, 2, and 12 directions are known when the stresses σ_1, σ_2, and τ_{12} are applied separately. These strengths are denoted as X, Y, and T respectively. Further, as the values of X and Y may be quite different, depending on whether the applied stresses are tensile or compressive, this must be taken into account when formulating a failure criterion.

Since a plane stress problem is involved with only three variables, a failure criterion may be defined in a three-dimensional space as illustrated in Figure 194. In this figure, normalizing stress ratios A, B, and C have been introduced (defined in Table LXIV) to avoid the distended shapes that would result if σ_1, σ_2 and τ_{12} were plotted directly. If the applied stresses are such that a point (A,B,C) is within the "solid" formed by the failure surface, then failure has not occured. If point (A, B, C) is outside the "solid", the strength has been exceeded and nonlinear analysis (see Section III G) is required generally to predict material behavior beyond yield to ultimate strength. The present work does not consider the more complicated effects of such nonlinearity .

TABLE LXIII

PREDICTED AND MEASURED MEMBRANE AND BENDING ELASTIC PROPERTIES FOR "THORNEL" 40/ERL2256 COMPOSITES

Property M - Membrane B - Bending	Number of Plies and Lay-Up Pattern 4(90°, 0°, 0°, 90°)	4(90°, 10°, -10°, 90°)	4(10°, -10°, -10°, 10°)	6(±10°, ±45°, ±10°)
E_1 M - Meas.	11.8	9.4	21.6	14.2
Pred.	12.81	12.11	22.48	15.88
E_1 B - Meas.	4.17	3.12	19.0	17.3
Pred.	3.91	3.64	22.48	21.75
E_2 M - Meas.	12.0	11.0	1.05	2.0
Pred.	12.81	12.82	0.98	2.75
E_2 B - Meas.	17.3	16.7	1.25	1.20
Pred.	21.64	21.65	0.98	1.05
G_{12} M - Meas.	0.62	0.84	1.5	2.7
Pred.	0.74	1.06	1.39	3.02
G_{12} B - Meas.				
Pred.	0.74	0.82	1.39	1.57
ν_{12} M - Meas.	0.03	0.05	0.98	0.86
Pred.	0.0216	0.0467	0.904	0.820
ν_{12} B - Meas.	0.01	0.03	0.76	0.8
Pred.	0.0127	0.0163	0.904	0.894
ν_{21} M - Meas.	0.03	0.06	0.047	0.12
Pred.	0.0216	0.0494	0.0396	0.142
ν_{21} B - Meas.	0.062	0.098	0.019	0.07
Pred.	0.0705	0.0968	0.0396	0.0430
V_f - Meas. (%)	64	57	69	56

Unit: Moduli in 10^6 psi. All predicted values are for a fiber volume of 65 percent and are based on the measured unidirectional composite properties given in Table LXII and a thickness per ply of 0.010 in.

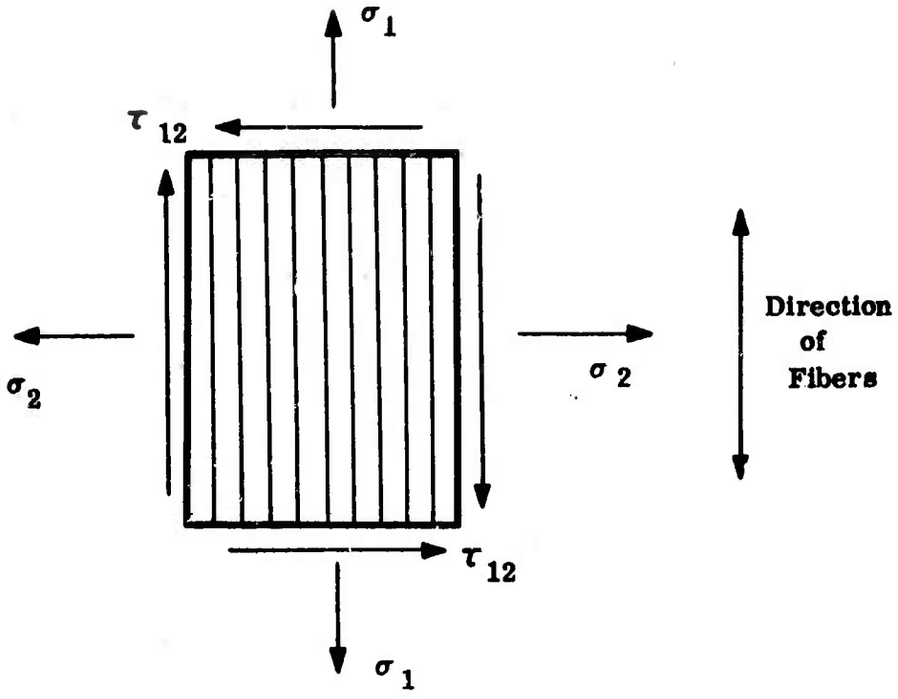

Figure 193. Stresses Applied to a Lamina

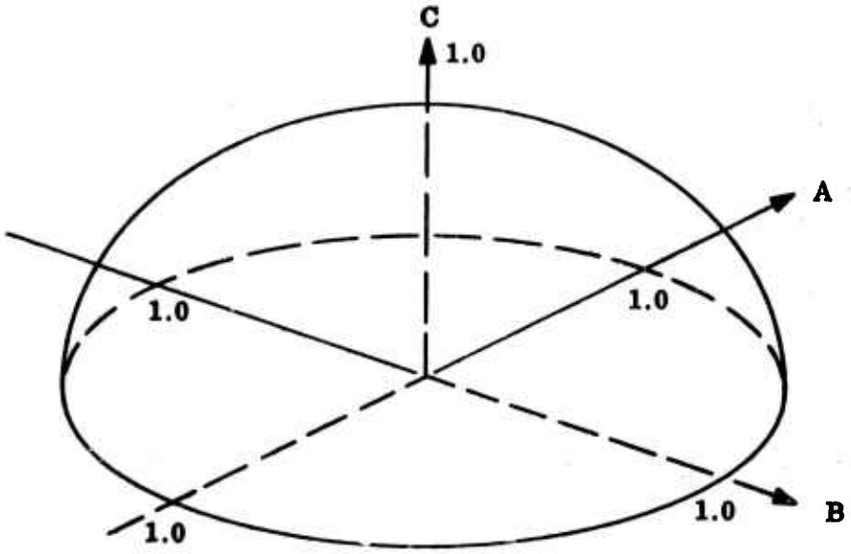

Figure 194. Representation of Failure Surface

1. Types of Criteria Available

The selection of a unique criterion to define the strength of composites is very difficult due to the high degree of material anisotropy and to their nonhomogeneous nature, which restricts the applicability of certain theories developed for anisotropic metals.

To define the strength of composites, the following criteria are available and may be divided into two types: (1) criteria derived from theories developed for anisotropic metals and (2) empirical interaction equations derived mainly from the study of test results for wood and glass composite materials. These criteria are summarized in Table LXIV.

TABLE LXIV

SUMMARY OF STRENGTH CRITERIA

Expression	Reference	Comment
(1) $A^2-(Y/X)AB+B^2+C^2=1$	17	Hill-type criterion developed for metals
(2) $A^2+B^2+C^2=1$	46	Based on wood technology (ANC-18)
(3) $A^2-AB+B^2+C^2=1$	47	Based on glass fiber work (MIL-HDBK-17)
(4) $A^2-KAC+B^2+C^2=1$	48	Based on glass fiber work (Grumman)

Definitions

$A = \sigma_1/X$

$B = \sigma_2/Y$

$C = \tau_{12}/T$

$$K = \frac{E_1 (1 + \nu_{21}) + E_2 (1 + \nu_{12})}{2\sqrt{E_1 E_2 (1 + \nu_{21}) (1 + \nu_{12})}}$$

In addition, criteria are available involving only two of the three variables A, B and C (Reference 49), which are not usable in the general case. Some involve these three quantities but use coefficients which are not specified directly (see Sections III F and IX F). The maximum strain approach (Reference 50) has also been applied to composite materials. This criterion has been shown to predict yield strength less well than the Hill-type criterion for boron laminates (Reference 50).

2. Comparison of Theories

The criteria given above may be compared by examining the traces in the BC, AC and AB planes as designated in Figure 195. For this purpose, A, B, and C are each in turn set equal to zero, and the resulting expressions are given in Table LXV. A comparison of the theories with experimental data is given in the next section.

TABLE LXV

COMPARISON OF FAILURE CRITERIA

	BC Plane	AC Plane	AB Plane
Expression	$A = \sigma_1 = 0$	$B = \sigma_2 = 0$	$C = \tau_{12} = 0$
(1)	$B^2 + C^2 = 1$	$A^2 + C^2 = 1$	$A^2 - \frac{Y}{X}AB + B^2 = 1$
(2)	$B^2 + C^2 = 1$	$A^2 + C^2 = 1$	$A^2 - AB + B^2 = 1$
(3)	$B^2 + C^2 = 1$	$A^2 + C^2 = 1$	$A^2 + B^2 = 1$
(4)	$B^2 + C^2 = 1$	$A^2 - KAC + C^2 = 1$	$A^2 + B^2 = 1$

In most cases, the four expressions become the same on a given plane. The traces are plotted for each of the three planes on Figure 195. Data currently in use for unidirectional "Thornel" 25 graphite yarn are used to determine the coefficients K (= 1.67) and Y/X (=8.56)* as defined in Table LXIV. These values are the averages of the tension and compression values and are used for the purpose of comparing the theories among themselves with a given set of composite inputs. The subsequent report section will treat separately tension and compression. The following features are of note: (a) All four expressions give the same trace (a circle) in the BC plane. (b) Expressions 1, 2 and 3 give the same trace (a circle) in the AC plane. Expression 4 gives an elongated ellipse, inclined at 45° to the A and C axes, due to the term involving K. (c) Expressions 3 and 4 give the same trace (a circle) in the AB plane, while expressions 1 and 2 give nearly coincident ellipses.

3. Comparisons with Test Results

Comparisons of the various failure criteria with fiberglass and graphite composites have been made using results for unidirectional specimens tested off-axis and the stress transformations given in Figure 196.

---

* For "Thornel" 40, K = 2.36. Values for Y/X (tension and compression) for "Thornel" 25 and 40 may be found in Table LXVI.

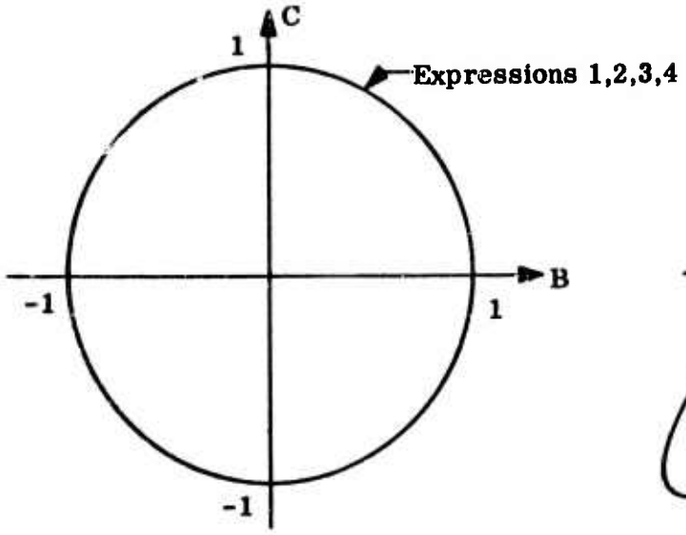

(a) Traces in BC (A=0) Plane

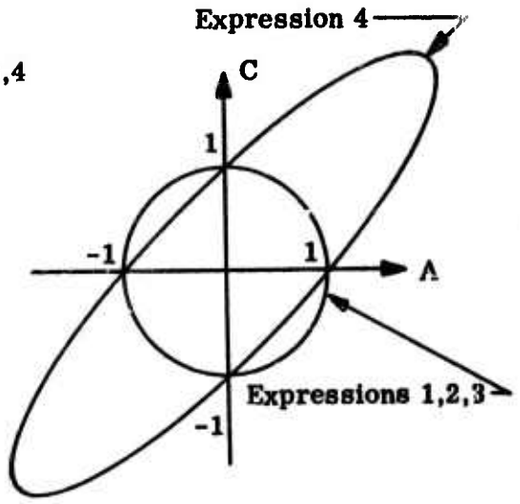

(b) Traces in AC (B=0) Plane

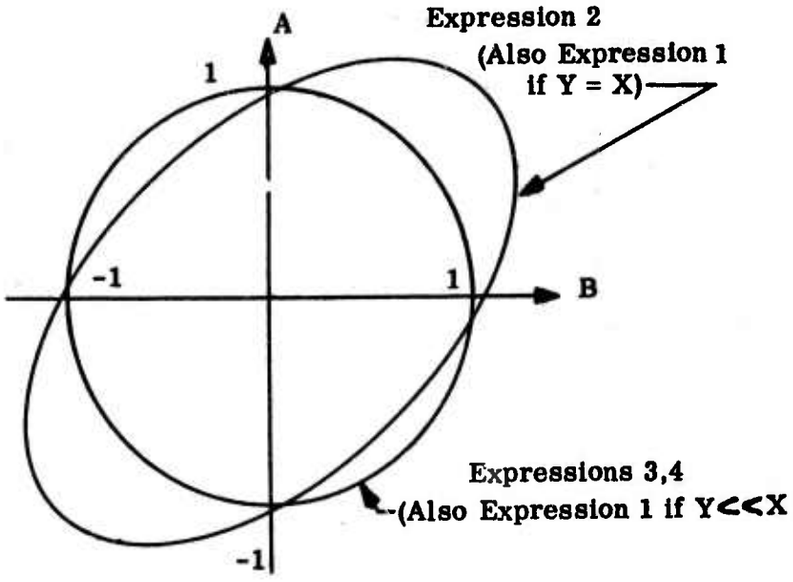

(c) Traces in AB (C=0) Plane

Figure 195. Traces of Failure Criteria in BC, AC, and AB Planes

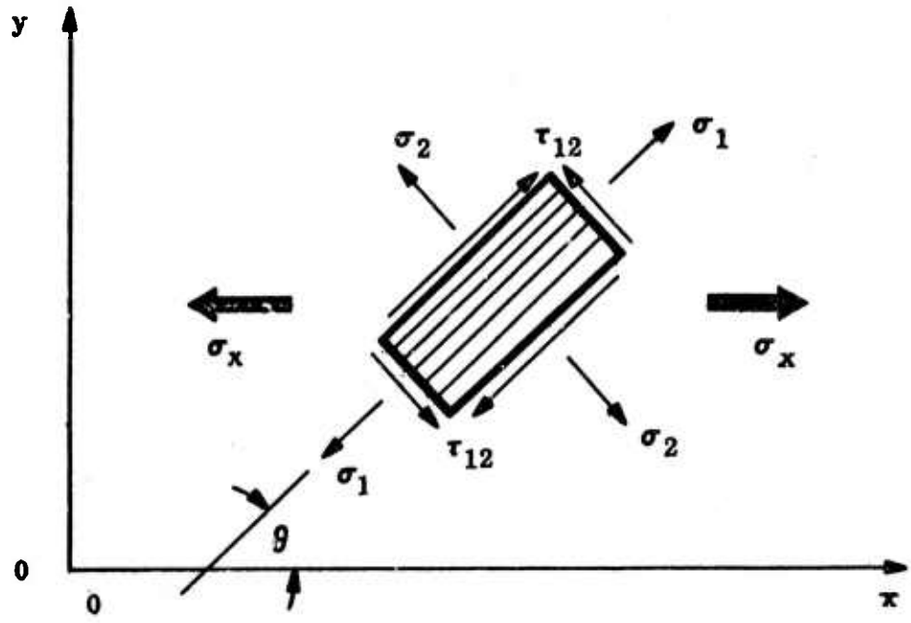

$$\sigma_1 = \sigma_x \cos^2\theta$$
$$\sigma_2 = \sigma_x \sin^2\theta$$
$$\tau_{12} = -\sigma_x \sin\theta \cos\theta$$

Figure 196. Stress Transformations

TABLE LXVI

COMPARISON OF ULTIMATE STRENGTH CRITERIA FOR GLASS AND GRAPHITE FIBER COMPOSITES

Test		σ (Pred.)/ σ (Meas.) for Criterion No.*			
	Angle	1	2	3	4
Case 1. Glass Fiber-Tension (Ref. 4)					
X=150	10°	0.939	0.938	0.959	1.071
Y=5.30	30°	0.934	0.933	0.949	0.960
T=6.05	60°	1.003	1.003	1.008	1.006
Case 2. Glass Fiber - Tension (Ref. 4)					
X=150	10°	1.030	1.029	1.052	1.176
Y=3.60	30°	1.001	1.000	1.018	1.021
T=6.05	60°	1.007	1.007	1.011	1.008
Case 3. "Thornel" 25 Fiber-Tension					
X=92	10°	1.003	1.003	1.040	1.233
Y=2.1	20°	0.963	0.962	0.990	1.031
T=4.0	45°	1.022	1.021	1.031	1.029
Case 4. "Thornel" 25 Fiber-Tension					
X=92	10°	0.871	0.870	0.894	1.040
Y=2.1	20°	0.859	0.858	0.878	0.915
T=3.4	45°	0.982	0.982	0.990	0.990
Case 5. "Thornel" 25 Fiber-Compression					
X=67	Y=21				
T=4.0	45°	0.715	0.714	0.717	0.747
X=67	Y=21				
T=5.0	45°	0.944	0.942	0.950	1.000
Case 6. "Thornel" 40 Fiber-Tension					
X=140	Y=2.0				
T=3.8	45°	1.023	1.023	1.029	1.030

*Criteria are defined in Table LXIV. Unit of X, Y, T - 10^3 psi.

For each test specimen, the strength was predicted by the criteria of Table LXIV. The ratio of the predicted strength to the measured strength is listed in Table LXVI. Cases 1 and 2 are based on a small amount of the data taken from Reference 17 for two glass fiber composites. Values predicted by criteria 1, 2, and 3 seem equally satisfactory and are within the scatter of the experimental measurements. Criterion 4 at 10 degrees gives appreciably poorer predictions. The experimental values of Y and T are not well established for the graphite fiber composites; the values (X=92, Y=2.1, T = 4.0 x 10^3 psi) used in Case 3 agree with the available measurements and give predicted tensile strengths with criteria 1, 2, and 3 which are as accurate as those for glass fiber composites. Criterion 4 at 10 degrees predicts a strength which is too high by 23 percent. When T is changed from 4.0 to 3.4 x 10^3 psi, criterion 4 gives better values, but they are still not in good agreement with measured values (Case 4); and criteria 1, 2, and 3 give low predicted values. Case 5 treats the compressive strength of a "Thornel" 25 composite at 45 degrees. Values of T of 3.4 and 4.0 x 10^3 psi give poor predicted strengths with all criteria; a value of 5.0 x 10^3 psi gives good predicted strengths with all criteria. The values of X, Y, and T used in Case 6 for a "Thornel" 40 composite tested at 45 degrees in tension are compatible with measured values given in Table XLIV - Section VI and give good predicted strengths with all criteria.

In summary, criteria 1, 2, and 3 seem equally satisfactory for the type of multiaxial stresses considered here; criterion 4 is less satisfactory. An unexplained problem is that the same value of T does not work well in both tension and compression. A limited survey indicates that criterion 1 also gives reasonably good predictions for the tensile strength of boron fiber composites. Basically, it is believed that more reliable experimental data for the Y and T strengths are required to evaluate adequately the available criteria.

D. Comparison of Predicted and Measured Composite Strengths
(S. Jordan and D.P. Hanley, Bell Aerosystems, and G.B. Spence, Union Carbide)

At Bell Aerosystems, attention has been turned toward composite strength predictions, not at the micromechanics level, but from an engineering standpoint with specific regard to establishing allowables for use in the component design. Consistent with this goal, the theory used for predicting strength and elastic properties has been applied to the generation of data for "Thornel" 25 and "Thornel" 40 graphite yarn composites*.

The procedure for the strength analysis of an arbitrary composite composed of a number of balanced laminates is outlined in Figure 197. It is assumed that a composite composed of balanced laminates "A", "B", and "C" is loaded by a biaxial state of stress. The stresses then distribute to the balanced laminates which make up the composite. In the figure, balanced laminate A is taken as an example.

*The development and implementation of theory to predict composite strength and elastic properties has been supported under Bell internal research funding.

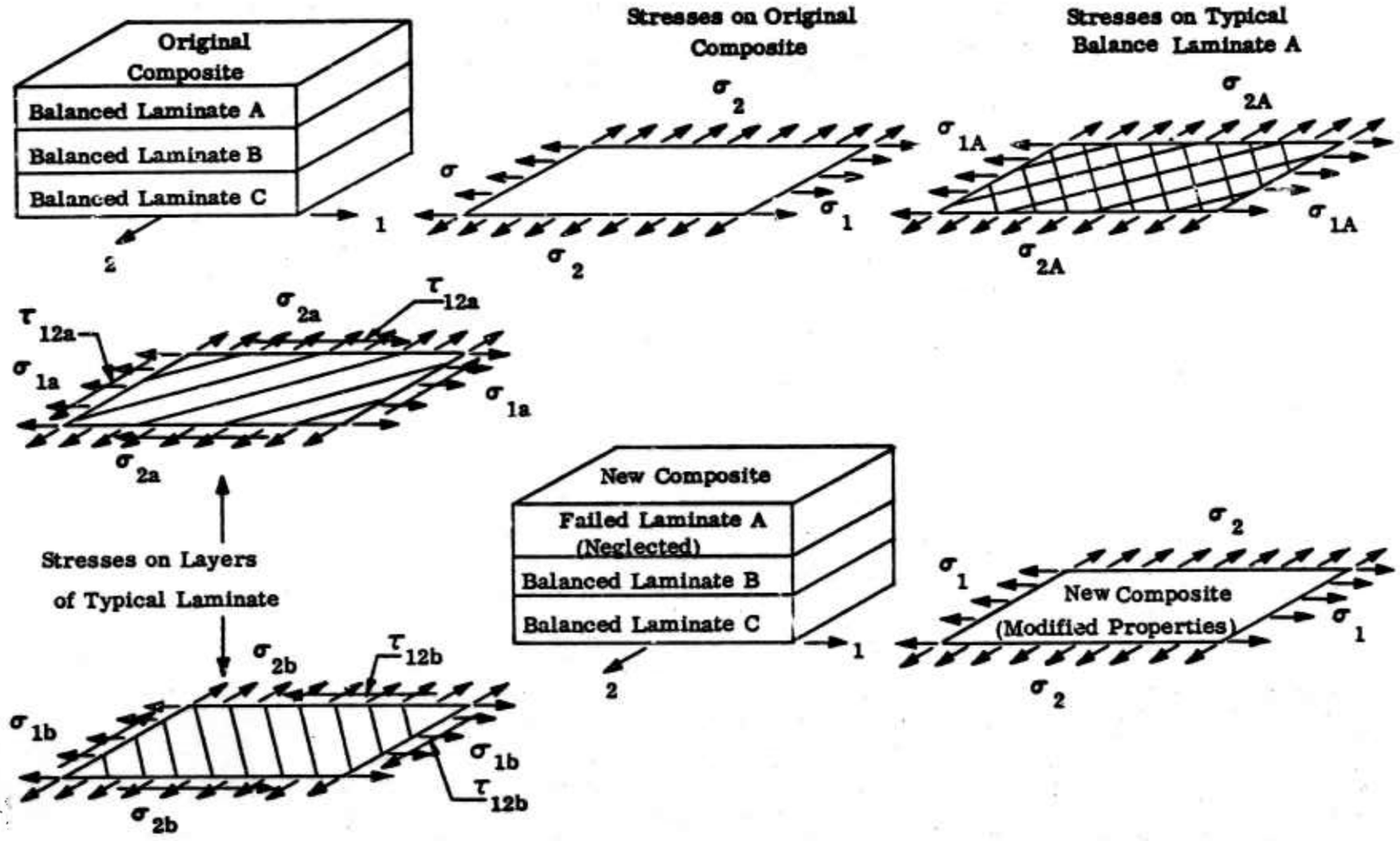

Figure 197. Strength Analysis Procedure

The stresses on each layer "a" and "b" of balanced laminate "A" are then computed. Based on these stresses and the principal strengths of the material, failure stresses are determined using the Tsai-type failure criteria (Reference 51, see Section VIII C). At the present time, it is assumed that when one layer of a balanced laminate fails, failure of the total balanced laminate is implied. After it has been determined which of the balanced laminates has failed, the elastic constants for the modified composite are recalculated and the process as described above is repeated. This procedure is then continued until ultimate failure of the composite (failure of the last lamina) is obtained.

This procedure is recognized to have flaws. First, the strongly nonlinear stress-strain curves obtained when cross-plied composites are tested at 45 degrees cannot possibly be predicted, even in a piece-wise linear manner. Second, when a yield point occurs the procedure predicts stress-strain curves of multidirectional composites which do not agree with experimentally observed curves.

Some predicted ultimate tensile strengths are given in Table XLIV which are based on the X, Y, and T values of Cases 3 and 6 of Table LXVI. The predicted values are 10 to 30 percent less than the measured values for the cross-plied composites tested in one of the fiber directions. Strength values predicted by the rule-of-mixtures method are 10 to 35 percent greater than the measured values. The higher predictions given by the rule-of-mixtures method (compared with the predictions given by the procedure outlined here) are due to the neglect of strain compatibility and the resulting biaxial stress state in the individual plies. Attempts to compare predicted and measured strengths for the multidirectional composites or cross-plied composites tested off-axis are complicated by the fact that the measured strengths depend on the size and shape of the test section. Preliminary experimental studies of the dependence of strength on gauge width have indicated two trends, for multidirectional composites. First, when many fibers lie at a small angle with respect to the test direction, the measured strength for a 1/4-inch gauge width is roughly 60 percent of the predicted value; and the measured strength approaches the predicted strength as the gauge width increases. Second, when no fibers lie at a small angle with respect to the test direction, the measured strength for a 1/4-inch gauge width is roughly the same as the predicted strength; and the measured strength becomes greater than the predicted strength as the gauge width is increased. In view of the fact that strengths from 1000 to over 100,000 psi occur for different lay-up patterns, the present analytical methods for predicting composite strengths, although not perfect, are still of considerable utility for preliminary design work. Further work is in progress on improved methods for predicting and measuring strengths of composites.

E. Microstress Analysis of Fiber Composites
(Professor Kicher and Mr. J.F. Stevenson)

Two formulations, each of which failed to yield a solution, are described. The first formulation is in terms of stresses and concerns the analysis of layered plates; the second seeks to effect a Ritz type solution by means of a displacement method discrete element and pertains to uni-directional fibrous composites. In the latter case, the composite is treated as a body in plane elasticity with the modeling element transverse to the fibers.

Laminated plates constructed with single layers of matrix-coated fibers are now of common enough occurrence to warrant a more sophisticated stress analysis than they have heretofore received. A possible idealization of such a construction consists in the replacement of each lamina with a homogeneous layer of material. Such an analysis, albeit a quasi-microstress analysis, in that within a layer each of the two identities-fiber and matrix-is lost, would be useful were it available. To this end, consider homogeneous, orthotropic, rectangular, parallelepiped the structural axes of which are aligned with a rectangular Cartesian coordinate system each axis of which is parallel to an edge of the body. It was assumed that three of the stresses could be represented by

$$\sigma_x = \sigma_x^{(0)}(x,y) + z\sigma_x^{(1)}(x,y) \qquad \text{(VIII F-1)}$$

$$\sigma_y = \sigma_y^{(0)}(x,y) + z\sigma_y^{(1)}(x,y) \qquad \text{(VIII F-2)}$$

$$\tau_{xy} = \tau_{xy}^{(0)}(x,y) + z\tau_{xy}^{(1)}(x,y) \qquad \text{(VIII F-3)}$$

where $\sigma_x^{(q)} = A_{00}^{(q)} + A_{10}^{(q)}x + A_{11}^{(q)}xy + A_{01}^{(q)}y + A_{20}^{(q)}x^2 + A_{02}^{(q)}y^2$ (VIII F-4)

$$\sigma_y^{(q)} = B_{00}^{(q)} + \ldots + B_{02}^{(q)}y^2 \qquad \text{(VIII F-5)}$$

$$\tau_{xy}^{(q)} = C_{00}^{(q)} + \ldots + C_{02}^{(q)}y^2 \qquad \text{(VIII F-6)}$$

$$q = 0, 1.$$

In order that the equilibrium equations be satisfied, it is necessary that

$$\sigma_z = \frac{z^3}{6}\left(\frac{\partial f_1}{\partial x} + \frac{\partial f_3}{\partial y}\right) - \frac{z^2}{2}\left(\frac{\partial f_2}{\partial x} + \frac{\partial f_4}{\partial y}\right) - z\left(\frac{\partial \phi_1}{\partial x} + \frac{\partial \phi_2}{\partial y}\right) + \phi_3 \qquad \text{(VIII F-7)}$$

$$\tau_{xz} = \frac{z^2}{2} f_1(x,y) + z f_2(x,y) + \phi_1(x,y) \qquad \text{(VIII F-8)}$$

$$\tau_{yz} = \frac{z^2}{2} f_3(x,y) + z f_4(x,y) + \phi_2(x,y) \qquad \text{(VIII F-9)}$$

where f_1, f_2, f_3, and f_4 are derivable from σ_x, σ_y, and τ_{xy}. The quantities ϕ_1, ϕ_2, and ϕ_3 are integration functions. With the assumption that the second partial derivatives of γ_{xz} and γ_{yz}, as they appear in the compatibility equations, are zero; it can be shown, after lengthy calculation, that the following must hold:

$$\psi = \frac{-\alpha}{2}\left(\frac{\nu_{13}}{E_1} x^2 + \frac{\nu_{23}}{E_3} y^2\right) + s_1\lambda + s_2 xy + s_3 y + s_4 \qquad \text{(VIII F-10)}$$

$$\phi = \frac{-\beta}{2}\left(\frac{\nu_{13}}{E_3} x^2 + \frac{\nu_{23}}{E_3} y^2\right) + r_1 x + r_2 y + r_4 \qquad \text{(VIII F-11)}$$

where

$$\phi = \frac{-\nu_{13}}{E_3} \sigma_x^{(0)} - \frac{\nu_{13}}{E_2} \sigma_y^{(0)} + \frac{1}{E_3} \phi_3 \qquad \text{(VIII F-12)}$$

$$\psi = \frac{-\nu_{13}}{E_1} \sigma_x^{(1)} - \frac{\nu_{23}}{E_2} \sigma_y^{(1)} - \frac{1}{E_3}\left(\frac{\partial \phi_1}{\partial x} + \frac{\partial \phi_2}{\partial y}\right). \qquad \text{(VIII F-13)}$$

In addition, eight equations relating the constants A_{ij}, B_{ij}, and C_{ij} can be deduced. All surface stresses are assumed to be of polynomial form in the coordinates of the face. If τ_{xz} is equated to the boundary values at the plus and minus faces, there results:

1. an expression for $\phi_1(x,y)$ and,
2. three relations among the polynomial coefficient for τ_{xz}.

Doing likewise for τ_{yz} yields:

1. an expression for $\phi_2(x,y)$ and,
2. three relations among the polynomial coefficients for τ_{yz}.

Thus, ϕ_1, ϕ_2, and ϕ_3 may be eliminated, and the problem may be viewed as having forty-five unknowns:

$(A_{ij}, B_{ij}, C_{ij}, r_i, s_i, \alpha, \beta) \rightarrow (12, 12, 12, 3, 4, 1, 1).$ (VIII F-14)

A set of forty-five equations was derived as follows. In the plus and minus z-faces, σ_z, τ_{xz}, and τ_{yz} were equated to the boundary values of these variables; on the plus and minus x-faces, the stress resultants N_x, N_{xy}, and M_x were equated to the respective applied values; on the plus and minus y-faces, the stress resultants N_y, N_{xy}, and M_y were equated to the corresponding applied values. Three eqautions are given by equating the x and y components of resultant couple and the z component of resultant force to zero. When these equations are combined with the eight deduced from the compatibility equations and the six found from matching the boundary conditions on τ_{xz} and τ_{yz}, a set of forty-five equations is found. When an attempt was made to solve these equations, it was found that only forty-two were linearly independent. An examination of the equations revealed that three of these could be shown to imply a restriction on the surface stresses that could not be deduced from the resultant force equilibrium equations. In view of this difficulty and the fact that stresses could not be matched on the x and y faces without inducing undue restrictions on the stress state in the interior, this problem was abandoned and attention was turned to a discrete element with a displacement formulation.

The plane stress element considered is rectangular and completely contains a circular fiber (see Figure 198). The assumed displacement functions to be discussed here involve fifty-six degrees of freedom and possess the following properties:

1. single-valued displacement components in the interior of the element,

2. continuous first partial derivatives of displacement and continuous mixed partial derivative of displacement at contiguous edges of two distinct elements, and

3. internal nodes on the fiber boundary to endow it with additional degrees of freedom relative to the matrix.

The circular fiber is replaced by an annulus with small inner radius (see Figure 199). At the centroid of the annulus, a rectangular coordinate system is established such that each axis is parallel to an edge of the element. Locate four points on each of the edge radii of the annulus where these boundaries are intersected by the coordinate axes. Radial lines joining such points divide the annulus into four sectors. Consider now the assumed displacement components $\tilde{u}$ and $\tilde{v}$.

$$\tilde{u} = \phi_1 + \hat{u}^{(s)} \qquad \text{(VIII F-15)}$$

$$\tilde{v} = \phi_2 + \hat{v}^{(s)} \qquad s = 1, 2, 3, 4 \qquad \text{(VIII F-16)}$$

where ϕ_1 and ϕ_2 are interpolations over the entire rectangle using only exterior degrees of freedom and $\hat{u}^{(s)}$ and $\hat{v}^{(s)}$ are interpolations over the s^{th} annular sector and use only interior degrees of freedom. $\hat{u}^{(s)}$ and $\hat{v}^{(s)}$ are, of course, identically zero for points not interior to sector s. Following Bogner et al.,[52] define

$$\psi(x,y) = \sum_{i=1}^{2}\sum_{j=1}^{2} \psi_{ij} H_{oi}^{(1)}(x) H_{oj}^{(1)}(y) + \sum_{i=1}^{2}\sum_{j=1}^{2} \psi_{xij} H_{1i}^{(1)}(x) H_{oj}^{(1)}(y)$$

$$+ \sum_{i=1}^{2}\sum_{j=1}^{2} \psi_{yij} H_{oi}^{(1)}(x) H_{1j}^{(1)}(y) + \sum_{i=1}^{2}\sum_{j=1}^{2} \psi_{xyij} H_{1i}^{(1)}(x) H_{1j}^{(1)}(y)$$

(VIII F-17)

$$\psi = u, v$$

where the $H_{ij}^{(1)}(t)$ are first order Hermitian interpolation polynomials for $t \in [a,b]$. These expressions may be expressed, equivalently, as:

$$u = \underline{H}^T \underline{u} \qquad v = \underline{H}^T \underline{v}$$

where

$$\underline{u} = \begin{bmatrix} u_{11} \\ u_{x11} \\ u_{y11} \\ u_{xy11} \\ \text{-----} \\ u_{12} \\ \cdot \\ \cdot \\ \cdot \\ \text{-----} \\ u_{22} \\ \cdot \\ \cdot \\ \cdot \\ \text{-----} \\ u_{21} \\ \cdot \\ \cdot \\ \cdot \end{bmatrix} \qquad \underline{v} = \begin{bmatrix} v_{11} \\ v_{x11} \\ v_{y11} \\ v_{xy11} \\ \text{-----} \\ v_{12} \\ \cdot \\ \cdot \\ \cdot \\ \text{-----} \\ v_{22} \\ \cdot \\ \cdot \\ \cdot \\ \text{-----} \\ v_{21} \\ \cdot \\ \cdot \\ \cdot \end{bmatrix}$$

(16 x 1) (16 x 1)

(VIII F-18) (VIII F-19)

$$\underline{H}(x,y) = \begin{bmatrix} H_{01}^{(1)}(x) & H_{01}^{(1)}(y) \\ H_{11}^{(1)}(x) & H_{01}^{(1)}(y) \\ H_{01}^{(1)}(x) & H_{11}^{(1)}(y) \\ H_{11}^{(1)}(x) & H_{11}^{(1)}(y) \\ \hline H_{01}^{(1)}(x) & H_{02}^{(1)}(y) \\ \vdots & \\ \hline H_{02}^{(1)}(x) & H_{02}^{(1)}(y) \\ \vdots & \\ \hline H_{02}^{(1)}(x) & H_{01}^{(1)}(y) \\ \vdots & \\ H_{12}^{(1)}(x) & H_{11}^{(1)}(y) \end{bmatrix}$$

(16 x 1).

A similar expression can be written for $\hat{u}^{(s)}$ (or $\hat{v}^{(s)}$) using r and θ as independent variables and empolying the "corner" values of $\hat{u}^{(s)}$ (or $\hat{v}^{(s)}$) and its partial derivatives as unknowns. In order to assure single-valued displacements at the matrix-fiber interface, the values of $\hat{u}^{(s)}$, $\hat{v}^{(s)}$, $\hat{u}_\theta^{(s)}$ and $\hat{v}_\theta^{(s)}$ were equated to zero. This fact means that corresponding to each node on the fiber boundary only two unknowns are introduced. On the inner boundary of the annulus, values of displacement and displacement derivatives were equated so that there remain four unknowns corresponding to each displacement component. For example, for the sector shown in Figure 200, these expressions are

$$\hat{u}^{(1)} = \underline{\hat{H}}^T \underline{\hat{u}}^{(1)} \qquad \hat{v}^{(1)} = \underline{\hat{H}}^T \underline{\hat{v}}^{(1)}$$

where

$$\underline{\hat{u}}^{(1)} = \begin{bmatrix} \hat{u}_{11} \\ \hat{u}_{r1,1} \\ \hat{u}_{\theta 1,1} \\ \hat{u}_{r\theta 1,1} \\ \text{------} \\ \hat{u}_{r2,1} \\ \hat{u}_{r\theta 2,1} \\ \text{------} \\ \hat{u}_{r2,2} \\ \hat{u}_{r\theta 2,2} \end{bmatrix} \qquad \underline{\hat{v}}^{(1)} = \begin{bmatrix} \hat{v}_{11} \\ \hat{v}_{r1,1} \\ \hat{v}_{\theta 1,1} \\ \hat{v}_{r\theta 1,1} \\ \text{------} \\ \hat{v}_{r2,1} \\ \hat{v}_{r\theta 2,1} \\ \text{------} \\ \hat{v}_{r2,2} \\ \hat{v}_{r\theta 2,2} \end{bmatrix}$$

(8 x 1) (8 x 1)

(VIII F-21) (VIII F-21a)

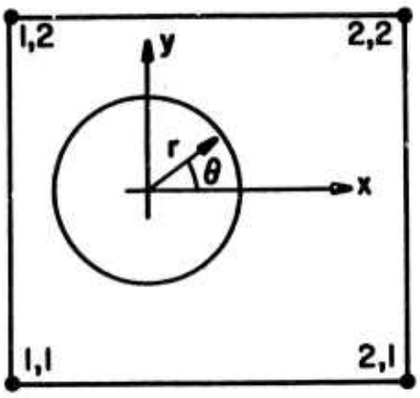

Figure 198. Rectangular Element Containing a Circular Fiber.

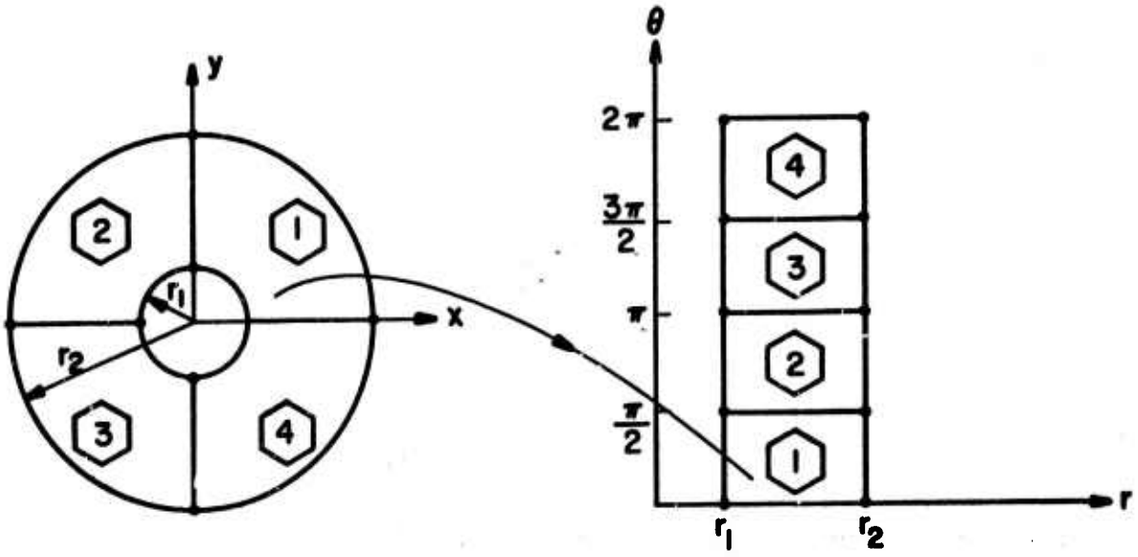

Figure 199. Annular Model of the Fiber.

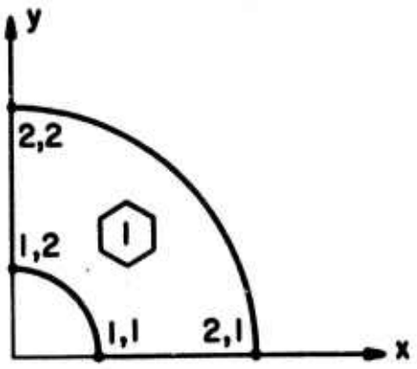

Figure 200. Annular Sector.

$$\underline{\hat{H}}(r,\theta) = \begin{bmatrix} H_{01}^{(1)}(r)\ H_{01}^{(1)}(\theta) + H_{01}^{(1)}(r)\ H_{02}^{(1)}(\theta) \\ H_{11}^{(1)}(r)\ H_{01}^{(1)}(\theta) + H_{11}^{(1)}(r)\ H_{02}^{(1)}(\theta) \\ \vdots \\ \hline H_{12}^{(1)}(r)\ H_{01}^{(1)}(\theta) \\ \vdots \\ H_{12}^{(1)}(r)\ H_{01}^{(1)}(\theta) \end{bmatrix}$$

(8 x 1).

(VIII F-22)

For the matrix material, $\phi_1 = u$ and $\phi_2 = v$. This assumption for $\tilde{u}$ and $\tilde{v}$ yields the following strain energy density expression for the matrix:

$$a_m(\underline{u},\underline{v}) = \frac{G_m}{1-\nu_m}\left[\underline{u}^T Q_{xx}\,\underline{u} + \underline{v}^T Q_{yy}\,\underline{v} + \nu_m(\underline{u}^T Q_{xy}\,\underline{v} + \underline{v}^T Q_{yx}\,\underline{u}\right]$$

$$+ \frac{G_m}{2}\left[\underline{v}^T Q_{xx}\,\underline{v} + \underline{v}^T Q_{xy}\,\underline{u} + \underline{u}^T Q_{yx}\,\underline{v} + \underline{u}^T Q_{yy}\,\underline{u}\right] \qquad \text{(VIII F-23)}$$

where $Q_{xx} = \underline{H}_x \underline{H}_x^T$ (VIII F-24)

$Q_{yy} = \underline{H}_y \underline{H}_y^T$ (subscripts on the $\underline{H}$ vector (VIII F-25)

$Q_{xy} = \underline{H}_x \underline{H}_y^T$ denote partial differentia- (VIII F-26)

$Q_{yx} = Q_{xy}^T$. tion) (VIII F-27)

Converting to radial transverse displacements in the fiber, ϕ_1 and ϕ_2 become

$$\phi_1 = \underline{G}^T\underline{u} \cos\theta + \underline{G}^T\underline{v} \sin\theta \qquad \text{(VIII F-28)}$$

$$\phi_2 = -\underline{G}^T\underline{u} \sin\theta + \underline{G}^T\underline{v} \cos\theta \qquad \text{(VIII F-29)}$$

$$\text{where } \underline{G} \equiv \underline{H}(r\cos\theta, r\sin\theta). \qquad \text{(VIII F-30)}$$

The assumed radial and transverse displacements for the fiber are then

$$u^f = \underline{G}^T\underline{u} \cos\theta + \underline{G}^T\underline{v} \sin\theta + \hat{H}^T\hat{u}(s) \qquad \text{(VIII F-31)}$$

$$v^f = -\underline{G}^T\underline{u} \sin\theta + \underline{G}^T\underline{v} \cos\theta + \underline{\hat{H}}^T\hat{v}(s). \qquad s = 1, 2, 3, 4 \qquad \text{(VIII F-32)}$$

The strain energy density function for the fiber is then given by

$$a_f(\underline{u},\underline{v};\hat{\underline{u}},\hat{\underline{v}}) = \alpha\, \underline{u}^T \{\underline{G}_r \underline{G}_r^T \cos^2\theta\}\, \underline{u} + \gamma \underline{v}^T \{\underline{G}_r \underline{G}_r^T \cos^2\theta\}\, \underline{v}$$

$$+ \alpha\, \underline{u}^T \{\underline{G}_r \underline{G}_r^T \cos\theta \sin\theta\}\, \underline{v} - \gamma \underline{u}^T \{\underline{G}_r \underline{G}_r^T \sin\theta \cos\theta\}\, \underline{v}$$

$$+ 50 \text{ addition terms}$$

$$\text{where } \alpha = \frac{G_f}{1-\nu_f} \qquad \gamma = \frac{G_f}{2}. \qquad \text{(VIII F-33)}$$

Close scrutiny of the integral of the strain energy density function revealed the existence of singularities of the $\frac{1}{r}$ type. These singularities arise as a consequence of products of $\frac{1}{r}$ and displacement derivatives that occur in the energy density expression. These singularities have the effect of placing unbounded entries in the stiffness matrix, thereby assigning zero values to the internal degrees of freedom. This difficulty can be avoided only if the constant terms and linear terms in r of $u^{(s)}$ and $v^{(s)}$ are set to zero. A study of displacements reported by Tsai et. al.[53] indicates that this restriction is so severe that the simplified displacement functions could not be expected to yield good results.

An alternative to the conventional Ritz type formulation of the displacement discrete element is a Trefftz inspired method wherein the assumed displacements satisfy the displacement equilibrium equations a priori and the degrees of freedom correspond to an approximation of the displacements along the boundary of the element. At present an effort is being made to exploit this approach systematically.

F. Elastoplastic Analysis of Cylindrical Inclusion in Uniformly Stressed Infinite Homogeneous Matrix

(Visiting Professor Mendelson, Case Institute)

1. Introduction

The importance of composite materials in aerospace applications, due primarily to their potentially high strength to weight ratios, is well known. The actual design strength of such material is, however, frequently much lower than their potential strength. One reason for this is the fact that there may be load components perpendicular to the fiber axes. The fibers then act as inclusions producing stress concentrations in the matrix which is to begin with considerably weaker than the fibers.

An elastic analysis on the effect of a circular inclusion in a homogeneous matrix presented by Schuerch[54]. Herein, a more realistic elastoplastic analysis is made to determine the stress and strain concentrations due to such inclusions. A complete analysis would have to include a large number of irregularly shaped inclusions irregularly spaced. It would also include the orthotropic character of the fibers. The present analysis is merely a first step, wherein a single circular inclusion in an infinite homogeneous matrix uniformly loaded at infinity is considered.

The method used in the analysis is the successive approximation or iterative technique for solving elastoplastic problems as outlined by Mendelson and Manson,[55] and Roberts and Mendelson.[56] This technique has been successfully used for the problem of an infinite plate with a hole by Davis,[57] Mendelson and Manson,[58] and Tuba,[59] and for a rigid inclusion by Tuba.[60] In both cases, the plane stress problem of a thin plate was considered. In the present analysis, the plane strain problem of an infinitely thick plate is treated for arbitrary matrix and inclusion properties. Furthermore, Hencky's total plasticity theory is used. Although the incremental theory can be used with equal ease, the results shown by Tuba[59] indicate that for this type of problem there is negligible difference between the total and incremental theory. If total plasticity theory is used, an appreciable amount of computer time can be saved.

2. Analysis

a. General Relations. Consider an infinite plate uniformly loaded at infinity as shown in Figure 201. Because of symmetry, the problem is most simply cast into polar coordinates. We define the following dimensionless quantities:

$$\rho = r/a \qquad \text{(VIII G-1)}$$

$$S_r = \frac{\sigma_r}{\sigma_o}, \quad S_\theta = \frac{\sigma_\theta}{\sigma_o}, \quad S_z = \frac{\sigma_z}{\sigma_o}$$

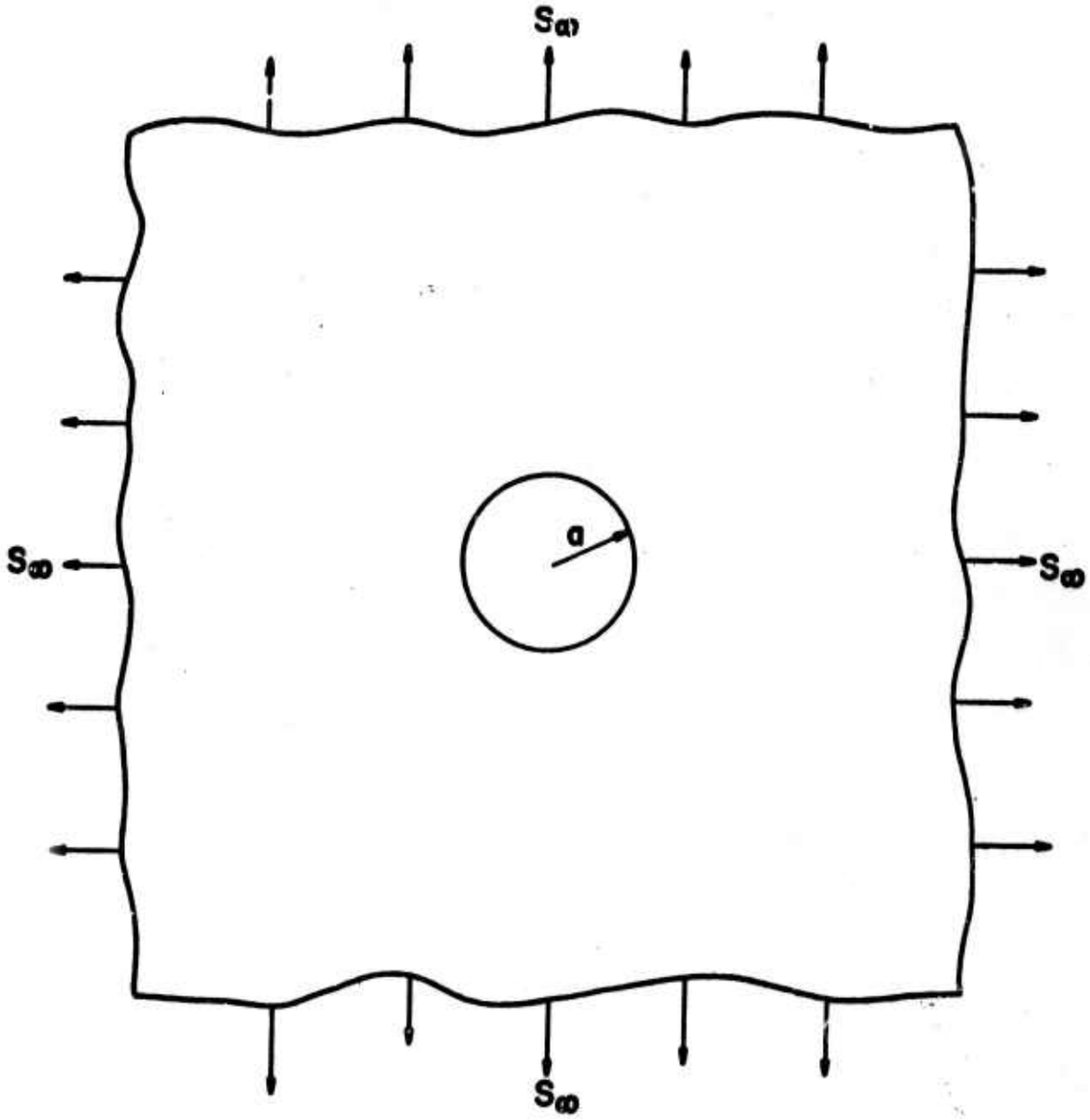

Figure 201. Infinite Body With Circular Inclusion.

$$e_r = \frac{\varepsilon_r}{\varepsilon_o}, \quad e_\theta = \frac{\varepsilon_\theta}{\varepsilon_o}, \quad U = \frac{u}{a\varepsilon_o}$$

where σ_o and ε_o are the yield stress and yield strain respectively. Furthermore, a is the radius of the inclusion and u is the radial displacement. The equilibrium, compatability and stress-strain relations can be written as

$$\frac{dS_r}{d\rho} = \frac{S_\theta - S_r}{\rho}, \qquad \frac{de_\theta}{d\rho} = \frac{e_r - e_\theta}{\rho}$$

$$e_r = S_r - \mu(S_\theta + S_z) + e_r^P \qquad \text{(VIII G-2)}$$

$$e_\theta = S_\theta - \mu(S_r + S_z) + e_\theta^P$$

$$e_z = 0, \quad \text{for plane strain.}$$

Equations (2) can be solved to give the following relations:

$$S_r = A + \frac{B}{\rho^2} + \frac{1}{2(1-\mu^2)} P(\rho) - \frac{1-2\mu}{2(1-\mu^2)} Q(\rho)$$

$$S_\theta = A - \frac{B}{\rho^2} + \frac{1}{2(1-\mu^2)} P(\rho) + \frac{1-2\mu}{2(1-\mu^2)} Q(\rho) + \frac{1}{1-\mu} R(\rho)$$

$$S_z = \mu(S_r + S_\theta) + e_r^P + e_\theta^P \qquad \text{(VIII G-3)}$$

$$e_r = (1-\mu-2\mu^2) A + (1+\mu) \frac{B}{\rho^2} + \frac{1}{2} \frac{1-2\mu}{(1-\mu)} P(\rho) - \frac{1-2\mu}{2(1-\mu)} Q(\rho) + \frac{1-2\mu}{1-\mu} e_r^P$$

$$e_\theta = (1-\mu-2\mu^2) A - (1+\mu) \frac{B}{\rho^2} + \frac{1}{2} \frac{1-2\mu}{1-\mu} (P(\rho) + Q(\rho))$$

$$U = (1-\mu-2\mu^2) A\rho - (1+\mu) \frac{B}{\rho} + \frac{1}{2} \frac{1-2\mu}{1-\mu} (P(\rho) + Q(\rho))\rho$$

where

$$P(\rho) \equiv \int_c^\rho \frac{e_r^P - e_\theta^P}{\rho} d\rho, \qquad R(\rho) \equiv \mu e_r^P - (1-\mu) e_\theta^P$$

$$Q(\rho) \equiv \frac{1}{\rho^2} \int_c^\rho \rho (e_r^P + e_\theta^P) d\rho. \qquad \text{(VIII G-4)}$$

The constants A, B and c will depend on the boundary conditions as will shortly be shown.

The plastic strains are related to the total strains by the modified Prandtl-Reuss relations.[55]

$$e_r^P = \frac{e_p}{3e_e}\ (2e_r - e_\theta), \qquad e_\theta^P = \frac{e_p}{3e_e}\ (2e_\theta - e_r) \qquad \text{(VIII G-5)}$$

where:

$$e_e = \frac{\sqrt{2}}{3}\ [(e_r - e_\theta)^2 + (e_r - e_z)^2 + (e_\theta - e_z)^2]^{1/2}$$

$$= \frac{2}{3}\ [e_r^2 + e_\theta^2 - e_r\, e_\theta]^{1/2} \qquad \text{(VIII G-6)}$$

and e_p is related to e_e through the stress strain curve and the relation

$$e_p = e_e - \frac{2}{3}\ (1 + \mu)\ S_e\ (e_p) \qquad \text{(VIII G-7)}$$

where S_e, the equivalent dimensionless stress, is the ordinate of the dimensionless uniaxial stress strain curve as shown in Figure 202. For the case of linear strain hardening, equation VIII G-7 can be solved for e_p to give

$$e_p = \frac{e_e - \frac{2}{3}\ (1 + \mu)}{1 + \frac{m}{1-m}\ \frac{2}{3}\ (1 + \mu)} \qquad \text{(VIII G-8)}$$

where m is the ratio of the slope of the stress-strain curve in the plastic range to the elastic modulus, as shown in Figure 203. For a perfectly plastic material VIII G-7 and VIII G-8 reduce to

$$e_p = e_e - \frac{2}{3}\ (1 + \mu) \qquad \text{(VIII G-8a)}$$

The above equations are completely general and are valid both in the inclusion and in the matrix. The constants A, B, and c will be different for the matrix and for the inclusion as will the material properties. We will henceforth distinguish between the matrix and the inclusion by using the subscripts M and I for matrix and inclusion respectively.

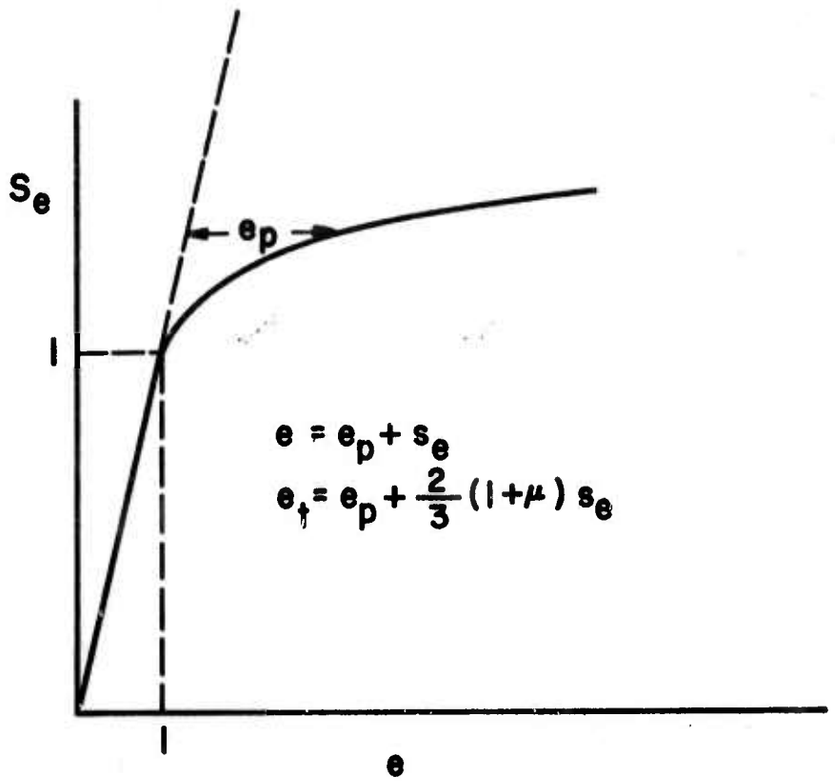

Figure 202. Dimensionless Uniaxial Stress-Strain Curve.

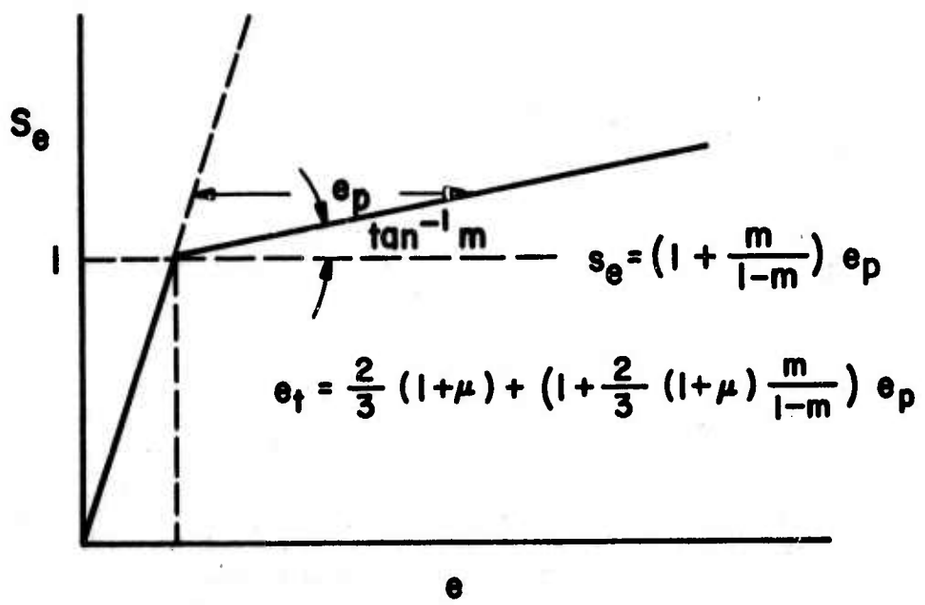

Figure 203. Dimensionless Uniaxial Stress-Strain Curve for Linear Strain Hardening.

b. Evaluation of Constants. To evaluate the constants, we make use of the boundary conditions.

$$c = \begin{cases} 0 & \text{for the inclusion } (0 \le \rho \le 1) \\ 1 & \text{for the matrix} \quad (1 \le \rho) \end{cases} \qquad \text{(VIII G-9)}$$

It also follows from the first or second of equations VIII G-3) that

$$B_I = 0. \qquad \text{(VIII G-10)}$$

Let the dimensionless stress at infinity be designated by

$$S_\infty \equiv \frac{\sigma_r(\infty)}{\sigma_{oM}}$$

where σ_{oM} is the yield stress of the matrix. Then, from the first of equations, VIII G-3:

$$A_m = S_\infty - \frac{1}{2(1-\mu_M^2)} P_M(\infty) + \frac{1-2\mu_M}{2(1-\mu_M)} Q_M(\infty)$$

where from VIII G-4:

$$P_M(\infty) = \int_1^\infty \frac{e^P_{rM} - e^P_{\theta M}}{\rho} \, d\rho, \qquad Q_M(\infty) = 0. \qquad \text{(VIII G-11)}$$

Hence,

$$A_M = S_\infty - \frac{1}{2(1-\mu_M^2)} P_M(\infty) \qquad \text{(VIII G-12)}$$

We note also that, since the plastic strains die out as ρ increases, we can replace the upper limit in equation VIII G-11 by some arbitrary radius R_M where R_M is greater than the radius of the plastic zone. Thus,

$$P_M(\infty) = \int_1^{R_M} \frac{e^P_{rM} - e^P_{\theta M}}{\rho} \, d\rho \, . \qquad \text{(VIII G-13)}$$

The two remaining constants A_I and B_M can be determined from the conditions that the radial stress and displacement should be continuous across the matrix-inclusion interface, i.e.,

$$\sigma_{rI}(a) = \sigma_{rM}(a) , \qquad u_{rI}(a) = u_{rM}(a) ,$$

or

$$S_{rI}(1) = \alpha S_{rM}(1) , \qquad \beta U_I(1) = \alpha U_M(1) \qquad \text{(VIII G-14)}$$

where

$$\alpha \equiv \frac{\sigma_{oM}}{\sigma_{oI}}, \quad \beta = \frac{E_M}{E_I} , \quad U_I = \frac{u_I E_I}{a \sigma_{oI}} , \quad U_M = \frac{u_M E_M}{a \sigma_{oM}} \qquad \text{(VIII G-15)}$$

and E_M, E_I are the elastic moduli of the matrix and inclusion, respectively.

From VIII G-3, 10, 12, and 14:

$$A_I = K_1 S_\infty + K_2 P_I(1) + K_3 Q_I(1) + K_4 P_M(\infty) \qquad \text{(VIII G-16)}$$

$$B_M = K_5 S_\infty + K_6 Q_I(1) + K_7 P_M(\infty)$$

where

$$K_1 = \frac{2(1-\mu_M^2)\,\alpha}{1+\mu_M + (1+\mu_I)(1-2\mu_I)\beta}$$

$$K_2 = -\frac{1}{2(1-\mu_I^2)}$$

$$K_3 = \frac{\frac{1-2\mu_I}{2(1-\mu_I)}\left(\frac{1+\mu_M}{1+\mu_I} - \beta\right)}{1+\mu_M + (1+\mu_I)(1-2\mu_I)\beta}$$

$$K_4 = \frac{-\alpha}{1+\mu_M + (1+\mu_I)(1-2\mu_I)\beta}$$

$$K_5 = \frac{(1+\mu_M)(1-2\mu_M) - (1+\mu_I)(1-2\mu_I)\,\beta}{1+\mu_M + (1+\mu_I)(1-2\mu_I)\,\beta} = \frac{K_1}{\alpha} - 1$$

$$K_6 = -\frac{(1-2\mu_I)\quad \beta/\alpha}{1+\mu_M + (1+\mu_I)(1-2\mu_I)\beta} = \frac{(1-2\mu_I)\,\beta}{\alpha^2} K_4$$

$$K_7 = -\frac{K_5}{2(1-\mu_M)^2}. \qquad \text{(VIII G-17)}$$

Note that the coefficients K_1 through K_7 are functions of the four material constants μ_I, μ_M, α and β.

c. Computation Procedure. The stresses, total strains, and plastic strains can now be computed by the successive approximation or iterative method.[55] The inclusion and the matrix are each divided into finite intervals. For the inclusion, the stations run from zero to 1. For the matrix, the stations run from 1 to R_M, where R_M is an arbitrary radius larger than the plastic zone. Since the plastic zone is not known to start with, one must guess at a reasonable value for R_M. It may be desirable to change this value after the first iteration so that most of the stations are in the plastic zone.

The coefficients K_1 through K_7 are computed only once from equation VIII G-17. Assuming all the plastic strains to be zero so that P_I, Q_I, P_M, Q_M are all zero, A_I and B_M are computed from equation VIII G-16 and A_M from VIII G-12. Equations VIII G-3 now give the complete elastic solution for the inclusion and the matrix. Beginning with the elastic solution, the iterative scheme for obtaining the elastoplastic solution proceeds as follows:

1. Using the values of total strains just computed, the equivalent total strain e_e is calculated at every station of the inclusion and the matrix by equation VIII G-6.

2. The equivalent plastic strain e_p at every station is determined from equation VIII G-7 and the stress-strain curve (or equation VIII G-8 for linear strain-hardening). If at any station e_p is less than zero, there is no plastic flow at that station, and the plastic strains are set equal to zero at that station.

3. The individual plastic strains are computed by means of equations VIII G-5.

4. The plastic strain integrals P_I, Q_I, P_M, Q_M are computed from VIII G-4.

5. A_M, A_I, and B_M are calculated from VIII G-12 and 16.

6. The stresses and strains are then computed from VIII G-3.

7. Return to step 1 and continue iterating until convergence is obtained, i.e., until two successive solutions differ by less than some arbitrarily preassigned value.

The above outlined computation scheme programmed for a digital computer gives rapidly and accurately the complete stress and strain fields both in the inclusion and the matrix. Both the elastic properties and stress-strain curves will, of course, be different in the two media.

3. Results and Discussion

The technique presented will now be illustrated for the two extreme cases of a plate with a void and a plate with a rigid inclusion and for the case of a relatively weak matrix with a relatively strong inclusion.

a. Plate with a hole or void. A plate with a hole represents the limiting case

$$\alpha \to \infty \qquad \beta \to \infty . \tag{VIII G-18}$$

The calculation proceeds as described above, except that A_I need not be computed. The stress and strain fields are obtained only in the matrix. Some results are shown in Figures 204-206.

In Figures 204 and 205 the effective stress and strain concentration factors are plotted against the applied stress at infinity for various values of the strain hardening parameter m_M. The effective stress concentration factor is here defined as the ratio of effective or equivalent stress at the edge of the hole to the equivalent stress at infinity, i.e.,

$$K_{\sigma_e} = \frac{S_{e(1)}}{S_{e(\infty)}} = \frac{S_{e\ (1)}}{(1-2\mu_M)S_\infty} \tag{VIII G-19}$$

with

$$S_e = \left[\frac{(S_r - S_\theta)^2 + (S_\theta - S_z)^2 + (S_z - S_r)^2}{2}\right]^{1/2} .$$

The elastic stress concentration factor as defined above is readily shown to equal

$$K_{\sigma_e}\ (\text{elastic}) = \frac{\sqrt{(1-2\mu_M)^2 + 3}}{1-2\mu_M} .$$

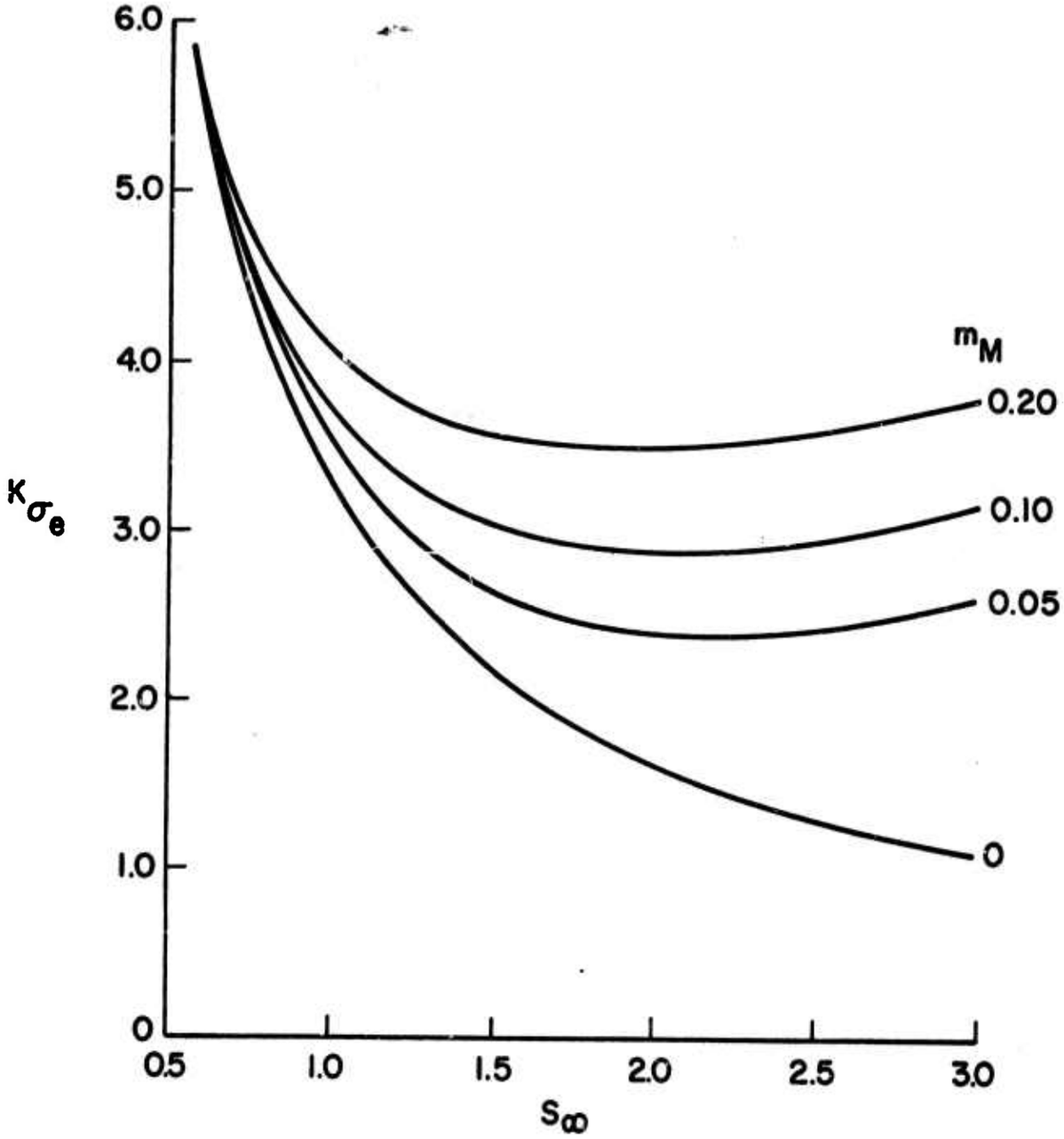

Figure 204. Effective Stress Concentration Factor For Plane Strain Case of Infinite Plate With Hole, $\alpha = \beta = \infty$.

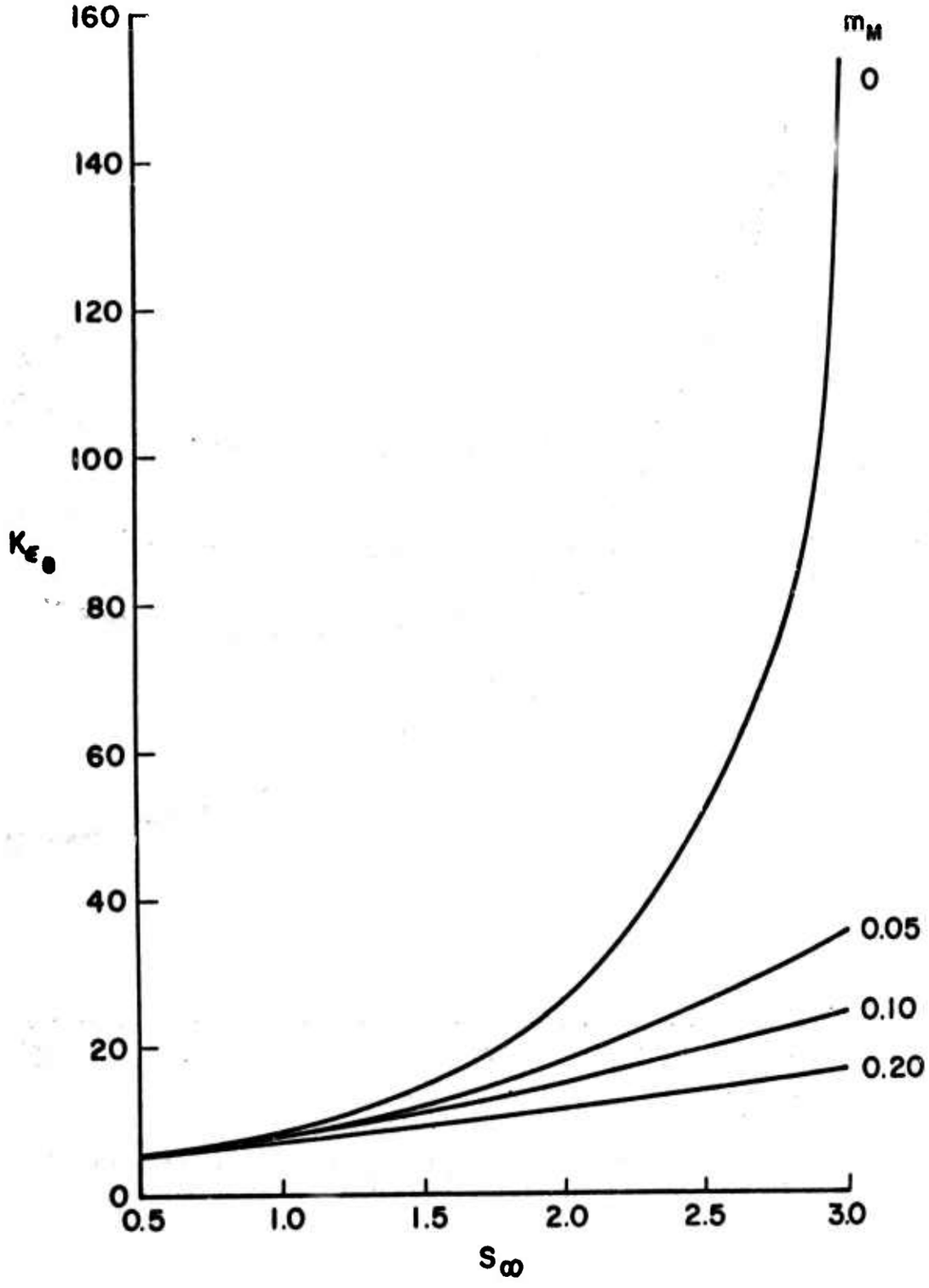

Figure 205. Effective Strain Concentration Factor For Plane Strain Case of Infinite Plate With Hole, $\alpha = \beta = \infty$.

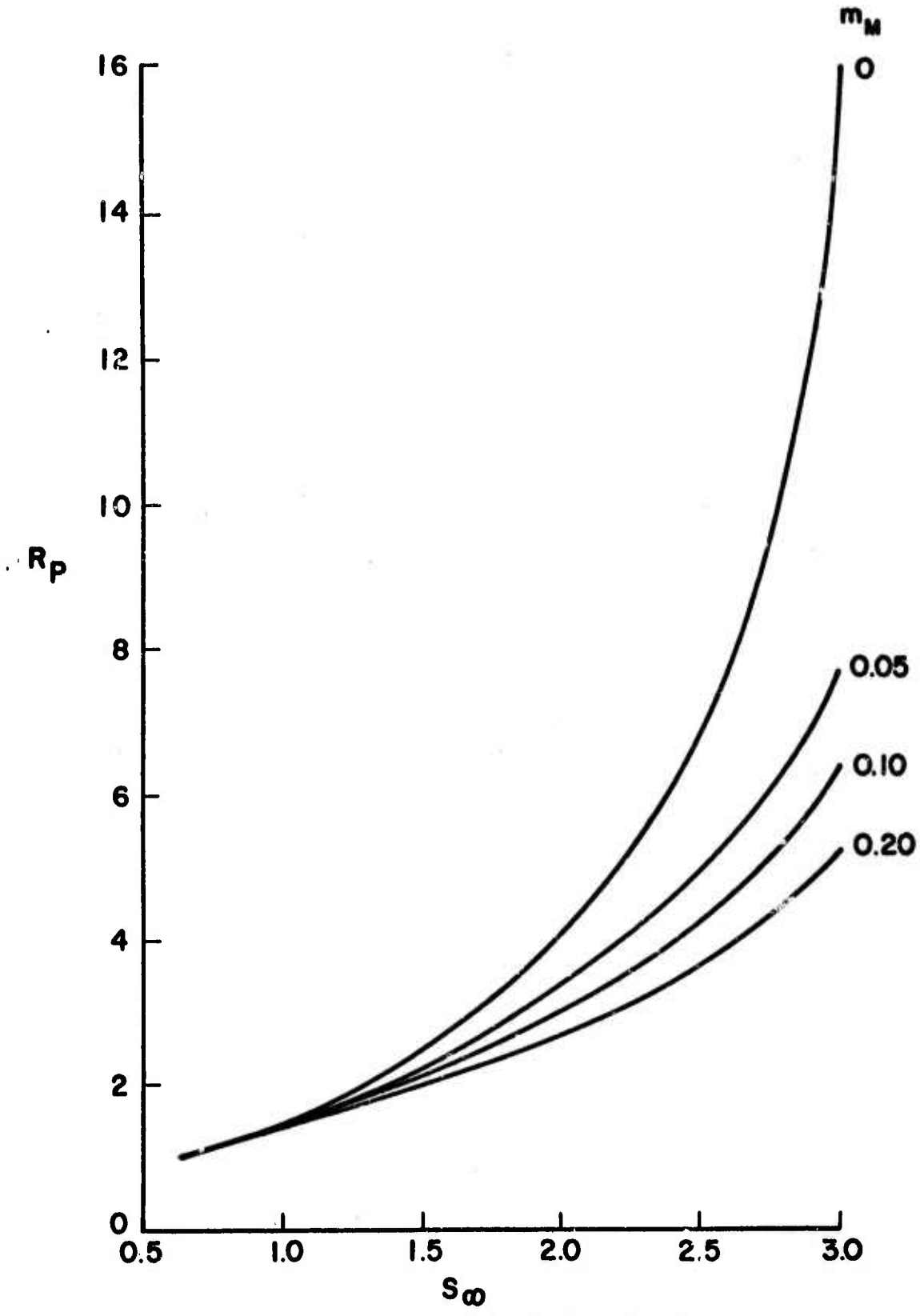

Figure 206. Plastic Zone Radius For Plane Strain Case of Infinite Plate With Hole, $\alpha = \beta = \infty$.

For a value of μ_M of 0.35, which is the value used in these calculations, the elastic stress concentration factor is equal to 5.86, the common starting point of all the curves of Figure 204.

Note that for the case of plane stress, the stress concentration factor is independent of Poisson's ratio and is equal to 2 for the elastic case. The large initial value of the stress concentration factor for the case of plane strain does not mean, however, that plastic flow will start at a lower load than for plane stress. On the contrary, it can readily be shown that the equivalent stress S_e will equal unity at the hole for a value of S_∞ equal to 0.569 compared to $S_\infty = 0.5$ for plane stress. Whether definition VIII G-19 is the appropriate one depends on how the stress concentration factor is to be used.

Figure 204 and 205 show how the stress concentration factor decreases with load and the strain concentration factor increases with load due to the material flowing plastically. The importance of strain hardening is readily evident. It is interesting to note that, although without strain hardening the stress concentration factor decreases monotonically with load, the introduction of strain hardening introduces a minimum point in the stress concentration-versus-load curve. For a high enough load, the strain hardening of the material is sufficient to overcome the stress relaxation due to plastic flow and the stress concentration factor starts rising. This effect does not occur for the plane stress case,[59] probably because the additional axial constraint inherent in the plane strain case is missing.

The strain concentration factor used in Figure 205 is defined by

$$K_{\varepsilon_e} = \frac{e_e(1)}{e_e(\infty)} = \frac{e_e(1)}{\frac{2}{3}(1+\mu_M)(1-2\mu_M)S_\infty} \qquad \text{(VIII G-20)}$$

For the elastic case

$$e_e(1) = \frac{2}{3}(1+\mu_M)\left[2 + (1-2\mu_M)^2\right]^{1/2} S_\infty$$

so that for $\mu_M = 0.35$

$$K_{\varepsilon_e} = 5.86 = K_{\sigma_e} .$$

Figure 206 shows the growth of the plastic zone with load. Again, the effect of strain hardening is very evident. The plate becomes completely plastic when S_∞ equals 3 1/3.

b. Plate with rigid inclusion. For a rigid inclusion

$$\alpha = \beta = 0. \qquad \text{(VIII G-21)}$$

The results using these values are shown in Figures 207-209. We note the very large difference between these results and those for the plate with the hole. The restraints produced by the inclusion greatly lower both the stress and strain concentration factors. Furthermore, the effect of strain hardening is no longer as great. The plastic zone size is greatly reduced as shown in Figure 209.

c. Inclusion with $\alpha = 0.1$, $\beta = .0.02$. As a final example, a matrix inclusion combination with $\alpha = 0.1$ and $\beta = .02$ was considered. This system corresponds roughly to a graphite fiber in a resin matrix. The results are shown in Figures 210-212. We note the similarity of these results to those of Figures 207-209 for the rigid inclusion. Of particular interest is the fact that the strain hardening properties of the matrix are relatively unimportant. Only one curve was drawn in Figure 212 since the difference between the different strain hardening parameter is very small. The complete plate becomes plastic for a value of S_∞ of about 3.35.

4. Summary

Equations have been derived and a method presented for performing an elastoplastic analysis of a system consisting of a circular inclusion in a homogeneous matrix uniformly stresses at infinity and in a condition of plane strain. The material properties of the inclusion and the matrix, including their stress-strain curves, are assumed to be arbitrary and independent of each other. Several examples, including the limiting cases of a hole and a rigid inclusion, are presented. It is shown that the constraints imposed by the rigid inclusion sharply reduce both the stress and strain concentration factors over those for the hole. The results for a system roughly approximating a graphite fiber in a resin matrix indicate that the fiber acts nearly as a rigid inclusion and that strain hardening properties of the matrix play only a minor role in determining the plastic strain concentration factor.

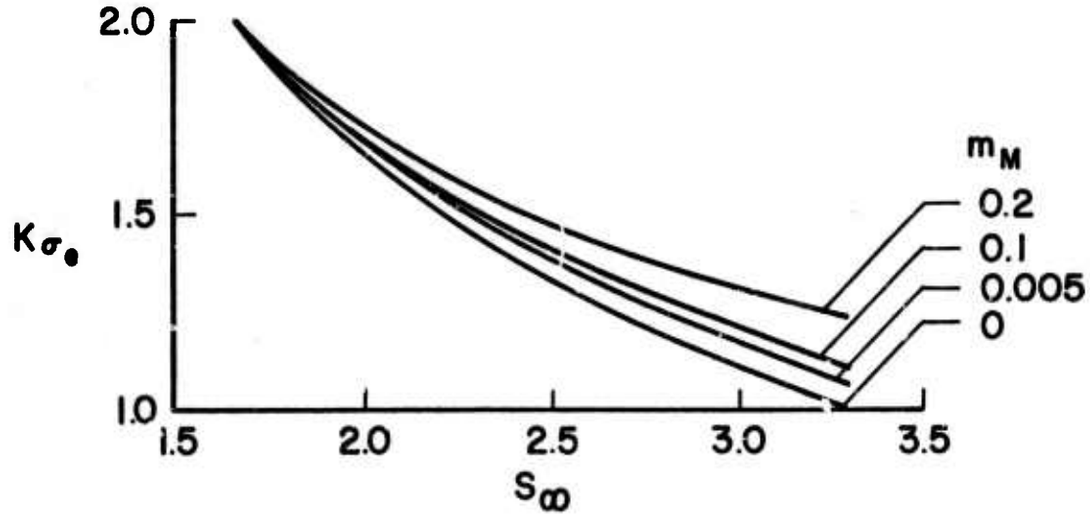

Figure 207. Effective Stress Concentration Factor For Plane Strain Case of Infinite Plate With Rigid Inclusion, $\alpha = 1$, $\beta = 0$.

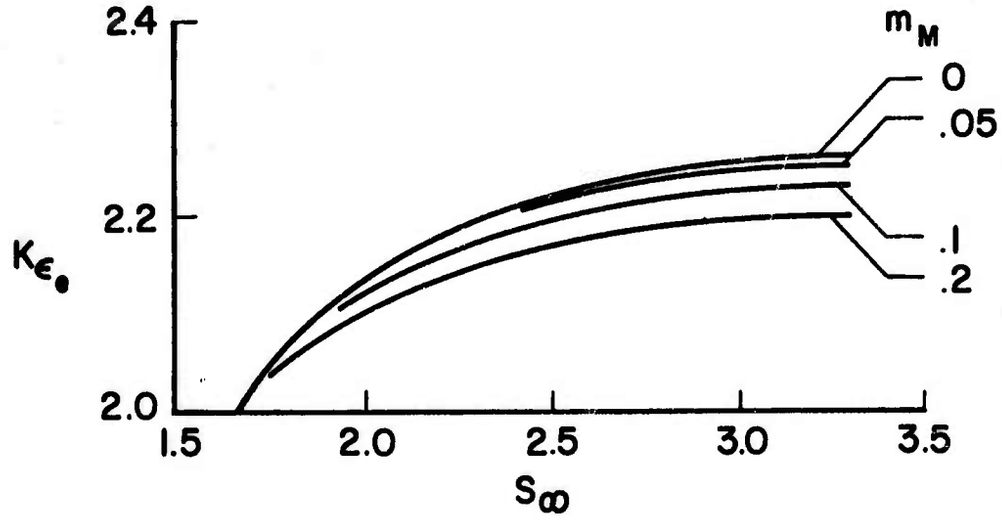

Figure 208. Effective Strain Concentration Factor For Plane Strain Case of Infinite Plate With Rigid Inclusion, $\alpha = 1$, $\beta = 0$.

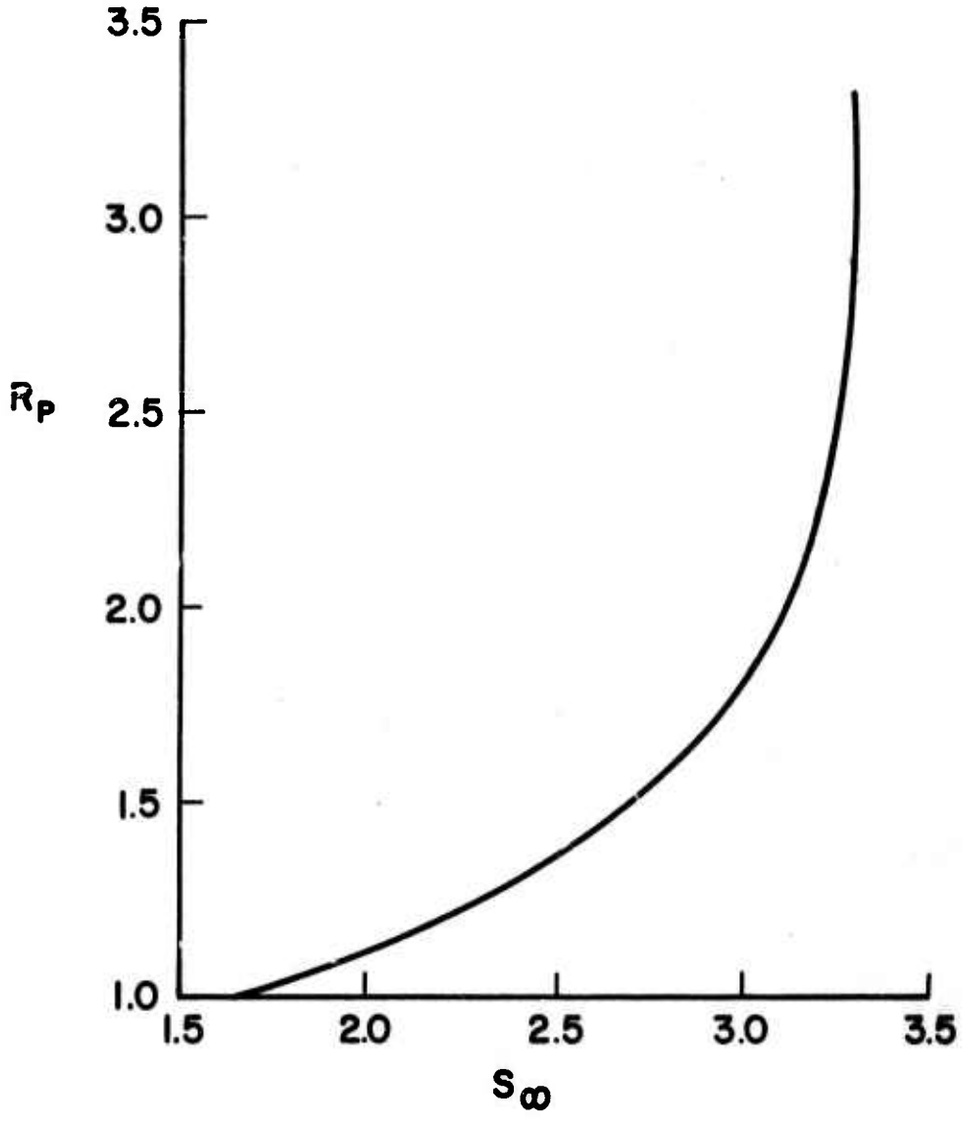

Figure 209. Plastic Zone Radius For Plane Strain Case of Infinite Plate With Rigid Inclusion; $\alpha = 1$, $\beta = 0$.

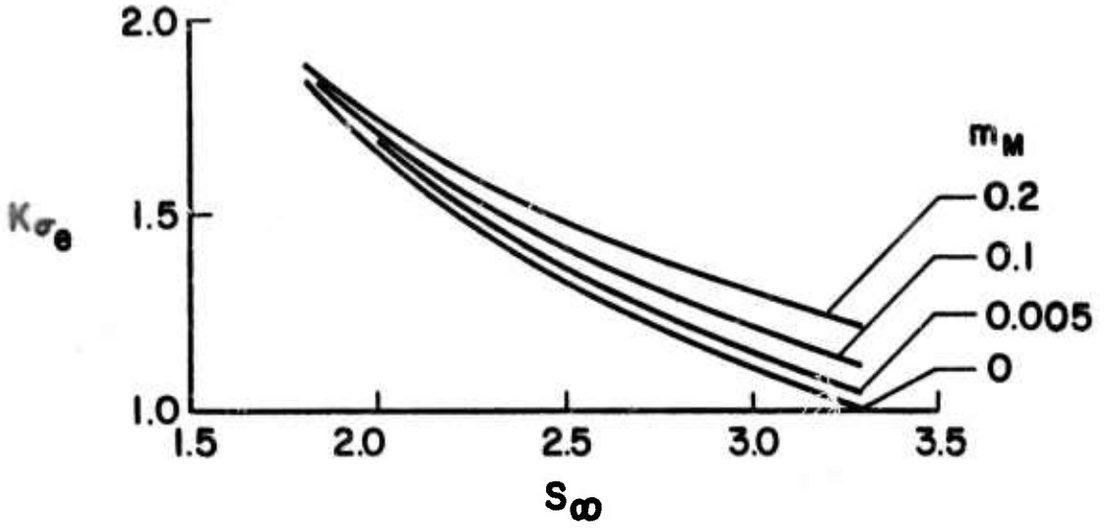

Figure 210. Effective Stress Concentration For Inclusion, $\alpha = 0.1$, $\beta = 0.02$.

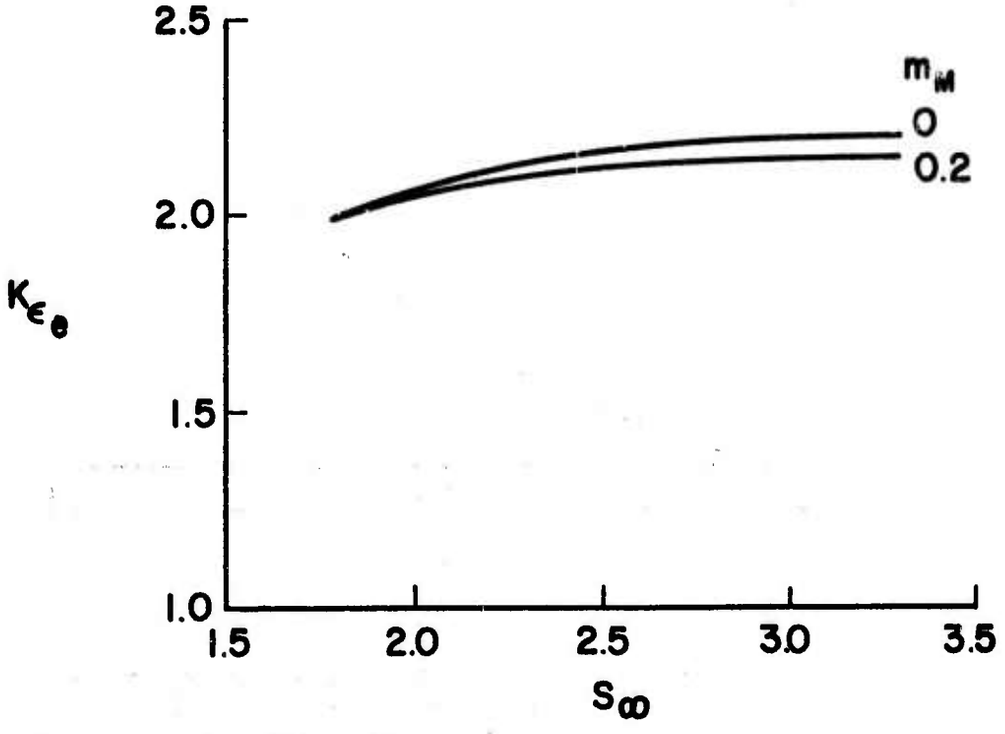

Figure 211. Effective Strain Concentration Factor For Inclusion, $\alpha = 0.1$, $\beta = 0.02$.

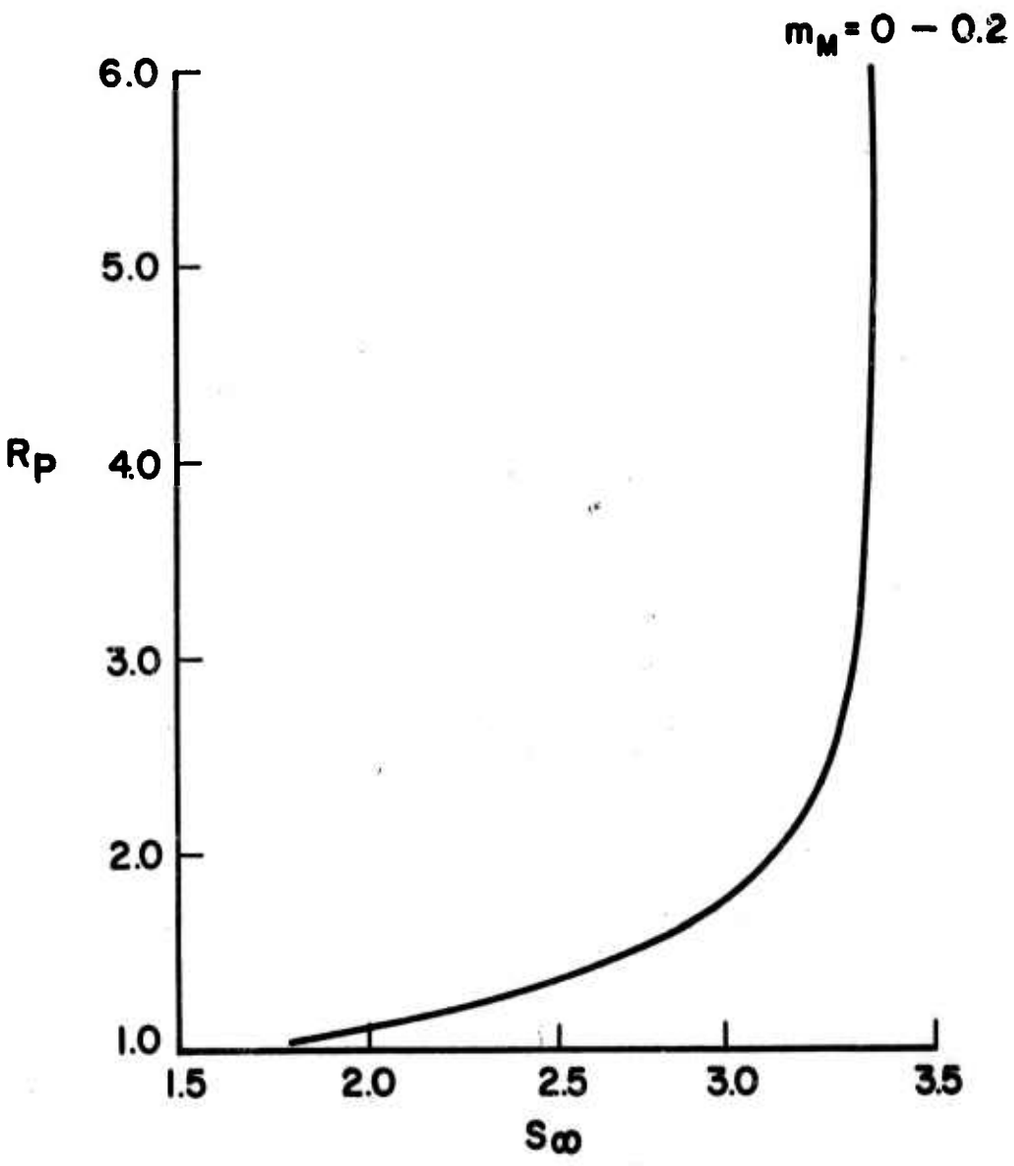

Figure 212. Plastic Zone Radius for $\alpha = 0.1$, $\beta = 0.02$.

G. Two and Three Dimensional Photoelastic Models of Fiber Composites
(Professor Wright and Mr. D. Weitzenhof)

The objective of this research is to develop a frozen stress photoelastic technique for accurate determination of the stresses caused by external loading of three-dimensional filamentary composites. The most obvious (and the most severe) problem encountered in this approach is the extraneous thermal stress pattern introduced into the two-component system by the stress-freezing cycle.

The thermal stress pattern is to be taken into account as follows. First, a model of the relevant composite system is "frozen" under load. At the same time, an unloaded model of the same configuration is subjected to the same "freezing" cycle. Both models are then analyzed, and the unloaded stress pattern is subtracted from the "load" stress pattern. The remaining stresses are the result of externally applied loads.

The two-step technique described above is being tested with two-dimensional models in which direct comparison of a stress pattern due solely to external load (model of Figure 213) can be made with those resulting from stress freezing (models of Figure 214). Good correlation in two-dimensions will permit extension to three-dimensional models to determine the relations between stresses and fibers end shapes and composite geometry. A sample three-dimensional model is shown in Figure 215.

Some results of the two-dimensional testing have been obtained. Isochromatic and isoclinic patterns for the two-dimensional models are shown in Figures 216 through 224.

Explanatory notes are as follows:

Figure 216. The dark field photograph of the stress frozen models (loaded model at right, unloaded at left) shows good symmetry of the stress pattern and a high stress concentration at the fiber tips. The shear stress concentration factor for the loaded model is approximately

$$SCF = \frac{\tau}{\tau_{Nominal}} \cong \frac{8}{1.5} = 5.33 \qquad \text{(VIII H-1)}$$

where the numbers 8 and 1.5 are the fringe numbers in the appropriate regions.

Figures 217, 218, 219. The isoclinic patterns show the symmetry of the stress distributions in these frozen stress models.

Figure 220. The dark field photograph of the room temperature comparison model also shows good symmetry and a high stress concentration. The shear stress concentration factor is approximately

$$SCF = \frac{\tau}{\tau_{Nom}} \cong \frac{9}{2} = 4.5 \qquad \text{(VIII H-2)}$$

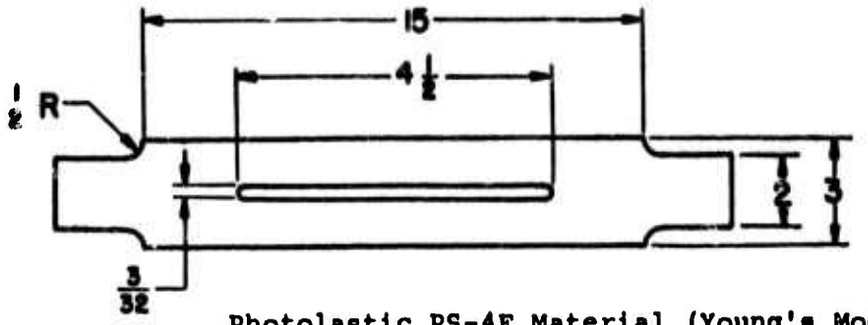

Photolastic PS-4F Material (Young's Modulus = 1 KSI)

Figure 213. Room Temperature Comparison Model

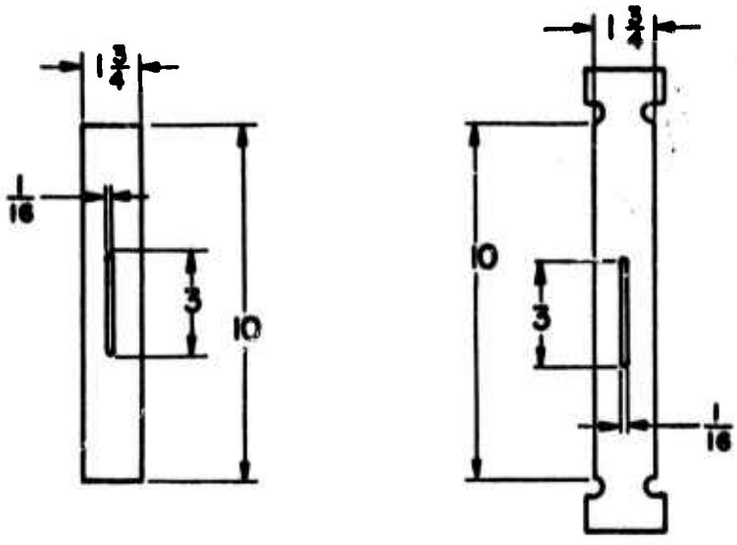

Unloaded Model Loaded Model

Figure 214. Two-Dimensional Models for Stress Freezing

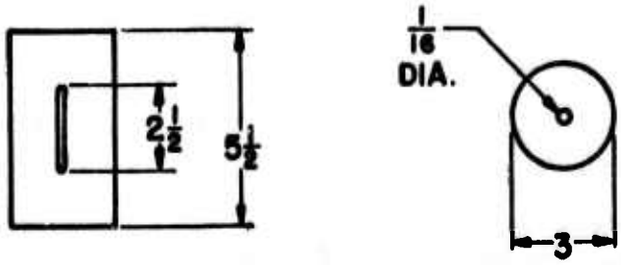

Side View End View

Figure 215. Three-Dimensional Models for Stress Freezing Compression Loading

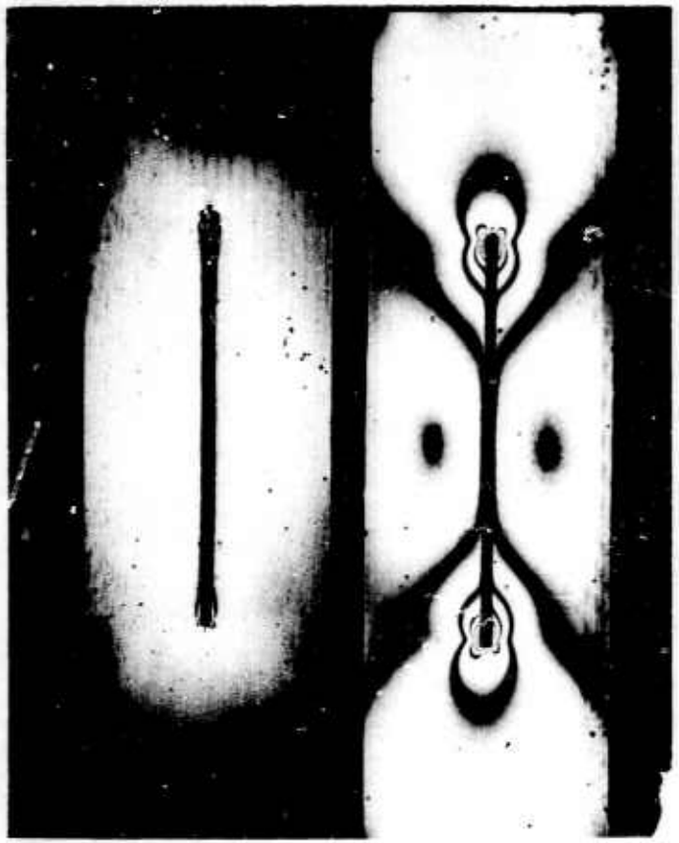

Figure 216. Two Dimensional Frozen Stress Patterns Unloaded-left, Loaded-right.

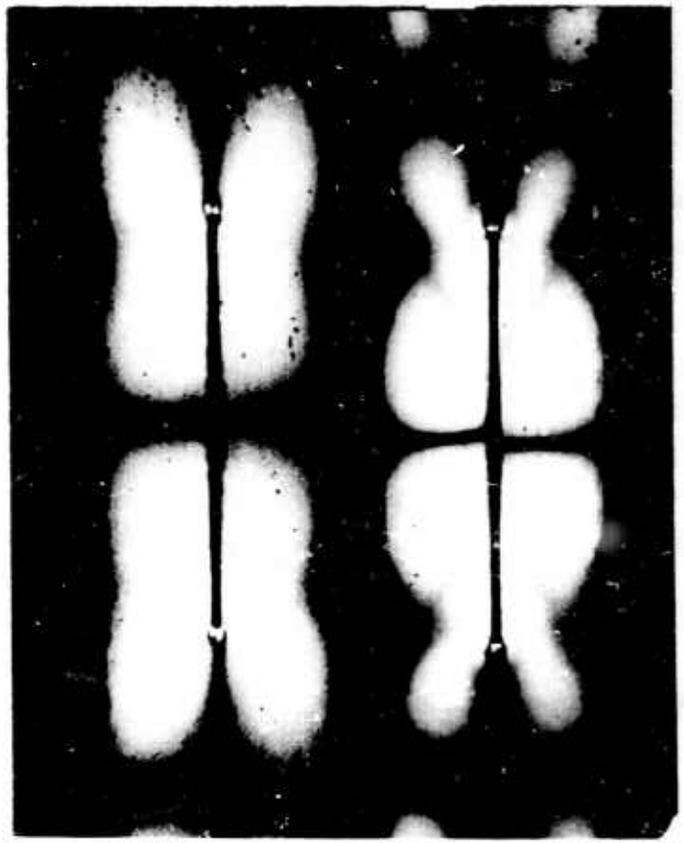

Figure 217. Two Dimensional Frozen Stress Patterns 0° Isoclinic Patterns.

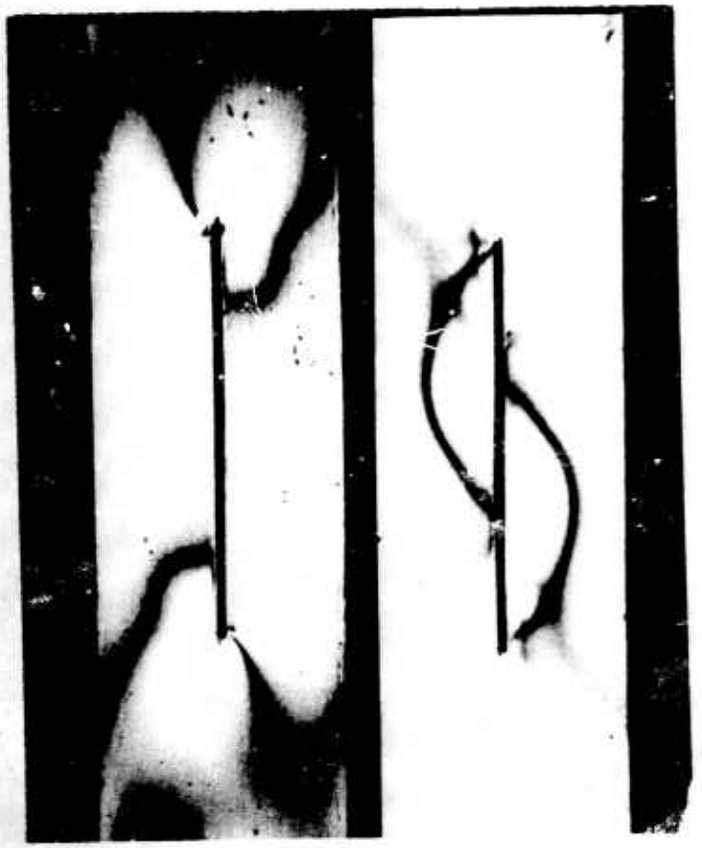

Figure 218. Two Dimensional Frozen Stress Patterns 22.5° Isoclinic Patterns.

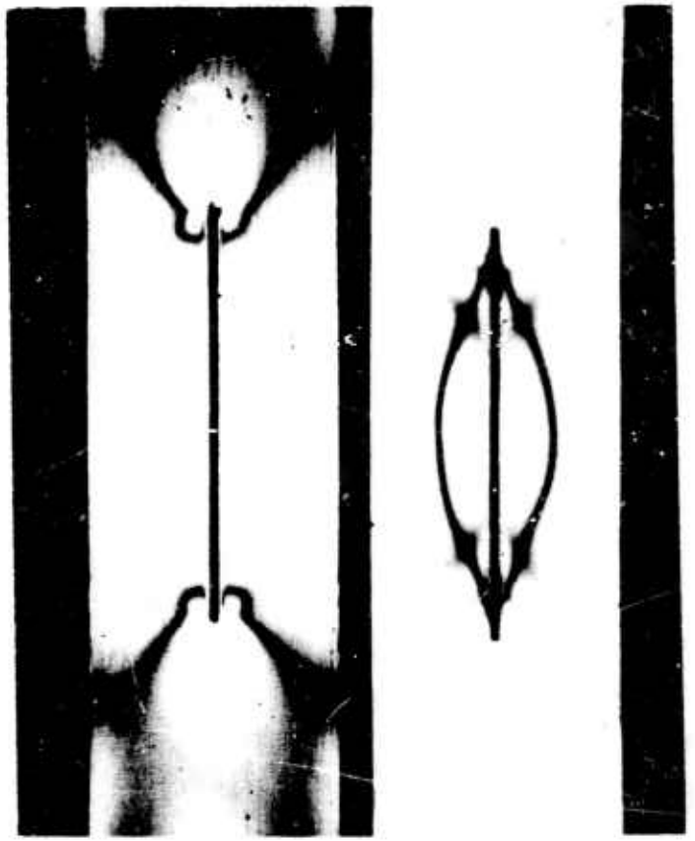

Figure 219. Two Dimensional Frozen Stress Patterns 45° Isoclinic Patterns.

Figure 220. Two Dimensional Room Temperature Model Under 15.91 lb. Axial Load.

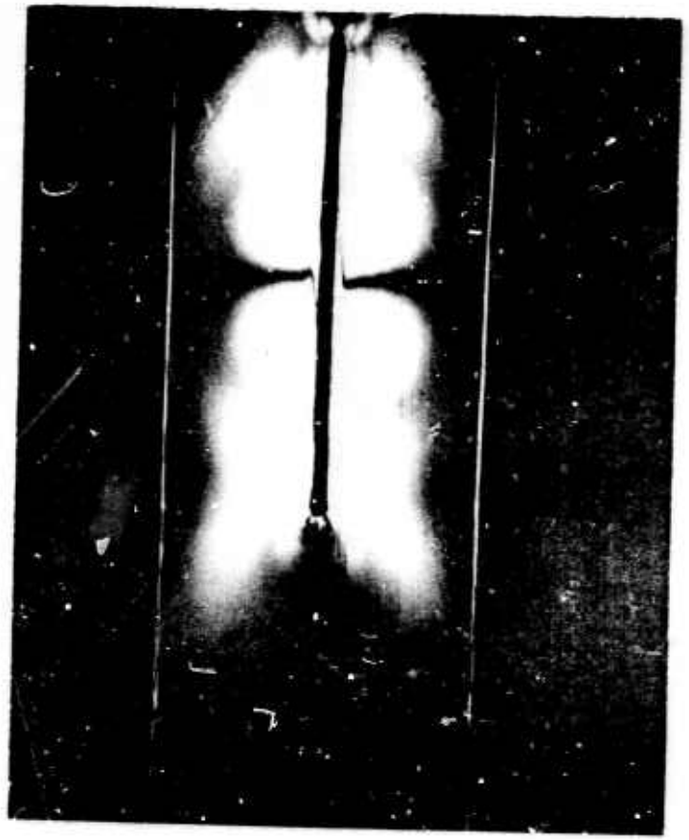

Figure 221. Two Dimensional Room Temperature Model 0° Isoclinic Pattern.

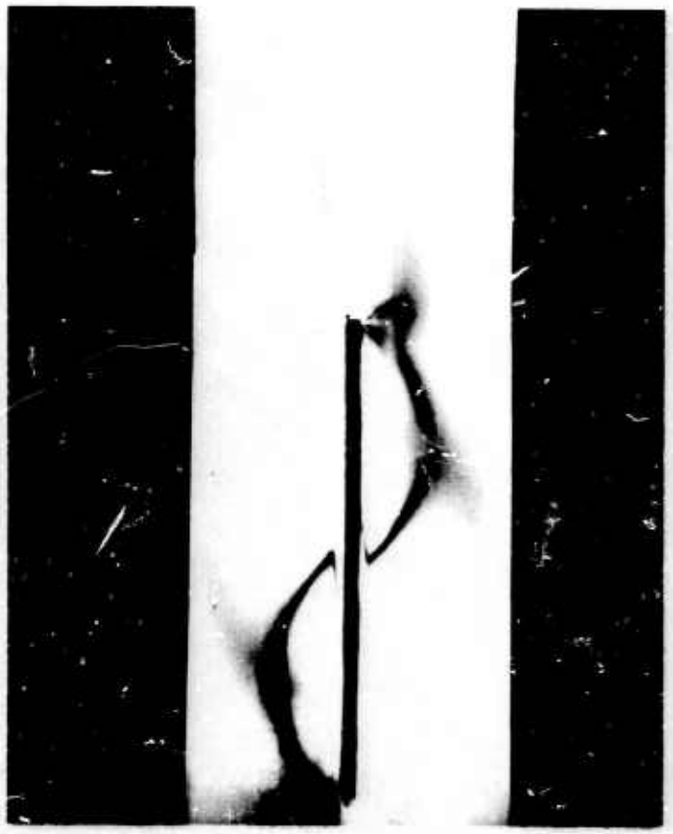

Figure 222. Two Dimensional Room Temperature Model 15° Isoclinic Pattern.

Figure 223. Two Dimensional Room Temperature Model 30° Isoclinic Pattern.

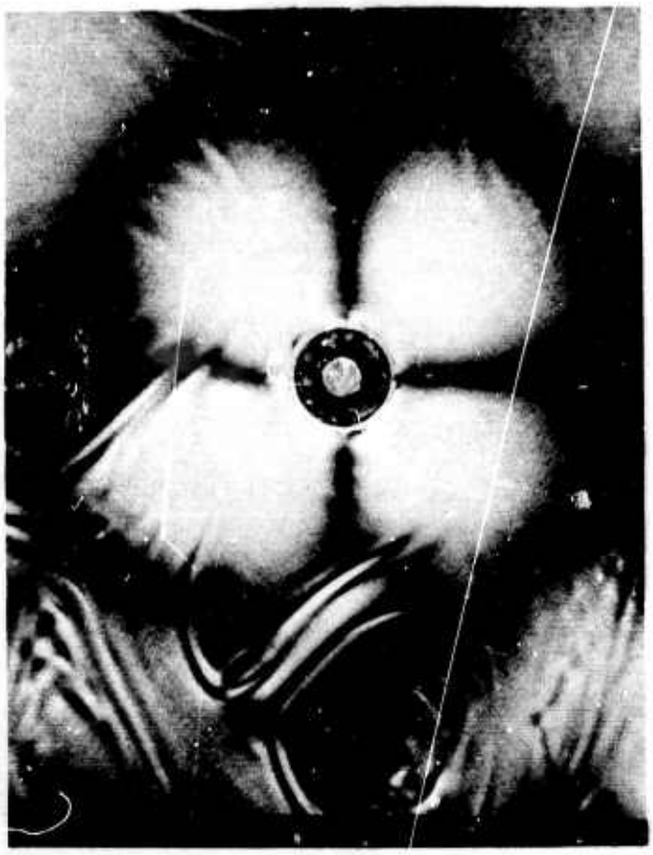

Figure 224. Mottle Observed in Early Models.

This value agrees fairly well with the value obtained in the frozen stress models.

Figures 221, 222, 223. The isoclinic patterns again show the symmetry of the stresses in the comparison model.

Conclusive results have not yet been obtained; however, shear stresses show excellent correlation between the frozen stress and comparison models. Further testing will evaluate the accuracy of the remaining stress components.

Previous investigators have concentrated on shear stress patterns. The technique outlined here will allow evaluation of the entire stress tensor at any desired points in the model. To aid in this work, a computer program has been devised to calculate the stresses from data obtained along any straight line leading from a region of known stress (free edge or previously calculated point) to any other point in the model. The method is the well-known three-dimensional shear difference integration of one of the equations of equilibrium.

Since the first Annual Report[1] several difficulties have been encountered and changes made to overcome them. The first obstacle met was bond failure caused by large relative thermal expansion between the 1/4-inch diameter aluminum "fiber" and the photoelastic material matrix. This difficulty was overcome by using 1/16-inch diameter wood "fibers" to increase the bond strength and the area to volume ratio. The mottling observed in the photos shown in the first Annual Report (see Figure 224 - a copy of Figure 102 of the Report) was eliminated by using higher quality photoelastic materials obtained from Photoelastic, Inc. Thermal stresses were reduced further by stress-freezing models at 200°F rather than the 220° - 250° F recommended by Photoelastic, Inc. The three-dimensional stress-freezing models are now designed for compression loading instead of the tensile loading first used. Reasons for the change are economy (less material and less machining result in much lower cost) and less likelihood of bond failure at the fiber tips (compressive loading produces stresses opposite in sign to the thermal stresses).

H. Failure Mechanics for Fiber Composites
(Professor Kicher and Mr. J.B. Koeneman)

The purpose of this project is to investigate experimentally on the microscale various continuum failure hypotheses. Methods are being developed to observe a regular arrangement of fibers in a polymer matrix during loading.

Figure 225 shows two 10μ glass fibers embedded in an Epon 828-TETA matrix. The sample was loaded transverse to the fibers. However, large plastic strains during the test also placed a compressive load along the axes of the fibers causing the buckling and debonding. The debonding can be identified by the darker areas along the fiber axes. Only two such areas are shown in the photograph due to the small exposure field. When this and similar specimens were examined through the reflected light microscope, areas of combined debonding and buckling were visible at regular intervals. Evidence of buckling is obvious in the region of the more drastic failure in the photograph. The other region failure indicates that buckling probably occurred but was immediately followed by brittle failure of the fiber both transverse and colinear with its axis. Note the excessive deformation of the fiber chip protruding under the undeformed fiber. This condition was possible because primary load was perpendicular to the fiber axes and only two fibers are imbedded in the specimen. It is difficult to determine if the debonding occurred first, permitting the buckling and brittle failure, or if the fibers buckled as columns in an elastic foundation, causing excessive stresses in the bond. Further microscopic examination during and after loading will be necessary to completely understand the phenomena of failure in fiber reinforced composites.

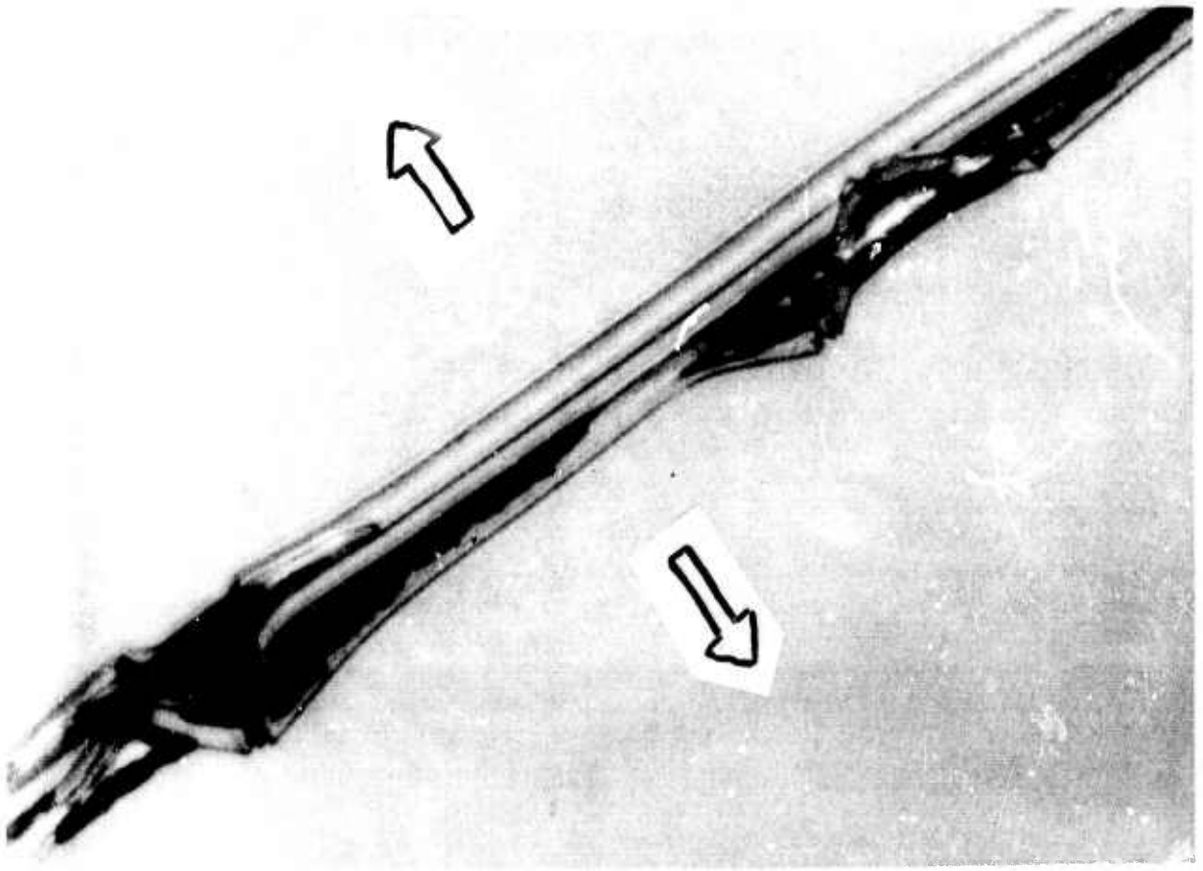

Figure 225. Two Glass Fibers in Epon 828 - TETA Matrix Loaded Transverse to the Fibers (600 X).

I. Bonding Stresses in Laminated Cylindrical Shells
(Professor Kicher and Dr. H.G. Franklin)

Composite material structures can fail in a variety of modes. A single ply of a laminated configuration can fail, leading to the total collapse of the structure. The bonding material between plys can fail, allowing excessive loads to develop in the structural layer. Consider, for example, a compressive load on a two-ply fiber reinforced cylindrical shell. The resistance to buckling is related to the material properties and the cube of the total thickness of the wall, through the flexural rigidities D

$$D = f(E, t^3). \qquad \text{(VIII J-1)}$$

If, during loading, the bond layer between the fiber reinforced structural layers fails prematurely, the reduced flexural rigidity, D', will be approximately twice the flexural rigidity of a single ply

$$D' \approx 2 f\left[E, \left(\frac{t}{2}\right)^3\right] \approx \frac{1}{4} f(E, t^3) \approx \frac{1}{4} D \qquad \text{(VIII J-2)}$$

or approximately one-quarter of the flexural rigidity of the wall before delamination. Therefore, the buckling load will be reduced by approximately a factor of four. Experimental buckling studies on composite cylinders have given extremely low results; although the cylinders appeared to fail in a buckling mode followed by delamination, they may fail first due to delamination followed by buckling. An understanding of the stress distribution in composite cylinders is necessary for an accurate prediction of the load carrying capacity.

As a means of explaining the structural model used for the analysis of the stress distribution in a composite cylinder, consider a simple bimetallic strip. Timoshenko[61] predicts a linear stress distribution in each layer and peak stresses of

$$\sigma_{max} = \frac{1}{2} E T(\alpha_1 - \alpha_2) \qquad \text{(VIII J-3)}$$

where

E = modulus of the materials (same in both materials)

T = temperature change

$\alpha_{1,2}$ = thermal expansion coefficients of layers 1 and 2, respectively.

At the mating surface of the two layers, there is a sharp stress discontinuity if the strip is forced to remain flat, a stress which must be sustained by the bond (see Figure 226). Since the bond layer was not included in this analysis, the prediction of stresses in the bond is not possible. A more

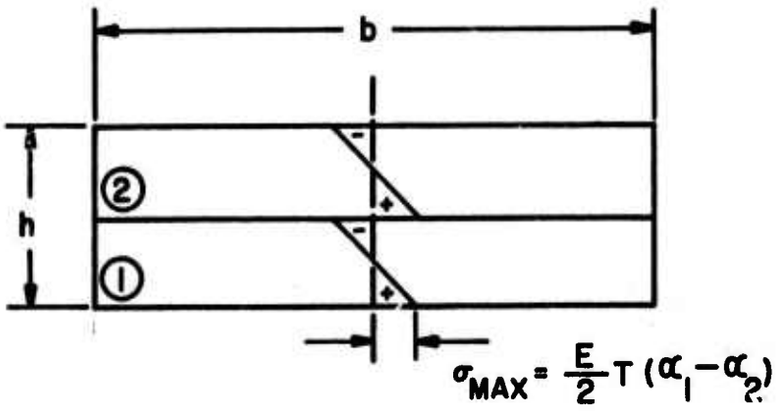

Figure 226. Stress Distribution in Bi-metallic Strip Held Flat and Subjected to a Temperature of T.

realistic model,[62] shown in Figure 227 includes the bond layer, thus allowing the prediction of stresses in the bond. The shear strain in the bond layer would be

$$\varepsilon_{xy} = \frac{u_1 - u_2}{c} = \frac{\tau_c}{G_c} \qquad \text{(VIII J-4)}$$

where u_1 and u_2 are the displacements of the layers due to a temperature change T. The axial strains in the structural layers can be expressed in full by:

$$\varepsilon_1 = \frac{du_1}{dx} = \alpha_1 \Delta T_1 + \frac{P_1}{E_1 t_1 b} \qquad \text{(VIII J-5)}$$

$$\varepsilon_2 = \frac{du_2}{dx} = \alpha_2 \Delta T_2 + \frac{P_2}{E_2 t_2 b} \qquad \text{(VIII J-6)}$$

from Hooke's Law. Equilibrium of the structural layers requires

$$\tau_c b = \frac{dP_1}{dx} = - \frac{dP_2}{dx} \qquad \text{(VIII J-7)}$$

as shown in Figure 228. Eliminating the strains and displacements gives

$$\frac{d\tau_c}{dx} = \left(\frac{G_c}{c}\right) \left[(\alpha_1 T_1 - \alpha_2 T_2) + \left(\frac{P_1}{E_1 t_1 b} - \frac{P_2}{E_2 t_2 b}\right)\right]. \qquad \text{(VIII J-8)}$$

Eliminating τ_c and one of the internal loads, say P_2, gives

$$\frac{d^2 P_1}{dx^2} = \left(\frac{G_c b}{c}\right) \left[(\alpha_1 T_1 - \alpha_2 T_2) + \frac{P_1}{b} \left(\frac{1}{E_1 t_1} + \frac{1}{E_2 t_2}\right)\right] \qquad \text{(VIII J-9)}$$

Now defining

$$\lambda = \left(\frac{G_c b}{c}\right) [\alpha_1 T_1 - \alpha_2 T_2] \qquad \text{(VIII J-10)}$$

$$K^2 = \left(\frac{G_c}{c}\right) \left[\frac{1}{E_1 t_1} + \frac{1}{E_2 t_2}\right] \qquad \text{(VIII J-11)}$$

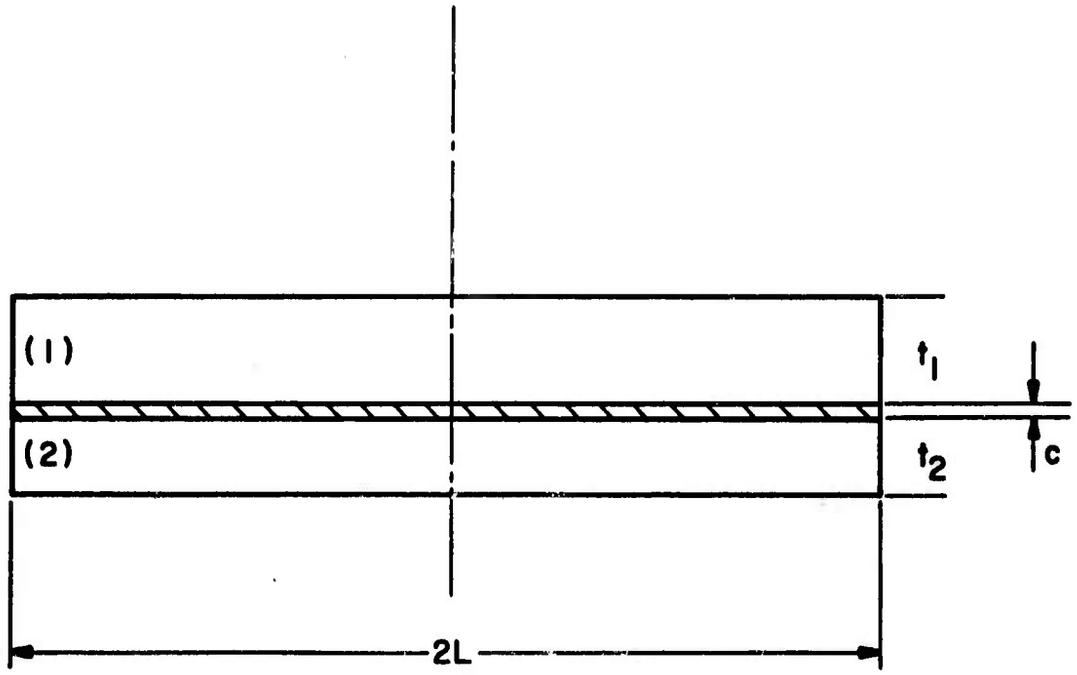

Figure 227. Three Element Model for Bi-metallic Strip Stress Analysis.

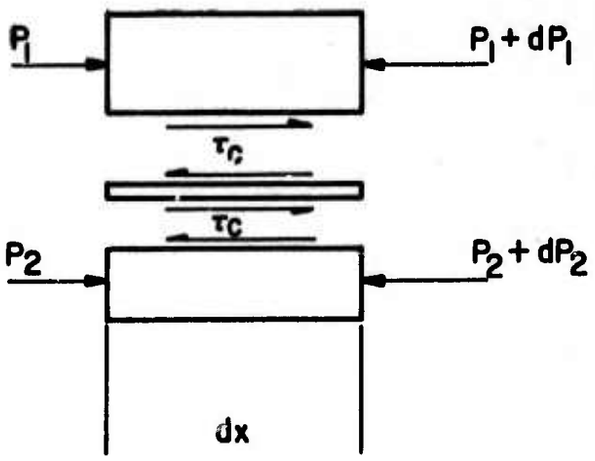

Figure 228. Differential Element of Bi-metallic Strip of Width d.

The governing differential equation becomes

$$\frac{d^2 P_1}{dx^2} - K^2 P_1 = \lambda \qquad \text{(VIII J-12)}$$

and the solution is of the form

$$P_1 = A \cosh Kx + B \sinh Kx - \frac{\lambda}{K^2} . \qquad \text{(VIII J-13)}$$

Applying conditions of symmetry about the midspan and $P_1 = 0$ at the ends leads to the following solution for P_1

$$P_1 = \frac{\lambda}{K^2} \left[\frac{\cosh Kx}{\cosh KL} - 1\right] . \qquad \text{(VIII J-14)}$$

The equation for τ is:

$$\tau = \frac{1}{b} \frac{dP_1}{dx} = \frac{\lambda}{Kb} \frac{\sinh Kx}{\cosh KL}$$

$$= \frac{[\alpha_1 T_1 - \alpha_2 T_2]}{\frac{c}{G_c}\left(\frac{1}{E_1 t_1} + \frac{1}{E_2 t_2}\right)} \frac{\sinh Kx}{\cosh KL} \qquad \text{(VIII J-15)}$$

which has its maximum value at $x = L$. There is a shear stress concentration in the bond at the free edge of the bi-metallic strip similar to the stress concentration at the end of a broken fiber in an epoxy matrix.[45] This minor modification of the analysis model makes possible the prediction of complete stress state, including the bond for laminated structures.

This project is concerned with the analysis of a laminated circular cylinder using a medium thick shell theory. The composite analyzed is composed of three layers, as shown in Figure 229. The inside and outside layers are fiber reinforced laminates with the fibers oriented at equal and opposite angles from the longitudinal axis and are considered to be orthotropic for the purposes of this analysis. The central layer represents the bonding agent and is considered isotropic. The main purpose of this analysis is to attempt to predict the stress distribution in the three layers with special emphasis on the estimation of the stresses in the bond layer and adjacent to it.

The following assumptions are made in this work:

1. The transverse shear stresses are negligible compared with the other stresses.

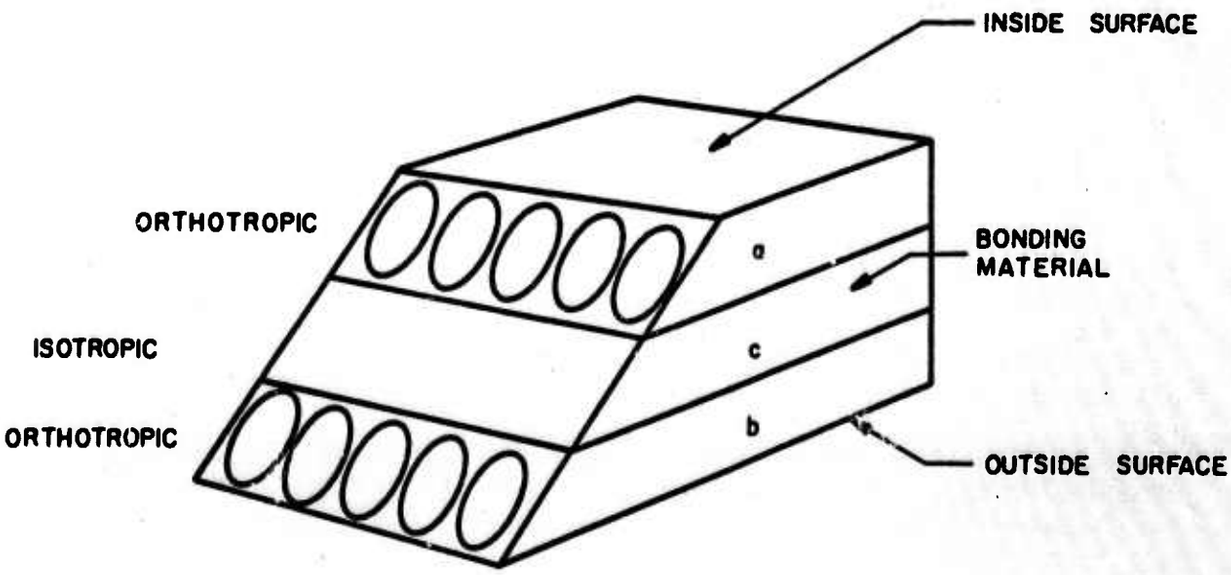

Figure 229. Trilayer Element.

2. The normal strain in the radial direction is negligible compared with the normal strains in the other two coordinate directions.

3. The external loading is distributed so that it does not cause any edge effects at the ends of the shells.

4. The stresses and displacements are independent of the circumferential coordinate (see Figure 230).

5. The ratio of shell thickness h to mean radius a is small enough to say that

$$1/(1 - h/a) \tilde{=} (1 + h/a).$$

Since the equations for the stresses and the displacements are developed separately for the isotropic and orthotropic layers, the displacements and transverse normal stresses are matched at the mating surfaces. In addition, it is assumed that the structure retains its cylindrical shape analogous to the assumption of the bi-metallic strip remaining flat. The mathematical details of this analysis along with extensive numerical results have been demonstrated by Franklin.[63, 64]

Some numerical results were obtained for fiberglass where the bonding agent is considered to have material constants similar to the resin or matrix material in the orthotropic layer. The maximum stresses are determined for the cases of axial, internal pressure and torsional loading. Figures 231 through 233 are typical results for the maximum stresses in the bond when the cylinder is subjected to axial, torsional, and internal pressure loading. Figures 234 through 236 present typical results for the maximum stresses in the outer layer when the cylinder is subjected axial, torsional, and internal pressure loading. The cylinders are two-layered, wound at $\pm \alpha$ (radians) with unidirectionally reinforced composites with the following properties

$E_L = 8 \times 10^6$ psi $\qquad E_T = 3 \times 10^6$ psi

$G_{LT} = 1.2 \times 10^6$ psi $\qquad \mu_{LT} = 0.25$

$\mu_{TL} = 0.10$ $\qquad h$ = ply thickness

while the bond has the following properties

$E_c = 5 \times 10^5$ psi $\qquad \mu_c = 0.35.$

h_c = bond thickness

The radius of the shell is "a", and the results are expressed as quantities nondimensionalized as some function of the load.

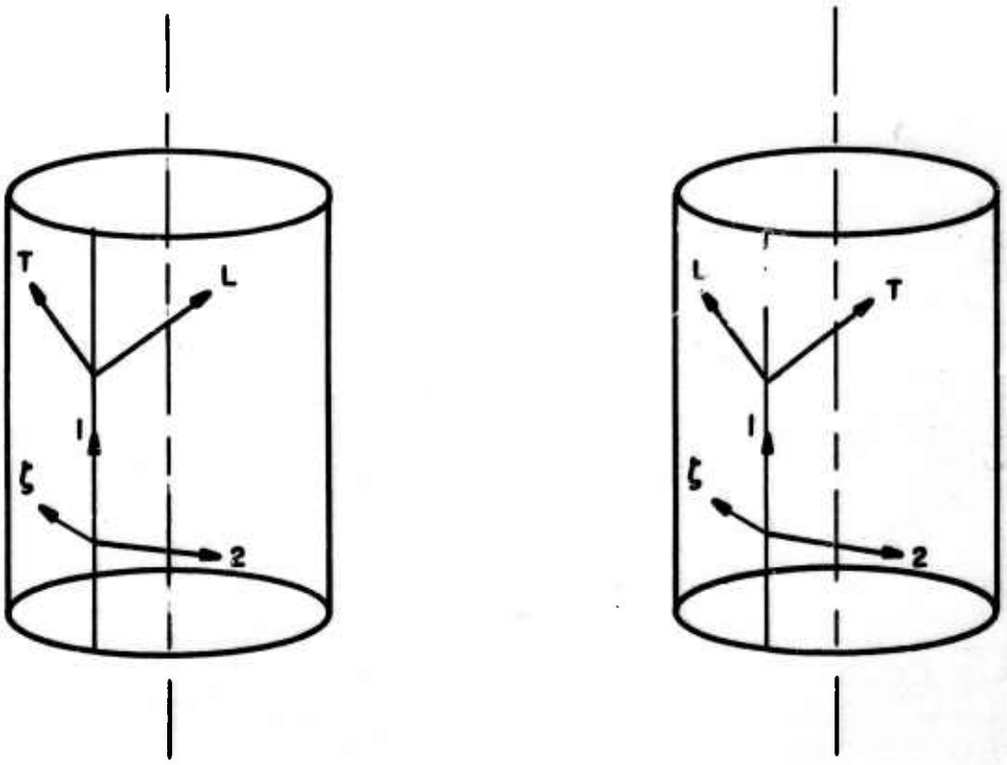

Figure 230. Orientation of Winding.

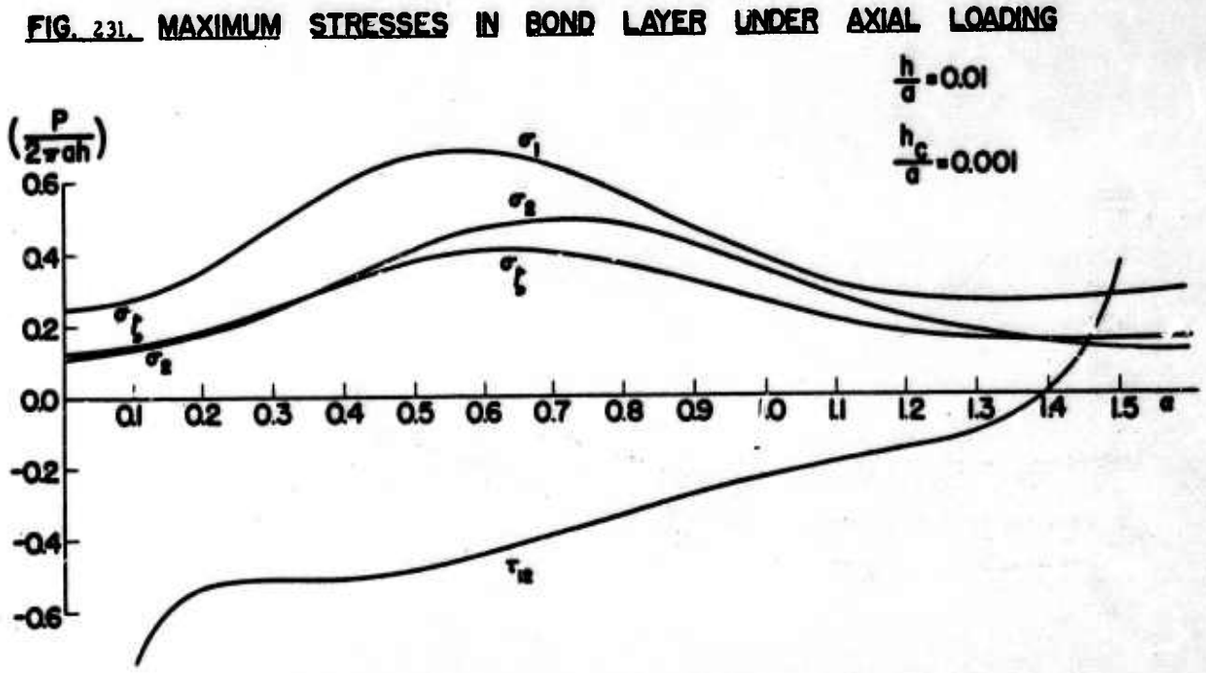

Figure 231. Maximum Stresses in Bond Layer under Axial Loading.

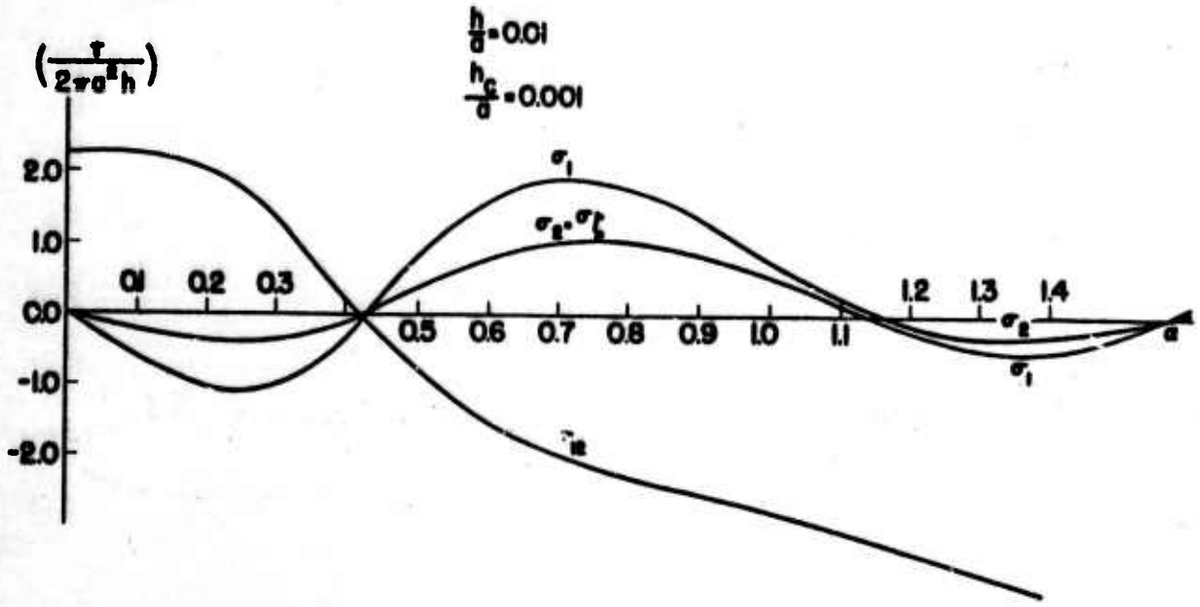

Figure 232. Maximum Stresses in Bond Layer under Torsional Loading.

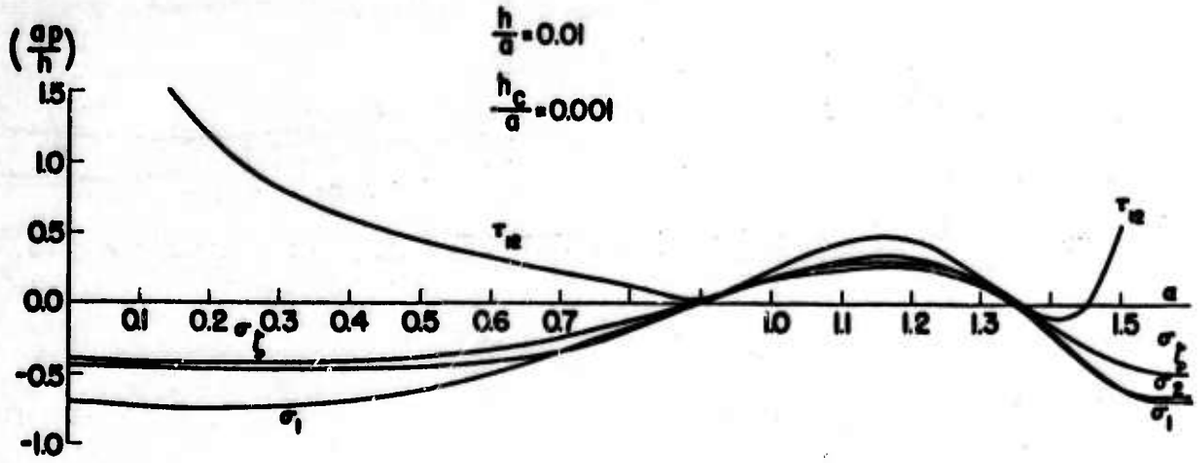

Figure 233. Maximum Stresses in Bond Layer under Internal Pressure.

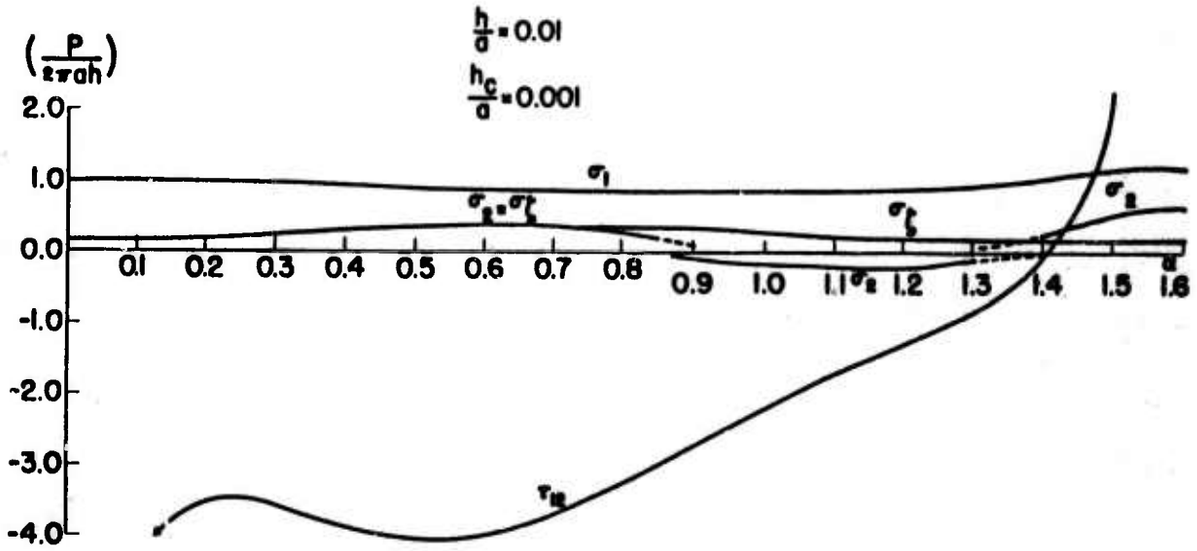

Figure 234. Maximum Stresses in Outer Layer under Axial Loading.

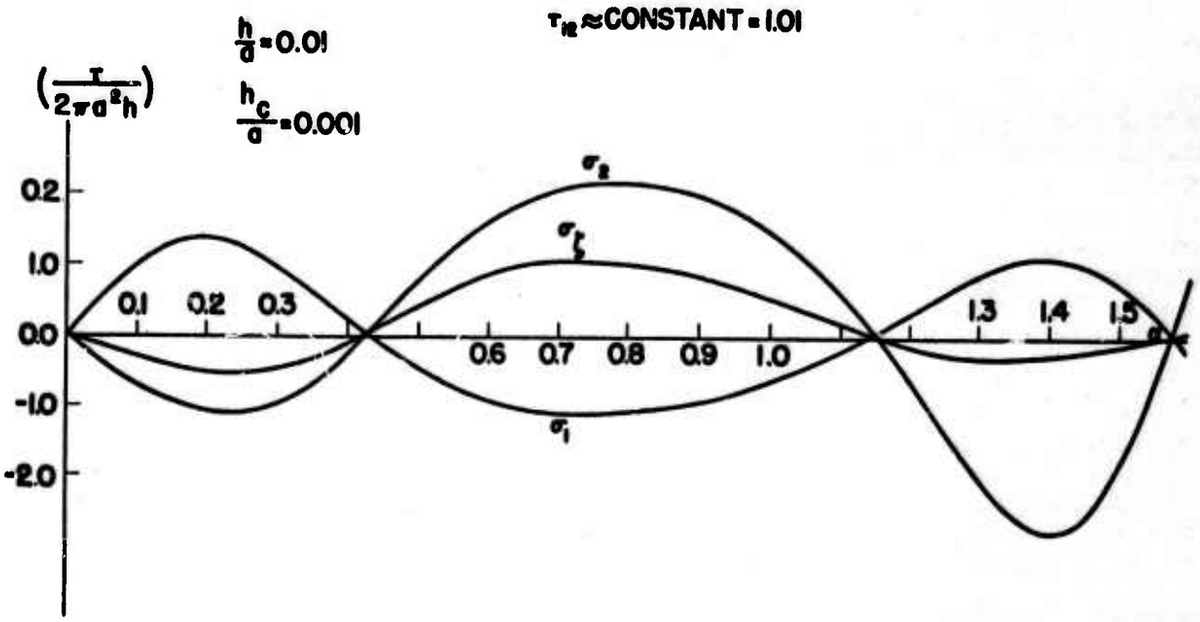

Figure 235. Maximum Stresses in Outer Layer under Torsional Loading.

FIG. 236. MAXIMUM STRESSES IN OUTER LAYER UNDER INTERNAL PRESSURE

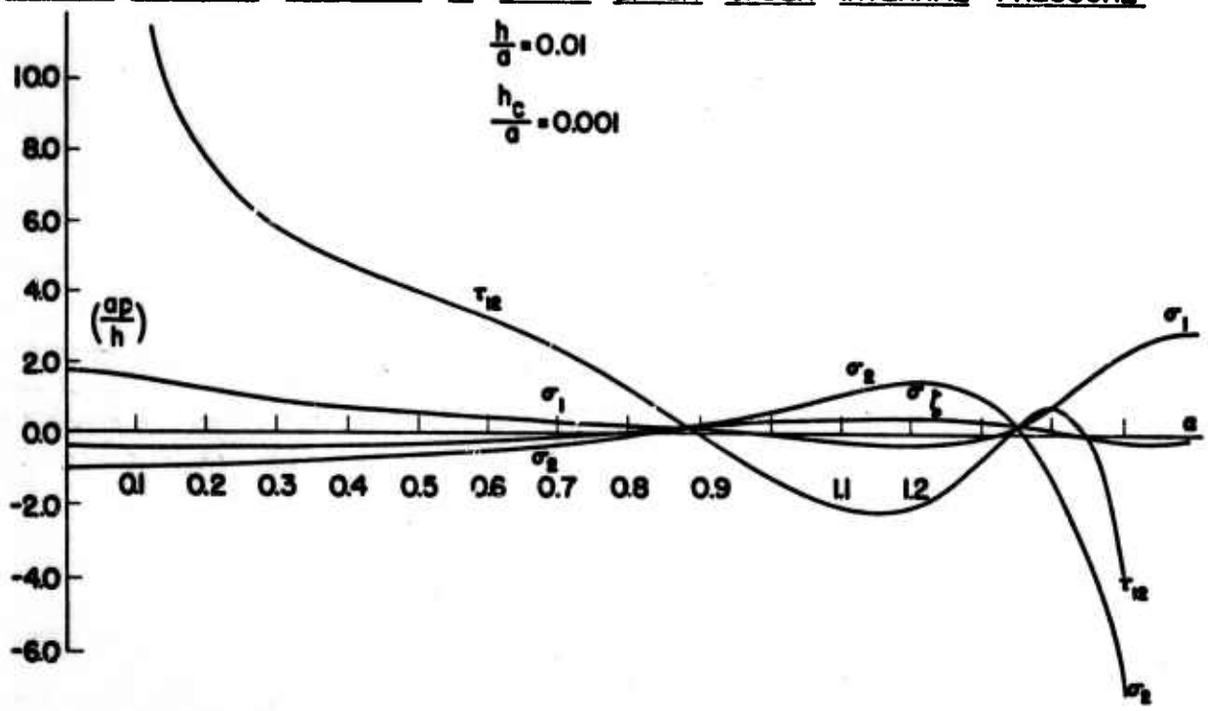

Figure 236. Maximum Stresses in Outer Layer under Internal Pressure.

A study of the numerical results indicates that the normal stresses σ_1, σ_2, and σ_ζ are well behaved for all values of α. However, the shear stress, τ_{12}, in the bond and the outer layer diverge for extreme values of α. Therefore, the solutions are questionable for α less than 0.2 radians or greater than 1.3 radians. This limitation is considered by assuming the transverse shear stresses to be negligible. Reissner[65] warns that this condition may occur when the moduli of elasticity are very different in adjacent layers. At intermediate values of α , the mismatch in elastic properties is something less than an order of magnitude; therefore, the approximation is valid. Some work was done using moduli of elasticity of approximately the same magnitude, and this limitation disappeared as did the stress discontinuities at the mating surfaces.

Note that, for the case of internal pressure, the minimum stress condition occurs at $\alpha = 0.9$ radians or 51.6°. This figure should be compared with 54.7° obtained from netting analysis for a uniform strength pressure vessel.

Figure 237 is a complete stress distribution for a cylindrical shell with $\alpha = \pm 0.7854$ subjected to axial, torsional, or internal pressure loading. It is found that large stress discontinuities exist at the mating surfaces, indicating the possible source of delamination. Further investigations[66,67] are underway to study the characteristics of bonding stresses in cylindrical shells.

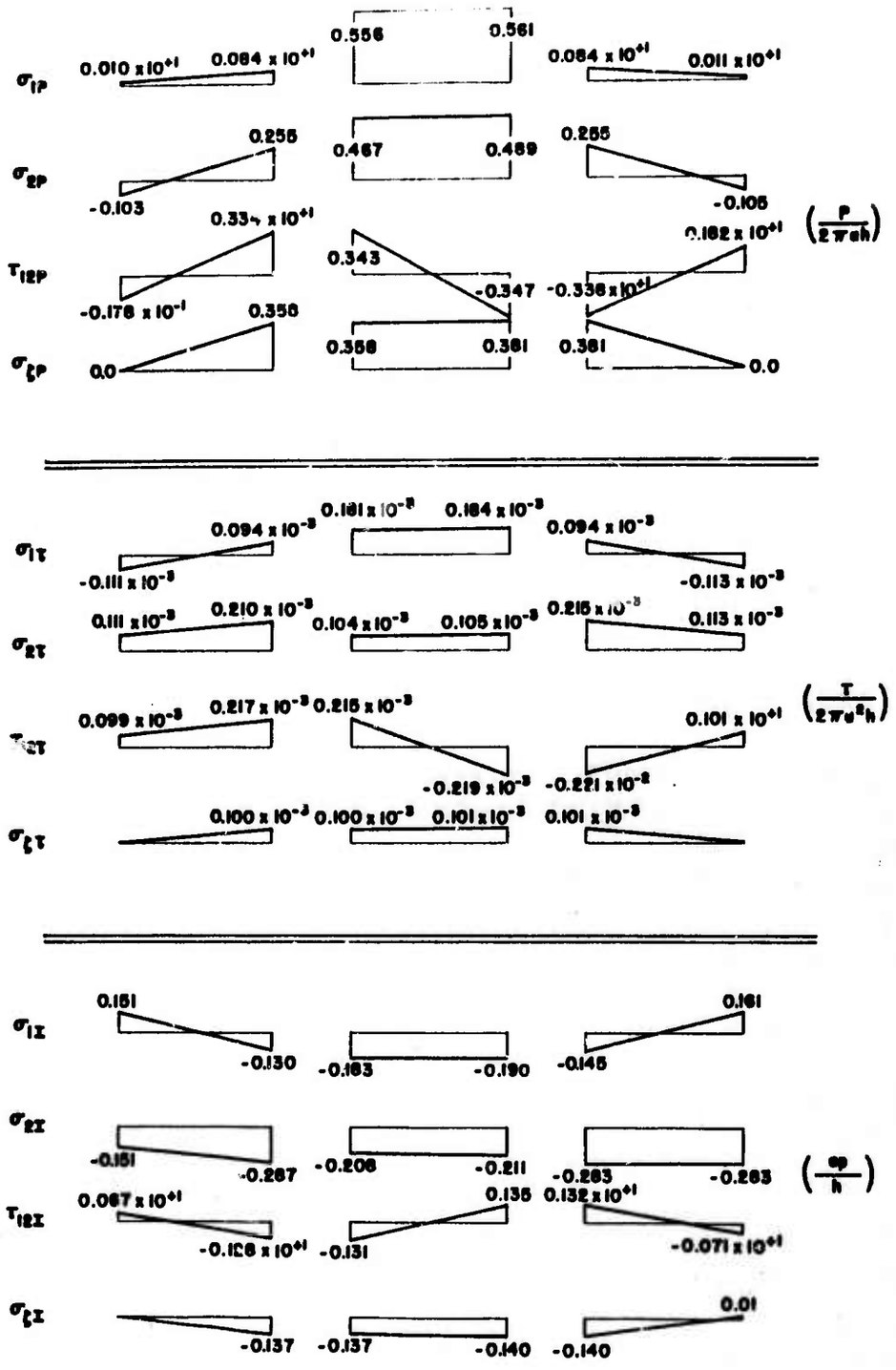

Figure 237. Stress Distributions of a Trilayer Fiber Reinforced Shell Subjected to Axial Torsional and Lateral Pressure Loading: $\frac{hc}{a}=1^{-3}, \frac{h}{a}=1^{-2}, \alpha=0.7854$

SECTION IX

STRUCTURAL ANALYSIS AND SYNTHESIS STUDIES

Superior structural designs can be obtained through design optimization and improved methods of structural analysis for any material. However, the introduction of materials with anisotropic and nonlinear properties requires the development of improved analysis methods in order to fully utilize such materials in any rational design procedure. Efforts to develop new and to improve existing analysis and synthesis capabilities were expanded during this report period.

The generation and verification of discrete elements for the design of anisotropic structures is presented in Section IX A. An adaptation of these analysis capabilities to various stiffened panel tests is reported in Section IX B. Section IX C gives a description of a new analytical tool for the structural behavioral study of nonlinear and nonisotropic materials subjected to multiaxial stress distributions. The development of algorithmic tools for new analysis methods and synthesis studies is contained in Section IX D. A structural synthesis study of a fiber composite flat plate that considers a material and a processing variable is presented in Section IX E.

A. Generation and Verification of Anisotropic Discrete Elements

(Dr. R.H. Mallett, Bell Aerosystems)

Structural analysis development has been directed toward generalization and extension of the best available analysis methods to accommodate the anisotropy and geometric complexity of composite structures, providing support for the representative component design studies.

The versatile matrix methods of structural analysis based on discrete element idealization have been employed in developing a unified approach to component analysis. The same basic analytical method and computer program which were used in the analysis of the rocket nozzle throat insert design, as described in Section IX C of the first Annual Report (Reference 1), have been used in this work.

For the rocket nozzle insert analysis, the triangular ring and other elements (Figure 238) were developed. For the fuselage component idealization, the discrete element models employed include the versatile triangular and quadrilateral thin shell (flat plate) elements (Figures 239b and 239c) which permit realistic representation of arbitrary thin shell structures. Anisotropy of elastic and thermal properties is assumed. The element representation further include matrices for distributed thermal and pressure loadings. Example problems have been solved for numerical check-out of these elements. These elementary problems (for which alternate analytic solutions are available) are designed to sequentially confirm proper operation of the various matrices in the element formulations.

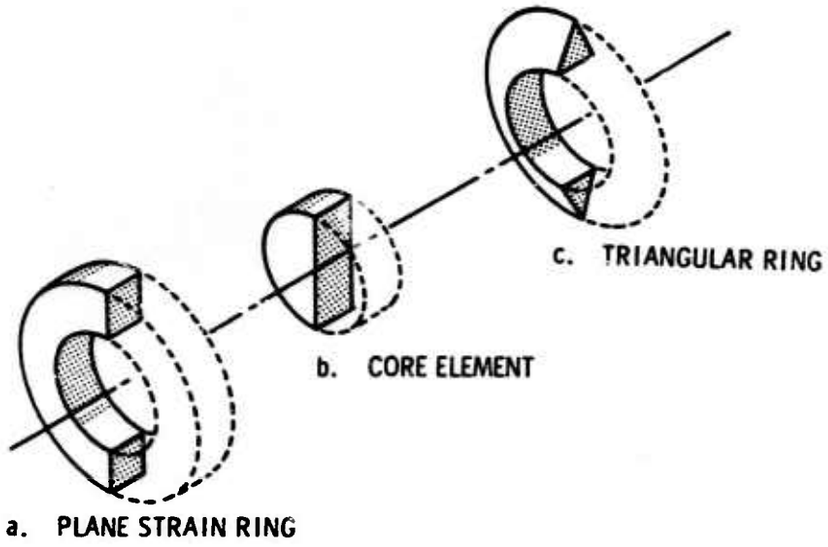

Figure 238. Discrete Elements For Analysis Of Thick Axisymmetric Structures

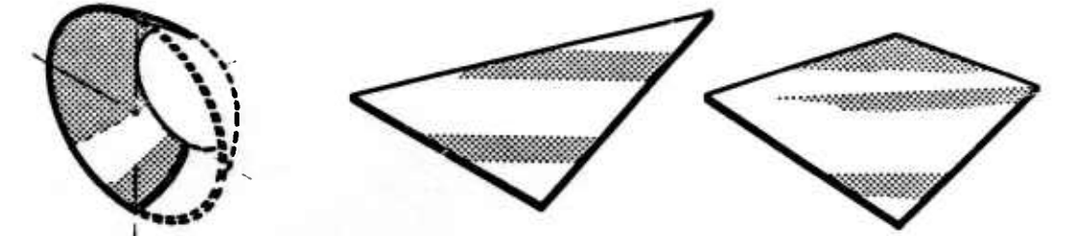

Figure 239. Discrete Elements For Analysis Of Thin Shell Structures

Subsequent to their evaluation, these elements have been checked-out in a more complex isotropic ring-stiffened cylinder problem for which both experimental and alternate analytical data were available. Following this check, which confirmed proper operation of the discrete element capability, analysis of the representative fuselage component was considered. Results of the element evaluation studies are presented in this report section, and stress analysis of the fuselage component is presented in Section X G.

1. Numerical Check Problems on Flat Plates

The first problem is defined in Figure 240, namely a square, isotropic, and unrestrained membrane subjected to parabolic edge loadings. The accuracy of the predicted displacement of the point "q" relative to the indicated plate origin is taken as a measure of the accuracy of the discrete element analysis. Displacement predictions based on triangular and quadrilateral discrete element idealizations are given in Figure 240 along with the analytic solution value (Reference 68). A maximum difference of 1.3 percent is observed among these values indicating very good agreement of results.

The second example treated is a rectangular orthotropic membrane subjected to self-equilibrating in-plane concentrated loads (Figure 241). The plate aspect ratio is four and the ratio of longitudinal modulus (E_x) to transverse modulus (E_y) is approximately six. Longitudinal stress profiles are shown in Figure 241 for four transverse sections through the membrane. Analytic solution values (Reference 69), shown as plotted points, reasonably confirm the stress profile lines obtained from a triangular element idealization.

Flexure characteristics of the elements are examined in the next several problems. The first plate considered (Figure 242) is square, isotropic, and elastic. The series of problems shown in Figure 242 is widely used for evaluation of plate elements. Two basic cases are treated by separately considering simple and fixed supports. In each case, point and pressure loadings are applied. The center point displacement is used to evaluate the reliability and accuracy of predicted behavior. Values based on triangular and quadrilateral discrete-element idealizations are compared with classical (Reference 70). Differences among the sets of three predictions are less than six percent.

Figure 243 illustrates a series of check problems derived from a rectangular orthotropic plate with an aspect ratio of two. In these problems, for both simple and fixed supports with point and pressure loads, the ratio of longitudinal to transverse moduli is six. Correlation of discrete element predictions and analytical values (Reference 42) is less favorable than that for the isotropic plate. These apparent differences are believed to be due to the simplified analysis employed in predicting the analytical values.

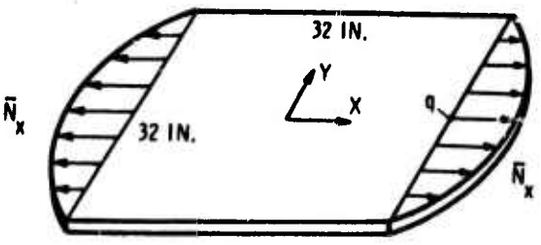

$t = 0.1$ IN.
$E = 10^7$ LB/IN.^{2}
$\nu = 0.3$
$\bar{N}_x = 100 \left[\frac{256 - Y^2}{256}\right]$ LB/IN.

DISPLACEMENT	
SOURCE	$\Delta q \times 10^3$ (IN.)
REFERENCE	1.4764
TRIANGULAR	1.4891
QUADRILATERAL	1.4722

Figure 240. Membrane Problem

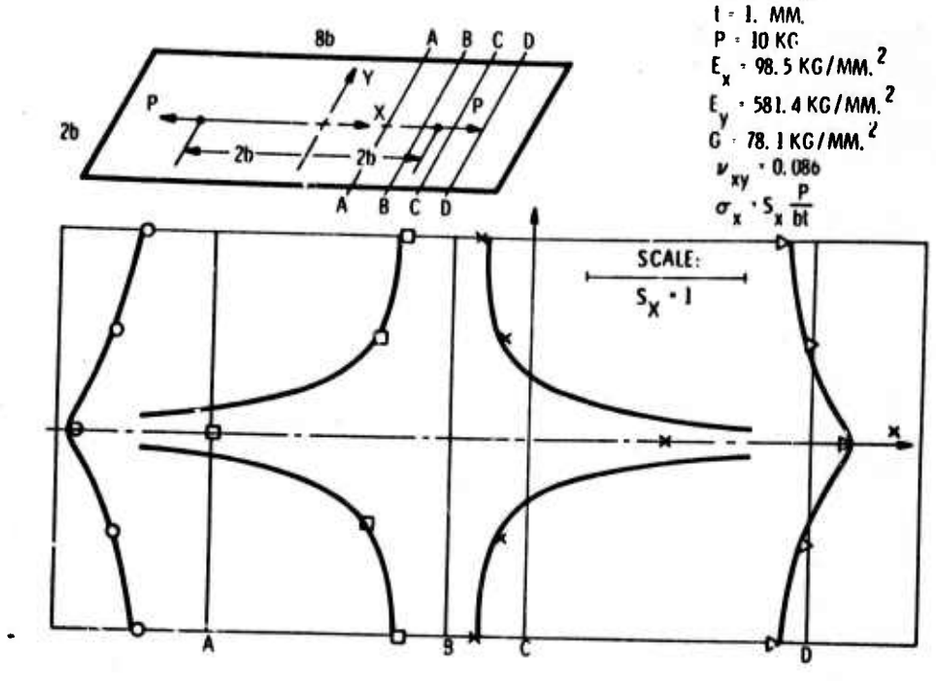

$b = 100$ MM.
$t = 1.$ MM.
$P = 10$ KG
$E_x = 98.5$ KG/MM.^{2}
$E_y = 581.4$ KG/MM.^{2}
$G = 78.1$ KG/MM.^{2}
$\nu_{xy} = 0.086$
$\sigma_x = S_x \frac{P}{bt}$

Figure 241. Membrane Stress Distribution

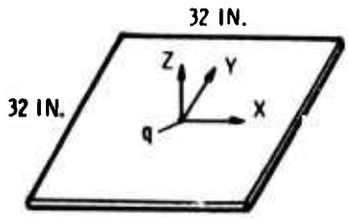

t = 0.1 IN.
E = 30×10^6 LB/IN.^{2}
ν = 0.3

SIMPLE SUPPORT

UNIT CENTER LOAD CENTER DISPLACEMENT	
SOURCE	$\Delta q \times 10^3$ (IN.)
REFERENCE	4.320
TRIANGLE	4.217
QUADRILATERAL	4.256

UNIT PRESSURE LOAD CENTER DISPLACEMENT	
SOURCE	Δq (IN.)
REFERENCE	1.545
TRIANGLE	1.532
QUADRILATERAL	1.546

FIXED SUPPORT

UNIT CENTER LOAD CENTER DISPLACEMENT	
SOURCE	$\Delta q \times 10^3$ (IN.)
REFERENCE	2.082
TRIANGLE	1.971
QUADRILATERAL	2.024

UNIT PRESSURE LOAD CENTER DISPLACEMENT	
SOURCE	Δq (IN.)
REFERENCE	0.4810
TRIANGLE	0.4774
QUADRILATERAL	0.4788

Figure 242. Plate Problem

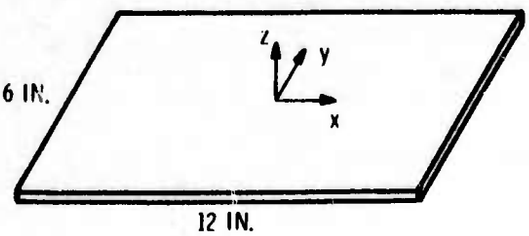

t = 0.1 IN.
E_x = 30×10^6 LB/IN.^{2}
E_y = 5×10^6 LB/IN.^{2}
G_{xy} = 10×10^6 LB/IN.^{2}
ν_{xy} = 0.3, ν_{yx} = 0.05

SIMPLE SUPPORT

UNIT CENTER LOAD CENTER DISPLACEMENT	
SOURCE	$\Delta q \times 10^3$ (IN.)
REFERENCE	0.4906
QUADRILATERAL	0.5810

UNIT PRESSURE LOAD CENTER DISPLACEMENT	
SOURCE	$\Delta q \times 10^3$ (IN.)
REFERENCE	14.479
QUADRILATERAL	14.128

FIXED SUPPORT

UNIT CENTER LOAD CENTER DISPLACEMENT	
SOURCE	$\Delta q \times 10^3$ (IN.)
REFERENCE	0.2581
QUADRILATERAL	0.3100

UNIT PRESSURE LOAD CENTER DISPLACEMENT	
SOURCE	$\Delta q \times 10^3$ (IN.)
REFERENCE	5.296
QUADRILATERAL	4.981

Figure 243. Plate Problem

The next example tests discrete element procedures with an orthotropic plate and stiffeners in combination as shown in Figure 244. In this problem, the with-grain axis is oriented at a counter-clockwise angle of 45° relative to the X-axis. The displacement profiles along Section A-A, based on a quadrilateral element idealization, are compared for the stiffened and unstiffened cantilevered plate, which is point-loaded at a corner.

2. Shell Problem Application

An example is presented here to complete the qualification of the analysis capability for application to the fuselage component. The problem, defined in Figure 245, is a ring-stiffened cylinder. The cylinder is rigidly supported at one end and point-loaded at the other. This cantilevered mode corresponds with one of the test conditions for the fuselage component. (See Section X A).

Both experimental and alternate analytical data are available for the ring-stiffened cylinder problem. By virtue of problem similarity and the previous check-out of orthotropic elements, the precision exhibited in the prediction of behavior should extrapolate to the fuselage component.

Displacement predictions for the ring-stiffened shell behavior are characterized by data in Figures 246 and 247. Figure 246 illustrates the longitudinal displacement profiles of the top, middle, and bottom of the cylinder. It is interesting to note, with reference to Figure 246, that the cylinder cross-section deforms in such a manner that the top moves downward in opposition to the upward load due to the ring-stiffening effect.

Figure 247 emphasizes the cross-section distortion implied in Figure 246 where the deformed cross-sections of the four rings are superposed. In Figure 247 the alternate analytical results of Reference 71 are identical to the present analytical results with the exception of the single plotted point marked "Reference" thus confirming the present discrete-element method predictions.

The longitudinal stress profiles for the example problem shown in Figure 248 are very significant. These profiles show excellent correlation of the predictions with alternate analytical and experimental data. At the same time the total inadequacy of conventional beam theory is brought to light, i.e., the deviation from the My/I predictions.

Figure 249 is an interesting plot of longitudinal stress contours which merits special mention because of the discontinuities shown. These discontinuities arise as a consequence of load transfer by the rings.

The foregoing discussion has treated the predication of behavior in the ring-stiffened cylinder shell. Figure 250 further treats the prediction of ring-stiffener behavior. Bending moments are taken to characterize stiffener action. The predicted

moments are seen to correlate well with alternate analytical (Reference 71) and experimental data (Reference 72).

This stiffened cylinder example, taken together with the problems treated earlier, serves to confirm proper operation of the linear analysis capability. Applications of discrete element methods to nonlinear materials are given in Section IIIG-2 and in Reference 73.

B. Discrete Element Applications to Analysis for Element Tests

(Drs. R.H. Mallett and K.H. Sayers, Bell Aerosystems)

A series of discrete element analyses are being conducted in support of the Element Test Program outlined in Section XA-12. Element configurations include stiffened compression and shear panels, and ring-beam elements. Comparison of the analytical and experimental results will serve to establish confidence in the discrete element analysis procedure with anisotropic elements as applied to graphite fiber composite structures.

1. Stiffened Compression Panel

A linear elastic discrete element idealization of the stiffened compression panel test specimen has been established and computer input data for the various cases to be considered is in preparation. The geometry of the specimen is given in Figure 251. Figure 252 shows an isometric view of the quadrant of the panel being considered which accounts for symmetry. The insert on Figure 252 indicates the quadrant location. Figure 253 shows the idealization employed, as established through the computer program plotting capability. Note that panel elements, bonding surfaces, and stiffeners are all represented, each element carrying its own appropriate orthotropic material properties. Thus, any of the various combinations of materials and bonding systems specified for test can be analyzed, simply by revising material properties and/or element thicknesses, orientations, etc. as required.

2. Stiffened Shear Panel

An idealization of the stiffened shear panel test specimen has been established, and computer input data for the various cases to be considered is in preparation as with the compression panels. The geometry of the specimen and test fixture are given in Figure 254. Figure 255 shows an isometric view of the quadrant of the panel being considered under antisymmetric conditions. Figure 256 shows the idealization established by the computer program. As in the case of the compression panels, analyses covering the desired range of materials and thicknesses can be carried out by simple input data changes.

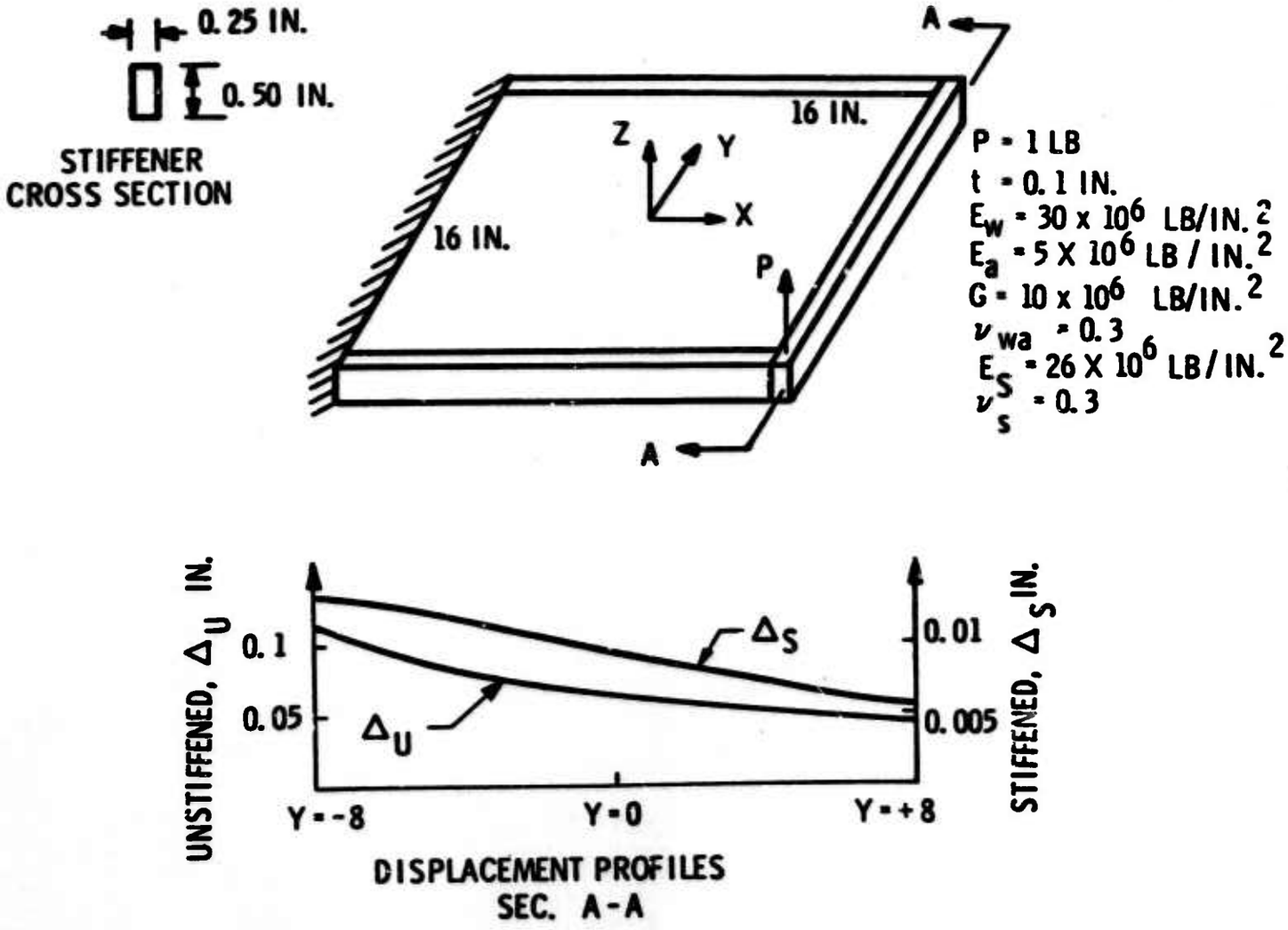

Figure 244. Stiffened Plate Problem

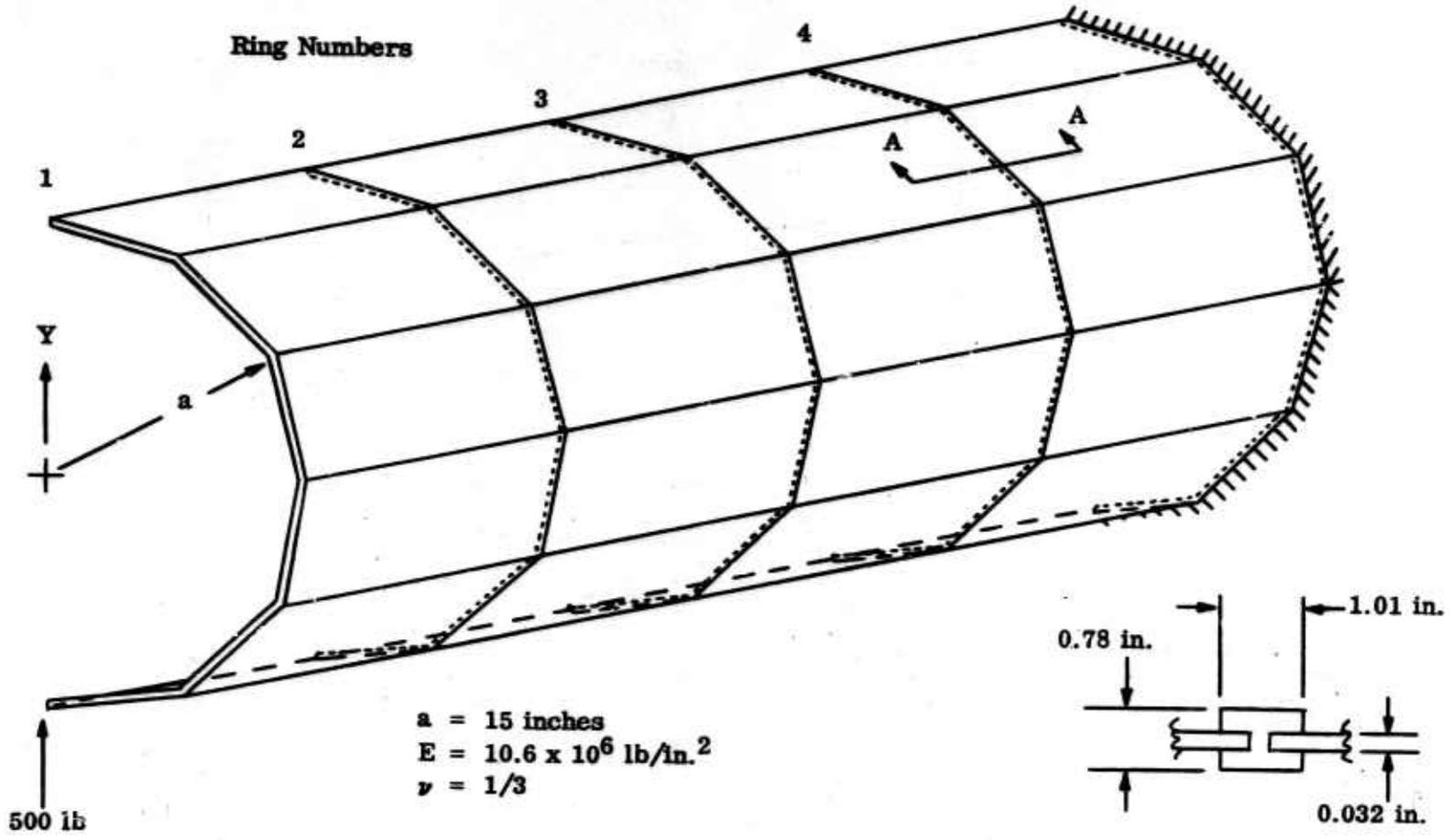

Figure 245. Stiffened Cylinder Problem Definition

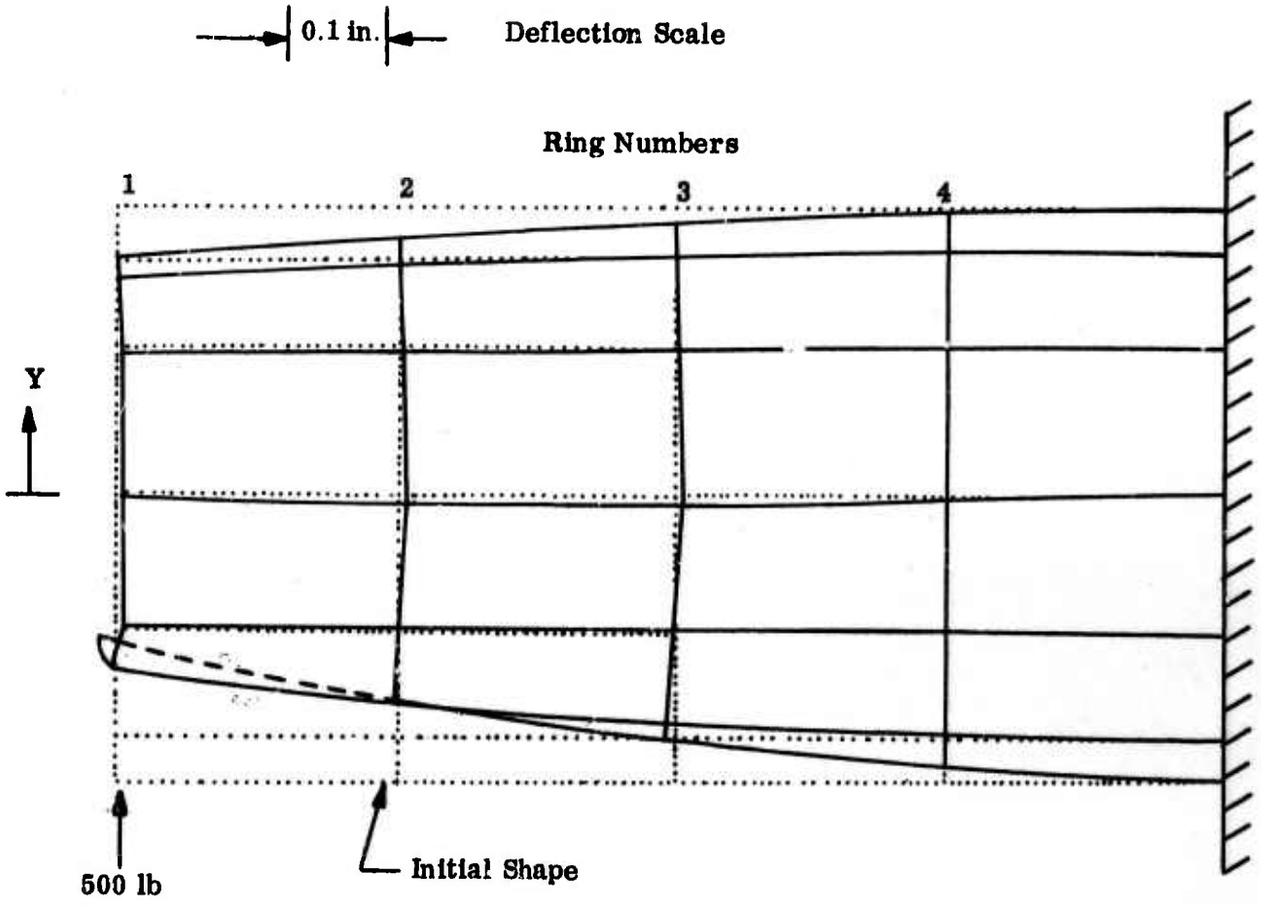

Figure 246. Stiffened Cylinder Longitudinal Displacement Profiles (Inches)

Notes:

1. Loading and ring numbers correspond to Figures 249 and 250
2. Plotted joints are present analytical results.

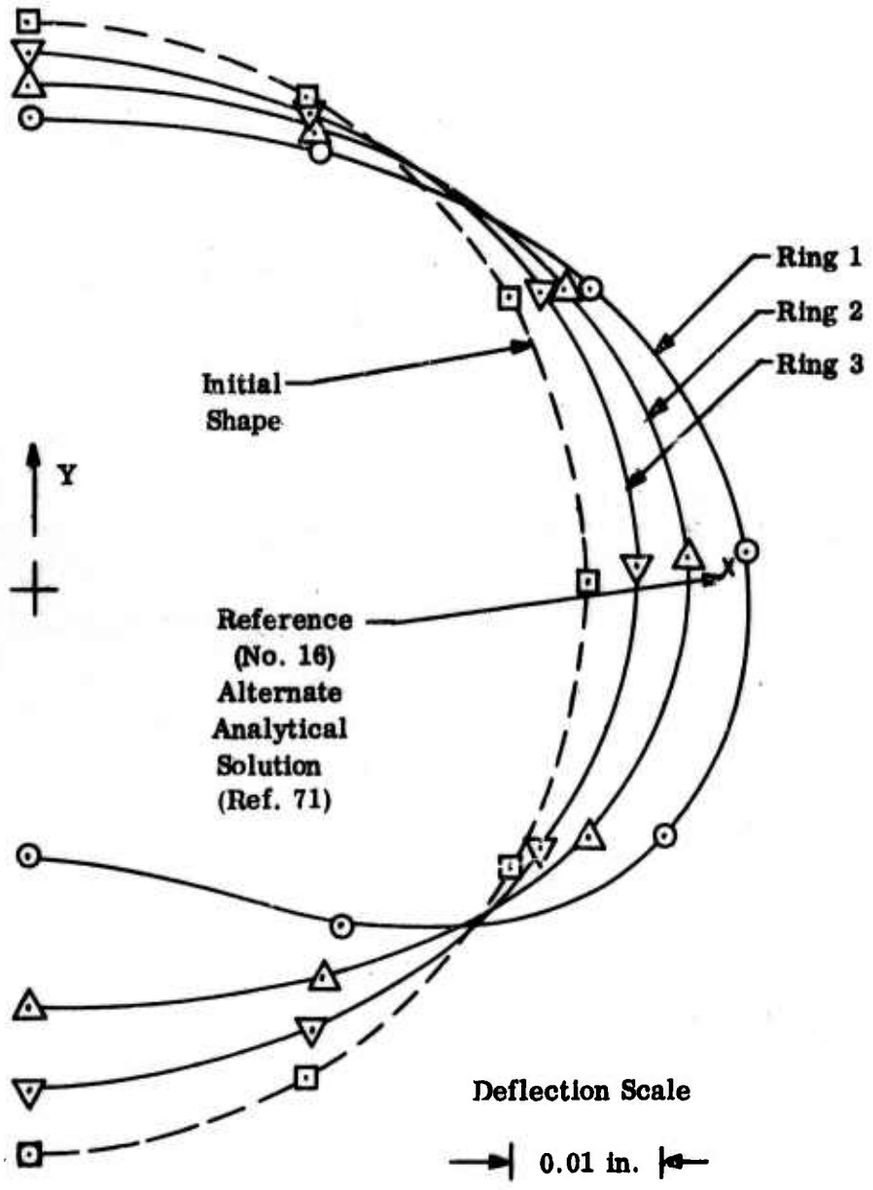

Figure 247. Predicted Stiffened Cylinder Deformed Cross Section (inches)

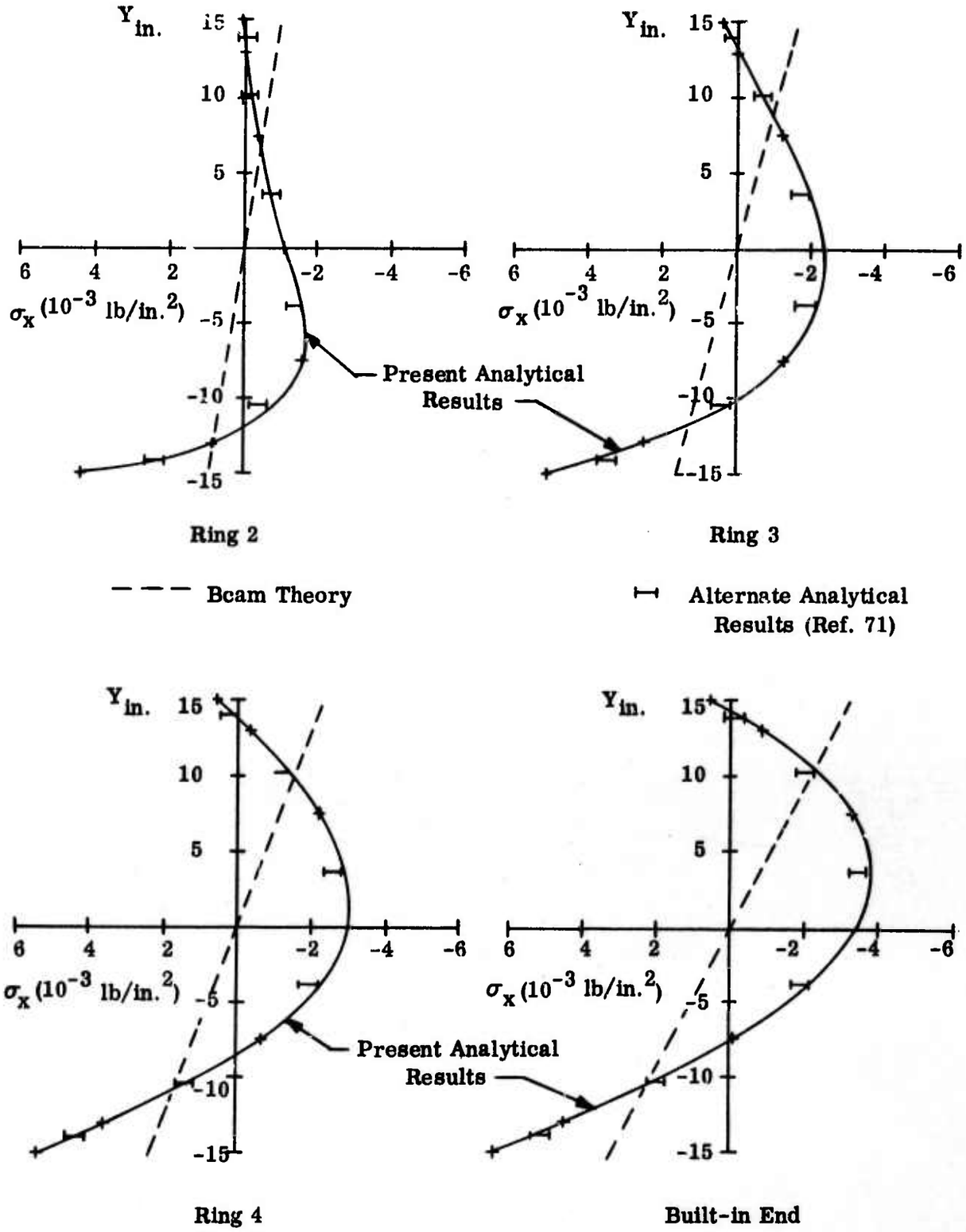

Figure 248. Stiffened Cylinder Longitudinal Stress Profiles

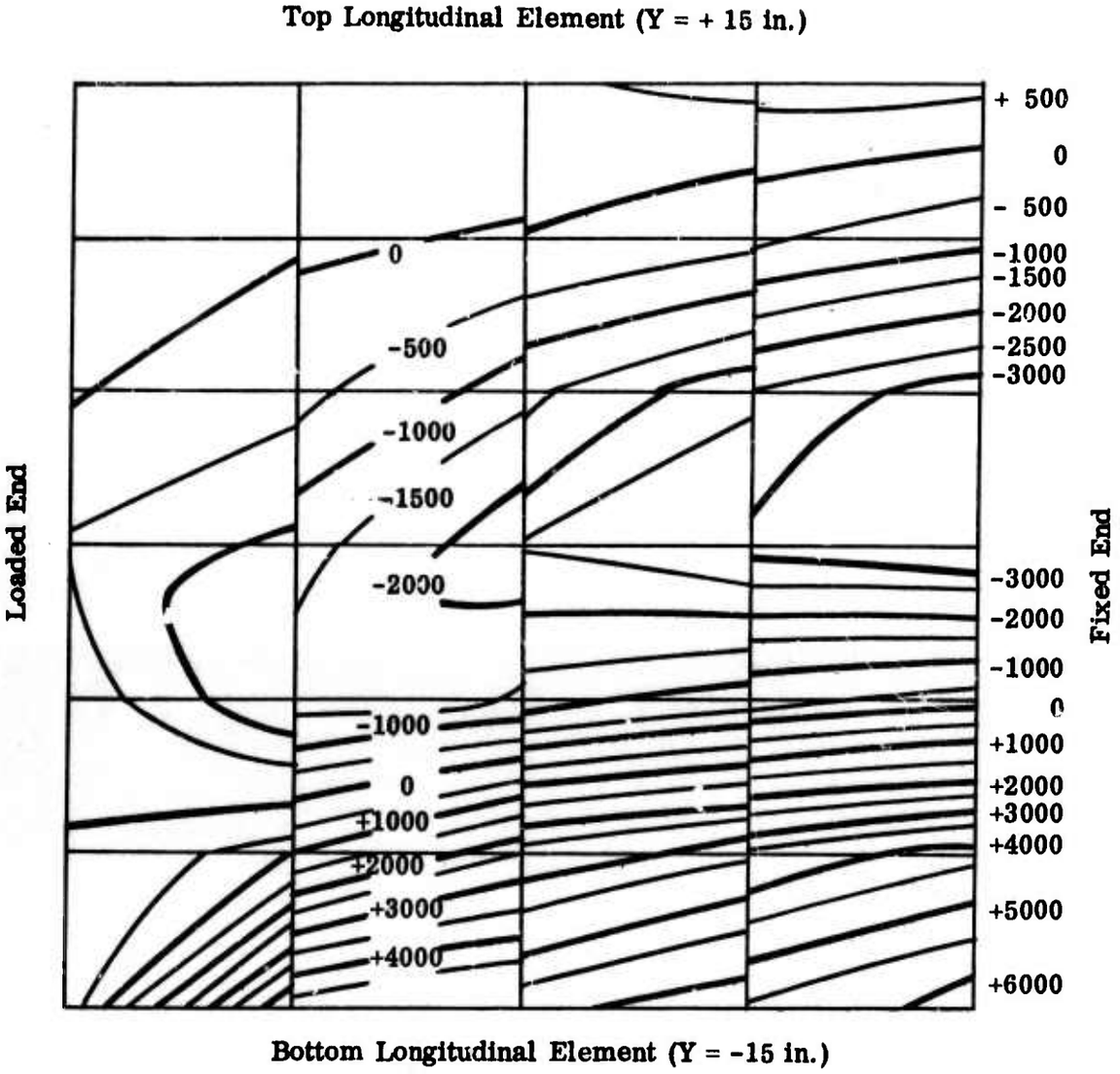

Figure 249. Stiffened Cylinder Longitudinal Stress Contours (psi)

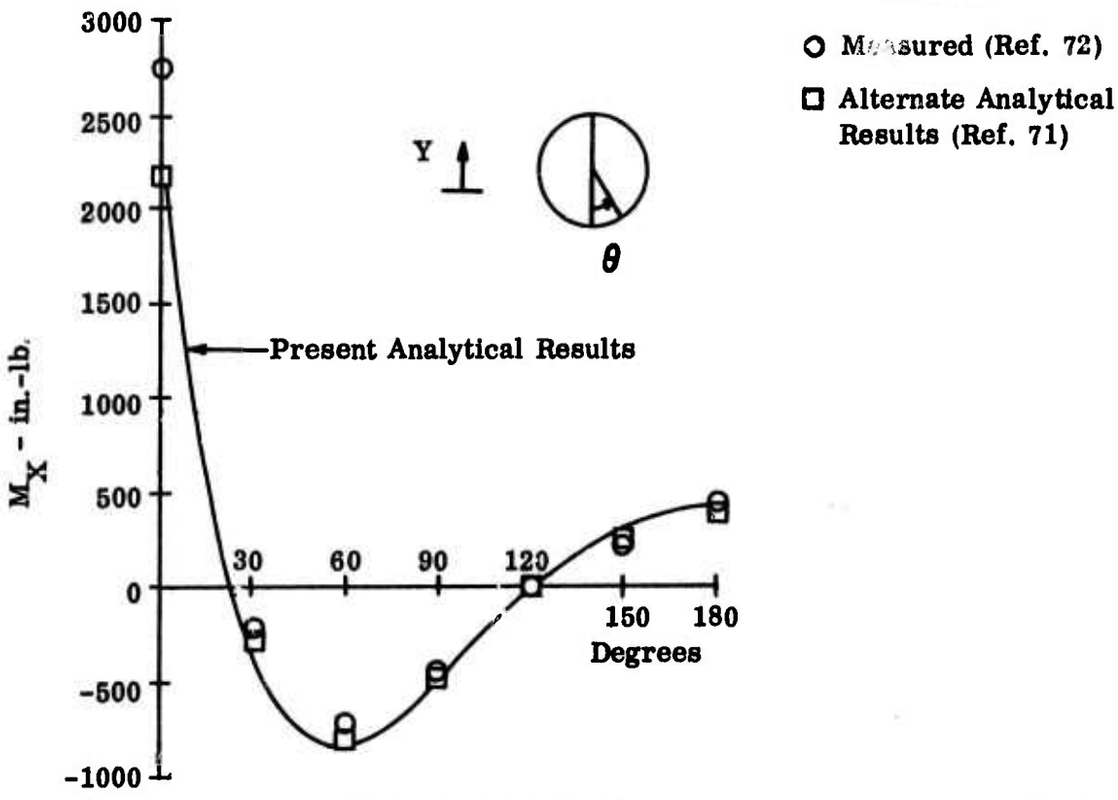

Ring 1 Bending Moments

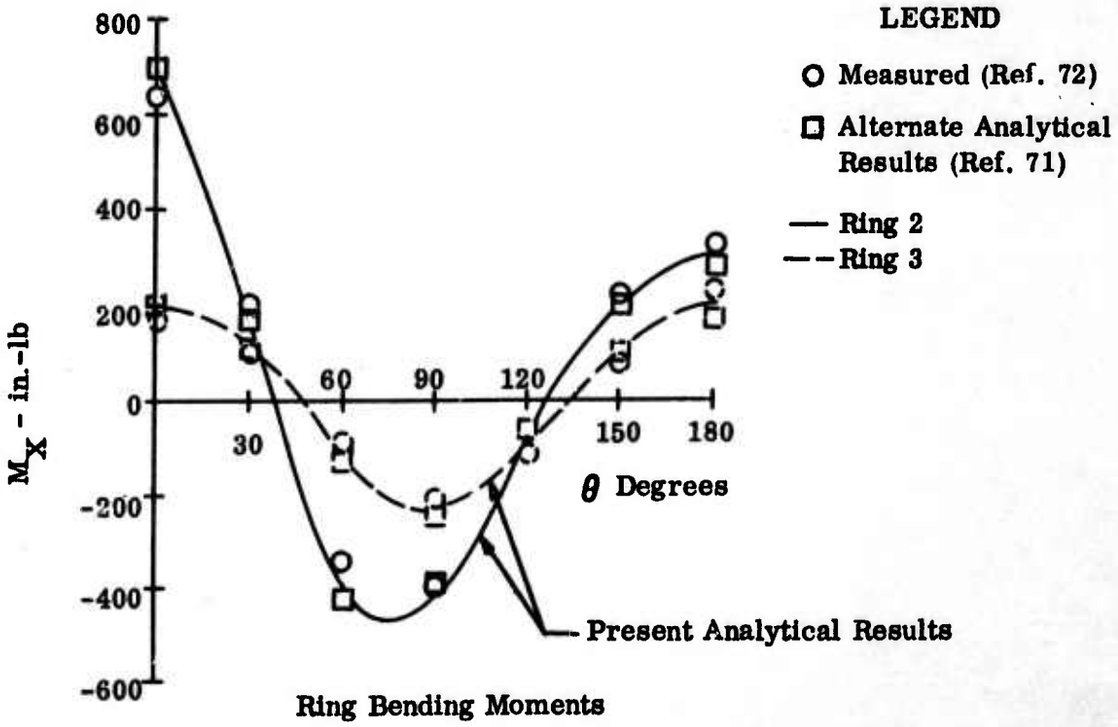

Ring Bending Moments

Figure 250. Stiffened Cylinder Ring Bending Moment Profiles

A.

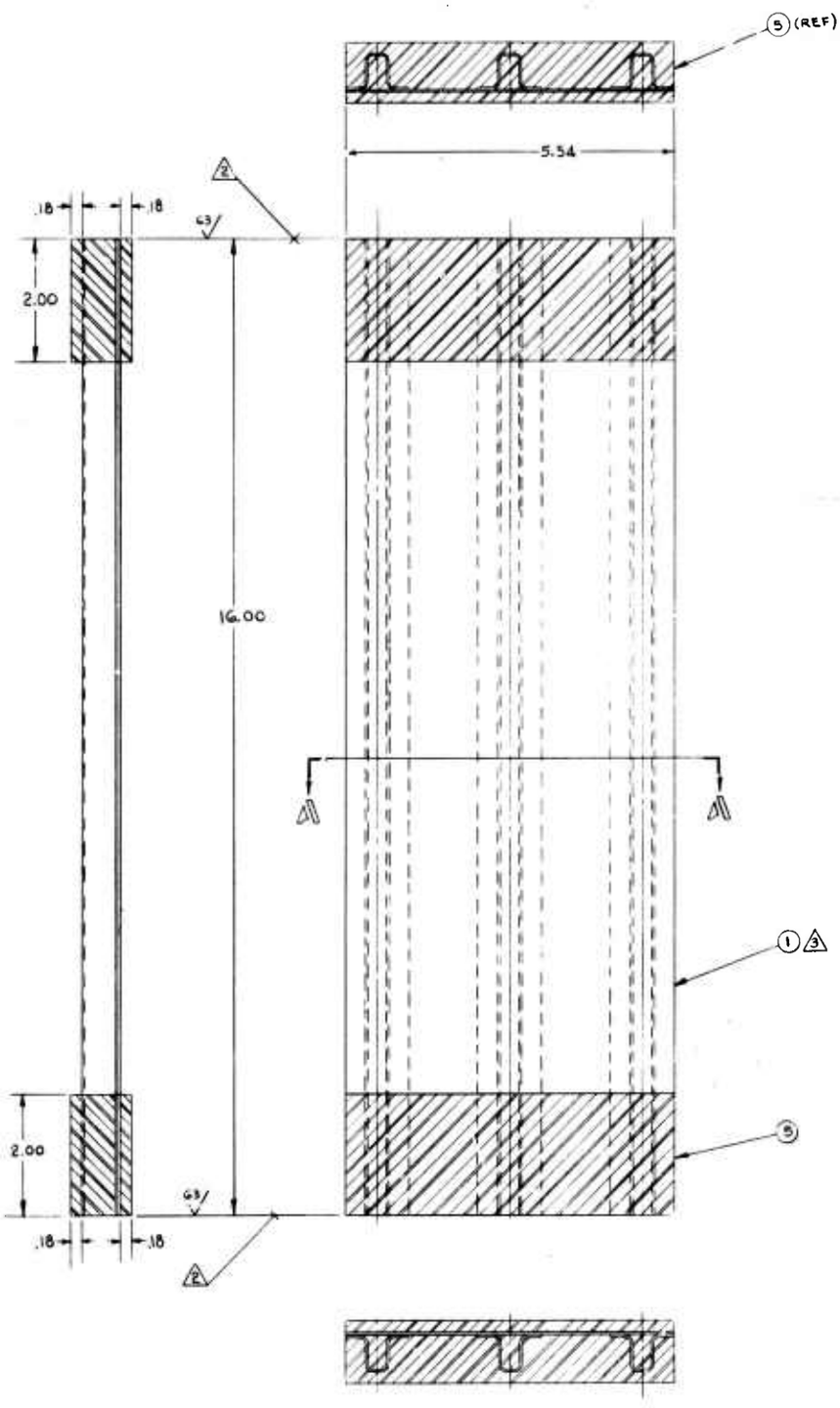

3 SUGGESTED FORMULA:
100 PARTS OF EPON 828
15 PARTS OF VERSAMID 140
8 PARTS OF DIETHYLENE TRIAMINE
50 PARTS OF INERT FILLER- CALCIUM CARBONATE
FABRICATE MOLD TO DRAWING DIMENSIONS
CURE AT ROOM TEMPERATURE OR 150°F

2 THESE SURFACES ARE TO BE PARALLEL TO EACH OTHER WITHIN .001 TIR

1 CFRP UCC PANEL Nº _____

NOTES:

EO NO.	SH OF SH	NU
EO TO COMPLETE PRINT		APP

B.

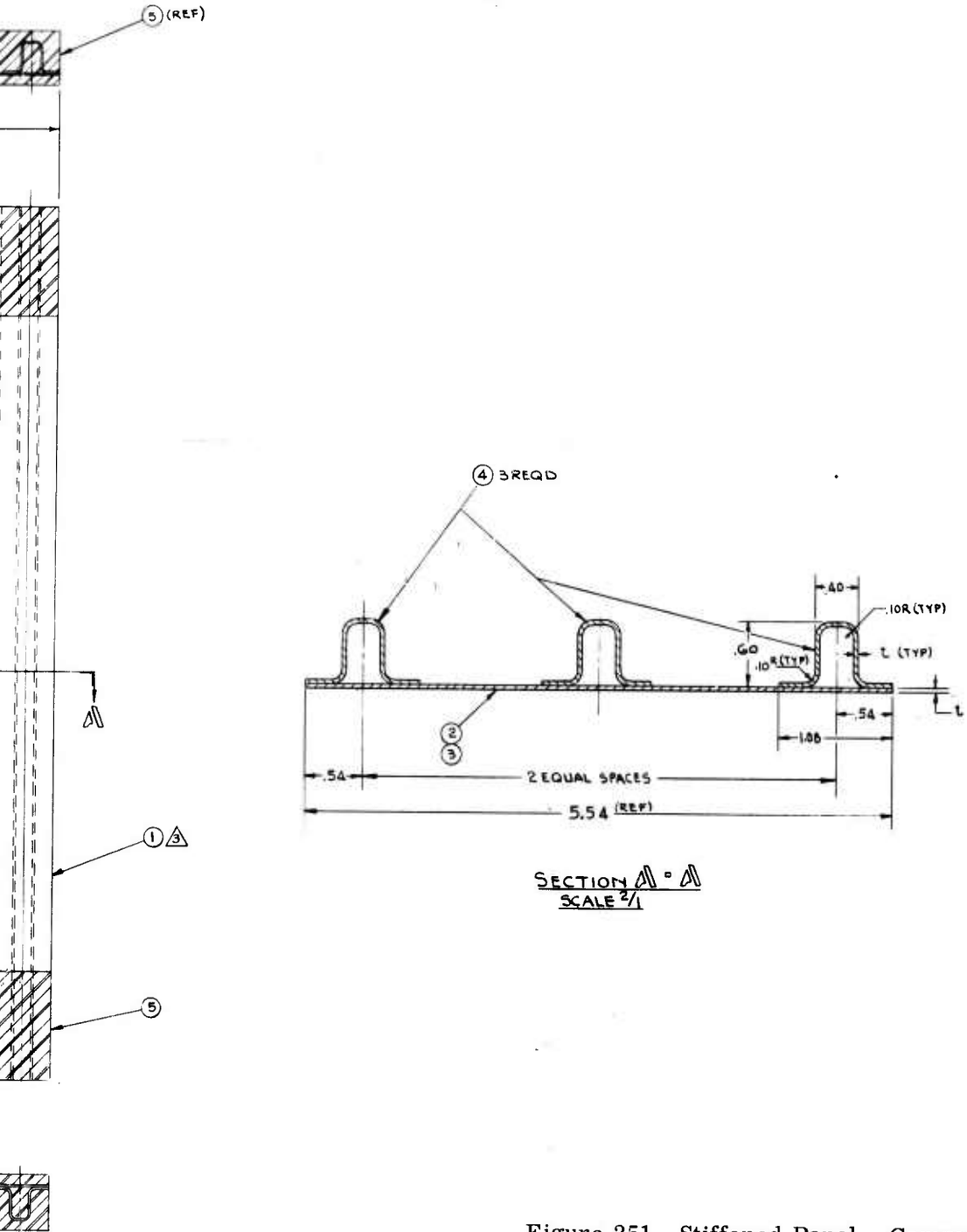

SECTION A-A
SCALE 2/1

Figure 251. Stiffened Panel - Compression Test

ZONE	LTR	REVISIONS DESCRIPTION	DATE	APPROVED

QTY REQD -3	QTY REQD -1	FIND NO.	CODE IDENT	PART OR IDENTIFYING NO.	NOMENCLATURE OR DESCRIPTION	MATERIAL OR NOTE	COMMERCIAL DESIGNATION	SPECIFICATION	DIA	THK	W	LG	13 DIGIT PART NO.	WGT/WT	ZONE
	AR	5		EPON 828	ADHESIVE FILLER MIXTURE 5										
3		4		8506-150006-7	STIFFENER										
		3		8506-150006-5	PANEL										
	1	2		8506-150006-3	STIFFENED PANEL	ASSY 1									
		1		8506-150006-1	PANEL ASSY	4									

PARTS LIST

ED NO.	SH OF SH	NUMBER	APPLICATION	BASIC NO.	NEXT ASSY	USED ON	NEXT ASSY QTY REQD	FINAL ASSY QTY REQD
ED TO COMPLETE PRINT		APPLICABLE SPECIFICATIONS			APPLICATION			

HOLE TOLERANCES EXCEPT AS SHOWN
.060 TO .129 +.002 -.000
.130 TO .250 +.002 -.000
.251 TO .499 +.003 -.000
.500 TO .750 +.010 -.000
.751 TO .999 +.010 -.000
1.000 AND LARGER ±.010

UNLESS OTHERWISE SPECIFIED DIMENSIONS ARE IN INCHES. TOLERANCES ON DECIMALS: .X ±.1, .XX ±.05, .XXX ±.010, ANGLES: ±0°30'
UNLESS OTHERWISE SPECIFIED BREAK ALL SHARP EDGES APPROX .015 R OR CHAMFER
MACHINED SURFACES EXCEPT AS NOTED ✓
SUPERSEDES | SUPERSEDED BY

DESIGN	T. PACHOL	3-27-67
GROUP	[illegible]	3/27/67
APPD	[illegible]	3-27-67
WT		
CHECR		
STRESS		
REL		
CONTRACT NO.		

BELL AEROSYSTEMS COMPANY
POST OFFICE BOX ONE BUFFALO, NEW YORK 14240

STIFFENED PANEL-COMPRESSION TEST

SIZE	CODE IDENT NO.	8506-150006
E	80070	

SCALE W/ NOTED | SHEET

8506-150006 B

A

BLANK PAGE

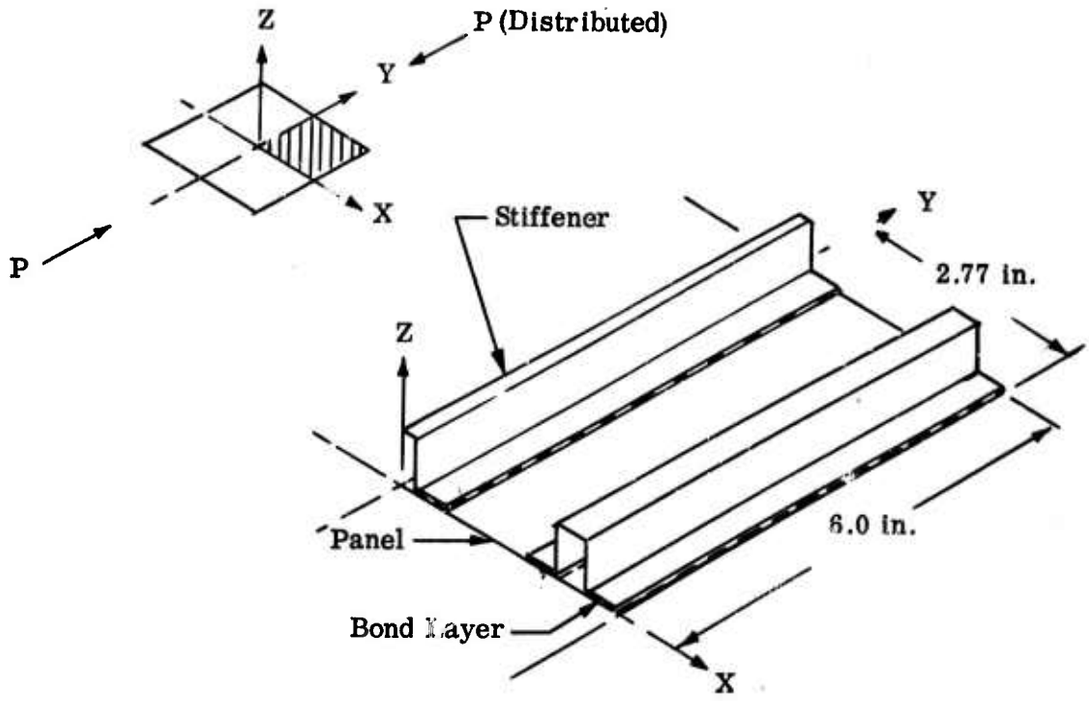

Figure 252. Composite Compression Panel - Test Specimen

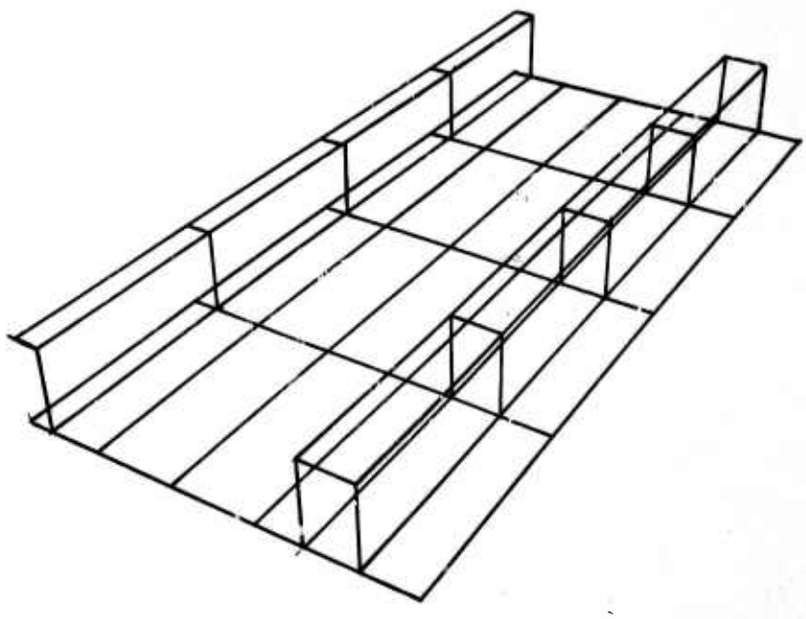

Figure 253. Composite Compression Panel - Test Specimen Idealization

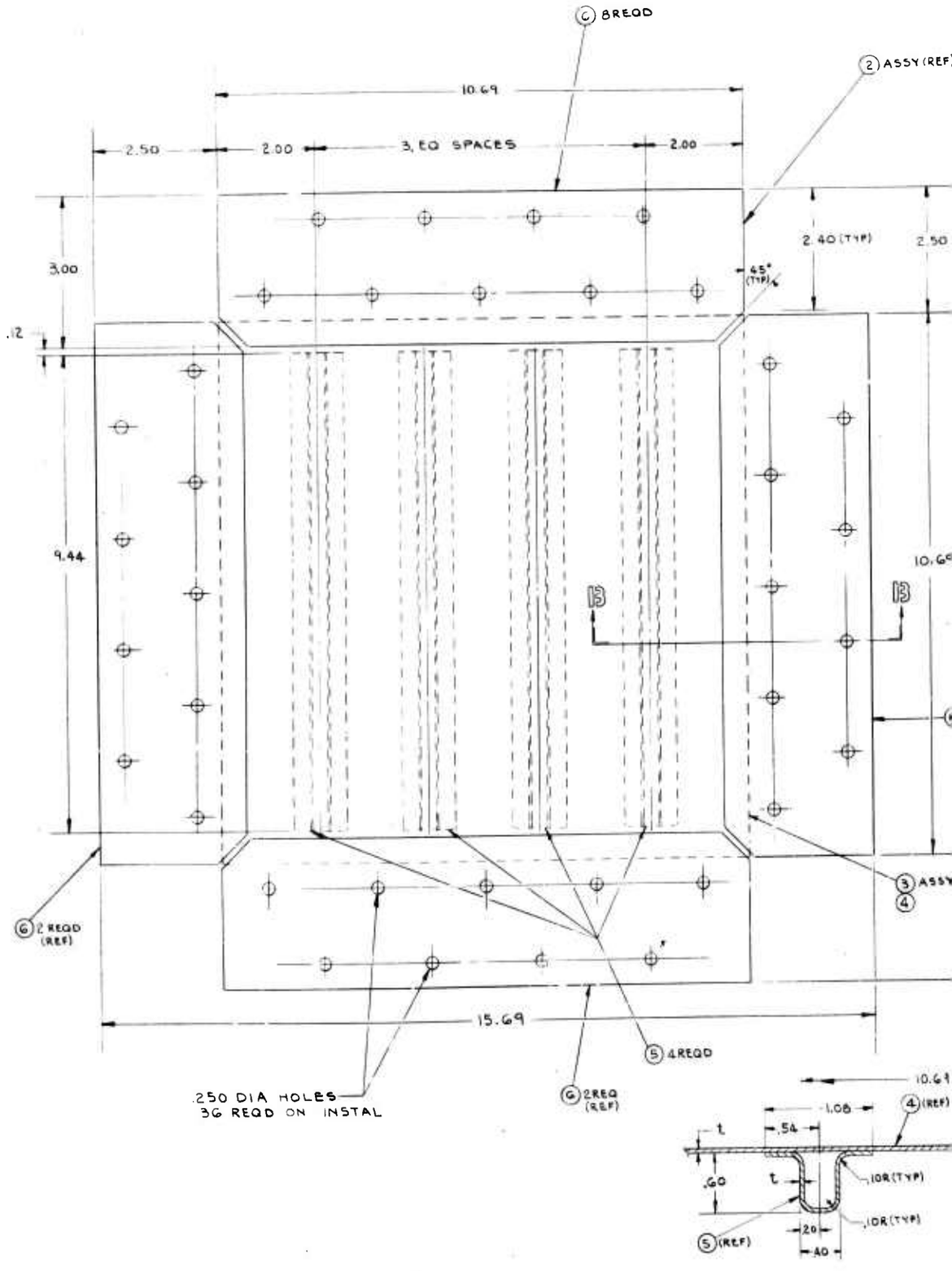
1 REQD
10.69
2.50
2.00
3 EQ SPACES
2.00
2 ASSY (REF)
2.40 (TYP)
2.50
3.00
45° (TYP)
.12
9.44
10.69
B
B
3 ASSY
4
6 2 REQD (REF)
15.69
5 4 REQD
.250 DIA HOLES
36 REQD ON INSTAL
6 2 REQ (REF)
10.69
1.08
4 (REF)
.54
t
.60
t
.10R (TYP)
.10R (TYP)
.20
.40
5 (REF)

A.

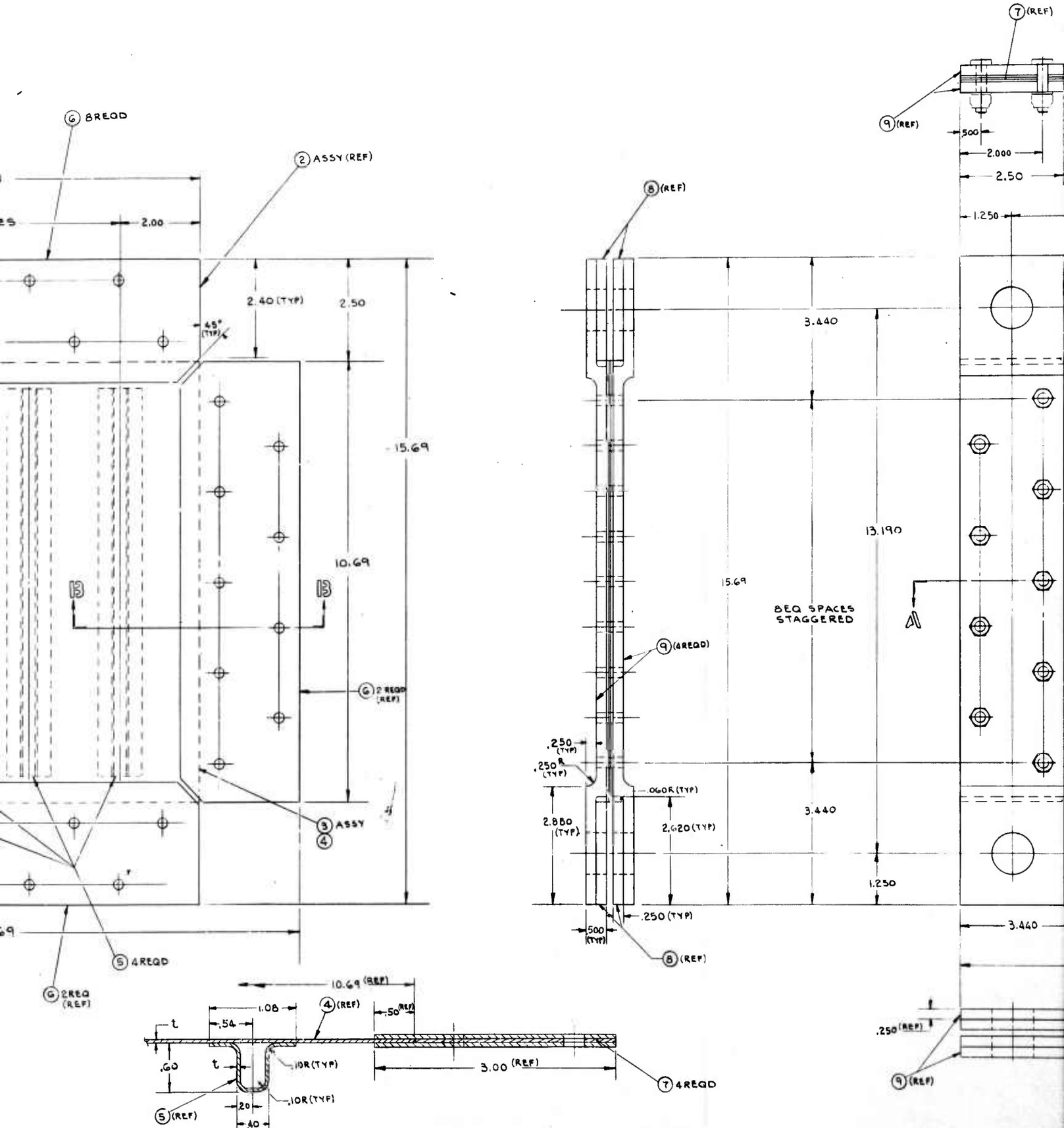

SECTION 13 - 13
SCALE 2/1

B.

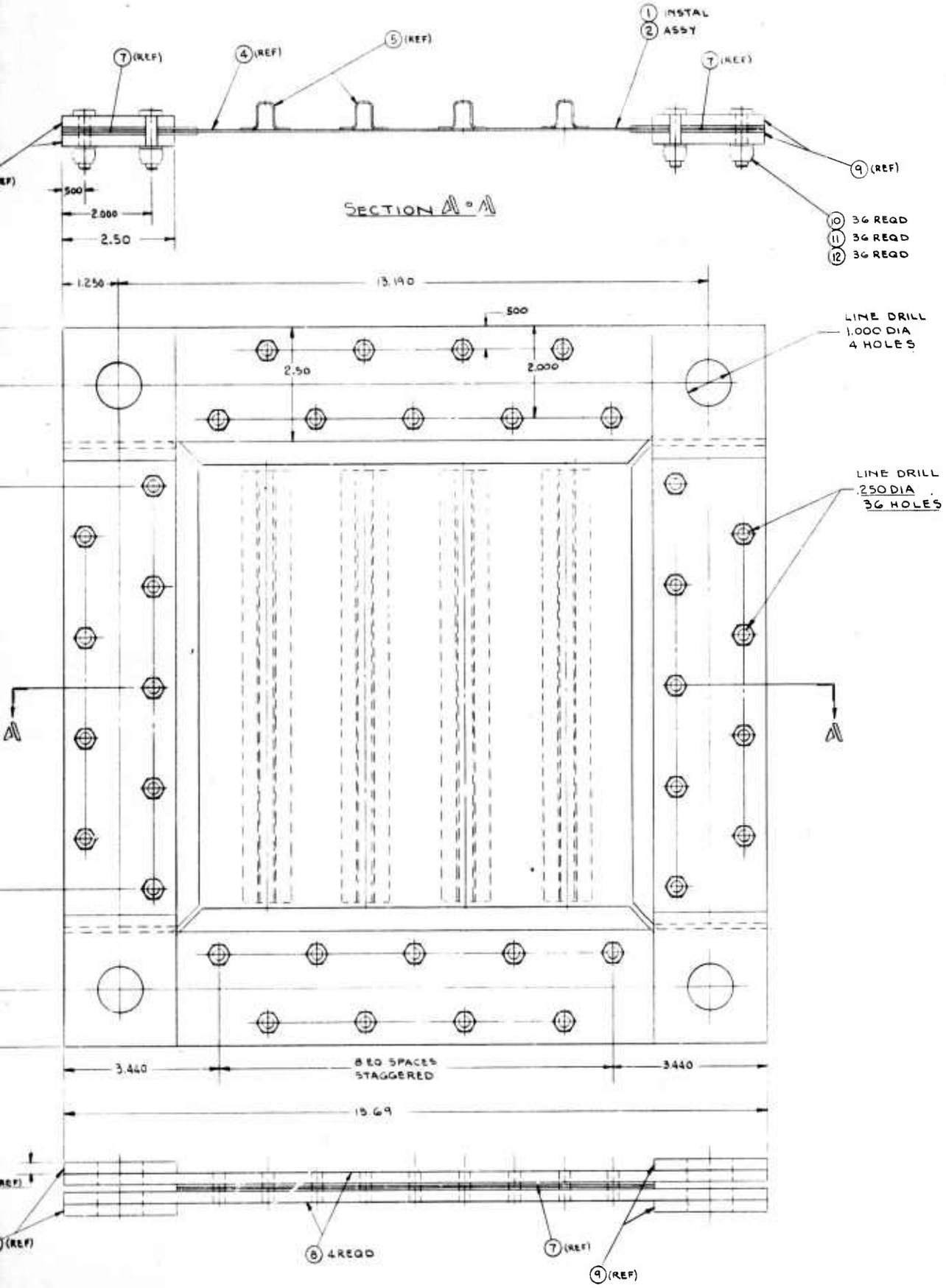

3 BOND -3 PANEL TO -11 ENDS WITH AF-126
SCOTCHWELD FIR BPS PURCHASE FROM 3M

2 THICKNESS OF -13 SHIM TO BE SAME AS THICKNESS OF

1 CFRP UCC PANEL ASSY Nº _____

NOTES:

C.

8506-150007

REVISIONS			
ZONE	LTR	DESCRIPTION	DATE	APPRDVED

D.

Figure 254. Stiffened Panel - Shear Test

QTY REQD -5	QTY REQD -3	QTY REQD -1	FIND NO.	CODE IDENT	PART OR IDENTIF. NO.	NOMENCLATURE OR DESCRIPTION	MATERIAL OR NOTE	COMMERCIAL DESIGNATION	SPECIFICATION	SIA	THK	W	LG	TS 1000 PSI	UNIT WT	ZONE
	AR		13		AF-126	SCOTCHWELD	A									
		36	12		AN960-416	WASHER	STD									
		36	11		MS21044N4	NUT	STD									
		36	10		AN4-15A	BOLT	STD									
		4	9		8506-150007-17	FRAME PLATE	ST PLATE	4130	MIL-S-18729		.560	2.7	16.0	90		
		4	8		8506-150007-15	FRAME PLATE	ST SHEET	4130	MIL-S-18729		.250	2.7	16.0	90		
	4		7		8506-150007-13	SHIM	ALCLAD SH	2024 T4	QQ-A-250/5	A	.063	2.7	11.0	62		
	8		6		8506-150007-11	END	ALCLAD SH	2024 T4	QQ-A-250/5		.063	2.7	11.0	62		
1			5		8506-150007-9	STIFFENER										
1			4		8506-150007-7	TEST PANEL										
	1		3		8506-150007-5	TEST SPECIMEN ASSY										
		1	2		8506-150007-3	PANEL ASSY										
			1		8506-150007-1	PANEL INSTALL										

PARTS LIST

8506-150007

ED NO.	SH OF SH	NUMBER	APPLICATION	DASH NO.	NEXT ASSY	USED ON	NEXT ASSY QTY REQD	FINAL ASSY QTY REQD
ED TO COMPLETE PRINT		APPLICABLE SPECIFICATIONS			APPLICATION			

HOLE TOLERANCES EXCEPT AS SHOWN
.040 TO .122 +.005,-.000
.123 TO .280 +.006,-.000
.281 TO .622 +.006,-.000
.623 TO .732 +.010,-.000
.733 TO .995 +.013, .000
.996 AND LARGER ±.010

UNLESS OTHERWISE SPECIFIED DIMENSIONS ARE IN INCHES. TOLERANCES ON DECIMALS: .X ±.1 | .XX ±.03 | .XXX ±.010 | ANGLES: ±0°30'
UNLESS OTHERWISE SPECIFIED BREAK ALL SHARP EDGES APPROX .010 R OR CHAMFER
MACHINED SURFACES 63 EXCEPT AS NOTED

SUPERSEDES | SUPERSEDED BY

DESIGN T. PACHOL 3-24-67
DROUP [illegible] 3/27/67
APPD [illegible] 3-27-67
WT
CHECK
STRESS
REL
CONTRACT NO.

BELL AEROSYSTEMS COMPANY
A TEXTRON COMPANY
POST OFFICE BOX ONE BUFFALO, NEW YORK 14240

STIFFENED PANEL
SHEAR TEST

SIZE J | CODE IDENT NO. 80070 | 8506-150007
SCALE 1/16 FULL | SHEET

OM 3M CO.
ESS OF -7 PANEL

BLANK PAGE

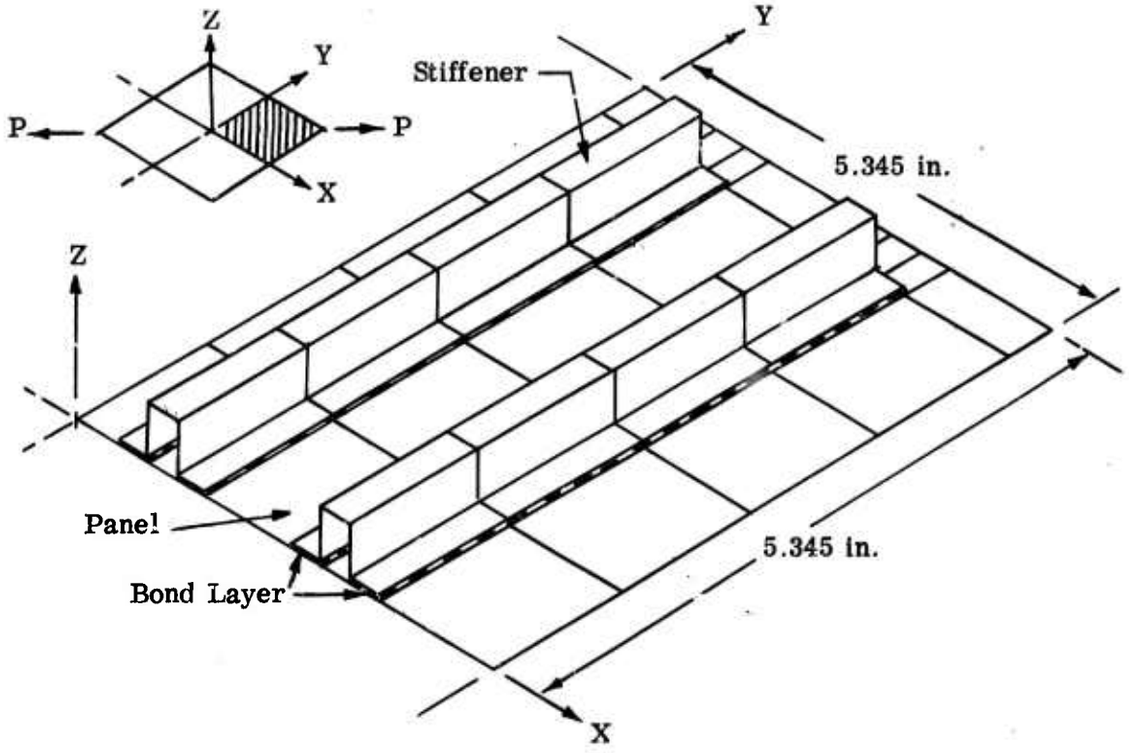

Figure 255. Composite Shear Panel - Test Specimen

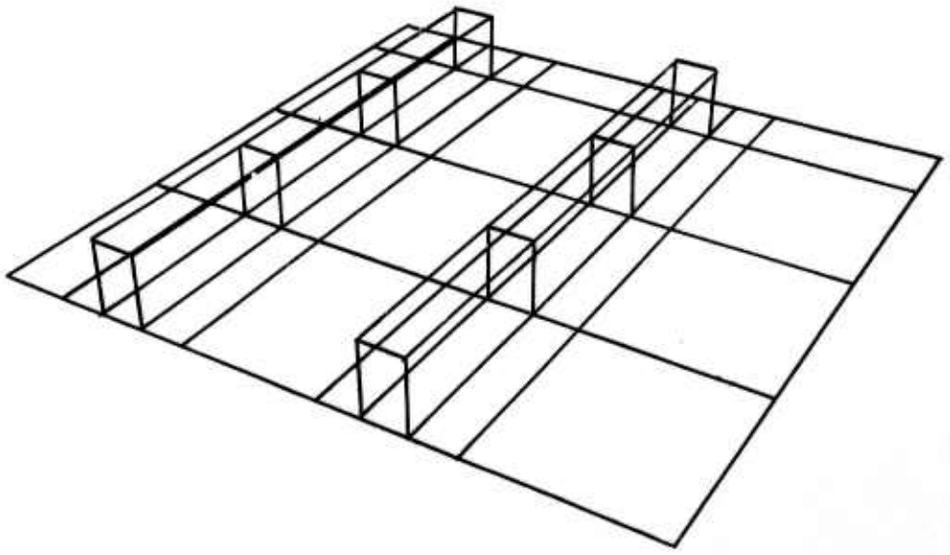

Figure 256. Composite Shear Panel - Test Specimen Idealization

3. Ring-beam Element

This element is a short, straight section of the ring section proposed for the fuselage component design (refer to Section X E and to Figure 257). Specimens of these types will be tested in bending to confirm strength predictions obtained through hand calculation. Discrete element analyses will only be employed here if hand analyses proven insufficient to predict adequately the strengths and failure modes observed from testing.

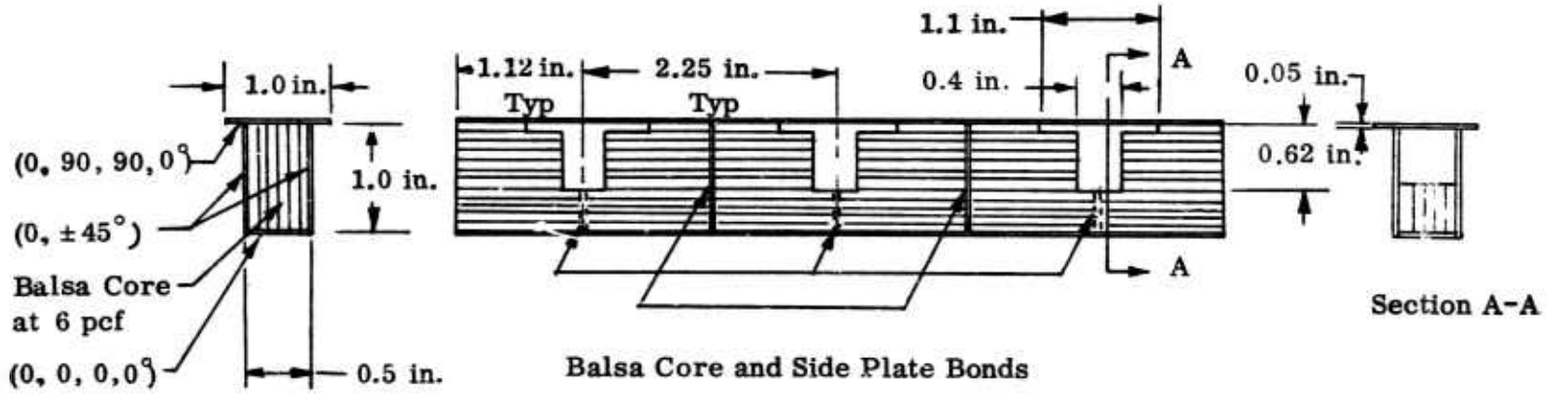

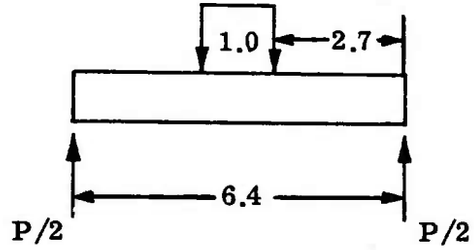

Test Loading

Figure 257. Ring-beam Element

C. Energy Search Methods for Nonlinear Materials
(Professor Schmit and Mr. E. Rybicki)

The incremental complementary energy approach to predicting multiaxial stress distribution behavior including material nonlinearity was described in Section IX A of the First Annual Report[1]. A numerical evaluation study has been carried out on a plane stress thermal problem for which Mendelson[74] has reported an independent solution. For this example, the material is isotropic, the stress-strain curve is bilinear, and the Prandtl-Reuss incremental strain stress relations are used to describe the material nonlinearities. The structure, shown in Figure 258, is a rectangular plate subjected to a parabolic temperature distribution $T = T_o y^2$. The stress solution for this problem[74] is used to evaluate the stress solution obtained by the incremental complementary energy approach. A total of five load increments were used, raising the temperature distribution to $T = 5.7\ (\sigma_0/\alpha E)y^2$ where σ_0 is the yield stress, α is the coefficient of linear thermal expansion, and E is the modulus of elasticity. Because of symmetry, only one quadrant of the plate is considered. The quadrant was divided into 4 elements as shown in Figure 259. A stress function in the form of the sum of products of hyperosculatory interpolation polynomials was assumed for each element. This representation provides 36 degrees of freedom for each element. However, after force boundary conditions and interelement equilibrium requirements are satisfied and the additional information that the stresses are continuous in the plate is employed, the total number of independent degrees of freedom reduces to 36 for the assemblage of four elements.

Three aspects of the stress solution obtained were compared with the solutions reported by Mendelson[74]:

1. The propagation of the plastic front, Figure 260
2. The normal stress σ_x (0,y) at the cross section (x=0) of the plate, Figure 261 and
3. The mechanical strain at the cross section (x=0) of the plate, Figure 262.

The curves in Figures 261 and 262 represent the solution for a plate infinite in the x direction[74]. The circles represent results at specific values of y obtained using the incremental complementary energy approach. The agreement between the reference solution and the results obtained with the incremental complementary energy method was very good. These results were obtained using 36 degrees of freedom for the structure and required 6.5 minutes of machine running time (Fortran IV program on a Univac 1107). The incremental complementary energy was minimized using the Fletcher-Powell minimization technique available as a preprogrammed procedure as a result of the effort first reported in Section IX B-2 of the First Annual Report[1]. On the basis of these results, the incremental complementary energy approach to the solution of nonlinear multiaxial stress problems was judged to be quite promising.

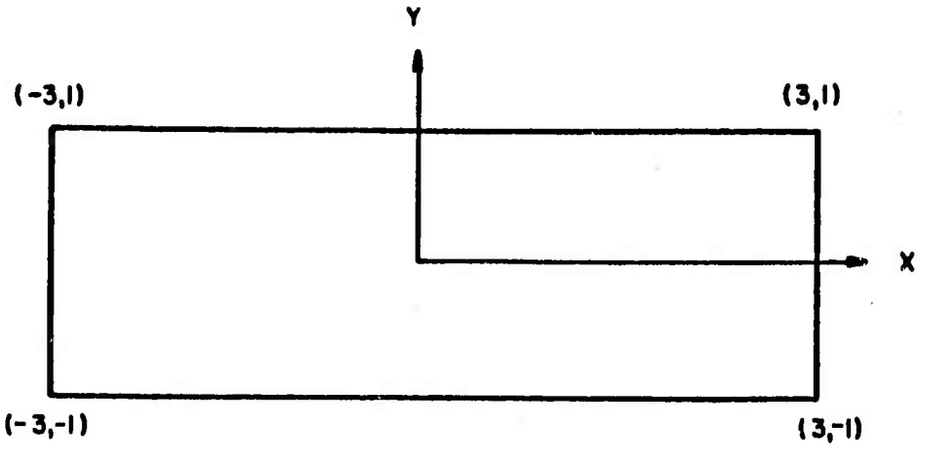

Figure 258. Rectangular Plate with Coordinate System.

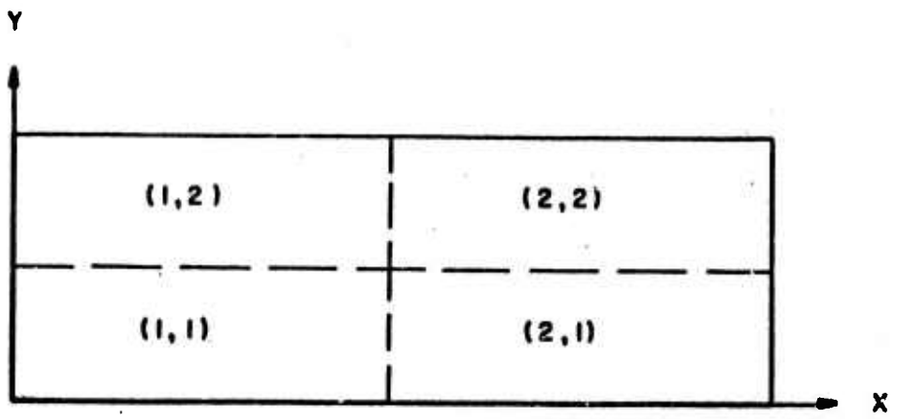

Figure 259. First Quadrant of Rectangular Plate Divided into Four Elements.

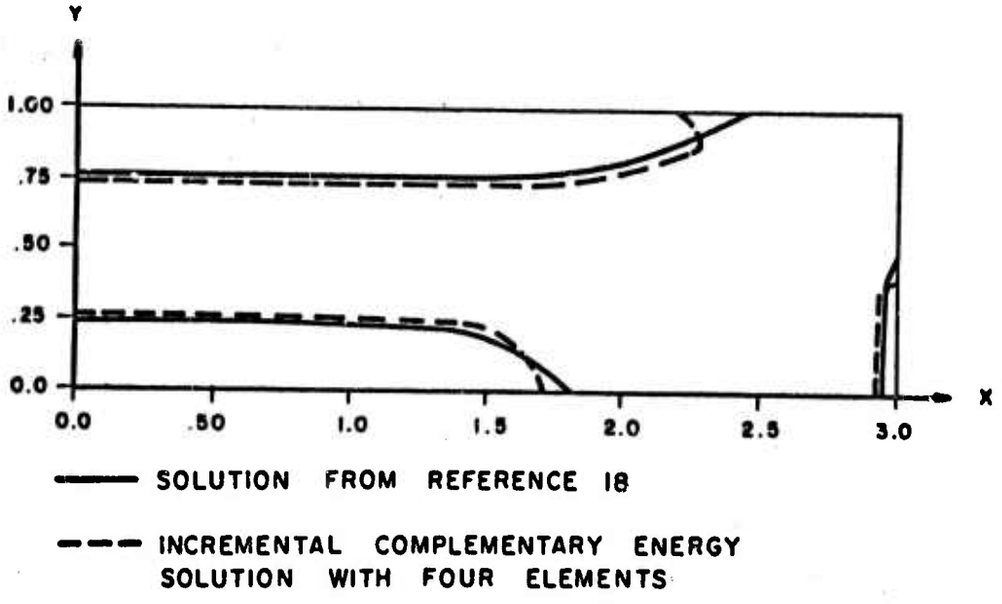

Figure 260. Plastic Front in First Quadrant.

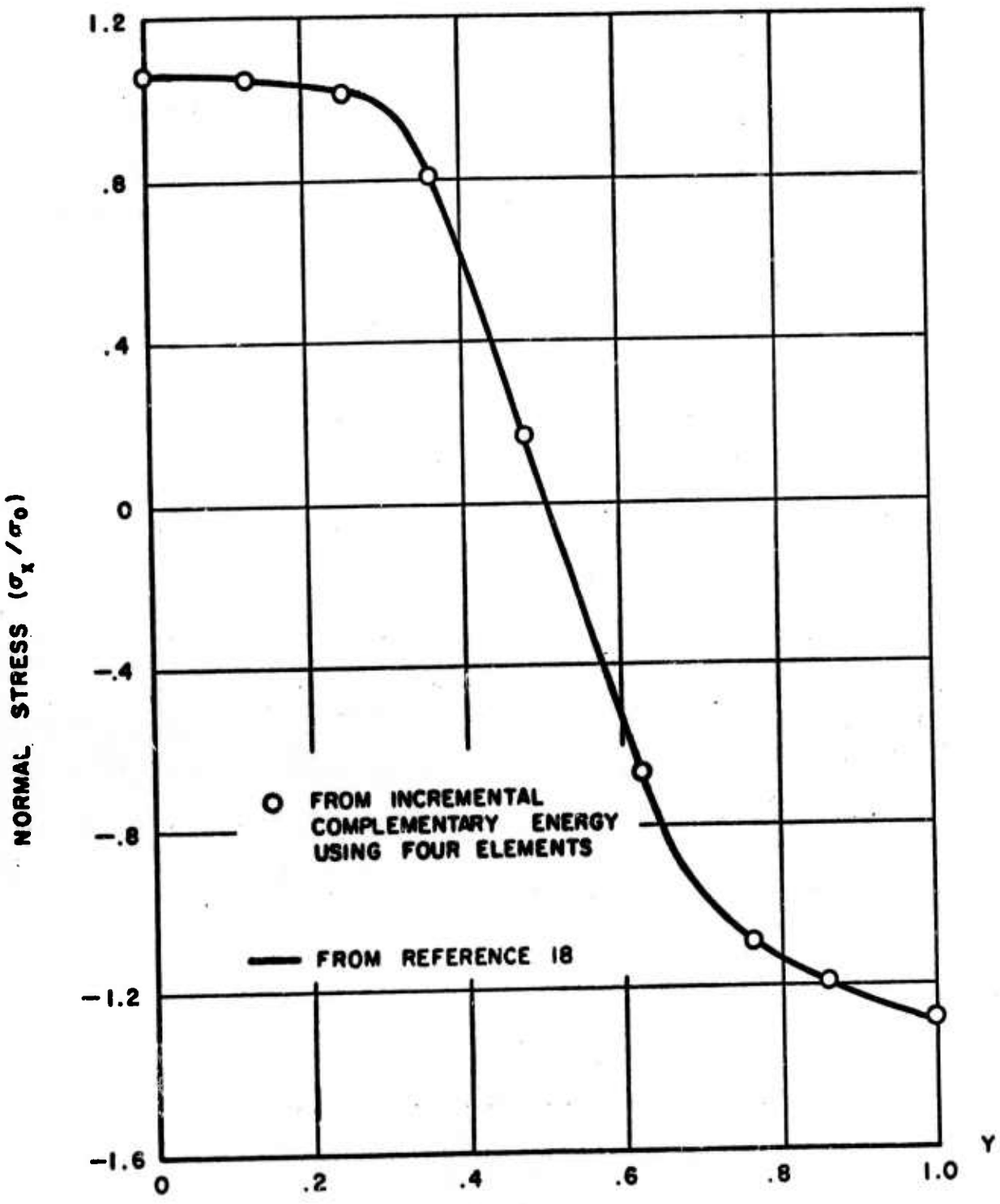

Figure 261. Normal Stress at Cross Section x = 0.

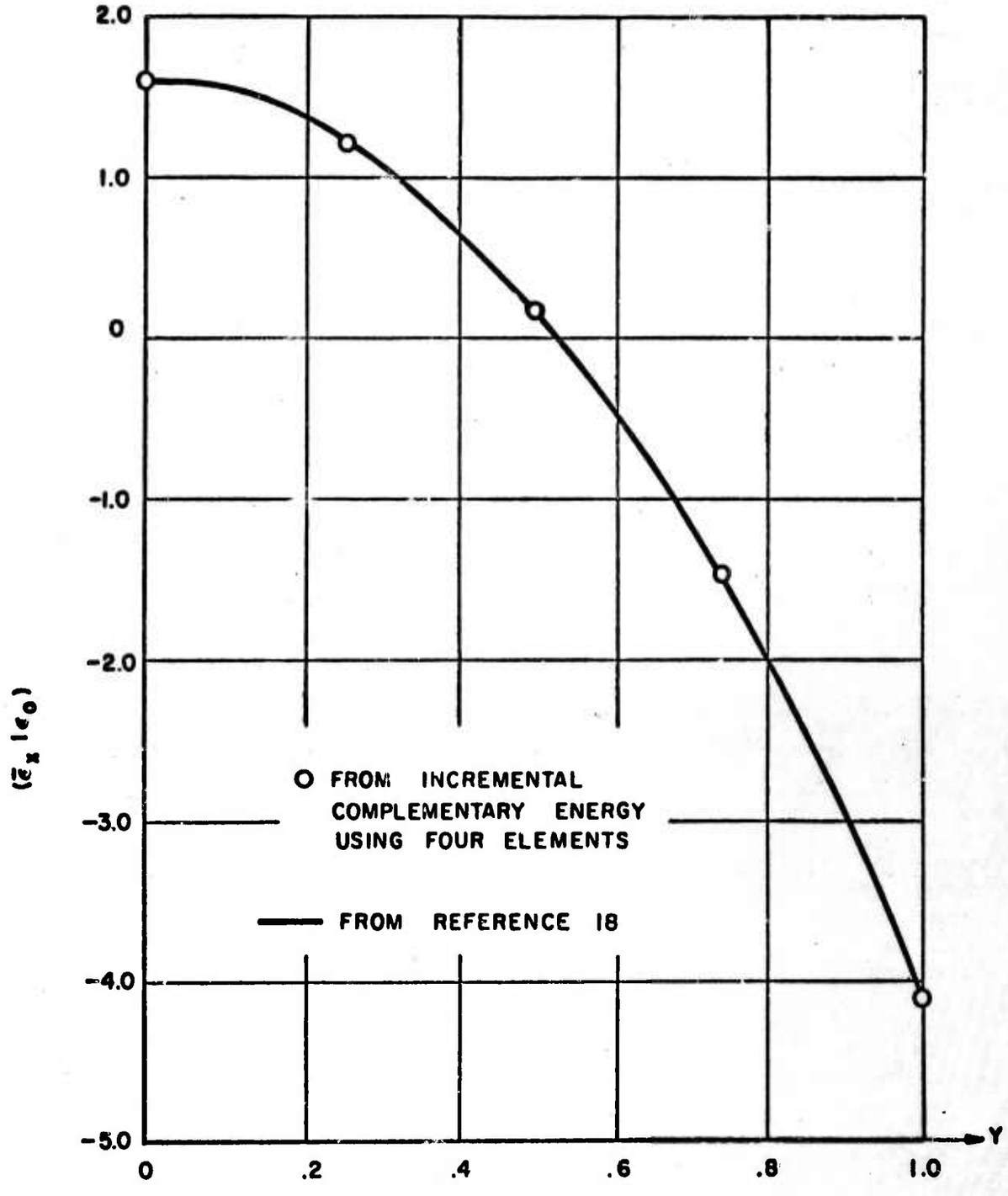

Figure 262. Mechanical Strain at Cross Section x = 0.

After the completion of the numerical verification study, efforts were directed toward extending the nonlinear multiaxial stress analysis capability to include transversely isotropic materials that behave differently in tension and compression. The structure to be analyzed is a thick-walled infinite cylinder constructed of transversely isotropic material. The stress distribution in the cylinder for axially symmetric temperature and pressure loadings is sought.

The formulation of this problem parallels that of the isotropic plate. The linear strain hardening representation for the stress strain curve has been extended to a multilinear strain hardening representation as shown in Figure 263.

The strains are assumed to be of the form

$$\varepsilon_r = \frac{\sigma_r}{E_r} - \frac{\mu_{r\theta}}{E_\theta}\sigma_\theta - \frac{\mu_{zr}}{E_z}\sigma_z + \alpha_r \Delta T + \sum_{q=1}^{Q-1} \Delta\varepsilon_r^{P(q)} + \Delta\varepsilon_r^{P(Q)} \qquad \text{(IX C-1)}$$

$$\varepsilon_\theta = \frac{\sigma_\theta}{E_\theta} - \frac{\mu_{\theta r}}{E_r}\sigma_r - \frac{\mu_{\theta z}}{E_z}\sigma_z + \alpha_\theta \Delta T + \sum_{q=1}^{Q-1} \Delta\varepsilon_\theta^{P(q)} + \Delta\varepsilon_\theta^{P(Q)} \qquad \text{(IX C-2)}$$

$$\varepsilon_z = \frac{\sigma_z}{E_z} - \frac{\mu_{zr}}{E_r}\sigma_r - \frac{\mu_{z\theta}}{E_\theta}\sigma_\theta + \alpha_z \Delta T + \sum_{q=1}^{Q-1} \Delta\varepsilon_z^{P(q)} + \Delta\varepsilon_z^{P(Q)} \qquad \text{(IX C-3)}$$

where the first three terms of each equation are the elastic strains, followed by the thermal strains, the accumulated plastic strains from the first Q-1 load increments, and, finally, the increment of plastic strain due to the Qth load increment. The incremental plastic strains are assumed to be given by

$$\Delta\varepsilon_r^P = \frac{\Delta\bar{\varepsilon}^P}{\bar{\sigma}}\left(\frac{\sigma_r}{F_r} - \frac{\sigma_\theta}{2F_\theta} - \frac{\sigma_z}{2F_z}\right)\frac{1}{F_r} \qquad \text{(IX C-4)}$$

$$\Delta\varepsilon_\theta^P = \frac{\Delta\bar{\varepsilon}^P}{\bar{\sigma}}\left(\frac{\sigma_\theta}{F_\theta} - \frac{\sigma_r}{2F_r} - \frac{\sigma_z}{2F_z}\right)\frac{1}{F_\theta} \qquad \text{(IX C-5)}$$

$$\Delta\varepsilon_z^P = \frac{\Delta\bar{\varepsilon}^P}{\bar{\sigma}}\left(\frac{\sigma_z}{F_z} - \frac{\sigma_r}{2F_r} - \frac{\sigma_\theta}{2F_\theta}\right)\frac{1}{F_z} \qquad \text{(IX C-6)}$$

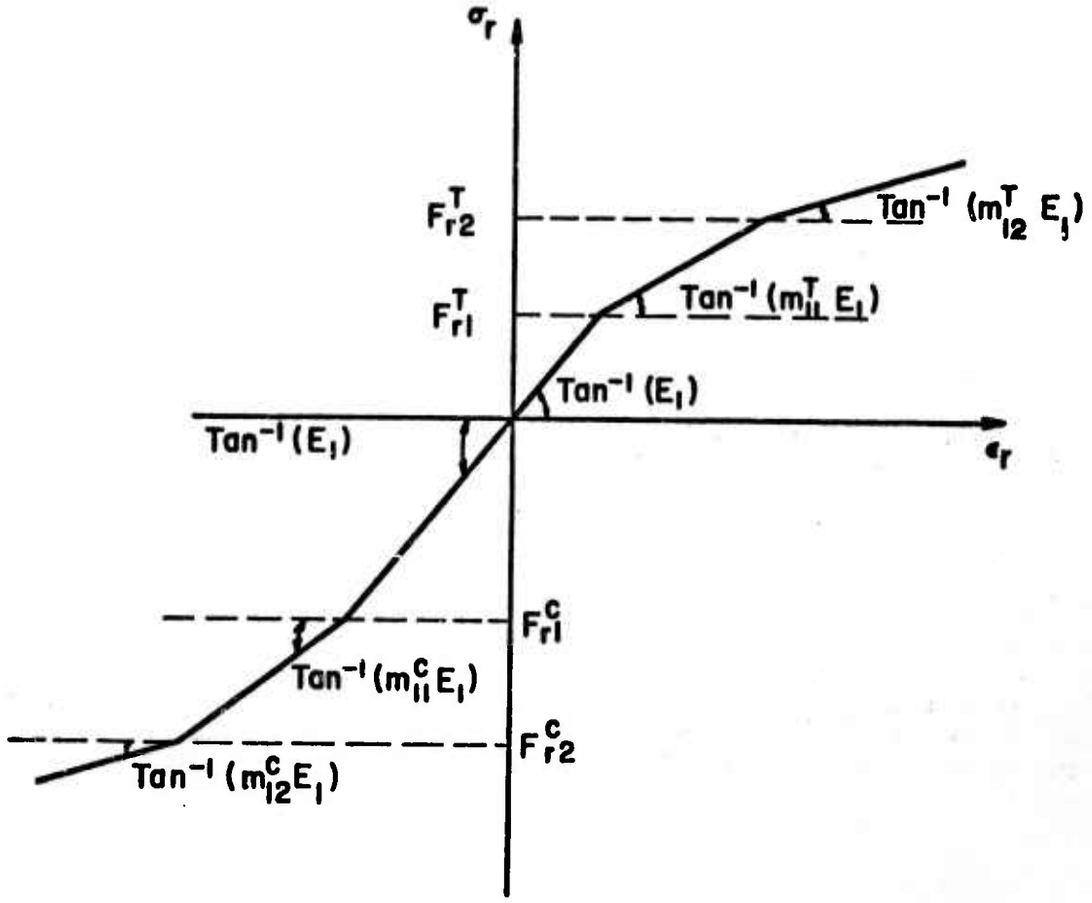

Figure 263. Multilinear Strain Hardening Representation of a Uniaxial Stress-Strain Curve for a Material that Behaves Differently in Tension and Compression.

where

$$\Delta\bar{\varepsilon}^{P} = \frac{2}{3}\left\{(F_r\,\Delta\varepsilon_r^P)^2 + (F_\theta\,\Delta\varepsilon_\theta^P)^2 + (F_z\,\Delta\varepsilon_z^P)^2 - F_r\,\Delta\varepsilon_r^P F_\theta\,\Delta\varepsilon_\theta^P - F_r\,\Delta\varepsilon_r^P F_z\,\Delta\varepsilon_z^P - F_\theta\,\Delta\varepsilon_\theta^P F_z\,\Delta\varepsilon_z^P\right\}^{1/2} \qquad \text{(IX C-7)}$$

and

$$\bar{\sigma}^2 = \left(\frac{\sigma_r}{F_r}\right)^2 + \left(\frac{\sigma_\theta}{F_\theta}\right)^2 + \left(\frac{\sigma_z}{F_z}\right)^2 - \frac{\sigma_r\sigma_\theta}{F_rF_\theta} - \frac{\sigma_r\sigma_z}{F_rF_z} - \frac{\sigma_\theta\sigma_z}{F_\theta F_z}. \qquad \text{(IX C-8)}$$

The quantities F_r, F_θ, and F_z describe the different behavior in tension and compression. For example, F_r is either the uniaxial yield stress in tension if σ_r is tensile or the uniaxial yield stress in compression if σ_r is compressive. The value of $\frac{\Delta\bar{\varepsilon}^P}{\bar{\sigma}}$ is found from a uniaxial stress-strain curve. For an isotropic material, a uniaxial stress-strain curve in any direction produces a unique value of $\frac{\Delta\bar{\varepsilon}^P}{\bar{\sigma}}$. However, this condition is not always true for an anisotropic material. For the case of a transversely isotropic material, this obstacle has been dealt with as follows. First, a multilinear strain hardening curve was used to represent the uniaxial stress strain curve in the strong material direction. Then a multilinear strain hardening stress-strain curve for the weak material direction was computed from the requirement

$$\left(\frac{\Delta\bar{\varepsilon}^P}{\bar{\sigma}}\right)_{\text{Strong Direction}} = \left(\frac{\Delta\bar{\varepsilon}^P}{\bar{\sigma}}\right)_{\text{Weak Direction}}. \qquad \text{(IX C-9)}$$

This idea was applied to the stress-strain curves for JTA material. The representation for the stress-strain curve in the weak direction obtained by using Equation IX C-9 was found to be a very good representation for the experimental stress-strain curve in the weak direction.

The conditions which insure conservative material behavior for the cylinder are

$$\frac{\partial \varepsilon_r}{\partial \sigma_\theta} = \frac{\partial \varepsilon_\theta}{\partial \sigma_r}$$

$$\frac{\partial \varepsilon_z}{\partial \sigma_r} = \frac{\partial \varepsilon_r}{\partial \sigma_z} \qquad \text{(IX C-10)}$$

$$\frac{\partial \varepsilon_\theta}{\partial \sigma_z} = \frac{\partial \varepsilon_z}{\partial \sigma_\theta} .$$

Using the unique value of $\frac{\Delta \bar{\varepsilon}^P}{\bar{\sigma}}$ obtained by assuming Equation IX C-9, it can be shown that the stress-strain relations in Equations IX C-1, 2, and 3 satisfy Equation IX C-10. This fact means that an incremental complementary energy approach can be utilized to obtain the stress solution of the transversely isotropic cylinder problem.

Thus, an incremental complementary energy approach can be utilized to obtain numerical stress solutions to various problems of interest. The simple thick walled cylinder subject to internal pressure loading and a radial temperature distribution can be solved taking into account nonlinear stress-strain behavior and transverse isotropy. These results will be compared with the corresponding elastic stress distribution, and it is anticipated that substantially lower stress levels will be predicted by the nonlinear theory. The problem of predicting the longitudinal load-elongation curve for an axisymmetric case with a solid core of different material will also be studied using the incremental complementary energy approach. Consideration is also being given to employing this approach to estimate residual stresses in metal matrix composites.

D. Algorithmic Tools for Analysis and Synthesis
(Professor Fox and Mr. T. Delivuk)

The major effort which has been carried out over this report period has been the development of a reliable and efficient version of the method of feasible directions. In parallel with this work, numerous small but essential programming tasks have been carried out, as have library maintenance and internal consultation on the application of the programs. In addition, during this period, the literature on optimization techniques has been studied for possible methods of value to this program. The result of this survey is that a method of Zoutendijk[75] is currently being considered for development.

The results of development work on a program for a method of feasible directions will be described here. A description of the method which appeared in the First Annual Report[1], section IX B, is summarized briefly as follows.

The concept involved in this class of optimization methods is that the iterative process

$$\vec{X}^{q+1} = \vec{X}^{q} + \alpha \vec{S}^{q} \qquad \text{(IX D-1)}$$

must produce an $\vec{X}^{q+1}$ such that

$$g_j(\vec{X}^{q+1}) \leq 0 \quad \text{for all } j \qquad \text{(IX D-2}$$

and

$$F(\vec{X}^{q+1}) < F(\vec{X}^{q}) . \qquad \text{(IX D-3)}$$

Defining $\vec{G} = \nabla F(X^q)$ and $\vec{q}_j \equiv \nabla g_j(\vec{X}^q)$ and a set of integers J_c such that j is in J_c if $g_j(\vec{X}^q) = 0$ (actually in practice j is in J_c is $|g_j| < \delta$, where δ is a reasonable tolerance on the constraint), we are assured that an α exists such that (a) and (b) are respected if $\vec{S}$ satisfies

$$\vec{S}^T \vec{q}_j \leq 0, \qquad j \in J_c \qquad \text{(IX D-4)}$$

$$\vec{S}^T \vec{G} \leq 0 . \qquad \text{(IX D-5)}$$

Given a point where some of the $g_j = 0$, an $\vec{S}$ satisfying IX D-4 and IX D-5 can be found (if such exists) by solving the following "direction finding problem".

Find $\vec{S}$ and a scalar σ such that

i $\quad \vec{S}^T \vec{q}_j + \theta_j \sigma \leq 0 \qquad j \in J_c$

ii $\quad \vec{S}^T \vec{G} + \sigma \leq 0$

iii Some norm of $\vec{S}$ is bounded

iv σ is maximized

where the θ_j are arbitrary positive scalars.

Different choices for requirement iii and different modes of choosing the constants θ_j form the basis for different algorithms for the method of feasible directions. Furthermore, once an $\vec{S}$ which satisfies these criteria has been found and $\sigma_{max} > 0$, there remains the logic of selecting an α such that IX D-2 and 3 are satisfied and so that the process is efficient. These were the areas of the method which needed to be developed. In the present program, the method used to calculate α is based upon the philosophy that it should be as large as possible without causing violation of any of the constraints. (Thus the program ignores the possibility that the value of F can increase after a certain finite distance has been stepped off in the direction). The method of accomplishing this choice of the α is relatively simple: the value of α is initially chosen so as to reduce the value of F, assuming linear dependence on α by some fixed percentage (for example 10% has been used in most of the runs):

$$\alpha = \frac{F(\vec{X}^q)\Delta}{\nabla F^T \vec{S}} \qquad \text{(IX D-6)}$$

where Δ is the desired percentage reduction of F. If this choice of α proves to be too large and some constraints are violated, a linear interpolation is applied to the constraint which is most in violation. If the initial move proves to be too small (that is, no constraints become active), then the procedure is repeated. No attempt has been made to try for less than the "maximum" step in as much as our experience to date has shown that the directions generated by this routine adhere fairly closely to the constraints and produce rapid convergence.

With respect to the direction finding process itself, two approaches have been taken: one in which requirement iii was taken to be the length of $\vec{S}$ and the second in which this requirement was taken to be the maximum component of $\vec{S}$. The first choice produces a nonlinear programming problem itself, and this problem was approached using a version of the Fiacco-McCormick unconstrained minimum algorithm. The penalty function used was

$$\phi(\vec{S},\theta,r) = -\sigma - r\left[\sum_{j\epsilon J_c} 1/(\vec{S}^T\vec{q}_j + \theta_j\sigma)\right.$$

$$\left. + 1/(\vec{S}^T\vec{G} + \sigma) + 1/(\vec{S}^T\vec{S} - 1)\right] . \qquad \text{(IX D-7)}$$

The directions resulting from this application were efficient without any particular directional bias but were so at the expense of solving the direction finding problem quite inefficiently. Although it is possible to convert this problem into a linear problem, the second alternative was chosen instead.

This second approach (and the one which is currently the recommended program) produces a linear programming problem for the direction finding problem:

$$\sum_{i=1}^{n} s_i q_{ij} + \theta_j\sigma \leq 0 \qquad j \epsilon J_c$$

$$\sum_{i=1}^{n} s_i G_i + \sigma \leq 0 \qquad \text{(IX D-8)}$$

$$s_i < 1 \qquad i = 1, \ldots, n$$

$$s_i > -1 \qquad i = 1, \ldots, n$$

$$\sigma \rightarrow \max$$

which was converted to a standard form, in which all s_i and σ are required to be positive and inequalities are converted to equalities by defining

$$\tilde{s}_i = s_i + 1 \qquad \text{(IX D-9)}$$

and introducing the slack variables U_k.

The final form of the problem is

$$\sum_{i=1}^{n} \tilde{s}_i q_{ij} + \theta_j \sigma + U_j = - \sum_{i=1}^{n} q_{ij} \qquad j \in J_c$$

$$\sum_{i=1}^{n} \tilde{s}_i G_i + \sigma + U_{k+1} = - \sum_{i=1}^{n} G_i \quad (k = \text{no. of active constraints})$$

$$\tilde{s}_i + U_{k+i+1} = 2 \qquad i = 1, 2, \ldots, n \qquad \text{(IX D-10)}$$

$$\sigma \rightarrow \max \qquad \tilde{s}_i, \sigma \geq 0 .$$

This LP is then solved with the simplex algorithm using a phase I for a basic feasible solution and a phase II for the final optimal search.

The coding of this program in ALGOL 60 is essentially complete. The development runs have been made on the traditional space truss optimization problem, and the results of this application are satisfactory. Our present effort involve isolating the component parts of the feasible directions program and assembling them into a modular package which can be used in conjunction with any appropriate analysis routine. We expect to be able to describe the use of this program at the procedural level.

E. Analysis and Synthesis of a Fiber Composite Flat Plate
(Professor Schmit and Mr. C. Chamis)

A study aimed at illustrating the role of the structural synthesis concept in design with fibrous composites has been undertaken. Consider a simply-supported rectangular multilayer resin-matrix fiber composite plate as shown in Figure 264. Let the planform dimensions (a,b) of the plate be preassigned parameters. The matrix material is assumed to be isotropic, and the following matrix properties are considered preassigned parameters:

ρ_m	weight density
E_m	modulus of elasticity
ν_m	Poisson's ratio
S_{mc}	compressive strength
ϵ_{mpt}	allowable tensile strain
ϵ_{mpc}	allowable compressive strain
ϵ_{mps}	allowable shear strain
ϵ_{mptor}	allowable shear strain (torsion test).

The fiber material is assumed to be transversely isotropic (see Figure 265 for orientation of fiber coordinate system), and the following properties of the fiber material are treated as preassigned parameters:

ρ_f	weight density of fiber
N_f	number of fibers per roving end
G_{f12}	shear modulus in the 1-2 plane
$E_{f22} = E_{f33}$	transverse modulus of elasticity
$\nu_{f12} = \nu_{f12}$	absolute ratio of the fiber transverse strain to fiber longitudinal strain due to longitudinal stress*
$\nu_{f23} = \nu_{f32}$	Poisson's ratio in the plane of transverse isotropy.

---

* The remaining Poisson's ratios are determined from the reciprocal theorem.

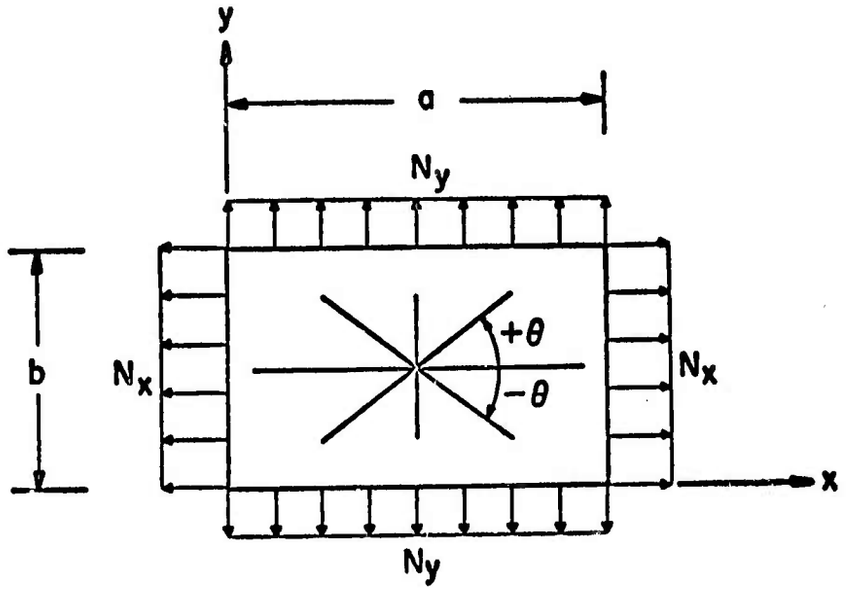

Figure 264. Simply Supported Fiber Composite Plate.

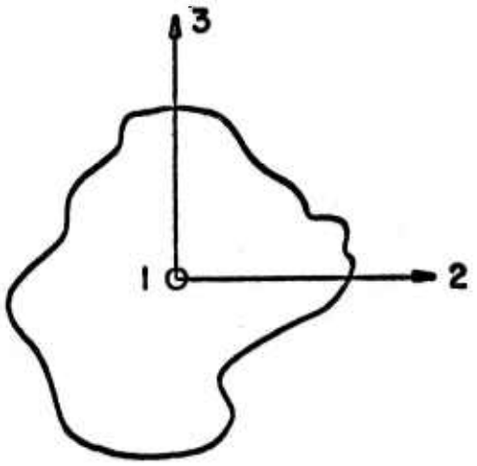

Figure 265. Fiber Coordinate System.

The bundle tensile strength of the fiber (S_{ft}) and the equivalent fiber diameter (d_f) are treated as preassigned functions of the longitudinal fiber modulus (E_{f11}) which is to be a design variable. The apparent volume of fiber k_f, the estimate volume fraction of voids in the matrix k_v, and several empirical factors, depending on the fabrication process, are also considered to be preassigned parameters.

Initially, this study will consider three design variables. The number of layers (N_ℓ) is taken as a design variable. The minimum number of layers is set at ten and the plate thickness is built up by adding two layers at a time symmetrically with respect to the reference plane as depicted in Figure 266. The layer pattern is such that linear bending-membrane coupling is precluded; however, the gross membrane behavior of the plate is symmetric only when the number of layers is an integer multiple of four (i.e., 12, 16, 20, etc.). The angle orienting the fiber direction in each layer (θ) is taken as the second design variable. This design variable is permitted to assume any value over the range from -90° to 90°. The longitudinal modulus of elasticity of the fiber material (E_{f11}) is treated as the third design variable*. This design variable may assume any value over the range from 10×10^6 lbs/in^2 to 100×10^6 lbs/in^2.

The plate is subject to a multiplicity of load conditions, each of which is given by specifying the uniform membrane loads N_x and N_y.

Three failure modes are considered, and each of these must be guarded against in each load condition. Let L denote the number distinct load conditions in the load system. Then the inequality constraints $g_j(\vec{D}) \leq 0$ for $j = 1 \rightarrow J$ can be written in the alternate form

$$g_{ik}(\vec{D}) \leq 0 \qquad k = 1 \rightarrow L; \quad i = 1, 2, 3 \qquad \text{(IX E-1)}$$

where it is understood that

$$j = k + (i-1)L \qquad j = 1 \rightarrow J \text{ and } j = 3L \, . \qquad \text{(IX E-2)}$$

The simple constraints on the range of values that the design variables may assume are numbered $j = 3L + 1$ through $j = 3L + 6$.

---

* It should be noted that the assumption that the fiber material properties treated as preassigned parameters remain fixed as E_{f11} varies is not strictly correct. This deficiency could be removed by expressing the pertinent fiber material properties (in addition to S_{ft} and d_f) as preassigned functions of the design variable E_{f11}.

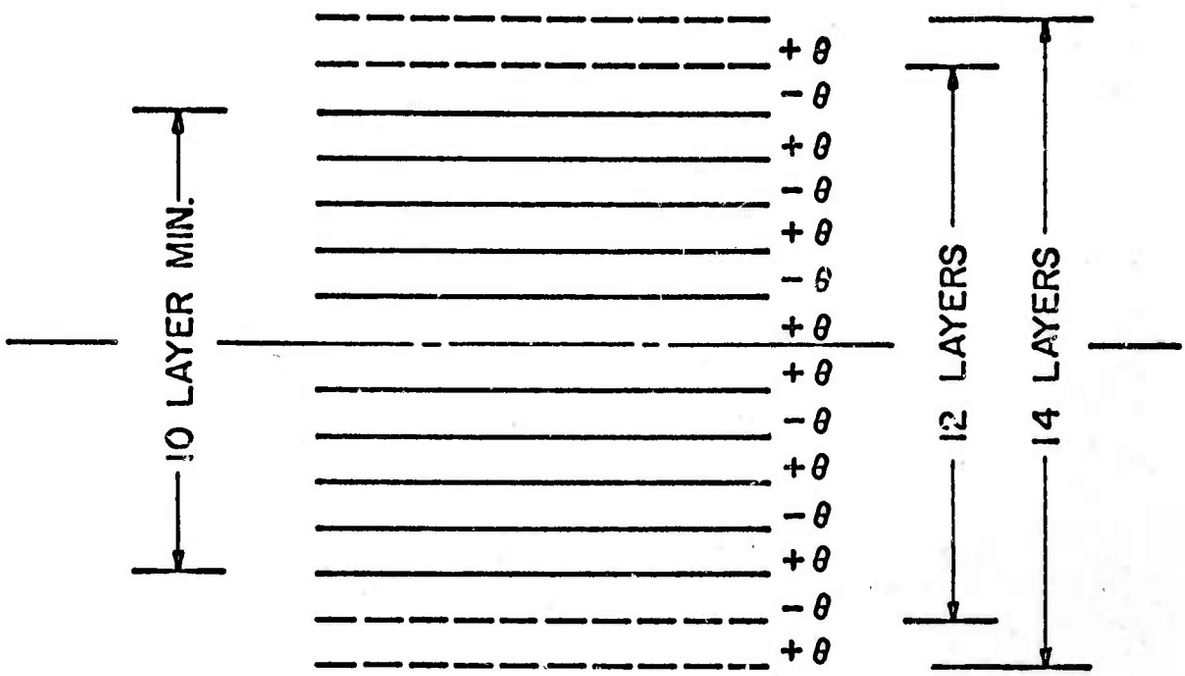

Figure 266. Balanced Lay Up Pattern.

The first failure mode (i = 1) considered is gross buckling of the composite plate. The gross buckling failure mode is represented by

$$g_{1k}(\vec{D}) = \frac{N_{xk}}{(N_x)_{crk}} + \frac{N_{yk}}{(N_y)_{crk}} - 1 \qquad \text{(IX E-3)}$$

where N_{xk} and N_{yk} represent the given applied loads in the x and y directions respectively in the kth load condition. The $(N_x)_{crk}$ and the $(N_y)_{crk}$ can be determined for a particular trial design (N_ℓ, θ , E_{f11}) and load condition by a procedure given in Reference 76. The essential point to be recognized here is that $g_{1k}(\vec{D})$ is computable according to a specified procedure given the preassigned parameters, the load condition k, and a trial design [$\vec{D}$, i.e., a set of values for N_ℓ, θ, and E_{f11}]. The values of $(N_x)_{crk}$ and $(N_y)_{crk}$ depend upon the critical buckling mode shape and the flexural rigidities of the composite plate. The flexural rigidities, in turn, depend upon the design variables (N_ℓ, θ,E_{f11}) and the preassigned parameters. Furthermore, if $g_{1k}(\vec{D})$ has a positive value, gross buckling failure in the kth load condition is predicted and the trial design is unacceptable. It should also be noted that, when the gradient $\nabla g_{ik}(\vec{D})$ is required, it is approximated by using central finite difference representations for each of the components.

The second failure mode (i = 2) considered is combined stress failure in a layer. Layers at $\pm\,\theta$ are checked, however, when N_ℓ is an integer multiple of four the results for + θ are identical with those for - θ, whereas when N_ℓ is not an integer multiple of four, the - θ layers are found to be critical. This second failure mode (i = 2) provides the constraints j = L + 1 through j = 2L, and it is represented by

$$g_{2k}(D) = \left(\frac{\sigma_{\ell 11k}}{S_{\ell 11\alpha k}}\right)^2 + \left(\frac{\sigma_{\ell 22k}}{S_{\ell 22\beta k}}\right)^2 + \left(\frac{\sigma_{\ell 12k}}{S_{\ell 12k}}\right)^2 - K_{\alpha\beta}\,\frac{\sigma_{\ell 11k}}{\left|S_{\ell 11\alpha k}\right|}\,\frac{\sigma_{\ell 22k}}{\left|S_{\ell 22\beta k}\right|} - 1 \qquad \text{(IX E-4)}$$

where σ_ℓ denotes layer stress, S_ℓ denotes layer strength, the one (1) direction coincides with the fiber direction in the layer, the two (2) direction is transverse to the fiber direction in the plane of the layer and the subscripts α and β are read as T(Tension) or C(Compression) depending upon whether the corresponding numerator (layer stress) is tensile (+) or compressive(-). Given the preassigned parameters, the load conditions k, and a trial design $\vec{D}(N_\ell, \theta, E_{f11})$, the layer stresses

and the layer strengths are determined according to the procedure given by Chamis[76]. If for $+\theta$ or $-\theta$ the function $g_{2k}(\vec{D})$ is greater than zero, the analysis predicts that failure under combined stress occurs in the kth load condition. When any of these combined stress failure modes $j = L+1 \rightarrow 2L$ become active, the gradient $\nabla g_j(\vec{D})$ for $j \in J_c$ is required, and it is approximated using central finite difference representations for each of the components.

The third failure mode ($i = 3$) considered is a delamination shear failure mode. Basically, this requirement limits the relative rotation between two adjacent layers. Relative rotations between layers imply high shear strains in the matrix material of the interlayer layers. The constraints $j = 2L + 1$ through $j = 3L$ are provided by this third failure mode which is represented by

$$g_{3k}(D) = \frac{|\Delta\phi_{jk}|}{(\Delta\phi_j)_{allow}} - 1 \qquad \text{(IX E-5)}$$

where $\Delta\phi_{jk}$ is the relative rotation between adjacent layers $j + 1$ and j in the kth load condition and $(\Delta\phi_j)_{allow}$ is the allowable relative rotation. When the preassigned parameters, the load condition k, and a trial design $D(N_\ell, \theta, E_{f11})$ are specified, the relative rotations and the allowable relative rotation can be determined according to the procedure given by Chamis[76]. Whenever $g_{3k}(\vec{D})$ is greater than zero, the analysis predicts that delamination failure occurs. When a delamination failure mode is active and the gradient is needed, it is determined using a central finite difference approximation for each of the components.

The objective function employed for the example problem is intended to represent cost of fiber material per unit surface area of plate. The cost of fiber is assumed to increase linearly with longitudinal fiber modulus (E_{f11}); hence, the objective function may be expressed as follows:

$$M(\vec{D}) = \rho_f \bar{k}_f t_p (K_1 + K_2 E_{f11}) N \qquad \text{(IX E-6)}$$

where ρ_f is the weight density of the fiber material, $\bar{k}_f$ is the actual fiber volume fraction, t_p is the thickness of a layer, $(K_1 + K_2 + E_{f11})$ expresses the cost per unit weight of fiber material as a linear function of longitudinal modulus, and N_ℓ is the number of layers. Note that this objective function is independent of the design variable θ. It should also be noted that the layer thickness (t_p) is assumed to depend upon the equivalent fiber diameter (d_f), the number of fibers per roving end (N_f), and the apparent volume fraction of fiber (k_f) as follows

$$t_p = \frac{d_f}{2} \left[\frac{\pi N_f}{k_f}\right]^{1/2} . \qquad \text{(IX E-7)}$$

Although this example is rather idealized, it nevertheless exhibits many of the features characteristic of more realistic composite material structural system design problems. The example involves only three design variables; however, the number of layers (N_ℓ) is a discrete sizing variable, the layer orientation angle (θ) is a configuration variable, and the longitudinal fiber modulus E_{f11} may be classified as a materials variable. The example also considers the loading system to be made up from several distinct loading conditions and a balanced optimum design is sought. The failure modes considered are intended to guard against buckling failure, combined stress failure, and delamination. Finally, the objective function employed (minimization of cost of fiber material per unit surface area of plate) is intended to suggest that minimization of total structural weight need not necessarily be the goal of every structural optimization capability.

Some preliminary numerical results obtained using a feasible directions method algorithm have been obtained and were reported by Schmit[77]. These results were only intended to illustrate the potential role of the structural synthesis concept in design with fibrous composite materials. Since these early results did not take into account the dependence of fiber bundle tensile strength (S_{ft}) or equivalent fiber diameter (d_t) on the longitudinal fiber modulus (E_{f11}), they are not repeated herein. Effort is being directed toward obtaining synthesis results when S_{ft} and d_t are treated as preassigned functions of the design variable E_{f11}. An assessment of sensitivity of the synthesis results to perturbations in preassigned parameters such as fiber volume fraction (k_f), volume fraction of voids in the matrix, and fiber transverse modulus of elasticity is planned.

SECTION X

FUSELAGE COMPONENT DESIGN AND ANALYSIS

Selection of a fuselage section for the representative fiber composite component was described in Section IV of the first Annual Report (Reference 1). The design, development, and test activities associated with this component provide a hardware performance demonstration of the advanced graphite fiber composite material. In addition, these activities serve to reveal present technological shortcomings and the need for improvements.

Section X A describes preliminary design studies, based on a pseudo-isotropic lay-up, which led to the choice of a basic structural arrangement for detailed study and identified the potential performance benefits of "Thornel" composites as compared with aluminum alloy construction. Design criteria and loading conditions are defined in Section X B. The influences of laminate configuration and geometric proportions are examined with respect to orthotropic shell buckling in Section X C and with respect to column and plate behavior in Section X D. Progress in the design of stiffening rings and the end attachment is discussed in Sections X E and X F, respectively. The anisotropic discrete elements, described previously in Section IX A, were used to conduct a stress analysis of the fuselage shell, the results of which are presented in Section X G.

A. Preliminary Design Studies

(D. P. Hanley and W. N. Meholick, Bell Aerosystems)

The preliminary design studies are presented under the four major groupings shown in Figure 267.

Most of the first area, Component Selection, was reported in Section IV of the first Annual Report (Reference 1). In this report, structural scaling parameters (item e) are considered in more detail in order to form a basis for relating dimensions and geometry of the representative component to full-scale applications.

The second area, Preliminary Design Studies, outlines briefly the iterative design loops and the 'first pass' accomplishments. This work provides a framework for the various analytical studies. An examination of typical comparative efficiencies of practical shell stiffening methods for a homogeneous, isotropic material was made first for the fuselage application. Study of the stiffened isotropic shell provides some insight into configuration effects that guided subsequent work with anisotropic materials, although more creative, yet realistic, design concepts for composite shell structures are obviously needed. Next, theoretical estimates of graphite fiber composite elastic properties and the methods used in their determination, as of the beginning of this report period, are presented. The studies then proceed into an evaluation of simple structural elements (such as plates,

1. COMPONENT SELECTION
   a. Applications Review
   b. Typical Environments
   c. Representative Loads
   d. Structural Concept
   e. Scaling Parameters
2. PRELIMINARY DESIGN STUDIES
   a. Stiffened Isotropic Shells
   b. Elastic/Strength Properties
   c. Plates, Columns, Stiffened Panels
   d. Unstiffened Orthotropic Shells
3. REPRESENTATIVE COMPONENT DESIGN
   a. Stiffened Composite Shell Approaches
   b. Comparison of a Conventional Material with Composites
4. TEST PLAN OUTLINES
   a. Simple Elements
   b. Representative Component

Figure 267. Airframe Component Selection and Preliminary Design

Scaling Method	Representative Component (22 - in.d)	Large - Scale Application (100 - in.d)
1. Equal Load Index		
$(M/D^3)^{1/3}$	4.0	4.0
N_x	1800 lb/in.	8200 lb/in.
t	0.017 in.	0.077 in.
2. Equal Skin Thickness I		
$(M/D^3)^{1/3}$	6.62	4.0
N_x	8200	8200
t	0.077	0.077
3. Equal Skin Thickness II		
$(M/D^3)^{1/3}$	4.0	2.4
N_x	1800	1800
t	0.017	0.017

NOTE: Calculations Based on Min. Wt. 7075 - T6 per WADC TR 59-18 PT II

Figure 268. Scaling Methods for Fuselage Components

columns, simple shells, and stiffened panels) which constitute the basic design problems associated with the fuselage-section. In each case, understanding of the significance of fiber properties and orientations was sought.

The third area, Representative Component Design, describes the two approaches which evolved from the preliminary design studies: a stringer/ring stiffening system and a honeycomb-stiffened system. Their principal features and anticipated performances are compared. Under Test Plans, in the fourth area, are presented the tentative experimental programs to evaluate simple structural elements and the representative component.

1. Scaling Methods

The low-to-intermediate loading ranges for both bending and shear conditions are frequently encountered in subsonic aircraft and present difficult problems because of conventional material and fabrication limitations. At the same time, these ranges offer tremendous potential for composites. Careful study is required, however, to define the greater design and fabrication freedoms within the range of practical constraints.

Of concern in selecting the overall dimensions of the fuselage section are structural scaling parameters which are shown in Figure 268. Given here are analytically determined skin thicknesses (not necessarily practical ones) for minimum weight shells in bending according to the general methods of Shanley and Micks (References 78 and 79) and those developed at Bell (Reference 80). The range of an $(M/D^3)^{1/3}$ loading index has been observed for many of Bell's aircraft fuselage designs as generally in the range of about 2.5 to 4, these values corresponding to the low-to-intermediate loadings previously mentioned. Two possible methods of scaling between the representative component (22-in. diameter) and a hypothetical large component (100-in. diameter) exist. The first such method (Case 1 on Figure 268) would design on an equal load index basis and the second method, as given by References 79 and 80 (Cases 2 and 3 on Figure 268), would be to design for equal skin thickness. In Case 1, unequal skin thicknesses and unequal loads per inch result. Consequently it is not desirable to attempt scaling between a thin-skinned model and a thick-skin large application. In Cases 2 and 3, however, if the structural indices are properly chosen, both thicknesses and load per inch can be matched to achieve good similitude. The major point here is that designing the fuselage component to an $(M/D^3)^{1/3}$ in the range of about 4 to 6 corresponds well with a large-scale structure having a realistic index of about 2.5 to 4. Loads per inch correspondingly are in agreement with Bell's design experience and skin thicknesses should be on the order of about 0.020 to 0.080 inch.

It is recognized that the above trends are based on isotropic theory for a widely used airframe aluminum alloy. Consistent with earlier comments on conventional materials, it is shown later however that a "Thornel" 40 graphite yarn pseudo-isotropic composite may in certain features be expected to behave like aluminum.

2. Design Procedure

The second major area of Figure 267 outlines basic areas of investigation that relate to the fuselage shell under preliminary design studies. The first several steps in the design process may be considered as: applications review, component selection, and materials and construction. These were discussed previously and led to the basic configuration of the fuselage component. Consideration of the stiffened shell led into further configuration and efficiency studies for isotropic materials. At the conclusion of studies on the isotropic stiffened shell, orthotropic material considerations were next treated. In the present work, preliminary design is conducted by going through several iterations which bring in the key analytical developments and critical basic tests. Initial preliminary design treats the idealization of the fuselage as a cylinder without substantial consideration of detailed boundary conditions. Completed preliminary design then accounts for better representation of more complex loads and the conical shell configuration. Final design should ultimately incorporate the synthesis activities in order to account for actual combined states of loading. Attachment concepts at this time require experimental validations.

Returning to the iterations in preliminary design, the best analytical steps that can be taken at an early time involve analytically predicting composite elasticity and strength properties, using these properties in analysis of simple structural elements (plates, columns, etc.), evaluating fiber and laminate configuration effects, and determining basic optimizations for simple elements. A second design cycle, uses experimentally-based specifications of fiber modulus and strength levels, resin properties, etc. Simple composite properties are then utilized in the design studies. A third pass involves fabrication and element testing of stiffeners, plates, and stiffened panels and recycling the design studies.

3. Minimum Weight Shells in Bending

Efficiencies for several stringer/ring and honeycomb systems were compared for isotropic shells. Figure 269 shows typical weights (in psf) for minimum weight aluminum cylinders in bending.

These curves are for the idealized cylinder and are based on standard design procedures. At the loading index of 4, two essential features are seen: (1) all of the stiffened shells are $\sim$ 50% lighter than the unstiffened shell and (2) although there appears to be a sizable weight saving among the stiffened shells, fabrication and material influences rarely allow minimum weight design. These factors tend to merge practical designs in-between the unstiffened shell and the minimum shell weights. Thus, fabrication enters the picture and it may be roughly concluded that efficient stringer shapes, such as hats and zees as later described, can be selected to tradeoff costs and design preferences. Although these trends are based on isotropic theory and are strictly applicable only to pseudo-isotropic composite layups, later discussion will show that the additional complexities of orthotropic material behavior and practical design constraints do not significantly change the weight/performance estimates for isotropic material assumptions.

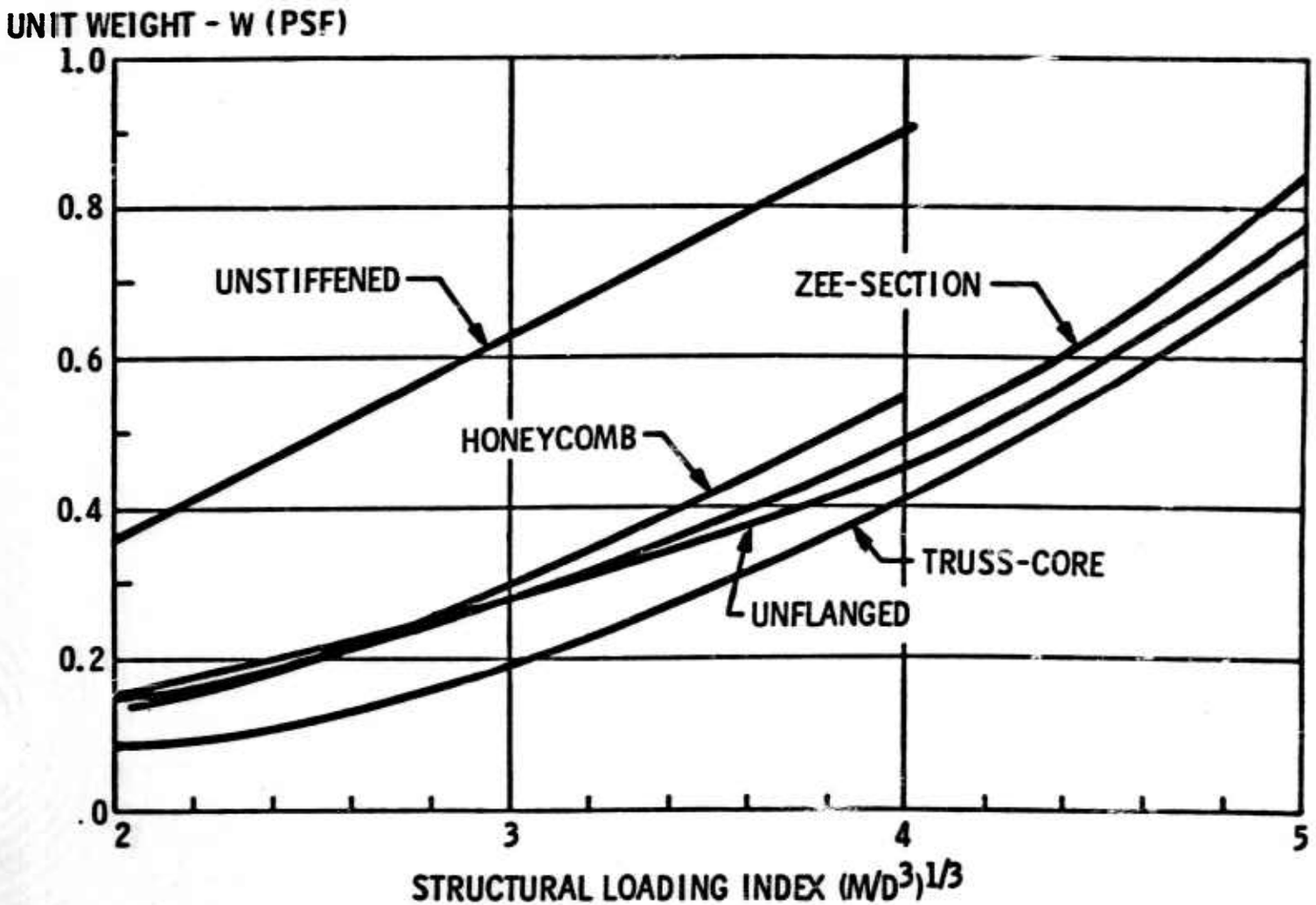

Figure 269. Minimum Weight Shells In Bending Comparison Of Structural Configurations

4. Graphite Fiber Composite Properties

Elastic properties for various laminate constructions were predicted with Whitney's equations using isotropic fiber properties (Reference 44) and Grezszcuk's transformations (Reference 45) for "Thornel" 25, 40 and 60 composites.

The prediction methods were verified by comparisons with boron fiber composite properties and the values were in good agreement with other investigations. These calculations showed that the ±45° graphite composite laminates yielded the lowest E but the highest G and Poisson's ratio. The isotropic construction for the "Thornel" 40 graphite yarn composite was seen comparable in modulus to aluminum with one-half the density of aluminum. It was also seen difficult to compare laminates with an entire set of elastic parameters. To do this required an examination of the structural behavior of simple components wherein the various basic laminate constructions could be studied. These are described briefly in the next several sections.

5. Plate Buckling Behavior

Plate buckling studies under edge compression and shear loads are shown in Figure 270. These calculations are for a 12 x 12 x 0.060 inch "Thornel" 25 plate with simply supported edges. They are based on the work of Seydel referenced in Dietz (Reference 49). The figure illustrates the influence of the elastic constants on the two types of buckling behavior: (1) For equal thickness plates in compression, the optimum construction is ±45°, followed by pseudo-isotropic, then uniaxial, then 0°-90°. (2) The characteristics of panels in shear buckling are strikingly different from those in compression buckling; i.e., for shear, the optimum constructions are in the order: isotropic highest, the ±45° only slightly less, and the uniaxial much less. Thus for buckling of panels under combined loads for general design, the concepts for layup optimization are indicated. It was recognized, however, that the curves shown for the rotated orthogonal plate were approximate by virtue of assumptions made regarding the magnitude of certain coupling terms, i.e., their being small.

For the fuselage-section designed for the low loading range, shear is small, ~ 80-90% less than axial load. Thus, with the higher shear buckling allowables and by assuming a conventional combined load interaction method applies, the effects of low shear loads may be assumed negligible. These studies, which are continuing as new information is cycled, have also been extended to account for other plate aspect ratios of interest, varying fiber modulus influence, and other boundary conditions. In most of the preliminary studies, a 65% fiber volume has been used. Recycling with other values is being investigated (see Section X D).

Recognizing that no established strength cut-offs were available early in preliminary design, the evaluation of other stability-critical elements proceeded on the basis of the elastic constants then available.

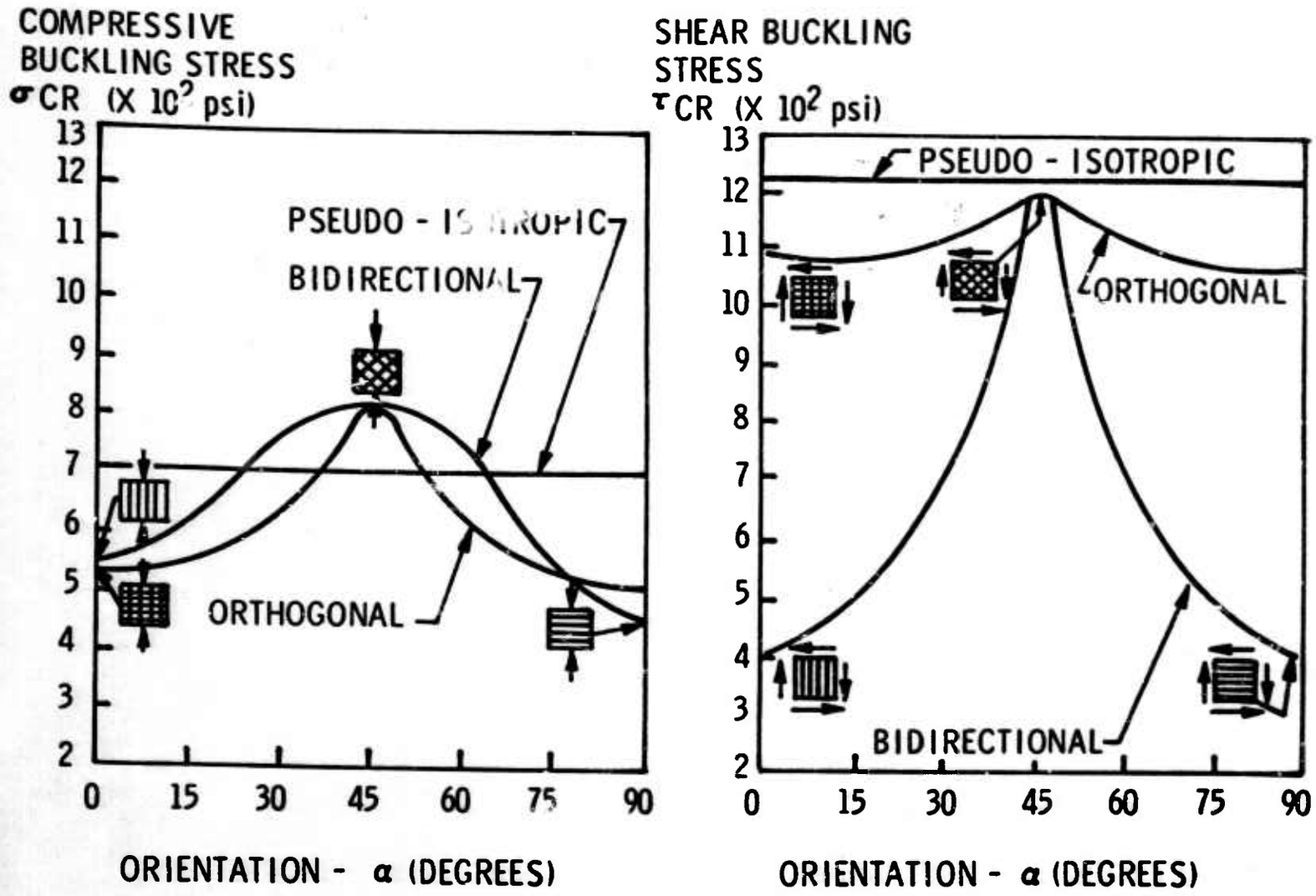

Figure 270. Influence Of Fiber Orientation On Composite Plate Buckling

6. Theoretical Column Buckling

Laminate configuration effects on columns were next examined. Compression members that buckle elastically as a result of the lateral bending induced by compression and are long in comparison to their other dimensions are termed long columns. The Euler equation is used to obtain the buckling stress as follows:

$$\sigma_{col} = \pi^2 E \Big/ (L' \Big/ \rho)^2 \qquad \text{(XA-1)}$$

When the load-deformation curve deviates from a straight line (whether at stresses beyond the material proportional limit or as a result of local crippling of the member elements), the columns are termed short. Columns are short or long depending on the L' / ρ slenderness ratio (pin-ended column length divided by radius of gyration) at which this nonlinearity occurs. Members with stable cross sections are analyzed by using a reduced modulus in the Euler equation. Members with cross sections where local crippling takes place are analyzed with the following equation (Reference 81)

$$\sigma_{col} = \sigma_{cc} \left[1 - \sigma_{cc} (L' \Big/ \rho)^2 \Big/ 4 \pi^2 E \right] \qquad \text{(XA-2)}$$

where σ_{cc} is the crippling stress.

A "Thornel" 25 graphite yarn composite Zee-section stiffener and skin section was used to determine attainable column stresses for a range of slenderness ratios and for pseudo-isotropic, ±45° bidirectional, and 0° unidirectional fiber orientations. The column curves thus generated for these fiber orientations are presented in Figure 271. At the short column lengths, where the plate characteristics largely predominate, the same order of effectiveness exists as with the plates: ±45°, isotropic, and unidirectional. In the long column region, where E_x is the controlling factor, a different order of optimum fiber orientation exists: namely, unidirectional, isotropic, and then ±45°.

Since the optimum configuration for plates is ±45° and for intermediate length columns is (±30°, 90°), a design consisting of ±45° skin ribbed with isotropic stiffeners appears very attractive. This mixed geometry system however is a difficult design problem and, as a simpler alternative, the pseudo-isotropic plate with the same type of stiffeners was next considered.

7. Wide-Column Stresses

Optimum wide-column stresses for Zee-section stiffened pseudo-isotropic panels are shown in Figure 272. These were developed using the transformation procedure of Reference 79.

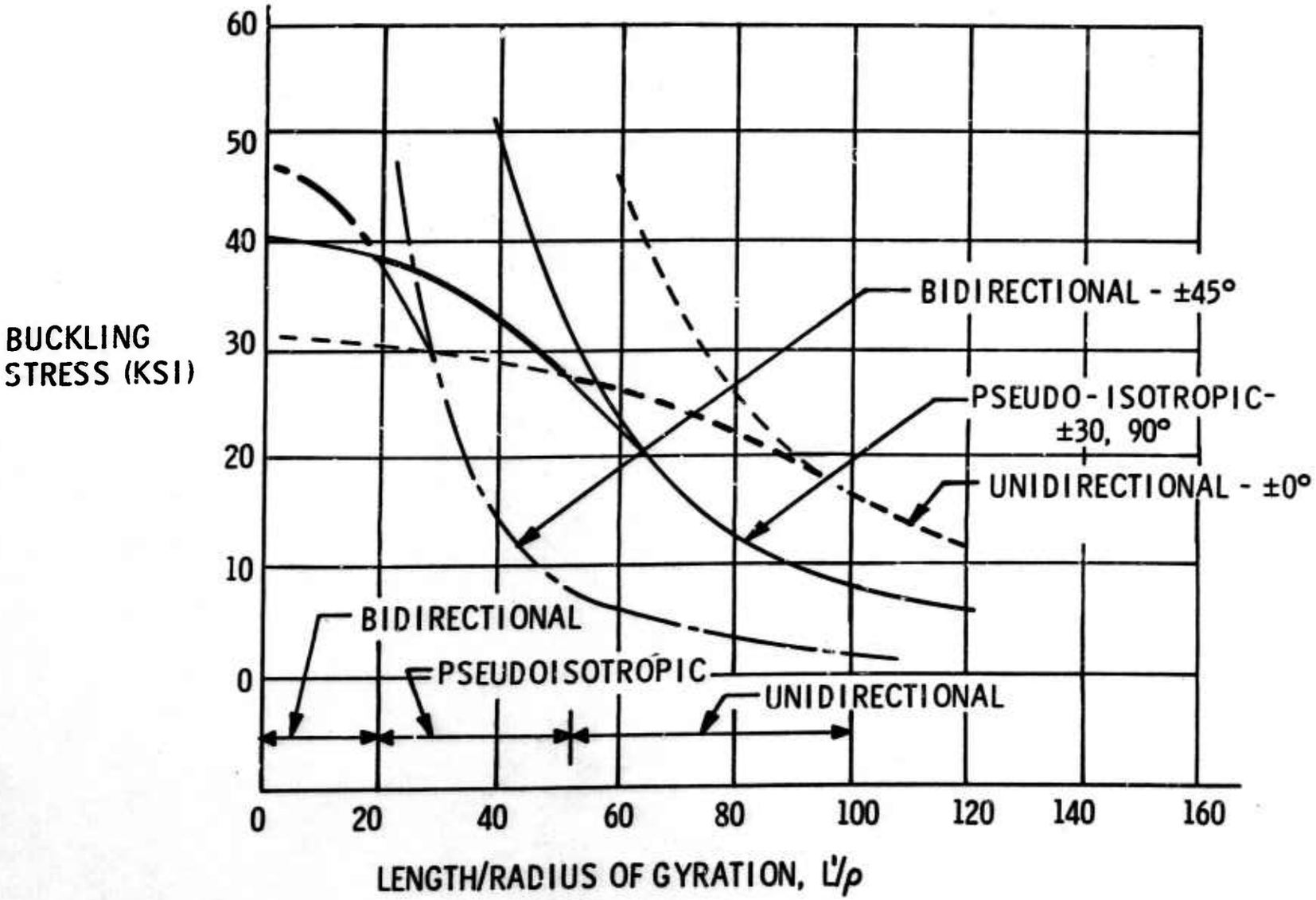

Figure 271. Theoretical Column Curves For Graphite/Resin Composites

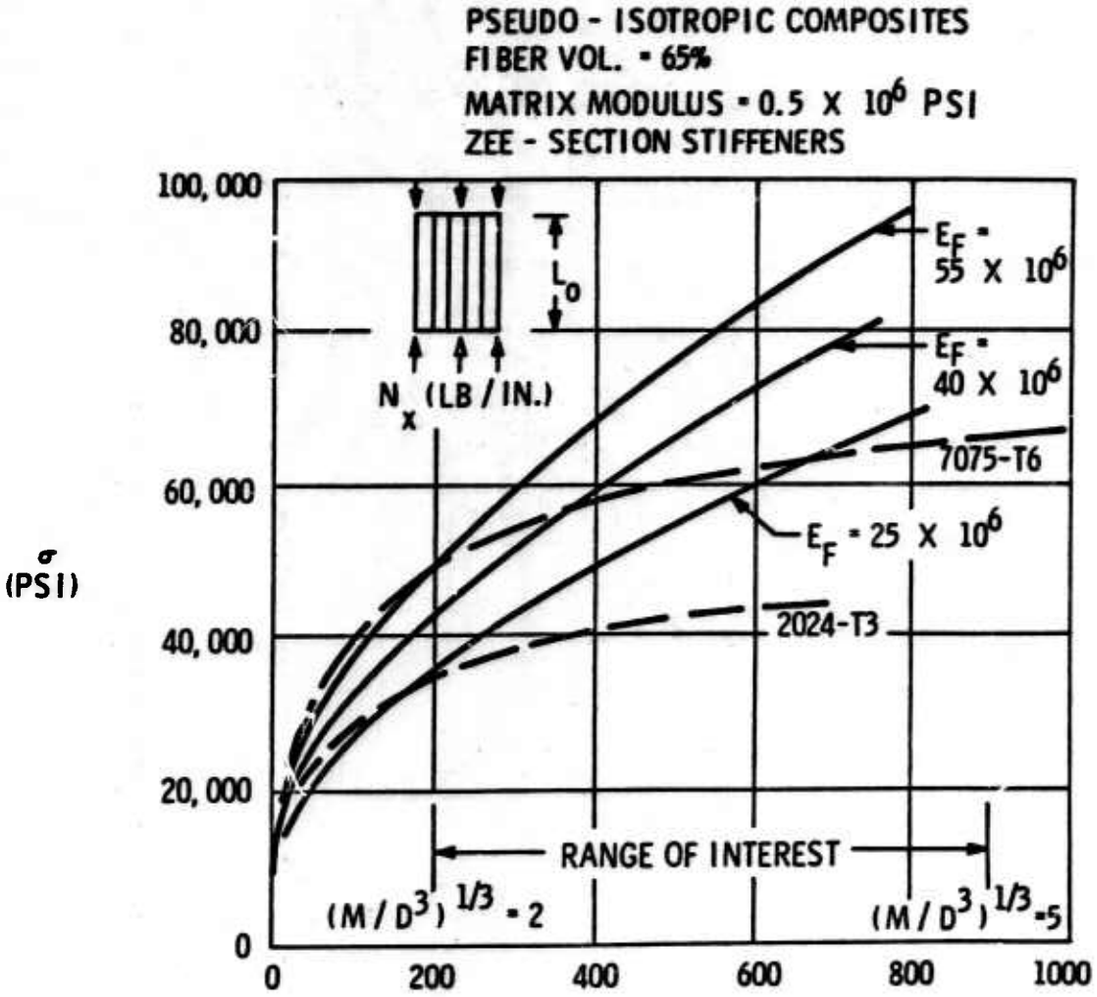

Figure 272. Optimum Wide Column Stresses versus Structural Loading Index

The strength cut-offs with the three values of fiber modulus are not shown for reasons already mentioned. The performance of composites in the range of interest is compared with the aluminum alloys shown. The overlap areas of the curves do not illustrate much higher compressive buckling stresses for composites; however, with equal stress/density ratios, the composites indicate a decided advantage.

8. Unstiffened Shell Efficiency

The fiber orientation influence on the efficiency of unstiffened orthotropic cylinders is shown on Figure 273. Based on the Dow and Rosen theory (Reference 82), the $\pm 45^{\circ}$ shell is slightly lighter than the pseudo-isotropic construction, a result which lends support to the previous plate buckling results. To this point in all of the preliminary design studies, it was assumed that classical linear orthotropic theory applied. This assumption includes the idealized homogeneous continuum. The studies indicate that the lower weight savings with composites require thin gauges; consequently, this assumption must be closely examined.

9. Flexural Modulus Dependence on Layers

The influence of the number of layers (plies) on plate flexural moduli was next investigated. Based on simple weighting procedures for orthogonal plates, wide divergence between the two principal moduli was shown to exist with very few layers. After $\sim$ 20 layers, the influence of number of plies was found to die out. In the case of a balanced even-ply (0°-90°) laminate, a more rapid rise in the moduli toward the "infinite number of layers" value was evident. These initial studies led to the theoretical and experimental agreements later found which are shown in Figure 192 (Section VIII B).

Applied to a basic plate construction, this study showed the significance in design for including finite layer effects. In preliminary design, this information is included in an approximate fashion. However, the need for reviewing the fundamental theory to more properly account for coupling of extensional/bending properties was pointed out for more basic university studies; secondly, the need for fabrication inputs on how many layers constitute a reasonably homogeneous continuum was also stressed.

10. Representative Fuselage Designs

After completion of the preliminary design studies as described above, efforts were directed toward defining fuselage-section design approaches shown on Figure 274. Two stiffening types, stringer/ring and sandwich were considered for an assumed minimum gauge limitation of 0.025 inch for a 55 million psi modulus graphite yarn isotropic construction. This minimum gauge limitation results in a higher weight (0.6 psf) sandwich design compared with the single-skin designs which are 0.4 psf $\pm \sim$ 10% for the various stiffeners shown. The single-skin designs result in lower weight capabilities at the representative loading index of 4. Other comparative features

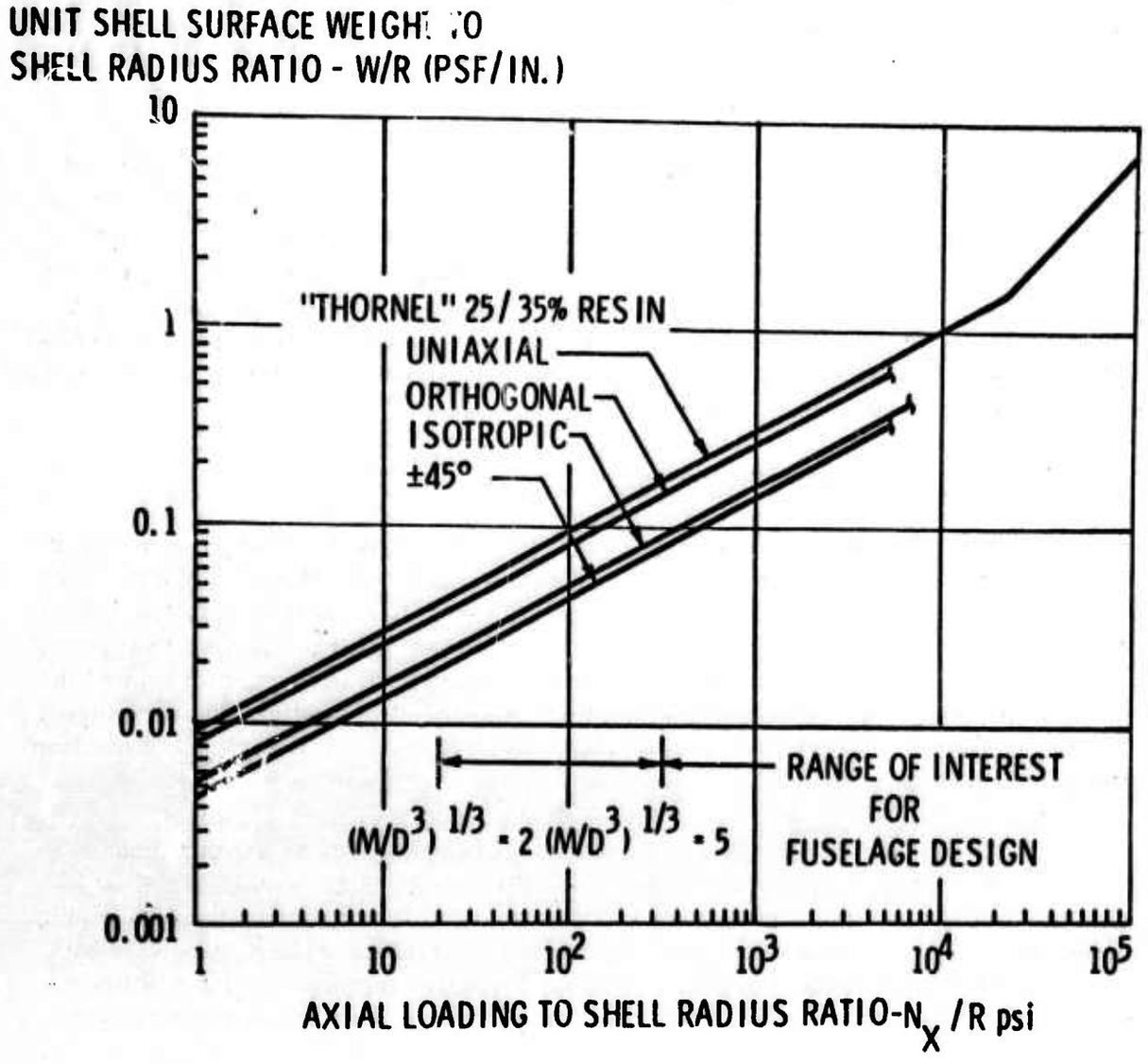

Figure 273. Influence of Fiber Orientation on Unstiffened Shell Efficiences

are given, primarily design flexibility and fewer anticipated attachment problems, both of which tend to favor the stringer-stiffened design.

Of these two design approaches, possible divergence effects of flexural moduli with thin skins would tend to increase weight of the single skin where bending effects are involved. The honeycomb design, however, being primarily dependent on membrane properties could probably be improved by changing the skin configuration to reduce its weight, thus bringing the two design approaches closer together. Further work is needed to explore these effects.

Comparisons of the stringer-skin combinations shown in Figure 274 with other stiffened wide-column concepts (Reference 83) were made and are summarized in Figure 275. Noted are comments concerning their applicability to the fuselage component. In Figure 275 the efficiency of a wide column was determined from:

$$\epsilon_{max} = \pi \nu \quad K_s K^{1/2}$$

where,

ν = Poisson's ratio for isotropic materials
K_s = stiffener shape factor
K = buckling coefficient

From consideration of the results shown in Figure 275, the hat and Zee-section types were selected as the best candidates for composite stringer fabrication. The closed-section or hollow-rectangular shape was included because of potential advantages obtained from filament winding. The other two types can be molded from wide-tape pressed between two matched dies.

11. Efficiency Comparisons of Designs

The potential impact of graphite-fiber composites on the aircraft industry is illustrated in Figure 276. Theoretical weight savings based on preliminary design on the order of 50% are indicated where large quantities of light-weight, stiff materials are used. The band on Figure 276 labeled "Refined Performance Envelope" is discussed later (Section X C).

Unit shell weights were determined for the 22-inch diameter fuselage component for practical (preliminary) designs using 7075-T6 aluminum alloy and pseudo-isotropic graphite-fiber/resin composites. The designs were for Zee-section longitudinal and ring-stiffened cylinders and covered a range in loading index. The graphite-fiber composites are for fiber moduli of 25, 40 and 55 x 10^6 psi, a resin modulus of 500,000 psi, and a fiber volume content of $\sim$ 65%.

The composite constructions were developed for three shell thicknesses and for stringer spacings of 1.1 inches and ring spacings of 12.0 inches, the same as those

STIFFENING TYPES	LOAD CAPACITY	EST. WEIGHTS $E_f = 55 \times 10^6$ psi	REMARKS
1. HAT SECTION 2. ZEE SECTION 3. CLOSED SECTION	N_X = 1800 LB/IN. $(M/D^3)^{1/3}$ = 4.0	0.400 psf	RING SPACING = 12 IN. SKIN THICKNESS = 0.025 IN. LOWER WEIGHT CAPABILITY AT MODERATE LOADS GREATER DESIGN FLEXIBILITY LESS ATTACHMENT PROBLEMS
4. SANDWICH	N_X = 4130 LB/IN. $(M/D^3)^{1/3}$ = 5.3	0.614 psf	NO RINGS SKIN = 0.025 IN. LOWER WEIGHT CAPABILITY AT HIGH LOADS GREATER PROBABLE EFFICIENCY FOR HIGH COMBINED LOADINGS BETTER RESISTANCE TO ACOUSTIC FATIGUE

Figure 274. Representative Fuselage Designs

CONFIGURATION	EFFICIENCY ϵ MAX	RATING	COMMENT
TRAPEZOIDAL CORRUGATION 	1.600	1ST	NO SHEAR CAP.
STRAIGHT Y-TEE STIFFENED 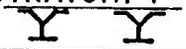	1.230	2ND	TOO COMPLICATED
TRUSS CORE CORRUGATION 	1.150	3RD	NO SHEAR CAP.
INTEGRAL ZEE 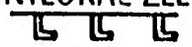	1.030	4TH	FAB. PROBLEMS
INTEGRAL TEE 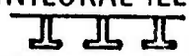	1.000	5TH	FAB. PROBLEMS
HAT SECTION STIFFENED 	0.928	6TH	SELECTED
ZEE STIFFENED 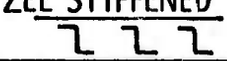	0.911	7TH	SELECTED
J STIFFENED 	0.793	8TH	POSSIBLE
STRAIGHT Y STIFFENED 	0.790	9TH	TOO COMPLICATED
SEMITRAPEZOIDAL CORR. SEMI. SANDWICH 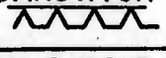	0.706	10TH	TOO COMPLICATED
SEMI-CIRCLE CORR. SEMI-SAND. 	0.706	11TH	IMPRACTICAL
TRUSS CORE SEMI-SANDWICH 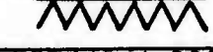	0.686	12TH	POSSIBLE
TRAPEZOIDAL CORR. SEMI-SAND. 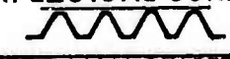	0.685	13TH	POSSIBLE
INTEGRALLY STIFFENED 	0.656	14TH	POSSIBLE
TRUSS CORE SANDWICH 	0.605	15TH	POSSIBLE FAB. PROBLEMS
CLOSED SECTION STIFFENED 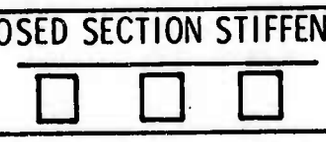	BETWEEN 0.656 & 0.928	HIGH	FAB. BY FIBER WINDING

Figure 275. Efficiencies Of Wide Column Concept

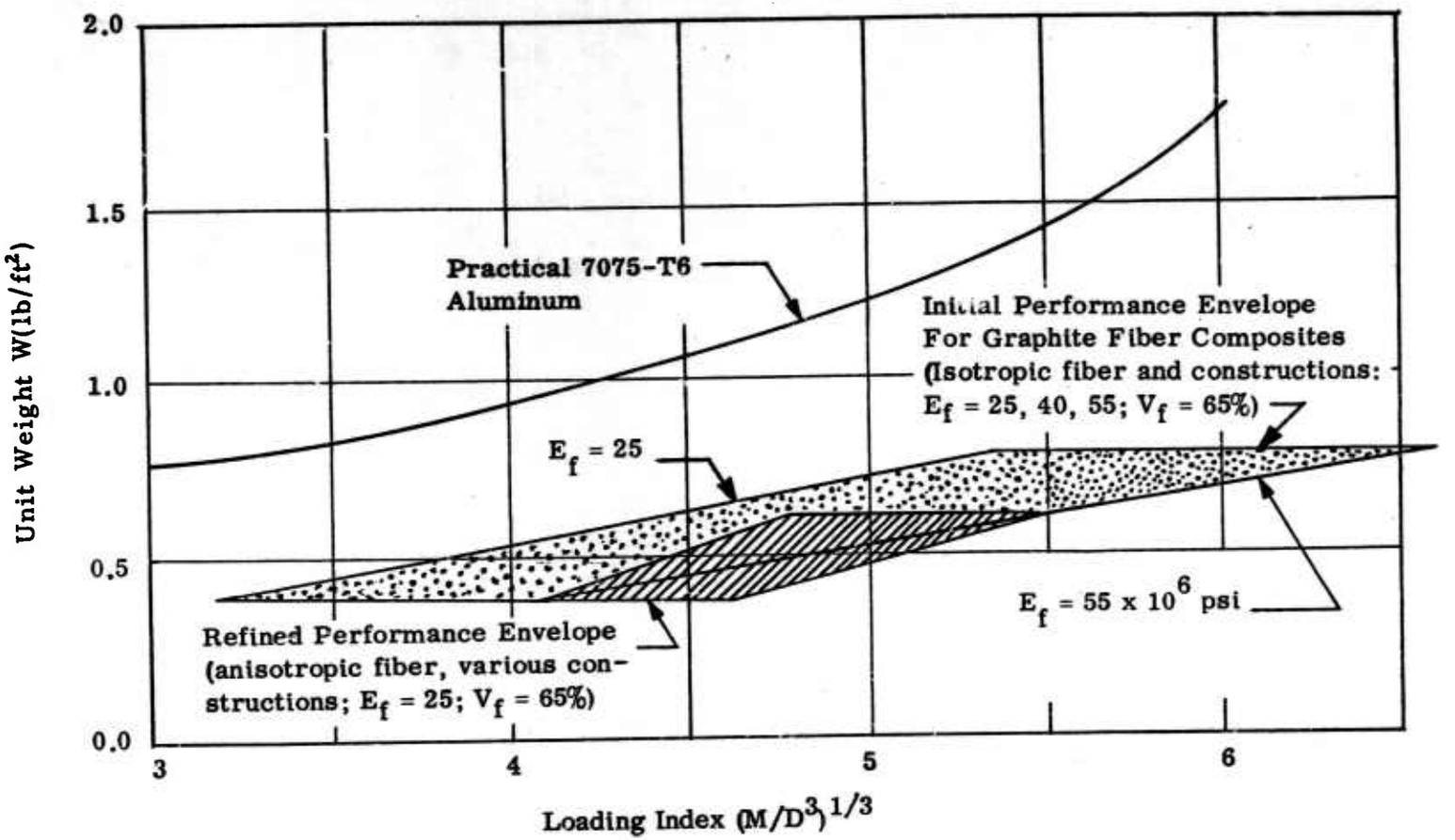

Figure 276. Weight Efficiency Comparison of Stiffened Cylinders of Graphite-Fiber, Epoxy-Resin Composites and Conventional Aluminum

of the aluminum construction. The three thicknesses are assumed minimum gauge cut-offs of 0.025, 0.032 and 0.040 inch. The 'preliminary design' composite band indicated on Figure 276 also applies closely to the hat-section stiffened shell, as shown later in Figure 279.

Optimum design curves for aluminum and graphite composites were also determined from methods given in Reference 84. The proportions of the minimum weight designs resulted in ring spacing-to-diameter ratios from 0.12 to 0.15, closely spaced stringers (~ 1/2 inch), and extremely thin material (~ 0.010-inch thicknesses). Consequently, there is greater interest in the practical designs given in Figure 276.

Other parts of this report section (particularly Sections X C and D) treat design refinements which consider factors such as fiber anisotropy, strength cut-offs, minimum gauges, and laminate configurations other than isotropic constructions.

12. Element Test Program

An element test program is being conducted, as shown in Figure 277. Here, the first two simple tests on flat coupons and "L" and "U" channels are being used to obtain web and flange crippling data. The data are being used for comparison of composites with conventional materials and for comparisons of fiber orientation effects (see Sections VII F and G). Ring beam-element tests are also being conducted.

Tests of stiffened panels in compression and shear are planned with the best candidate configurations for the fuselage application. In these tests various bonding systems, buckling stress levels and instability modes will be evaluated. Data from these tests will be applied directly to the fuselage-section design.

13. Preliminary Design and Test Plan

A test set-up schematic for the representative fuselage component is shown in Figure 278. The component is shown as it will be placed in the static test facility with a series of tension jacks tied to the end fixtures and loading frame. Sections X E and F and Figure 279 present in detail the design work on stabilizing rings, end attachments, and the stiffener reinforcement system.

As shown in the test plan on Figure 278, tests will be conducted by load-response measurements on the component to compare measurements with theory. These will involve: tension, compression, bending, torsion, transverse shear, and several combinations of loads. The shell will then be loaded to destruction in bending.

As a planning and coordination tool, a configuration and assembly drawing for the fuselage section has been prepared as shown in Figure 279. This drawing has been distributed to the Association with the areas "to be specified" so marked in

SPECIMEN	TEST	OBJECTIVE
1. FLAT COUPONS	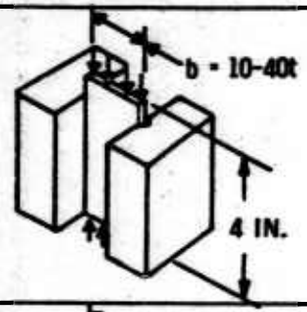	WEB ELEMENT CRIPPLING STRESS DATA CORRELATE WITH NACA TN 3600
2. "L" AND "U" CHANNELS	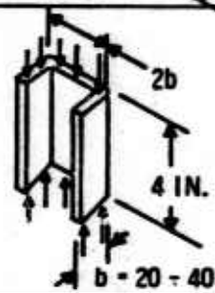	FLANGE ELEMENT CRIPPLING STRESS DATA, CORRELATE WITH NACA TN 3553 AND TN 3784
 3. STIFFENERS	SAME AS (2)	VALIDATE PREDICTIONS OF σ_{cc} FROM (1) AND (2)
4. STIFFENED PANELS	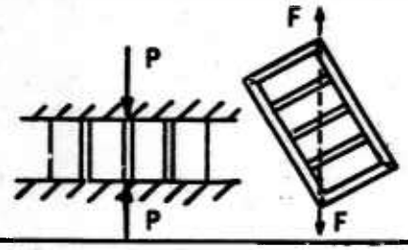	EVALUATE BONDING SYSTEMS VALIDATE STIFFENED PANEL PREDICTIONS

Figure 277. Initial Element Test Outline

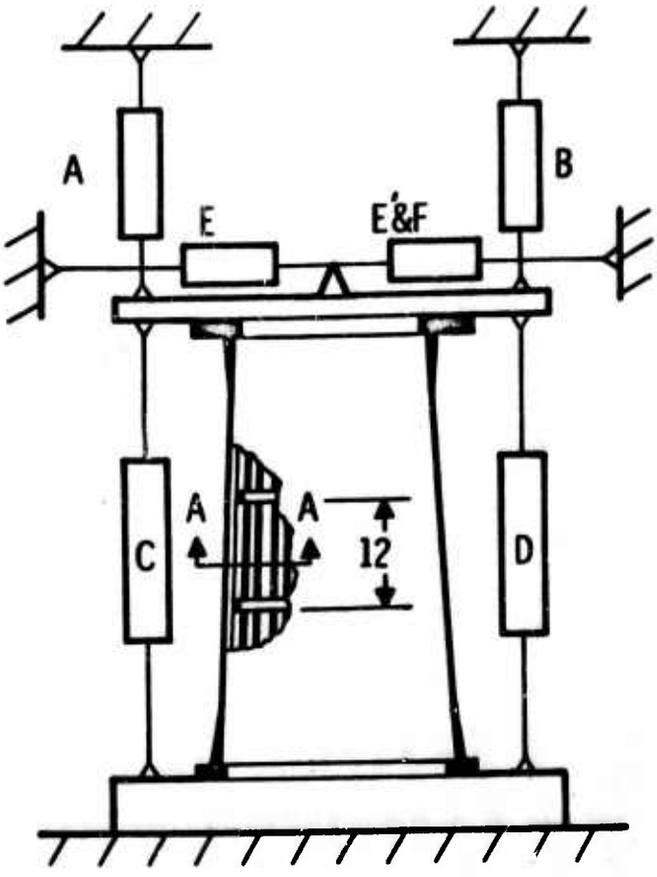

TEST SET-UP

TEST PLAN	
TYPE OF LOADING	JACKS
STRUCTURAL RESPONSE TO:	
(a) TENSION	A AND B
(b) COMPRESSION	C AND D
(c) BENDING	A AND D
(d) TORSION	E AND F
(e) SHEAR	E' AND F
(f) COMBINED LOADS	A – F
BENDING DESTRUCTION	A AND D

Figure 278. Preliminary Fuselage Design and Test Plan

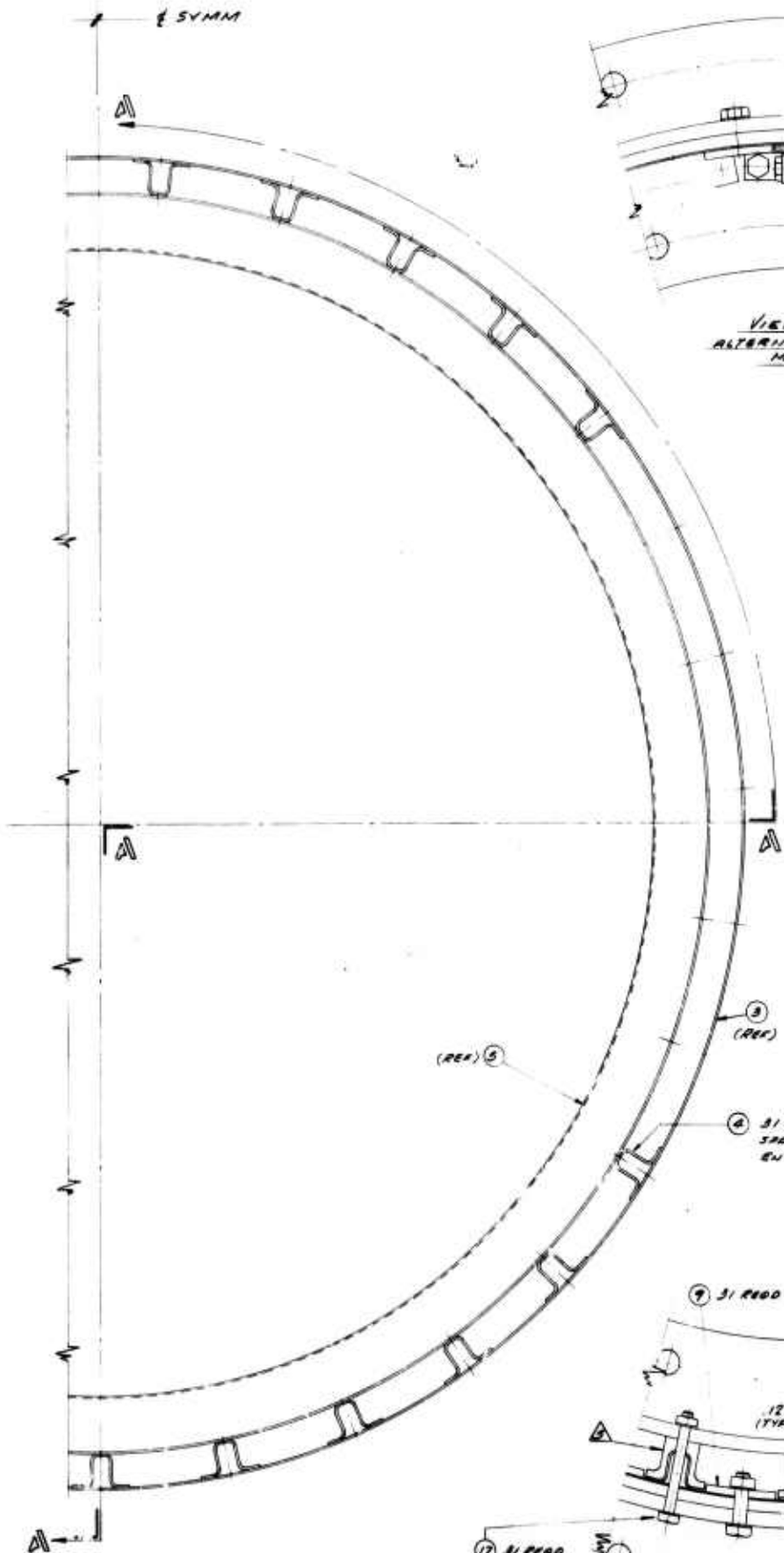

VIEW C$_0$ - C$_0$
ALTERNATE ATTACHMENT METHOD

SECTION D - D

VIEW B - B

A

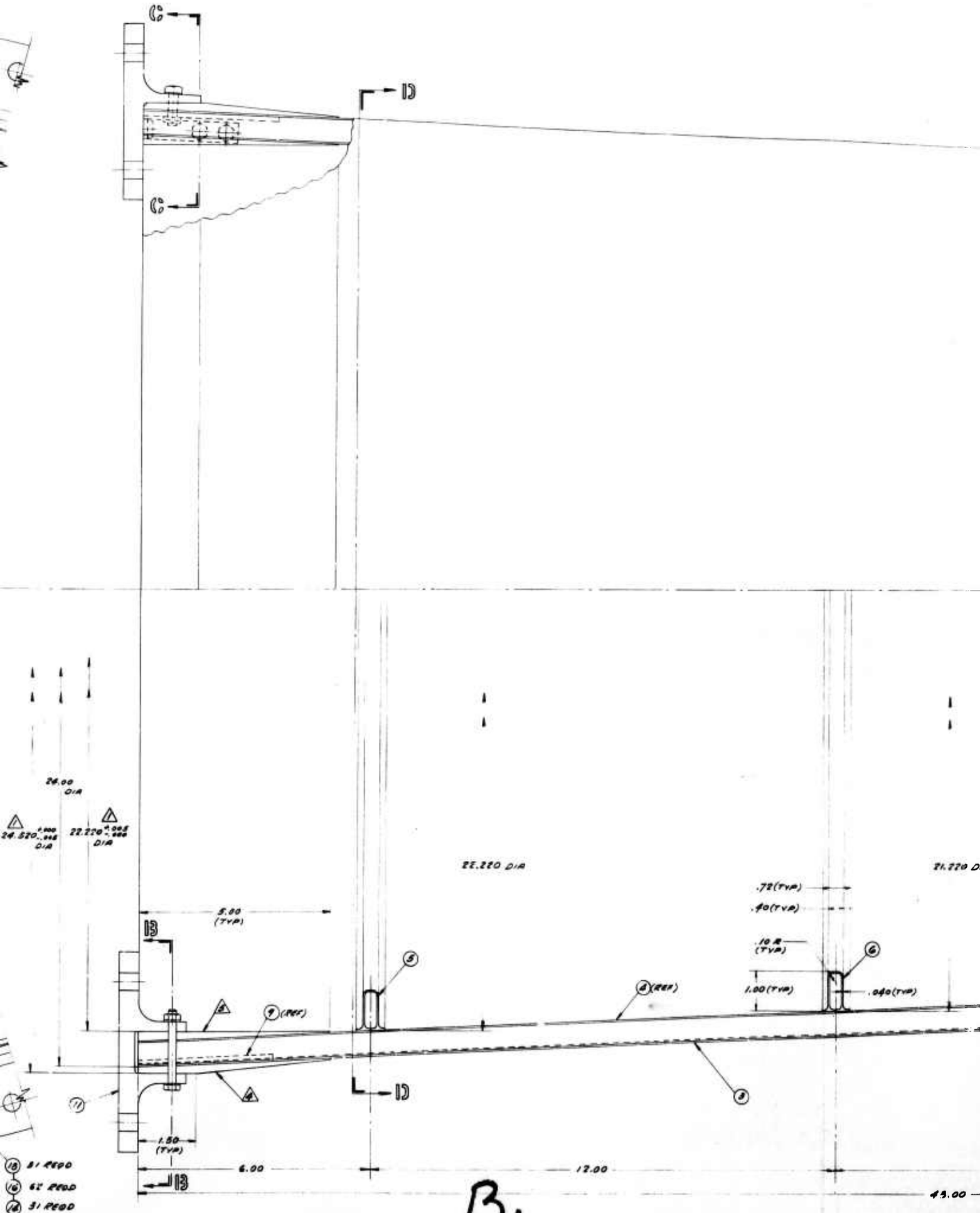
C
C
13
13
13
24.00 DIA
24.520 DIA
22.220 DIA
22.220 DIA
21.220 D
5.00 (TYP)
.72(TYP)
.40(TYP)
.10 R (TYP)
1.00(TYP)
.040(TYP)
9 (REF)
8 (REF)
1.50 (TYP)
6.00
12.00
45.00
18 81 REQD
16 62 REQD
14 31 REQD

B.

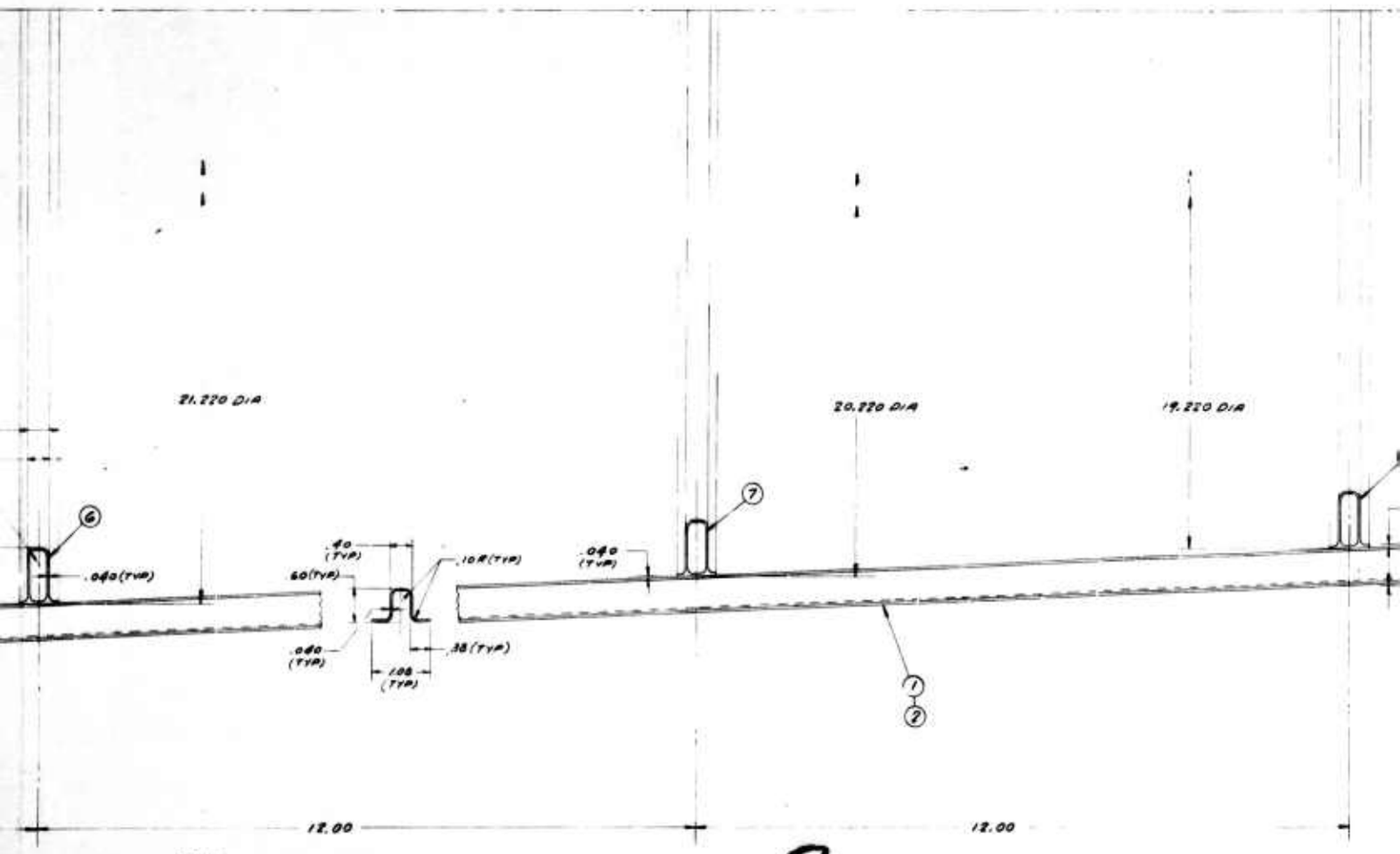

SECTION A1-A1-A1-A1

C.

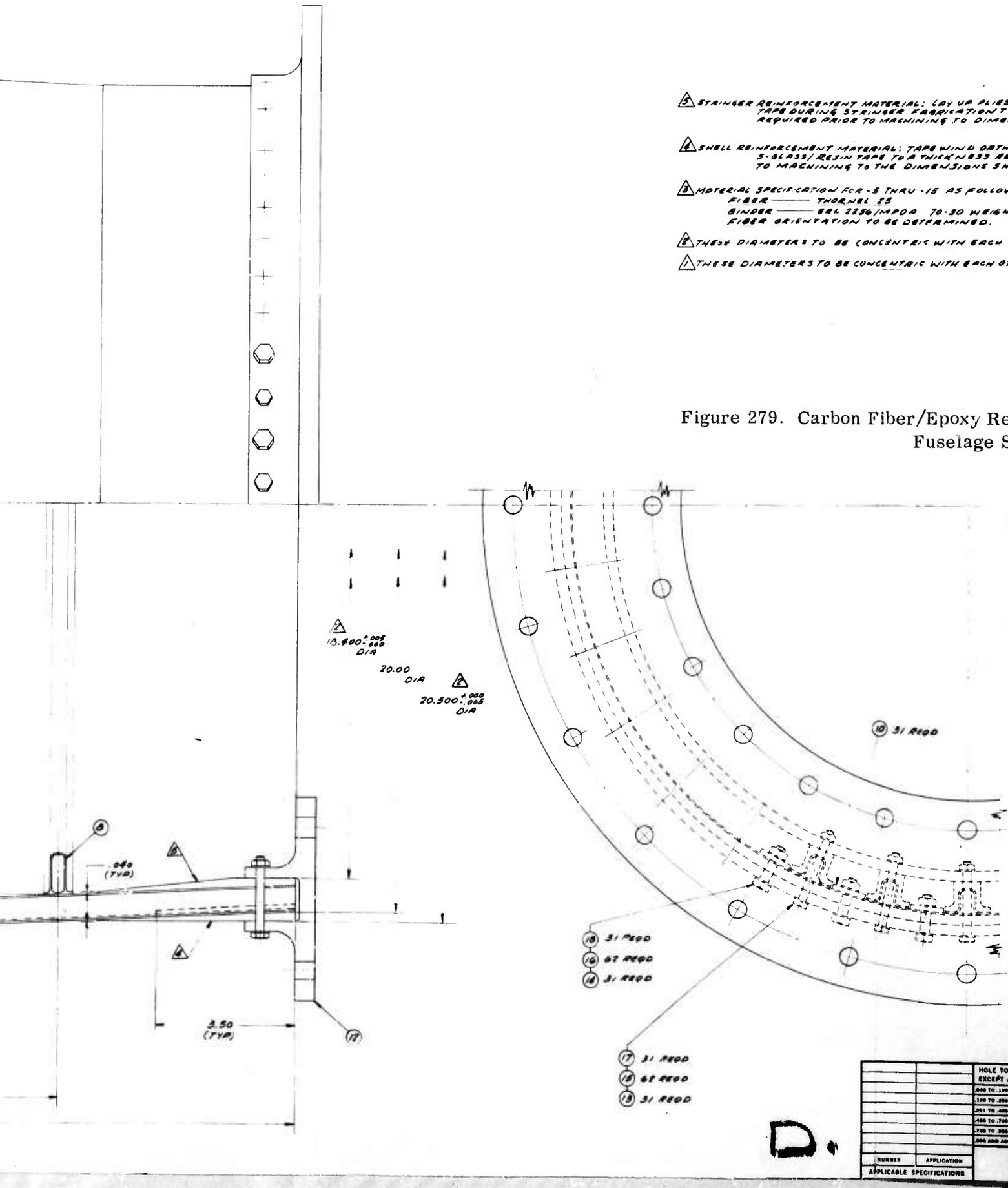

Figure 279. Carbon Fiber/Epoxy Res
Fuselage St

REVISIONS

SYM	ZONE	DESCRIPTION	DATE	APPROVED

REINFORCEMENT MATERIAL: LAY UP PLIES OF ORTHOGONAL TAPE DURING STRINGER FABRICATION TO THE THICKNESS REQUIRED PRIOR TO MACHINING TO DIMENSIONS SHOWN.

NFORCEMENT MATERIAL: TAPE WIND ORTHOGONAL PLIES OF S-GLASS/RESIN TAPE TO A THICKNESS REQUIRED PRIOR TO MACHINING TO THE DIMENSIONS SHOWN.

SPECIFICATION FOR -5 THRU -15 AS FOLLOWS:
IR ——— THORNEL 25
ER ——— 826 2256/MPDA 70-30 WEIGHT RATIO.
R ORIENTATION TO BE DETERMINED.

METERS TO BE CONCENTRIC WITH EACH OTHER WITHIN .005 TIR

AMETERS TO BE CONCENTRIC WITH EACH OTHER WITHIN .005 TIR.

279. Carbon Fiber/Epoxy Resin Component No. 1 - Representative Fuselage Structure

E.

(10) 31 REQD

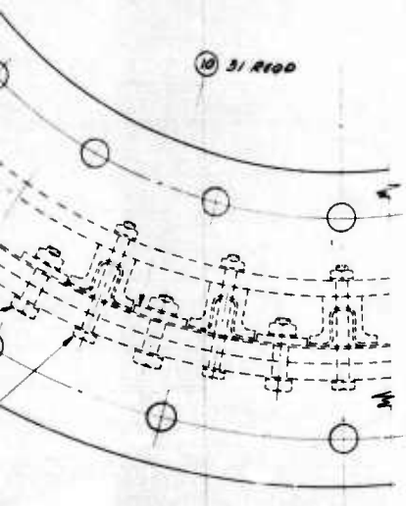

QTY REQD	FIND NO	CODE IDENT	PART OR IDENTIFYING NO.	NOMENCLATURE OR DESCRIPTION	MATERIAL OR NOTE	SPECIFICATION	DIA	TBK	W	LG	TS	UNIT WT	ZONE
62	18		MS 1308-24W	BOLT									
62	17		MS 1308-24W	BOLT									
124	16		AN 960C416L	WASHER									
124	15		AN 960C416	WASHER									
62	14		AN 316C8	NUT									
62	13		AN 316C8	NUT									
1	12		8506-150001-3	PLATE, MTG									
1	11		8506-150001-1	PLATE, MTG									
31	10		8506-150001-9	STIFFENER PLATE									
31	9		8506-150001-7	STIFFENER PLATE									
1	8		8506-150001-13	RING									
1	7		8506-150001-15	RING									
1	6		8506-150001-11	RING									
1	5		8506-150001-9	RING									
1	4		8506-150001-7	STRINGER									
1	3		8506-150001-5	SHELL									
	1	2	8506-150001-3	STRUCTURE, ASSY GP									
		1	8506-150001-1	STRUCTURE ASSY									

LIST OF MATERIALS OR PARTS LIST

8506-150001

D.

HOLE TOLERANCES EXCEPT AS SHOWN	
.060 TO .129	+.005, -.000
.130 TO .290	+.005, -.000
.291 TO .480	+.005, -.000
.481 TO .720	+.010, -.000
.730 TO .980	+.015, -.000
.986 AND ABOVE	±.010

UNLESS OTHERWISE SPECIFIED DIMENSIONS ARE IN INCHES TOLERANCES ON .X ±.1, .XX ±.02, .XXX ±.010, ANGLES ±1°

UNLESS OTHERWISE SPECIFIED BREAK ALL SHARP EDGES APPROX .015 R OR CHAM

MACHINED SURFACES EXCEPT AS NOTED ✓

DESIGN Polanowski 10/21/66
GROUP
APPD
CHK
STRESS
WT
REL

SUPERSEDES | SUPERSEDED BY

BELL AEROSYSTEMS COMPANY
DIVISION OF BELL AEROSPACE CORPORATION
POST OFFICE BOX 1 BUFFALO 5, NEW YORK

CARBON FIBER/EPOXY RESIN COMPONENT NO 1 - REPRESENTATIVE FUSELAGE STRUCTURE

CODE IDENT NO. 80078 | SIZE J | 8506-150001

SCALE | SHEET

NUMBER	APPLICATION
APPLICABLE SPECIFICATIONS	

DASH NO.	NEXT ASSY	USED ON	NEXT ASSY	FINAL ASSY	ED NO.	SH OF DWG
	APPLICATION		QTY REQD		ED TO COMPLETE PRINT	

order to focus attention on the critical areas of design. As the iterations proceed, this control drawing will be revised and changes documented.

B. Design Criteria and Loading Conditions

(W. N. Meholick and D. P. Hanley, Bell Aerosystems)

To finalize the representative fuselage component design requires the establishment of a design criteria and a set of loading conditions. The criteria discussed in this report section establish a means of evaluating various materials and methods of construction on the same reference basis. The loads specify the strength objectives required and will be presented later in detail.

1. Definition of Loads and Factors

The USAF General Specifications contained in MIL-A-8860 to 8870 for military aircraft strength and rigidity are used as a guide. The requirements from these specifications are the definition of loads and the factors of safety that are applied:

(a) Limit load is defined as the maximum load expected in service with at least two occurrences.
(b) Ultimate load is defined as the limit load times a factor of 1.5.
(c) Yield load is defined as being equal to the limit load. A requirement for the airframe when subjected to yield loads is that no permanent structural deformation is permitted that prevents the proper functioning of any structural or mechanical component.

General criteria governing the definition of allowable stresses and elastic constants for design for filamentary composites need to be established and verified. The criteria in use for conventional isotropic materials need revision for application to composite materials because of anisotropy and nonlinear effects. The following criteria will be used in the present program until more experience with graphite fiber composites has been obtained.

2. Allowable Stresses

(a) Limit stress analysis will be based on the linear elastic constants of the material.
(b) Ultimate stress will be taken to be the lower stress of either 1.5 times the limit stress or the failure stress of the material as determined experimentally.
(c) Ultimate stress analysis will be based on the material elastic constants at the ultimate stress.

3. Buckling Stresses

The initial buckling stress of any plate element in shear or compression shall be equal to or greater than the stress occurring in the plate element at limit load. This recommendation is made because the behavior of graphite composites in the post buckling region has not yet been firmly established. The post buckling or crippling stress allowable in compression is being studied, however, as reported in Section VII G.

4. Stiffness

The General Specifications previously mentioned merely state that adequate bending (EI) and torsional (GJ) stiffness shall be provided.

The EI and GJ values for the representative component, as described in the previous report section, if made with 0.040-inch thick skin and stringers of 7075-T6 aluminum, are summarized in Table LXVII.

TABLE LXVII

ALUMINUM FUSELAGE STIFFNESS CHARACTERISTICS

Dia.	I	EI	J	GJ	EI/GJ
	$in.^4$	$(x\ 10^{-7}\ lb\text{-}in.^2)$	$in.^4$	$(x\ 10^{-6}\ lb\text{-}in.^2)$	
20 in.	231	242	251	987	2.45
22 in.	312	328	337	1330	2.45
24 in.	406	427	442	1740	2.45

The Aerodynamics Section at Bell Aerosystems has been consulted to establish a meaningful design requirement for the "aft fuselage torsional stiffness" of the representative component. Levels of aerodynamic stiffness acceptable for good handling qualities are obtained from parametric static and dynamic analyses. These results are unique to each aircraft design. Effects of flexibility are accounted for by corrections applied to the rigid aerodynamic stiffness parameters. As long as the aerodynamic parameters corrected for flexibility meet the levels established for good handling qualities, the design is considered satisfactory. For composite materials which can have structural stiffness characteristics appreciably different from those of conventional materials, it would be desirable to have a criteria that relates stiffness directly to aircraft handling qualities. Although at present there are no such criteria, some thought has been given toward establishing limits on the aft fuselage torsional stiffness that will maintain aerodynamic parameters within a reasonably satisfactory range relative to: (1) stability and (2) control levels provided by the usual static and dynamic analyses. At the critical steady sideslip condition, in case (1), where the vertical tail

develops its maximum load, fuselage torsional flexibility can result in reduced static directional stability due to a loss in vertical tail effectiveness. In case (2), a pitching moment trim requirement arises due to the component of the tail load acting in the vertical plane.

The reduced tail load, Y_{VT}, in case (1) can be expressed as $Y_{VT} \cos^2 \phi$ where ϕ is the angle of twist of the fuselage under load. For conventional configurations having an aft tail arrangement, a restriction which maintains the reduction in vertical tail load due to twist within 0.97 to 0.95 of the rigid value (three to five percent reduction) is considered reasonable. This criterion can be written quantitatively as $\cos^2 \phi \leq 0.95$ to 0.97.

The pitching moment coupling for case (2) due to the component of vertical tail side-force acting vertically is

$$\Delta M = Y_{VT} \ell_{VT} \cos \phi \sin \phi$$

where ℓ_{VT} is the distance between the aerodynamic center of the vertical tail and the center of gravity. A reasonable control of this effect is to keep it less than the trim requirement for a 0.5 g-pullup with a 10% static margin which is written quantitatively as follows:

$$M = Y_{VT} \ell_{VT} \cos \phi \sin \phi \leq 0.05 W\bar{c}$$

As will be seen shortly in Table LXVIII, this equation sets another limit on ϕ, the permissible angle of twist for the fuselage.

It is recognized that there are many other criteria that might be developed to relate structural stiffness requirements directly to handling qualities. However, in their absence, it is felt that adherence to the general limits prescribed by the two rules given above should result in flexible aerodynamic characteristics within the range required for acceptable handling qualities.

For typical aircraft design, a permissible twist angle ϕ per foot of fuselage length can be derived from the above two criteria with the lower value of ϕ being the governing requirement. Torsional stiffnesses (GJ) of the representative component designed according to the above criteria have been calculated. Table LXVIII summarizes the resulting values. These data, derived from aerodynamic considerations, yield requirements for the net shear modulus of the fuselage shell.

TABLE LXVIII

SUMMARY OF TORSIONAL STIFFNESS (GJ) REQUIRED

Criteria	Twist Angle (1)	Twist Angle/ft (2)	GJ (3)	G (J=337 in.^{4})
(1) Reduced Tail Load $\cos^2\phi \leq 0.95$	$\phi \leq 13°$	0.0114 rad/ft	95.6×10^6 lb-in.^{2}	284,000 psi
(2) Pitching Moment Coupling $\cos\phi \sin\phi = \frac{0.05\,W\bar{c}}{Y_{VT}\ell_{VT}}$	$\phi = 3°$	0.00262 rad/ft	415×10^6 lb-in.^{2}	1,230,00 psi

(1) Typical Aircraft: $W = 20{,}000$ lb, $\bar{c} = 10$ ft, $\ell_{VT} = 20$ ft, $Y_{VT} = 10{,}000$ lb } $\cos\phi \sin\phi = 0.05$

(2) Typical Aft Fuselage Length = 20 feet

(3) $\phi = \frac{TL}{GJ}$ where T is the torsion due to 180/1.5 = 120 lb/in. shear flow

$$T = \frac{180}{1.5}\,\pi\,(22)(11) = 91{,}200 \text{ in.-lb}$$

C. Orthotropic Shell Buckling Predictions

(K. H. Sayers, W. N. Meholick, and D. P. Hanley, Bell Aerosystems)

Initial work on the fuselage shell design was given in Section X A, Preliminary Design Studies. The tentative ring- and stringer-stiffened shell design was defined in Figure 279 and the following analysis efforts were recognized as necessary to finalize the design: (1) orthotropic cylindrical shell buckling predictions examining various layup angles and thicknesses, and (2) discrete-element stability analysis accounting for the conical (tapered cylinder) shape.

This report section describes progress in these two areas. In the first area the method of analysis is described with results given for "Thornel" 25 and 40 designs; in the second area, an approximate comparison of a "Thornel" 25 and aluminum shell design is made.

1. Cylindrical Shell Analysis

a. Theoretical Method

The analytical method employed considers the buckling of eccentrically stiffened orthotropic cylinders under pure bending in the manner of Reference 85. A nontapered cylinder is considered. Analysis uses small-deflection linear orthotropic buckling theory. The buckling mode has the form given by

$$w = \sin \frac{m \pi x}{a} \sum_{n=o}^{\infty} a_n \cos \frac{ny}{R} \qquad \text{(XC-1)}$$

where:

w	=	radial displacement
m, n	=	buckling half-wave numbers
x, y	=	longitudinal and hoop reference axes
a	=	cylinder length
a_n	=	undetermined coefficients
R	=	cylinder radius

This function assumes simply-supported ends, a sinusoidal waveform in the axial direction, and a waveform in the circumferential direction defined by the undetermined a_n coefficients. Solutions to this equation have been obtained by a computer program supplied by NASA/Langley. Results include the number of axial buckling half-waves and the critical maximum load/inch of circumference.

b. Application to "Thornel" 25 Fuselage Component

The analysis was applied to the fuselage shell using elastic constants accounting for fiber anisotropy of the "Thornel" 25 fiber*. The fiber volume content was initially assumed to be 65% with flexural moduli calculated from the membrane elastic constants. The shell was, as required by the analysis, assumed to be simply-supported at the stiffening rings and the effects of taper were not considered. (The discrete-element stability analysis in the final design will more realistically account for these effects.) Consideration was given to performance comparisons of an aluminum alloy and the graphite fiber composites with various gauge thicknesses, the basic geometry and type of stiffening remaining unchanged.

Three groups of skin/stiffening construction were analyzed as shown in Table LXVIX. For each separate case, two types of buckling were considered: overall shell buckling and panel buckling between rings. In each case, panel buckling was critical. Results were obtained for each group of constructions by plotting structural weight against the loading index. The following trends were observed.

TABLE LXVIX

SKIN AND STIFFENER COMBINATIONS
CONSIDERED IN ORTHOTROPIC BUCKLING ANALYSIS

	Different Lay-Ups Degrees	Thicknesses for Each Lay-Up Inch
Group 1		
Skin	0, ±15, ±30, ±45, and 0-90	0.025, 0.032, 0.040
Ring and Stringer	0	0.040
Group 2		
Skin	0, ±15, ±30, ±45 and 0-90	0.025, 0.032
Ring and Stringer	0	Same as skin
Group 3		
Skin	±15, ±30, ±45 and 0-90	0.025, 0.032, 0.040
Ring and Stringer	Same as skin	Same as skin

*At the time when this work was done, the fiber properties were not as well established as those given in Table LXVIX; the only discrepancy between values, however, was in E_{TF} in the present work it was taken as 1.5×10^6 psi compared to 1.2×10^6 psi shown in Table LXVIX.

With unidirectional 0.040-inch thick hat-section stringers and hollow rings, close grouping of critical loadings was found for the Group 1 configurations, as shown in Figure 280. The orthogonal (0-90°) skin lay-up resulted, weight-for-weight, in the greatest load capability. The effects of the high-modulus 0° stringers is evident here since changes in the skin construction (lay-up angles and thickness) did not appreciably shift the performance curves.

Critical loadings were considerably reduced when unidirectional hat-section stringers and rings were employed, as in the Group 2 configurations, with thicknesses equal to the shell thickness, as shown in Figure 281. For a given structural weight, the orthogonal skin pattern still was found to give the greatest load capability. Correspondingly, for $4.5 < (M/D^3)^{1/3} < 5.5$, the 0-90° skin configuration resulted in the lightest shell weight compared with the other skin configurations.

The critical loadings were still further reduced when the stringers and skins have the same lay-up pattern and thickness as the basic skin as in the Group 3 configuration as shown in Figure 282. Now, however, the orthogonal lay-up resulted in the lowest load capability for equal weight shells.

With the same geometry and thicknesses, the comparative performance of an aluminum alloy cylinder is shown in Figures 280, 281, and 282 with its indicated compressive yield cutoff. The weight advantage of composite construction is evident. Comparison with the preliminary design weight-structural index curves is shown on Figure 276. The band labeled Preliminary Design Performance Envelope considered fiber moduli levels of 25, 40, and 55 x 10^6 psi, assumed all pseudo-isotropic construction, and used isotropic fiber properties for calculation. The band labeled Refined Performance Envelope considers 25 x 10^6 psi fiber modulus, various skin-stringer constructions, and anisotropic fiber properties. The significance of the latter band is that in the low-to-moderate loading range of interest, the performance of the graphite composites is still seen to offer ~ 50% weight savings potential in comparison with conventional aluminum construction.

To verify the significance of the above cited weight savings potential, the strength cutoffs must be established. Reliable test data substantiating analytical predictions are necessary to define these with confidence. For a shell where stiffeners and skin have different effective moduli, stresses in the two elements will not be the same for a given loading even in the elastic range. Therefore, an examination of these stresses was made for two configurations which resulted in high panel-buckling loads: orthogonal skin and uniaxial rings and stringers, each with thicknesses of 0.040 and 0.032 inch. These results are shown in Figure 283. The compressive ultimate stresses are rough estimates based on current analytical work and composite test results. The data shown in Figure 283 indicate that slight skin buckling would be present before failure occurs due to panel buckling between rings. Complete buckling failure would then be accompanied by skin crushing under the stringers. The sequence of failure for the 0.032-inch design was predicted to be the same as for the 0.040-inch design, but the onset of skin buckling occurs at a lower skin stress level.

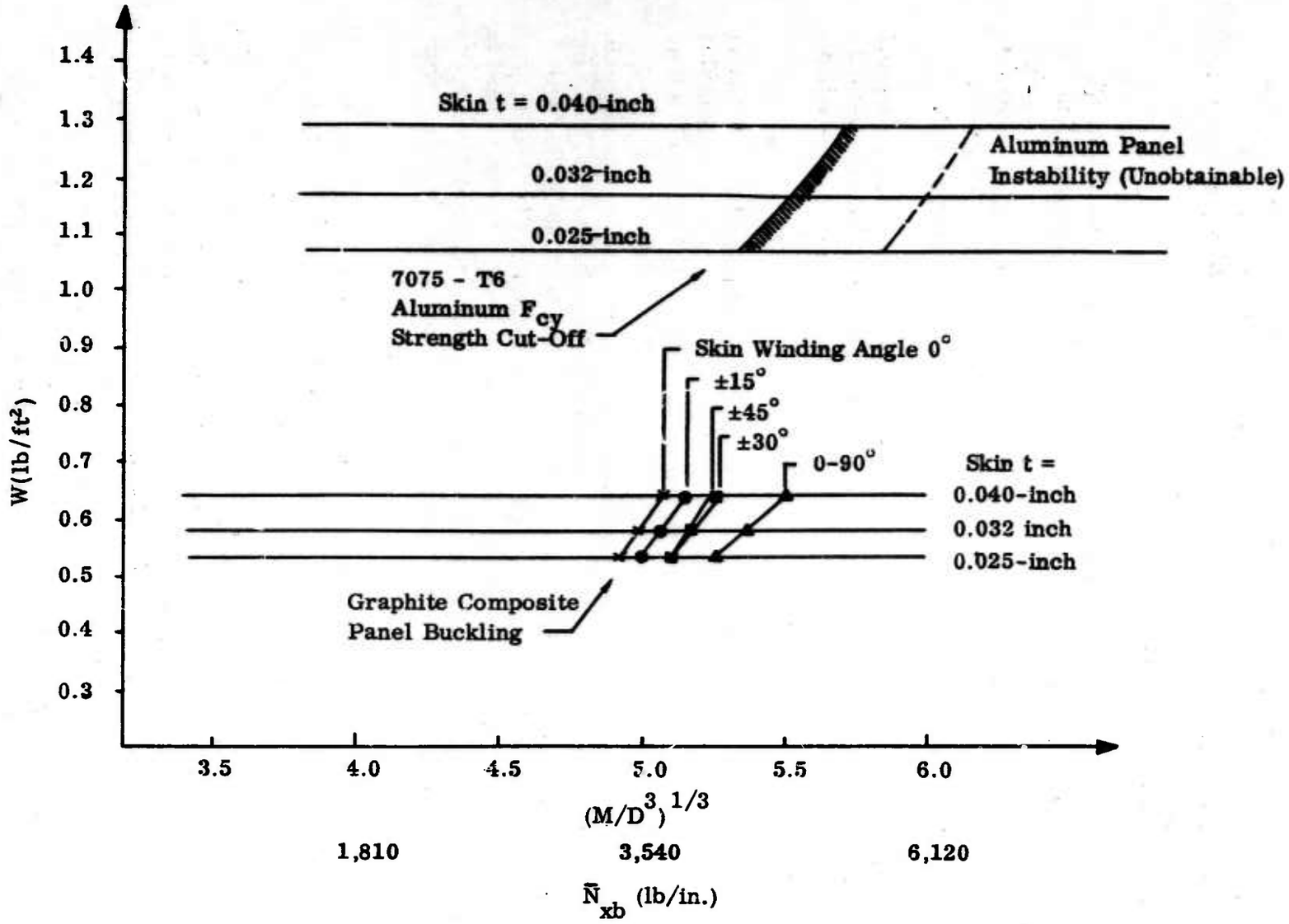

Figure 280. Graphite Composite Shell Weight - Strength Comparisons
(Gp. 1: Uniaxial Rings and Stringers with t = 0.040 inch)

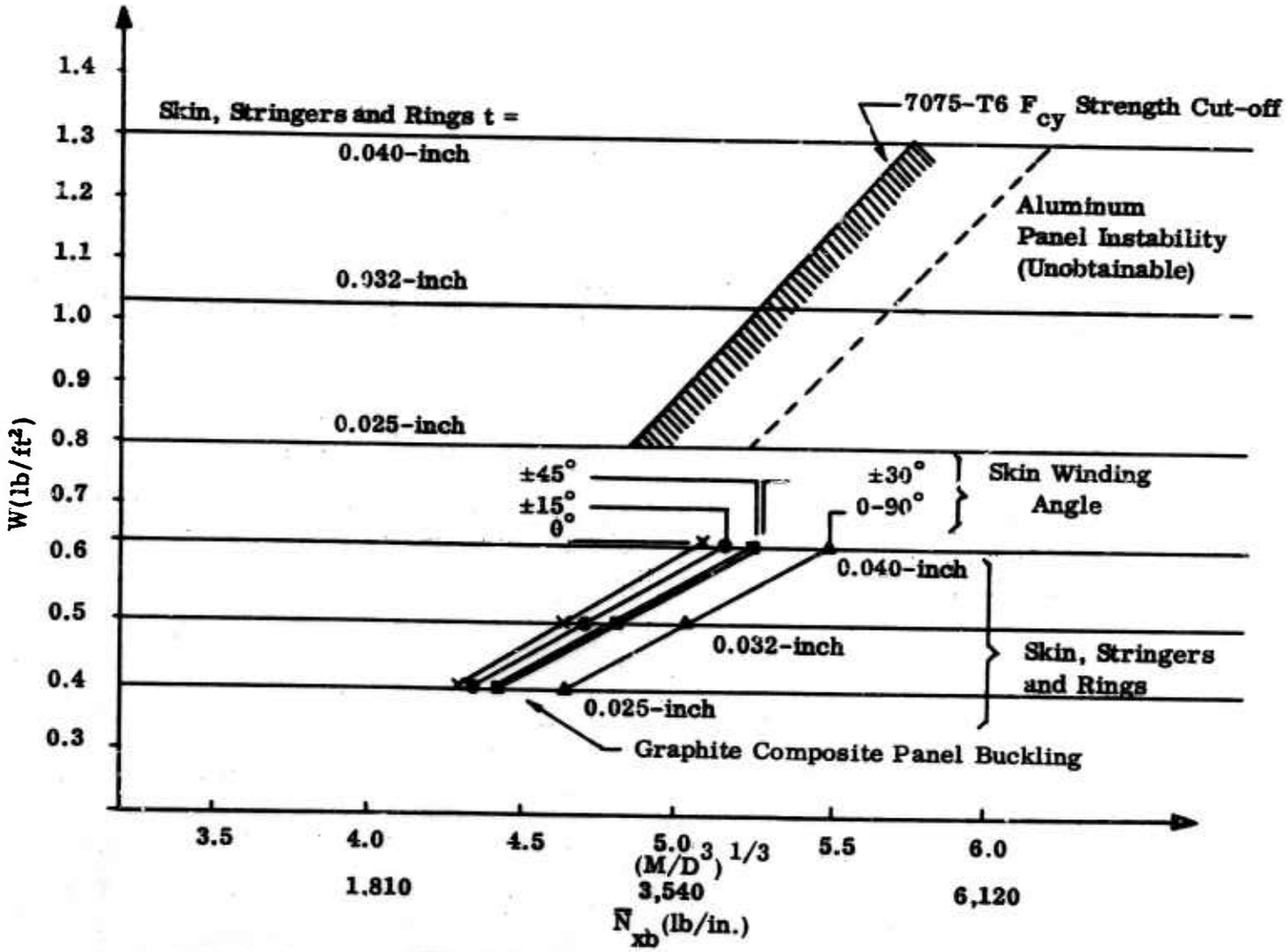

Figure 281. Graphite Composite Shell Weight-Strength Comparisons
(Gp. 2: Uniaxial Rings and Stringers)

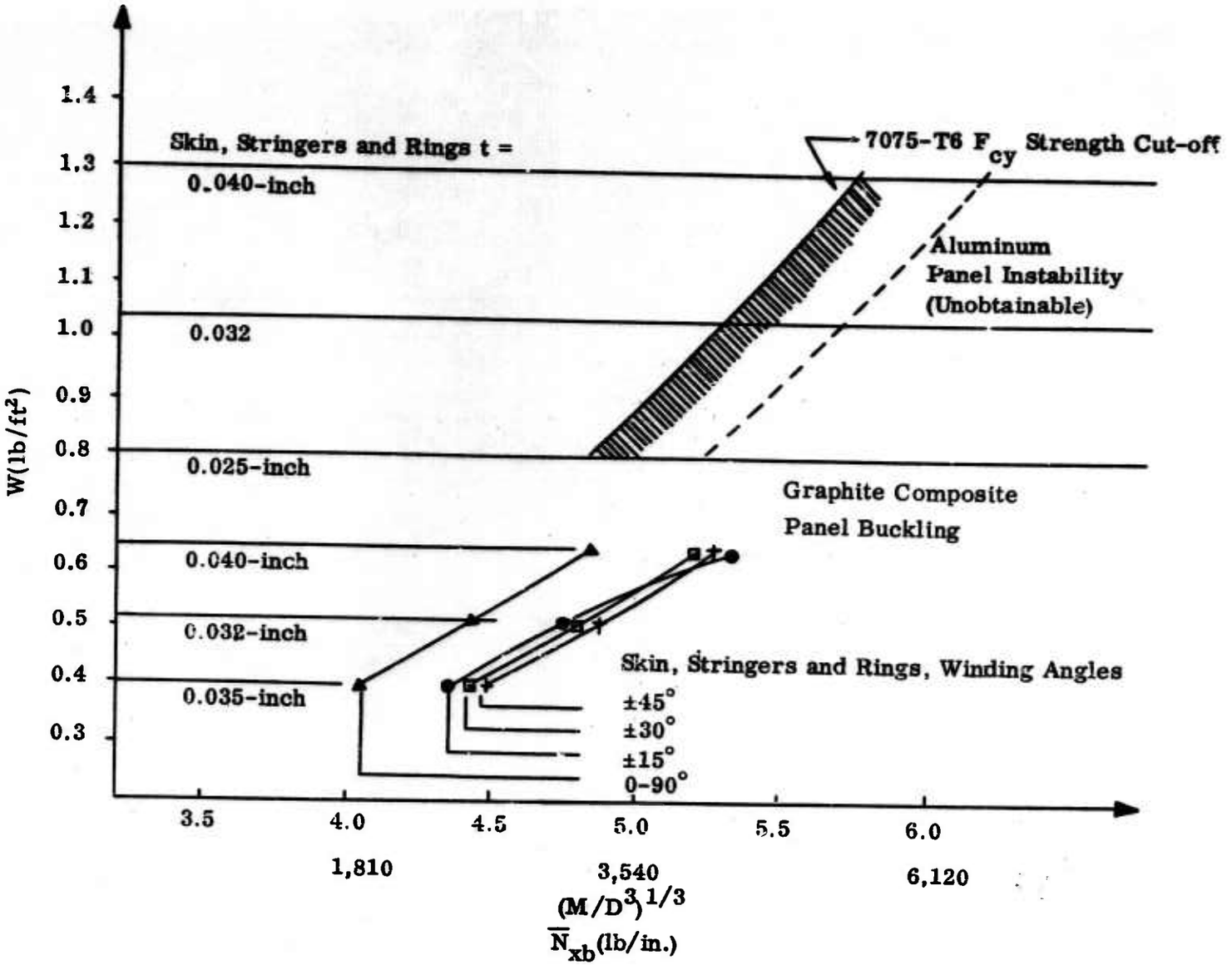

Figure 282. Carbon Composite Shell Weight-Strength Comparisons
(Gp. 3: Varing Angle Skin, Stringer, and Rings)

Uniaxial 0.040-inch stringers and rings with a 0.040-inch orthogonal skin	Uniaxial 0.032-inch stringers and rings with a 0.032-inch orthogonal skin
Orthotropic analysis predicts panel instability between rings at $(M/D^3)^{1/3} = 5.49$ $\overline{N}_{xb} = 4510$ lb/in.	Orthotropic analysis predicts panel instability between rings at $(M/D^3)^{1/3} = 5.02$ $\overline{N}_{xb} = 3570$ lb/in.
At this loading based on elastic analysis σ stringer = 73,500 psi σ skin = 40,200 psi	At this loading based on elastic analysis σ stringer = 72,800 psi σ skin = 39,900 ft
These stresses are compared with the assumed strength allowables of: $(F_{cu}) = (F_{tu})$ stringer = 90,000 psi $(F_{cu}) = (F_{tu})$ skin = 40,000 psi	These stresses are compared with the assumed strength allowables of: $(F_{cu}) = (F_{tu})$ stringer = 90,000 psi $(F_{cu}) = (F_{tu})$ skin = 40,000 psi
and an assumed local instability allowable of $1.5 \times F_{cr} = 30,100$ psi for the skin between stringers.	and an assumed local instability allowable of $1.5 \times F_{cr} = 19,400$ psi for the skin between stringers.
This local instability corresponds to: $(M/D^3)^{1/3} = 4.91$ $\overline{N}_{xb} = 3350$ lb/in. W = 0.645 psf	This local instability corresponds to: $(M/D^3)^{1/3} = 3.95$ $\overline{N}_{xb} = 1740$ lb/in. W = 0.516 psf

Figure 283. Summary of Panel and Local Instability Allowables for Two Component Designs

The initial analysis indicated that the most promising fuselage component construction is the orthogonal (0°-90°) skin combined with uniaxial (0°) rings and stringers. However, the skin may have to be modified to include $\pm \alpha$ balanced lamina to resist shear and/or multiple loads. Stringer and ring lay-ups may also have to be modified to reduce the danger of splitting due to the low transverse strength of unidirectional configurations.

c. Application to "Thornel" 40 Fuselage Component

In the previous section, a wide range of possible laminate constructions for the shell, stiffeners, and rings were investigated to obtain load/weight performance comparisons in order to select likely candidates. These calculations were made using "Thornel" 25 graphite yarn properties with 65% fiber volume content. The inplane elastic constants were used to obtain approximate values for the bending constants. The greatest performance potential for the loads specified appeared to be with an orthogonal skin and unidirectional stringers and rings.

Additional results of orthotropic shell buckling studies have been obtained using "Thornel" 40 properties with 50% fiber content, since "Thornel" 40 will be used in the component fabrication. Fifty percent fiber content is expected in the fabrication process. The bending elastic constants have been evaluated in a more consistent manner with the methods used to generate the bend data of Table LXIII. A (0°, 90°, 0°, 90°) orthogonal skin 0.040-inch thick was considered. The stiffeners had the same cross sections and spacings as in the previous work. The four types of stringer and ring designs were: (1) unidirectional lay-up, 0.040-inch thick; (2) unidirectional lay-up, 0.032-inch thick; (3) orthogonal lay-up, 0.040-inch thick; and (4) orthogonal lay-up, 0.032-inch thick. The stringers and rings were assumed to have four plies. Input properties are given in Table LXX.

Four strength limitations were investigated for each shell configuration.

(1) General Instability: an overall instability failure mode of the shell involving ring deformations, which implies catastrophic failure and is an ultimate condition;
(2) Panel Instability: a catastrophic (ultimate) failure buckling mode which occurs between rings with no ring deformation;
(3) Static Strength: an ultimate condition characterized by material failure of the stringer and/or skin; and
(4) Initial Skin Buckling: a limit condition characterized by no buckling at limit load.

For each of the four shell configurations, the panel buckling instability mode between rings occurred at much lower loads than did the general instability mode (as before) and, hence, was the more critical loading. The panel buckling loadings, load indices, and associated stringer and skin stresses are given in Table LXXI.

TABLE LXX

CALCULATED ELASTIC CONSTANTS FOR "THORNEL" 40 GRAPHITE YARN COMPOSITES

(50 v/o fiber content, 10 mils/layer)

	Unidirectional	Orthogonal	
	4 (0)	4 (0-90-0-90)	4 (0-90-90-0)
Membrane			
E_1, 10^6 psi	20.28	10.78	
E_2, 10^6 psi	1.17	10.78	
G_{12}, 10^6 psi	0.56	0.56	Same as 0-90-0-90 Membrane
ν 12	0.310	0.034	
ν 21	0.018	0.034	
Bending			
D_1, lb-in.^{2}	108.8	48.8	95.6
D_2, lb-in.^{2}	6.32	48.8	19.1
D_3, lb-in.^{2}	3.01	3.40	3.01
ν 12	0.310	0.045	0.102
ν 21	0.018	0.045	0.020

At the panel buckling load, the calculated stringer and skin stresses are on the order of the expected ultimate composite strengths. Thus, panel instability and static strength limitations are expected to occur at approximately the same ultimate loads. All of the panel buckling loads are well above the design load of 1,800 lb/in. However, initial instability of the skin between stringers occurs at loads well below panel instability loads. Since we are designing to an ultimate loading of 1,800 lb/in. due to overall shell bending, initial instability must not occur at loads below 1,800 ÷ 1.5 = 1,200 lb/in. (limit load). The loads to cause initial instability are presented in Table LXXI. For all four of the present designs, initial buckling occurs above limit load. Examination of Table LXXI shows that design number 4 is closer to the required limit and ultimate loads then are the other three designs; but this design is not the most efficient, since design number 2 develops greater load capability at the same weight. However, design number 4 has the attraction that the orthogonal layers used for the stringers and rings will reduce the danger of axial splitting in these members. Also, the orthogonal configurations tend to improve transverse bending rigidity to the stringer flats and, hence, increase support of the skin between stringers. This improvement is important for the local buckling strength and, in a flightworthy structural application, would also help the skin/stringer combination to better resist normal pressure loadings.

The orthogonal skin, although it gives good panel buckling and initial skin instability strengths and has a reasonable static strength, is suspected to have limitations of low shear strength and stiffness. This factor, as discussed under Design Criteria, Section X B will be taken into account in prescribing shear and torsion test loads. (A maximum of 180 lb/in. has been provisionally proposed, requiring a skin shear strength of 4,500 psi.)

The data for design number 4 in Table LXXI show that initial skin buckling may be expected at a loading of approximately 1,400 lb/in. Panel buckling between rings is predicted at approximately 3,000 lb/in. The actual panel buckling load will be lower because of the loss of skin effectiveness due to local buckling. Thus, catastrophic failure may be expected at a loading greater than 1,400 lb/in. but less than 3,000 lb/in. If it is assumed that the skin/stringer combination can support a loading 50% greater than that causing initial instability of the skin, an ultimate load of approximately 2,300 lb/in. can be carried. Since the ultimate design load is 1,800 lb/in., the 2,300 lb/in. predicted ultimate load provides a safe margin. Further analysis of the strength and crippling test results on "Thornel" 40 composites will enable more reliable predictions of the shell strength.

At present, design number 4 is predicted to be slightly conservative in bending and design number 2 even more conservative. Both designs fall within the refined performance envelope for graphite fiber composites shown in Figure 280, a fact which further substantiates the expected appreciable weight savings possible with composites.

TABLE LXXI

FUSELAGE COMPONENT LOADS AND STRESSES

		Design No. 1	Design No. 2	Design No. 3	Design No. 4
Ultimate Condition					
Shell Load/Inch	(lb/in.)	5416	4596	3613	3083
Associated Moment	(10^6 lb/in.)	2.09	1.77	1.38	1.18
Loading Index	$(M/D^3)^{1/3}$	5.74	5.43	5.00	4.75
Stringer Stress	(psi)	88100	80300	44500	42300
Skin Stress	(psi)	46900	45700	44500	42300
Limit Condition					
Skin Initial Instability Stress	(psi)	19400	19400	19400	19400
Shell Load/Inch	(lb/in.)	2210	1920	1550	1380
Unit Shell Weight	(lb/ft^2)	0.645	0.574	0.645	0.574

Limit Design Load - 1200 lb/in.
Ultimate Design Load - 1800 lb/in.
Orthotropic Shell Buckling - Panel Buckling is Critical

2. Conical Shell Analysis

A discrete element instability analysis was conducted to determine the initial loading for the conical fuselage component. Only two types of construction have been considered thus far, due to the computer time needed to obtain each solution. The details of these two types of construction are given as follows: (1) The first was an isotropic aluminum construction with a Young's modulus of 10×10^6 psi and all element thicknesses equal to 0.040 inch; in this case, a comparative calculation with the cylindrical idealization described in the previous section was also run. (2) The second construction used "Thornel" 25 fiber (assumed isotropic) and all element thicknesses were equal to 0.040 inch. Skin, stringer and ring properties used were as follows:

Skin: $\pm 20^\circ$, $E_1 = 12 \times 10^6$ psi, $E_2 = 3.5 \times 10^6$ psi, $\nu_{21} = 0.204$
$G = 2.4 \times 10^6$ psi, $\nu_{12} = 0.7$,

Stringers and rings: Pseudo-isotropic, $E = 8.27 \times 10^6$ psi

The discrete element method has the attraction that the effects of taper and end restraint may be properly considered. The degrees of freedom at one end of the shell were completely restrained. Those at the other end, except the axial displacements, were also fixed, and an axial load was applied there by a system of equivalent nodal loads. A relatively coarse structural grid was dictated, since the number of degrees of freedom per node (three translations and two rotations) meant that the computer limitation of 150 degrees of freedom was quickly reached.

The analysis yielded the following results for the two constructions under a pure compressive load uniformly distributed around the shell periphery:

Case (1): Critical Load = 455,800 lb; Stringer stress = 79,000 psi
Skin stress = 87,000 psi

Case (2): Critical Load = 460,000 lb; Stringer stress = 62,000 psi
Skin stress = 105,000 psi

The comparative calculation for Case (1) indicated an initial axial load of 448,000 lb.

These loads correspond to stresses somewhat above the strength cutoffs of the materials considered. The main objective in treating the above cases, however, was to properly validate the program as is indicated by the above data. When the shell design is completed, the program will be used again in final predictions of the buckling collapse loads under the types of loading to be applied in the test program. Initial buckling, crippling and ultimate strength cutoffs will be more firmly established by that time.

D. Parametric Design Studies for Columns and Plates

(K. H. Sayers and D. P. Hanley, Bell Aerosystems)

Current work uses the "Thornel" 40 two-ply yarn. Until recently, "Thornel" 25 was being used. There is the prospect of "Thornel" 60 for use in the future. This report section therefore compares some basic lamina properties for these three fiber types. It also considers the effects of varying fiber content in simple structural columns and plates.

1. Resin Content/Ply Thickness Relationships

An important parameter in composite structures is the fiber content. It has been found with graphite composites that as fiber content increases, the basic ply thickness decreases. In composites with a uniform array of rod-like reinforcing filaments, such as boron fibers, the variation of lamina thickness with fiber content is relatively easy to establish mathematically. This situation is considerably more complicated with graphite fiber composites because of basically different filament characteristics. Since attempts to apply simple packing theories have been found inadequate, an experimental curve of fiber content against ply thickness is required for reliable lamina property predictions.

Figure 284 shows experimental data obtained for both "Thornel" 25 and 40, with a curve approximated through the points. This approach seems justified, since yarn characteristics and filament cross sections are similar for the "Thornel" types. This curve is used subsequently to examine the effects on buckling strength of columns and plates of varying fiber content and moduli.

Since the thickness per ply varies with fiber content, as shown in Figure 284, the thicknesses of laminates built up of plies will vary also. This is an important effect, since although membrane stiffnesses are increased by increasing the fiber content, the bending stiffnesses are decreased for a fixed number of plies, as shown in Section X D-3. Figure 285 shows the variation of laminate thickness as a function of n for different fiber contents. It is based on the curve of Figure 284

At low fiber contents ($\lesssim$ 40%), the ply microstructure has been observed with matrix material both within the yarn, surrounding the individual filaments, and en masse around each yarn. At the higher fiber contents ($\gtrsim$ 60%), the yarns tend to coalesce and the yarn boundaries become difficult to distinguish. The type of microstructure thus varies radically with fiber content.

2. Simple Column Studies

The buckling strength/weight performances of built-up thin-walled unidirectional columns (of the types considered for the fuselage component stiffeners) may be compared by examining the quantity Et/W which is proportional to P_{cr} divided by column weight, where E is the principal column modulus, t is the wall thickness, P_{cr} is the Euler buckling load, and W is the weight per unit surface area, given by

$$W = t \left[V_F (\rho_F - \rho_M) + \rho_M \right] \qquad \text{(XD-1)}$$

The variation of W with fiber content is given by Figure 286. The combinations of t and V_F are obtained from Figure 284. The values of ρ_F and ρ_M used in the present calculations were 0.0541 and 0.0441 pci, respectively. "Thornel" 40 and 60 have slightly greater densities.

Figure 287 shows the buckling load/weight efficiency parameter Et/W as a function of fiber content for "Thornel" 25, 40, and 60. These curves show the relative performance tradeoffs and the desirability of low resin contents for simple unidirectional columns.

3. Plate Initial Instability Studies

It has been shown that as fiber content is increased, ply thickness decreased (Figure 284). For a fixed number of layers this is accompanied by a reduction of the laminate weight per unit area (Figure 286). Although it has been shown that extensional stiffness E_L increases with increasing fiber content, the bending stiffnesses of a

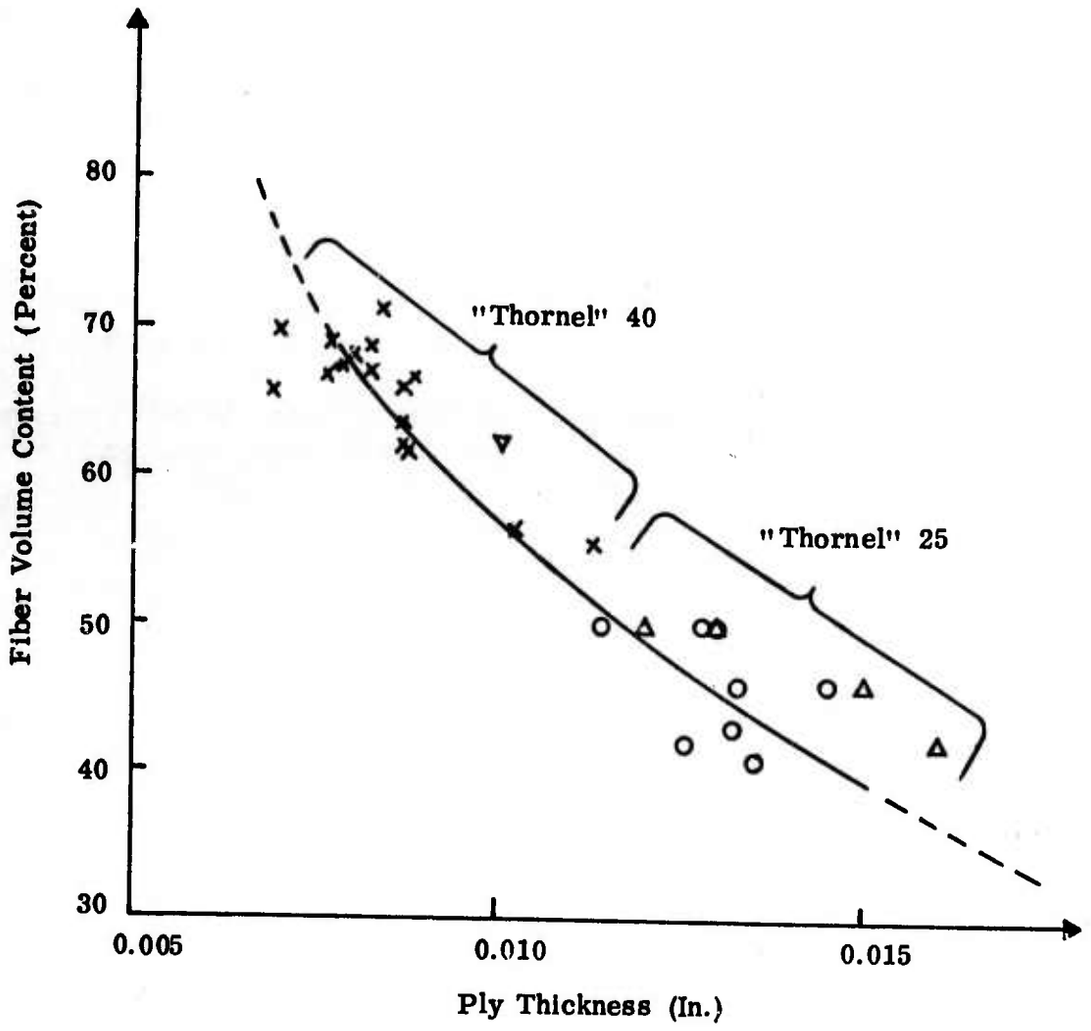

Figure 284. Fiber Volume Content as a Function of Ply Thickness

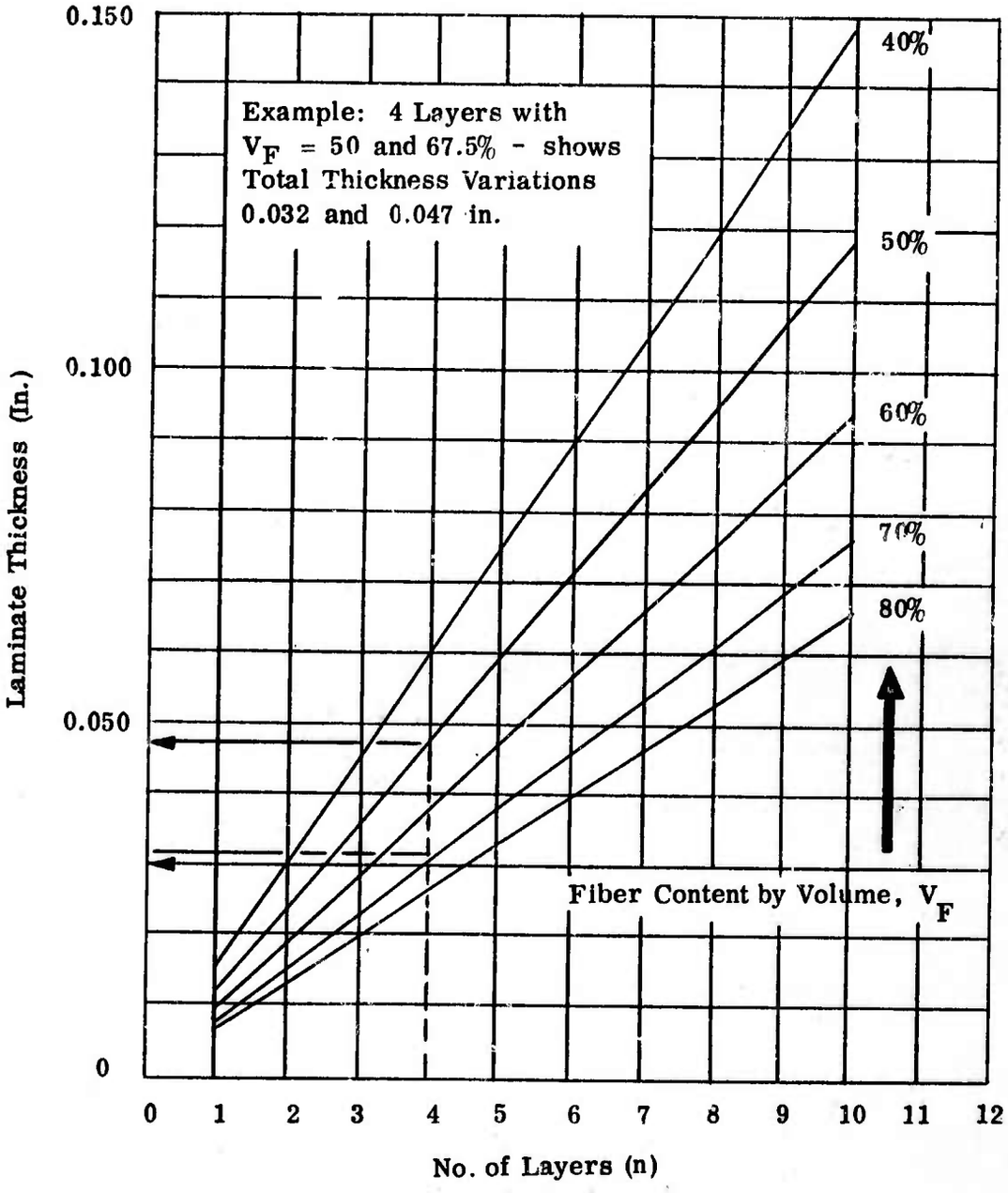

Figure 285. Variation of Laminate Thickness with Number of Layers and Fiber Content

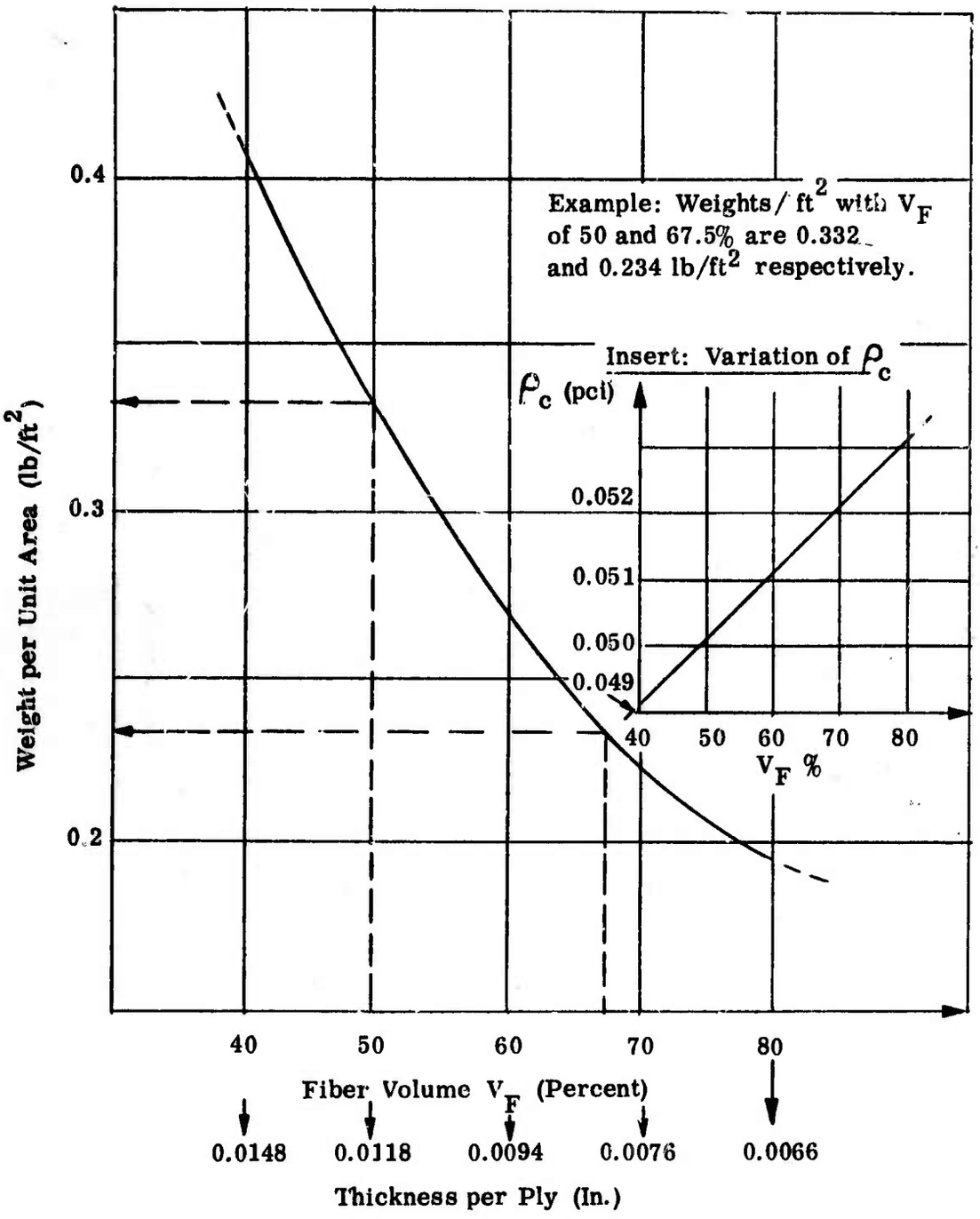

Figure 286. Variation of Weight per Square Foot (4 Layers) with Fiber Content

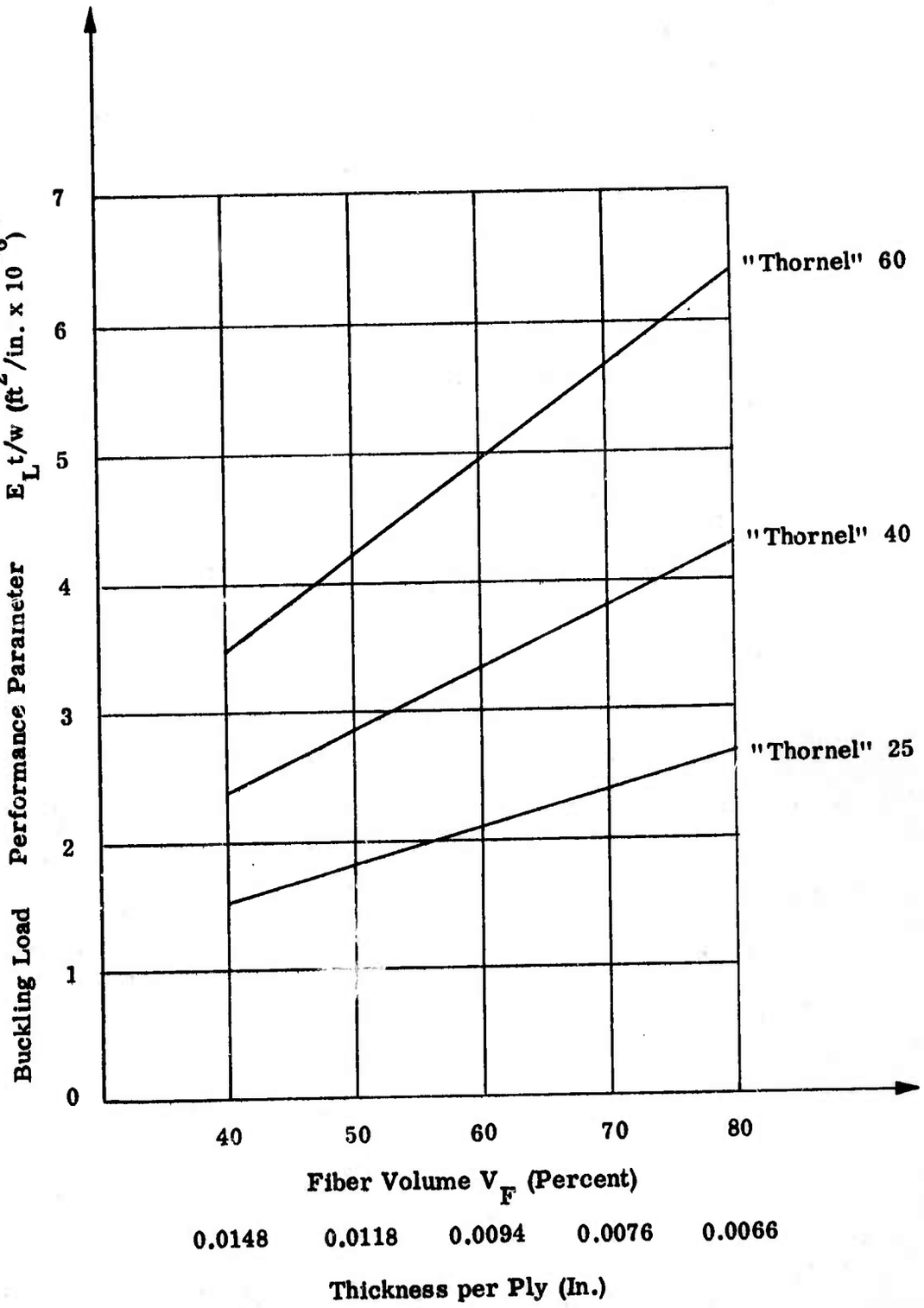

Figure 287. Variation of Column Buckling Performance Parameter with Fiber Content

laminate may be greatly decreased. This result is due to the fact that the thickness per layer is decreased, an effect which more than balances out the beneficial increase in E_L. This effect is next examined for a particular laminate type being considered for the fuselage component skin.

Two four-layer orthogonal laminates have been evaluated, a (0, 90, 0, 90°) and a (90, 0, 0, 90°) lay-up. Laminates in "Thornel" 25, 40, and 60 were examined, having fiber contents varying from 25 to 80%. The variation of thickness per layer was obtained using the curve on Figure 284 and extrapolations thereof. The basic fiber (anisotropic) and matrix properties of Section VIII B were used as inputs to determine the bending stiffnesses.

The initial buckling stresses for a long, flat, simple-supported orthotropic plate are (Reference 86):

Compression - $$\sigma_{CR} = \frac{2\pi^2}{tb^2} \left\{ D_3 + \sqrt{D_1 D_2} \right\}$$

Shear - $$\tau_{CR} = \frac{2\pi^2}{tb^2} \left\{ D_3 + 1.65\sqrt{D_1 D_2} \right\} \sqrt[4]{D_2/D_1}$$

where b is the plate width.

These parameters were calculated for each type of plate, and the results are presented as curves on Figures 288-291 inclusive. The curves are shown dotted for $V_F < 40\%$ and $V_F > 75\%$, indicating lack of confidence in the calculated results because of no experimental data for the V_F-t curve in these ranges.

Figures 288-291 show that, for a fixed number of plies (4), increasing the fiber content reduces the buckling performances in all cases. The highest performances are predicted using the lower fiber contents (40-50%). The use of higher fiber moduli gives increased performances for a fixed resin content over the whole range of V_F used. Alternatively, equal performances (strength/weight ratios) are seen for low modulus, low resin content systems compared with high modulus, high resin content systems. Also, for all combinations of "Thornel" type and V_F, the (0, 90, 0, 90°) plate is more efficient in both compression and shear than the (90, 0, 0, 90°) plate. As noted in the preliminary design work (Section X A), the shear buckling allowables are found to be greater than the compression buckling allowables.

At very low fiber contents (< 40%), there will exist a strength cutoff due to reduced laminate longitudinal strength. In the higher range of fiber contents (> 70%), matrix strain magnification effects will reduce transverse strength and give a second strength cutoff. Within these limits ($40 < V_F < 70\%$), buckling strength may best be provided using the lower fiber contents, except in those cases where the addition of extra layers is possible and does not result in over-design.

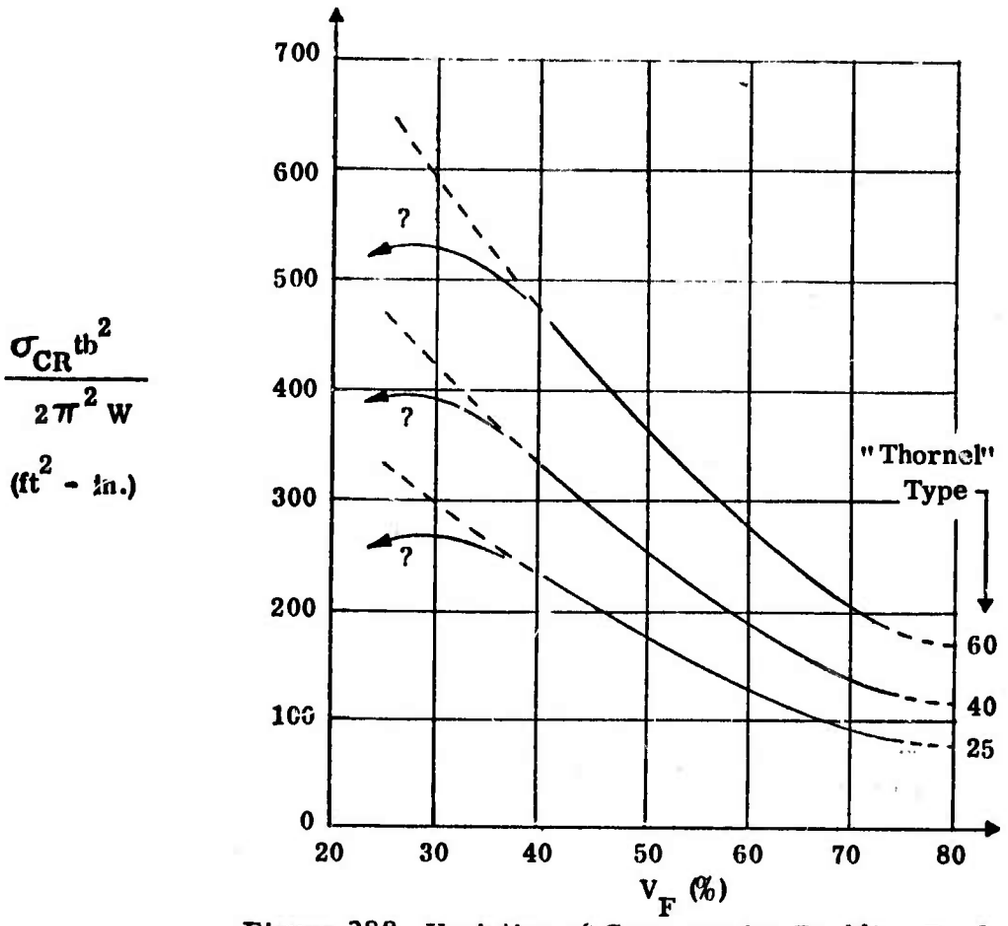

Figure 288. Variation of Compressive Buckling Performance with Fiber Content for a (0, 90, 0, 90°) Plate

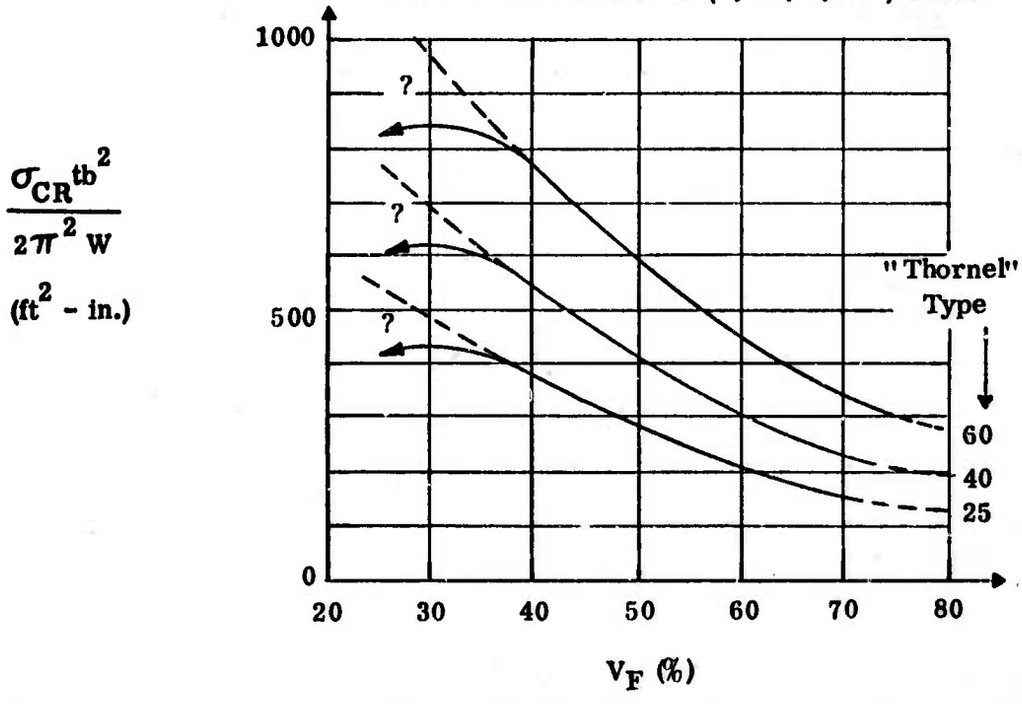

Figure 289. Variation of Shear Buckling Performance with Fiber Content for a (0, 90, 0, 90°) Plate

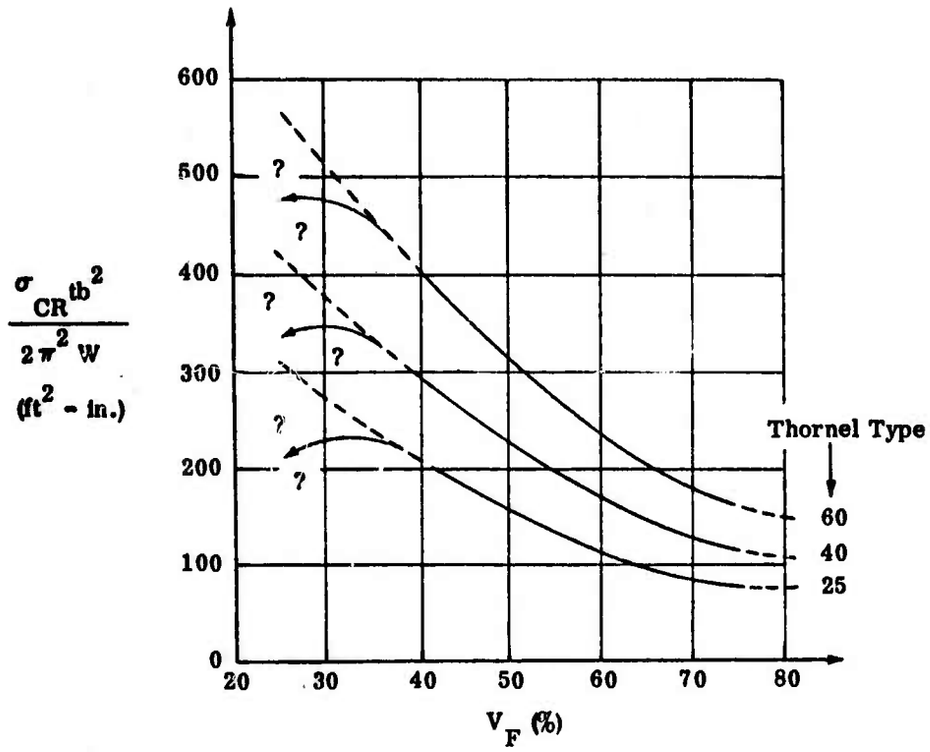

Figure 290. Variation of Compressive Buckling Performance with Fiber Content of a (90, 0, 0, 90°) Plate

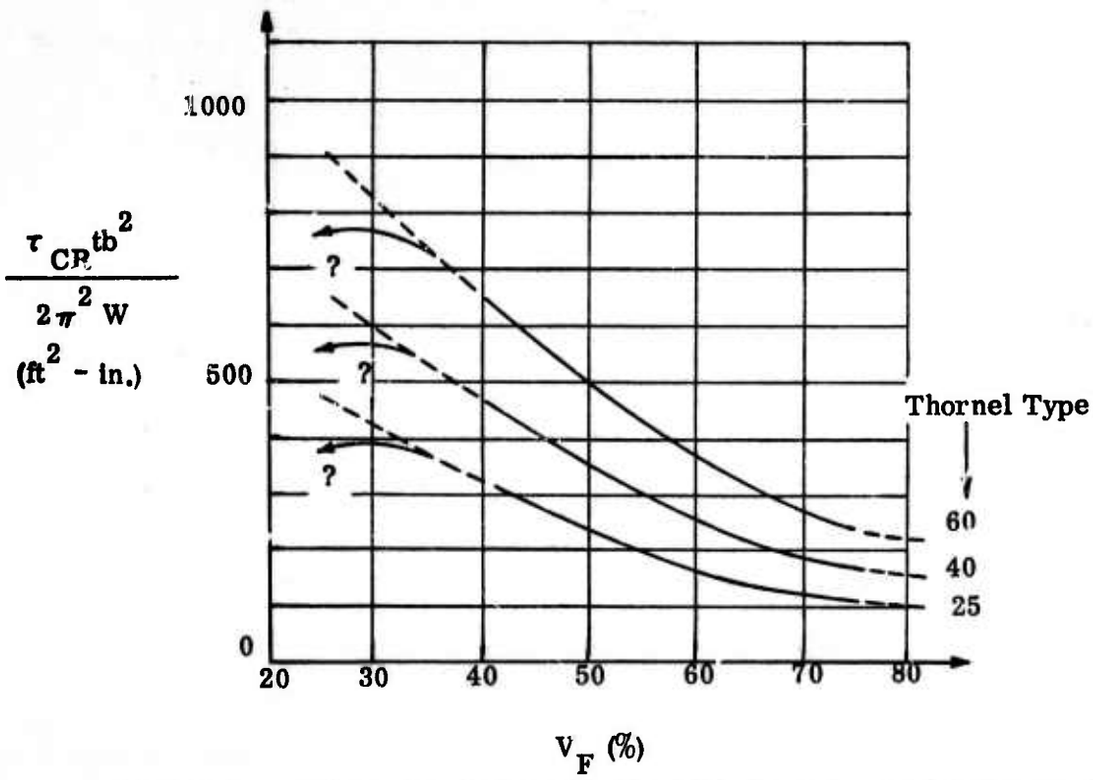

Figure 291. Variation of Shear Buckling Performance with Fiber Content of a (90, 0, 0, 90°) Plate

Throughout this study, the fiber content-lamina thickness relationship has been of over-riding importance. Due to the peculiar microstructure of graphite reinforced composites, this relationship is not obtainable analytically. This thought underlines the fact that although sophisticated analytical methods are available for composite structures, they are severely restricted without inputs which reflect sufficiently well the physical realities of the problem. This work is thus considered to open up further both design and fabrication optimization studies for composite structures i.e., optimizing resin content, ply thicknesses, etc. for various elements (skin, stiffeners, and rings) of the representative fuselage component.

E. Design of Stiffening Rings

(W. N. Meholick, K. H. Sayers, and D. P. Hanley, Bell Aerosystems)

Design studies have been made on various structural configurations for the fuselage component stiffening rings. These studies were made for the purpose of analyzing the existing and alternate designs to determine their respective strength and stiffness characteristics in conjunction with the possibilities of simplifying fabrication.

Illustrated in Figure 292 are three basic alternate stiffening ring configurations (Designs 1A, 2A, and 3A) and three simplified versions of these (Designs 1B, 2B, and 3B). These configurations differ from the ring concept presented in Section X A in that they utilize the skin of the component to provide bending stiffness for the ring.

The ring concept shown previously (Section X A) is called the "floating" ring type because the ring is placed inside the stringers and is not attached to the skin in a continuous manner. Because of this, the floating ring type excludes the skin stiffness in resisting "rolling" of the ring and does not have good stringer-to-ring interconnection. The addition of shear ties between the stringers that connect the skin to the stringer web and outer flange of the ring can improve this interconnection appreciably at the expense of weight and hand-assembly of shear clips, etc. The magnitude of the forces between the stringers and ring design described in Section X A has been obtained from the analysis of Section X G and will be applied in evaluation of the final ring design.

Presented in this section are descriptions of the alternate ring designs, the structural function the ring serves, and the methods used for including ring stiffness properties in the component analysis. Included also is a summary of various core materials that have potential use in the fabrication of each ring type.

1. Description of Alternate Rings

Design 1 in Figure 292 is made from two separate pieces bonded with a core material separating them. Each piece for Type A has a channel cross-sectional shape while each piece for Type B eliminates the channel "sides" utilizing mostly flat elements. Both types trap the stringer between the ring and the outer skin to restrain its radial displacement. Another important feature of this design is that stresses across the thickness of the stringer webs are practically eliminated. Such stresses

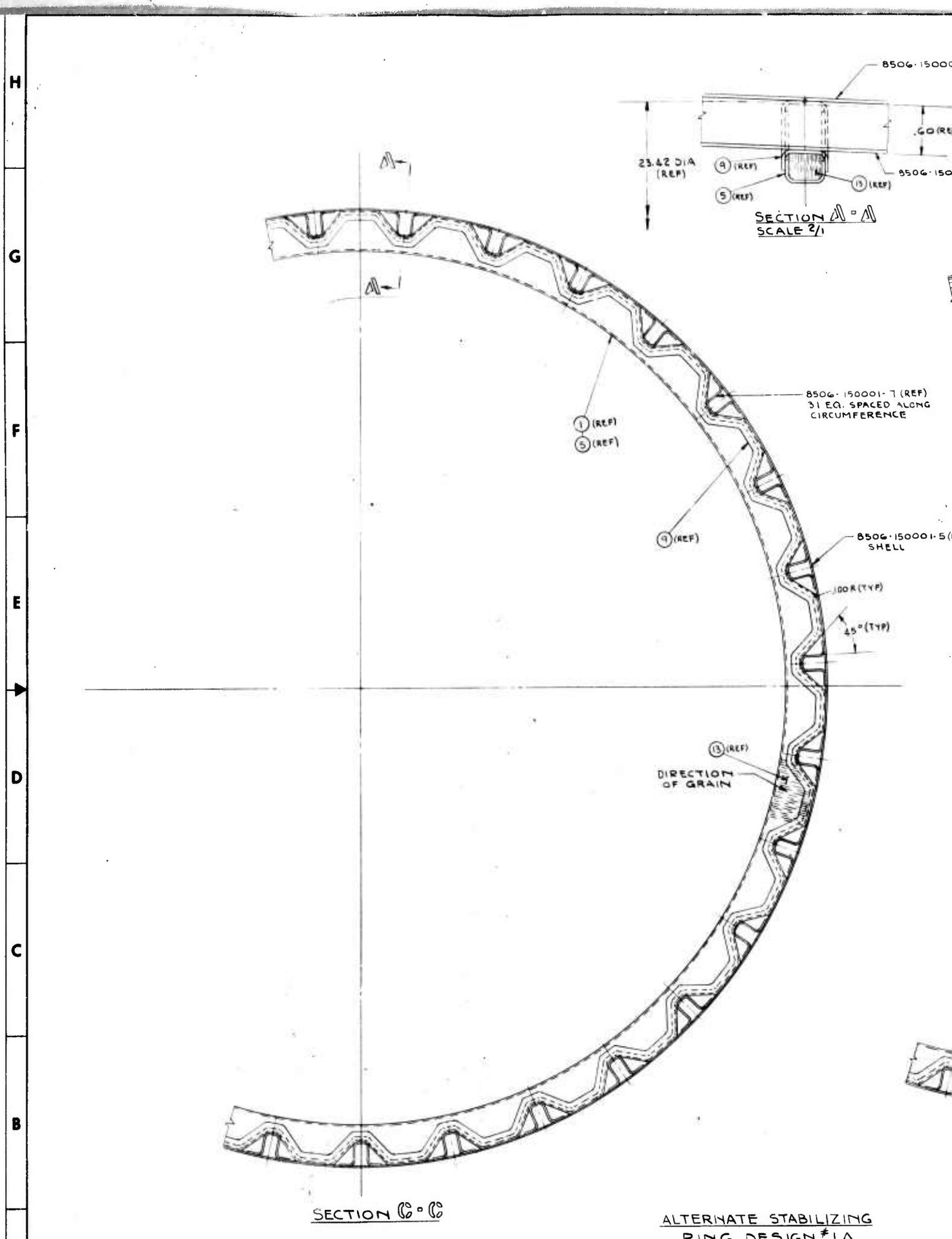

ALTERNATE STABILIZING RING DESIGN #1A

A.

8506-150001-5 (REF)

.60 (REF)

8506-150001-7 (REF)

(12) (REF)

SECTION A-A
SCALE 2/1

8506-150001-5 (REF)

.040 .08R (TYP)

.25 (TYP)

(12) (REF)

1.00

DIRECTION OF GRAIN

(9) (REF)

.040

(16) (REF)

.08R (TYP)

.50

20.42 DIA (REF)

SECTION B-B
SCALE 2/1

20.42 DIA (REF)

(88) (REF)

1.00

(92)

.50

.040

.040

SECTION D-D
SCALE 2/1

8506-150001-7 (REF)
EQ. SPACED ALONG
CIRCUMFERENCE

(4) (REF)

(8) (REF)

(12) (REF)

20.42 DIA (REF)

(96) (REF)

(88) (REF)

(92) (REF)

SECTION C-C
SCALE 2/1

8506-150001-5 (REF)
SHELL

.100R (TYP)

45° (TYP)

(96) (REF)

(92) (REF)

(84) (REF)

(86) (REF)

C C

B B

A A

SECTION D-D (PARTIAL)

ALTERNATE STABILIZING
RING DESIGN 1B

(16) (REF)

DIRECTION OF GRAIN

B.

SECTION D-D

2 82
6 86
10 90
14 94

3 83
7 87
11 91
15 95

C C

D D

22.42 DIA

21.42 DIA

20.42 DIA

4 84
8 88
12 92
16 96

23.42 DIA

81 1
85 5
89 9
93 13

6.00 (REF)

12.00 (REF)

12.00 (REF)

12.00 (REF)

C C

D D

IZING
#1A

8506-150003

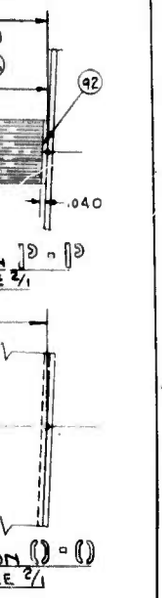

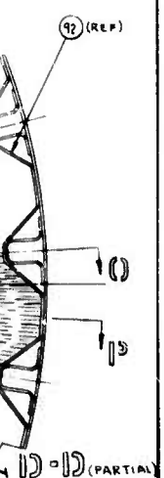

ABILIZING
N 1B

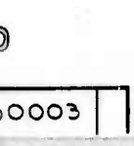

50003

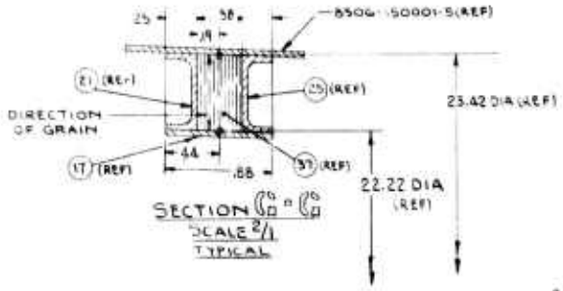

SECTION ⌀ ⌀
SCALE 2/1
TYPICAL

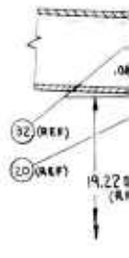

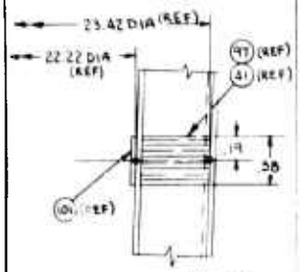

SECTION ⌀ ⌀
SCALE 3/1

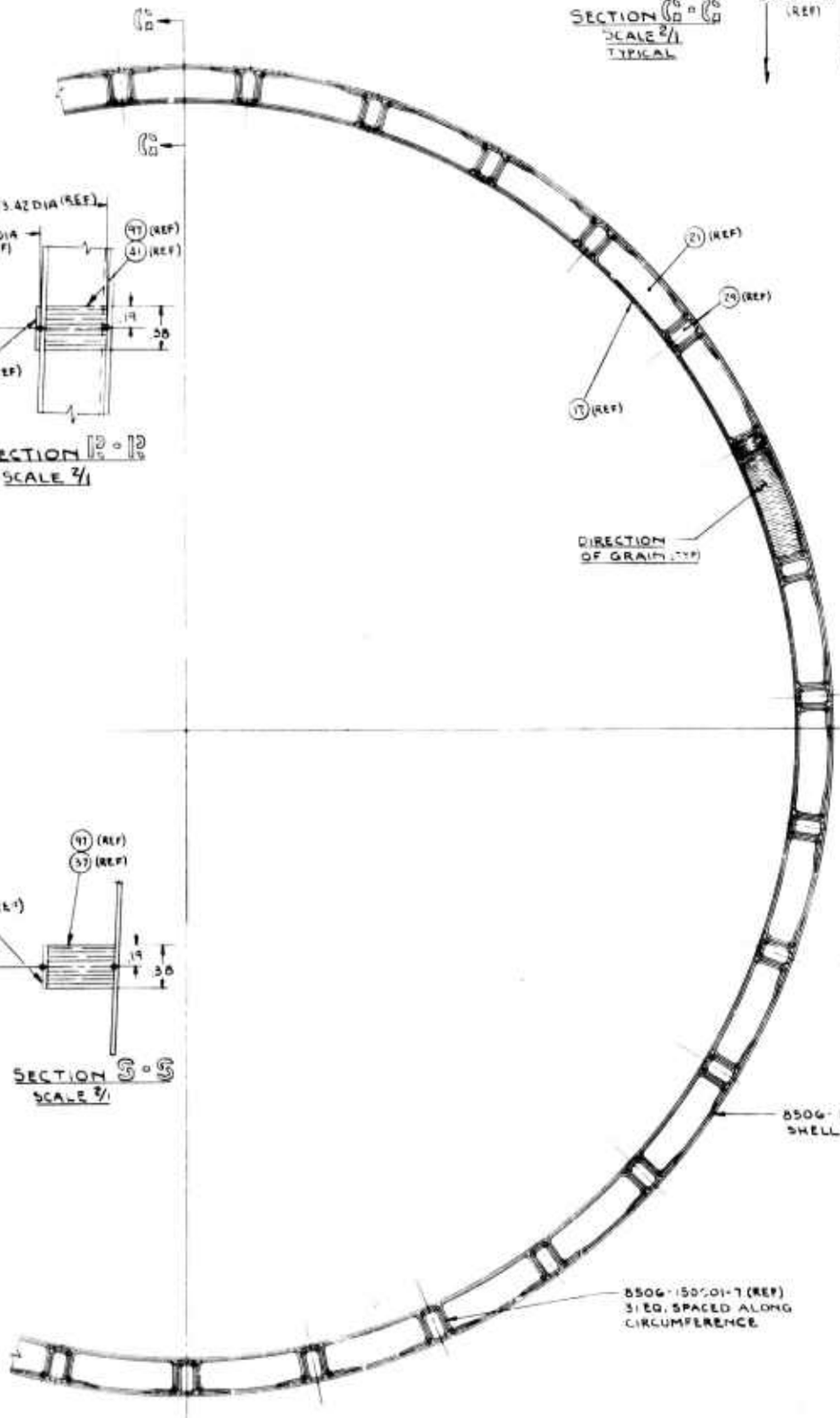

SECTION ⌀ ⌀

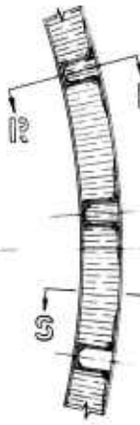

SECTION ⌀ ⌀ (PARTIAL)
ALTERNATE STABILIZING
RING DESIGN #2B

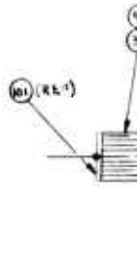

SECTION S-S
SCALE 3/1

SECTION ⌀ ⌀

ALTERNATE STABILIZING
RING DESIGN #2A

2.

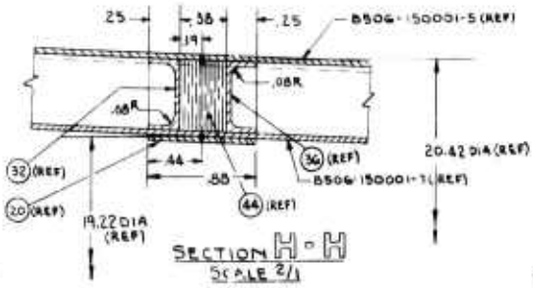

SECTION H-H
SCALE 2/1
TYPICAL

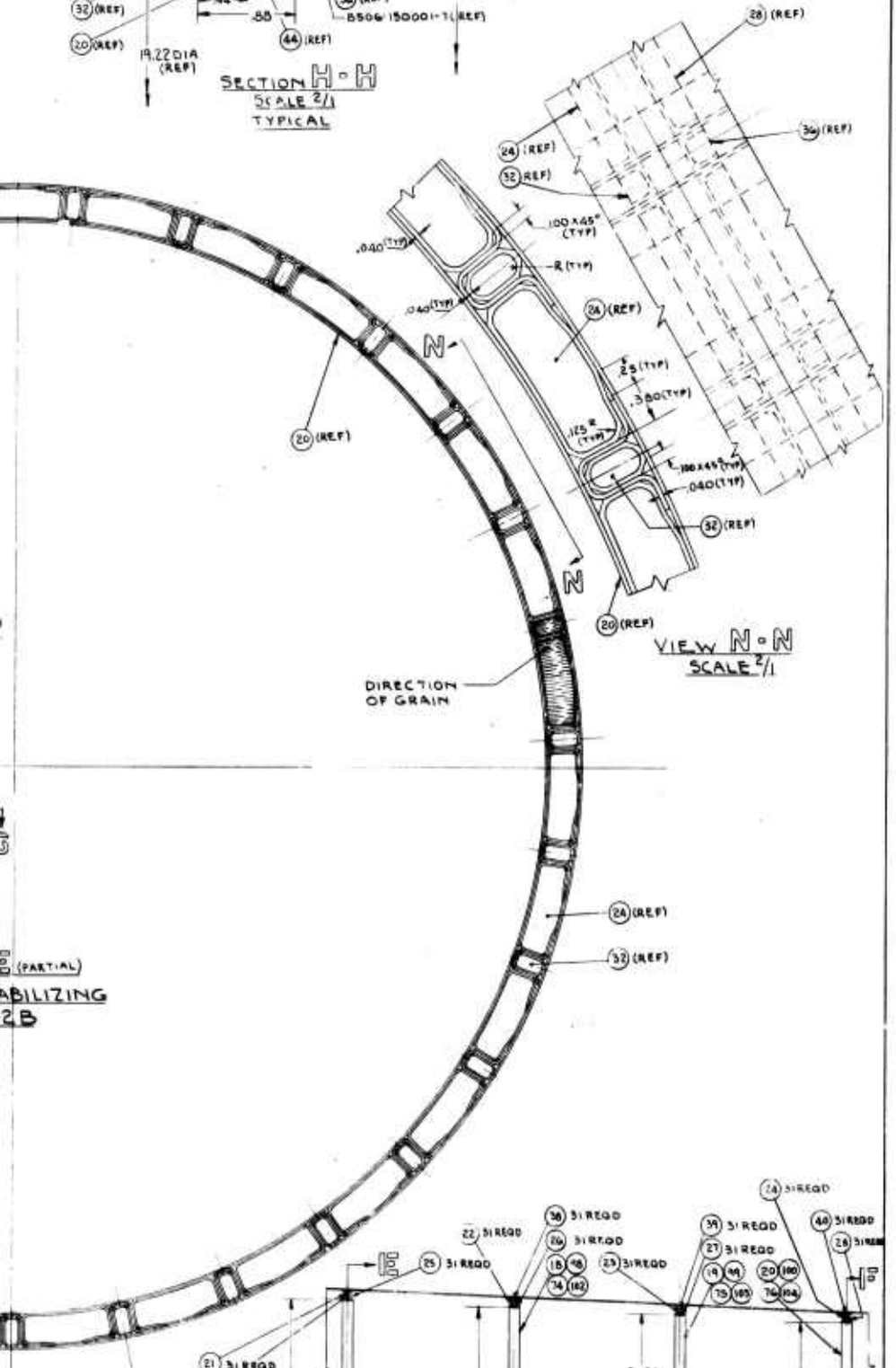

VIEW N-N
SCALE 2/1

ABILIZING
2B

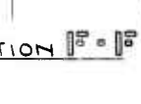

TION 1"=1"

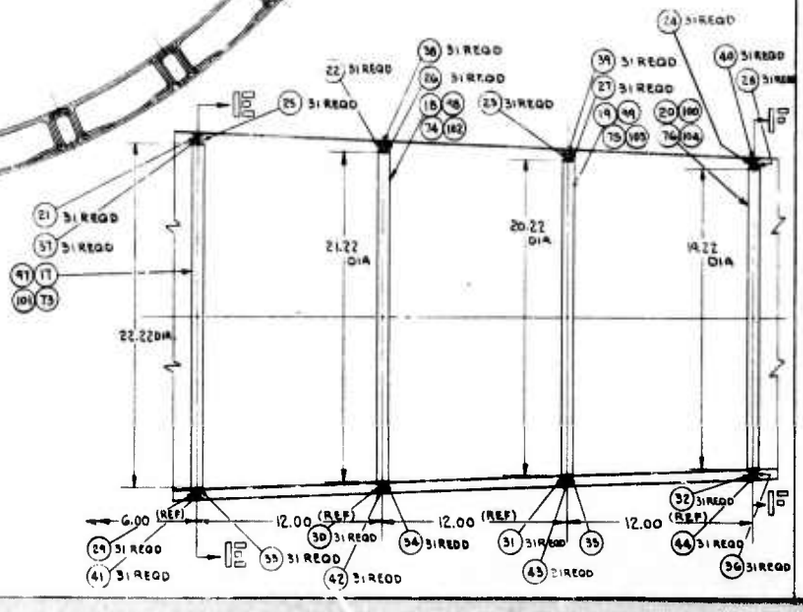

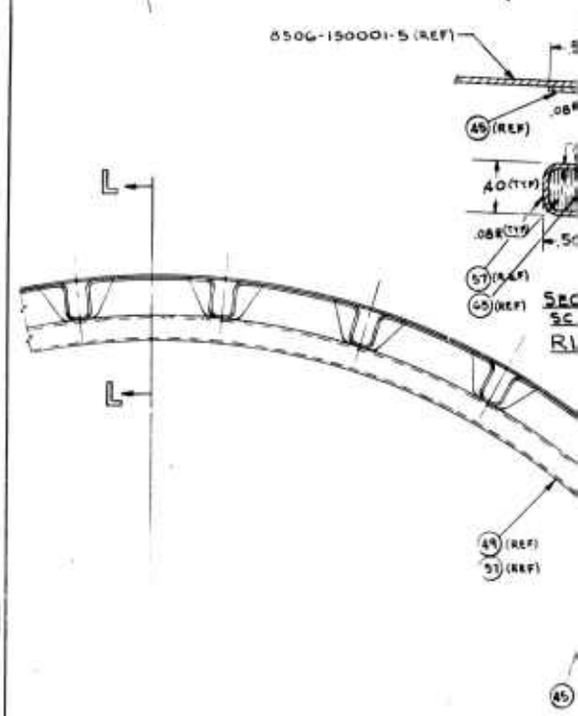

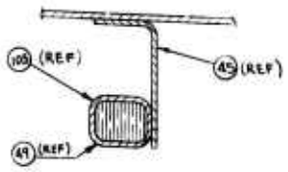

SECTION L-L
SCALE 2/1
RING DESIGN #3B

D.

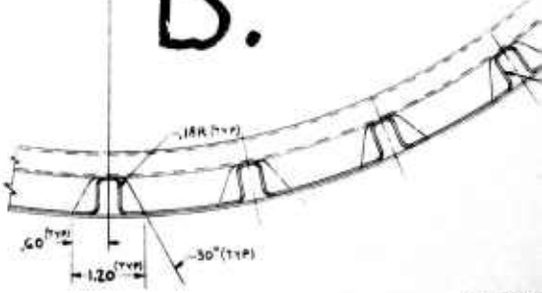

SECTION J-J

ALTER
RING

8506-150003

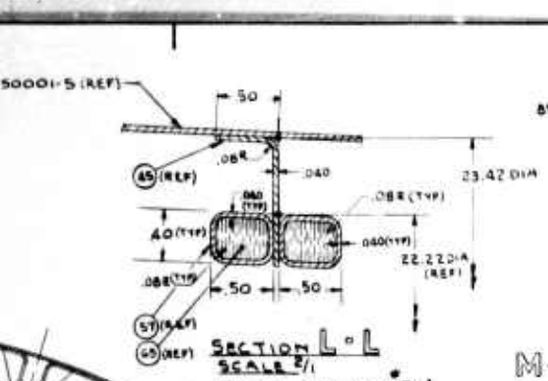

SECTION L-L
SCALE 2/1
RING DESIGN #3A

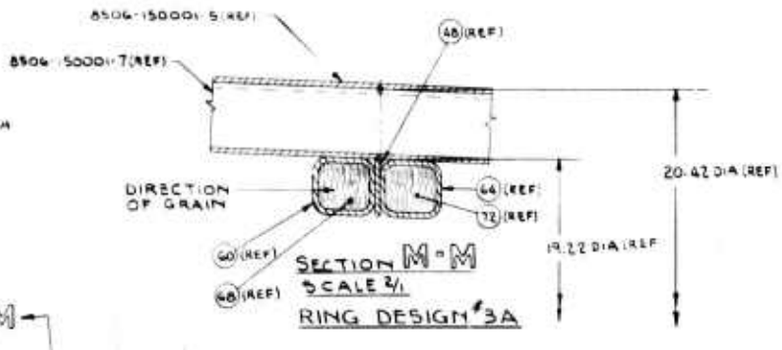

SECTION M-M
SCALE 2/1
RING DESIGN #3A

4 APPLY EPOX
ASSEMBLY PE
SUGGESTED
100 PARTS
5 PARTS
8 PARTS
AND CURE

3 PURCHASE FR
KILN DRIED

1 MATERIAL S
FIBER
BINDER
FIBER OR

NOTES

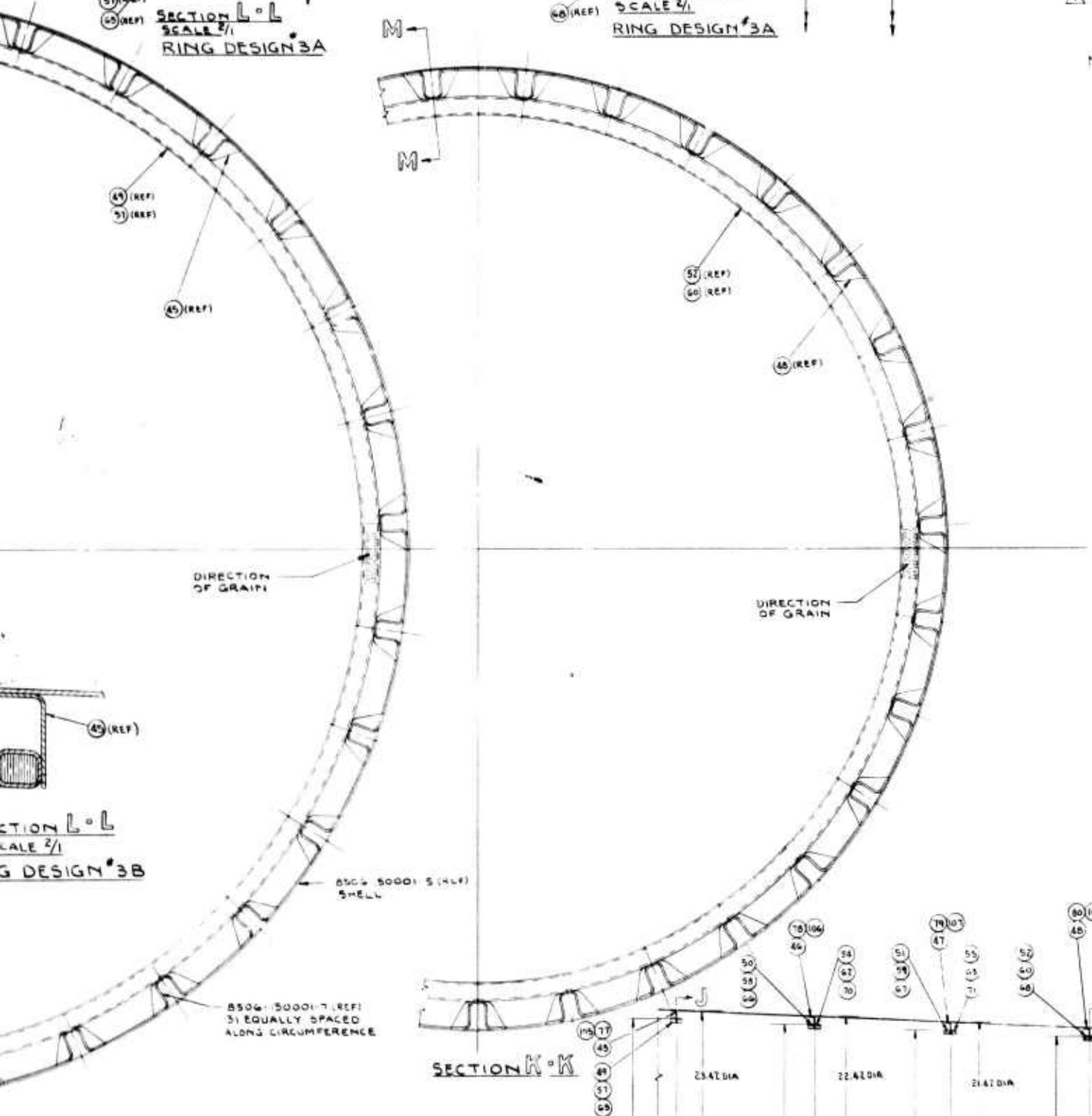

CTION L-L
CALE 2/1
G DESIGN #3B

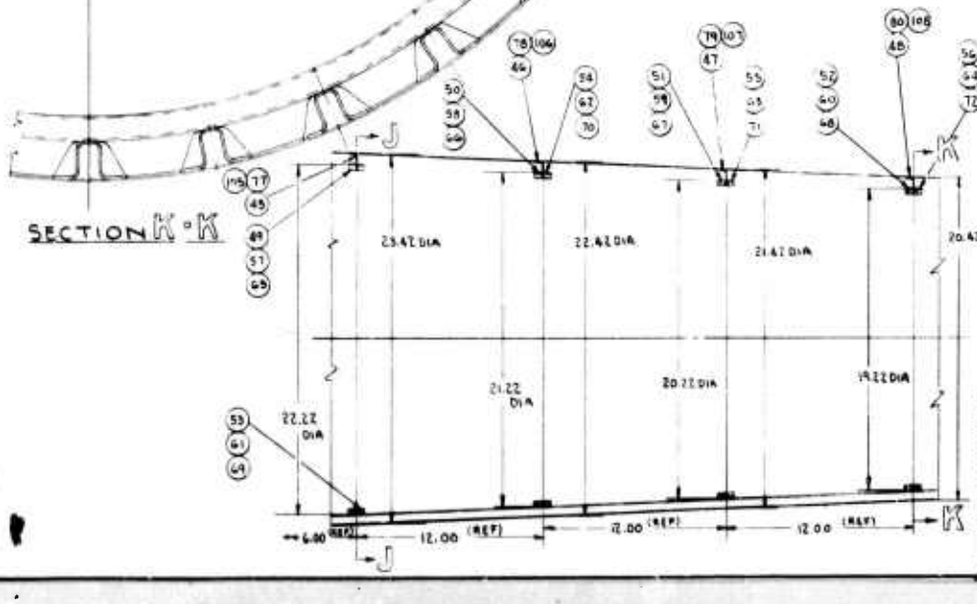

SECTION K-K

ALTERNATE STABILIZING
RING DESIGN #3A & 3B

E.

60003

4. APPLY EPON 828 ADHESIVE TO THE CORE AS A SEALER PRIOR TO ASSEMBLY PER THE REQUIREMENTS OF PARA 6.3 OF BPS 42.74 A
SUGGESTED FORMULA:
100 PARTS OF EPON 828
15 PARTS OF VERSAMID 140
8 PARTS OF DIETHYLENE TRIAMINE
AND CURE AT ROOM TEMPERATURE OR 150°F

3. PURCHASE FROM BALSA EQUADOR LUMBER CORP
KILN DRIED WITH 12% MOISTURE CONTENT AT 6LBS PER CU. FT. DENSITY

1. MATERIAL SPECIFICATION AS FOLLOWS:
FIBER — THORNEL 25 70-30 WEIGHT RATIO
BINDER — ERL 2256/MPDA
FIBER ORIENTATION TO BE DETERMINED

F.

NOTES.

FIND NO.	CODE IDENT	PART OR IDENTIFYING NO.	NOMENCLATURE OR DESCRIPTION	MATERIAL OR NOTE	COMMERCIAL DESIGNATION	SPECIFICATION
81			EPON 828 ADHESIVE FILLER MIXTURE 4			
80		8506-150003-85	FRAME INSTALL			
79		8506-150003-87	FRAME INSTALL			
78		8506-150003-53	FRAME INSTALL			
77		8506-150003-55	FRAME INSTALL			
76		8506-150003-51	FRAME INSTALL			
75		8506-150003-49	FRAME INSTALL			
74		8506-150003-47	FRAME INSTALL			
73		8506-150003-45	FRAME INSTALL			
72		8506-150003-103	CORE		BALSA	BPS 42.74 A
71		8506-150003-41	CORE			
70		8506-150003-39	CORE			
69		8506-150003-137	CORE			
68		8506-150003-135	CORE			
67		8506-150003-33	CORE			
66		8506-150003-131	CORE			
65		8506-150003-129	CORE		BALSA	BPS 42.74 A
64		8506-150003-127	RING			
63		8506-150003-125	RING			
62		8506-150003-123	RING			
61		8506-150003-121	RING			
60		8506-150003-119	RING			
59		8506-150003-117	RING			
58		8506-150003-115	RING			
57		8506-150003-113	RING			
56		8506-150003-111	FRAME ASSY			
55		8506-150003-189	FRAME ASSY			
54		8506-150003-83	FRAME ASSY			
53		8506-150003-105	FRAME ASSY			
52		8506-150003-109	FRAME ASSY			
51		8506-150003-101	FRAME ASSY			
50		8506-150003-99	FRAME ASSY			
49		8506-150003-97	FRAME ASSY			
48		8506-150003-95	FRAME			
47		8506-150003-93	FRAME			
46		8506-150003-91	FRAME			
45		8506-150003-89	FRAME			
44		8506-150003-87	CORE		BALSA	BPS 42.74 A
43		8506-150003-85	CORE			
42		8506-150003-83	CORE			
41		8506-150003-81	CORE			
40		8506-150003-79	CORE			
39		8506-150003-77	CORE			
38		8506-150003-75	CORE			
37		8506-150003-73	CORE		BALSA	BPS 42.74 A
36		8506-150003-71	STRINGER REINF.			
35		8506-150003-69	STRINGER REINF			
34		8506-150003-67	STRINGER REINF.			
33		8506-150003-65	STRINGER REINF			
32		8506-150003-63	STRINGER REINF			
31		8506-150003-61	STRINGER REINF			
30		8506-150003-59	STRINGER REINF			
29		8506-150003-57	STRINGER REINF			
28		8506-150003-55	INTERCOSTAL			
27		8506-150003-53	INTERCOSTAL			
26		8506-150003-51	INTERCOSTAL			
25		8506-150003-49	INTERCOSTAL			
24		8506-150003-47	INTERCOSTAL			
23		8506-150003-45	INTERCOSTAL			
22		8506-150003-43	INTERCOSTAL			
21		8506-150003-41	INTERCOSTAL			
20		8506-150003-39	BAND			
19		8506-150003-37	BAND			
18		8506-150003-35	BAND			
17		8506-150003-33	BAND			
16		8506-150003-31	CORE		BALSA	BPS 42.74 A
15		8506-150003-29	CORE			
14		8506-150003-27	CORE			
13		8506-150003-25	CORE		BALSA	BPS 42.74 A
12		8506-150003-23	RING CAP			
11		8506-150003-21	RING CAP			
10		8506-150003-19	RING CAP			
9		8506-150003-17	RING CAP			
8		8506-150003-15	RING			
7		8506-150003-13	RING			
6		8506-150003-11	RING			
5		8506-150003-9	RING			
4		8506-150003-7	RING ASSY			
3		8506-150003-5	RING ASSY			
2		8506-150003-3	RING ASSY			
1		8506-150003-1	RING ASSY			

QTY REQD: -105 -97 -95 -93 -91 -89 -87 -85 -83 -81 -79 -77 -75 -73 -71 -69 -67 -65 -63 -61 -59 -57 -55 -53 -51 -49 -47 -45 -43 -41 -39 -37 -35 -33 -31 -29 -27 -25 -23 -21 -19 -17 -15 -13 -11 -9 -7 -5 -3 -1

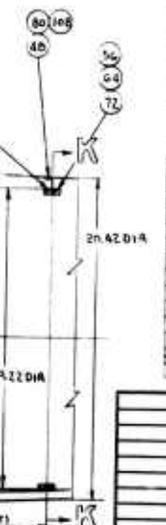

PARTS LIST

ECO NO.	NUMBER	NEXT ASSY	USED ON
APPLICABLE SPECIFICATIONS		APPLICATION	

HOLE TOLERANCES EXCEPT AS SHOWN
.000 TO .120 ± .002 — .000
.130 TO .250 ± .004 — .000
.251 TO .499 ± .006 — .000
.500 TO .750 ± .010 — .000
.750 TO .999 ± .012 — .000
.000-000 LARGER ± .015

UNLESS OTHERWISE SPECIFIED DIMENSIONS ARE IN INCHES. TOLERANCES ON DECIMALS: X ± .1, XX ± .03, XXX ± .010, ANGLES ± 0° 30'
UNLESS OTHERWISE SPECIFIED BREAK ALL SHARP EDGES APPROX .015 R OR CHAMFER
MACHINED SURFACES EXCEPT AS NOTED ✓
SUPERSEDES | SUPERSEDED BY

DESIGN T. PAHOL 3/5/67
GROUP
APPD 1-27-67
WT
CHECK
STRESS
REL
CONTRACT NO.

BELL AEROSYSTEMS COMPANY
A TEXTRON COMPANY
POST OFFICE BOX ONE BUFFALO, NEW YORK 14240

ALTERNATE STABILIZING RING DESIGNS-CARBON FIBER/EPOXY RESIN
COMPONENT #1

SIZE J | CODE IDENT NO. 80070 | 8506-150003
SCALE 1/4 INCH | SHEET 1 OF 2

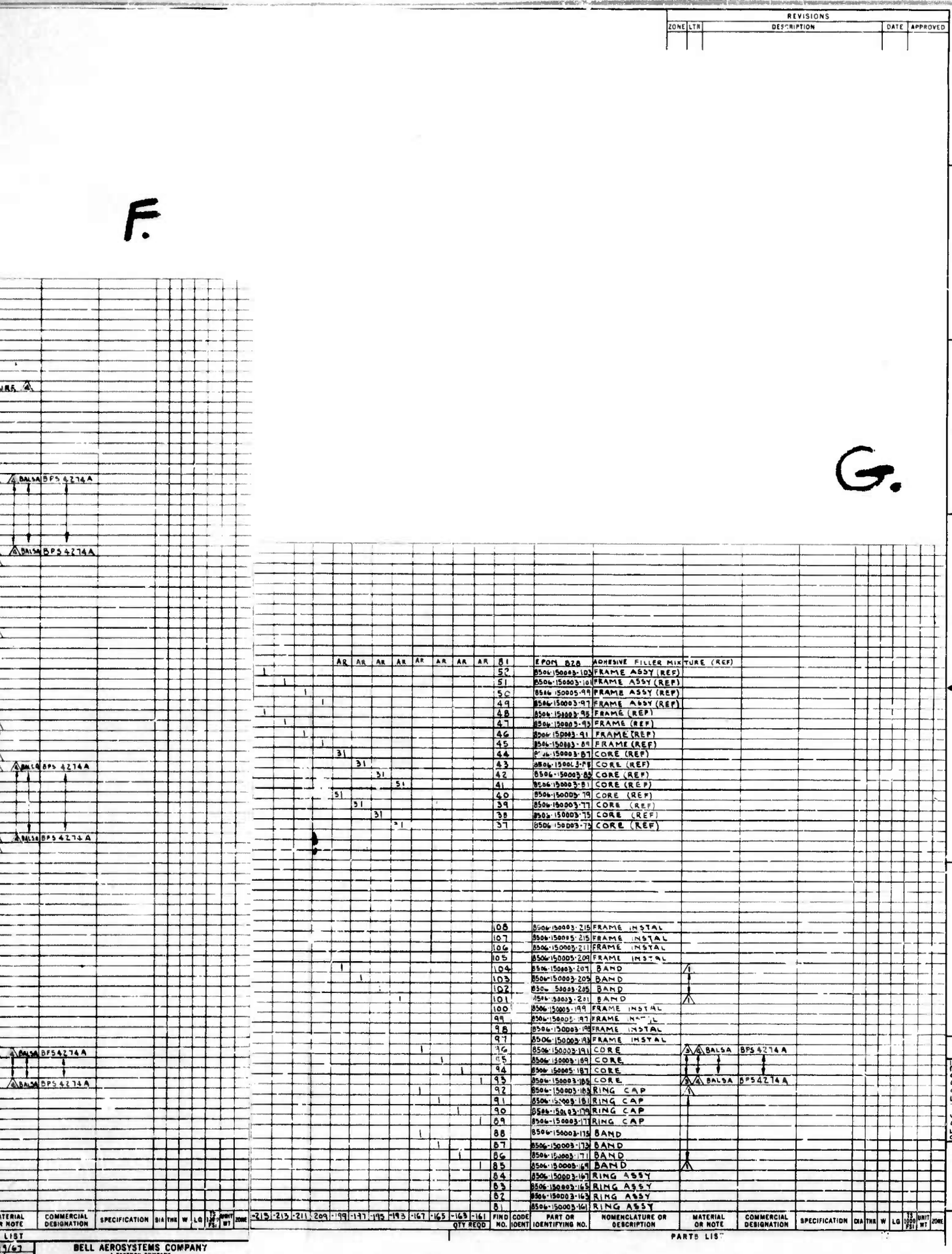

Figure 292. Alternate Stabilizing Ring Designs Carbon Fiber/Epoxy Resin Component

might cause splitting of the stringer webs, especially if unidirectional stringers are used.

Design 2A is made by running a plate element around the periphery just inside the stringer and filling the space between and inside the stringer with core material and side elements (intercostals). The side elements in Type A are "bath-tub" shapes fabricated in a matched mold process; in Type B, the intercostals are eliminated. Stresses across the stringer webs might be serious for Type A because of the intercostal attachment to the stringers. Design 2B, although the simplest to fabricate, is inefficient if high stiffness is desired. The former design, Type A, is considered structurally efficient but could cause fabrication problems with respect to cost and control of tolerances.

Design 3 is intended to improve on the floating ring type concept by making the cross section simpler and adding a shear tie to the skin. Type A merely adds another ring to eliminate the eccentricity of the shear tie characteristics of Type B.

In summary of the concepts presented thus far and with due regard to the discussion to follow in this report section, the approach offered by design concept 1A is presently favored. Further work will concentrate on this design approach with the alternates held as "back-up".

2. Core Materials

The ring designs shown on Figure 292 require a core material to provide stability and to carry shear loads. Summarized in Table LXXII are the physical and mechanical properties of several high strength "military grade" aluminum honeycomb, balsa wood, and hetro and syntactic foam core materials.

The core material presently considered most promising is balsa wood at six pcf with an Epon 828 mixture as a surface sealer. This core is relatively inexpensive and is expected to provide adequate strength and modulus pending further studies of output data as in Section X G. The aluminum honeycomb core is the strongest of all those presented at the same weight; however, its initial and fabrication costs are higher. The reliability of aluminum honeycomb in corrosive environments makes it the preferred choice for actual aircraft fuselage structures.

3. Ring Structural Functions

The prime function of a stiffening ring is to break the stringers into short column lengths so they are stable when loaded in compression. Ring stiffness that restrains radial displacement affects the number of half-wave buckles in the longitudinal direction (Reference 87). When the half-wave number m is equal to the number of rings minus one, the ring stiffness is sufficient to provide a simple support to the stringer column and the general instability mode is of the Euler or panel buckling (instability) type. The effect of ring stiffness on the general instability allowable and the corresponding values of m is shown on Figure 293 and will be discussed later.

TABLE LXXII

SUMMARY OF VARIOUS STABILIZING CORE MATERIALS

Aluminum Alloy Honeycomb			Balsa Wood	Balsa Ecuador Lumber Corporation 12% Moisture			Hetro Foam-Durez Plastics				Syntactic Foam-PVC. (Polyvinyl Chloride)			
Property	Military Grade 1/8-5052-0.0015	Flexcore	Property	6 pcf	11 pcf	15 1/2 pcf	Property	6 pcf	10 pcf	20 pcf	Property	Vinylcor	Rigicell	Plasticell
Supplier	Hexcell	Hexcell	Compression Strength P.L. psi				Compr. Strength 75°F (psi)	150	320	1000	Supplier	Johns Manville	B.F Goodrich	
Cell Size	1/3 in.	3/8 in.	(a) Crush	500	1450	2310					Compression Strength	230-320	206	180
				750	1910	2950					Density	6 pcf	5.5 pcf	5.6 pcf
Foil Type Alloy	5052	5052	E	330	768000	1164000	Tensile Strength (psi)	200	380	980				
			Perpend to Grain											
Foil Gage	0.0015 in.	0.0037 in.		50 [illegible]		145-198	Flexural Strength (psi)	250	500	1200	Compression Modulus	7900-10000	3220	40000
			(b) Crush		100-144									
Density	6.1 pcf	5.7 pcf		5100-16000	13000-37000	19000-53000	Shear Strength (psi)	75	150	370	Flex Strength	355-500		200
							Modulus (psi)							
Compression Strength	950 psi	870 psi	Perpend to Grain				Flexural Compression Shear	4800	10500	30000	Flex Modulus	10000-13000		
			Static Bending											
Compression Modulus	182000	-	Strength P.L.	825	1725	2535		3200	8000	28000				
Shear Strength (Ribbon)	550 psi	355 psi	Modulus of Rupture	1375	3050	4525		1600	3900	13000	Shear Strength		178	150
			E	280000	625000	925000	Description	Hetrofoam 368 Polyphenyl Isocyanates in Fire Retardant High Density Rigid Urethane Foam			Shear Modulus		4380	4000
Shear Modulus (Ribbon)	90000 psi	48000 psi	Tensile Strength											
			(a) Para to Grain	1375	3050	4525					Tensile Strength			250
Shear Strength (Transvese)	325 psi	197 psi	(b) Perpen to Grain	72-118	118-170	156-223								
Shear Modulus (Transverse)	42800 psi	23400 psi	Shear Strain	158-180	298-360	425-522								
Crush Strength	445 psi	382 psi	Recommended Usage End Grain Orientation											
Application	Flat Surfaces	Curved Surfaces												
Adhesive used in Panel Constr	AF-111 Scotch Weld	AF-111 Scotch Weld												
Supplier	3M	3M												
Weight	0.08 psf	0.08 psf												
Thickness	0.015 in.	0.015 in.	Balsa is dipped into liquid adhesive to form a coating. Bonding to carbon fiber pre-preg. tape is accomplished with this coating; therefore, no film adhesive is required. 0.010 in. coating thickness is equivalent to 7.1 x 0.010=0.07 psf											
Peel Strength	18 in.-lb/in.	18 in.-lb/in.												
Flatwise Tens.	1190 psi	1190 psi												
Cure Temp.	250°F	250°F												
Time	60 min.	60 min.												
Pressure	10 psi	10 psi												

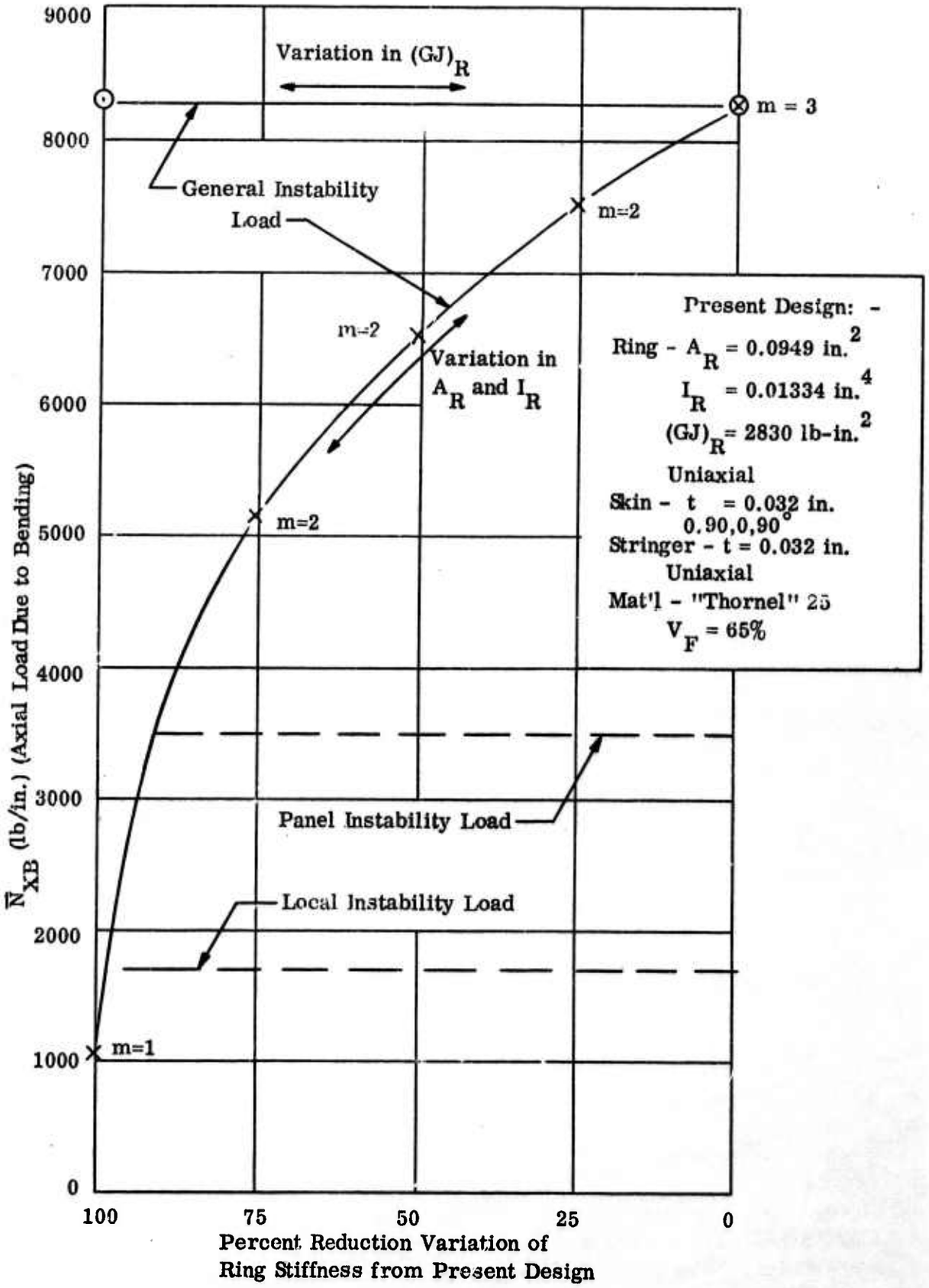

Figure 293. Variation in $\bar{N}_{xb}$ with Ring Stiffeners

Weight variations between designs are small since the ring weight for the representative component is approximately 10 to 15 percent of the total weight. This relationship is true because the design has been based on a fixed ring spacing of 12 inches as a practical geometric constraint. The effects of ring spacing on weight are to be further studied, however. Primarily, though, selecting a design is strongly dependent on the fabrication method and its cost. Some designs offer growth potential if additional area and stiffness are required such as, for example, if the ring had to distribute a concentrated load from a point on the frame to a shear flow in the skin. Qualitative advantages and disadvantages of each design from strength, stiffness, and fabrication standpoints are summarized in Table LXXIII.

TABLE LXXIII

COMPARISONS OF ALTERNATE STABILIZING RING DESIGNS

Alternate Design No.	Comparison/Remarks
1	Type A is torsionally strong - broad range of area and stiffness possibilities - eliminates the possibility of stresses across the stringer thickness - moderately difficult to fabricate.
	Type B is torsionally weak with the same remarks as Type A except that fabrication is simpler.
2	Type A is torsionally strong - limited in area and stiffness possibility, damaging stresses across the stringer thickness may be created - difficult to fabricate.
	Type B is torsionally weak - minimizes stringer transverse stresses - simpler to fabricate.
3	Type A is torsionally strong - symmetric design with respect to skin shear tie - minimizes stringer transverse stresses - fabrication difficulties are moderate.
	Type B is torsionally weak - minimizes stringer transverse stresses - fabrication difficulties are improved.

The individual effect of the ring on the stringer column when cylindrical effects are neglected can be considered as shown in Figure 294 for two stiffening rings stabilizing the column. Timoshenko (Reference 88) states that the spring rate, (here shown provided by the ring) must be equal to $\alpha = \frac{81\ Pe}{L}$ where Pe is the Euler pin - ended column load, $\pi^2\ EI/L^2$, and the buckle mode is as shown. The difficulty

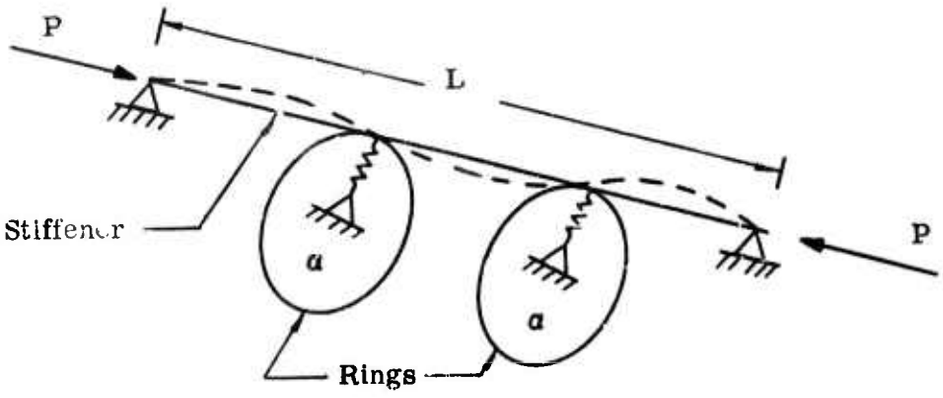

Figure 294. Effect of Ring on Stringer Column

here is determining the effective spring rate to the critical stringer column when several stringers are loaded in compression due to a bending moment. This difficulty can be overcome conservatively with a few simplifying assumptions.

The torsional stiffness of the ring in combination with the bending stiffness that restrains out-of-plane displacements provides an additional stabilizing effect to the stringer column. Appendix B of Reference 89 presents the method for determining this effect. What results, according to the following formula

$$\left(\frac{M}{\theta}\right) = \frac{(EI)_{ring}}{R^2} \qquad \text{(XE-1)}$$

where,

M	=	local stringer bending moment
θ	=	local stringer rotational deflection
EI	=	ring flexural stiffness
R	=	ring radius

is that the ring stiffness provides some column end fixity thus increasing the Euler pin-ended stringer column allowable. This principle illustrates the basic mechanism of ring/stringer column stiffening.

4. Analysis Methods for the Component

The influence of ring stiffness on the instability of orthotropic cylinders in axial compression or bending is presented in Reference 90. This analysis is similar to that of Reference 87.

Small deflection theory is used and the equations include the effects of discrete ring stiffness characterized by a bending stiffness that restrains radial deformation of the shell. Compression and bending loads are treated equally and the rings

are considered torsionally weak, therefore, the analysis neglects the ring torsional stiffening described in the previous report section. The results of the analysis are presented for one shell of a given orthotropy and indicate that the Shanley criterion (Reference 91) for ring stiffness is conservative for small ring spacing ($\ell/R < 0.7$) and is not conservative for large ring spacings ($\ell/R > 0.7$). The representative fuselage component has a ring spacing-to-radius ratio of approximately one, consequently, the Shanley criterion is not adequate for determining minimum ring stiffness.

Referring to Figure 293, shows that the effects of ring torsional stiffness $(GJ)_R$ variation from 2830 lb-in.^{2} to a 100% stiffness reduction (no rings) on the general instability allowable is very slight; however, there is a large effect due to variations in ring area (A_R) and stiffness (I_R). The shape of this curve is similar to that given by Timoshenko (Reference 88). On the basis of this analysis, the ring designs may be compared quantitatively according to torsional rigidity $(GJ)_R$, adequate effective area (A_R), and stiffness, (I_R).

Also, included on Figure 293 are the local and panel stability allowables shown as a comparison with the general instability allowables. The local allowable is based on the compressive buckling stress for the skin plate element between the stringers because this is the widest, hence, most critical, of the skin and stringer plate elements. The panel instability is determined with the assumption that the rings provide simple supports for a shell with a length equal to the ring spacing. The m value for this buckle mode would have to be equal to three. The adequacy of this assumption is obvious; its effect is conservative with regard to the allowable for the shell.

F. Design of End Attachment

(Drs. R. H. Mallett and K. H. Sayers, Bell Aerosystems)

Initial design of the fuselage component (described in Section X A) featured end attachments reinforced with fiberglass elements bonded between the stiffened shell and aluminum loading rings. The main load path from the attachment rings to the shell was through a ring of bolts. Preliminary analysis has shown that this type of attachment is weak due to the low bearing strength of the fiberglass inserts. Two rings of bolts would be required to provide adequate bearing strength. In view of assembly simplifications, however, the design has been modified and present work uses 7075-T6 aluminum reinforcing elements of similar shape to the previous fiberglass ones. Complete "potting" of the end attachment fixtures was also considered briefly, but was discarded because of possible assembly and inspection difficulties. Final analyses will be conducted using discrete element methods, the development of which is now described.

The primary discrete element analysis of the fuselage (Section X G) establishes overall load transfer mechanisms between points of loading and points of support. For the most part, stresses are also available either directly or with limited data reduction.

Refined predictions of stresses are invariably required in localized regions of loading. The fuselage structure demands close examination of the stresses in the

attachment regions, with the objective of determining the stresses arising within and around the joint as load is transferred from the fixtures.

The physical model appropriate for this secondary analysis is shown in Figure 295. This model encompasses a typical circumferential segment in the region between the rigid p tion of the test fixture and the first ring. Figure 296 shows the idealization employed, as established from input data through use of the plotting capability of Bell's computer program.

The secondary analysis model will be subjected to select combinations of axial, shear, and bending loading determined from the primary analysis model. Study of the secondary analysis results will be used to verify the attachment design adequacy.

G. Discrete Element Stress Analysis of Fuselage Shell
(Dr. R. H. Mallett, Bell Aerosystems)

Details of the ring and stringer stiffened fuselage shell together with test fixture attachments were given earlier in this report section and property data were given in Section VIII B. The shell discrete element idealization, based on these inputs, is shown in Figure 297. Orthotropic thin-shell quadrilateral elements are employed to model the conic shell. Frame elements are employed to model the eccentric stabilizing rings and longitudinal s' feners as well as the end attachment loading rings.

Linear stress and displacement analyses have been conducted for each of the loading conditions defined in the experimental testing program. The numerical results for the shear loading condition have been converted to a graphical presentation. The loading condition was considered in the previous stiffened cylinder example problem of Section IX (Figure 245). The displacement predictions are shown in Figures 298 and 299. In contrast with the ring stiffened cylinder example, no appreciable ring deformations are induced in the fuselage structure. Two factors account for this difference in displacement behavior. Firstly, the stiffness of the rings relative to the shell is much greater for the fuselage component. Secondly, the end shear loading on the fuselage component is distributed over the end ring.

Based on preliminary data reduction, a longitudinal stress profile at the cantilever root-section is illustrated in Figure 300 This plot indicates that the combination of ring and stringer stiffening employed yields a gross behavior pattern closely resembling a beam for the transverse cantilever loading; however, the skin stress discontinuities produced by the stiffeners are clearly seen.

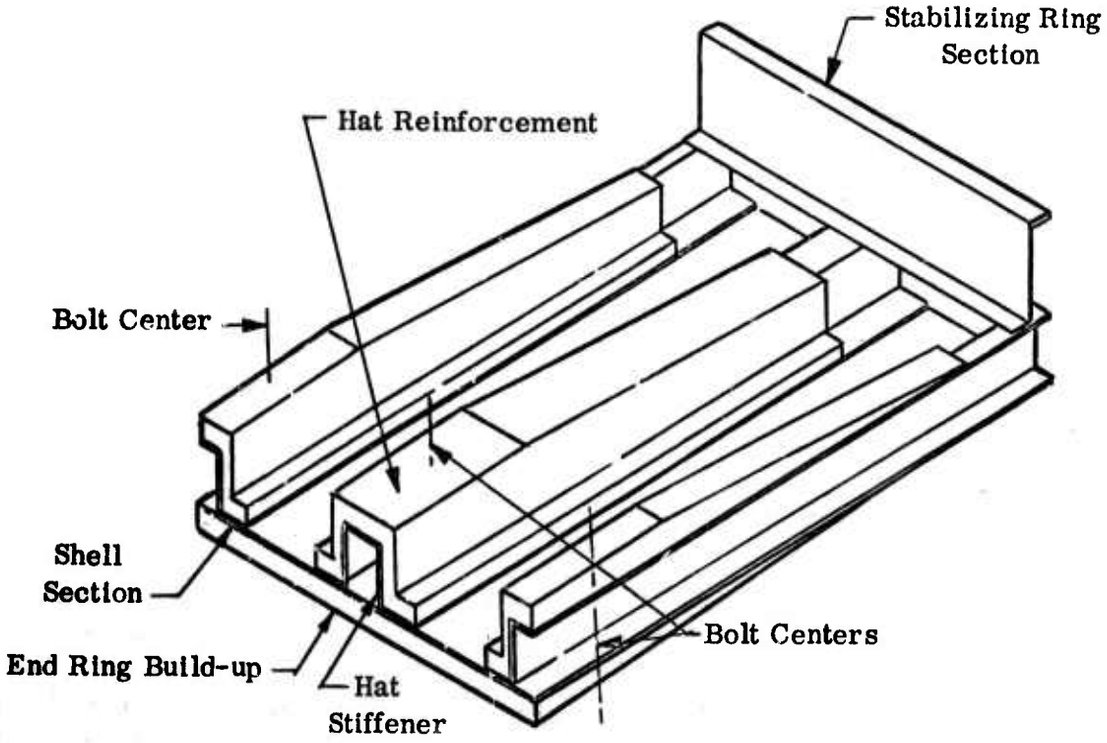

Figure 295. Fuselage Component Secondary Analysis Model

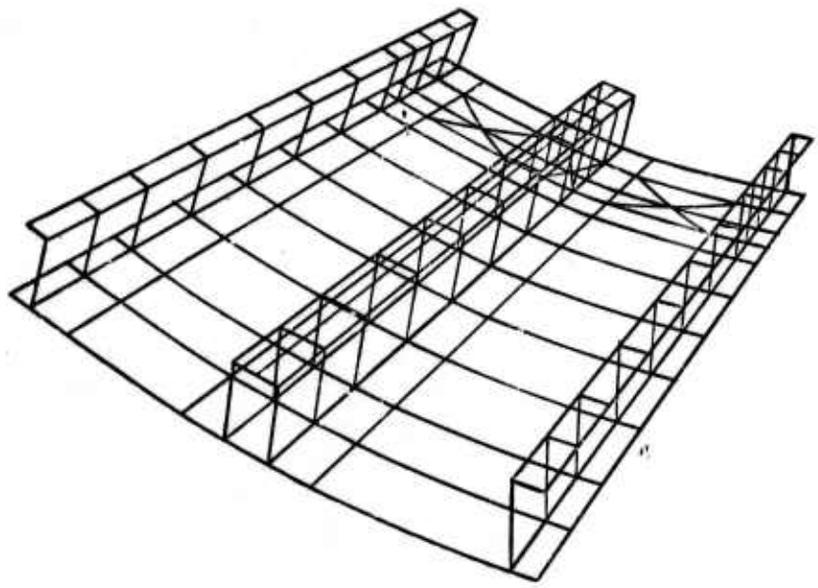

Figure 296. Idealization for Secondary Analysis of Composite Cylinder

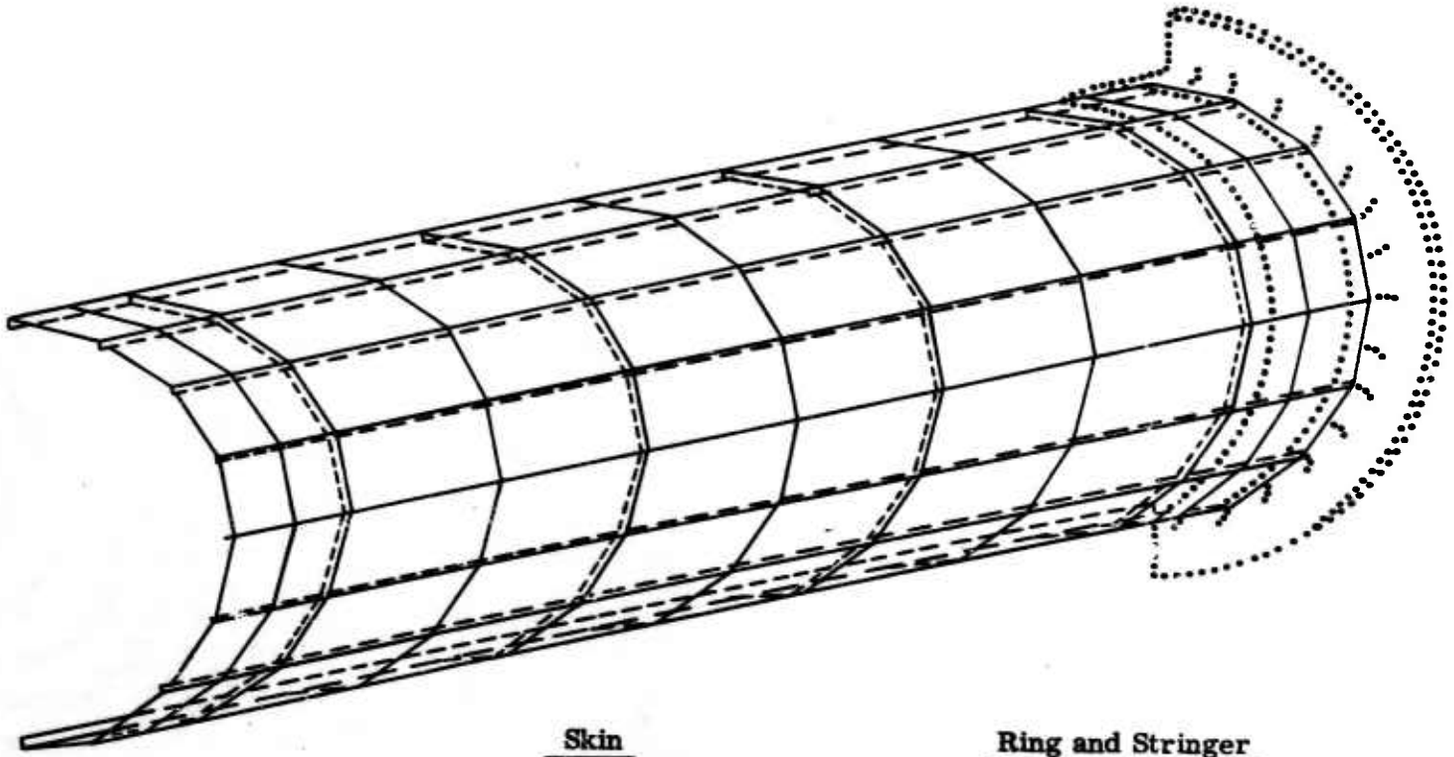

Skin	Ring and Stringer
$E = 10.78 \times 10^6$ psi	$E = 20.28 \times 10^6$ psi
$\nu = 0.034$	$\nu = 0.31$
$G = 0.5 \times 10^6$ psi	$G = 0.5 \times 10^6$ psi

Figure 297. Fuselage Component Discrete Element Idealization

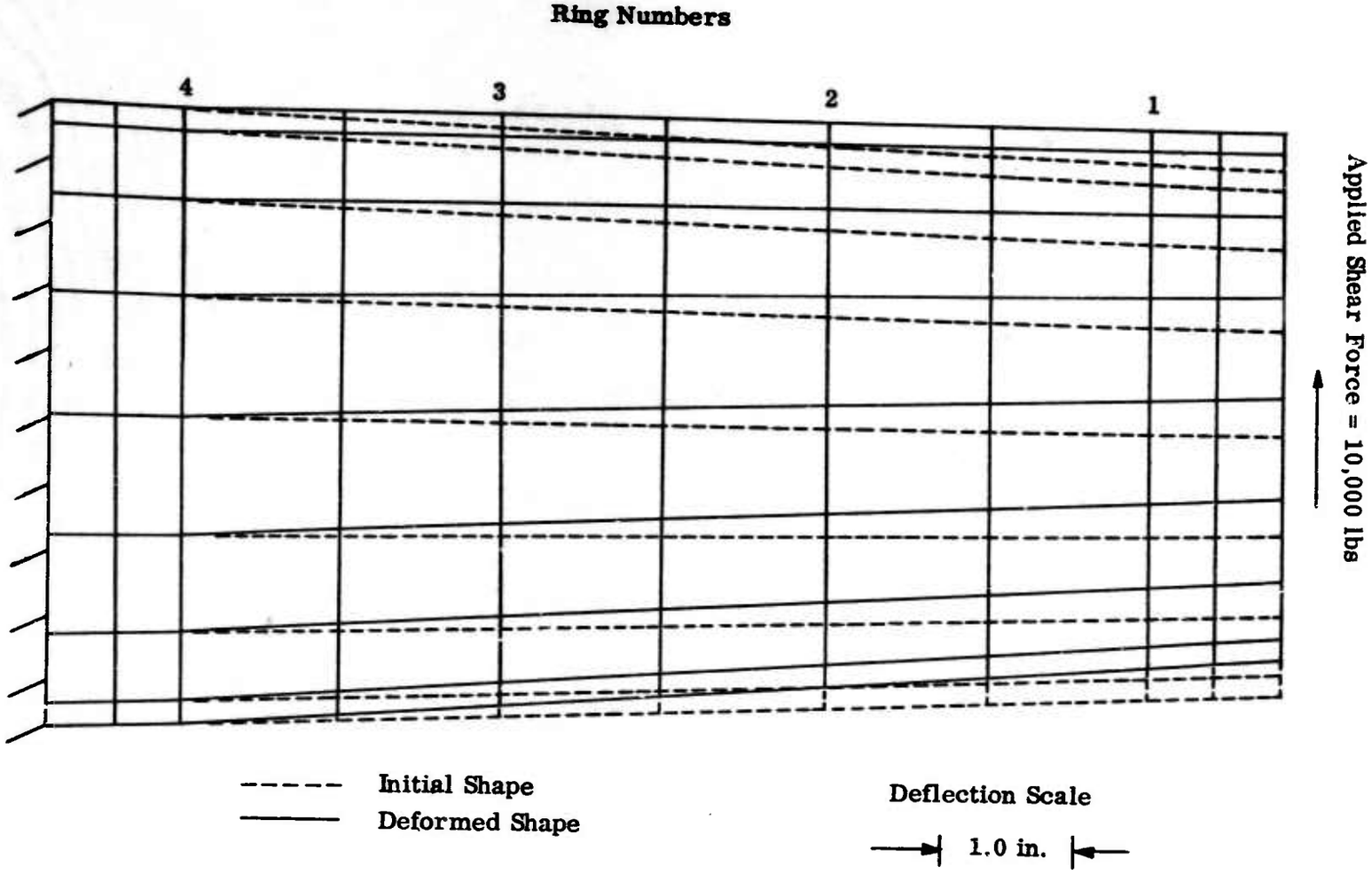

Figure 298. Fuselage Component Displacement Profiles (in.)

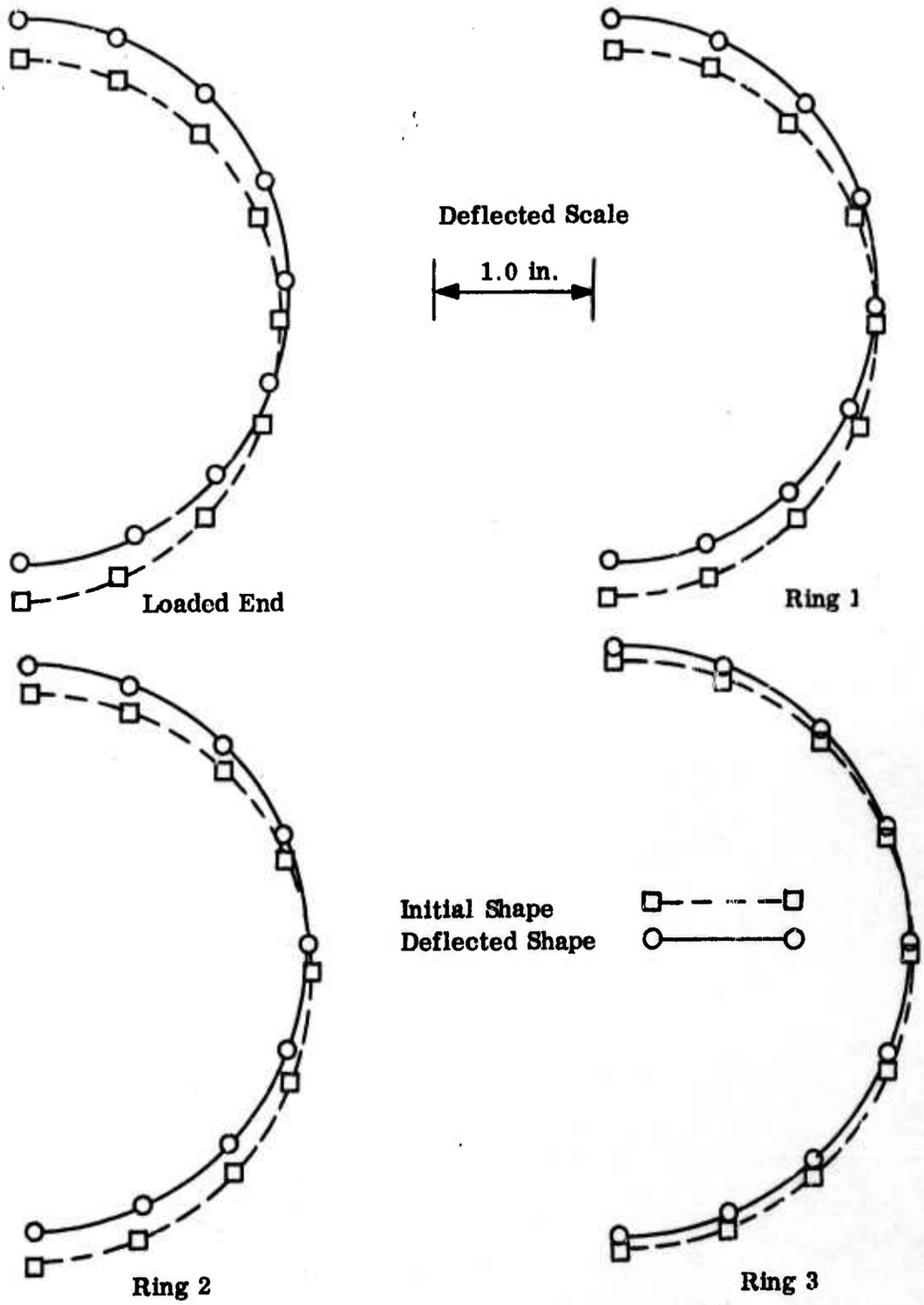

Figure 299. Fuselage Component Deformed Cross-Section (In.)

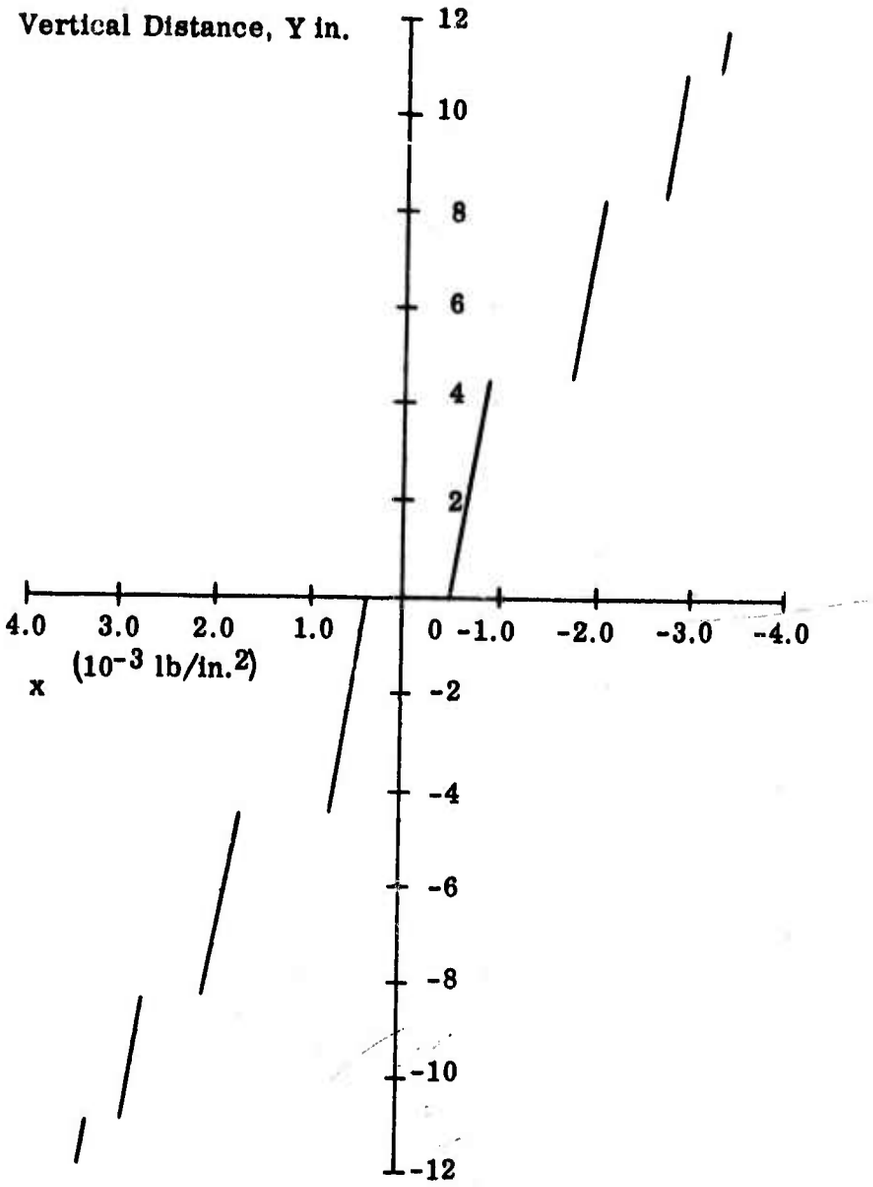

Ring 4

Figure 300. Fuselage Component Stress Profile at Fixed End (psi)

REFERENCES

1. Technical Report AFML-TR-66-310, Part I, Air Force Materials Laboratory, Wright-Patterson Air Force Base, Ohio, October 1966.

2. A. Naidai, Theory of Flow and Fracture of Solids, Vol. I, (McGraw-Hill Book Company, New York, 1950), pp. 353-359.

3. W. J. Parker, R. J. Jenkins, C. P. Butler, and G. L. Abbott, "Flash Method of Determining Thermal Diffusivity, Heat Capacity, and Thermal Conductivity," J. Appl. Phys. 32, 1979-1684 (1961).

4. Union Carbide Corporation, National Carbon Company, Research and Development on Advanced Graphite Materials - Survey and Analytical Representation of the Measurements of the Specific Heat of Graphite, by G. B. Spence, WADD TR 61-72, Vol. XLI, (November 1963), (AF33(616)-6915).

5. Battelle Memorial Institute (Columbus), Refractory Ceramics of Interest in Aerospace Structural Applications--A Materials Selection Handbook, by J. R. Hague, J. F. Lynch, A. Rudnick, F. C. Holden, and W. H. Duckworth, RTD-TDR-63-4102 (1963), p. 55, (AF33(657)-8326).

6. A. Goldsmith, T. E. Waterman, and H. J. Hirschhorn, Handbook of Thermophysical Properties of Solid Materials, Vol. III: Ceramics, (MacMillan Company, New York, 1961), p. 925.

7. See Reference 2, pp. 347-352.

8. H. W. Swift, "Length Changes in Metals Under Torsional Overstrain," Engineering, 163, 253-257 (1947).

9. R. Hill, The Mathematical Theory of Plasticity, (Oxford University Press, London, 1950) pp. 325-328.

10. R. C. Grassi and I. Cornet, "Fracture of Gray-Cast-Iron Tubes Under Biaxial Stresses," J. of Appl. Mech. 16, Trans. ASME 71, 178-182 (1949).

11. I. Cornet and R. C. Grassi, "Fracture of Inoculated Iron Under Biaxial Stress," J. of Appl. Mech. 22, Trans. ASME 77, 172-174 (1955).

12. L. F. Coffin, "The Flow and Fracture of a Brittle Material," J. of Appl. Mech. 17, Trans. ASME 72, 233-248 (1950).

13. F. M. Anthony, A. L. Mistretta, J. Y. L. Ho, L. Marcus, Selection Techniques for Brittle Materials (The Evaluation of JTA Graphite Composite as a Structural Refractory Ceramic Body), AFML-TR-67-78, May 1967.

REFERENCES (Cont'd.)

14. V. Genberg, "Optimization of Particulate Composites for Layered Orthotropic Thick Cylinders." M. S. Thesis, Case Institute of Technology, Cleveland, Ohio, June 1967.

15. P. V. Marcal and I. P. King, "Elastic-plastic Analysis of Two Dimensional Stress Systems by the Finite Element Method" International J. of Mech. Sci. 9, 143-155 (1967).

16. R. Hill, Mathematical Theory of Plasticity, (Clarendon Press, 1950).

17. V. D. Azzi and S. W. Tsai, "Anisotropic Strength of Composites," Exptl. Mech. 5, 283 (September 1965) or Proc. Soc. Exptl. Stress Anal. 22, 283 No. 2, 1965).

18. Plastics for Flight Vehicles, Armed Forces Supply Support Center, MIL-HDBK-17, Part 1, (November 5, 1959).

19. V. Zentner, A. Brenner and C. W. Jennings, Physical Properties of Electrodeposited Metals. I. Nickel, A. E. S. Research Report, Serial No. 20, American Electroplaters Society. 445 Broad Street, Newark, New Jersey.

20. D. Cratchley and A. A. Baker, Metallurgia 69, 153 (1964).

21. International Nickel Company, Inc., Engineering Properties of Nickel, Technical Bulletin T-15, (New York, New York, October, 1957).

22. P. R. Gage and T. M. Place, Aeronutronics Division, Philco Corporation, Data Presented at Second Metal Matrix Composites Working Group Meeting, Wright-Patterson Air Force Base, Ohio, June 14-15, 1966.

23. H. Hahn, A. P. Direcho, P. Lane, and B. Dennison, Research on Reinforced Metal Composites, Melpar, Job No. 5192 under Contract No. W 65-0387-f, Final Report, April 30, 1966, (Melpar, Inc.).

24. J. B. Nelson and D. P. Riley, "The Thermal Expansion of Graphite from 15°C to 800°C: Part I. Experimental," Proc. Phys. Soc. 57, 4770486 (1945).

25. Plastics Properties Chart Part II: Thermosets, Supplement to Modern Plastics Encyclopedia Issue, (Sept. 1962), Plastics Catalogue Corporation, New York.

26. Data obtained from Union Carbide Corporation, Plastics Division.

27. A. H. Lasday and C. P. Talley, "Boron Filament for Structural Composites," in Advanced Fibrous Reinforced Composites, SAMPE, Vol. 10 (Western Periodicals Company, North Hollywood, California, November 1966) pp. D-1 to 12.

28. T. J. Humphrey, "New Glass Fibers," 21st Annual Technical Conference, SPI Reinforced Plastics Division, Chicago, Illinois (February 1966) Section 8-B, pp. 1-8.

29. University of Dayton, "Determining Fiber Content of Graphite Yarn - Epoxy Resin Composites," by R. Kuhbander, V. D. Tech. Memo. No. UDRI-TM-66-103 (January, 1966), Contract No. AF 33(657)-10688.

30. S. P. Timoshenko, "Transverse Vibrations of Prismatic Bars," Phil. Mag. 41, 744 (1921).

31. R. Simon, S. P. Prosen, and J. Duffy, "Carbon Fiber Composites," Nature 213, 1113 (1967).

32. J. P. Ellington, "On Obtaining the Shear Stress-Strain Relationship from a Hollow Specimen in Torsion," J. of Roy. Aeron. Soc. 60, 806-808 (December 1956).

33. J. D. Thornburgh and C. D. Pears, "Prediction of the Thermal Conductivity of -illed and Reinforced Plastics," ASME Paper 65-WA/HT-4 presented at the ASME Winter Annual Meeting, Chicago, Illinois (November 1965).

34. G. S. Springer and S. W. Tsai, "Thermal Conductivities of Unidirectional Materials," S. Composite Mater. 1, 166-173 (1967).

35. L. B. Greszczuk, "Thermoelastic Considerations for Filamentary Structures," Proc. 20th Tech. Conf. SPI Reinforced Plastics Div., Section 5-C, Chicago, Illinois (February 1965).

36. R. Lansard, "Fillets without Stress Concentrations," Proc. of S. E. S. A., V. XIII, N. 1, p. 97 (1955).

37. Whitney, J. M. et al., "Experimental Methods for Determining Shear Modulus of Fiber Reinforced Composite Materials," Technical Report AFML-TR-65-42, Sept. 1965.

38. Tsai, S. W., "Experimental Determination of the Elastic Behavior of Orthotropic Plates," ASME Journal of Eng. for Ind., Vol. 83, Series B, August 1965, pp. 315-318.

39. Foye, R. L., "Deflection Limits of the Plate Twisting Test," Journal of Composite Materials, Vol. 1, No. 2, April 1967, pp. 194-198.

40. M. M. Frocht, Strength of Materials, (The Ronald Press Company, New York, 1951), pp. 370-373.

41. N. F. Dow, "Applications and Optimizations of Structural Composites for Aircraft Wings," presented at the 23rd Meeting of the Structures and Materials Panel, AGARD, NATO, Paris, France (October 1966).

42. R. F. S. Hearmon, Introduction to Applied Anisotropic Elasticity, (Oxford University Press, Oxford, England, 1961).

43. Chao, T. L., "A Study of Elastic Properties of Filamentary Composites, Part I - Two Dimensional Mechanical Properties," Report No. 3, Solid Mechanics, Structures and Mechanical Design Group, Case Institute of Technology, 1967.

44. Whitney, J. M., "Elastic Moduli of Composite Materials Reinforced with Orthotropic Filaments," Technical Report AFML-TR-65-411, January, 1966.

45. Greszczuk, L. B., "Elastic Constants and Analysis Methods for Filament [illegible]nd Shell Structures," Douglas Aircraft Company, Report SM45849, January, 1964.

46. Army-Navy-Civil Committee on Aircraft Design Criteria, Design of Wood Aircraft Structures, bull. ANC-18 (U. S. Gov. Printing Office, Washington, D. C., 1944).

47. U. S. Department of Defense, Plastics for Flight Vehicles, Military Handbook MIL-HDBK-17 (U. S. Gov. Printing Office, Washington, D. C., 1959).

48. L. Fisher, "How to Predict Structural Behavior of RP Laminates," Modern Plastics 37 120ff (June, 1960).

49. A. G. H. Dietz, Engineering Laminates, (John Wiley and Sons, Inc., 1949).

50. M. E. Waddoups, Advanced Composite Material Mechanics for the Designer and Stress Analyst, General Dynamics, Fort Worth Division, Report No. FZM-4763, (January 19, 1967).

51. S. W. Tsai, "Strength Characteristics of Composite Materials," National Aeronautics and Space Administration Contractor Report CR-224 (April, 1965).

52. F. K. Bagner, R. L. Fox, and L. A. Schmit, Jr., "The Generation of Inter-Element-Compatible Stiffness and Mass Matrices by the Use of Interpolation Formulas." Matrix Methods in Structural Mechanics, Proceedings of the Conference held at Wright-Patterson Air Force Base, Ohio, pp. 26-28, October, 1965.

53. S. W. Tsai, Adams, D. F., Doner, D. R., "Analysis of Composite Structures," NASA CR-620.

54. H. Schuerch, A Contribution to the Micromechanics of Composite Materials and Failure Mechanisms Induced by Inclusions. NASA CR-482, Sept. 1966.

55. A. Mendelson, and S. S. Manson, Practical Solution of Plastic Deformation Problems in Elastic-Plastic Range NASA TR R-28, 1959.

56. E. Roberts and A. Mendelson, Analysis of Plastic Thermal Stresses and Strains in Thin Finite Plate of Strainhardening Material, NASA TND-2206, 1964.

57. E. A. Davis, Extension of Iterative Method for Determining Strain Distributions Due to Uniformly Stressed Plate with a Hole. J. Appl. Mech., Vol. 30, 1963, pp. 210-214.

58. Discussion on above paper, Ibid, June, 1964, pp. 362-364, by A. Mendelson and S. S. Manson.

59. I. S. Tuba, Elastic-Plastic Stress and Strain Concentration Factors at a Circular Hole in Uniformly Stressed Infinite Plate, J. Appl. Mech., Sept., 1965, p. 710-712.

60. I. S. Tuba, Elastic-Plastic Analysis of a Flat Plate with a Circular Rigid Inclusion, Appl. Sci. Res., Vol. 16, pp. 241-255.

61. S. P. Timoshenko, "Strength of Materials," Part I - Elementary Theory and Problems, D. Van Nostrand Co., Inc., Princeton, New Jersey, Third Edition, September, 1958, pp. 219-221.

62. R. McChesney, Unpublished Notes.

63. H. G. Franklin, "Bonding Stresses in a Laminated Orthotropic Shell, Part I - Membrane Analysis, "Division of Solid Mechanics, Structures and Mechanical Design, Case Western Reserve University, Report No. 1.

64. H. G. Franklin, "Bonding Stresses in a Laminated Orthotropic Shell, Part II - Thick Shell Analysis, " Division of Solid Mechanics, Structures and Mechanical Design, Case Western Reserve University, Report No. 2.

65. F. B. Hildebrand, E. Reissner, and G. B. Thomas, "Notes on the Foundations of the Theory of Small Displacements of Orthotropic Shells," Massachusetts Institute of Technology, NACA Technical Note No. 1833, March, 1949.

66. H. G. Franklin, "Bonding Stresses in a Laminated Orthotropic Shell, Part IV - Thick Shell Analysis with Arbitrary Parameters," report in preparation.

67. H. G. Franklin, "Bonding Stresses in a Laminated Orthotropic Shell, Part V - Equations for an n-Layered Shell," report in preparation.

68. S. Timoshenko and J. N. Goodier, Theory of Elasticity, 2nd ed. (McGraw-Hill Book Company, New York, 1951).

69. H. D. Conway, "Stress Distribution in Orthotropic Strips," J. of Appl. Mech. 22, No. 3 (1955).

70. S. Timoshenko and Woinowsky-Kreiges, Theory of Plates and Shells, (McGraw-Hill Book Company, New York, 1959).

71. R. H. Gallagher, J. Padlog, and R. D. Huff, Thermal Stress Determination Techniques for Supersonic Transport Aircraft Structures, Part III - Computer Programs for Beam, Plate and Cylindrical Shell Analysis, ASD-TDR63-783, (July 1963).

72. P. Kuhn, J. E. Duberg, and G. E. Griffith, The Effect of Concentrated Loads on Flexible Rings in Circular Shells, NACA ARR No. L5H23, (December 1945).

73. P. V. Marcal, A Comparative Study of Numerical Methods of Elastic-Plastic Analysis, AIAA/ASME Structures, Structural Dynamics, and Materials Conference, Palm Springs, California, March 29-31, 1967.

74. A. Mendelson, Solutions of Some Plane Thermal and Crack Problems for Strain Hardening Materials,Ph.D. Thesis, Case Institute of Technology (1965).

75. G. Zoutendijk, "Nonlinear Programming: A Numerical Survey," J. SIAM Control 4, No. 1, 194-210 (1966).

76. C. C. Chamis, Structural Synthesis of Multilayer Fiber Composite Panesl, Ph.D. Thesis, Case Institute of Technology, in preparation.

77. L. A. Schmit, The Structural Synthesis Concept and its Potential Role in Design with Composites, presented at the International Conference on the Mechanics of Composite Materials, May 9, 1967, Philadelphia, Pennsylvania.

78. R. F. Crawford and A. B. Burns, Strength, Efficiency, and Design Data for Beryllium Structures, ASD TR-61-692 (February 1962).

79. W. R. Micks, "A Method of Estimating the Compressive Strength of Optimum Sheet-Stiffener Panels for Arbitrary Material Properties, Skin Thickness, and Stiffener Shapes," J. Aeron. Sci. 16, 705-715 (1948).

80. I. Rattinger and R. H. Gallagher, Investigation and Design Study for Fuel Storage in High Performance Aircraft, (U) Part II Appendices, WADC TR 59-18, (May 1959).

81. E. F. Bruhn, Analysis and Design of Flight Vehicle Structures, Tri- State Offset Co. (January 1965).

82. N. F. Dow and B. Rosen, Evaluations of Filament-Reinforced Composites for Aerospace Applications, NASA CR-207 (April 1965).

83. D. H. Emero and L. Spunt, "Optimization of Multirib and Multiweb Wing Box Structures under Shear and Moment Loads," AIAA Sixth Structures and Materials Conference, (April 5-7, 1965), p. 330.

84. W. D. Kroll, G. P. Fisher, and G. J. Heimerl, Charts for Calculation of the Critical Stress for Local Instability of Columns with I, Zee, Channel, and Rectangular Tube Sections, NACA ARR 3K04, (November 1943).

85. D. L. Block, Buckling of Eccentrically Stiffened Orthotropic Cylinders under Pure Bending, NASA TN D-3351 (March 1966).

86. A. Krivetsky, "Buckling of Orthortopic Plates (Corrugated Plate Applications), Bell Aerosystems Co., Report No. 7-60-961001, July 3, 1961.

87. K. H. Sayers and W. N. Meholick, Computer Program Description - Buckling of Eccentrically Stiffened Orthotropic Cylinders under Pure Bending, Bell Aerosystems Co. Report No. 8506-941001.

88. S. Timoshenko, Theory of Elastic Stability, First Edition (McGraw-Hill Book Co., 1936), p. 107.

89. J. P. Peterson and J. K. Anderson, Bending Tests of Large Diameter Ring - Stiffened Corrugated Cylinders NASA-D-3336, (March 1966).

90. D. L. Block, Influence of Ring Stiffeners on Instability or Orthotropic Cylinders in Axial Compression, NASA TN-D-2482, (October 1964).

91. F. R. Shanley, Weight-Strength Analysis of Aircraft Structures, (McGraw-Hill Book Co., 1952) pp. 65-71.

UNCLASSIFIED
Security Classification

DOCUMENT CONTROL DATA · R&D
(Security classification of title, body of abstract and indexing annotation must be entered when the overall report is classified)

1. ORIGINATING ACTIVITY (Corporate author)
Union Carbide Corporation, Case Western Reserve University, and Bell Aerosystems Company

2a. REPORT SECURITY CLASSIFICATION
UNCLASSIFIED

2b. GROUP

3. REPORT TITLE
INTEGRATED RESEARCH ON CARBON COMPOSITE MATERIALS

4. DESCRIPTIVE NOTES (Type of report and inclusive dates)
Summary Technical Report June 1966 to June 1967

5. AUTHOR(S) (Last name, first name, initial)
Union Carbide Corporation, Carbon Products Division, in Association with Case Western Reserve University and Bell Aerosystems Company, a Textron Company

6. REPORT DATE	7a. TOTAL NO. OF PAGES	7b. NO. OF REFS
December 1967	437	91

8a. CONTRACT OR GRANT NO.
AF 33(615)-3110

b. PROJECT NO.
ARPA Order No. 719

c.
Program Code No. 5950

d.

9a. ORIGINATOR'S REPORT NUMBER(S)

9b. OTHER REPORT NO(S) (Any other numbers that may be assigned this report)
AFML-TR-66-310, Part II

10. AVAILABILITY/LIMITATION NOTICES
Each transmittal of this document outside the agencies of the U. S. Government must have prior approval of the Air Force Materials Laboratory, MAP, Wright-Patterson Air Force Base, Ohio 45433

11. SUPPLEMENTARY NOTES

12. SPONSORING MILITARY ACTIVITY
Air Force Materials Laboratory
Research and Technology Division
Wright-Patterson AFB, Ohio

13. ABSTRACT Results are reported on a continuing program directed toward developing a fabrication and structural design capability for graphite-fiber composites and toward extending the methods of structural synthesis to include material variables. Part of the current work is centered on the first phase of the design and fabrication of a ring- and stringer-stiffened tapered shell, representative of a subscale fuselage section. Other longer-range projects include work on analytical and experimental methods for obtaining reliable design data, on nonlinear analysis, and on synthesis studies. Studies on graphite-base refractory composites, begun before fiber composites were available, have been concluded; these include work on multiaxial stress failure criteria, statistical strength distributions for anisotropic materials, structural synthesis problems involving the selection of the best material, and nonlinear-analysis of a rocket throat insert. Work on graphite-fiber, metal-matrix composites has been on processing studies and high temperature strength measurements of nickel-matrix composites. Graphite-fiber, resin-matrix composites have been fabricated with an epoxy (ERL 2256) matrix. The physical properties of the constituents have been determined; plates fabricated; and measurements made for membrane and bending stiffnesses, strengths, stress-strain behaviors, and thermal properties. Theoretical predictions of membrane and bending stiffnesses and tensile strengths correlated sufficiently well with experimental results for preliminary design purposes. Several common mechanical testing procedures for composite materials have been assessed; and a nondestructive plate buckling test apparatus and a new NOL ring test device have been (cont'd)

DD FORM 1 JAN 64 1473

UNCLASSIFIED
Security Classification

13. ABSTRACT - (cont'd)
built and applied. Structural element tests include angle bend and crippling tests on composite stringers as well as crippling and acoustic fatigue tests on composite panels. Several micromechanics and design data prediction investigations are reported. An elasto-plastic analysis of a cylindrical inclusion and a study of bonding stresses in laminated cylindrical shells have been completed. Projects in progress include microstress analysis and studies of photoelasticity and failure mechanisms. Several structural analysis and syntheses investigations aimed at developing the tools necessary to achieve superior structural designs with composite materials are reported. Several anisotropic discrete element formulations have been generated and numerically verified. New procedures are being developed for multiaxial stress analysis involving nonlinear and nonisotropic materials. Computer program packages have been created for unconstrained and inequality-constrained minimization techniques. The extension of structural synthesis to fiber composites is illustrated with a plate problem which treats material variables within the optimization process. Design activities associated with the tapered, stiffened cylinder began with weight efficiency comparisons of many candidate constructions and composite lay-up patterns. Parametric studies of the influence of fiber content and ply thickness on plate and column behavior are reported. Discrete element analyses are being made of stiffened panel element test configurations and of the behavior of the stiffened shell and end attachment.

14. KEY WORDS	LINK A		LINK B		LINK C	
	ROLE	WT	ROLE	WT	ROLE	WT
Carbon Graphite Fibers Graphite Fibers Composites Plastic Matrix Metal Matrix Properties Analysis Synthesis Mechanical Properties						

INSTRUCTIONS

1. ORIGINATING ACTIVITY: Enter the name and address of the contractor, subcontractor, grantee, Department of Defense activity or other organization *(corporate author)* issuing the report.

2a. REPORT SECURITY CLASSIFICATION: Enter the overall security classification of the report. Indicate whether "Restricted Data" is included. Marking is to be in accordance with appropriate security regulations.

2b. GROUP: Automatic downgrading is specified in DoD Directive 5200.10 and Armed Forces Industrial Manual. Enter the group number. Also, when applicable, show that optional markings have been used for Group 3 and Group 4 as authorized.

3. REPORT TITLE: Enter the complete report title in all capital letters. Titles in all cases should be unclassified. If a meaningful title cannot be selected without classification, show title classification in all capitals in parenthesis immediately following the title.

4. DESCRIPTIVE NOTES: If appropriate, enter the type of report, e.g., interim, progress, summary, annual, or final. Give the inclusive dates when a specific reporting period is covered.

5. AUTHOR(S): Enter the name(s) of author(s) as shown on or in the report. Enter last name, first name, middle initial. If military, show rank and branch of service. The name of the principal author is an absolute minimum requirement.

6. REPORT DATE: Enter the date of the report as day, month, year; or month, year. If more than one date appears on the report, use date of publication.

7a. TOTAL NUMBER OF PAGES: The total page count should follow normal pagination procedures, i.e., enter the number of pages containing information.

7b. NUMBER OF REFERENCES: Enter the total number of references cited in the report.

8a. CONTRACT OR GRANT NUMBER: If appropriate, enter the applicable number of the contract or grant under which the report was written.

8b, 8c, & 8d. PROJECT NUMBER: Enter the appropriate military department identification, such as project number, subproject number, system numbers, task number, etc.

9a. ORIGINATOR'S REPORT NUMBER(S): Enter the official report number by which the document will be identified and controlled by the originating activity. This number must be unique to this report.

9b. OTHER REPORT NUMBER(S): If the report has been assigned any other report numbers *(either by the originator or by the sponsor)*, also enter this number(s).

10. AVAILABILITY/LIMITATION NOTICES: Enter any limitations on further dissemination of the report, other than those imposed by security classification, using standard statements such as:

(1) "Qualified requesters may obtain copies of this report from DDC."

(2) "Foreign announcement and dissemination of this report by DDC is not authorized."

(3) "U. S. Government agencies may obtain copies of this report directly from DDC. Other qualified DDC users shall request through

_____."

(4) "U. S. military agencies may obtain copies of this report directly from DDC. Other qualified users shall request through

_____."

(5) "All distribution of this report is controlled. Qualified DDC users shall request through

_____."

If the report has been furnished to the Office of Technical Services, Department of Commerce, for sale to the public, indicate this fact and enter the price, if known.

11. SUPPLEMENTARY NOTES: Use for additional explanatory notes.

12. SPONSORING MILITARY ACTIVITY: Enter the name of the departmental project office or laboratory sponsoring *(paying for)* the research and development. Include address.

13. ABSTRACT: Enter an abstract giving a brief and factual summary of the document indicative of the report, even though it may also appear elsewhere in the body of the technical report. If additional space is required, a continuation sheet shall be attached.

It is highly desirable that the abstract of classified reports be unclassified. Each paragraph of the abstract shall end with an indication of the military security classification of the information in the paragraph, represented as *(TS), (S), (C), or (U)*.

There is no limitation on the length of the abstract. However, the suggested length is from 150 to 225 words.

14. KEY WORDS: Key words are technically meaningful terms or short phrases that characterize a report and may be used as index entries for cataloging the report. Key words must be selected so that no security classification is required. Identifiers, such as equipment model designation, trade name, military project code name, geographic location, may be used as key words but will be followed by an indication of technical context. The assignment of links, rules, and weights is optional.